Exploring Potential of Silk 3D Matrices for Bioartificial Liver and Regenerative Applications

A Thesis

Submitted in Partial Fulfillment of the Requirements for the Degree of

DOCTOR OF PHILOSOPHY

by

JANANI G

Department of Biosciences and Bioengineering
Indian Institute of Technology Guwahati
Guwahati-781039, Assam, India

July 2022

Dedicated to my beloved parents

To my life companion, Boopathy

To my tiny tingling baby in the womb

INDIAN INSTITUTE OF TECHNOLOGY GUWAHATI

DEPARTMENT OF BIOSCIENCES AND BIOENGINEERING

STATEMENT

I do hereby declare that the research findings of this thesis is the result of research work carried out by me in the Department of Biosciences and Bioengineering, Indian Institute of Technology Guwahati, Guwahati, India, under the supervision of **Prof. Biman B. Mandal**.

As per the general norms of reporting research findings, due acknowledgments have been made, wherever the research findings of other researchers have been cited in this thesis.

Date: 27/07/2022

Janani G

INDIAN INSTITUTE OF TECHNOLOGY GUWAHATI

DEPARTMENT OF BIOSCIENCES AND BIOENGINEERING

CERTIFICATE

It is certified that the work described in this thesis entitled ***"Exploring Potential of Silk 3D Matrices for Bioartificial Liver and Regenerative Applications"*** by ***Ms. Janani G*** for the award of degree of Doctor of Philosophy is an authentic record of the results obtained from the research work carried out under my supervision in the Department of Biosciences and Bioengineering, Indian Institute of Technology Guwahati, India, and this work has not been submitted elsewhere for the award of any other degree.

Janani G
(Candidate)
Roll No: 166106010

CERTIFIED

Biman B. Mandal, Ph.D.
(Thesis Supervisor)

Date: 27.07.2022

ACKNOWLEDGEMENT

I take this opportunity to thank and record my deepest acknowledgments to everyone who has generously extended their support throughout my Ph.D. journey.

Foremost, I would like to express my sincere gratitude and warmest thanks to my supervisor and mentor, Prof. Biman B. Mandal for providing me with the opportunity to work on this project and be a part of his dynamic research group. His continuous support, guidance, invaluable advice, and patience have encouraged and motivated me in this project. I am deeply indebted to him for his scientific discussions, insightful suggestions, and plentiful experience over the years that have shaped this project and sculpted me as an independent researcher. From the bottom of my heart, I am grateful to him for having confidence in me and making this journey an inspiring and wonderful experience, both personally and professionally.

I would like to extend my sincere thanks to my Doctoral committee members, Prof. Bithiah G. Jaganathan, Dr. Rajkumar P. Thummer from the Department of Biosciences and Bioengineering, IITG; and Dr. Uttam Manna from the Department of Chemistry, IITG for their advice, scientific inputs, and critiquing queries from defining objectives till this project completion.

I would also like to thank the present and former Heads of the Department of Biosciences and Bioengineering, IITG; Prof. Rakhi Chaturvedi, Prof. Latha Rangan, Prof. Kannan Pakshirajan, and Prof. V. Venkata Dasu for extending their support through various academic and research activities.

I am extremely grateful to my Fulbright mentor, Prof. Stephen F. Badylak, McGowan Institute for Regenerative Medicine, University of Pittsburgh, USA, for hosting me as a Fulbright Nehru Doctoral Research fellow in his laboratory and whose insights and knowledge into the project steered me through my research activities. Special thanks to Li Zhang, McGowan Institute for Regenerative Medicine, University of Pittsburgh, USA, for her guidance, scientific discussions, and for making my stay more impactful and truly memorable. The support and scientific inputs of Dr. Andrew W. Duncan, Scott A. Johnson, Dr. Nairita Roy, and Dr. Bharat Bhushan have significantly benefitted this thesis work. Thank you for scientifically nurturing me and providing an enriching learning experience during my short stay. I would also like to thank Dr. Ahmed

Bendari, Jordan Chang, Dr. Neil Turner, Dr. William D'Angelo, Dr. Anjani Ravindra, Dr. Maddie Cramer, Salma El-Mossier, Dr. Catalina P. Molina, Dr. Lina Q. Luque, Dr. Evan R. Delgado, Lori Walton, and Julia Hart from the University of Pittsburgh, USA, for extending their support for experimental work.

I record my heartfelt gratitude to thank all the collaborators, Prof. Samit K. Nandi, West Bengal University of Animal and Fishery Sciences, Kolkata, India; Dr. Pawan K. Samudrala, National Institute of Pharmaceutical Education and Research (NIPER), Guwahati; and Dr. VGM Naidu, NIPER, Guwahati for their help in animal experiments.

My special thanks to Dr. Nandana Bhardwaj, Sr. scientist, STANVAC for her generous support, scientific opinions, motivation, caring, and appreciation throughout my tenure.

I would like to offer my special thanks to the infrastructural support provided by Central Instruments Facility (CIF), IITG; Centre for Nanotechnology, IITG; Centre for Excellence in Nanoelectronics & Theranostic Devices, IITG; Departmental CIF (DCIF), Department of Biosciences and Bioengineering, IITG through various administrative staff, technical scientific personal, and student operators for the high-end instrumentation support used for various experiments in this thesis.

I want to thank all the funding agencies for providing financial assistance during my Ph.D. tenure. I acknowledge the Ministry of Education (MoE), formerly the Ministry of Human Resource Development (MHRD), Government of India for my Ph.D. fellowship. Thank you so much, Institute of International Education (IIE), New York, and the United States-India Educational Foundation (USIEF) for awarding me the Fulbright-Nehru Doctoral Research Fellowship to pursue research in a USA laboratory.

I had the pleasure of working with extraordinary young minds in our Biomaterials and Tissue Engineering Laboratory, IITG, who never failed to motivate me during tough times and provide a home away from home environment. I appreciate the scientific inputs from Dr. Manishekhar Kumar, Dr. Jadi Praveen Kumar, Dr. Bibhas Kumar Bhunia, Dr. Dimple Chouhan, Dr. Prerak Gupta, Dr. Ankit Gangrade, Dr. Yogendra Pratap Singh, Dr. Shreya Mehrotra, Dr. Rocktotpal Konwarh, Dr. Deepika Arora, and Mr. Joseph Christakiran Moses around the clock. I am so grateful and privileged to work with all of them. I cherished working with Mr. Ashutosh Bandyopadyay, Ms. Bibrita Bhar, Ms. Chitra Jaiswal, Mr. Souradeep Dey, Ms. Shivanshi Kumar, Ms. Tarishi Gupta, Ms. Monisha V, Ms. Smriti Priya, Ms. Ayushi Mukherjee, Mr. Saptarshi

Biswas and Mr. Apoorv Bajpai, and many thanks to them. I am also thankful to current and former lab members: Dr. Ashang Luwang Laiva, Dr. Biswajit Chakraborty, Dr. Aparjita Ghosh, Dr. Rajiv Bora, Dr. Bhaskar Bhirru, Dr. Chandramouli Ghosh, Dr. I Puttu Mahindra, Dr. Priyanka Shaw, Ms. Mimi Adhikary, Mr. Prateek Hemani, Mr. Sai Chand, Mr. Sadanand Kumar, Mr. Bhat Waseem, Ms. Sakshi Gupta, Ms. Princy Aggarwal, Ms. Vaishali Soni, Ms. Swapnil Tyagi, Mr. Omkar Majumder, Ms. Sohenii Bhattacharjee, Mr. Sonu Rudra, Ms. Prerna Pant, Ms. Triya Saha, Mr. Namit Dey, Mr. Suvro Kanti Chowdhury, Mr. Nikhil Gnanavel, Mr. Rishabh Deo Singh, Ms. Sangeetha Pillai, Mr. Nakhul Pai, Mr. Anupam Mishra, Ms. Priyanka Korgaonkar, Mr. Shubham Choudhari, Ms. Sayanti Shome, Ms, Ananya Das, Ms. Amritha Bhat, Mr. Rupam Khatua, Ms. Rachita Pattanaik, Ms. Dimpal Das, Mr. Rajat Dadheech, Mr. Kodieswaran M., Ms. Baishali Ghibhela, Ms. Eshani Das, Ms. Shruti Agnihotri, Mr. Animesh Mishra, and Ms. Shruti More. I am blissful for their great company and scientific discussions and will always cherish their memories.

I would like to offer my special thanks to all members of the SFB lab, Dr. George Hussey, Dr. Joseph Bartolacci, Dr. Lindsey Saldin, Dr. Jonas Eriksson, Yoojin C Lee, Rachel T Beckel, Emily Henderson, and Nicole Wenturine for extending their valuable help and support in every possible manner. I wish to thank my dear friends: Padma, Vignesh, Johny, Sunitha, Monisha, Privita, Brindha, Devaki, Sruthi, Padmapriya, and Gomathi, who have been with me at all times.

This endeavor would not have been possible without thanking my dear hubby, Mr. Boopathy N., for being the Love of my Life, and motivating me at all the vulnerable times over the past 15 years and for many more years to come. I am forever grateful to evident of our love, my tiny tingling baby in the womb for supporting me to stay awake and active during the thesis writing. Words cannot express my sincere gratitude to my beloved parents, amma and appa, and my sister Meenu for their unconditional love and support throughout my life. Finally, I would like to remember all my family members and extend my gratitude for their support, patience, and countless personal sacrifices that have empowered me to persistently make extra efforts toward my academic pursuits.

Thanks to the Lord, the Almighty, for showering his blessings and grace during this beautiful journey!

Janani G

CONTENTS

Abbreviations

3D	-	Three-dimensional
3ITT	-	Three interval thixotropic test
A1AT	-	Apha-1 antitrypsin
AA/ *A. assamensis*	-	*Antheraea assamensis*
ADMSCs	-	Adipose-derived mesenchymal stem cells
ADR	-	Adverse drug reaction
AFP	-	Alpha-fetoprotein
ALB	-	Albumin
ALD	-	Alcoholic liver disease
ALF	-	Acute liver failure
ALT	-	Alanine transaminase
AST	-	Aspartate transaminase
ANOVA	-	Analysis of variance
APAP	-	Acetaminophen/ N-acetyl-para-aminophenol
ApoA4	-	Apolipoprotein A-IV
ASS	-	Argininosuccinate synthase
AU	-	Arbitrary units
AVMA	-	American Veterinary Medical Association
BA	-	Blend of *Bombyx mori* and *Antheraea assamensis*
BAL	-	Bioartificial liver
bFGF	-	Basic fibroblast growth factor
BM/ *B. mori*	-	*Bombyx mori*
BMDM	-	Bone marrow-derived macrophages
BMMSCs	-	Bone marrow-derived mesenchymal stem cells
BSA	-	Bovine serum albumin
C3A	-	Clonal derivative of hepatoblastoma-based HepG2 cell line
CAD	-	Computer-aided design
CCl_4	-	Carbon tetrachloride

CCR7	-	C-C chemokine receptor type 7
CD163	-	Cluster of Differentiation 163
CD68	-	Cluster of Differentiation 68
CD86	-	Cluster of Differentiation 86
CD31	-	Cluster of Differentiation 31
CD206	-	Macrophage mannose receptor/Cluster of Differentiation 206
cDNA	-	Complementary deoxyribonucleic acid
CK	-	Cytokeratin
CK-19	-	Cytokeratin-19
CLEC7A	-	C-type lectin domain family 7 member A
CLSM	-	Confocal laser scanning microscopy
C_{max}	-	Average maximum drug concentration in plasma
cm	-	Centimeter
CO_2	-	Carbon dioxide
CPR	-	Cytochrome P450 Reductase
CS	-	Cross-section
CV	-	Central vein
CYP	-	Cytochrome P450
CYP1A1	-	Cytochrome P450 1A1
CYP1A2	-	Cytochrome P450 1A2
CYP2A6	-	Cytochrome P450 2A6
CYP2E1	-	Cytochrome P450 2E1
CYP3A4	-	Cytochrome P450 3A4
CYP2B	-	Cytochrome P450 2B
CYP7A	-	Cytochrome P450 7A
DAMPs	-	Damage-associated molecular patterns
DAPI	-	4', 6-diamidino-2-phenylindole
DILI	-	Drug-induced liver injury
dLECM	-	Decellularized liver extracellular matrix
DLM	-	Decellularized liver matrix

DLP	-	Digital light processing
dLS	-	Decellularized liver stroma solution
DMEM	-	Dulbecco's Modified Eagle Medium
DMEM-F12	-	Dulbecco's Modified Eagle Medium/ Nutrient Mixture F-12
DMSO	-	Dimethyl sulfoxide
DNA	-	Deoxyribonucleic acid
DNase	-	Deoxyribonuclease
DPX	-	Dibutylphthalate polystyrene xylene
E. coli	-	*Escherichia coli*
EC_{50}	-	A 50% decrease in cell viability
ECM	-	Extracellular matrix
ECGM	-	Endothelial cell growth medium
EDC	-	Ethyl(dimethylaminopropyl) carbodiimide
EDTA	-	Ethylene diamine tetraacetic acid
EGF	-	Epidermal growth factor
EGFR	-	Epidermal Growth Factor Receptor
EGTA	-	Ethylene glycol tetraacetic acid
ELISA	-	Enzyme-linked immune sorbent assay
ELSS	-	Extracorporeal liver support systems
ETO	-	Ethylene oxide
EVs	-	Extracellular vesicles
F4/80	-	EGF-like module-containing mucin-like hormone receptor-like 1/ pan-macrophage marker
FASN	-	Fatty acid synthase
FBS	-	Fetal Bovine Serum
FDA	-	Food and Drug Administration
FESEM	-	Field emission scanning electron microscopy
FGF	-	Fibroblast growth factor
FGF2-SPIONs	-	FGF 2 was conjugated to dextran-coated superparamagnetic iron-oxide nanoparticles

FHF	-	Fulminant hepatic failure
FIB	-	Fibronectin
FITC	-	Fluorescein isothiocyanate
Fizz1	-	Resistin-like molecule alpha 1/Found in inflammatory zone 1
FLT1	-	Vascular endothelial growth factor receptor 1 precursor
FOV	-	Field of view
FTIR	-	Fourier transform infrared spectroscopy
FTIR-ATR	-	Fourier transform infrared-attenuated total reflectance
G	-	Gauge
G’	-	Storage modulus
G”	-	Loss modulus
g	-	Gram
G6P	-	Glucose-6-phosphate
GAG	-	Glycosaminoglycan
GAPDH	-	Glyceraldehyde-3-phosphate
GGT	-	Gamma-glutamyl transferase
GOI	-	Gene of interest
GSTA1	-	Glutathione S-transferase alpha 1
h	-	Hour
H&E	-	Hematoxylin and Eosin
HBSS	-	Hank’s balanced salt solution
HCl	-	Hydrochloric acid
HDMEM	-	High glucose Dulbecco’s Modified Eagle Medium
HepaRG	-	Immortalized human hepatic progenitor cell line
HEPES	-	Hydroxyethyl piperazineethanesulfonic acid
HepG2	-	Hepatocarcinoma cells
HGF	-	Hepatocyte growth factor
HHSCs/ HSCs	-	Human hepatic stellate cells

hiPSCs	-	Human induced pluripotent stem cells
HLCs	-	Hepatocyte-like cells
HNF4α	-	Hepatocyte nuclear factor 4alpha
H_2O_2	-	Hydrogen peroxide
HRP	-	Horseradish peroxidase
HUVECs	-	Human umbilical vein endothelial cells
iHep	-	hiPSC-derived iCell 2.0 hepatocytes
i.p.	-	Intraperitoneal
IACUC	-	Institutional Animal Care and Use Committee
IAEC	-	Institutional Animal Ethical Committee
IFN-γ	-	Interferon-gamma
IgG	-	Immunoglobulin G
IHC	-	Immunohistochemistry
IL-1β	-	Interleukin-1β
IL1-Ra	-	Interleukin-1 receptor antagonist
IL-4	-	Interleukin-4
IL-6	-	Interleukin-6
IL-10	-	Interleukin-10
IL-13	-	Interleukin-13
iNOS	-	Inducible nitric oxide synthase
IR	-	Infrared
ITS	-	Insulin-Transferrin-Selenium
KCs	-	Kupffer cells
KCl	-	Potassium chloride
kDa	-	Kilo Dalton
Ki67	-	Marker of proliferation
kPa	-	Kilopascal
kN	-	Kilonewton
kV	-	Kilovolt
L	-	Liter
L929	-	Mouse fibroblast cell line

LDH	-	Lactate dehydrogenase
LECM	-	Liver extracellular matrix
LECM-SF	-	Liver extracellular blend silk scaffolds
LLOC	-	Liver lobule on a chip
LOC	-	Liver-on-a-chip
LPS	-	Lipopolysaccharide
LS	-	Longitudinal section
LSECs	-	Liver sinusoidal endothelial cells
LVER	-	Linear viscoelastic region
LX-2	-	Hepatic stellate cells
M	-	Molar
Mϕ	-	Naive macrophages
M1	-	Classically activated pro-inflammatory macrophages
M2	-	Alternatively activated pro-remodeling macrophages
MCP1	-	Monocyte chemoattractant protein 1
MCSF	-	Macrophage-colony-stimulating factor
MEM	-	Minimal Essential Medium
MGC	-	Multinucleate giant cells
mg	-	Milligram
min	-	Minute
mL	-	Milliliter
mm	-	Millimeter
mm/s	-	Millimeter per second
mmHg	-	Millimeter of mercury
mM	-	Millimolar
MMPs	-	Matrix metalloproteases
MMP9	-	Matrix metalloprotease 9
mRNA	-	Messenger ribonucleic acid
MRP2	-	Multidrug resistance-associated protein 2
MSCs	-	Mesenchymal stem cells
MT	-	Masson's Trichrome

MTT	-	3-(4,5-Dimethylthiazol-2-yl)-2,5-diphenyltetrazolium bromide
mU	-	Milliunits
MSCs	-	Mesenchymal stem cells
N	-	Newton (unit of force)
N	-	Normality
NAC	-	N-acetylcysteine
NaCl	-	Sodium chloride
NADH	-	Nicotinamide adenine dinucleotide
NADPH	-	Nicotinamide adenine dinucleotide phosphate
NAFLD	-	Non-alcoholic fatty liver disease
NAPQI	-	N-acetyl-p-benzoquinone imine
NBF	-	Neutral buffered formalin
NCCS	-	National Centre for Cell Sciences
ng	-	Nanogram
NHS	-	N-Hydroxysuccinimide
NIH	-	National Institute of Health
nm	-	Nanometer
nmol	-	Nanomoles
NPCs	-	Non-parenchymal cells
OLT	-	Orthotopic liver transplantation
p21	-	Cyclin-dependent kinase inhibitor 1
Pa	-	Pascal
PAA	-	Peracetic acid
PBS	-	Phosphate-buffered saline
PC	-	Pericentral
PCL	-	Poly(ε-caprolactone)
PCR	-	Polymerase chain reaction
PCNA	-	Proliferating cell nuclear antigen
PDGF-BB	-	Platelet derived growth factor with two B subunits
PDGFRα	-	Platelet-derived growth factor receptor α

PDMS	-	Polydimethylsiloxane
pg	-	Picogram
PHH	-	Primary human hepatocytes
PLA	-	Polylactic acid
PLGA	-	Poly(lactic acid-glycolic acid)
PLLA	-	Poly(L-lactic acid)
PMH	-	Primary mouse hepatocytes
PNRHs	-	Primary neonatal rat hepatocytes
pNIPAAm	-	Thermoresponsive polymer
PP	-	Periportal
PP mesh	-	C.R. BARD polypropylene surgical mesh
PRH	-	Primary rat hepatocytes
PRP	-	Platelet rich plasma
P/S	-	Pencillin/Streptomycin
PT	-	Portal triad
PVA	-	Poly(vinyl alcohol)
qRT-PCR	-	Quantitative real time-polymerase chain reaction
rad/s	-	Radian per second
RAW 264.7	-	Murine macrophage cell line
RGD	-	Arginine-glycine-aspartate
RNA	-	Ribonucleic acid
ROS	-	Reactive oxygen species
rpm	-	Rotations per minute
RT	-	Room temperature
S. griseus	-	*Streptomyces griseus*
SCGM	-	Stellate cell growth medium
SD	-	Standard deviation
SDS	-	Sodium dodecyl sulfate
SEM	-	Standard error of mean
SF	-	Silk fibroin
sec/ s	-	Seconds

SIS	-	Small intestinal submucosa extracellular matrix
SLA	-	Stereolithography
Sox9	-	SRY-Box Transcription Factor 9
STAT6	-	Signal transducer and activator of transcription 6
STL	-	Standard Triangle Language
TAA	-	Thioacetamide
TCP	-	Tissue culture plate
TGF-β1	-	Transforming growth factor β1
THP1	-	Human leukemia monocytic cell line
TNF–α	-	Tumor necrosis factor-alpha
TRIS	-	Tris(hydroxymethyl)aminomethane
U	-	Units
U/L	-	Units per litre
VEGF	-	Vascular endothelial growth factor
vWF	-	von Willebrand Factor
v/v	-	Volume/ volume
w/v	-	Weight/ volume
WBUAFS	-	West Bengal University of Animal and Fishery Sciences
WEM	-	William's E Medium
WJMSCs	-	Wharton's Jelly derived mesenchymal stem cells
Wnt	-	Wingless-related integration site
YAP	-	Yes-associated protein
YM1	-	Chitinase-like protein 3
β	-	Beta
γ	-	Shear strain
ε	-	Porosity
ω	-	Oscillatory strain
°C	-	Degree Celsius
µL	-	Microliter
µg	-	Microgram

µm	-	Micrometer
µM	-	Micromolar
>	-	Greater than
<	-	Lesser than

LIST OF TABLES

LIST OF FIGURES

CHAPTER 1

Introduction and Review of Literature

Patients with advanced liver cirrhosis are limited with liver transplants as the only therapeutic option; indeed, the practical applications of liver transplantation possess several drawbacks. This chapter provides a progressive overview of liver tissue engineering, liver microarchitecture, spatial heterogeneity of multicellular components, hepatocyte zonation, clinical manifestations of liver cirrhosis, and available treatment strategies. Different tissue engineering-based therapeutics in liver regenerative medicine emphasizing on natural biomaterials and decellularized liver extracellular matrix, followed by their promising prospects in the bioartificial liver, drug screening, and regenerative medicine are discussed. The insights on emerging strategies employed in designing native-like liver models are presented, focusing on the latest 3D bioprinting and microfluidic liver on a chip technique, and an update on commercially available tissue-engineered *in vitro* liver models.

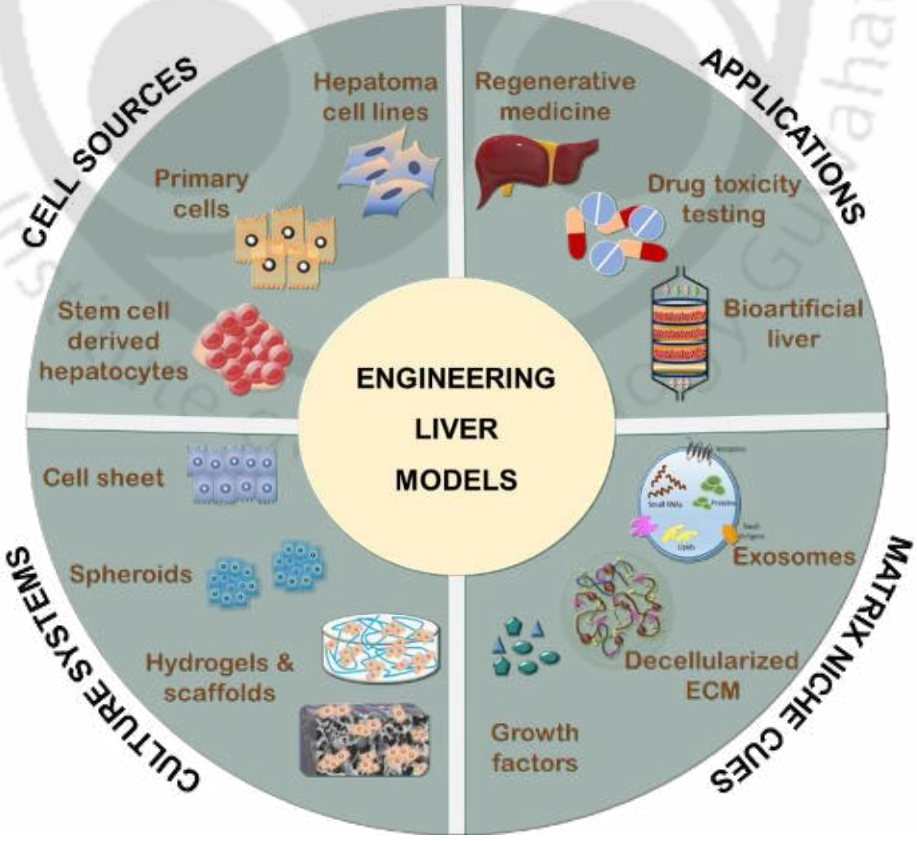

भारतीय प्रौद्योगिकी संस्थान गुवाहाटी
Indian Institute of Technology Guwahati

1.1 Introduction

The liver, the highly regenerative internal organ with complex microarchitecture, accounts for 1.4 – 1.6 kg representing 1.5 – 2.5% of lean body mass, and performs over 500 functions to maintain the metabolic homeostasis of the human body [1, 2]. The highly vascularized liver (13% of blood supply) is responsible for various physiological functions ranging from the metabolism of complex compounds, synthesis of serum proteins, bile secretion, drug detoxification, coagulation, and immunoregulation [3, 4]. The human liver consists of four lobes and is composed of millions of smaller functional subunits acinus or lobule, which is hexagonal in shape with a remarkable existence of 3-6 portal triads at the periphery of the lobule [5, 6]. Each portal triad comprises a hepatic artery, portal vein, and bile duct; the portal vein and hepatic artery supply nutrient-rich blood (80%) and oxygenated blood (20%), respectively to the lobule through vascular conduits (sinusoidal capillaries) and drain to the central efferent vein [7]. The microarchitecture of the liver lobule is intricate with a radial pattern of parenchymal and non-parenchymal cells (NPCs) originating from the central vein to the portal triad. The active interaction of parenchymal hepatocytes with NPCs (sinusoidal endothelial cells, stell ate cells, and Kupffer cells) and the surrounding extracellular matrix (ECM) is a prerequisite for retaining liver functionality [8]. The liver bud arises from the definitive endoderm, and the release of growth factors and cytokines from cardiac mesoderm and septum transversum mesenchyme induces differentiation and hepatogenesis [9]. Following acute liver injury and partial hepatectomy, a healthy liver recovers by self-regenerative mechanisms using all hepatic cell types, that involves extracellular and intracellular signaling pathways, inflammatory reaction, fibrinolysis, and matrix remodeling process [10]. Interestingly, cholangiocytes and hepatocytes act as facultative stem cells during liver injury and gradually transdifferentiate into each other to restore normal functions highlighting the plasticity of the liver [11].

Moreover, recurrent insults due to viral infections, genetic disorders, alcohol intake, and metabolic disorders from toxins and drugs result in chronic liver damage, called liver cirrhosis [12]. Chronic liver disease is highly prevalent, affecting around 800 million people worldwide with 2 million deaths every year [13]. Recurring acute liver failure (ALF) leads to cirrhosis and is associated with collagen deposition in the space of disse, dysregulated wound healing, an imbalance between matrix synthesis and altered matrix degradation, and loss of compensatory hepatocyte regeneration [14, 15]. Cirrhosis or end-stage liver disease is a chronic condition

characterized by the necrosis of liver cells, loss of compensatory hepatocyte proliferation, sinusoidal hypertension, and scar tissue formation [16]. Orthotopic liver transplantation (OLT) represents the definitive gold standard clinically accepted therapeutic option for patients with cirrhosis, with an overall one-year survival rate of about 65%. However, OLT presented several limitations, such as organ shortage, the possibility of allogeneic rejection, the use of immunosuppressants, and secondary complications [17]. Meanwhile, potential alternative strategies such as extracorporeal liver support systems, cell-based therapies, and liver tissue engineering have been explored to treat patients with decompensated liver diseases. However, the minimally invasive cell transplantation method in treating ALF has shown a low degree of cell engraftment and cannot support major liver functions [18]. Therefore, researchers have explored various tissue engineering techniques to fabricate an *in vitro* liver model for bioartificial liver (BAL) and liver transplantation applications.

A growing enthusiasm has favored the discovery and engineering of various biomaterials [2, 19], cell sources [20], fabrication techniques [21, 22], and culture systems [23] in liver tissue engineering. The standard monolayer hepatic culture based on surface coating with ECM molecules or collagen has been employed to study drug effects; however, hepatocytes de-differentiate and rapidly lose their morphology and functions [24, 25]. To combat this, researchers have developed a sandwich configuration of culture, wherein hepatocytes are cultured between two layers of gel to retain the polarity and augment the survival, morphology, and functions *in vitro* [26, 27]. In the native conditions, the liver cells are embedded in the complex hepatic 3D ECM microenvironment network that has a defined stiffness and regulates cellular morphology and functionality [28]. Then, the fabrication of 3D matrices using biomaterials into a range of formats from hydrogels, scaffolds, and nanofibrous mats to bioprinted constructs and microfluidic organ on a chip, enabled the 3D culture of hepatocytes, cell-matrix interactions, and enhanced liver-specific synthetic and metabolic functions [29]. Further, a heterotypic organoid culture in well-defined 3D matrices encompassing parenchymal and NPCs enhances cell-cell interactions, cell-matrix interactions, and functionality [30]. The maintenance of liver functions has been regulated by the epithelial-mesenchymal properties and paracrine signaling between the hepatocytes and non-parenchymal cells [31]. In order to emulate a more physiological environment and culture for a longer period, these developed 3D constructs were matured in bioreactor culture

systems like perfusion, hollow fiber, and a packed bed that imparted efficient mass transfer of nutrients and metabolites [32].

In vitro liver models emphasizing native-like microenvironmental niche, cell-cell interactions, and cell-matrix interactions deliver a potential platform for understanding liver biology that applies in drug toxicity studies, designing implantable constructs, and extracorporeal BAL support systems [33]. Liver zonation, a distinct metabolic heterogeneity of hepatocytes based on their position along the liver sinusoid, is often not wholly focused in *in vitro* liver systems [5, 34, 35]. Previous studies have developed *in vitro* liver zonation-based models by implementing native-like oxygen gradient and Wnt/β-catenin signaling [36-38]. Natural biomaterials including collagen, gelatin, chitosan, alginate, and silk fibroin have been extensively explored for liver tissue engineering applications owing to their bioactive attributes: biocompatibility, minimally immunogenic, possess cell-stimulating factors, and promote cell-matrix interactions [2, 8]. Among the natural polymers, silk fibroin endowed with easy processability, long-term stability, and mechanical strength has been employed as surgical sutures since ancient times and extensively explored for various tissue engineering applications. Silk fibroin (SF), isolated from mulberry *Bombyx mori* and non-mulberry *Antheraea assamensis,* is a low-density structural protein with a high content of β sheet or α helices with a core domain of random coils making it more crystalline and robust in nature [39]. SF protein acts as a carrier and supporting matrix for cell adhesion and proliferation, facilitating tissue regeneration [40]. Much research work has been carried out on mulberry SF in the biomedical field, with a few translated medical products in the market. The presence of intrinsic arginine-glycine-aspartic acid (RGD) tripeptide sequence, natural healing property, and high mechanical strength of *Antheraea assamensis* SF over mulberry SF have riveted biomedical engineers to exploit non-mulberry SF as a potential biomaterial [41]. Amino acid sequences of silk vary from species to species imparting unique physical and chemical properties to the protein, which substantiates its use as a biomaterial in numerous biomedical fields such as tissue engineering, *in vitro* models, and drug delivery [42]. *Bombyx mori* silk fibroin-based nanofibrous mats and scaffolds supported hepatic functions and has been explored for *in vitro* liver model and disease model [40, 43]. Besides the culture of liver cells in lab-developed scaffolds using different biomaterials, the transplantation of bioengineered whole liver in ALF animals has shown promising clinical outcomes [44, 45]. Scaffolds composed of ECM provide dynamic biomechanical and biochemical interplay between cells and matrix, thus promoting growth,

functionality, cell-cell, and cell-matrix communication [46]. Furthermore, the decellularized liver extracellular matrix (dLECM) was solubilized and used as a scaffold in various formats, and dLECM has been emerging as a key biomaterial to accomplish the biochemical cues of native ECM in liver regenerative medicine over the past decade [46, 47].

The main goal of this thesis is to bioengineer a physiologically relevant *in vitro* liver model for BAL and drug toxicity screening and to develop bioactive functional 3D matrices for liver regenerative applications. Towards this end, mulberry *Bombyx mori* silk fibroin, non-mulberry *Antheraea assamensis* silk fibroin, and decellularized liver ECM are explored in the domain of liver tissue engineering. In this chapter, we briefly introduced liver microarchitecture, liver zonation, and various cell sources and discussed different scaffold matrices focusing on cell-cell and cell-matrix interactions. Furthermore, insights on emerging fabrication techniques such as bioprinting and microfluidic organ on a chip in developing liver models and their prospective applications in BAL and drug toxicity screening are provided. By implementing defined objectives, we have employed novel strategies and progressively developed a physiologically relevant *in vitro* liver model encompassing liver ECM and silk fibroin resembling biomimetic cues and cellular arrangement towards the maintenance of long-term liver-specific functions. Further, we investigated the detailed host response, macrophage activation state, and therapeutic potential of liver ECM and silk biomaterials in the pre-clinical models.

1. The literature review about silk presented in this chapter are published in a peer reviewed journal:

Janani G., Kumar M., Chouhan D., Moses J.C., Gangrade A., Bhattacharjee S., and Mandal B.B. "*Insight into silk-based biomaterials: From physicochemical attributes to recent biomedical applications*". **ACS Applied Bio Materials**, 2019, 2 (12), 5460-5491.

2. The literature review about liver tissue engineering presented in this chapter are under preparation for manuscript submission:

Janani G., and Mandal B.B. "*Bioengineered 3D liver constructs for bioartificial liver, drug screening models, and liver regeneration*". **Manuscript under preparation**

Review of Literature

भारतीय प्रौद्योगिकी संस्थान गुवाहाटी
Indian Institute of Technology Guwahati

1.2 Liver microstructure and metabolic zonation

The liver is responsible for a plethora of biological functions, including (i) detoxification of xenogenic compounds, (ii) production of serum proteins, (iii) cholesterol production, (iv) regulation of blood composition, (v) bile production, (vi) amino acid synthesis, (vii) protein synthesis (albumin and urea), and (viii) glycogen storage **(Figure 1.1 A)**. The liver lobule, microanatomy of the liver, is heterogeneous in terms of cell types and is composed of hepatocyte plates radiating outward from the central vein to the portal triad [48] **(Figure 1.1 B)**. The portal triad at the corners of the liver lobule is embedded with the hepatic artery, portal vein, and bile duct that carries oxygenated blood, nutrient-rich blood, and bile products, respectively [49] **(Figure 1.1 C)**. The liver parenchymal hepatocytes encompass two-thirds of the liver population, 80% of total liver volume, and perform synthetic and metabolic functions [3, 50]. While, liver sinusoidal endothelial cells (LSECs), hepatic stellate cells (HSCs), Kupffer cells (KCs), cholangiocytes, and dendritic cells constitute the NPCs population [48]. The anchorage-dependent hepatocytes are polarized cells, and the polarity is retained by a gradient of growth factors and soluble factors presented by native liver ECM [51]. The apical membrane of hepatocytes forms tight junctions, resulting in the bile canaliculi formation for the transport of bile juice [52]. Highly specialized LSECs represent a permeable barrier associated with fenestrae, retain the highest endocytosis ability, and regulate hepatic vascular tone [53, 54]. The hepatic stellate cells reside in the “space of disse” between the anti-luminal side of the LSECs and the basolateral surface of hepatocytes [55]. HSCs store vitamin A, maintain ECM, and facilitate liver regeneration by producing cytokines and growth factors [31, 55]. The liver-resident macrophages known as Kupffer cells are largely immotile cells localized within the sinusoidal network and play a critical component in the mononuclear phagocytic system by removing foreign particles and dead liver cells [56, 57]. Interestingly, the liver shows a remarkable metabolic heterogeneity in the hepatocytes along the vascular sinusoid due to the oxygen gradient resulting in different functions creating liver zonation [58] **(Figure 1.1 C)**. The liver lobule has been divided into zone 1 periportal, zone 2 midlobular, and zone 3 pericentral. Comparatively, the mitochondria of hepatocytes in the periportal region were larger and spherical than the elongated mitochondria of the pericentral hepatocytes [51, 59]. The oxygen-rich periportal hepatocytes predominantly

perform gluconeogenesis, β-oxidation, cholangiocyte functions, protein synthetic functions, and ureagenesis. While oxygen concentration is low in the pericentral zone, functions such as glycolysis, ketogenesis, lipogenesis, Wnt signaling, and xenobiotic metabolism are dominant in pericentral hepatocytes [6, 60]. Further, zonation and the functional difference were also noted in non-parenchymal cells along the sinusoid. New hepatocytes are produced in the periportal zone and slowly migrate towards the central vein during liver damage and regeneration [61]. Therefore, resembling the cellular complexity and metabolic hepatocyte heterogeneity of native liver lobule is a prerequisite in *in vitro* liver model systems.

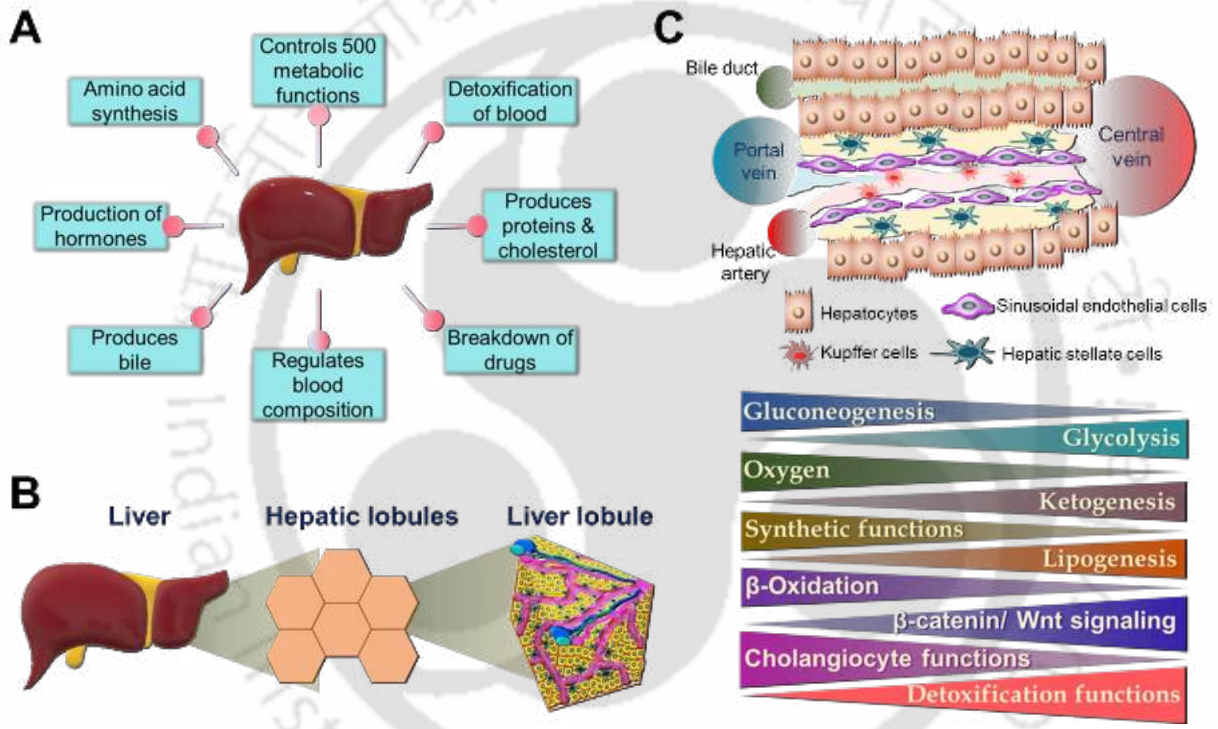

Figure 1.1. Liver functions and their anatomical microstructure. *Schematic illustration depicting (A) Liver functions. (B) Multiscale system of liver. (C) Microarchitecture, cellular arrangement of parenchymal and non-parenchymal cells, and metabolic zonation of the liver lobule.*

1.3. Liver tissue engineering and cell sources

The origin of liver tissue engineering can be traced to five decades ago, beginning with the application of cell sheets, spheroids, and scaffold culture to bioprinted liver models and microfluidic liver on a chip for cell culture and biological functions. The progress in liver regenerative medicine could be a promising strategy to develop a native-mimicking liver model for extracorporeal support to overcome the shortage of organ donors and limitations in cell

transplantation and implantable constructs. All these methods emphasized on the restoration of partial or complete liver functions in *in vitro* BAL liver model and the preservation of viability and functionality of hepatocytes for a longer period. Crucial components in developing liver models include (i) biomaterial choice, (ii) type of scaffold, and (iii) liver cell source. Given that hepatocytes are anchorage-dependent cells, the biomaterials employed for scaffold fabrication in liver tissue engineering should be biocompatible, porous, biologically active, and should provide robust topography and mechanical strength supporting the liver cells to adhere, grow, and differentiate [2]. The different cell types used for various liver tissue engineering applications with their advantages and limitations are presented and discussed in **figure 1.2**. While selecting an appropriate cell source for *in vitro* liver culture systems, the critical considerations include (i) hepatocyte polarity, (ii) secreting hepatocyte-specific synthetic proteins such as albumin, alpha-1 antitrypsin (A1AT), bile acids, and clotting factors, (iii) storing glycogen, (iv) metabolizing nitrogenous compounds to urea, (v) metabolizing xenobiotic compounds, (vi) reproducibility, (vii) physiological relevance, and (viii) availability, cost, and scalability. Herein, we have discussed the progress in conventional and emerging tissue engineering strategies for developing liver models with the limitations for a wide range of applications.

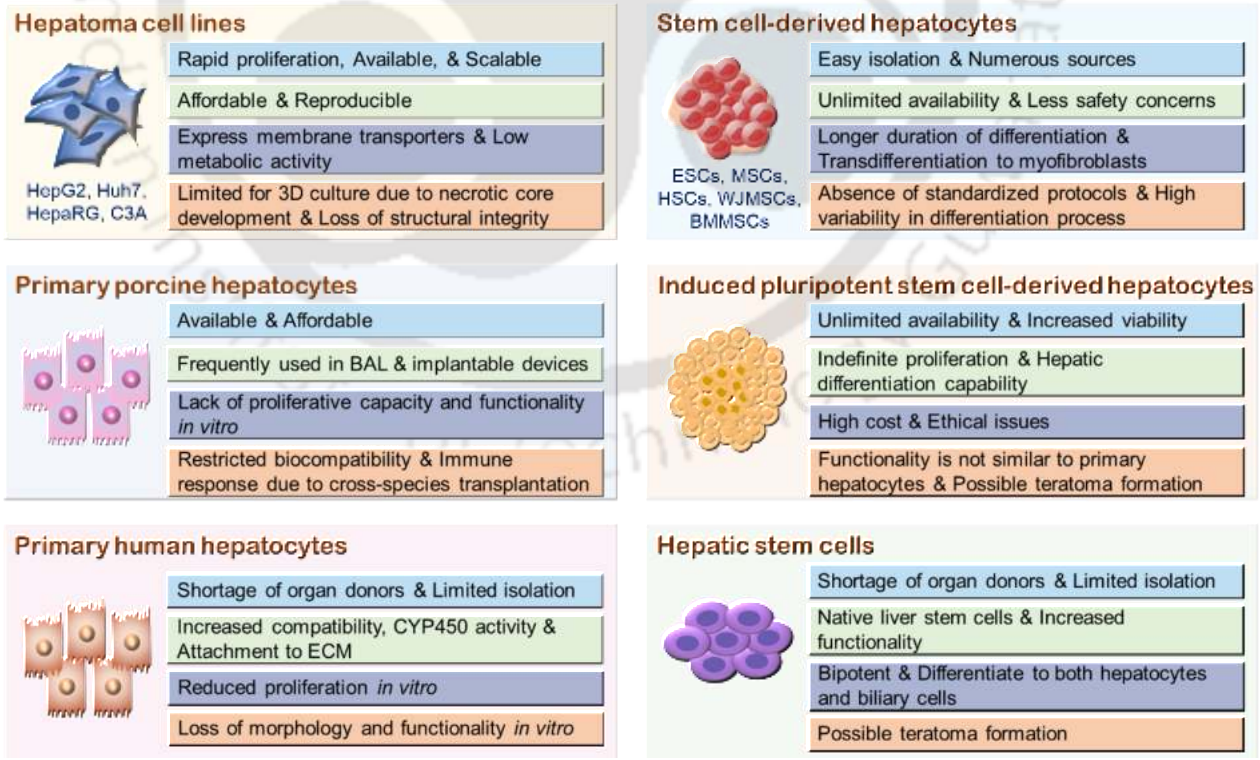

Figure 1.2. Assessment of various cell sources for liver tissue engineering and its advantages and limitations.

1.4 Tissue engineered therapeutic interventions in liver regenerative medicine

1.4.1 Bioengineered liver models centering cell-cell communication

A growing body of evidence demonstrated that hepatocyte culture as 3D spheroids or organoids facilitates cell-cell communication, hepatocyte polarity, and overcomes the drawbacks associated with rapid de-differentiation of hepatocytes in monolayer and sandwich culture [48, 62]. Spheroids mediated by cellular interactions and cell-secreted ECM offer biomechanical cues, oxygen gradient, and nutrient gradient resembling the oxygen gradient from the periportal to the pericentral region in the liver lobule [63-65]. The self-organizing spheroids with improved uniformity and functionality were developed using various micropattern arrays such as hanging-drop, microwell array, and magnetic assembly [48, 66]. The gap distance between the spots in a micropatterned culture system regulates the spheroid behavior, and studies suggested that an increased spheroid separation distance improved the growth and functionality of HepG2 spheroids by overcoming the anaerobic metabolism [63, 67]. Miniaturization of *in vitro* spheroid model into a 384-well high-throughput drug screening platform improved the hepatotoxicity prediction of 3D primary human hepatocyte spheroids as tested with 199 compounds and could be employed in the early drug discovery process [62]. However, modulating the size, morphology, and shape of spheroids is crucial to enhance the efficiency and reproducibility of spheroids for liver tissue engineering and drug toxicity applications [68]. Zhu *et al*. fabricated a decellularized liver matrix (DLM) coated micropattern array platform with a diameter of 100 μm each to generate an optimal size-controllable, homogenous, and arrangement-orderly HepG2 spheroids for drug screening [69]. DLM as coating substrate enhanced the cellular adhesion rate, viability, and functions of HepG2 spheroids compared to Matrigel and Collagen I coating [69].

Spheroids comprising only hepatocytes emphasize on homotypic cellular interactions, hepatocyte-specific synthetic (albumin, urea), and detoxification functions; however, they fail to recapitulate the complexity of the native tissue microenvironment. Multilineage spheroids comprising hepatocytes and NPCs facilitate heterogeneous cell-cell interactions and replicate the pathophysiology *in vivo*, which is crucial while developing *in vitro* liver models for various liver tissue engineering applications. Stellate cells in multicellular genetically-induced non-alcoholic fatty liver disease (NAFLD) model composed of HepG2 and LX-2 (hepatic stellate cells) facilitated compactness of spheroids, intercellular fat accumulation, and collagen deposition upon exposure to free fatty acids, and this model was further evaluated for disease reversal using

Liraglutide or Elafibranor [70]. A multilineage 3D spheroid system developed by co-culturing primary human hepatocytes (PHH) and NPC (stellate, Kupffer cells, and biliary cells) at a ratio of 2:1 in a chemically-defined serum-free condition was morphologically stable and remained functionally and metabolically active over a period of 5 weeks as compared to only PHH spheroids [71]. The preserved long-term NPC functionality, proteomes, and hepatic phenotypes in the co-culture spheroid system closely resembled native conditions and were employed as an *in vitro* platform for drug screening and disease models [71]. Similarly, a co-culture spheroids generated using PHH and mixed NPCs predicted acetaminophen-induced hepatotoxicity better than only PHH spheroids by inducing inflammation and steatosis. Several studies highlighted the protective effect and cellular crosstalk of NPCs with hepatocytes in *in vitro* liver model system [71, 72]. Furthermore, hepatic organoids or spheroid models generated from a human-induced pluripotent stem cell (hiPSCs) derived hepatocyte-like cells (HLCs) exhibited significantly increased hepatic marker gene expression, drug-metabolizing activity [73], and recapitulated functional bile canaliculi system [74]. The hiPSCs-derived hepatic organoids were evaluated as an *in vitro* model to study liver diseases like non-alcoholic hepatitis (NASH) [74] to predict drug-induced liver injury (DILI) [73], and liver regeneration [75].

Spheroid-based *in vitro* models are benefitted in terms of scalability, homogeneity, high-throughput reproducibility, and intercellular communications. However, these systems fail to recapitulate the cell-ECM interactions and continuous perfusion in a 3D environment, which is decisive during the fabrication of complex microtissues.

1.4.2 Bioengineered liver models ameliorating cell-matrix interaction

1.4.2.1 Hydrogels

A hydrogel is a network of natural or synthetic hydrophilic polymer chains and possesses fundamental attributes including hydrophilicity, degree of flexibility, biocompatibility, biodegradability, bioactivity, and mimic native ECM properties for tissue engineering applications [76]. Two different approaches were used to generate cell-loaded hydrogels: cells were either encapsulated within the hydrogel matrix while forming the gel or seeded on the surface of the prefabricated hydrogel matrix. Several synthetic polymers have been utilized as hydrogel matrices for disease modeling, drug delivery, and hepatocyte growth, including poly(acrylic aid), poly(vinyl alcohol) (PVA), poly(ethylene glycol), poly(lactide-co-glycolide), owing to their robust mechanical structure [77, 78]. However, these synthetic hydrogels are less bioactive and

biodegradable compared to natural hydrogels due to their similarity to native ECM. To combat this, researchers modified the PVA hydrogels with natural polymers like collagen and ECM proteins to accomplish increased hepatocyte viability, albumin secretion, and urea synthesis [79, 80]. Similarly, a synthetic supramolecular hydrogel was fabricated by assembling RGD peptides on squaramide synthons, and these supramolecular hydrogels assisted self-assembly of HepG2 spheroids (~ 150 μm) and showed increased expression of drug transporters, liver markers, and drug-metabolizing enzymes compared to Matrigel [81].

Many natural polymers such as proteins (gelatin, collagen, and fibrin), and polysaccharides (agarose, hyaluronic acid, alginate, and chitosan) have been widely exploited to construct complex 3D hydrogels either in pristine or in combination with other polymers for liver tissue engineering applications [82, 83]. Over the last decade, researchers have exploited gelatin derivatives-based hydrogels such as fibrin incorporated alginate dialdehyde–gelatin hydrogel [84], gelatin methacrylol hydrogel [82], glycidyl methacrylate functionalized gelatin hydrogel [85], galactose containing PVA/gelatin hydrogel [86], hyaluronan-gelatin [87], and gelatin blended glycosaminoglycans for hepatocyte culture to promote hepatic functions. A photocrosslinkable glycidyl methacrylate functionalized gelatin hydrogel was synthesized using Irgacure I2959 as an initiator, and these hydrogels improved mass diffusional properties that assisted in enhanced proliferation and differentiation of cultured Huh-7.5 cells over 14 days [85]. The fibrillar collagen on soft elastic polyacrylamide hydrogels cultured with primary rat hepatocytes promoted hepatocyte survival, self-aggregation, and metabolic functions for longer periods of time [88]. Alginate-galactosylated chitosan with collagen hydrogels supported higher Young's modulus, long-term viability, interactions between encapsulated HepG2 cells and the matrix, and increased liver-specific functions [89]. Several studies demonstrated that the enrichment of alginate with collagen and galactosylated chitosan enhances the bioactivity of the hydrogel by reducing the swelling ratio and degradation behavior [88, 89]. Jiang *et al*. fabricated a viscoelastic bifunctional hyaluronan-collagen hydrogel matrix that replicated the mechanical properties of the native liver and showed great potential in the development of *in vitro* alcoholic liver disease (ALD) model using HepG2 cells [90]. The ALD model induced lipogenesis, expression of fatty acid synthase, and reduced metabolic activities of albumin, urea, and glutathione over 21 days culture period, thereby leading to liver fat lesions. Furthermore, the intervention effect of epigallocatechin gallate

was evaluated in the ALD model both *in vitro* and *in vivo* which alleviated liver disease and improved liver functions [90].

The physicochemical versatility, biocompatibility, and biodegradability of hydrogels can serve as an effective system for transplantation applications and local delivery of therapeutic molecules [91, 92]. The alginate capsule hydrogel encapsulated with hiPSC-derived HLC aggregates together with stroma cells showed persistently increased albumin secretion over 8 days *in vitro* and 24 days *in vivo* after engraftment in immunocompetent C57BL/6 mice [92]. Seale *et al*. developed a vascularized dual compartment hydrogel system with an outer compartment housing supporting cells and hollow inner core housing PHH to facilitate vascularization and host cell infiltration [91]. The minimally invasive cell-loaded hydrogel grafts assisted anastomosis and acted as ectopic liver by supporting the viability and functionality of transplanted hepatocytes over 1 month upon subcutaneous transplantation [91]. The bioengineered hepatic units formulated using collagen hydrogel and neonatal rat liver cells allowed site-specific intrahepatic transplantation into the parenchyma and attenuated liver cirrhosis by promoting engraftment and hepatic functions [93].

With the combination of several advantages of hydrogel-based 3D matrices such as water imbibing capacity, degradation, and swelling under physiological conditions for *in vivo* liver transplantation, many of them are less bioactive and exhibit diffusional limitations while employed for the development of *in vitro* liver model. Various design strategies and culture systems could be employed to impart larger pores and mechanical strength to augment culture time.

1.4.2.2 Scaffolds

Scaffolds with interconnected pores and tunable mechanical strength assure the nutrient and metabolite diffusion in addition to structural support for the cells to grow in a 3D environment allowing high cell growth and liver microtissue formation. The scaffolds in various formats, namely cryogels, freeze-dried structures, and nanofibrous mesh have been investigated for liver tissue engineering. Several studies have reported that structural characteristics of scaffolds like pore size and geometry would influence the hepatocyte morphology and function [94, 95]. They can be classified by material as (i) synthetic polymers such as poly(L-lactic acid) (PLLA), Poly(ε-caprolactone) (PCL), poly(lactic acid-glycolic acid) (PLGA), and (ii) natural polymers such as collagen, gelatin, chitosan, alginate, and silk. Electrospun PCL nanofibrous scaffolds supported the growth and functionality of hepatocytes as assessed using HepG2, PHH, and primary mouse

hepatocytes [94, 96, 97]. Increased fiber size and higher porosity of PCL nanofibrous scaffold allowed nutrient diffusion and cell-cell interactions to facilitate the organoid arrangement of hepatocytes [94, 97]. The PLLA scaffold blended or coated with PCL [98] and collagen [99] provided a 3D platform for the hiPSCs differentiation into hepatocytes. Liu *et al.* co-cultured rat bone marrow-derived mesenchymal stem cells (BMMSCs) with murine hepatocytes at a ratio of 1:5 on PLGA scaffolds that demonstrated hepatocyte metabolism *in vitro* and further implantation into the abdominal cavity restored ALF in mice [100]. Moreover, the synthetic materials have been modified with lecithin [101], galactose [102-104], and chitosan [102] to significantly augment hepatocyte attachment by improving the softness, elasticity, and hydrophilicity and introducing biologically active functional groups.

Compared to synthetic polymers, natural polymers-based scaffolds are biocompatible, bioactive, and mimic ECM better, as liver ECM is enriched with polysaccharides and proteins. Collagen, an abundant component of native ECM has been limited for its use as a whole scaffold matrix for liver tissue engineering owing to faster degradation and minimal stiffness [105]. Chitosan is biodegradable, exhibits antibacterial properties, and is often modified with other materials as it lacks bioactivity and cell-binding domain [2]. Silk, a biocompatible protein isolated from various silkworms, has been explored for various tissue engineering applications due to its tunable mechanical strength, biocompatibility, biodegradability, and bioactivity [106]. Particularly, the non-mulberry *Antheraea assamensis* silk provides an additional advantage due to the intrinsic RGD motifs [42]. The use of several natural biomaterials as a whole or in combination with other natural biomaterials for various liver tissue engineering applications, including cell source, culture time, and characteristics, is discussed in **Table 1.1**.

The macroporous scaffolds succored self-aggregation of hepatocytes and extended culture periods compared to hydrogels; indeed, cell fibrosis occurs at the core of the scaffolds due to lack of oxygen and nutrient diffusion [107]. Maturation of scaffolds in a bioreactor would enhance the functionality of cultured hepatocytes

Table 1.1. *Natural polymer-based 3D scaffolds for liver tissue engineering applications*

Biomaterials	Cell type	Fabrication strategy	Efficacy	Culture time	Research applications	References
Gelatin	ADMSCs	Cryogel	Increased albumin, AFP, CK-18 and CK-19 expression, urea production, and glycogen storage	3 weeks	3D matrix for hepatogenic differentiation	[108]
	PHH	Solution blow spinning	Maintenance of hepatic metabolic activity and polarization; Increased CYP expression in response to drugs	3 weeks	*In vitro* model for drug testing	[109]
Chitosan + Gelatin	Primary rat hepatocytes	Rapid-prototyping, microreplication, and freeze-drying method	Scaffolds possessed a flow-channel network and hepatic chambers; increased albumin and urea secretion	7 days	*In vitro* liver model	[110]
	HepG2	Freeze-drying method	Maintained spherical morphology; Increased albumin and lactate dehydrogenase activity	3 weeks	*In vitro* liver model	[111]
	HepG2	Freeze-drying method	Increased albumin and urea secretion	8 days	*In vitro* liver model	[112]

	HepaRG + HUVECs + LSECs	Freeze-drying method	Increased albumin and urea secretion, and CYP3A4 activity; Highest acetaminophen conversion after exposure to acetaminophen for 1 day	8 days	*In vitro* model for drug testing	[113]
Galactosylated chitosan	Primary rat hepatocytes	Electrospinning	Supported hepatocyte aggregate culture; Increased albumin, urea, and CYP activity	7 days	*In vitro* liver model	[114]
Chitosan + Galactosylated hyaluronic acid	Primary rat hepatocytes	Freeze-drying method	Induced cellular aggregates; Increased albumin secretion and urea synthesis	13 days	*In vitro* liver model	[115]
Chitosan + Fibronectin	Primary rat hepatocytes + 3T3-J2 fibroblasts	Electrospinning	Increased albumin and CYP activity	29 days	*In vitro* liver model	[116]
Collagen + Heparin	WJMSCs	Freeze-drying method	Increased albumin, HNF4, CK-18, CK-19, G6P, and CYP2B expression	3 weeks	3D matrix for hepatogenic differentiation	[117]
Bombyx mori silk	Murine ADMSCs	Electrospinning	Engraftment of MSC seeded electrospun matrices into injured liver and recovery	3 months	Transplantation and Liver regeneration	[118]

	and BMMSCs		from CCl_4 induced ALF; neovascularization on day 5; bile canaliculi-like structure at one month; the appearance of hepatocyte-like cells after two months			
	HepaRG	Freeze-drying method	Supported proliferation for the first 14 days and differentiation in the last 14 days; Increased albumin, CYP1A1, and CYP3A4 expression	4 weeks	*In vitro* liver model	[40]
	HepaRG	Freeze-drying method	Increased ApoA4, FASN expression	4 weeks	*In vitro s*teatosis liver model	[40]
Bombyx mori silk + Collagen	PHH + 3T3-J2 fibroblasts	Freeze-drying method	Increased albumin secretion and CYP2A6 activity	1 month	*In vitro* liver model	[43]
Alginate	C3A	Freeze-drying method	Induction of hepatocyte spheroids; Increased CYP1A2 and CYP3A4 activity	7 days	*In vitro* model for drug testing	[119]
	BMMSCs	Freeze-drying method	Albumin and urea production; increased albumin, AFP,	4 weeks	3D matrix for hepatogenic differentiation	[120]

			CYP7A and CK-18 expression			
Alginate + Galactosylated chitosan	Primary rat hepatocytes + 3T3-J2 fibroblasts	Freeze-drying method	Expressed HGF; increased albumin and urea secretion	6 days	Delivery of hepatocyte growth factor plasmid	[121]

ADMSCs – Adipose-derived mesenchymal stem cells; BMMSCs – Bone marrow-derived mesenchymal stem cells; WJMSCs – Wharton's Jelly-derived mesenchymal stem cells; PHH – Primary human hepatocytes; HepG2 – Human hepatocarcinoma cell line; HUVECs – Human umbilical vein endothelial cells; LSECs – Liver sinusoidal endothelial cells; HepaRG – Human bipotent progenitor cell line; C3A – Human hepatocyte cell line; CYP1A1 – Cytochrome P450 1A1; CYP1A2 – Cytochrome P450 1A2; CYP3A4 - Cytochrome P450 3A4; CYP2A6 – Cytochrome P450 2A6; CYP2B - Cytochrome P450 2B; CYP7A - Cytochrome P450 7A; CYP – Cytochrome P450; ApoA4 – Apolipoprotein A-IV; FASN – Fatty acid synthase; AFP – Alpha-fetoprotein; CK – Cytokeratin; HNF4 – Hepatocyte nuclear factor 4; G6P – Glucose-6-phosphate; CCl_4 – Carbon tetrachloride; ALF – Acute liver failure; HGF – Hepatocyte growth factor

1.4.2.3 Decellularized extracellular matrix and extracellular vesicles

Decellularized liver ECM (dLECM) from xenogeneic animals and discarded human livers act as a natural ECM scaffold in hepatic regenerative medicine owing to its intrinsic native ECM composition, growth factors, cytokines, flexibility, and mechanical strength [122]. Increasing evidence suggests that the dLECM scaffolds maintain hepatocyte interaction and polarity for longer culture periods and promote hepatocyte functionality [122, 123]. The chemical, enzymatic and physical methods alone or in combination have been employed for effective decellularization, which comprises the removal of host cells to evade inflammatory reactions and preservation of ECM composition with the vascular network for eventual endothelialization, anastomosis, and transplantation [124, 125]. The whole liver decellularization was first introduced in 2010, with the preservation of intact architecture, microvascular network, and ECM composition, allowing the transplantation of recellularized liver grafts with primary rat hepatocytes [126]. Further, revascularization of the decellularized whole porcine liver with HUVECs followed by transplantation into immunosuppressed pigs colonized liver sinusoids, expressed endothelial markers, and succored perfusion up to 15 days [127]. Over the years, whole liver bioscaffold revolved around implementing a cocktail of chemicals for decellularization; and optimizing cell seeding with primary hepatocytes, ADMSCs, BMMSCs, and iPSCs for recellularization [124]. However, numerous pitfalls remain in the utilization of whole liver bioscaffolds such as (i) establishment of a non-thrombotic vascular network, (ii) poor colonization of the vascular and bile network with functional cells, (iii) limited availability of primary hepatocytes, (iv) deliver of all liver cell types, and (iv) limited reproducibility in decellularization.

Recent studies have attempted to functionalize 3D matrices with solubilized decellularized liver stroma (dLS) solution in the form of coating, hydrogel, and scaffolds to augment the cellular organization and hepatic functionality [128]. Hussein *et al*. subjected the decellularized mice livers to enzymatic digestion to produce a liver hydrogel [129]. The liver hydrogel retained glycosaminoglycans, collagen, elastin, and growth factors and significantly enhanced the angiogenesis, proliferation, and migration of hepatic cells and endothelial cells *in vitro*. Liver hydrogel inhibited the activation of TGF-β1 (Transforming growth factor β1)-induced LX-2 cells by downregulating collagen α-1 and blocking TGF-β1/Smad pathway. Further, the injectable liver hydrogel intra-parenchymally attenuated thioacetamide (TAA)-induced liver fibrosis by improving the morphology and albumin level and reducing the collagen deposition,

hydroxyproline content, and oxidative stress over 3 weeks [129]. Several groups have recently attempted to implement whole liver bioscaffolds and dLECM-based matrices for liver tissue engineering applications, and details including ECM source, decellularization method, cell source, characteristics, culture time, and research applications are discussed in **table 1.2**.

Extracellular vesicles (EVs), membrane-derived nanovesicles that are released by various cell types in the extracellular space comprising exosomes and microvesicles, represent an emerging field in liver therapeutics [130]. The HSCs-derived EVs enriched in platelet-derived growth factor receptor α (PDGFRα), and inhibition of HSCs autophagy by mTOR signaling participated in liver fibrosis progression [131, 132]. An allosteric inhibitor of SHP2, SHP099 treatment reduced the activated HSCs-derived EVs and attenuated liver fibrosis [132]. Recently, researchers showed that administration of EVs derived from hiPSCs [133], hiPSC-derived mesenchymal stromal cells [134], human liver stem cells [135], and MSCs [136] attenuates liver injury and exerts a beneficial protective effect on hepatocytes. Multiple assets of EVs offer great interest in developing therapeutic strategies in the field of liver tissue engineering, and studies aimed at successful clinical application of EVs are in progress.

Table 1.2. *Whole liver bioscaffolds and decellularized liver extracellular matrix-derived scaffolds in liver regenerative medicine*

Source of ECM	Decellularization approaches	Scaffold	Cell type	Efficacy	Culture time	Research applications	References
Human	Perfusion of 4% Triton X-100/1% ammonium hydroxide – 6 days; perfusion of 0.9% NaCl and 2 mg/L DNAse-I solution	Whole liver bioscaffold	HUVECs	Supported endothelialization	5 days	Bioengineered livers for transplantation	[137]
Rat	Perfusion of 0.1% SDS – 3 h; perfusion of 0.1% Triton X-100 -30 min	Whole liver bioscaffold	Primary rat hepatocytes	Recellularized liver expressed albumin, CK-18, CK-19, GGT, G6P, AFP, and produced albumin and urea	2 weeks	Bioengineered livers for transplantation	[138]
Porcine	Perfusion of 1% Triton X-100 -5 h; perfusion of 0.6% SDS – 8 h; perfusion of peracetic acid	Whole liver bioscaffold	HUVECs	Revascularized grafts retained vascular patency and endothelialization in immunosuppressed pigs	15 days	Bioengineered livers for transplantation	[127]

Human	0.01% SDS – 4h; 0.1% SDS – 1h; 0.2% SDS – 1h; 0.5% SDS – 1h; 1% Triton X-100 – 15 min	dLECM hydrogel	hiPSCs	Improved hepatic differentiation and increased expression of functional hepatic markers	20 days	3D matrix for hepatogenic differentiation	[139]
Porcine	0.1% SDS	dLECM hydrogel	Mouse cholangiocytes	Induced biliary network; exhibited polarization and transporter activity	3 weeks	Bile duct tissue engineering	[140]
Porcine	0.02% Trypsin/ 0.05% EGTA – 2 h; 1% Triton X-100/ 0.1% ammonium hydroxide – 72 h	dLS coated chitosan	C3A	Increased albumin secretion, urea synthesis	7 days	*In vitro* liver model and BAL	[141]
Porcine	1% Triton X-100/0.1% ammonium hydroxide – 5 days	dLECM hydrogel	PHH	Promoted cell growth and metabolic activity	7 days	*In vitro* liver model	[128]
Caprine	2% Triton X-100/0.05 mM EDTA; 0.025% ammonium hydroxide – 72 h	dLECM scaffold	HepG2	Supported hepatocyte differentiated phenotype and functionality; Exhibited pro-	2 weeks	Liver tissue engineering applications	[142]

				angiogenic properties			
Mice	Perfusion of 0.1% SDS – 2 h; perfusion of 0.1% peracetic acid – 2 h	dLECM hydrogel	NA	Liver hydrogel upregulated hepatic functions and downregulated fibrotic markers in TAA-induced liver fibrosis	3 weeks	Injectable hydrogel for treating liver fibrosis	[129]
Rat	Perfusion of 1% Triton X-100/0.1% ammonium hydroxide	Conjugated dLECM scaffold coated with dLS	HepG2	Intrahepatic transplantation of grafts improved functionality and increased the expression of albumin, CK-19, HGF, FLT1, and Ki67	10 days	Bioengineered livers for transplantation	[143]
Rat	0.5% SDS – 4 h, 1.5% Triton X-100 – 72 h	dLECM incorporated pNIPAAm hydrogel	Human ADMSCs	Induced differentiation into HLCs and increased levels of albumin, urea, hepatogenic markers, and glycogenesis	3 weeks	*In vitro* liver model	[144]

ADMSCs – Adipose-derived mesenchymal stem cells; AFP – Alpha-fetoprotein; BAL – Bioartificial liver; C3A - Human hepatocyte cell line; CK – Cytokeratin; DNAse-I – Deoxyribonuclease I; dLECM – Decellularized liver extracellular matrix; dLS – Decellularized liver stroma solution; EGTA - Ethylene glycol tetraacetic acid; EDTA - Ethylene diamine tetraacetic acid; FLT1 – Vascular endothelial growth factor receptor 1 precursor; G6P – Glucose-6-phosphate; GGT – Gamma-glutamyl transferase; HepG2 - Hepatocarcinoma cell line; hiPSCs – Human induced pluripotent stem cells; HGF – Hepatocyte growth factor; HLCs – Hepatocyte-like cells; HUVECs – Human umbilical vein endothelial cells; Ki67 – Marker of proliferation; NaCl - Sodium chloride; pNIPAAm – Thermoresponsive polymer; PHH – Primary human hepatocytes; SDS – Sodium dodecyl sulfate; TAA – Thioacetamide

1.5 Emerging strategies in bioengineering liver models: The road ahead for improving hepatic functionality

In conventional monolayer, spheroid, hydrogel, and scaffold culture systems, the cultured hepatocytes were limited in maintaining native cellular morphology, spatial arrangement of various cell types, diffusion gradient, long-term viability, and key hepatic functions [145]. Emerging technologies namely bioprinting, microfluidics, and perfusion culture systems offer a vision to generate functional liver constructs with spatiotemporal structure and flow patterns similar to their native counterparts, addressing the need in tissue engineering [2].

1.5.1 Bioprinted liver models recapitulating native microarchitecture

Bioprinting, an extended application of rapid prototyping, is a bottom-up strategy and offers the advantage of bioprinting functional bioinks embedded with multiple cell types in a layer-by-layer (LBL) fashion to formulate 3D biomimetic cell-laden constructs in desired shapes and size [146]. A combination of biomimicry, self-association, and building blocks is a prerequisite to bioprint a functional *in vitro* liver model reproducing mechanical, cell-cell, and cell-matrix interactions [147]. Based on the working principle, different bioprinting modalities based on inkjet, laser, extrusion, stereolithography (SLA), acoustic, and magnetic have been used to accomplish the desired constructs [22, 148]. Extrusion-based bioprinting of donut-shaped hiPSC-derived hepatoorganoids using alginate/pluronic F-127 bioink retained the liver functions after 18 days of culture [149]. Further, hepatoorganoids bioprinted with HLCs remained stable for up to 10 days and expressed hepatic markers, transporters, and phase I enzymes, paving the way for drug toxicity assessment [150]. Another study showed that extrusion-based bioprinting of hepatoorganoids using HepaRG cells differentiated after 7 days of culture and presented glycogen storage, albumin secretion, and drug metabolism [151]. Transplantation of these organoids into the abdominal cavity of Fah-deficient mice showed functional vascular systems, drug metabolism activities, increased synthesis of liver-specific proteins, and prolonged the survival of mice with liver failure [151]. Nevertheless, bioprinting constructs mimicking the functional units of liver lobule are challenging. Very few research works focused on bioprinting an *in vitro* liver lobule model recapitulating the structural and biological features of the native liver for applications such as drug screening and disease modeling.

Ma *et al*. generated a 3D bioprinted liver lobule platform consisting of physiologically relevant hexagonal units of hiPSC-derived HLCs and supporting cells with endothelial

mesenchymal cells using digital light processing (DLP)-based bioprinting [152]. Following 7 days of bioprinting, hepatic triculture demonstrated cell reorganization in their designated patterns and enhanced albumin synthesis, urea secretion, and drug-metabolizing markers [152]. In another study, Kang *et al*. employed extrusion-based bioprinting and sodium alginate, Atelo-collagen, and gelatin as bioink to bioprint a hepatic lobule structure (1 mm) embedded with HepG2/C3A and human umbilical vein endothelial cell line including a central vein of 150 μm [153]. The hepatic lobule structure showed protein levels of albumin, multidrug resistance-associated protein 2 (MRP2), CD31, and activities of CYP3A4 and CYP1A1 over 7 days, and further assessed for hepatotoxicity prediction using Amiofarone [153]. In another study by Hong *et al*., structured multicellular spheroids laden with HepG2/C3A and human umbilical vein endothelial cell line resembling lobule-like structures were generated following a unique technique combining extrusion bioprinting and microfluidic emulsification systems [154]. The structured multicellular spheroids with a higher resolution of 20 μm and structural integrity showed enhanced MRP2, albumin, and CD31 expression and were successfully engrafted with increased viability and vascular network over 2 weeks [154] **(Figure 1.3)**. A multiscale perfusable liver lobule-like microvasculature composed of hexagonal endothelialized channels, a radial bridge pattern with angiogenic sprouts, and a dotted normal human dermal fibroblasts pattern was bioprinted by applying a gradient of angiogenic factors along the bridge pattern [155]. The manual loading of primary mouse hepatocytes-laden fibrin hydrogel into the microvasculature followed by culturing for 3 days generated a vascularized liver tissue with improved liver functions compared to constructs without a capillary network [155].

Bioprinting has several challenges: (i) choosing a bioactive biomaterial containing biophysical and biochemical cues that enable printability and cell adhesion, (ii) vascularization, (iii) complex patterning of heterocellular types, and (iv) maintaining functionality for a longer period.

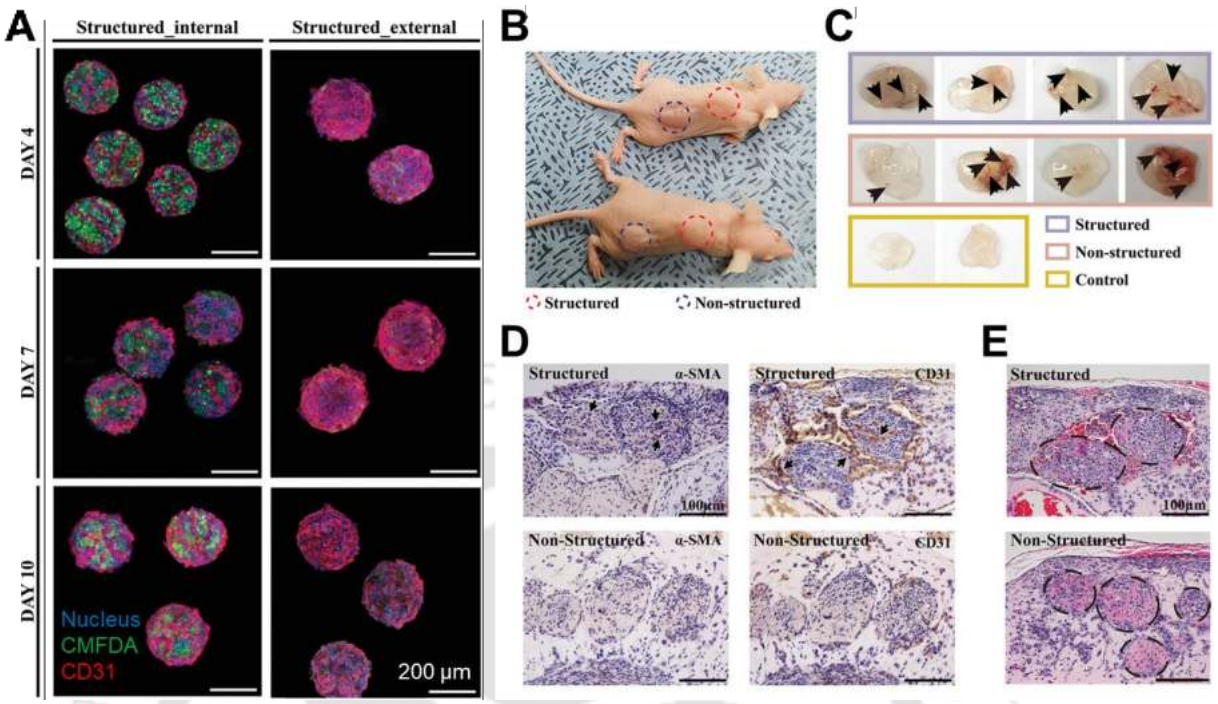

Figure 1.3. Bioprinting of multicellular hepatic lobule-like structured spheroids and subcutaneous transplantation of bioprinted spheroids. *(A) External and internal morphology of structured spheroids maintaining structural integrity on 4, 7, and 10 days. (B) Subcutaneous injection of structured spheroids encapsulated in Matrigel. Explants of matrigel sections of structured and non-structured spheroids showing (C) Blood vessel formation. (D) Immunohistochemical images of α-SMA and CD31. (E) H&E images. Reprinted (adapted) with permission from [154] under Creative Commons Attribution-NonCommercial-NoDerivs License.*

1.5.2 Physiologically relevant microfluidic liver on a chip models

The microfluidic liver-on-a-chip (LOC) platform holds great potential in replicating the physiologically relevant liver lobule microarchitecture in respect of sinusoidal structure, multicellular arrangement, hepatocytes-NPC communication, and fluid dynamics while fabricating functional liver constructs [156]. Microfluidic LOC devices, also designated as microphysiological systems, provide ECM, chemical concentration gradients, biophysical cues, and mechanical stimulations with high sensitivity and precision, and have been envisaged for disease modeling and drug screening [157]. Numerous fabrication approaches such as micro-cutting, ultrasonic machining, energy-assisted methods, laser fabrication, lithography, 3D printing, injection moulding, roller embossing, microthermoforming, and mould fabrication on curved surfaces have been employed for developing microfluidic devices with each having characteristic features [158]. The LOC devices aim to simulate liver sinusoid, liver lobule, and zonation present

in vivo [159]. These microfluidic LOC devices have shown advantages in reducing the cost, cell number, and reagents and possess wide biomedical applications in drug screening, disease modeling, and liver regenerative medicine by increasing the efficiency for translation into product [156, 158].

A dual microchannel liver sinusoid model co-cultured with primary rat hepatocytes and bovine aortic endothelial cells under continuous perfusion maintained morphology and produced urea for up to 30 days. The sinusoid model was also extended to develop Hepatitis B-induced liver disease model [160]. In another study Mi *et al*., a biomimetic liver sinusoid on a chip was constructed by injecting HepG2-laden collagen gel and HUVECs-laden collagen gel by taking advantage of laminar flow [161]. The liver sinusoid on a chip maintained liver functions for 7 days and showed benefits for hepatotoxicity prediction [161]. Banaeiyan *et al*. developed a liver lobule on a chip (LLOC) device by incorporating hexagonal tissue-culture chambers with a diameter of 1.2 – 2.4 mm and a central outlet simulating the central vein for seeding hiPSC-derived HLCs [162]. However, the structure specificity, oxygen gradient concentration, and perfusable sinusoid networks in LOC models are limited. Multiple liver lobules with self-assembled perfusable hepatic sinusoid networks as well as physiologically relevant oxygen concentrations were designed by reconstructing a flow-guided angiogenesis technology to form radiating hepatic sinusoids [163]. The primary liver cells comprising hepatocytes, LSECs, HSCs, and KCs were encapsulated in collagen and loaded into the cell co-culture zone to generate liver constructs that maintained metabolic activity and albumin secretion over 14 days [163] **(Figure 1.4)**. Heart-liver microfluidic chip system with a synthetic Start-M skin surrogate developed by Mello *et al*. improved the drug toxicity prediction following acute and chronic drug exposure by resembling dermal absorption and transport dynamics through the skin barrier [164]. The LLOC reproducing dual blood supply through the hepatic portal vein and the hepatic artery was developed for modeling NAFLD [165]. The co-culture of fibrinogen-laden HepaRG, LX-2, and human LSECs over 14 days in LLOC exhibited high viability and formed hepatic microtissues with vascularized sinusoid, endothelial fenestrations, and bile canaliculi network. Further, steatosis was successfully induced in the on-chip NAFLD model with lipid zonation in the liver lobule, and prevention and reversibility of drugs in the NAFLD model were investigated using obeticholic acid and elafibranor [165]. The metabolic gradients of hepatocytes in the native liver lobule occur from the zone-1 periportal region performing synthetic functions to the zone-3 perivenous region performing metabolizing

functions [5]. The metabolic patterning on a chip stemmed from microfluidic technology demonstrated a hepatocyte metabolic pattern across the cultured tissue by generating a differential concentration of modulators such as hormones, enzymes, and small molecules [166].

The LOC recreating the structure and functions of liver lobule have been highlighted for various applications; indeed, LOC models posed challenges in operation simplicity, cost efficiency, appropriate cell source, and resembling spatiotemporal anisotropy of cell-cell and cell-matrix interactions.

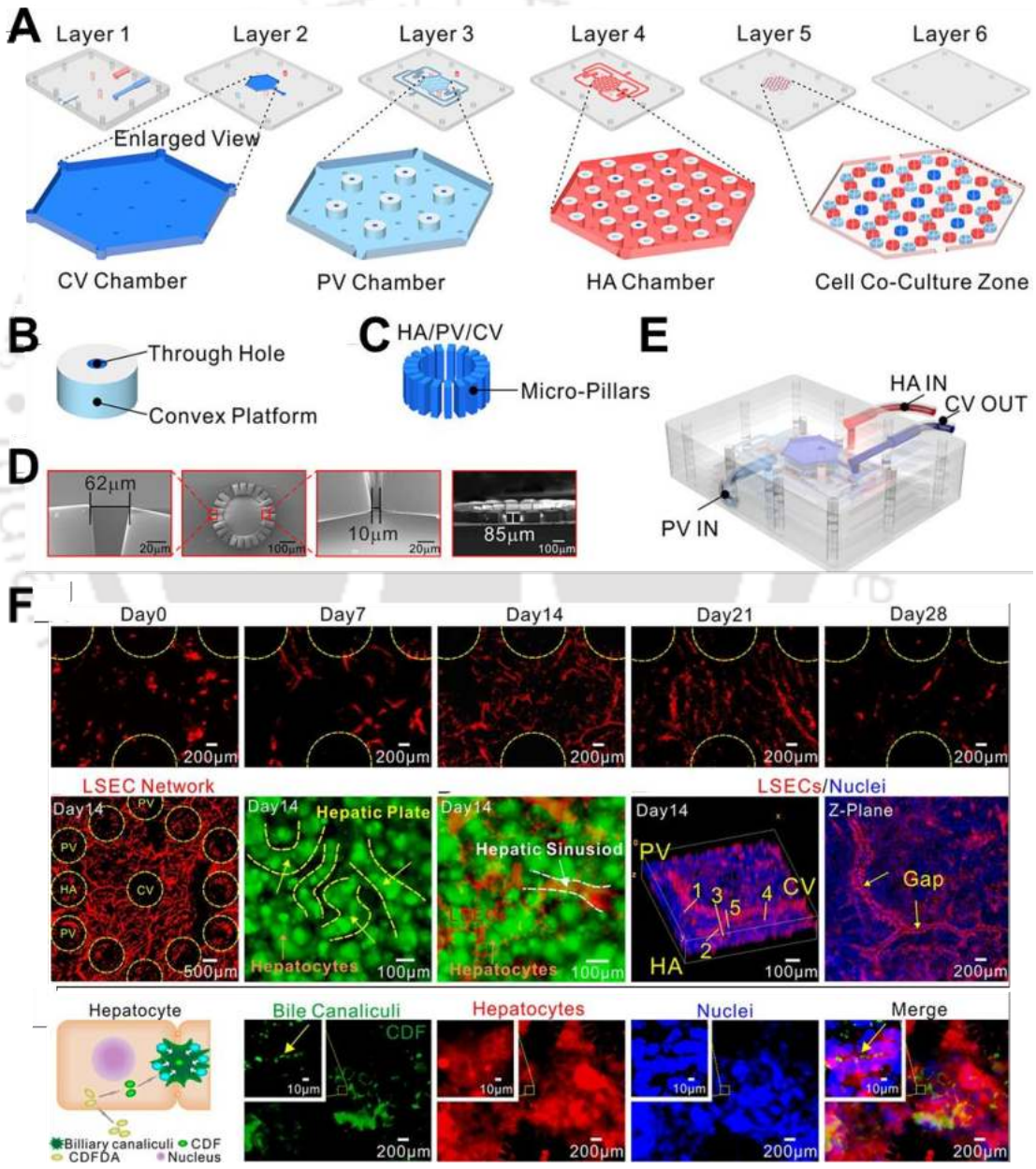

Figure 1.4. Multiple liver lobule on a chip with self-assembled perfusable hepatic sinusoids. *(A) Components of liver-on-a-chip composed of six layers. (B) Circular convex platforms through*

holes on third and fourth layers. (C) Circular micropillar arrays with HA/PV/CV on fifth layer. (D) SEM images of micropillar arrays. (E) Assembled LOC. (F) Assembled LOC with sinusoid formation, hepatic plates, hepatic sinusoids, perfusable channels connected to CV, and bile canalicular network. HA: hepatic artery, PV: portal vein, CV: central vein (CV). Reprinted (adapted) with permission from [163]. Copyright 2021 American Chemical Society.

1.5.3 Culture systems

Perfusion bioreactor culture and supplementation of bioactive molecules, including growth factors, cytokines, and peptides, offer the advantages of flow dynamics, mechanical stimulation, intercellular signaling, and culture medium as in the native environment. The emerging bioprinted liver models and LOC models, in combination with bioreactor culture, facilitate the control of oxygen concentration, shear stress, mass transport with continuous perfusion of nutrients and removal of metabolites and have great potential in translational medicine. Maturation of the constructs in any bioreactor aims to provide vascularization by enabling continuous perfusion of nutrients and influencing cell signaling [167]. Compared to static cultures, bioreactor culture supported cell survival and mature hepatic metabolic functions over an extended period [32]. Flat plate, hollow fiber, perfused bed, packed bed, and encapsulation are the principal bioreactors used for liver tissue engineering. A packed bed bioreactor was developed for BAL applications, wherein the biocompatible gelatin and gum arabic hybrid scaffold loaded with functionally active hepatocytes acted as a biological compartment and as a matrix for hepatocyte culture [168]. For drug toxicity testing applications, double well vertical-flow bioreactor array [23] and stirred-tank bioreactors [169] under perfusion operation mode were developed to support and maintain the liver-specific functions over 2 weeks culture period. A custom-designed perfusion bioreactor designed by Sassi *et al*. allowed the whole organ upscale, and supported the functions (albumin production and expression of CYP enzymes) of cultured PHH in decellularized rat whole liver bioscaffold and longitudinal non-invasive analysis up to 30 days [32]. Further, the nutrient distribution characteristics by cell-seeded porous scaffolds in a bioreactor culture were analyzed experimentally using the combination of residence time distribution and computational fluid dynamic simulation to understand the effect of mechanical stimulus on the growth of hepatocytes [170]. Lee-Montiel *et al*. developed an improved model of human liver acinus microphysiology systems recreating the liver sinusoid physiology by controlling the 3D matrix and oxygen tension [107]. The zone-1 and zone-3 microenvironments were established by maintaining a flow rate of 15 µL/h and 5 µL/h to achieve oxygen tension comparable to periportal and pericentral region,

respectively. The liver acinus models demonstrated zonation-dependent functions of albumin, urea, A1AT secretion, and oxidative phosphorylation, followed by assessed for generating steatosis model and determining acetaminophen toxicity [107].

The supplementation of various growth factors, natural extracts, and cytokines has been reported to modulate hepatocyte growth and attenuate liver injury [171]. The LECM scaffold immobilized with HGF promoted hepatocyte migration and functions in cultured primary rat hepatocytes [172]. Similarly, intrahepatic implantation of scaffolds loaded with a combination of HGF, epidermal growth factor (EGF), fibroblast growth factor (FGF) 1, FGF 2, and LECM into animals following partial hepatectomy modulated growth and regeneration over seven days [173]. Recently, extracts from the honeyberry plant showed advantages in mitigating NAFLD in an animal model [174]. Among various growth factors, FGF 2 has been shown to regulate HSCs function and inhibit HSCs activation by interacting with FGFR 1 expressed on activated HSCs [175]. In a recent study by Kurniawan *et al*., human FGF 2 was conjugated to dextran-coated superparamagnetic iron-oxide nanoparticles (FGF2-SPIONs) to enhance the half-life and stability of FGF 2, and attenuate TGF-β1 induced LX-2 activation, migration, and contraction *in vitro* [171]. Further, the therapeutic potential of FGF2-SPIONs assessed in the CCl_4 induced ALF mouse model significantly reduced alanine transaminase (ALT) levels, collagen I, and F4/80 positive macrophages, improved hepatocyte proliferation, and promoted liver regeneration [171]. Despite the great progress in the scaffold fabrication and culture systems, the requirement of a higher number of primary hepatocytes, media, and recapitulating essential liver functions in *in vitro* liver models is still limited.

1.6 Liver models: Applications and challenges

1.6.1 Bioengineered liver tissue models for extracorporeal bioartificial liver devices

Extracorporeal BAL support systems comprising functional hepatocytes are the external bioreactors and constitute one of the promising alternate solutions to carry out the lost liver metabolic functions in patients with end-stage liver cirrhosis due to the limited availability of healthy organ donors and tissue engineering liver transplants [176]. BAL is integrated with hollow fibers to perform plasma perfusion and acts as an eventual liver support system for many clinicians and researchers [177]. Acellular components in BAL encompass a scaffold matrix, a chamber for cell seeding, and capillary networks for supplying nutrients and gas essential to support cell viability and cell signaling [176, 177]. Most BAL support systems employ primary porcine

hepatocytes and immortalized human hepatocyte cell lines (HepG2, HepaRG, C3A) [178-180]. Pertinently, the cellular components should allow the exchange of nutrients, oxygen, and metabolites and satisfy the minimal functional requirements of gluconeogenesis, ureagenesis, enzymatic detoxification, drug metabolism, synthetic functions, and blood protein synthesis [8, 20].

The bioreactor designs such as hollow fiber bioreactor, packed bed bioreactor, perfused bed bioreactor, and flat membrane bioreactor are being assessed for their utility in BAL [181]. Till now, the commercially available BAL devices in the market are HepatAssist, Extracorporeal Liver Assist Devices (ELAD®), Amsterdam Medical Center-Bioartificial Liver Device (AMC-BAL), Modular Extracorporeal Liver Support (MELS), and Bioartificial Liver Support Systems (BLSS). HepatAssist, AMC-BAL, and BLSS use porcine hepatocytes, and only MELS uses human hepatocytes; indeed, ELAD uses HepG2/C3a cells [8]. In HepatAssist (Arbios, Waltham, WA), the patient's plasma was separated by plasmapheresis, passed through an activated charcoal (cellulose-coated) filter and an oxygenator, and then circulated through cryopreserved porcine hepatocytes in the extracapillary space of a modified hollow fiber module to perform liver functions [182, 183]. Similarly, the plasma is passed through the hemodialysis cartridge containing C3A cells in the extracapillary space of ELAD (Vital Therapies, San Diego, CA) to perform gluconeogenesis, ureagenesis, protein synthesis, and drug metabolism for longer periods [184, 185]. However, the plasma is in direct contact with the hepatocytes cultured in nonwoven polyester fibers in AMC-BAL (Academic Medical Center, Amsterdam, The Netherlands), enabling direct cell-plasma contact with only one barrier [186, 187]. BLSS (ExcorpMedical, Minneapolis, MN) employs patients' whole blood and houses porcine hepatocytes within hollow fibers separated by a cellulose acetate bioreactor membrane from blood [8]. Nevertheless, MELS (Charite, Berlin, Germany) is comprised of primary human hepatocytes and was designed by combining different extracorporeal medical devices, wherein two dialysis modules perform venovenous hemodiafiltration and remove albumin-bound toxins [187, 188]. Herein, hollow fiber membranes and hydrophobic membranes were interwoven into four independent 3D compartments supporting oxygenation, carbon dioxide elimination, perfusion of patient's plasma, seeding of functional hepatocytes, and enabling an effective exchange of nutrients and metabolite removal [181, 188]. Therefore, it is pivotal to develop a bioactive functional 3D scaffold for BAL to create a uniform environment for maintaining functional hepatocytes and for scale-up. A freeze-dried 3D

chitosan/gelatin scaffold was developed for the BAL platform facilitating hepatocyte adhesion, proliferation, albumin expression, and ureagenesis over one week [189]. Bonalumi *et al*. designed a multilayered bioreactor with stacked cryogel discs, wherein RGD-containing p(HEMA)-alginate cryogel was modified with alginate and RGD to overcome fouling and increase hepatocyte adhesion, respectively [190]. The developed cryogels improved the exchange between the cultured hepatocytes and perfused blood, and augmented hepatocyte adhesion, cell viability, and metabolic functions. Further, assessment in *in vivo* bile-duct ligation rat model improved its safety and blood biochemistry [190].

BAL support systems are expensive and are limited by reliable cell sources, risk of xeno-infection, metabolic incompatibility, and large requirements of cells (~10 billion), which is almost 10% of total liver mass. Likewise, maintenance of hepatocyte aggregate culture in high-density culture and preservation of liver-specific synthetic and detoxification functions for an extended period is decisive [191]. Recent advancements in stem cell technology show promising cell sources in clinical-scale BAL devices enabling researchers to utilize MSCs and hiPSCs to generate functional hepatocytes in the future.

1.6.2 Bioengineered liver tissue models for hepatotoxicity prediction

The drug development process starts with drug identification to *in vitro* validation, followed by lengthy and expensive preclinical and clinical investigations that have been estimated to cost approximately 1 billion dollars and take 10-15 years [192]. The utilization of experimental animal models in pharmaceutical and industrial research in the drug discovery process fails to meet the ends as they are not predictive modalities for human hepatotoxicity response [193]. However, drug withdrawal after drug approval occurs due to adverse drug reactions and organ-specific toxicity, and the most frequent cause is associated with hepatotoxicity and drug-induced liver injury (DILI) [194]. Therefore, there is a need to develop better *in vitro* liver model platforms for drug-induced hepatotoxicity prediction that can be applied in the pharmaceutical industry in the new drug development.

In recent years, a considerable effort has been made in bioprinted liver models and LOC models to create miniature structures that resemble the spatiotemporal arrangement and physiology of the human liver. These *in vitro* liver models have been organically incorporated into the drug development pipeline from early drug discovery to preclinical screening that replaces animal testing. A multicellular bioprinted liver model manufactured by Organovo (San Diego, USA) with

a thickness of 250 µm retained the compartmentalization of PHH and NPCs [195]. The bioprinted liver tissue showed collagen deposition, produced ECM during vasculogenesis, and sustained basal expression of CYP enzymes over 28 days. The potential of bioprinted liver tissues in hepatotoxicity prediction was assessed by testing the effect of Levofloxacin and idiosyncratic drug Trovafloxacin at various drug concentrations following 7 days of dosing. Trovafloxacin significantly decreased the albumin and ATP at all doses; however, Levofloxacin showed decreased albumin only at a higher dose of 100 µm [195]. A grid-shaped bioprinted construct laden with HepaRG in an alginate/gelatin/Matrigel-based hydrogel showed a dose-dependent toxicity effect after treatment with aflatoxin B1 and survived up to 3 weeks compared to a 2D HepaRG culture [196]. In another study by Gori *et al*., the bioprinted constructs laden with HepG2/C3A cells in a thermoresponsive hydrogel maintained liver-specific functions and demonstrated increased sensitivity to the well-known hepatotoxic drug acetaminophen [197]. Both bioprinting and organoid technology were employed by Bouwmeester *et al*. to generate bioprinted constructs using intrahepatic cholangiocyte organoids embedded in a gelatin-based hydrogel, wherein the hepatic differentiation was started directly after bioprinting [150]. After 10 days of differentiation, the bioprinted human organoids showed increased expression of albumin, CYP3A4, hepatocyte nuclear factor 4α (HNF4α), argininosuccinate synthase (ASS), and multidrug resistance protein 1 (MDR1) revealing the differentiation and polarization of liver organoids. Further, the bioprinted humanized testing platform exposed to acetaminophen for 72 h allowed accurate hepatotoxicity prediction with a decreased cell viability and increased miRNA-122 expression [150]. Among different emerging strategies, microfluidic technology provides high-precision and recreates the liver lobule environment, including the nutrient flow and removal of metabolites, so the combination of microfluidic technology with bioprinting formed advanced *in vitro* liver tissue for drug screening [198]. The bioprinted hepatic spheroids comprising HepG2/C3A cells suspended in gelatin-based hydrogel were patterned directly into the microfluidic device, and LOC showed increased bioactivity and acetaminophen-induced hepatotoxicity prediction similar to animal models [198]. Ma *et al*. designed a biomimetic liver lobule-like microfluidic chip with a radially patterned network of hepatic cords and hepatic sinusoids and primed it with a collagen-I overnight for loading HepG2 cells and human aortic endothelial cell line at the desired position [199]. These microtissues maintained higher expression of phase I/II drug metabolism enzymes (CYP1A2 and uridine 5'-diphospho-glucuronosyltransferase) and analyzed the hepatic drug metabolism of

acetaminophen, rifampicin, and isoniazid [199]. The conventionally available OrganoPlate 2-lane (Mimetas, The Netherlands) liver-on-a-chip comprising co-cultures of hiPSC-derived iCell 2.0 hepatocytes (iHep), differentiated THP-1, and immortalized human microvascular endothelial cell line at a ratio of 5:5:1 was validated to screen hepatotoxicity using 159 compounds [200]. Over treatment with 180 µm Troglitazone for 72 h, the iHep viability, iHep nuclear size, albumin secretion, and urea level of OrganoPlate LiverTox model compared with vehicle control were assessed to yield robust Z' factor analysis to determine endpoints for hepatotoxicity prediction. Further, experimental evidence of 159 test compounds revealed that 34 out of 159 screened compounds were toxic by Toxicological Prioritization score, and the OrganoPlate LiverTox model provided a robust, high-throughput model to predict immune-mediated hepatotoxicity [200].

Tremendous progress has been made in developing physiologically relevant *in vitro* liver microtissues for drug screening applications; indeed, these platforms fail to emulate the physiological crosstalk between the tissue-resident KCs, HSCs, and hepatocytes and predict chronic drug dosing over prolonged periods by reducing the cost and time

1.7 Commercially available *in vitro* liver models

Advances in tissue-engineered technologies and cell culture methodologies have facilitated the commercial availability of liver model systems for drug toxicity assessment and disease modeling. The use of primary human hepatocytes (both fresh and cryopreserved) in most liver models afford several advantages, including increased compatibility, CYP450 activity, and major metabolic functions as in the native liver. Visikol, Emulate, CN-BIO Innovations, and MIMETAS companies have adopted microfluidic technology to design HµREL® Micro Livers, Emulate Liver-chip, PhysioMimix™ Liver-on-a-Chip, OrganoPlate®, respectively that recapitulate the vascularization, flow pattern, and liver acinus. Furthermore, 3D InSight™ Human Liver Microtissues, ExVive™ 3D Bioprinted Human Liver Tissue, Emulate Liver-chip, PhysioMimix™ Liver-on-a-Chip, and OrganoPlate® employed liver-specific NPCs facilitating the cellular crosstalk. Herewith, we have discussed commercially available *in vitro* tissue-engineered liver models in the market and their application with the employed cell source and technology **(Table 1.3)**. These readily available liver model systems also offer a platform to study liver disease pathologies.

Table 1.3. *Commercially available in vitro liver models.*

Company/ Manufacturer	Product	Technology	Cell Source	Applications	References
BioIVT	HepatoPAC™	Micropatterned hepatocyte islands surrounded by stromal cells	PHH + 3T3-J2 fibroblasts	Drug toxicity assessment	[201]
InSphero	3D InSight™ Human Liver Microtissues	Spheroids by hanging drop method	PHH + human KCs + human LSECs	Drug toxicity assessment	[202]
Visikol	HμREL® Micro Livers	Microfluidic device and self-assembled co-cultures forming spheroids	Primary hepatocytes + stromal cells	Drug toxicity assessment	[203]
Organovo	ExVive™ 3D Bioprinted Human Liver Tissue	Bioprinted spheroids	PHH + HUVECs + human HSCs	Drug toxicity assessment	[195]
Emulate	Emulate Liver-chip	Microfluidic liver on a chip	PHH + human LSECs + human KCs + human HSCs	Drug toxicity assessment	[204]

CN-BIO Innovations	PhysioMimix™ Liver-on-a-Chip	Microphysiological system with multicellular spheroids and perfusable capillary-like flow	Human or rat primary hepatocytes + NPCs	Drug toxicity assessment and liver disease modeling	[205]
MIMETAS	OrganoPlate®	Microfluidic liver on a chip	PHH, HepaRG, hiPSC-derived HLCs, HepG2 + HSCs + KCs	Drug toxicity assessment	[200]

PHH – Primary human hepatocytes; KCs – Kupffer cells; LSECs – Liver sinusoidal endothelial cells; HSCs – Hepatic stellate cells; HUVECs – Human umbilical vein endothelial cells; HepaRG - Human bipotent progenitor cell line; hiPSC – Human induced pluripotent stem cells; HLCs – Hepatocyte-like cells; HepG2 - Hepatocarcinoma cell line; NPCs – Non-parenchymal cells

भारतीय प्रौद्योगिकी संस्थान गुवाहाटी
Indian Institute of Technology Guwahati

Motivation and Objectives of the Present Investigation

भारतीय प्रौद्योगिकी संस्थान गुवाहाटी
Indian Institute of Technology Guwahati

Motivation and Objectives of the Present Investigation

Liver regenerative medicine includes cell transplantation, microtissues, biomaterial implantation, and extracorporeal bioartificial liver support to enable the restoration of liver functions; indeed, they possess critical setbacks in clinical translation settings. The criteria for engineering 3D hepatic constructs for liver regenerative medicine are (i) cell-cell and cell-matrix interactions assisting long-term cell viability, (ii) heterotypic culture of liver cells maintaining cell functionality, (iii) long-term liver-specific synthetic, metabolic, and detoxification functions, and (iv) facilitating the regeneration of damaged tissue. Multiple aspects must be considered while designing a matrix for liver tissue engineering. A suitable 3D matrix with appropriate biocompatibility, hemocompatibility, topography, and physicochemical attributes facilitates hepatocyte aggregation, polarity, differentiation, and proliferation. Aggregate morphology of hepatocytes displayed higher functionality, emphasizing both cell-cell and cell-matrix interactions, which solely relies on the physicochemical properties of the scaffold. Further, mimicking the physiological conditions such as the use of various liver cell types, zonal distribution of the unique cell types, cytokine release, diffusion properties, cell-material interactions, and cellular crosstalks play an important role in the development of organotypic *in vitro* liver models. Some of the key pitfalls in the field of liver regenerative medicine are listed as follows:

i. Formulation and fabrication of a bioactive 3D matrix that provides biomimetic cues and influences the aggregation of cultured hepatocytes.
ii. Advancements in finding an adequate cell source and maintenance of survival, physiological, zone-specific functions, and functional phenotypes of hepatocytes for an extended period.
iii. Modulating biophysical aspects of culture systems to improve nutrient diffusion, oxygen supply, metabolites removal, and shear stress.
iv. Need for liver models resembling the complex microarchitecture, vascularization, and cellular arrangement of parenchymal and non-parenchymal cells as in the native liver.
v. Minimal inflammation, host tissue acceptance, and promoting hepatocyte regeneration upon implantation in liver fibrosis model.

The current thesis takes into consideration these challenges to develop a robust physiologically relevant scaffold matrix composed of silk fibroin and decellularized tissue-specific liver extracellular matrix (LECM) for liver tissue engineering applications. Herein, silk fibroin and LECM are chosen due to their biochemical composition, mechanical stiffness, biocompatibility, biodegradability, and hemocompatibility. Natural silkworm silk isolated from mulberry *Bombyx mori* and *Antheraea assamensis* has gained more acceptance as a biomaterial for various biomedical applications, including optical devices, implantable medical devices, tissue engineering, and drug delivery. The BM silk fibroin is a heterodimer of a heavy chain (~390 kDa), light chain (~25 kDa), a P25 glycoprotein (27 kDa) and has polyglycine alanine repeats; AA silk fibroin is homodimers of a heavy chain (~230 kDa) and has polyalanine repeats [42]. Mechanically resilient and easily processable regenerated silk fibroin solution is amenable for fabrication into diverse 2D and 3D matrices: films, microparticles, electrospun nanofibrous mats, hydrogels, scaffolds, and 3D bioprinted matrices with defined cytocompatibility and resorbability characteristics. The presence of intrinsic RGD (arginine-glycine-aspartic acid) motifs and the high mechanical strength of AA silk fibroin have riveted biomedical engineers to exploit AA as a potential biomaterial as it enhances cellular attachment and cell-matrix interactions [42, 206]. In recent years, the prominent role of LECM hydrogel in liver tissue engineering has been emerging, owing to the presence of growth factors, cytokines, and cell-secreted exosomes in LECM [207]. The LECM hydrogels have been reported to maintain the phenotype, polarity, and functions of cultured primary hepatocytes *in vitro* [47], and improve the survival of transplanted hepatocytes *in vivo*, providing a suitable matrix for liver tissue engineering [44]. Thus, the current thesis deliberates on designing a 3D matrix with biomimetic cues from LECM and AA silk fibroin supporting the long-term hepatocyte polarity and functionality for its applications in regenerative medicine for clinical translation. Various crucial facets addressed in this thesis for the development of a scaffold platform that could provide biomimetic cues, physiochemical attributes, microarchitectural features of the native liver, hepatocyte metabolic zonation, minimal inflammation, and promote hepatocyte regeneration are described in **Figure 1.5.**

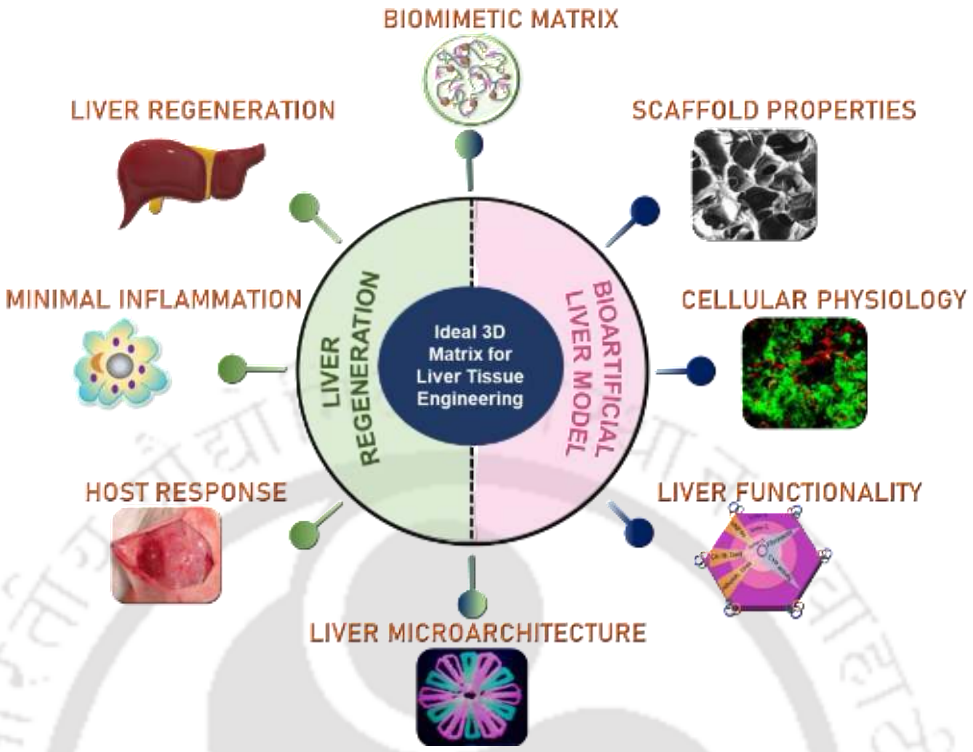

Figure 1.5. *Scheme illustrating the various crucial facets addressed in this thesis for BAL model development and liver regenerative applications.*

Different hypothetical strategies are analyzed for developing a bioactive 3D matrix for bioartificial liver and liver regenerative applications through the following defined objectives:

1. Functional hepatocyte clusters on bioactive blend silk matrices towards generating bioartificial liver constructs
2. Mimicking physiologically relevant hepatocyte zonation using immunomodulatory silk liver extracellular matrix scaffolds toward a bioartificial liver platform
3. Mimicking native liver lobule microarchitecture *in vitro* with parenchymal and non-parenchymal cells using 3D bioprinting for drug toxicity and drug screening applications
4. Silk fibroin bioscaffold from *Bombyx mori* and *Antheraea assamensis* elicits a distinct host response and macrophage activation paradigm *in vivo* and *in vitro*
5. Intraperitoneal administration of liver-derived extracellular matrix hydrogel promotes regeneration and alleviates liver fibrosis in acetaminophen-induced liver injury model

CHAPTER 2

Functional hepatocyte clusters on bioactive blend silk matrices towards generating bioartificial liver constructs

This chapter investigates the potential of a novel blend (BA) silk scaffold fabricated by blending mulberry (*Bombyx mori*, BM) silk fibroin with cell adhesion motif (RGD) rich non-mulberry (*Antheraea assamensis*, AA) silk fibroin in maintaining long-term functional hepatocyte clusters. Silk scaffolds fabricated from *Bombyx mori*, *Antheraea assamensis*, and blend present distinct physicochemical properties (surface morphology, pore size, swelling, biochemical composition). The hepatocyte adhesion, growth, and functionality were evaluated using HepG2 cells and primary neonatal rat hepatocytes. Understanding the hepatocyte-silk matrix interaction offers a befitting environment to generate functional *in vitro* liver constructs.

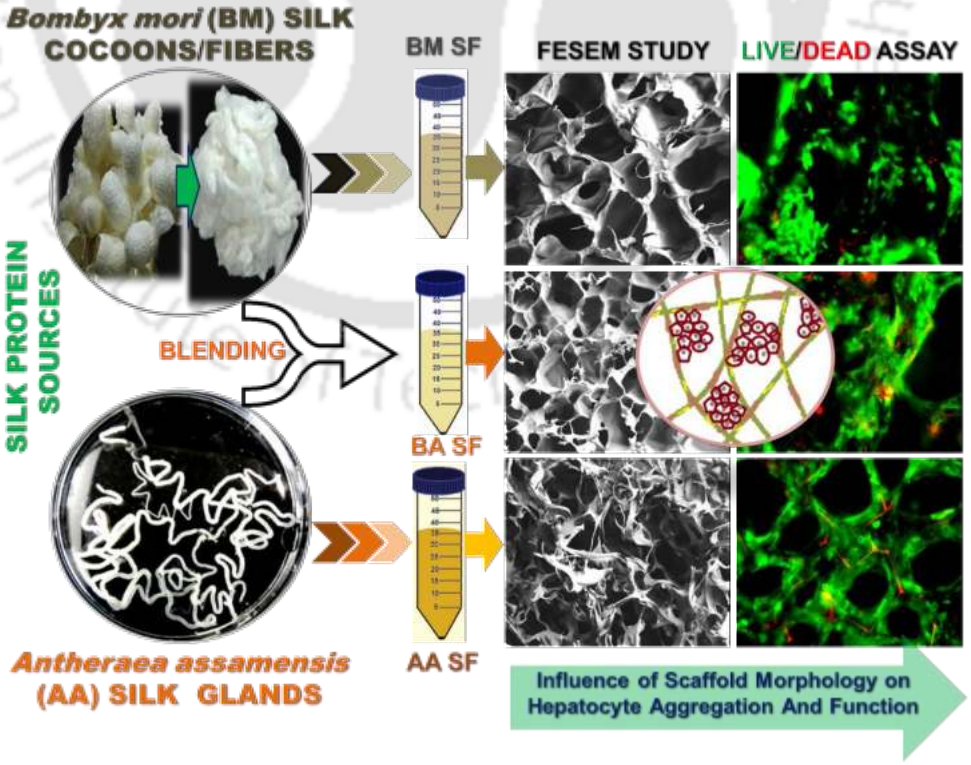

ABSTRACT

The creation of *in vitro* functional hepatic tissue simulating the micro-environmental niche of native liver is a keen area of research due to its demand in the bioartificial liver (BAL) and cell-based tissue engineering. Here, we investigated the potential of a novel blend (BA) silk scaffold fabricated by blending mulberry (*Bombyx mori*, BM) silk fibroin with cell adhesion motif (RGD) rich non-mulberry (*Antheraea assamensis*, AA) silk fibroin, in generating a functional liver construct. Three-dimensional (3D) porous silk scaffolds (BM, AA, and BA) were physicochemically characterized and functionally evaluated using human hepatocarcinoma cells (HepG2) and primary neonatal rat hepatocytes. The growth and distribution of hepatocytes within the scaffolds were tracked by FESEM, alamar blue proliferation assay, and live/dead staining. Hemocompatible BA scaffolds supported the formation of high-density hepatocyte clusters, facilitating cell-matrix and cell-cell interactions. Blend scaffolds evinced enhanced liver-specific functions of cultured hepatocytes in terms of albumin synthesis, urea synthesis, and cytochrome P450 enzyme activity over 21 days. Subcutaneous implantation of scaffolds demonstrated minimal macrophage infiltration in blend scaffolds. These findings substantiate that the integral property of the blend (BA) scaffold offers a befitting environment by influencing the spheroidal growth of hepatocytes with enhanced biological activity. Collectively, the present study provides a new 3D bio-matrix niche for growing functional liver cells that would have future prospects in BAL and regenerative medicine.

The findings of this chapter are published in a peer reviewed journal:

Janani G., Nandi S.K., and Mandal B.B. "*Functional hepatocyte clusters on bioactive blend silk matrices towards generating bioartificial liver constructs*". **Acta Biomaterialia**, 2018, *67*, 67-182.

2.1 Introduction

Liver, the largest internal organ with complex microarchitecture is highly regenerative, metabolically active, and regulates physiological homeostasis by performing over 500 functions [208]. Acute or chronic liver injury occurs due to various scenarios like hepatitis, hepatocellular carcinoma, autoimmune disorders, drug toxicity, alcoholic and non-alcoholic fatty liver disease [209]. Cirrhosis, an end-stage liver disease, affects approximately 10% of the world's population and is estimated to be the 12th leading cause of mortality in 2020 [210, 211]. Cirrhosis is characterized by necroinflammation, portal hypertension, and fibrotic tissue formation perturbing the normal physiological functions and self-healing ability of the liver [210]. In India alone, the total liver transplants performed till 2016 was around 7500, with higher than 75 liver transplants per annum in each of the seven major liver transplantation centers [212]. Organ transplantation is limited by immune rejection, high cost, and scarcity of healthy donors resulting in 50 million deaths annually (World Health Organization) [213]. Alternate approaches, such as extracorporeal liver support systems (ELSS), and cell and tissue engineering-based therapies have been studied to overcome the above-mentioned limitations. Artificial liver dialysis units like Molecular Adsorbent Recirculating System and Prometheus are FDA (Food and Drug Administration) approved and attempts to eliminate toxins and protein bound substances from the plasma, still they fail to achieve essential cell-based synthetic and metabolic functions [214]. Hepatocyte loaded bioartificial liver (BAL) system acts as a 'clinical bridge' by performing hepatocyte specific functions and convalescence of damaged liver [50]. To achieve enhanced hepatocyte-specific functions, hepatocyte spheroid culture in a suitable niche mimicking *in vivo* cuboidal geometry of liver cells exhibiting high cell-cell interaction was employed in recent BAL device configurations like modular ELSS [16, 215, 216]. Strategies like the incorporation of galactose [114, 217], blood compatible polymers [50], PLA (Polylactic acid) coating over collagen [218], and co-culture with mesenchymal stem cells [219] have been explored to establish hepatocyte aggregate culture. However, long term maintenance of functional hepatocytes was not achieved. Thus, matrix design considering both material properties and cell-matrix interactions is essential to bring improvement in the cellular component of BAL systems.

Matrix for culturing hepatocytes should be highly porous and mechanically stable, where nutrient and metabolite diffusion occurs through convection, supporting high cell growth and migration [220]. Scaffold-based hepatocyte culture in polyethylene glycol hydrogel with

micropatterned polycaprolactone fibers [221], 3D porous polystyrene scaffolds [222], composite silk/gelatin scaffolds [223], and decellularized liver hydrogel [224] assisted in achieving high cell density. Amalgamated chitosan/galactosylated hyaluronic acid/heparin matrices induced hepatocyte clusters with enhanced liver functions over 2 weeks [225]. Similarly, fibronectin coating over a 3D collagen scaffold enhanced albumin synthesis and cytochrome P450 activity [226]. Further, primary hepatocyte culture signifies the physiologically relevant system for ELSS by accomplishing the major liver functions [114]. Maintaining the differentiated hepatic phenotype and long-term functions of primary hepatocytes have been a major goal [227]. Therefore, the criteria for designing a scaffold for liver tissue engineering include tunable porosity, low shear stress, mechanical stability, hemocompatibility, and promoting high cell-cell interactions followed by cell attachment [228]. Current research focuses on fabricating a readily available and biocompatible matrix that retains better hepatocyte functionality through a scaffold-based biomimetic approach to exploit in BAL devices.

Silk, a highly explored natural biomaterial, possesses valuable bioactive properties like tunable mechanical strength, non-thrombogenicity, biocompatibility, and the ability to acquire micro molded formats [41, 229]. Several reports have demonstrated the applicability of silk scaffolds in tissue regeneration. Silk fibroin composite scaffolds exhibit high potential as a wound dressing material by accelerating skin regeneration through regulated extracellular matrix (ECM) deposition [230, 231]. Recent reports elucidate the effect of BM nanoridges towards *in vitro* differentiation of mesenchymal stem cells (MSCs) into osteoblasts and *in vivo* bone tissue formation without additional factors [232]. Further, regenerated BM silk matrices seeded with MSCs assisted in liver regeneration in an acute liver failure rat model along with enhanced angiogenesis and formation of bile canaliculi over a period of 3 months [118]. To date, porous scaffolds fabricated from BM silk fibroin blended with collagen [233], chitosan [234], and galactosylated chitosan [235] guided the growth of hepatocytes. Similarly, non-mulberry silk *Antheraea assamensis* (AA) is known to provide additional advantages due to its intrinsic RGD motif that has been found role in promoting cell attachment and proliferation [236]. Growth and proliferation of HepG2 cells on AA cryogels were studied [237]. However, an extensive study on functional attributes of primary hepatocyte culture on silk-based scaffolds has not yet been explored.

Hepatocytes are majorly anchorage-dependent cells, and modulating the cell-matrix interactions aids in maintaining primary hepatocellular clusters [218]. As primary hepatocyte clusters retain their differentiated state, the potential of silk scaffold in maintaining long-term functional hepatocyte clusters has been investigated in the present study. The current study focuses on (i) blending mechanically resilient RGD containing AA with BM to fabricate a 3D porous scaffold (BA) and (ii) assessing the potential of a developed 3D silk construct (BM, AA, and BA) in supporting hepatocyte adhesion, growth and functionality by culturing with HepG2 cells and primary neonatal rat hepatocytes over 3 weeks. Furthermore, scaffolds were physicochemically characterized, and metabolic functions such as albumin secretion, urea synthesis, and cytochrome P450 activity were analyzed for their potential application in BAL devices.

2.2 Materials and methods

2.2.1 Silk fibroin isolation

Silk fibroin solution was extracted from the BM cocoons and silk glands of AA, as mentioned in the earlier protocols [231, 238]. Briefly, BM cocoons were chopped and degummed in boiling 0.02 M sodium carbonate solution to remove the sericin. The degummed fibers were air-dried and subsequently dissolved in 9.3 M lithium bromide solution at 60°C for 4 h. Regenerated BM silk fibroin solution was acquired by performing dialysis against Milli-Q water for 48 h using a molecular weight cutoff (12 kDa) dialysis membrane. Similarly, silk glands from the 5th instar AA silkworms were harvested and squeezed in an aqueous environment to extrude the native fibroin protein. Isolated protein was dissolved in 1% (w/v) sodium dodecyl sulfate followed by dialysis for 4 h at 4°C against Milli-Q water. The concentration of regenerated silk fibroin solution (BM and AA) from both the species was estimated by the gravimetric method, and final concentration of 3% (w/v) was used for further studies.

2.2.2 Silk scaffold fabrication

Three-dimensional (3D) porous silk scaffolds of three variants: (i) *B. mori* (BM), (ii) *A. assamensis* (AA), and (iii) blend *B. mori/A. assamensis* (BA) were fabricated by the freeze-drying method [229]. For preparing blend (BA) scaffolds, 3% (w/v) of BM and AA silk fibroin was mixed in an equal ratio, frozen at -20°C overnight, followed by lyophilization for 48 h. Similarly, respective 3% (w/v) BM and AA scaffolds were fabricated to assess the influence of individual silk protein on the hepatocytes. All three freeze-dried scaffolds (BM, AA, and BA) were treated

with 90% (v/v) and 70% (v/v) ethanol for 3 h and 12 h, respectively to induce β-sheets in the samples [229]. For further cell culture studies, the scaffolds were washed with Milli-Q water, autoclaved, and maintained under sterile conditions.

2.2.3 Physicochemical characterization

2.2.3.1 Field emission scanning electron microscopy (FESEM)

Surface morphology of scaffolds was analyzed through FESEM analysis (Zeiss, Sigma, USA). After 21 days of the culture period, scaffolds cultured with HepG2 cells were washed in phosphate-buffered saline (PBS, pH 7.4) to remove the cell debris and fixed in 10% (v/v) Neutral buffered formalin (NBF). Both scaffolds and cell-seeded scaffolds were dehydrated using graded ethanol (35%, 50%, 70%, 80%, 90%, 95%, and 100%), lyophilized, and sputter-coated with gold for further analysis. Samples were scanned at an applied voltage of 2.00 kV, and the acquired image was processed using Image J software (NIH, USA). Average pore size and pore wall thickness were estimated by measuring at 50 different points. Hepatocyte arrangement on cell-seeded scaffolds was further investigated from FESEM images.

2.2.3.2 Swelling behavior

The swelling behavior was examined to comprehend the nutrient uptake capacity of freeze-dried scaffolds by the gravimetric method [231]. Initial dry weight (W_1) of the scaffolds was noted, and the swelling study was executed in PBS (pH 7.4) until it reached the equilibrium swelling point. Samples were removed at regular time intervals by draining excess PBS, and the weight of the scaffolds (W_t) at time (t) was inscribed till it reached the equilibrium point. The swelling index of scaffolds was calculated from the formula,

Swelling ratio = $(W_1 – W_t)/W_1$

2.2.3.3 Mechanical strength

Compressive strength and Young's Modulus of scaffolds were estimated using INSTRON Universal Testing Machine (Model: 5944, USA) equipped with a load cell of 100 N at a cross head speed of 1 mm/min. Experiments were executed with scaffolds of equivalent size 12 mm × 12 mm (height × diameter) in PBS at ambient temperature and humidity. Four samples (n = 4) were analyzed, and the average strength of the material was calculated.

2.2.3.4 Porosity

The porosity of various silk scaffolds was measured as described in the established protocol using the liquid displacement method [239]. Hexane, a displacement solvent, was chosen as it easily permeates through pores without destructing the microarchitecture of the scaffolds. Dry scaffolds of equal size 10 mm × 10 mm (height × diameter) was immersed in a known volume of hexane (V_1) for 20 min, and the total volume of hexane along with hexane impregnated scaffold (V_2) was measured. Subsequently, the sample was removed, and the final volume of hexane without scaffold was noted as V_3. The porosity (ε) of scaffolds was determined using the formula,

$$\varepsilon\ (\%) = [(V_1 - V_3)/(V_2 - V_3)] \times 100$$

where $(V_1 - V_3)$ = Volume of hexane impregnated within silk scaffold

$(V_2 - V_3)$ = Total volume of silk scaffold

2.2.3.5 Fourier transform infrared spectroscopy

Structural transition of scaffolds due to ethanol treatment and blending of two different silk fibroin was analyzed by FTIR spectroscopy (Nicolet iS 10). Dry pellets of ethanol-treated and untreated scaffolds were prepared using potassium bromide for further examination. Absorbance values were recorded in the spectral region of 4000 to 500 cm^{-1} at a resolution of 4 cm^{-1} by an accumulation of 32 scans per spectra. The variation in the FTIR spectra of scaffolds was analyzed using Origin Pro 8 (Microcal version, USA).

2.2.3.6 Protein release study

Amount of leached out protein from various scaffolds over 28 days was assessed using the Bradford method. Scaffolds of equal weight (10 mg) were incubated at 37°C in 500 µL of PBS (pH 7.4) supplemented with 0.05% (w/v) sodium azide. After every 3 days, 20 µL of solution (PBS) containing leached out protein was collected and treated with 200 µL of Bradford reagent for 20 min. Absorbance was measured spectrophotometrically at 525 nm and the amount of unknown protein in the leached out environment was calculated from the standard curve plotted with different concentrations of respective BM and AA silk fibroin. Protein release (%) was calculated using the given formula,

Protein release (%) = $(C_2/C_1) \times 100$

where, C_1 = Initial amount of scaffold (mg)

C_2 = Amount of leached protein in the solution (mg)

2.2.3.7 *In vitro* degradation study

The *in vitro* degradation profile of scaffolds in both hydrolytic and enzymatic environments was examined over 28 days at 37°C, as mentioned in the earlier protocol [236]. Protease XIV isolated from *S. griseus* was chosen for carrying out degradation studies. Initial dry weight (W_i) of the scaffolds was measured and immersed in both hydrolytic (PBS) and enzymatic (PBS supplemented with 2 U/mL of protease) solution. At predefined time points, samples were removed and lyophilized to measure the dry weight of the sample (W_t). Enzyme solution was replenished every 3 days, and the percentage mass remaining of the scaffolds was calculated from the formula,

Percentage of mass degraded (MD) $= [(W_i - W_t)/ W_i] \times 100$

Percentage of mass remaining in the scaffolds $= 100 - MD$

2.2.4 Primary neonatal rat hepatocytes isolation

All *in vivo* studies were approved by the Institutional Animal Ethical Committee (IAEC), West Bengal University of Animal and Fishery Sciences (WBUAFS), West Bengal, India. Primary neonatal rat hepatocytes were isolated from Wistar rats (1-3 days old) of either sex according to a two-step in situ collagenase digestion method with slight modifications [114, 218]. Briefly, the harvested whole liver was washed in ice-cold Kreb's Ringer buffer solution to remove the blood clots and perfused with EGTA (ethylene glycol tetraacetic acid) containing buffer 1 at 37°C for chelation. Then, the whole liver was treated with buffer 2 containing antibiotics for 30 min followed by enzymatic digestion (buffer 3) with 0.02% (w/v) collagenase type IA (> 3.5 U/mg, Sigma Aldrich, USA) for 30-40 min. Outer capsule layer of the digested liver was removed with the help of a surgical blade and gently dispersed in ice cold 1X HBSS (Hank's balanced salt solution, Sigma Aldrich, USA) to collect the primary hepatocytes. All the buffer compositions are given in **Table 2.1**. Isolated primary neonatal rat hepatocytes were washed twice and maintained in serum-free William's E Medium (WEM) for 2-3 days allowing initial cell attachment. Harvested hepatocytes maintained >90% viability as evaluated by trypan blue dye exclusion assay.

Table 2.1. *Buffer composition used for isolation of primary neonatal rat hepatocytes*

Buffer 1

S. No.	Components	Composition (g/L)
1.	Sodium chloride	8.30
2.	Potassium chloride	0.50
3.	HEPES	2.40
4.	EGTA	0.19

Buffer 2

S. No.	Components	Composition (g/L)
1.	Sodium chloride	8.30
2.	Potassium chloride	0.50
3.	HEPES	2.40

Buffer 3

S. No.	Components	Composition (g/L)
1.	Sodium chloride	3.90
2.	Potassium chloride	0.50
3.	HEPES	2.40
4.	Calcium chloride	2.40
5.	Collagenase type IA	0.20

2.2.5 Cell seeding and culture

Hepatocarcinoma (HepG2) cells were acquired from National Centre for Cell Sciences (NCCS), Pune, India, and cultured in Minimal Essential Medium (MEM) complemented with 10% Fetal Bovine Serum (FBS), 100 U/mL Penicillin, 0.25 µg/mL Amphotericin B and 0.1 mg/mL Streptomycin. Primary hepatocytes were cultured in serum-free WEM supplemented with 0.5 µg/mL Insulin, 0.5 mg/mL Bovine serum albumin (BSA), 10 ng/mL Epidermal growth factor (EGF), 5 nM Dexamethasone, 50 mg/mL Penicillin, 50 mg/mL Streptomycin and 100 ng/mL Neomycin. Medium was replenished every 2 days, and cells were subcultured in the ratio of 1:2

once they reached 90% confluence. For cell culture studies, sterilized scaffolds were preconditioned in respective MEM and WEM medium. Prior to cell seeding, the medium in the scaffold was gently aspirated with care, making sure that the pores were not damaged to support cell infiltration. Concurrently, the hepatocytes were trypsinized, counted, seeded onto respective scaffolds and left for 3 - 4 h for initial cell attachment, followed by addition of complete medium.

2.2.6 Cell viability

Cell viability and distribution of HepG2 and primary neonatal rat hepatocytes seeded on different scaffolds were analyzed using a live/dead assay kit. After 20 days of the culture period, cell-seeded scaffolds were gently washed with PBS to remove the debris and incubated in PBS containing 4 μM Calcein–AM and 2 μM Ethidium homodimer (Sigma Aldrich, USA) for 20-30 min. Calcein-AM stains live cells green due to intracellular esterase activity, whereas, Ethidium homodimer binds with the nucleus of dead cells and stains red. Prior to live cell imaging, samples were washed with PBS, and images were acquired using a fluorescent microscope (EVOS FL, Life Technologies, USA).

2.2.7 Cell proliferation study

Proliferation rate of hepatocytes (HepG2 and primary neonatal rat hepatocytes) seeded on different scaffolds was measured at specific time points using an alamar blue dye reduction assay. Alamar blue (Invitrogen, USA), a non-toxic and cell permeable dye (blue) reduces to a highly fluorescent (pink) compound in response to the intracellular metabolic reaction. Hepatocytes were seeded at a density of 5×10^4 cells on scaffolds and cultured for 21 days with regular media changes. As per the manufacturer's protocol, hepatocyte seeded scaffolds were incubated with alamar blue along with medium in the ratio of 1:10 for 4 h in dark conditions. Absorbance of the reduced solution was spectrophotometrically measured at 570 nm and 600 nm using a microplate reader (Tecan Infinite Pro, Switzerland). Cell proliferation of both HepG2 and primary hepatocytes was normalized with day 1 value and represented in the form of arbitrary units (AU).

2.2.8 Gene expression analysis

Synthetic and metabolic functions of hepatocytes cultured on various scaffolds were examined by quantitative real-time polymerase chain reaction (qRT-PCR) (Applied Biosystems 7500, USA) at days 1, 7, 14, and 21 for HepG2 and days 1, 10, and 21 for primary hepatocytes.

Samples were lysed using TRIzol reagent (Sigma Aldrich, USA) and centrifuged at 13,000 rpm for 10 min to collect the cell lysate. Upper aqueous layer containing the RNA pool was separated by treating with chloroform. Further, RNA was precipitated using ice cold isopropanol and ethanol. For cDNA synthesis, an equal amount of RNA resuspended in RNase free water (Sigma Aldrich, USA) was reverse transcribed using high capacity cDNA synthesis kit (Applied Biosystems, Invitrogen, USA). Expression levels of liver-specific synthetic genes namely, albumin (ALB), alpha-fetoprotein (AFP), fibronectin (FIB), and detoxification gene namely, cytochrome P450 2E1 (CYP2E1) were analyzed in a real-time PCR machine (Applied Biosystems 7500) using Power SYBR Green PCR master mix (Applied Biosystems, USA). Primer sequence along with gene ID has been listed in **Table 2.2**. A denaturation program (95°C for 3 min), followed by the amplification (95°C for 15 sec) and quantification program (60°C for 30 sec) was repeated for 40 cycles. Expression level of functional genes in hepatocyte seeded scaffolds was examined by normalizing to glyceraldehyde-3-phosphate (GAPDH), housekeeping gene, and corresponding day 1 expression by $2^{(-\Delta\Delta Ct)}$ method.

Table 2.2. *Primer sequence for real-time PCR*

S. No.	Gene	Source	Sequence	References
1.	ALB	Human	F 5'-TGCTAATTTCCCTCCGTTTG-3'	[240]
	NM_000477.6		R 5'-CTGAGCAAAGGCAATCAACA-3'	
2.	AFP	Human	F 5'-AGCTTGGTGGTGGATGAAAC-3'	[240]
	NM_001134.2		R 5'-CCCTCTTCAGCAAAGCAGAC-3'	
3.	CYP2E1	Human	F 5'-CGTGGAAATGGAGAAGGAAA-3'	[240]
	NM_000773.3		R 5'-GGTGATGAACCGCTGAATCT-3'	
4.	FIB	Human	F 5'-CCATCGCAAACCGCTGCCAT-3'	[241]
	XM_017003695.1		R 5'-AACACTTCTCAGCTATGGGCTT-3'	
5.	GAPDH	Human	F 5'-GACCTGACCTGCCGTCTA-3'	[242]
	NM_001289746.1		R 5'-GTTGCTGTAGCCAAATTCGTT-3'	
6.	ALB	Rat	F 5'-GATGCCGTGAAAGAGAAAGC-3'	[243]
	NM_134326.2		R 5'-CGTGACAGCACTCCTTGTTG-3'	

7.	AFP NM_012493.2	Rat	F 5'-ACTACTTACAAAATCTGTTCCTCATTGG-3' R 5'-ATGTAAATGTCGGCCAGTCC-3'	[244]
8.	CYP2E1 NM_031543.1	Rat	F 5'-TGCGGAGGTTTTCCCTAAGC-3' R 5'-GCGCAGCCAATCAGAAATGT-3'	[245]
9.	FIB NM_019143.2	Rat	F 5'-GGATCCCCTCCCAGAGAAGT-3' R 5'-GGGTGTGGAAGGGTAACCAG-3'	[246]
10.	GAPDH XM_017593963.1	Rat	F 5'-TGACTCTACCCACGGCAAGTTCAA-3' R 5'-ACGACATACTCAGCACCAGCATCA-3'	[247]

2.2.9 Hepatic function assessment

2.2.9.1 Urea synthesis

Culture medium was collected on days 1, 7, 14, and 21 for HepG2 and on days 1, 10, and 21 for primary neonatal rat hepatocytes cultured on scaffolds and stored at -20°C. The amount of urea in the medium was estimated using a calorimetric urea assay kit (Sigma Aldrich, USA) as per the manufacturer's protocol. Supernatant was collected after centrifuging the culture medium at 1000 rpm for 5 min. Samples were incubated with an equal amount of reaction mix containing peroxidase substrate, enzyme mix, developer, and converting enzyme for 60 min followed by absorbance measurement at 570 nm. The standard curve was plotted using the urea standard (0 – 5 nmol/well), and the unknown concentration of urea in the culture medium was calculated from the given formula,

$$(S_a/S_v) = C$$

where, S_a = Amount of urea in samples (nmol) calculated from the standard curve

S_v = Volume of sample (µL) added in the wells

C = Concentration of urea in the samples

2.2.9.2 Cytochrome P450 activity

Cytochrome P450 enzyme activity of HepG2 cells and primary neonatal rat hepatocyte cells cultured on various silk scaffolds at predefined time points was measured using Cytochrome

P450 Reductase (CPR) Activity Assay Kit (Abcam, UK). Cell seeded samples were homogenized by treating with lysis buffer containing 1% Nonident P40, 2 mM Tris HCl, 10% glycerol, 13.7 mM NaCl and protease inhibitors (EDTA, Aprotinin, Phenyl methyl sulfonyl fluoride, and Sodium orthovanadate) at 4°C for 4 h. Cell lysate was treated with reaction buffer containing NADPH substrate, CPR assay buffer and 20 mM G6P for 10 min followed by absorbance measurement at 460 nm in kinetic mode for 25-30 min. Simultaneously, the cell lysate was treated with CPR inhibitor (1 mM), and the same series of steps was followed. Specific CPR activity of hepatocytes was assessed by normalizing with activity obtained along with inhibitor. The intracellular protein concentration after cell lysis was estimated using Bradford's reagent (Sigma Aldrich, USA). Finally, the concentration of CPR in the cell lysate was calculated from the standard curve using the formula,

$$\text{Total CPR Activity (mU/mg)} = (B/ (\Delta T \times P)) \text{ nmol/min/mg}$$

where, B = Amount of G6P consumed in the reaction calculated from the standard graph (Absorbance at T_2 – Absorbance at T_1)

ΔT = Reaction time in min (T_2 - T_1)

P = Total amount of intracellular protein as calculated from Bradford assay.

Pure CPR activity in sample (mU/mg) = (Total CPR activity) – (CPR activity with inhibitor)

2.2.9.3 Albumin secretion

HepG2 cells were seeded at a density of 2×10^6 on scaffolds, and secreted albumin at predefined time points (days 1, 7, 14, and 21) was measured using human albumin ELISA quantification kit (Abcam, UK) as per the manufacturer's protocol. Briefly, the culture medium was centrifuged at 500g for 10 min, and the supernatant was stored at -20°C. All the samples and reagents were equilibrated to room temperature before use. 50 µL of sample was incubated in primary antibody coated wells for 1 h. Subsequently, the sample was serially treated with 50 µL of biotinylated albumin antibody and 50 µL of streptavidin conjugate for 30 min. The reaction mixture was removed, and chromogen substrate (50 µL) was added to the wells. Stop solution was added, and absorbance was measured at 450 nm and 570 nm. Concentration of albumin in the culture medium was determined from the standard curve plotted using albumin standard (0-200 ng/mL).

2.2.10 Histology and immunohistochemistry

Scaffolds seeded with HepG2 cells were examined for cell distribution and expression of functional markers after 21 days of the culture period. Briefly, cell-seeded scaffolds were fixed in 10% NBF, dehydrated with graded ethanol (50% - 100%), cleared with xylene, followed by paraffin embedding. Scaffolds were sectioned at 5 μm thickness using a manual microtome (Leica Biosystems, USA). Thin scaffold sections were stained with Hemotoxylin & Eosin (H&E) to examine the distribution and arrangement of hepatocytes on different scaffolds. Hemotoxylin stains the nucleus purple, and eosin stains the cytoplasm pink. For immunohistochemistry, thin scaffold sections were initially permeabilized using 0.1% (v/v) Triton X-100 for 10 min and blocked using 1% (w/v) BSA for 20 min to minimize the nonspecific binding. Further, the scaffold sections were incubated for 1 h with a specific primary antibody, mouse monoclonal against human serum albumin (Abcam, UK, 1:300 dilution), and mouse monoclonal against fibronectin (Abcam, UK, 1:200 dilution). Then, the sections were repeatedly washed and incubated with FITC conjugated anti-mouse secondary antibody IgG (Sigma-Aldrich, USA) for 30 min followed by counterstaining with Hoechst-33342 (1:1000, Sigma-Aldrich, USA) to stain the nucleus. The localization of proteins (albumin and fibronectin) in the HepG2 cultured scaffolds was captured using an inverted fluorescence microscope (EVOS FL, Life Technologies, USA).

2.2.11 Hemocompatibility assay

Hemocompatibility and antithrombogenic property of scaffolds was analyzed by measuring the amount of adhered platelets on scaffolds as described in the earlier protocol [248]. Briefly, whole blood collected from healthy porcine was primed with heparin and centrifuged at 100g for 15 min to separate platelet-rich plasma (PRP). Sterilized scaffolds of equal size 6 mm × 2 mm (diameter × height) were incubated with 1 mL of PRP at 37°C for 2 h. After 2 h, the scaffolds were repeatedly washed with PBS, and Lactate Dehydrogenase (LDH) activity of adhered platelets was measured by using the LDH assay kit (Sigma-Aldrich, USA). Adhered platelets were lysed with 1% (v/v) Triton X-100 for 1 h, centrifuged at 10,000 rpm, and LDH activity of the cell lysate was measured as per the manufacturer's protocol.

2.2.12 *In vitro* inflammatory response

In vitro immunogenic response of silk scaffolds was investigated using RAW 264.7 cells (mouse macrophages) by measuring the amount of released Tumor Necrosis Factor-alpha (TNF–

α) as reported in the earlier protocol [236]. RAW 264.7 cells were cultured at a density of 6×10^4 per well, and scaffolds of equal size 6 mm × 2 mm (diameter × height) were placed in the wells. Tissue culture plate (TCP) containing 250 pg/mL of lipopolysaccharide (LPS) from *E. coli* (Sigma Aldrich, USA) and RAW 264.7 cells were considered as a positive and negative control, respectively. After 12 h of exposure to scaffolds, the culture medium was collected to quantify the TNF–α release due to immunogenic response using the TNF–α ELISA kit (Invitrogen, USA) as per the manufacturer's instructions. Briefly, the media was incubated with 50 µL of biotinylated secondary antibody for 90 min and treated with 100 µL of streptavidin-HRP solution for 30 min. Further, chromogen solution (100 µL) was added, and the reaction was stopped using stop solution. Absorbance was measured spectrophotometrically at 450 nm.

2.2.13 *In vivo* immunogenic response by subcutaneous implantation

In vivo immunogenicity and host integrity of scaffolds were investigated by performing subcutaneous implantation of silk scaffolds in swiss (I.B.) mice of either sex weighing around 30-35 g. Animal experiments were performed according to "Principles of laboratory animal care" under guidance from IAEC, WBUAFS, West Bengal, India. Prior to implantation, animals were anesthetized by giving isoflurane as an inhalant with 1-3% oxygen using a precision vaporizer, and the operative regions were wiped with 70% (v/v) ethanol. Subcutaneous pocket located on the lateral side of thoraco-lumbar region was incised (5 mm diameter), and sterile scaffolds of equal size 5 mm × 2 mm (diameter × height) were implanted. The wound region in mice was covered with non-absorbable nylon sutures, and progressive wound healing was examined regularly with due care to avoid infections. Animals were sacrificed by cervical dislocation post 2 weeks and 4 weeks, and implanted samples along with the surrounding host tissue were collected for further examination. Retrieved samples were fixed in 10% NBF, sectioned, and stained with H&E to assess the host response towards implants. To detect the immune cell infiltration, sections were stained with macrophage specific marker (CD68). Briefly, sections were permeabilized with 0.1% (v/v) Triton X-100, blocked with 1% (w/v) BSA for 30 min and stained with rabbit polyclonal against CD68 (Abcam, UK, 1:500 dilution). Further, the sections were incubated with FITC labeled secondary antibody IgG (Abcam, UK, 1:2000 dilution) followed by counterstaining with Hoechst-33342. Macrophage stained samples were mounted and visualized using an inverted fluorescence microscope (EVOS FL, Life technologies, USA).

2.2.14 Statistical analysis

Data were obtained from n = 4 samples in each experiment and stipulated as mean ± standard deviation (SD). Significance level among the samples at predefined time points was analyzed by performing Tukey's method of one-way ANOVA test. All statistical analysis was carried out using OriginPro 8 software (Originlab Corporation, USA) by considering $^{\#}p \leq 0.05$ as significant and $^{**}p \leq 0.01$ as highly significant among the groups.

2.3. Results

2.3.1 Physicochemical characterization studies

2.3.1.1 Surface morphology

Scaffold microarchitecture plays a significant role in cell infiltration, attachment, and proliferation [229]. The surface morphology, pore thickness, and pore size of fabricated freeze-dried scaffolds were analyzed from FESEM images **(Figure 2.1 A).** Scaffolds displayed a well-defined interconnected porous microstructure with the pore size ranging between 70 and 140 µm. The pore size distribution of BM, AA, and BA scaffolds ranged around 89.72 ± 15.93 µm, 113.8 ± 18.6 µm, and 105.78 ± 15.5 µm, respectively ($p > 0.05$, **Figure 2.1 B**). Cross-sectional FESEM images of scaffolds depicted smooth homogenous pores in BM scaffolds and heterogeneous fibrillar pores in AA scaffolds. Blend (BA) scaffolds displayed homogeneous pores with a fibrillar protrusion at the pore junctions. The pore wall thickness of BM, AA, and BA scaffolds was found to be in the range of 10.60 ± 4.89 µm, 12.10 ± 3.80 µm, and 13.96 ± 1.45 µm, respectively ($p > 0.05$).

2.3.1.2 Swelling behavior

Physicochemical characteristics of a material determine its water uptake behavior that aids in nutrient diffusion [239]. Swelling behavior of various scaffolds was monitored at predefined time points till it reached equilibrium **(Figure 2.1 C)**. BM, AA, and BA scaffolds swelled rapidly in 60 min with a swelling ratio of 19.51 ± 1.27, 13.02 ± 0.62, and 16.86 ± 1.11, respectively ($p \leq 0.05$). Maximum swelling ratio was observed in BM (19.62 ± 1.18) and BA (18.07 ± 0.08) scaffolds that were approximately 1.4 times greater than AA scaffolds ($p \leq 0.01$).

2.3.1.3 Mechanical strength

Matrices designed for BAL devices and *in vivo* implantation require considerable mechanical strength to withstand the physiological stress during plasma infusion. Stiffness of scaffolds was measured in terms of compressive modulus **(Figure 2.1 D).** Similarly, compressive strength was calculated in hydrated conditions, and the results are displayed in **Table 2.3**. AA scaffolds presented higher compressive strength and modulus of 22.66 ± 3.68 kPa and 25.73 ± 1.59 kPa, respectively ($p \leq 0.01$). BM scaffolds exhibited minimum compressive strength and modulus as compared to AA and BA scaffolds.

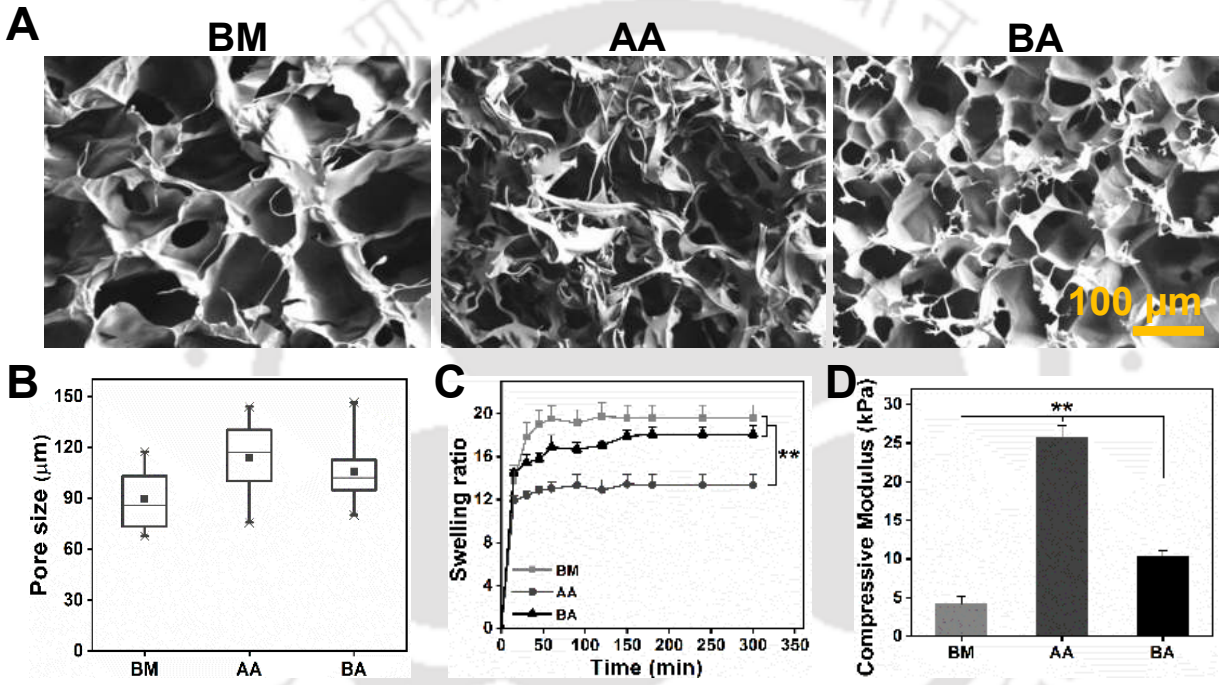

Figure 2.1. Surface morphology and physical characterization studies of silk scaffolds. *(A) FESEM images representing the microarchitecture of freeze-dried mulberry (BM), non- mulberry (AA), and blend (BA) silk scaffolds. Scale bar: 100 µm. (B) Pore size distribution analysis (C) Swelling ratio and (D) Compressive modulus of various silk scaffolds. ** signifies the statistical difference between the groups at $p \leq 0.01$.*

2.3.1.4 Porosity

Porosity, as determined by the volumetric displacement method signifies the mass transport of nutrients in scaffolds. Porosity (%) of BM, AA, and BA scaffolds is reported in **Table 2.3**, with significantly higher porosity in BM scaffolds ($p \leq 0.05$). The porosity of all freeze-dried scaffolds was found to be in the range of 88-93%, indicating the suitability of scaffolds for cell-based applications [239].

Table 2.3. *Porosity and compressive strength of silk scaffolds*

S. No.	Samples	Porosity (%)	Compressive Strength (kPa)
1.	BM	92.83 ± 0.41	12.81 ± 1.66
2.	AA	88.86 ± 0.50	22.66 ± 3.68
3.	BA	89.45 ± 0.45	8.24 ± 1.38

2.3.1.5 Fourier transform infrared spectroscopy

Characteristic absorption bands in the infrared spectrum provide information about the secondary structure of proteins, including amide I and amide II linkages. FTIR spectra of silk scaffolds in the range of 4000-400 cm^{-1} were recorded **(***Appendix* **Figure A2.1)**. The difference in the peak intensity was observed at 3460 cm^{-1} (amide A), 2920 cm^{-1} (alkanes), 1660 cm^{-1} (amide I), and 1530 cm^{-1} (amide II) for blend scaffolds as compared to BM and AA due to additional hydrogen bonding and amide linkages. Peak shift at 3500 cm^{-1} (amide A) is characterized due to the resonance between amide II and N-H stretching vibration [249]. Frequency variation observed at 2920 cm^{-1} is attributed to alkane C-H bending [249]. Secondary structure transition of ethanol-treated scaffolds (BM-E, AA-E, and BA-E) as compared to untreated scaffolds (BM, AA, and BA) was detected in the range of 1800-1000 cm^{-1} **(Figure 2.2 A).** Beta sheet induced scaffolds presented shift in vibration bands at 1620 cm^{-1}, 1514 cm^{-1} and 1230 cm^{-1} from 1650 cm^{-1}, 1540 cm^{-1} and 1240 cm^{-1} respectively. Peptide bonds (-CONH-) give rise to characteristic amide signature peaks ranging 1610-1660 cm^{-1} (amide I), 1510-1560 cm^{-1} (amide II), and 1210-1260 cm^{-1} (amide III) that is related to C=O stretching, N-H bending and C-N stretching respectively [250].

2.3.1.6 Integral stability and *in vitro* degradation studies

Integral stability of silk scaffolds was assessed by quantifying the leached out protein over 28 days **(Figure 2.2 B)**. Leached out fraction from all the three scaffold variants was found to be less than 2% (w/v) of the total scaffold which is negligible thus confirming the matrix stability. Degradation pattern of implanted bio-matrix is crucial during the repair and regeneration of host tissues [236]. The *in vitro* degradation profile of scaffolds until 4 weeks in hydrolytic (without protease) and enzymatic (with protease) environment was determined in terms of percentage mass remaining **(Figure 2.2 C)**. Silk scaffolds maintained their integrity in PBS with minimal weight

loss over 4 weeks (*Appendix* **Figure A2.2)**. However, BM, AA, and BA scaffolds in the protease environment displayed time-dependent degradation with 82%, 39%, and 65% weight loss, respectively ($p \leq 0.01$) post 28 days. Non-mulberry (AA) and blend (BA) scaffolds retained a final mass of about 3.43 and 1.97 fold greater than BM.

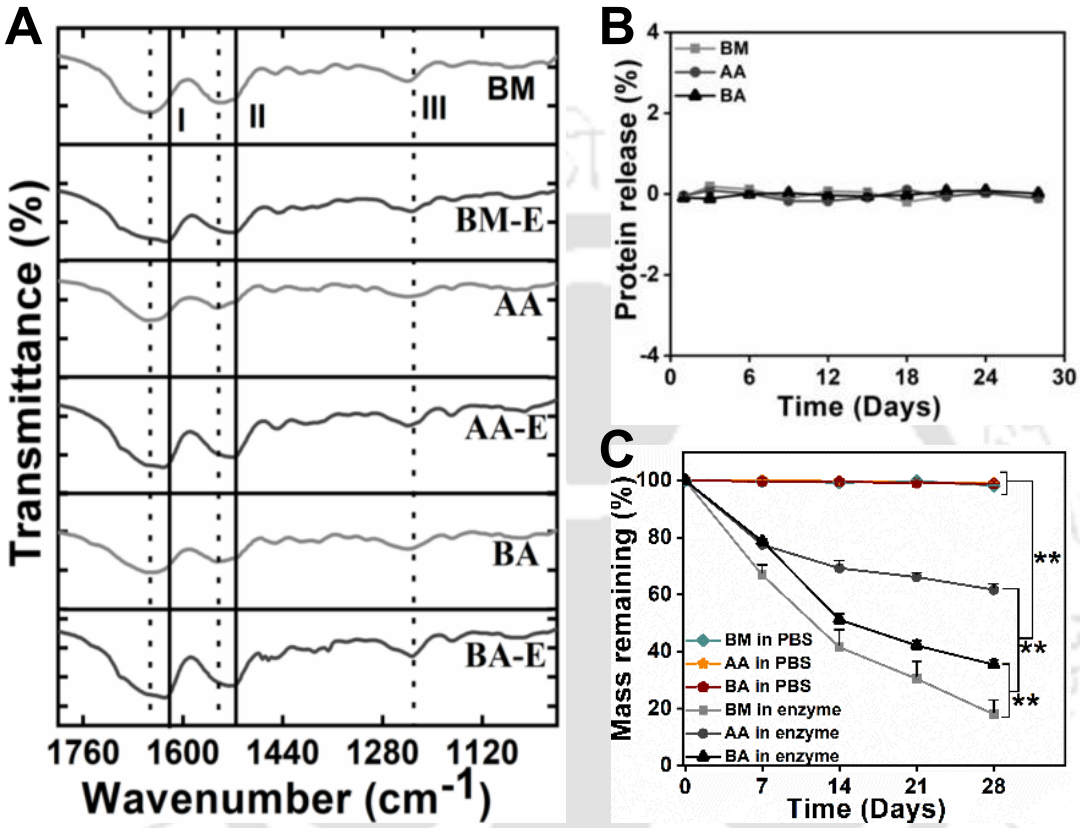

Figure 2.2. Secondary structure transition showing amide peaks and integral stability of silk scaffolds. *(A) Fourier Transform Infrared Spectra (FTIR) of ethanol-treated (BM-E, AA-E, and BA-E) and untreated (BM, AA, and BA) scaffolds over the range of 1800 – 1000 cm^{-1}, (B) Protein leaching in the presence of PBS and (C) Degradation profile of silk scaffolds over 28 days in the presence of PBS and protease XIV. ** signifies the statistical difference between the groups at $p \leq 0.01$.*

2.3.2 Cell viability and attachment studies

The potential of silk scaffolds in supporting hepatocyte attachment and growth was assessed using FESEM and live dead imaging. FESEM and fluorescent images of hepatocytes cultured on silk scaffolds over a period of 20 days are displayed (**Figure 2.3 A)**. Each variant of silk scaffold influenced the unique distribution of hepatocytes along the pore wall of scaffolds. From FESEM and live dead images, it is clearly observed that large hepatocellular clusters were

found in BM scaffolds with less cell attachment along the pores as compared to AA and BA. Whereas, hepatocytes were uniformly distributed along the pore walls of AA scaffolds due to favorable cell-matrix interaction. Blend (BA) scaffolds supported the formation of stable hepatocyte clusters exhibiting both cell-cell and cell-matrix interactions. Both HepG2 and primary hepatocytes cultured on scaffolds maintained spherical morphology and were also viable which were stained green. Few dead cells stained in red were detected in the core of cell clusters in BM and BA scaffolds.

2.3.3 Cell proliferation study

Proliferation of HepG2 cells and primary neonatal rat hepatocytes cultured on silk scaffolds (BM, AA and BA) was analyzed over 21 days **(Figure 2.3 B-C)**. After 1 week of culture of HepG2 cells on different scaffolds, AA and BA scaffolds supported high cell proliferation with respect to BM scaffolds. On day 21, HepG2 proliferated significantly in BA, about 1.38 and 1.14 fold greater than BM and AA, respectively ($p \leq 0.05$). A 2.21 fold increment in cell number was observed in BA scaffold over the culture period of 21 days. Primary hepatocytes cultured on BA scaffolds displayed 1.9 fold increment in cell number with a fold increase of 1.40 than BM scaffolds over 21 days ($p \leq 0.01$). Also, the proliferation rate of primary hepatocytes in AA scaffolds was 1.30 fold greater than BM ($p \leq 0.01$).

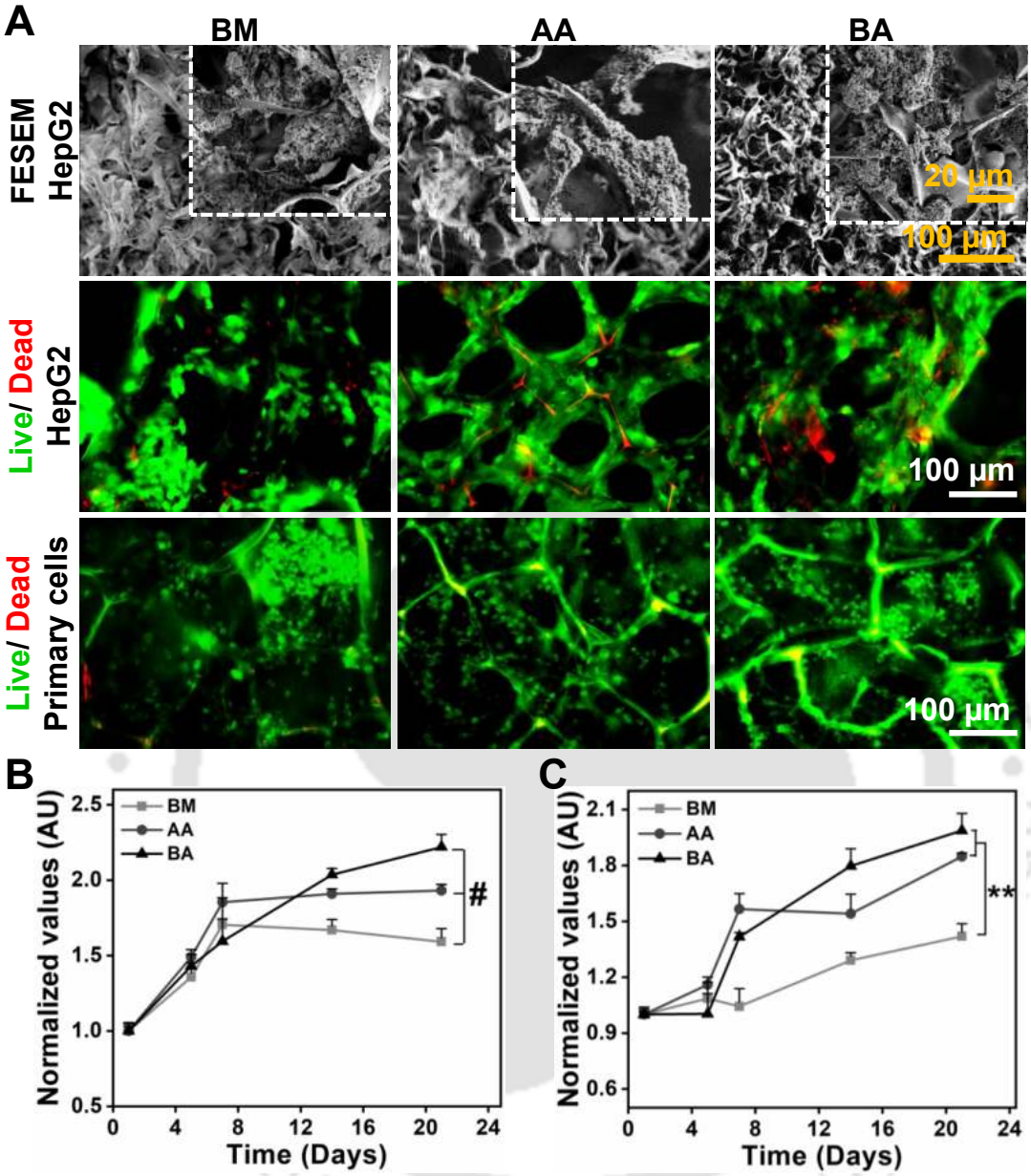

Figure 2.3. Cellular arrangement, live/dead staining, and in vitro proliferation profile of HepG2 and primary neonatal rat hepatocytes cultured on silk scaffolds. *(A) FESEM images of HepG2 cells cultured on BM, AA, and BA scaffolds. Scale bar is 100 µm and 20 µm in the main and insert image, respectively. Fluorescence microscopic images of HepG2 and primary neonatal rat hepatocytes cultured on BM, AA, and BA scaffolds stained with calcein-AM and ethidium homodimer after 20 days. Scale bar: 100 µm. Viable cells were stained in green, and dead cells were stained in red. Cell proliferation assessment by alamar blue dye reduction assay for (B) HepG2 cells and (C) primary neonatal rat hepatocytes cultured over 21 days on various silk scaffolds. Data are represented as mean ± SD. (n=4).* $^{\#}$ *and* ** *signify the statistical difference between the groups at* $p \leq 0.05$ *and* $p \leq 0.01$*, respectively.*

2.3.4 Gene expression analysis

Expression of hepatocyte specific genes encoding ALB, AFP, CYP2E1, and FIB in HepG2 and primary neonatal rat hepatocytes cultured on various silk scaffolds were analyzed at predefined time points (**Figure 2.4 and 2.5).** ALB and AFP expression levels increased gradually throughout the culture period in HepG2 cells cultured on BA scaffolds with a fold of 1.40 and 3.04, respectively compared to BM scaffolds ($p \leq 0.01$). On the other hand, expression levels of detoxification gene (CYP2E1) and ECM synthesizing gene (FIB) in HepG2 cultured BA scaffolds increased rapidly after 2 weeks and were about 1.55 and 3.09 times higher than BM scaffolds on day 21 ($p \leq 0.01$). Moreover, BA scaffolds showcased superior cell supporting potential (a fold increase of 1.25 (ALB), 1.77 (AFP), 1.22 (CYP2E1), and 2.08 (FIB)) as compared to AA scaffolds on day 21. However, the functional attributes of primary hepatocytes are strongly correlated with their morphology. Expression levels of the aforementioned markers were highest in primary hepatocytes as compared to HepG2 over 21 day culture period **(Figure 2.5)**. It was observed that BA supported significantly greater expression of ALB, AFP, CYP2E1, and FIB in primary hepatocytes with a fold increase of 1.26, 1.78, 1.94, and 1.59, respectively compared to BM scaffolds ($p \leq 0.01$). Expression of ALB and CYP2E1 on BA was increased with a fold change of 1.50 and 1.54, respectively than AA scaffolds. Hence, these results suggested that HepG2 and primary hepatocytes exhibit higher liver-specific functions on the BA scaffold than BM and AA.

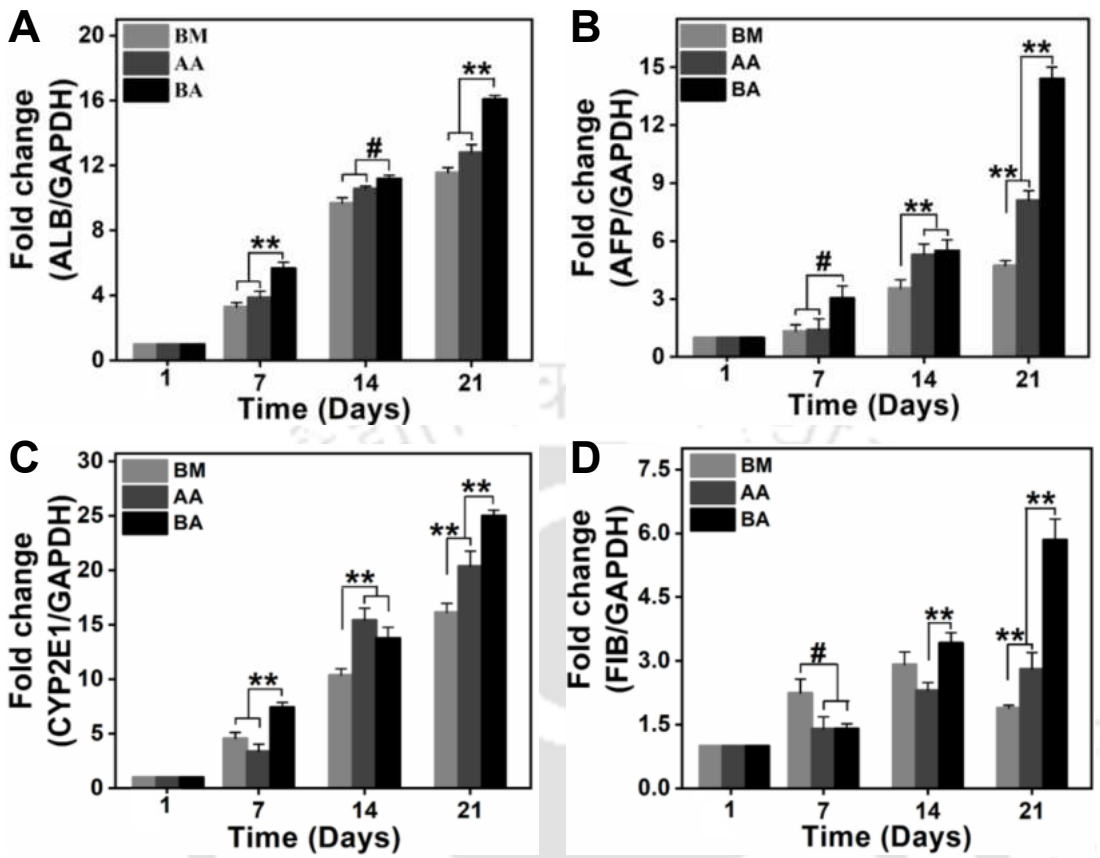

Figure 2.4. Real-time gene expression analysis of functional hepatic markers in HepG2 cells cultured on various silk scaffolds (BM, AA, and BA) over 21 days. *Synthetic gene (A) ALB, (B) AFP, (C) detoxification gene, CYP2E1 and (D) ECM secretion gene, FIB. Data are represented as mean ± SD. (n=4).* $^{\#}$ *and* ** *signify the statistical difference between the groups at* $p \leq 0.05$ *and* $p \leq 0.01$*, respectively.*

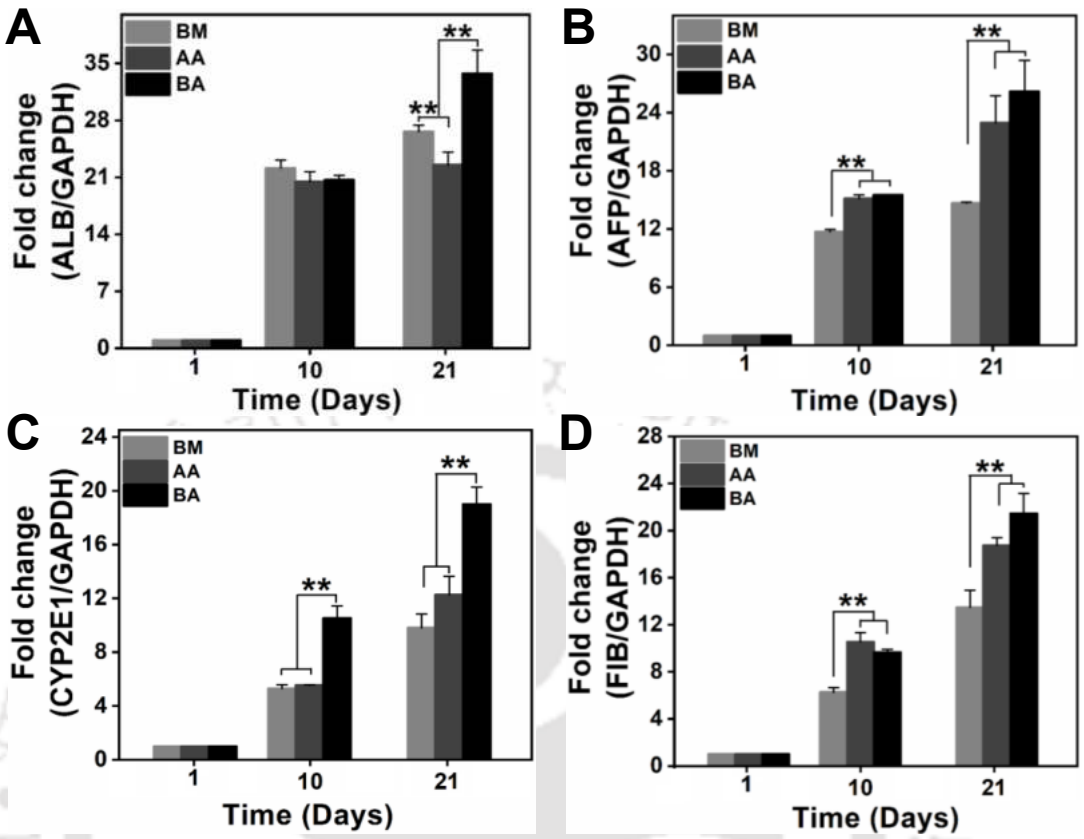

Figure 2.5. Real-time gene expression analysis of functional hepatic markers in primary neonatal rat hepatocytes cultured on various silk scaffolds (BM, AA, and BA) over 21 days. *Synthetic gene (A) ALB, (B) AFP, (C) detoxification gene, CYP2E1 and (D) ECM secretion gene, FIB. Data are represented as mean ± SD. (n=4).* $^{\#}$ *and* ** *signify the statistical difference between the groups at* $p \leq 0.05$ *and* $p \leq 0.01$*, respectively.*

2.3.5 Functional assessment

Individual variant of silk scaffold demonstrated diverse behavior in hepatocyte attachment, proliferation, and expression of signature markers. Further, the bioactivity of HepG2 and primary neonatal rat hepatocytes cultured on silk scaffolds were analyzed by estimating urea production, cytochrome P450 activity, and albumin synthesis for its application in BAL devices.

2.3.5.1 Urea synthesis

Total amount of urea secreted into the medium by HepG2 and primary neonatal rat hepatocytes was estimated **(Figure 2.6 A)**. Urea synthesized by HepG2 and primary hepatocytes cultured on BA scaffolds was comparable to that of other scaffolds till day 7 and day 10, respectively. Both the cells signified a similar pattern with an increase in urea level between days

14 and 21 ($p \leq 0.01$). However, HepG2 cells cultured on BA scaffold demonstrated higher urea synthesis than other scaffolds on day 14 and day 21 ($p \leq 0.05$). Primary hepatocytes cultured on BA scaffold revealed a significantly higher amount of urea on day 21 with a fold increase of about 1.20 and 1.18 than cells cultured on BM and AA scaffolds, respectively ($p \leq 0.01$). These results indicated that the bioactivity of hepatocytes was well maintained in hepatocytes cultured on blend silk scaffolds.

2.3.5.2 Cytochrome P450 activity

Activity of Cytochrome P450 Reductase (CPR) enzymes involved in Phase I detoxification of xenobiotic compounds was quantified in HepG2 and primary hepatocytes cultured on various silk scaffolds. CPR activity of hepatocytes cultured on scaffolds was normalized with the activity of CPR in the presence of an inhibitor and represented with respect to total intracellular protein **(Figure 2.6 B)**. CPR activity of hepatocytes with and without inhibitor for all the scaffolds over the culture period **(***Appendix* **Figure A2.3)**. HepG2 cultured on both BM and AA retained a similar level of CPR activity till day 7 (0.18 mU/mg of total intracellular protein). However, on day 21, HepG2 cultured on BA revealed significantly higher CPR activity (0.36 mU/mg of total intracellular protein) with a fold increase of ~1.38 than BM and AA ($p \leq 0.01$). Interestingly, the highest metabolic activity exhibited by HepG2 cells cultured on BA was similar to positive human CPR control. Primary hepatocytes cultured on scaffolds also presented a similar trend in the CPR activity with remarkably increased enzymatic activity from day 10 of the culture period. CPR activity of primary hepatocytes cultured on BA scaffolds increased significantly from day 1 (0.10 mU/mg of total intracellular protein) to day 21 (0.22 mU/mg of total intracellular protein) than BM and AA scaffolds ($p \leq 0.01$). After 21 days of the culture period, CPR activity of primary hepatocytes cultured on BA scaffolds increased significantly with a fold change of 2.0 and 1.69 than BM and AA, respectively. Hence, these results represented that BA scaffolds are effective in preserving the detoxification and metabolic function of both HepG2 and primary neonatal rat hepatocytes.

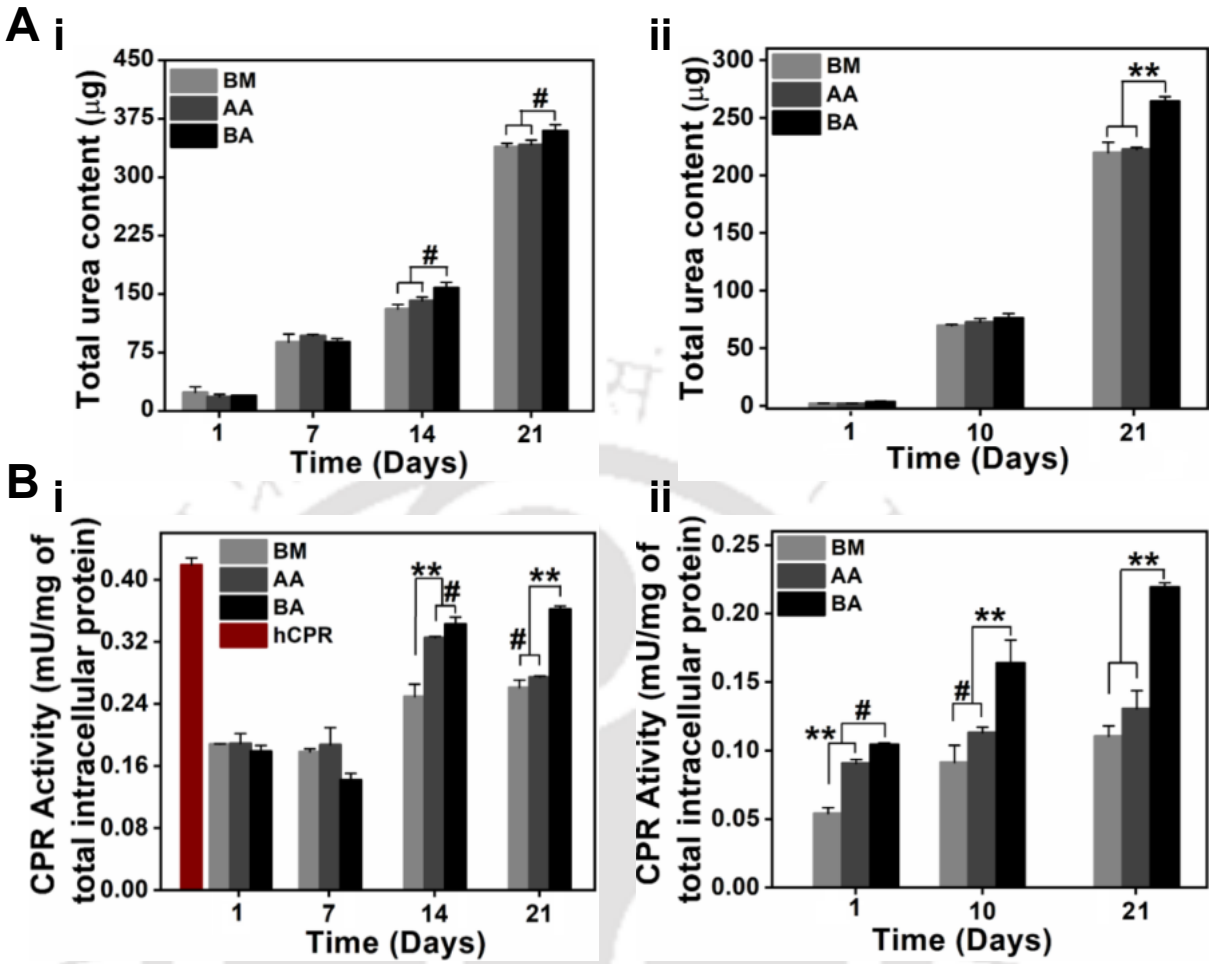

Figure 2.6. Metabolic activity assessment of HepG2 and primary neonatal rat hepatocytes cultured on silk scaffolds over 21 days by estimation of urea and cytochrome P450 activity. *Biochemical assay estimating (A) Total urea content and (B) Cytochrome P450 activity of (i) HepG2 cells and (ii) primary neonatal rat hepatocytes cultured on scaffolds (BM, AA, and BA). Data are represented as mean ± SD. (n=4).* $^{\#}$ *and* ** *signify the statistical difference between the groups at* $p \leq 0.05$ *and* $p \leq 0.01$*, respectively.*

2.3.5.3 Albumin secretion

Activity of total albumin and albumin per scaffold mass secreted by HepG2 cells cultured on scaffolds was estimated **(Figure 2.7 A-B)**. Amount of total secreted albumin increased progressively over the culture period of 21 days. On day 14, HepG2 cells cultured on AA and BA secreted ~12 µg of albumin with significantly higher activity than BM ($p \leq 0.05$). Albumin activity was almost similar for hepatocytes cultured in AA and BA till day 14; however, the albumin activity was dramatically increased in AA on day 21. Over 21 days, HepG2 cultured on BA scaffolds exhibited maximum albumin activity (23.11 µg) as compared with cells cultured on BM

and AA scaffolds ($p \leq 0.01$) with a fold increase of 1.42 and 1.13, respectively. These results revealed that hepatocytes cultured in blend silk scaffolds secreted a higher amount of albumin over the culture period.

2.3.6 Histology and immunofluorescence

Hematoxylin and eosin (H&E) stained sections revealed the attachment and distribution of HepG2 cells along the pores of the matrix **(Figure 2.7 C)**. All the variants of silk scaffolds assisted the infiltration of HepG2 cells with varied distribution pattern in an individual scaffold. HepG2 was distributed evenly along the pores of the AA matrix, whereas hepatocyte clusters were observed in BM and BA scaffolds. Optimal sized hepatocyte clusters were noticed in BA scaffolds; however, bigger clusters were formed in BM scaffolds. Fluorescent microscopic images displayed the expression of albumin (synthetic marker of hepatocytes) and fibronectin (ECM deposition) in HepG2 cultured on silk scaffolds supporting its functional attributes **(Figure 2.7 C)**. Expression of marker proteins was higher in hepatocytes cultured on AA and BA scaffolds, whereas limited expression in the core of clusters was displayed in BM scaffolds.

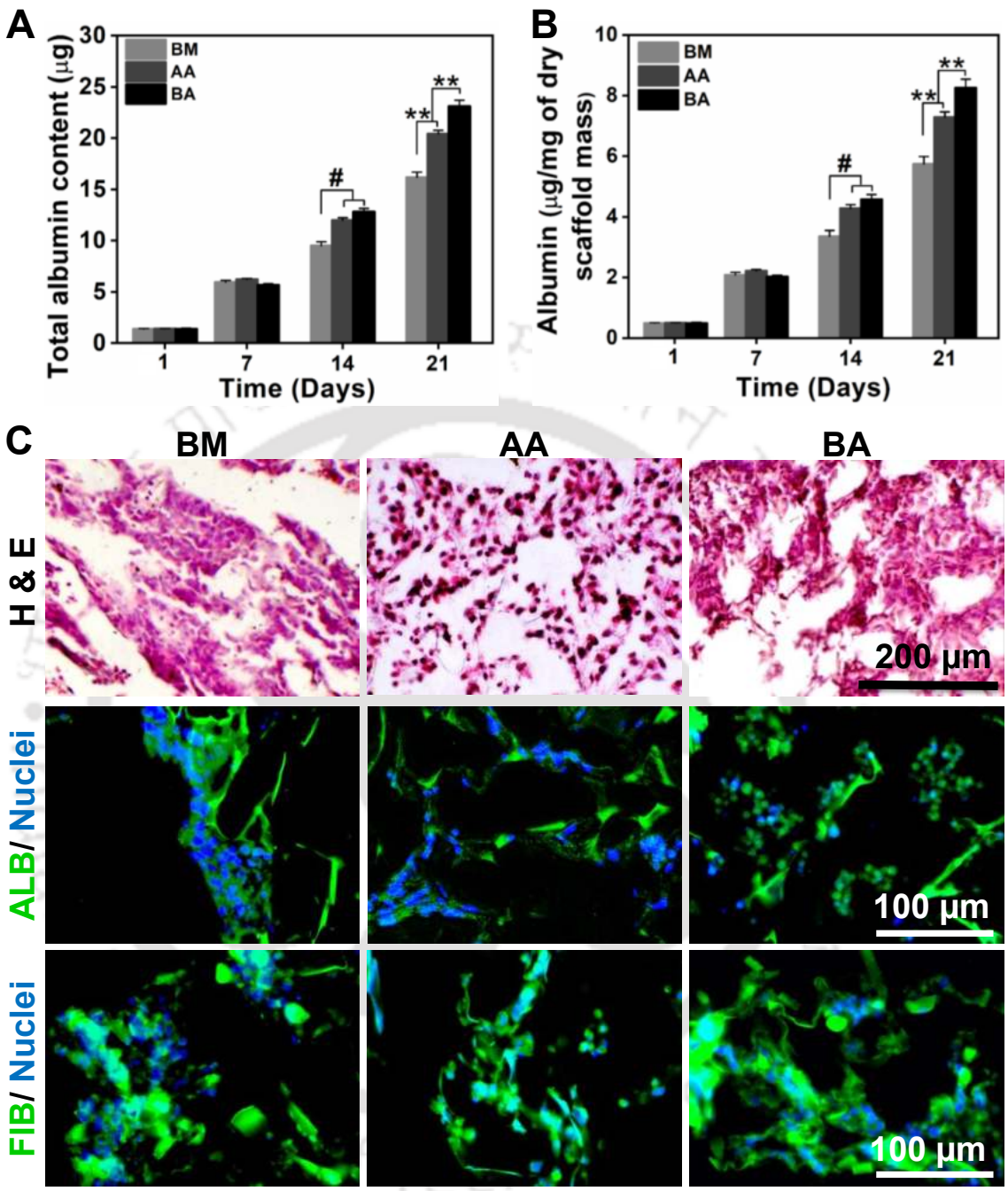

Figure 2.7. Albumin synthesis, H&E staining, and representative fluorescent microscopic images depicting functional marker expression of hepatocytes cultured on silk scaffolds. *ELISA quantification of (A) Total albumin content and (B) Albumin per dry scaffold mass secreted by HepG2 cells cultured on various silk scaffolds. Data are represented as mean ± SD. (n=4).* $^{\#}$ *and* ** *signify the statistical difference between the groups at* $p \leq 0.05$ *and* $p \leq 0.01$*, respectively. (C) H&E staining and immunofluorescence staining (green) of albumin (ALB) and fibronectin (FIB) in HepG2 cultured on various silk scaffolds. Cell nuclei were counterstained with Hoechst (blue). Scale bar represents 200 µm and 100 µm in H&E and immunofluorescence images, respectively.*

2.3.7 Hemocompatibility assay

Matrices used in BAL devices should be hemocompatible and antithrombogenic as it comes in contact with the patient's plasma. Hemocompatibility and antithrombogenic property of silk scaffolds (BM, AA, and BA) were evaluated by quantifying the LDH activity of adhered platelets **(Figure 2.8 A)**. Among all the scaffolds, a higher population of adhered platelets was observed in AA scaffolds with a maximum LDH activity of 1.01 milliunits/mL. BA scaffold was found to be minimally thrombogenic than AA, with a significant difference in the LDH activity ($p \leq 0.05$). LDH activity of adhered platelets on BM and BA was in the same range with a value of 0.77 and 0.68 milliunits/mL, respectively.

2.3.8 *In vitro* inflammatory response

Biomaterials elicit an immune response by provoking the macrophages, which in turn regulate lymphocyte activation by releasing pro-inflammatory cytokines (TNF-α). Immunogenicity of various silk scaffolds was assessed by quantifying the TNF-α release from RAW 264.7 cells in response to silk scaffolds **(Figure 2.8 B)**. TNF-α release from macrophages exposed to silk scaffolds was compared with the LPS treated group (positive control) and TCP (negative control). TNF-α release in the presence of silk scaffolds (BM, AA, and BA) was in the range of 200-300 pg/mL, which was significantly lower (4 fold) as compared to a positive control ($p \leq 0.01$). Moreover, TNF-α release in response to scaffolds was similar to the TNF-α release in the negative control (TCP). Non-mulberry (AA) and blend (BA) silk scaffolds exhibited a significantly lower amount of TNF-α than BM and TCP ($p \leq 0.05$), suggesting lower immunological responses.

2.3.9 *In vivo* immunogenic response by subcutaneous implantation

Implanted samples were stained with anti CD68 antibody (macrophage specific marker) and H&E to evaluate the immunogenicity, and implant integration with the host tissue, respectively post 2 and 4 weeks of implantation **(Figure 2.8 C)**. Histological examination after 2 weeks revealed the occurrence of host cells at the interface between BM scaffolds and host tissue. Whereas, AA and BA implanted samples exhibited more host cell infiltration and early tissue ingrowth supporting early implant integration. Presence of macrophages (stained in green), a characteristic immune cell at the host scaffold (H-S) interface, suggested an early immune response elicited by the host for the scaffolds. In 4 weeks stained samples, few macrophages were

observed in BM implanted sections indicating mild inflammatory reaction; however, AA and BA scaffolds didn't display the presence of immune cells. Subsequently, scaffolds were relatively degraded and surrounded by fibrotic tissue with host cells, as evident from the fragmented scaffold in the implant site.

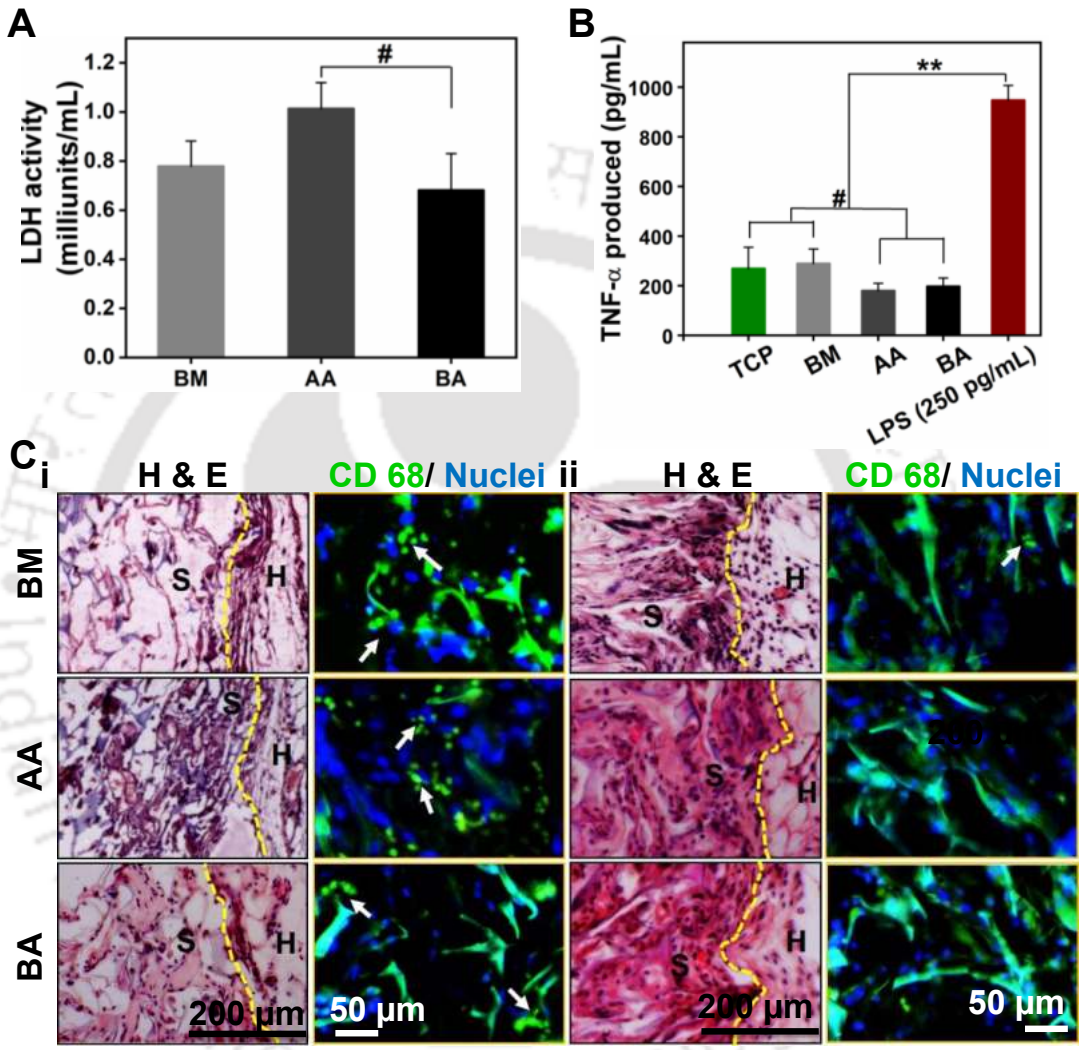

Figure 2.8. Assessment of hemocompatibility, in vitro immunogenicity, and in vivo response of silk scaffolds. *(A) Lactate Dehydrogenase Activity (LDH) of platelets adhered to various silk scaffolds. (B) TNF-α production by RAW 264.7 (mouse macrophages) in response to various silk scaffolds. Lipopolysaccharide (250 pg/mL) and standard Tissue Culture Plate (TCP) were considered as positive and negative controls, respectively. Data are represented as mean ± SD. (n=4).* $^{\#}$ *and* ** *signify the statistical difference between the groups at* $p \leq 0.05$ *and* $p \leq 0.01$*, respectively. (C) Histological analysis and CD68 staining (green) of subcutaneously implanted scaffolds after (i) 2 weeks and (ii) 4 weeks. Cell nuclei were counterstained with Hoechst (blue).*

Yellow dashed line highlights the host-scaffold interface in H&E staining images. Fibroblast infiltration was observed at the host-scaffold interface, where H- Host tissue and S- Scaffolds. White arrows in CD68 staining represent macrophage occurrence at the H-S interface

2.4 Discussion

Development of a suitable 3D matrix that promotes the growth of hepatocytes with maximum functional attributes is an important module in bioartificial liver (BAL) devices and cell-based tissue engineering approaches. Though HepG2 is reported as a human primary hepatocyte model [50], primary hepatocyte culture is expected to be a suitable cell source in BAL development, drug screening, *in vitro* liver models, and liver tissue engineering, as it can perform major synthetic and metabolic functions [218]. Hepatocyte clusters displayed higher functionality, emphasizing both cell-cell and cell-matrix interactions, which solely relies on the physicochemical properties of the scaffold [251]. Various biochemical factors like galactose [114], collagen [218], and RGD (arginine-glycine-aspartate) [252] have been conjugated with surface polymer to generate the hepatocyte clusters, but they failed to retain their functionality for a prolonged period [253]. Therefore, engineering a biocompatible and mechanically stable 3D *in vitro* liver construct using a scaffold-based approach to preserve the long-term bioactivity of hepatocytes is a major concern in liver tissue engineering.

In the present study, fabricated 3D silk scaffolds (BM, AA, and BA) were evaluated for its potential in liver tissue engineering and validated against HepG2 and primary neonatal rat hepatocytes. Surface morphology of the scaffolds, pore size, and pore interconnectivity have a great impact on cell-matrix interactions, cellular infiltration, attachment, and migration [229]. Silk scaffolds presented interconnected pores in the range of 70 – 130 µm in diameter that recapitulates *in vivo* liver microarchitecture to maintain hepatic physiology [225, 254]. Structural integrity and surface morphology of scaffolds were attributed to the amino acid composition and crystallinity of silk fibroin. Silk fibroin heavy chain is primarily composed of hydrophilic amorphous α-helices domains interspaced with crystalline β-sheets [255]. Rough fibrillar pores of AA scaffold is attributed to abundant poly-alanine repeats in AA silk fibroin assisting additional β-sheets, better hydrophobicity, and crystallinity (34.7%) [255-257]. Moreover, the basic/acid amino acid ratio is high in AA (~1.24) as compared to BM (~0.60) silk fibroin [256, 258]. The structural transition of ethanol-treated silk scaffolds from native random coils to β-sheets lead to absorption in the frequency range of amide I, II, and III bands, as evidenced by the IR spectrum. Comparatively, BA scaffolds exhibited greater amide linkages and β-sheets due to blending BM and AA,

confirming their integrity. Characteristic peaks detected in the range around 1648–1554 cm^{-1} and 1610–1630 cm^{-1} confirmed the secondary structure conformation of silk I and silk II, respectively [236]. Amide I band is associated with C=O and C-N stretching vibration, amide II corresponds to N-H bending vibration and stretching vibration of C-N and C-C groups, whereas amide III is of complex bands due to a mixture of several coordinate displacements from side chains and hydrogen bonding [250]. Therefore, peak shifts and increases in their intensity signified additional amide linkages and hydrogen bonds attributing to the stability of scaffolds. Further, structural integrity was confirmed from the minimal protein release and *in vitro* degradation profile of silk scaffolds in PBS over 4 weeks. Matrix incorporating hepatocytes in BAL devices should maintain integral stability to evade host immune response [50]. For tissue engineering applications, the developed matrix should exhibit a controlled degradation rate to support the regeneration of native tissues [259]. Under *in vivo* conditions, various ECM modulatory enzymes like matrix metalloproteases (MMPs) regulate tissue regeneration [260]. To mimic MMPs, a nonspecific proteolytic enzyme protease XIV was chosen to perform *in vitro* degradation studies [236]. Scaffolds showed a time-dependent degradation profile over 28 days with structural changes in BM and BA scaffolds. Slower degradation and superior mechanical strength of AA scaffold are attributed to intrinsic hydrophobic amino acids, poly-alanine repeats, and greater β-sheets, as confirmed by FTIR studies [42]. Matrices employed in liver tissue engineering applications are expected to possess suitable mechanical strength to promote the growth of hepatocytes and withstand physiological forces [114, 261]. All variants of silk scaffolds displayed porosity around 88-92% demonstrating high surface area to volume ratio that assists in bidirectional mass transfer of nutrients to diffuse in and metabolites to diffuse out of cell-seeded matrix [262]. However, increased swelling ratio of BM scaffold may be attributed to its high hydrophilicity and lesser degree of crystallinity that governs the absorption of nutrients [257]. Pore size and swelling capacity of the 3D scaffold influences their mechanical strength. During load, water molecules in BM scaffolds with high swelling capacity migrate towards unloaded regions allowing extended deformation. BA scaffold presented similar water imbibing capacity in accordance with BM and suitable mechanical strength required for maintaining cellular functions in soft tissue engineering [263].

Due to differential physicochemical traits of mulberry, non-mulberry, and blend silk scaffolds, their influence on hepatocyte attachment, growth, and functional properties were

explored. The potential of silk scaffolds for liver tissue engineering has been studied using HepG2 cells [223, 237]. As primary hepatocyte culture is a suitable hepatic model, there is a need to assess its functional attributes on silk scaffolds. In this regard, we have analyzed the synthetic and metabolic activity of both HepG2 and primary neonatal rat hepatocytes cultured on silk scaffolds. Intrinsic cell attachment motifs (RGD) [42] and high arginine repeats (3.9%) in hydrophobic and crystalline AA silk fibroin favored high cell-matrix interactions facilitating hepatocytes attachment along the pores of the AA scaffold. Whereas, BM and BA scaffolds displayed bigger hepatocyte clusters and optimal sized stable hepatocyte clusters, respectively in both elliptical and circular form, as evidenced from H&E stained images. Hepatocyte clusters in the blend scaffolds might be attributed to the matrix roughness and presence of both poly-glycine-alanine repeats (from BM) and RGD motifs (from AA). Therefore, BA scaffolds favored optimal cell-matrix interaction along with cell-cell interaction in achieving hepatocellular clusters by supporting our hypothesis. Physical cues offered by a 3D matrix direct the cellular assembly [264, 265]. Hepatocytes are highly sensitive to the surface topography and biochemical composition of the matrix [114]. Previous studies have reported the induction of cellular clusters using nanofibers such as parotid epithelial cells on polycaprolactone nanofibrous microwells [265], breast tumor cells on silica microfibers [266], primary neonatal rat hepatocytes on galactosylated chitosan nanofibers [114] and so on. In the case of hepatocyte clusters, the inner core starts to lose its viability during the later phase of culture (after 1 week) [114]. In this study, we have succeeded in maintaining the stability of hepatocyte clusters over a period of 3 weeks using blend silk scaffolds comprised of a natural biocompatible polymer possessing superior physicochemical attributes (surface topography, intrinsic RGD motifs, and high mechanical stability). Further, the metabolic activity of hepatocytes cultured on silk scaffolds was evaluated based on percentage alamar reduction. Enhanced proliferation of HepG2 and primary neonatal rat hepatocytes was observed in BA scaffolds over the culture period, confirming the superior proliferative potential of clusters. Earlier study on fibronectin coated collagen sponge demonstrated enhanced HepG2 proliferation [226], highlighting the significance of cell binding motifs in hepatocyte bioactivity. Furthermore, basolateral side of hepatocytes are organized towards ECM in native liver tissue emphasizing both cell-cell and cell-matrix interactions [267].

Intricate organization of 3D cultured hepatocytes within porous scaffolds reflects its functional behavior [251]. Hepatocyte clusters formed on BA scaffolds revealed enhanced

expression of liver-specific markers (ALB, AFP, CYP2E1, and FIB) over 21 days. However, increased fibronectin expression in HepG2 cultured on BM scaffold during the initial days might be attributed to the early formation of clusters. Albumin production and urea synthesis are involved in regulating blood oncotic pressure and protein metabolism, respectively [1]. Minimal functional properties of hepatocytes cultured on BM scaffolds might be attributed to the larger clusters (> 100 μm) with reduced proliferation after day 14. Previous studies also highlighted the influence of cluster size in maintaining hepatocyte functions over a long-term culture period; clusters greater than 100 μm exhibited low functionality due to limited oxygen diffusion in the central core [216]. Also, these clusters were not mechanically stable and encountered shear stress against the plasma and nutrients flow [268]. Stable hepatocyte clusters (< 100 μm) formed in BA scaffolds supported increased albumin production and urea synthesis over 21 days which is in line with previous studies where the spheroidal culture of liver cells presented high metabolic and detoxification functions [217]. Intrinsic RGD motif in AA exalts cell-matrix attachment through integrin mediated pathway [257] which in turn activates Rho signaling leading to YAP localization resulting in hepatocyte dedifferentiation [50]. Hence, RGD dependent Rho signaling pathway might attribute to the enhanced proliferation and functionality of primary hepatocytes. Gene expression studies and functionality assessment demonstrated that hepatocyte clusters formed in BA scaffolds maintained a higher level of liver-specific functions for a prolonged period. The possible key factor for improved cell functionality involves controlling the microarchitecture of the developed cell construct with the maximum mass transfer of oxygen and nutrients [251]. Further, immunohistochemical analysis demonstrated higher expression of albumin in AA and BA scaffolds as supported, which is comparable to functional analysis. Reduced albumin expression in the core of hepatocyte clusters formed in BM scaffold might be due to formation of necrotic core. However, higher fibronectin expression in hepatocyte cultured on BM and BA scaffolds showcased enhanced functionality traits (ECM synthesis) by hepatocyte clusters.

A functionally engineered *in vitro* liver construct for BAL systems demands hemocompatibility and immunocompatibility to minimize thrombogenesis and host immune response, respectively. LDH activity of adhered platelets on silk scaffolds (BM, AA, and BA) demonstrated minimal platelet adhesion owing to its hemocompatibility. This is in accordance with earlier works [236]. *In vitro* immune response towards scaffolds after 12 h incubation with macrophages (RAW 264.7) was comparable to that of negative control, presenting its negligible

immunogenicity. Further, the scaffolds were subcutaneously implanted to investigate the *in vivo* immune response. Post 2 weeks of implantation, retrieved sections indicated macrophage infiltration at the scaffold-host (S-H) interface that may aid in tissue repair [231]. Surplus invasion of the host cell in non-mulberry-based scaffolds (AA and BA) due to the presence of RGD motifs favored early graft acceptance and initiated the remodeling process [231]. This further promoted the formation of host tissue at the implant site after 4 weeks with structural modulations of scaffolds supporting the host-implant integration. Graft remodeling with cellular ingrowth and vascularization substantiated the immunocompatibility of silk scaffolds. The proposed methodology here is beneficial; as it involves economical, biocompatible natural polymer in developing a large bioactive 3D hepatic culture system highlighting both cell-cell and cell-matrix interactions. Hence, blend silk scaffolds assisted in retaining stable primary hepatocyte clusters by overcoming the challenges of long-term functional maintenance for its prospects in liver tissue engineering. Ensuring other non-parenchymal cells of the liver to fabricate heterotypic hepatocyte clusters mimicking native tissue will aid in forwarding the fabricated 3D *in vitro* liver construct. Further, the modular assembly of liver cells has to be optimized for its application in BAL devices.

2.5 Significant findings

1. In this chapter, we have fabricated porous silk scaffolds using a facile approach to maintain long-term hepatic functions for its prospects in the bioartificial liver (BAL) development and liver tissue engineering approaches.
2. Cell attachment, proliferation, and functional properties of both HepG2 and primary neonatal rat hepatocytes were found to be correlated with the physicochemical properties of the scaffolds.
3. Coalescing mulberry and non-mulberry silk fibroin is predicted to assist the formation of stable and optimal sized hepatocyte clusters (< 100 μm) with enhanced functionality that might enable better nutrient and oxygen diffusion.
4. High cell density accomplished in blend silk scaffolds was found to be metabolically active and retained maximum functional attributes of the liver (albumin synthesis, urea synthesis, and Cytochrome P450 enzymatic activity) for 3 weeks as compared to BM and AA.

5. Engineered bioactive 3D primary hepatocyte construct found its prospects in drug toxicity studies and biohybrid devices. Future advancements in biocompatible 3D porous scaffold system (BA) for achieving various functional properties of hepatocytes would lead to clinical applications.

CHAPTER 3

Mimicking physiologically relevant hepatocyte zonation using immunomodulatory silk liver extracellular matrix scaffolds toward a bioartificial liver platform

This chapter demonstrates the establishment of a physiologically relevant *in vitro* liver model mimicking nativelike metabolic zonation facilitating physiological cues, hepatocyte polarity, and phenotypic functions. A hepatocyte metabolic heterogeneity in an *in vitro* liver model was developed encompassing liver extracellular matrix-functionalized silk scaffolds (LECM-SF) by altering ECM proportion. A single *in vitro* liver system comprising primary neonatal rat hepatocytes seeded LECM-SF scaffolds assisting periportal to pericentral gradient functions was stacked and matured in a perfusion bioreactor to simulate oxygen gradient, supporting its promising avenue in the bioartificial liver.

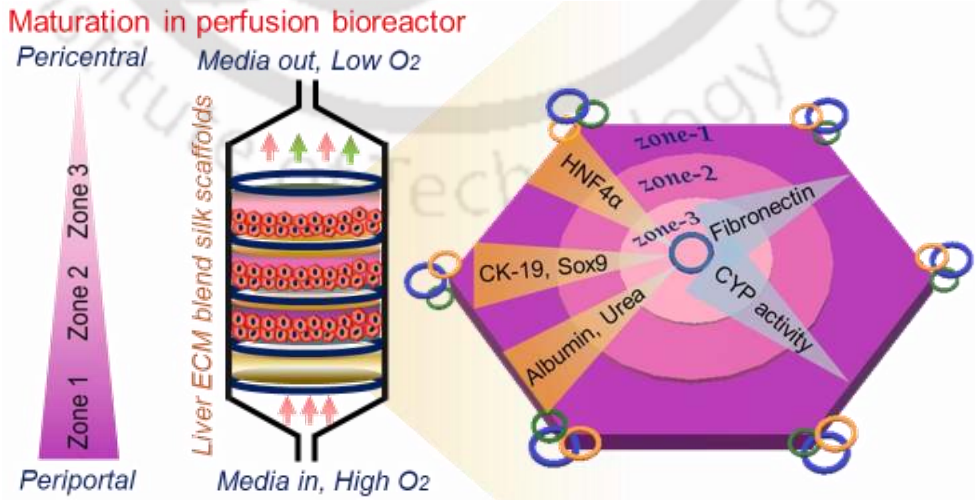

Liver Model Recapitulating Native Metabolic Zonation

ABSTRACT

Mimicking nativelike metabolic zonation is indispensable to develop an efficient bioartificial liver model, as it facilitates physiological cues, hepatocyte polarity, and phenotypic functions. The present study shows the first evidence of hepatocyte metabolic heterogeneity in an *in vitro* liver model encompassing liver extracellular matrix (ECM)-functionalized silk scaffolds (LECM-SF) by altering ECM proportion. Upon static culture, individual LECM-SF scaffold supports differential synthetic and metabolic functions of cultured primary neonatal rat hepatocytes (PNRHs), owing to discrete biophysical attributes. A single *in vitro* liver system comprising PNRHs seeded LECM-SF scaffolds assisting periportal to pericentral gradient functions is stacked and matured in a perfusion bioreactor to simulate oxygen gradient. The scaffold with high ECM supports periportal-specific albumin synthesis, urea secretion, and bile duct formation, albeit the scaffold with low ECM supports pericentral-specific cytochrome P450 activity. Extensive physicochemical characterizations confirmed the stability and interconnected porous network of scaffolds, signifying cellular infiltration and bidirectional nutrient diffusion. Furthermore, scaffolds demonstrate minimal thrombogenicity, reduced foreign body response, and enhanced pro-remodeling macrophage activation, supporting constructive tissue remodeling. The developed liver model with zone-specific functions would be a promising avenue in bioartificial liver and drug screening.

The findings of this chapter are published in a peer reviewed journal:

Janani G., and Mandal B.B. "*Mimicking physiologically relevant hepatocyte zonation using immunomodulatory silk liver extracellular matrix scaffolds toward a bioartificial liver platform*". **ACS Applied Materials & Interfaces**, 2021, 13 (21), 24401-24421.

3.1 Introduction

Acute or fulminant hepatic failure (FHF) is a severe life-threatening clinical condition, where liver functions and self-regenerative ability deteriorate, affecting one-third of the total world population with an 80% mortality rate [194, 269]. Orthotopic liver transplantation (OLT) is a gold standard treatment option for FHF; however, OLT remains limited due to organ shortage, use of immunosuppressants, and secondary complications [270]. Meanwhile, artificial liver support systems, bioartificial liver (BAL), cell-based therapies, and implantable tissue constructs are being explored to treat FHF [50, 271]. Developing cell-based liver supports, including BAL, implantable tissue-engineered constructs, and liver models are prime research areas to complement crucial hepatocyte-specific synthesis, regulatory, and detoxifying functions [272]. Three-dimensional (3D) *in vitro* functional hepatocyte models emphasizing nativelike microenvironmental niche, cell-cell interactions, and cell-matrix interactions deliver a potential platform to bring advancements in cellular components [271]. Significant challenges in hepatic tissue engineering include (i) biocompatible and hemocompatible scaffold choice, (ii) cell source, (iii) achieving maximum liver functions, and (iv) long-term functional stability [271]. Research efforts continue to aim at designing 3D matrices and employing hepatocytes from primary and stem cell sources (embryonic, adipose, induced pluripotent stem cells) for liver support systems. In particular, primary hepatocytes cultured in well-defined 3D matrices have been advantageous, as it demonstrates effective cell-cell signaling by maintaining their functionality [271, 273]. However, such primary hepatocyte liver models are incapable of assisting essential functions comparable to the native liver due to phenotypic instability and limited polarity [274].

Scaffolds composed of extracellular matrix (ECM) provide dynamic biomechanical and biochemical interplay between cells and matrix, thus promoting growth, functionality, cell-cell, and cell-matrix communication [275, 276]. Liver ECM fabricated as coating and hydrogels supported survival and maturation of primary rat hepatocytes (PRH) over 8 days culture period [114]. In the same way, silk scaffolds fabricated by blending mulberry (*Bombyx mori*, BM) and non-mulberry (*Antheraea assamensis*, AA) silk fibroin supported optimal aggregate growth of PRH, which in turn enhanced albumin secretion, urea synthesis, and cytochrome P450 activity [271]. Nevertheless, *in vitro* liver models are limited in recapitulating hepatocyte metabolic heterogeneity; therefore, achieving hepatocyte polarity, maximum liver functions, and long-term stability are difficult, which is indeed observed in the native liver [33, 277]. Liver zonation, a

distinct metabolic gradient of hepatocytes based on their position along the liver sinusoid, is often not wholly focused in *in vitro* liver systems [278, 279]. The oxygenated blood, nutrients, and drugs enter the liver lobule through the portal vein, get metabolized by resident hepatocytes, and resultant metabolites along with synthesized molecules exit the lobule through the central vein, thus creating a non-overlapping metabolic gradient in hepatocytes [34, 279]. Based on oxygen gradient and distinct metabolic patterning, hepatocytes along the sinusoid are compartmentalized into three distinct regions: zone 1, periportal (PP); zone 2, midzonal; and zone 3 pericentral (PC) regions [277]. A multitude of complementary liver functions, including synthesis of plasma proteins, storage of glycogen, production of bile, metabolism of complex glucose and lipid molecules, and detoxification of drugs, are regulated explicitly by defined zonal hepatocytes to maintain physiological homeostasis [277, 279]. For instance, periportal hepatocytes perform ureagenesis, albumin secretion, gluconeogenesis, and cholesterol synthesis; perivenous hepatocytes perform glycolysis, lipogenesis, glutamine synthesis, and metabolism of xenobiotics and drugs through cytochrome P450 activity (CYP) [280]. Metabolic plasticity of hepatocytes was shown to be regulated by oxygen gradient, ECM composition, nutrient diffusion, and distribution of hormones and non-parenchymal cells [34, 277, 280]. Also, the apical membrane of polarized hepatocytes toward the PP region joins together and forms a continuous bile canaliculi network [194].

Previous studies have developed *in vitro* liver zonation-based models by implementing nativelike oxygen gradient and Wnt/β-catenin signaling (a key regulator in activating drug-metabolizing enzymes) [5, 34, 277, 281]. The oxygen gradient generated in a microfluidic device achieved metabolic zonation during human embryonic stem cell differentiation to mature hepatocytes [281]. Moreover, Wnt/β-catenin signaling was modulated to achieve zone-specific hepatocyte heterogeneity in a 3D HepaRG/agarose channel [277], and *in vitro* cultured murine and human hepatocytes [279]. Recently, biomimetic oxygen levels induced in PRH cultured PDMS tissue culture plates achieved both zone-specific metabolism heterogeneity and β-catenin signaling [5]. Other methods include attempts to resemble hormone gradients using exogenous hormones and chemical inducers in a microfluidic device to accomplish native liver zonation-based carbohydrate and nitrogen metabolism in PRH [282], and human hepatocytes [36]. Despite the importance of liver zonation, existing liver models do not account for achieving long-term zone-specific liver functions and resembling the continuous perfusion system as in the native liver.

Thus, in an effort to recapitulate liver metabolic zonation, we have designed liver ECM blend silk (LECM-SF) scaffolds housing primary neonatal rat hepatocytes (PNRHs) and matured them in a perfusion bioreactor to imitate the oxygen gradient and nutrient diffusion. In this study, we incorporated porcine liver ECM in the blend silk scaffold for the first time and fabricated LECM-SF scaffolds by varying ECM proportion. In static conditions, PNRHs cultured on LECM-SF scaffolds self-assembled into optimal aggregates and presented a gradient of synthetic (albumin, urea), detoxification (cytochrome P450), ECM production (fibronectin), and cholangiocyte (CK-19, Sox9) functions. Using the perfusion system coupled with distinct functional attributes supported by individual scaffold variant, we matured a whole *in vitro* liver construct over 45 days and examined the role of oxygen and ECM proportion on the induction of hepatocyte metabolic functions. Functional characterizations revealed that scaffolds with high ECM supported zone 1 PP functions (synthetic and cholangiocyte); and scaffolds with low ECM supported zone 3 PC functions (detoxification and ECM production). Furthermore, host response and macrophage activation toward LECM-SF scaffolds were evaluated in the subcutaneous rat model.

3.2 Materials and Methods

3.2.1 Liver decellularization and its biochemical characterization

The chemical decellularization approach reported previously was followed with few modifications to obtain organ-specific liver ECM [44]. Briefly, porcine liver tissue was chopped into small cubes with an area of 1 cm^2 and a thickness of 2 mm, washed alternatively with 0.1 M phosphate-buffered saline (PBS) and Milli-Q water for 24 h, followed by incubation with 1% (v/v) Triton X-100 and 0.1% (v/v) ammonium hydroxide solution for 3-4 days. Liver decellularization was validated from histological analysis and quantification of DNA, glycosaminoglycan (GAG), and collagen. Native and decellularized liver samples were sliced into 10 µm thickness sections. The sections were stained with hematoxylin and eosin (H&E), and Alcian blue to assess the removal of cellular components and GAG preservation, respectively, as per the manufacturer's instructions. The images were captured via bright field microscopy using an EVOS FL inverted microscopy (Life Technologies, USA). Native liver and decellularized liver ECM were lyophilized, pulverized into a fine ECM powder, and digested in papain buffer solution at 60°C for 16 h. DNA, GAG, protein, and collagen content in native and decellularized liver samples were

estimated using Quant-iT PicoGreen dsDNA assay, dimethylmethylene blue assay, Bradford assay, and Sirius Red Dye method, respectively, as previously described [114].

3.2.2 Silk fibroin isolation

The BM and AA silk fibroin solution was isolated from BM cocoons and AA silk glands, as reported previously [271, 283]. Briefly, BM cocoons were degummed in boiling sodium carbonate solution (0.02 M), dissolved for 4 h in lithium bromide solution (9.3 M, 60°C), and dialyzed against Milli-Q water for 48 h to obtain a regenerated BM silk fibroin solution. However, extruded AA silk fibroin from silk glands harvested from fifth instar silkworms was dissolved in sodium dodecyl sulfate solution (1% (w/v)) and dialyzed for 4 h against Milli-Q water (4°C). The gravimetric method was employed to measure the concentration of silk fibroin solution, followed by 3% (w/v) BM and 3% (w/v) AA were blended at a 1:1 ratio to obtain 3% (w/v) BA silk solution as previously described [271].

3.2.3 Fabrication of liver ECM blend silk scaffolds

The pulverized decellularized liver ECM powder of 10 mg was solubilized with 1 mg/mL pepsin in 0.01 N HCl solution for 48 h at 37°C. The 3% (w/v) decellularized liver stroma (dLS) solution was employed for scaffold fabrication after adjusting the pH to 7.4 [114]. Four variants of porous liver ECM blend silk (LECM-SF) scaffolds were fabricated using a conventional freeze-drying method, where 3% (w/v) BA and 3% (w/v) dLS solution were blended at various ratios (**Table 3.1)**, frozen at -20°C, and lyophilized for 48 h. Then, scaffolds were crosslinked following carboxyl-to-amine crosslinking using EDC/NHS for 12 h to augment β-sheets and then washed repeatedly with Milli-Q water to ensure the removal of the residual crosslinking solution.

Table 3.1. *Description and proportion of liver ECM blend silk scaffolds*

Sample	Scaffold description	Volume of 3% (w/v) BA silk solution (µL)	Volume of 3% (w/v) dLS solution (µL)	Ratio of BA:dLS solution
1	BA:dLS (2:0)	1000	0	2:0
2	BA:dLS (1.5:0.5)	750	250	1.5:0.5
3	BA:dLS (1:1)	500	500	1:1
4	BA:dLS (0.5:1.5)	250	750	0.5:1.5

3.2.4 Physicochemical characterization

3.2.4.1 FTIR analysis

The structural transition in LECM-SF scaffolds before and after EDC/NHS crosslinking was characterized using Fourier Transform Infrared-attenuated total reflectance (FTIR-ATR) method. The absorbance spectra were recorded with 32 scans per spectra in the range of 2000-800 cm^{-1} at 4 cm^{-1} spectral resolution. Concurrently, isolated BM, AA, and dLS solution were also FTIR characterized before and after EDC/NHS crosslinking. The conformation changes in the secondary structure of LECM-SF scaffolds before and after EDC/NHS crosslinking were further characterized by deconvolution of amide I spectra covering 1700–1600 cm^{-1}, as previously described [284]. The secondary structures were determined by fitting Gaussian peaks in the second derivative of baseline-corrected absorption spectrum using Origin Pro 8 (Microcal version, USA), followed by band assignments as (i) β-sheets (1620–1640 cm^{-1}), (ii) disordered structures (1640–1650 cm^{-1}), (iii) α-helices (1650-1658 cm^{-1}), and (iv) loops (1660-1680 cm^{-1}) [277, 284, 285]. Subsequently, the percentage area of secondary structures in each scaffold before and after crosslinking was examined from the deconvoluted spectrum's normalized area.

3.2.4.2 Surface topography and pore size distribution

The surface topography of LECM-SF scaffolds was analyzed using Zeiss Field Emission Scanning Electron Microscopy (FESEM, Sigma, USA) with an accelerative voltage of 2 kV. Scaffolds were dehydrated by a sequential gradient of ethanol treatment, immersed in hexamethyldisilazane, sputter-coated with gold, and high-resolution FESEM images were captured at 500× magnification under high vacuum conditions. The pore size distribution in the scaffold was quantified using Image J software (NIH, USA) by randomly measuring at 60 different places.

3.2.4.3 Porosity

The porosity was analyzed using the hexane displacement method, as previously described, [271] where LECM-SF scaffolds of equal size (10 mm height × 10 mm diameter) and equal weight were immersed in 10 mL of hexane. The total volume of hexane with impregnated scaffold was noted as V_1, and the resultant hexane volume after scaffold removal was noted as V_2. The porosity was calculated by

$$\text{Porosity (\%)} = [(10 - V_2)/ (V_1 - V_2)] \times 100$$

3.2.4.4 Swelling ratio

The swelling ratio of scaffolds was assessed by incubating samples in PBS, pH 7.4 for 24 h, and measuring the water uptake until it reaches the equilibrium swelling point [271]. Initially, the dry weight of scaffolds (W_1) was noted, incubated in PBS, and at predetermined time points, the weight (W_t) of scaffolds was measured after draining excess PBS. The swelling ratio was calculated by

Swelling ratio = $(W_1-W_t)/ W_1$

3.2.4.5 Protein release

The stability of crosslinked LECM-SF scaffolds was examined using the Bradford method by incubating the scaffolds in 0.1 M PBS and quantifying the amount of leached-out protein, as previously described [271]. The initial weight of the scaffolds (W_1) was noted and incubated at 37°C in 1 mL of 0.1 M PBS (pH 7.4) over 10 days. At specified time points (30 min and 1, 3, 6, 12, 24, 72, 120, and 240 h), 20 µL of PBS encompassing leached out protein was collected and incubated with Bradford reagent (200 µL, 20 min) followed by absorbance measurement at 525 nm. From the standard curve plotted using a respective concentration of BA and dLS solution, the unknown concentration of leached out protein (W_2) was calculated and represented in terms of percentage of protein release (%) by

Protein release (%) = $(W_2/W_1) \times 100$

3.2.4.6 *In vitro* enzymatic degradation

The degradation pattern of LECM-SF scaffolds was evaluated *in vitro* using Protease XIV, derived from *Saccharomyces griseus* (Sigma-Aldrich, USA) over 45 days. The initial dry weight (DW_i) of scaffolds (5 mm diameter × 12 mm height) was noted and incubated in 2 U/mL of Protease XIV solution. Every 5 days, the enzyme solution was removed, samples were gently rinsed in Milli-Q water to remove residual enzyme solution, and dry weight was noted (DW_t). The mass remaining (%) of LECM-SF scaffolds was calculated using

Mass remaining (%) = $100-\{[(DW_i - DW_t)/ DW_i] \times 100\}$

3.2.4.7 Mechanical compliance of scaffolds

The stress-strain relationship and compressive modulus of LECM-SF scaffolds of equal size (10 mm diameter × 10 mm height) were determined using an Instron 5944 Universal Testing Machine, USA. The mechanical studies were carried out under hydrated conditions (PBS, pH 7.4)

with a load cell of 0.1 kN at a 1 mm/min crosshead speed, and an offset-yield approach was followed to determine the compressive modulus from the stress-strain curve.

3.2.5 Isolation of primary parenchymal hepatocytes from neonatal rats and cell culture characterization

The widely employed two-step in situ collagenase digestion protocol was adapted from previous reports of Shen *et al*. [286] and others [114, 271] to isolate parenchymal hepatocyte population from 1 to 3 days old Wistar neonatal rats of either sex. The isolation method was in accordance with the Institutional Animal Ethical Committee (IAEC) guidelines, West Bengal University of Animal and Fishery Sciences (WBUAFS), West Bengal, India. The harvested whole liver was washed in an ice-cold Kreb's Ringer Buffer solution and incubated in buffer 1 (EGTA, HEPES, NaCl, KCl) at 37°C for 30 min until the liver blanches. Subsequently, the whole liver was enzymatically digested in buffer 2 (HEPES, NaCl, KCl) comprising 0.05% (w/v) Collagenase type IA at 37°C for 30 min. The digested liver tissue was gently dispersed in an ice-cold 1X HBSS solution to disassociate liver cells using a sterile cell scraper. The liver cell suspension was filtered through a 100 µm cell strainer followed by a 70 µm cell strainer to remove the undigested connective tissue fragments. Then, the parenchymal hepatocytes were pelleted out from the liver cell suspension by differential centrifugation (350 rpm, 5 min, 4°C), while non-parenchymal cells remained in the supernatant. The cell pellet comprising only parenchymal hepatocytes was suspended in serum-free William's E Medium (WEM), labeled as primary neonatal rat hepatocytes (PNRHs); PNRHs maintained >80% cell viability and cultured for 2-3 days in serum-free WEM.

Cellular proliferation, viability, and distribution of PNRHs seeded on different LECM-SF scaffolds were evaluated by alamar blue assay, confocal live-cell imaging, FESEM, and H&E staining, respectively. The LECM-SF scaffolds of 5 mm height × 5 mm diameter preconditioned in serum-free WEM were seeded with PNRHs at a density of 1×10^5 cells and cultured in serum-free WEM supplemented with 1X antibiotics, 10 ng/mL EGF, 0.5 µg/mL Insulin, 0.5 mg/mL BSA, and 5 nM Dexamethasone, denoted as the culture medium in the present study. The proliferation rate of PNRHs cultured on LECM-SF scaffolds was evaluated over 30 days culture period at predetermined time points using alamar blue dye reduction assay, as per manufacturer's instructions. Briefly, PNRHs cultured on scaffolds were incubated with a 1:10 ratio of alamar blue dye in the WEM for 4 h followed by absorbance measurement at 570 nm and 600 nm using Tecan Microplate Reader.

After 21 days of the culture period, the PNRHs cultured on scaffolds were treated with 4 µM Calcein-AM suspended in 1mL of 0.1 M PBS for 20 min to stain live cells. The live cells were stained green, and the scaffold microarchitecture is seen in red owing to the silk's integral autofluorescence property. At specific depths, the Z-stack imaging was recorded using Carl Zeiss Confocal Laser Scanning Microscopy (CLSM 880) at 20× magnification to investigate both PNRHs viability and infiltration. Ten Z-stacks covering 100 µm area at 10 µm intervals were recorded and processed using FIJI to obtain representative CLSM live-cell images. For FESEM imaging and H&E staining, the PNRHs cultured on LECM-SF scaffolds were fixed in 10% (v/v) NBF after 21 days culture period and serially dehydrated with gradient ethanol treatment. For FESEM imaging, the samples were sputter-coated with gold, scanned at 2.00 kV applied voltage, and acquired images were processed using FIJI. Subsequently, the PNRHs cultured scaffolds were cryosectioned at 10 µm thickness, stained with H&E, and images were captured at the bright field to comprehend cellular distribution.

3.2.6 Static and perfusion bioreactor culture experimental design

The zonation functions of PNRHs seeded LECM-SF scaffolds were assessed upon culturing in both static and perfusion bioreactor conditions. For static culture, the PNRHs at a density of 1×10^6 were seeded on preconditioned BA:dLS (2:0), BA:dLS (1.5:0.5), BA:dLS (1:1), and BA:dLS (0.5:1.5) scaffolds of 5 mm diameter and 2 mm height placed in a 24-well plate. After 24 h of cell attachment, 1 mL of culture media was added, and the cells were maintained at 37°C and 5% CO_2 in a humidified incubator. The media was replenished every 48 h, and all functional studies were carried out on days 1, 10, 20, and 30 of the 30 day static culture period. The conditioned media was collected for albumin and urea assessment, and PNRHs cultured on scaffolds were snap-frozen and stored for gene expression analysis and cytochrome P450 activity at preset time points. Subsequently, the PNRHs cultured on scaffolds after 30 days were fixed in NBF for immunolabeling the functional liver-specific markers.

The zone-specific functions of cultured PNRHs in LECM-SF scaffolds, including albumin synthesis, urea secretion, and cytochrome P450 activity, were determined as described in section 3.2.7. From the investigations, we found that comparatively BA:dLS (0.5:1.5) supported zone 1 (PP) functions and BA:dLS (1.5:0.5) assisted zone 3 (PC) specific functions. On the basis of these results, we anticipated stacking LECM-SF scaffolds as a single whole system following the zonal functions starting with BA:dLS (0.5:1.5) followed by BA:dLS (1:1) and BA:dLS (1.5:0.5), and

maturing them in perfusion bioreactor over 45 days culture period **(Figure 3.7 A)**. Initially, the PNRHs at a density of 5×10^6 were seeded in BA:dLS (0.5:1.5), BA:dLS (1:1), and BA:dLS (1.5:0.5) scaffolds of 14 mm diameter and 3 mm height and cultured for 2 days under static conditions. Simultaneously, the 3D Biotek perfusion bioreactor set up along with tubing, chambers, and medium reservoirs were sterilized and equilibrated with 20 mL of culture medium, as described previously [283]. The PNRHs cultured on BA:dLS (0.5:1.5), BA:dLS (1:1), and BA:dLS (1.5:0.5) scaffolds were stacked in the bioreactor chamber, and the culture medium circulated at a flow rate of 0.5 mL/min, wherein the inlet is close to BA:dLS (0.5:1.5), and the outlet is from BA:dLS (1.5:0.5) scaffolds. Acellular BA:dLS (2:0) scaffold with high mechanical strength was placed at the bottom to withhold physiological stress during perfusion. After 35 days of maturation, the scaffolds were examined for cellular distribution along the longitudinal section (LS) and cross-section (CS) by H&E staining, per manufacturer's instructions, and images were captured via bright field microscopy using an EVOS FL inverted microscopy (Life Technologies, USA). The functional liver zone-specific markers after maturing in perfusion bioreactors were assessed by immunolabeling against specific markers, as explained in **section 3.2.7.2**. The conditioned media on days 1, 15, 30, and 45 were quantified for albumin and urea secretion by the whole system. Individual scaffold variant was separated aseptically on days 1, 15, 30, and 45 and analyzed for gene expression and cytochrome P450 activity.

3.2.7 Functional characterization

3.2.7.1 Gene expression analysis

The expression of liver-specific synthetic genes (albumin, ALB; fibronectin, FIB); detoxification genes (glutathione S-transferase alpha 1, GSTA1; cytochrome P450 1A2, CYP1A2; alpha-1 antitrypsin, A1AT; cytochrome P450 2E1, CYP2E1); and cholangiocyte genes (hepatocyte nuclear factor 4α, HNF4α; cytokeratin 19, CK-19; SRY-box transcription factor9-Sox9) in PNRHs cultured on scaffolds grown under both static and perfusion bioreactor conditions were investigated using quantitative real-time polymerase chain reactions systems (RT-PCR, 7500 Fast, Applied Biosystems, USA). The primer sequences with accession numbers are listed in **Table 3.2.** The scaffolds collected at predetermined time points were equilibrated to room temperature, incubated in TRIzol reagent for 20 min to ensure cell lysis, and then cell lysate was treated with chloroform for 20 min.

Table 3.2. *Forward and reverse primer sequence for real-time polymer chain reaction*

S. No.	*Gene Name*	*Accession Number*	*Sequence*
1.	r-GAPDH	XM_032905640.1	**F** 5'-TGACTCTACCCACGGCAAGTTCAA-3'
			R 5'-ACGACATACTCAGCACCAGCATCA-3'
2.	r-ALB	XM_032916218.1	**F** 5'-GATGCCGTGAAAGAGAAAGC-3'
			R 5'-CGTGACAGCACTCCTTGTTG-3'
3.	r-FIB	XM_032901307.1	**F** 5'-GGATCCCCTCCCAGAGAAGT-3'
			R 5'-GGGTGTGGAAGGGTAACCAG-3'
4.	r-GSTA1	XM_032909659.1	**F** 5'-ATGAGAAGTTTATACAAAGTCC-3'
			R 5'-GATCTAAAATGCCTTCGGTG-3'
5.	r-CYP1A2	XM_032911352.1	**F** 5'-CGGTGGCTAATGTCATCGGAG-3'
			R 5'-TTGCTGCTCTTCACGAGGTTGA-3'
6.	4-A1AT	XM_032908315.1	**F** 5'-AACAATGGGGCTGACCTC-3'
			R 5'-CCACAAAGATGGGGCTCT-3'
7.	r-CYP2E1	XM_032891525.1	**F** 5'-TGCGGAGGTTTTCCCTAAGC-3'
			R 5'-GCGCAGCCAATCAGAAATGT-3'
8.	r-HNF4α	XM_032904886.1	**F** 5'-AGTGCTGCCTTGGACCCAGCCT-3'
			R 5'-GGCACACAGGGCACTGACACCC-3'
9.	r-CK-19	XM_032913310.1	**F** 5'-CTAATGGCGAGCTGGAGGTGAAG-3'
			R 5'-GGCGGGCATTGTCGATCTGTAGGA-3'
10.	r-Sox9	XM_032913232.1	**F** 5'-TGGCAGAGGGTGGCAGACAGC-3'
			R 5'-CGTTGGGCGGCAGGTATTGG-3'

The aqueous layer containing RNA was separated, and RNA pellet was extracted by sequential washing with isopropanol and DNA diluent. A 1 µg sample of RNA was reverse transcribed to DNA using a high-capacity cDNA synthesis kit (Applied Biosystems, USA) followed by the expression of functional genes was assessed using the SYBR Green PCR master mix (Applied Biosystems, USA) in the RT-PCR system. The relative expression levels of functional genes (GOI) in PNRHs cultured on LECM-SF scaffold groups at a predefined time point were quantified according to the comparative CT ($2^{-(\Delta\Delta Ct)}$) method in line with the previous

reports [279]. Briefly, the GOI expression of PNRHs cultured on the LECM-SF scaffold at a predefined time point was normalized to housekeeping glyceraldehyde-3-phosphate-GAPDH expression and represented as in relative to day 1 expression value (as baseline) in the appropriate scaffold group.

3.2.7.2 Immunofluorescence staining

The immunolabeling for liver-specific functional synthetic markers, ALB and FIB; metabolic marker, arginase-1; and cholangiocyte markers, HNF4α, CK-19, and Sox9 was carried out in PNRHs cultured on LECM-SF scaffolds in both static and perfusion bioreactor conditions. The NBF fixed samples were paraffin-embedded, sectioned at 10 µm thickness (using Leica Biosystems microtome, USA), cleared with xylene, and hydrated with a gradient of ethanol treatment. For immunofluorescence staining, each scaffold section was incubated independently for primary antibodies against ALB (1:300 dilution), FIB (1:200 dilution), HNF4α (1:500 dilution), and CK-19 (1:100 dilution) suspended in blocking buffer at 4°C overnight. Next, the sections were washed with 0.1 M PBS and incubated for 1 h in Alexa Fluor 488 secondary antibody at 1:200 dilution in blocking buffer, followed by counterstaining with DAPI and mounting with Dako fluorescent mounting medium. Using Carl Zeiss CLSM, 10 *z*-stacks covering a 10 μm^2 area at 1 µm intervals were imaged and processed using FIJI to obtain representative fluorescence CLSM images. The localization of markers is visualized in green, and the nucleus is stained in blue. The percentage of area positive for each marker ($albumin^+$, $fibronectin^+$, $HNF4\alpha^+$, and $CK\text{-}19^+$) was evaluated relative to the total scaffold area per field of view (FOV) following color deconvolution and thresholding of fluorescence images using the ImageJ program. Subsequently, the hydrated sections were incubated individually with primary antibodies against arginase-1 (1:200 dilution) and Sox9 (1:100 dilution) using the VECTASTAIN Elite-ABC Universal Kit per the manufacturer's protocol, and images were captured using bright field inverted microscopy.

3.2.7.3 Biochemical analysis

3.2.7.3.1 Albumin secretion

The albumin secreted by PNRHs cultured on scaffolds in the conditioned medium was quantified on days 1, 10, 20, and 30 for static culture and on days 1, 15, 30, and 45 for perfusion bioreactor culture using rat albumin ELISA kit (Abcam, UK), as described previously [271]. Briefly, 50 µL of the collected media was serially incubated in a primary antibody-coated well for

1 h and treated with an equal amount of biotinylated albumin antibody and streptavidin conjugate solution. After completion of the reaction, 50 µL of chromogen substrate was added, followed by absorbance measurement at 450 nm and 570 nm. The unknown albumin concentration was estimated from the standard curve plotted with an albumin standard of 0-200 ng/mL.

3.2.7.3.2 Urea release assessment

The urea secreted by PNRHs cultured on scaffolds in the conditioned medium in both static and perfusion bioreactor conditions was quantified calorimetrically using a urea assay kit (Sigma-Aldrich, USA), as per the manufacturer's protocol. The culture medium collected at predefined time points was centrifuged at 1000 rpm for 5 min to collect the supernatant and incubated with an equal amount of reaction mix comprising enzyme mix, peroxidase substrate, and converting enzyme for 60 min. The absorbance was measured at 570 nm, and the unknown urea concentration was calculated from the urea standard curve by

$$(U_s/V_s) = C$$

where U_s = urea in samples (nmol) as calculated from the standard curve

V_s = sample volume (µL)

C = urea concentration (µg) in unknown samples

3.2.7.3.3 Cytochrome P450 activity determination

The metabolic activity of PNRHs cultured on LECM-SF scaffolds in static and perfusion bioreactor conditions was determined by quantifying cytochrome P450 reductase (CPR) enzyme activity using a CPR Activity assay kit (Abcam, UK). The cultured hepatocytes were harvested from scaffolds at predefined time points, and cell lysate microsomal fractions were obtained by differential centrifugation [271]. The cell lysate at respective dilutions was treated with reaction buffer (NADPH substrate, CPR assay buffer, glucose-6-phosphate) for 10 min at 37°C, and the absorbance was measured in kinetic mode at 460 nm to obtain total CPR activity. Correspondingly, the CPR activity of samples in the presence of a CPR inhibitor was estimated by following a similar reaction procedure. The total protein concentration in the cell lysate was quantified using Bradford's method. The total CPR activity was normalized with the CPR activity in the presence of an inhibitor, and the specific CPR activity of the sample was calculated using,

Total CPR Activity (mU/mg) = (A/ (ΔT × IP)) nmol/ min/ mg

where A = G6P consumed, as calculated from the standard graph (absorbance at T_2 – absorbance at T_1)

ΔT = reaction time (T_2 - T_1) (min)

IP = total intracellular protein (mg)

Specific CPR activity (mU/mg) = (CPR activity with inhibitor) – (Total CPR activity)

3.2.8 *In vitro* immunogenic response and hemocompatibility assessment

The *in vitro* inflammatory reaction toward LECM-SF scaffolds was assessed using RAW 264.7 (mouse macrophages) by quantifying the amount of released anti-inflammatory cytokine, interleukin-1β (IL-1β). Briefly, RAW 264.7 cells were seeded at a density of 1×10^5 in a 24-well microtiter plate and cultured in high glucose Dulbecco's Modified Eagle Medium (HDMEM). The RAW 264.7 macrophages stimulated with 500 ng/mL lipopolysaccharide (LPS, *E. coli* origin) were designated as positive pro-inflammatory control, and those cultured in only HDMEM were defined as the negative control. For treatment, RAW 264.7 macrophages were exposed to sterile LECM-SF scaffold discs of 6 mm diameter and 2 mm thickness for 12 h. The medium was then collected, and the amount of released IL-1β was quantified using IL-1β ELISA Kit (Invitrogen, USA) as per the manufacturer's instructions.

The antithrombogenic property of LECM-SF scaffolds was investigated by measuring the lactate dehydrogenase (LDH) activity of adhered platelets on scaffolds [271]. Briefly, the porcine blood was anticoagulated and centrifuged at 100g for 15 min to obtain platelet-rich plasma (PRP). All the variants of sterile LECM-SF scaffold discs of 6 mm diameter and 2 mm thickness were incubated with an equal volume of PRP for 2 h at 37°C. The residual PRP suspension was then removed by repeated washing using 0.1 M PBS, and the adhered platelets were quantified using the LDH activity kit (Sigma-Aldrich, USA), as per the manufacturer's instructions.

3.2.9 *In vivo* host response and macrophage activation analysis in the subcutaneous rat model

The foreign body response and macrophage activation toward LECM-SF scaffolds were studied in the subcutaneous mice (Swiss, I.B.) model of either sex weighing around 30-35 g. Strict sterility measures were followed throughout the animal surgery, and all animal experiments were carried out per the IAEC, WBUAFS, West Bengal, India. Animals were anesthetized using 1-2% isoflurane with oxygen, followed by exposing the subcutaneous pocket located on both the lateral sides. In each mouse, two scaffolds of 5 mm diameter and 2 mm thickness were implanted

randomly in a subcutaneous pocket, and incisions were sutured using 6-0 polypropylene suture. Antibiotics were given two times a day for 3 days to avoid infection. At 1 and 3 weeks post implantation, the mice were sacrificed by cervical dislocation, and the explants along with surrounding host tissue were retrieved and fixed in 10% (v/v) NBF. The paraffin-embedded samples were sectioned and stained with H&E and Masson's trichrome to assess host cellular response and native ECM (collagen) deposition, respectively, following the standard protocol. The multinucleate giant cells were manually counted from H&E images to determine the foreign body response. The blood vessels or angiogenesis toward the LECM-SF scaffolds were assessed by immunostaining for CD31 and quantifying the number of CD31 positive blood vessels. Briefly, the sectioned samples were incubated with CD31 (1:200 dilution) at 4°C overnight and treated with Alexa Flour 488 (1:200 dilution) for 1 h, followed by counterstaining with DAPI. The CD31 positive blood vessels were quantified from the fluorescence images captured using Carl Zeiss CLSM. Furthermore, the sectioned samples were immunostained for CD68 (pan-macrophage marker), CCR7 (M1-like pro-inflammatory marker), and CD163 (M2-like pro-remodeling marker) to investigate macrophage response toward LECM-SF scaffolds. The samples were incubated with primary antibodies against CD68 (1:100 dilution), CCR7 (1:100 dilution), and CD163 (1:100 dilution) at 4°C overnight, followed by secondary antibody treatment for 1 h with Alexa Flour 488 (for CD68) and DyLight 594 (for CCR7 and CD163) at 1:200 dilution. The sections were then counterstained with DAPI and mounted with fluorescent Dako medium, and fluorescence images were captured using Carl Zeiss CLSM. The percentage area of $CCR7^+$ and $CD163^+$ cells was evaluated relative to the total scaffold area per FOV following the color deconvolution and thresholding program using FIJI software.

3.2.10 Statistical analysis

All the results presented were obtained from triplicates (n = 3 samples) in both static and perfusion bioreactor culture, unless otherwise mentioned. The host response study of the liver ECM blend silk scaffolds was studied randomly in n = 3 animals. Data are represented as average ± standard error of mean (SEM). The statistical analysis was carried out by one-way analysis of variance (ANOVA) test, followed by posthoc Dunn's multiple comparison test. The p-values ≤ 0.05, ≤ 0.01, and ≤ 0.001 was considered statistically significant, as denoted by *, **, and ***, respectively.

3.3 Results

3.3.1 Porcine liver tissue decellularization and biochemical characterization

H&E staining revealed the absence of purple-stained nuclear material in decellularized liver, validating effective cell removal **(Figure 3.1 A)**. The positive staining for GAG confirmed ECM preservation at the end of decellularization **(Figure 3.1 A).** Furthermore, biochemical estimation of DNA, collagen, protein, and GAG in native and decellularized liver tissues evidenced the removal of cellular components and ECM preservation **(Figure 3.1 B).** DNA content in decellularized tissue was reduced to 0.06 ± 0.01 µg/mg dry weight compared to 0.87 ± 0.003 µg DNA/mg dry weight in the native liver ($p \leq 0.001$). The isolated liver ECM met the established decellularization criteria of having less than 50 ng DNA/mg dry weight of decellularized tissue **(Figure 3.1 B, i) [287]**. Higher collagen in the decellularized liver (3.0 ± 0.5 µg/mg dry weight) than native liver (1.8 ± 0.02 µg/mg dry weight) might be due to increased exposure of ECM in decellularized tissues **(Figure 3.1 B, ii)**. The total protein and GAG content were not significantly different among native and decellularized liver, confirming ECM structural preservation **(Figure 3.1 B, iii-iv)**.

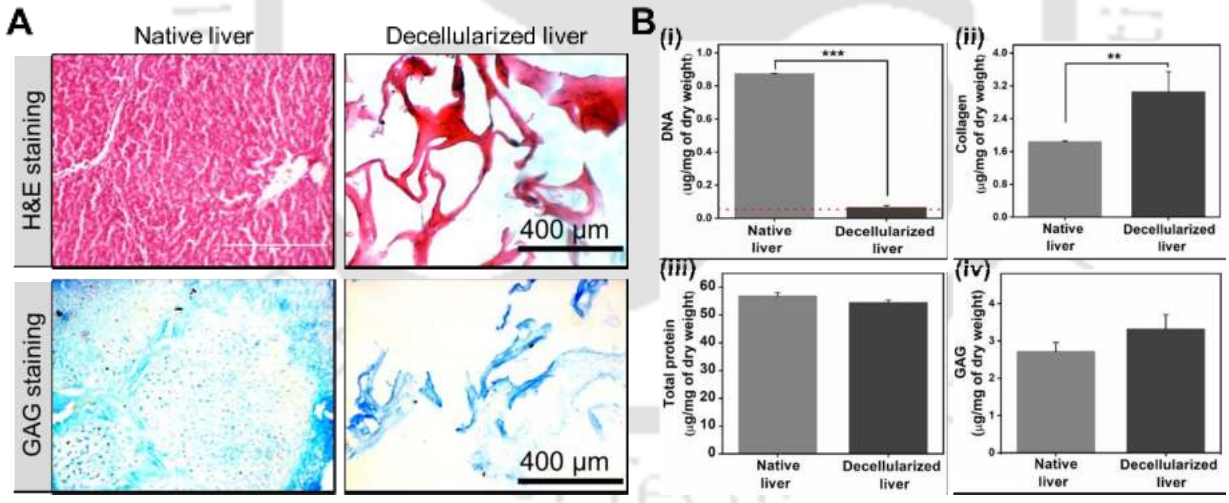

Figure 3.1. Decellularization of porcine liver and its characterization. *(A) H & E and Alcian blue stained images of native and decellularized porcine liver tissues. Scale bar: 400 µm. (B) Biochemical characterization of native and decellularized liver (i) DNA content, (ii) Collagen content, (iii) Total protein content, and (iv) GAG content. Data are expressed as µg per mg of the dry weight of the tissue (n=9). The red dashed line in DNA content represents the reported permissible limit of DNA (50 ng) in decellularized ECM. ** and *** signify the statistical difference between the groups at $p \leq 0.01$ and $p \leq 0.001$, respectively.*

3.3.2 Liver ECM blend silk scaffold fabrication and physicochemical characterization

LECM-SF scaffolds were fabricated from 3% (w/v) decellularized liver stroma solution (dLS) and BA silk fibroin following freeze-drying and EDC/NHS crosslinking **(Table 3.1, Figure 3.2 A)**. The scaffolds after crosslinking showed a shift in the characteristic amide peaks, amide I (C=H stretching at 1700-1600 cm^{-1}), amide II (C=N stretching at 1580-1510 cm^{-1}), and amide III (C-N stretching at 1260–1210 cm^{-1}), denoted by a, b, and c in the spectrum, respectively **(Figure 3.2 B)**, indicating a conformational change in the secondary structure of crosslinked scaffolds. Amide I spectra deconvolution revealed a discrete secondary structure composition in EDC/NHS crosslinked and untreated LECM-SF scaffolds **(***Appendix* **Figure A3.1)**, which was further quantified and summarized in **Table 3.3**. The cumulative higher percentage of β-sheets in EDC/NHS crosslinked LECM-SF scaffolds confirmed the scaffold stability and β-sheet induction. Similarly, the discrete BM silk, AA silk, and dLS prior and after EDC/NHS crosslinking exhibited amide I, II, and III peaks as denoted by a, b, and c in the spectrum, with a shift in crosslinked scaffolds **(***Appendix* **Figure A3.2)**. Remarkably, characteristic peaks at 1370–1450 cm^{-1} and 1150–1085 cm^{-1} denoted by d and e, were noted high in pure dLS, indicating the presence of methyl group and C-O stretching, respectively. Surface morphological analysis through FESEM images demonstrated that each LECM-SF scaffold variant presented an interconnected porous network with distinct pore morphology, thus supporting hepatocyte infiltration. With an increase in ECM proportion in scaffolds, the pore architecture was found to be more rough and fibrous **(Figure 3.2 C)**. All scaffolds exhibited similar pore size **(Figure 3.2 D)** and porosity above 80% **(Figure 3.2 E)**, supporting the hepatocyte infiltration and nutrient diffusion. LECM-SF scaffolds with a higher amount of ECM, (BA:dLS (1:1) and BA:dLS (0.5:1.5)) showed increased ($p \leq 0.01$) porosity over 90% and a higher swelling ratio of 18.9 compared to other variants **(Figure 3.2 E-F)**. The leached out protein from all variants of LECM-SF scaffolds was less than 1% (w/w) of the initial weight, which was insignificant, thus confirming the integral stability of scaffolds after crosslinking **(***Appendix* **Figure A3.3)**. In line with porosity and swelling ratio data, BA:dLS (0.5:1.5) and BA:dLS (1:1) scaffolds degraded significantly ($p \leq 0.01$) at a higher rate with a remaining mass of 8.0 ± 2.4% and 23.4 ± 5.1%, respectively, compared to BA:dLS (2:0) and BA:dLS (1.5:0.5) with a remaining mass of 51.2 ± 8.1% and 56.6 ± 4.4% respectively **(Figure 3.2 G)**. Comparatively, BA:dLS (0.5:1.5) degraded at a higher ($p \leq 0.05$) rate than BA:dLS (1:1). Under hydrated conditions, scaffolds with a higher amount of ECM, BA:dLS (1:1) and BA:dLS (0.5:1.5) presented

($p \leq 0.01$) compressive modulus values of 1.7 ± 0.6 kPa and 1.5 ± 0.02 kPa, respectively, lower than that of BA:dLS (1.5:0.5) **(Figure 3.2 H-I)**. BA:dLS (1:1) and BA:dLS (0.5:1.5) scaffolds exhibited compressive modulus values similar to that of the decellularized human liver (indicated in green dashed line). Among all scaffolds, BA:dLS (2:0) exhibited a remarkably increased ($p \leq 0.001$) compressive modulus of 12.4 ± 3.5 kPa, which is similar to the reported compressive modulus of the native liver (indicated in red dashed line).

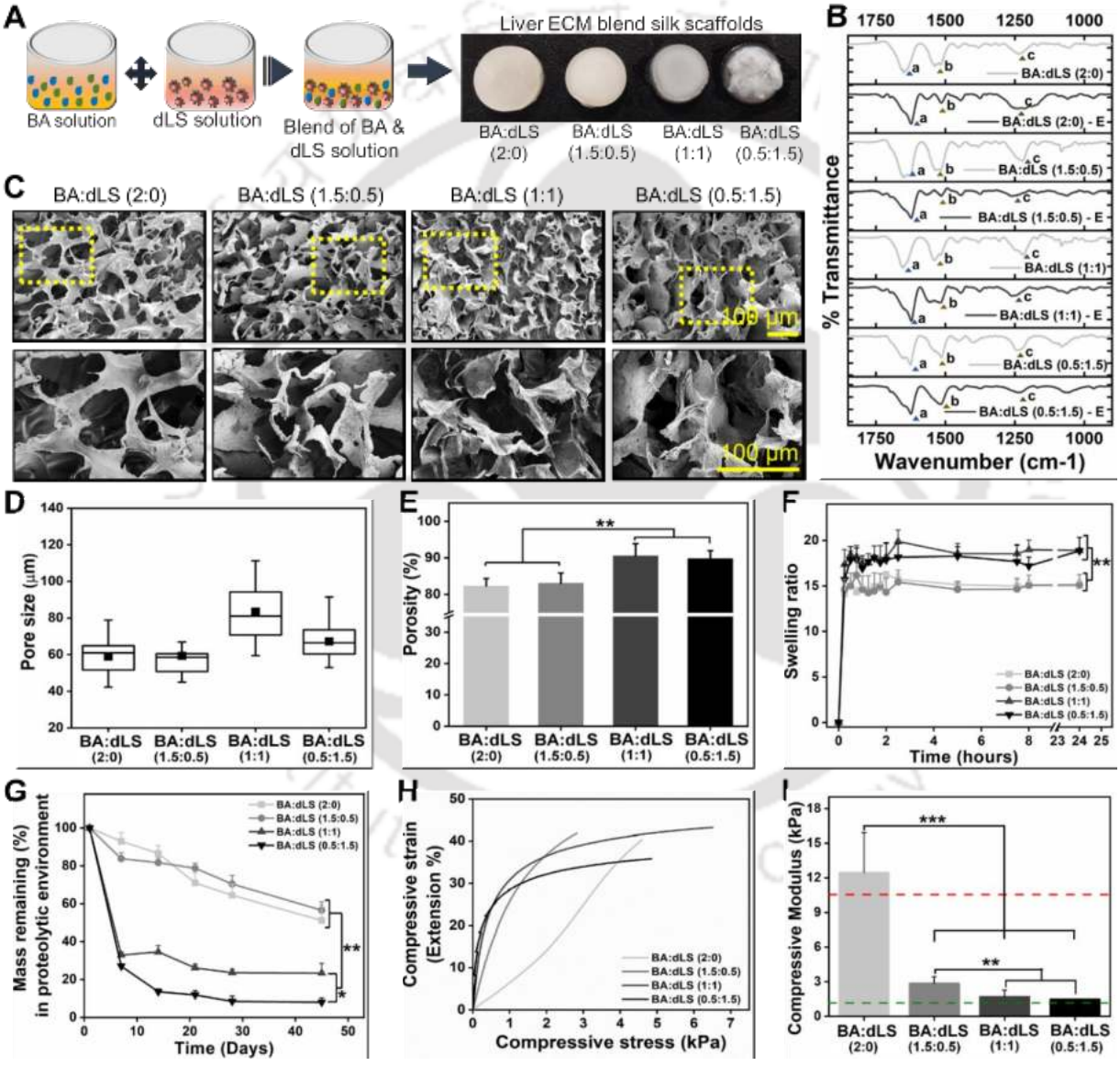

Figure 3.2. Fabrication of liver ECM blend silk scaffolds and their physicochemical characterization. *(A) Schematics representing the fabrication of liver ECM blend silk scaffolds. Physicochemical characterizations of LECM-SF scaffolds by (B) FTIR spectrum of untreated LECM-SF scaffolds, BA:dLS (2:0), BA:dLS (1.5:0.5), BA:dLS (1:1), and BA:dLS (0.5:1.5), and*

*EDC/NHS crosslinked scaffolds, BA:dLS (2:0)-E, BA:dLS (1.5:0.5)-E, BA:dLS (1:1)-E, BA:dLS (0.5:1.5)-E, where "–E" represents EDC/NHS crosslinked scaffolds. "a", "b", and "c" represent amide I, II, and III peaks respectively. (C) FESEM images. The yellow box represents the area shown in the higher magnification image. Scale bar: 100 µm. (D) Pore size. (E) Porosity. (F) Swelling ratio. (G) In vitro degradation profile. (H) Stress-strain curve. (I) Compressive modulus. The red and green dashed line represents the reported compressive modulus of native and decellularized human liver tissue, respectively. Data are represented as average ± standard error of mean, processed from n=6 from each group. *, ** and *** signify the statistical difference between the groups at $p \leq 0.05$, $p \leq 0.01$, and $p \leq 0.001$, respectively.*

Table 3.3. *Secondary structure composition of untreated and EDC/NHS crosslinked LECM-SF scaffolds*

Secondary Structures	Percentage (%)							
	BA: dLS (2:0)	**BA: dLS (2:0)-E**	**BA: dLS (1.5:0.5)**	**BA: dLS (1.5:0.5) -E**	**BA: dLS (1:1)**	**BA: dLS (1:1)-E**	**BA: dLS (0.5:1.5)**	**BA: dLS (0.5:1.5) -E**
β-sheets	63.8	68.9	47.9	55.1	46.6	59.0	38.4	55.8
Disordered structure	16.2	-	-	25.1	30.4	-	-	10.8
α-helices	9.1	31.1	33.1	-	12.2	31.3	46.5	10.6
Loops	10.8	-	19.0	19.7	10.8	9.7	15.0	22.0

3.3.3 Cellular viability and proliferation of hepatocytes cultured on liver ECM blend silk scaffolds

The isolated PNRHs using the two-step collagenase digestion method exhibited >80% cell viability, and a majority of isolated cells expressed characteristic hepatocyte marker albumin **(Figure 3.3 A)**. In static culture, alamar blue proliferation assessment of PNRHs cultured on LECM-SF scaffolds signified that all variants augmented the PNRHs proliferation until 25 days, about 1.4 to 1.5 fold greater than that of day 1, and the proliferation rate was maintained until 30 days **(Figure 3.3 B)**. No significant difference was noted in the proliferation of cultured PNRHs between the scaffolds variants until 10 days. PNRHs proliferation was higher ($p \leq 0.05$) in BA:dLS (1.5:0.5) scaffolds than other scaffolds at days 20 and 25. The CLSM z-stack live-cell images of PNRHs cultured on LECM-SF scaffolds confirmed the viability and hepatocyte infiltration into scaffolds over the culture period **(Figure 3.3 C)**. Further, FESEM and H&E stained images of

PNRHs cultured on LECM-SF scaffolds demonstrated the cellular attachment along the pore wall and PNRHs growth as clusters. Collaboratively, the distribution pattern of PNRHs was uniform in BA:dLS (1.5:0.5) and BA:dLS (1:1), whereas BA:dLS (0.5:1.5) scaffolds supported more aggregate formation of hepatocytes **(Figure 3.3 C)**.

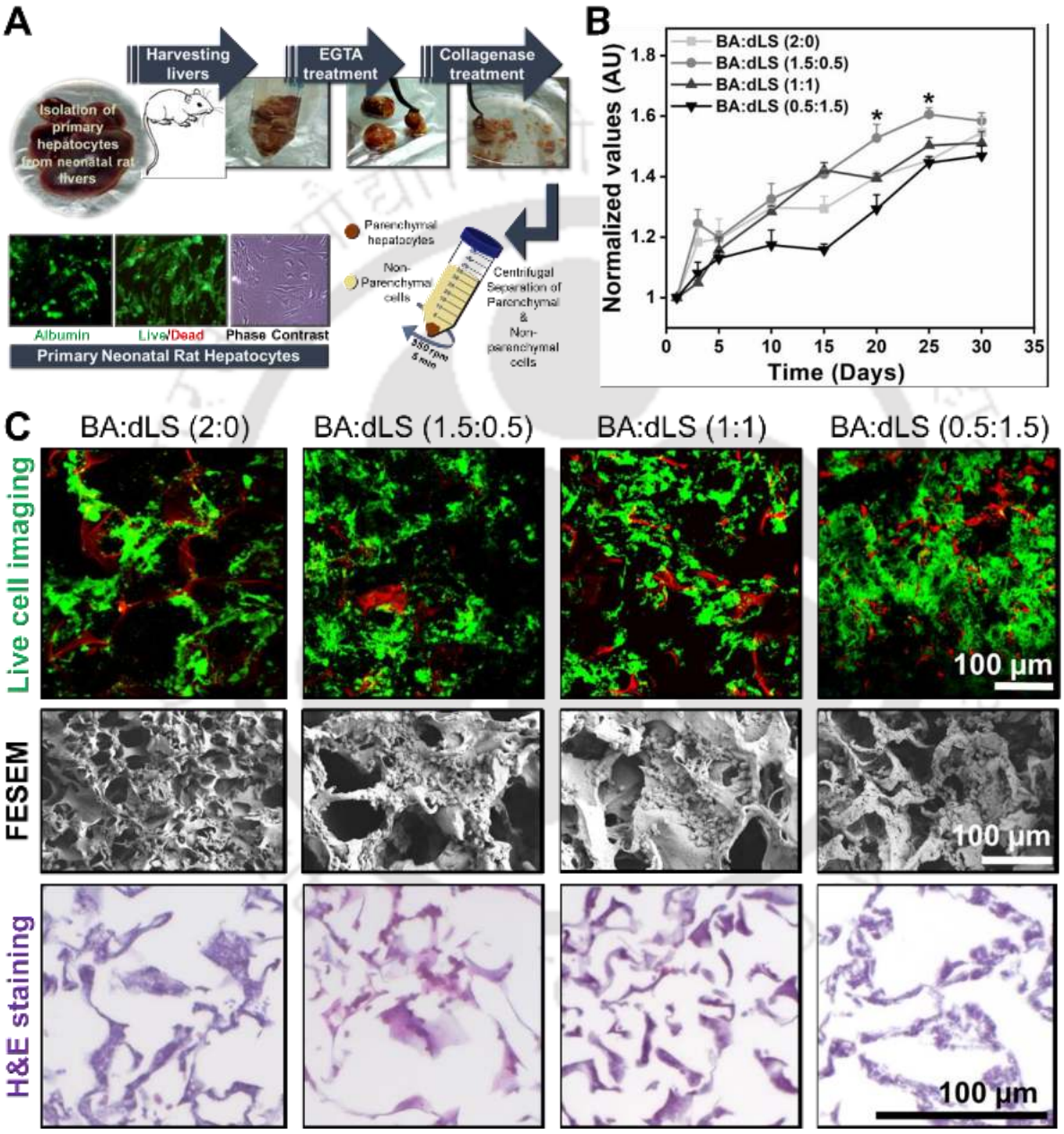

Figure 3.3. Isolation of primary neonatal rat hepatocytes (PNRHs), cellular viability, and proliferation of PNRHs cultured on liver ECM blend silk scaffolds. *(A) Schematics illustrating the PNRHs isolation process from neonatal rat livers, showing the phase contrast and live/dead images of PNRHs, and PNRHs that were positive for hepatocyte marker albumin (shown in green). (B) Proliferation assessment using alamar blue assay. (C) CLSM, FESEM, and H&E images*

*showing the viability and distribution of cultured PNRHs. Scale bar: 100 µm. Data are represented as average ± standard error of mean (n=6). * signifies the statistical difference between the groups at $p \leq 0.05$.*

3.3.4 Zonation biased synthetic and metabolic function profiling upon hepatocyte culture in various liver ECM blend silk scaffolds under static culture conditions

3.3.4.1 Gene expression analysis

The relative expression levels of synthetic genes (ALB and FIB), phase-I and phase-II drug-metabolizing genes (GSTA1, CYP1A2, A1AT, and CYP2E1) were distinct in PNRHs cultured on LECM-SF scaffolds under static conditions **(Figure 3.4 A-B)**. Over 30 days, ALB expression increased ($p \leq 0.01$) about 1.7 - 2.2 fold upon culturing PNRHs in BA:dLS (0.5:1.5) compared to that in BA:dLS (1.5:0.5) and BA:dLS (1:1) **(Figure 3.4 A, i)**. FIB expression were remarkably higher in PNRHs cultured on BA:dLS (1.5:0.5) and BA:dLS (1:1) compared to those cultured on BA:dLS (2:0) and BA:dLS (0.5:1.5) scaffolds over 20 days ($p \leq 0.01$) and 30 days ($p \leq 0.001$) **(Figure 3.4 A, ii)**. The GSTA1 expression in PNRHs cultured on BA:dLS (1:1) was 2.6 and 1.6 fold higher ($p \leq 0.001$) than those in PNRHs cultured on BA:dLS (2:0) and BA:dLS (0.5:1.5), respectively. Similarly, PNRHs cultured on BA:dLS (1.5:0.5) showed an increased GSTA1 expression about 2.2 and 1.4 fold higher ($p \leq 0.001$) than that in PNRHs cultured on BA:dLS (2:0) and BA:dLS (0.5:1.5), respectively **(Figure 3.4 B, i)**. However, CYP1A2 expression levels was comparable in PNRHs cultured on BA:dLS (1.5:0.5), BA:dLS (1:1) and BA:dLS (0.5:1.5) over 30 days **(Figure 3.4 B, ii)**. A1AT expression levels were comparable in PNRHs cultured on BA:dLS (1.5:0.5) and BA:dLS (1:1), and 3.2 fold higher ($p \leq 0.01$) than those in PNRHs cultured on BA:dLS (2:0) and BA:dLS (0.5:1.5) **(Figure 3.4 B, iii)**. The CYP2E1 expression was remarkably higher ($p \leq 0.001$) in PNRHs cultured on BA:dLS (1.5:0.5) and BA:dLS (1:1) than that in PNRHs cultured on BA:dLS (2:0) and BA:dLS (0.5:1.5) **(Figure 3.4 B, iv)**.

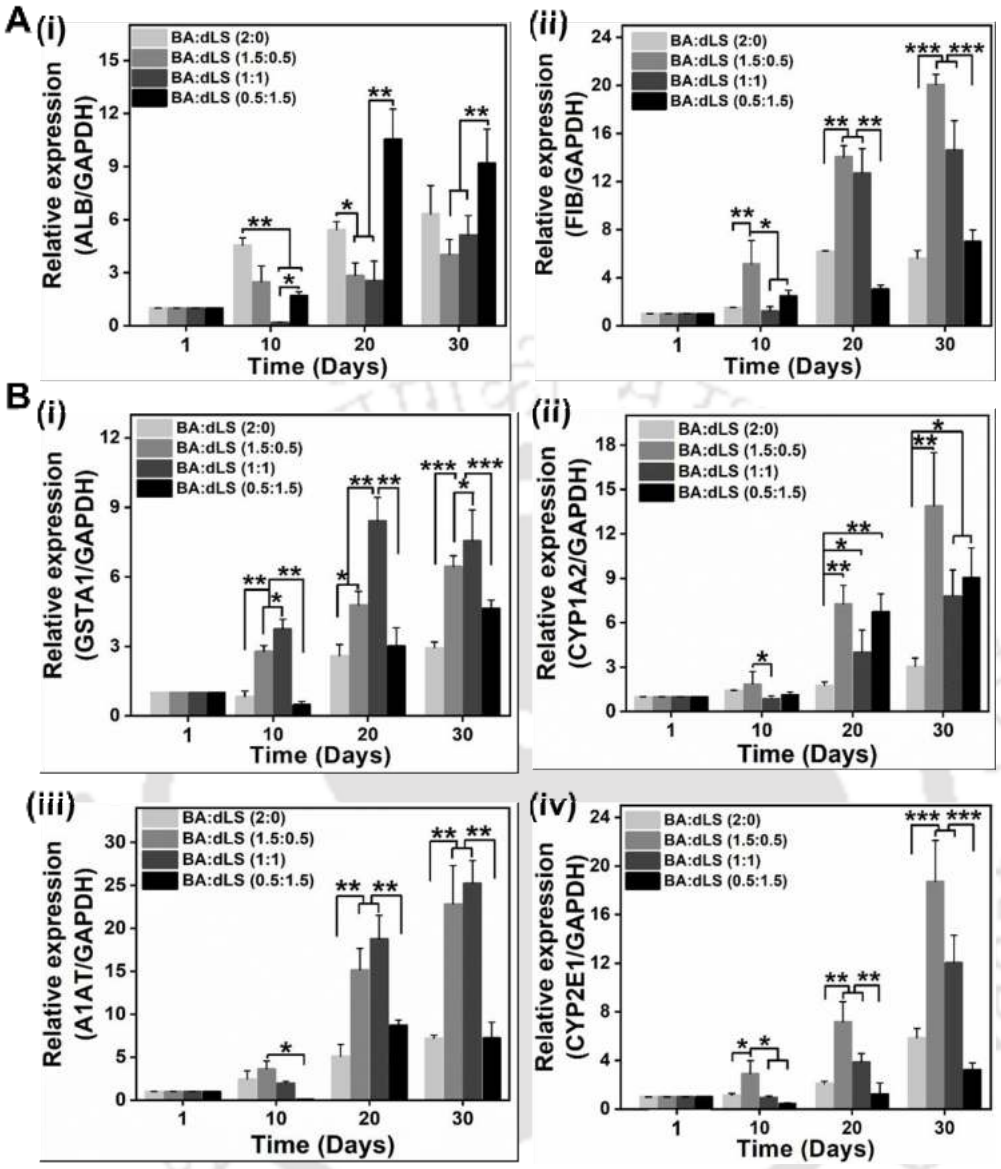

Figure 3.4. Liver-specific synthetic and detoxification functions in the static culture of PNRHs seeded liver ECM blend silk scaffolds over 30 days. *Relative expression of (A) synthetic gene markers (i) ALB and (ii) FIB, and (B) detoxification gene markers (i) GSTA1, (ii) CYP1A2, (iii) A1AT, and (iv) CYP2E1. Data are represented as average ± standard error of mean (n=3). *, ** and *** signify the statistical difference between the groups at $p \leq 0.05$, $p \leq 0.01$, and $p \leq 0.001$, respectively.*

3.3.4.2 Immunostaining for protein expression

Immunostaining for albumin and fibronectin in PNRHs cultured on LECM-SF scaffolds confirmed the differential expression of synthetic proteins **(Figure 3.5 A, i-ii)**. The scaffold with higher ECM, BA:dLS (0.5:1.5) supported an increased albumin expression in cultured PNRHs

than the other three scaffold variants, as validated from immunostaining and percentage area of albumin$^+$ cells ($p \leq 0.01$) **(Figure 3.5 A, i, iii)**. The percentage area of albumin$^+$ cells in PNRHs cultured on BA:dLS (2:0), BA:dLS (1.5:0.5), BA:dLS (1:1), and BA:dLS (0.5:1.5) were 3.9 ± 0.5, 1.6 ± 0.4, 3.3 ± 0.7, and 10.9 ± 1.4 respectively **(Figure 3.5 A, iii)**. Although fibronectin expression increased in PNRHs cultured on BA:dLS (1.5:0.5) and BA:dLS (1:1) compared to that in PNRHs cultured on BA:dLS (2:0) and BA:dLS (0.5:1.5), as corroborated from immunostaining and percentage area calculation ($p \leq 0.01$) **(Figure 3.5 A, ii-iv)**. The percentage area of fibronectin$^+$ cells in PNRHs cultured on BA:dLS (2:0), BA:dLS (1.5:0.5), BA:dLS (1:1), and BA:dLS (0.5:1.5) were 1.4 ± 0.4, 4.6 ± 0.7, 7.8 ± 0.8, and 1.9 ± 0.3 respectively **(Figure 3.5 A, iv)**. Moreover, immunostaining for arginase-1 evidenced an equivalent expression in PNRHs cultured on LECM-SF scaffold variants **(Figure 3.5 B)**.

3.3.4.3 Effect on albumin synthesis, urea secretion, and cytochrome P450 activity

The total albumin in the conditioned media increased over the 30 day culture period in all PNRHs cultured on LECM-SF scaffold variants **(Figure 3.5 C, i)**. Improved albumin secretion was noticed in PNRHs cultured on BA:dLS (0.5:1.5) than PNRHs cultured on BA:dLS (2:0), BA:dLS (1.5:0.5), and BA:dLS (1:1) at day 10 ($p \leq 0.05$) and day 20 ($p \leq 0.01$). Notably, total albumin secreted over 30 days in PNRHs cultured on BA:dLS (0.5:1.5) was 19.6 ± 0.5 µg, which was 2.1 fold higher than that in PNRHs cultured on BA:dLS (2:0) with 9.3 ± 0.9 µg and 1.5 fold higher than that in PNRHs cultured on BA:dLS (1.5:0.5) and BA:dLS (1:1), 13.5 ± 0.9 µg and 12.3 ± 0.6 µg, respectively. Similarly, a steady increase in urea secretion was witnessed by all PNRHs cultured on LECM-SF scaffolds over 30 days **(Figure 3.5 C, ii)**. The PNRHs cultured on BA:dLS (1.5:0.5) and BA:dLS (1:1) secreted similar urea levels until day 30. However, PNRHs cultured on BA:dLS (0.5:1.5) demonstrated increased ($p \leq 0.01$) urea secretion at day 30 and 1.2 fold higher than urea secreted by PNRHs cultured on BA:dLS (2:0), BA:dLS (1.5:0.5) and BA:dLS (1:1). The total CPR activity was unique and improved among PNRHs cultured on LECM-SF scaffold variants over 30 days **(Figure 3.5 C, iii)**. At day 30, the PNRHs cultured on BA:dLS (1:1) presented ($p \leq 0.05$) CPR activity (0.40 ± 0.04 mU/mg) 1.5 times higher than that of PNRHs cultured on BA:dLS (2:0) (0.27 ± 0.04 mU/mg). Similarly, at day 30, the CPR activity of PNRHs cultured on BA:dLS (1.5:0.5) (0.34 ± 0.06 mU/mg) and BA:dLS (1:1) (0.40 ± 0.04 mU/mg) were 2 fold higher ($p \leq 0.01$) than that of PNRHs cultured on BA:dLS (0.5:1.5) (0.17 ± 0.02 mU/mg).

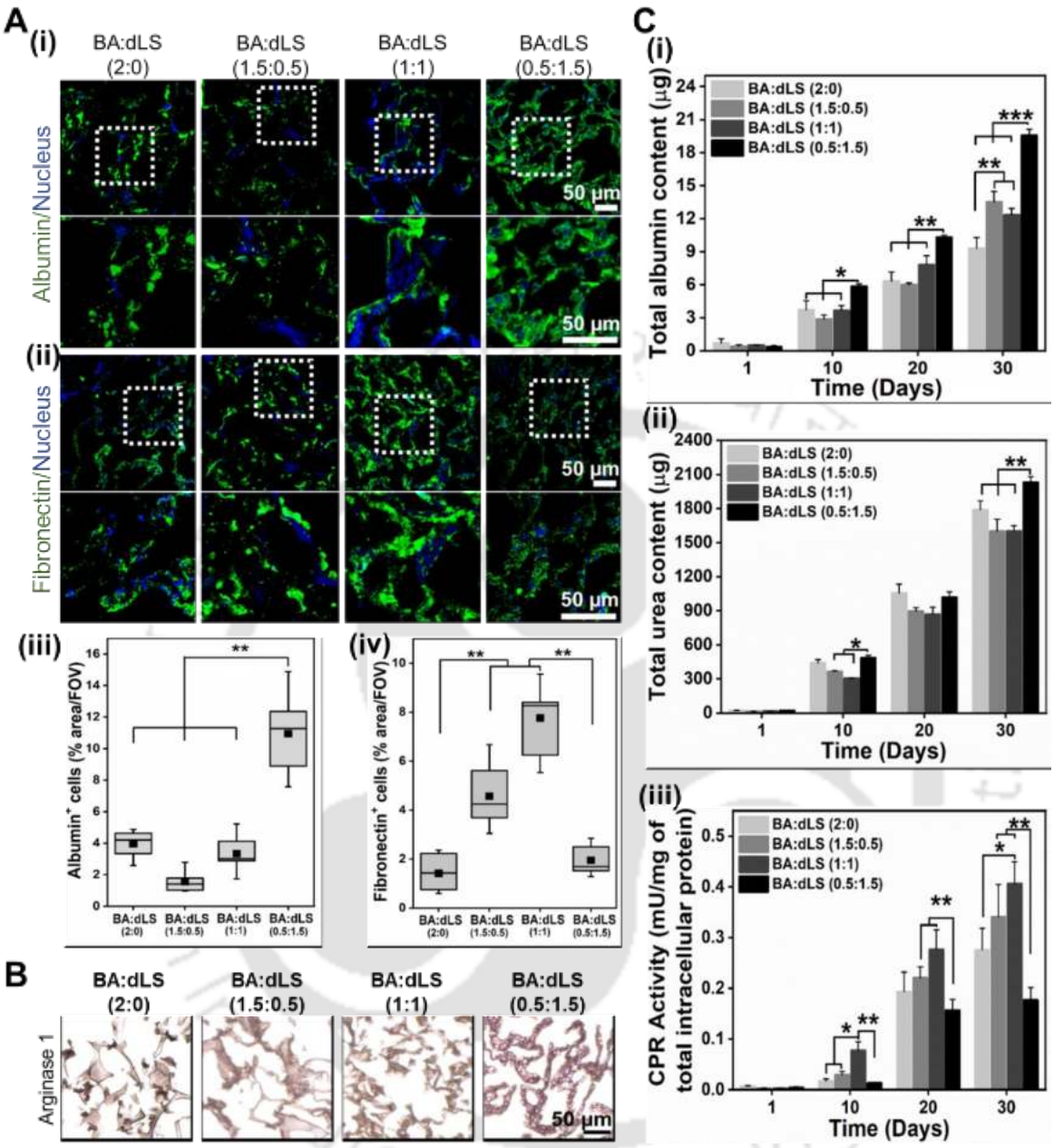

Figure 3.5. Liver-specific synthetic and detoxification functions in the static culture of PNRHs seeded liver ECM blend silk scaffolds over 30 days. *(A) Representative CLSM immunofluorescence images showing the expression of (i) albumin and (ii) fibronectin, and quantification of percentage area of (iii) albumin- and (iv) fibronectin-positive cells per scaffold FOV processed from immunofluorescence images (n=9 from each group). The white box represents the area shown in the high magnification image. Scale bar: 50 µm. (B) Immunostained images showing arginase-1 expression. Scale bar: 50 µm. (C) Biochemical estimation of total (i) albumin, (ii) urea, and (iii) cytochrome P450 activity. Data are represented as average ± standard error of mean (n=3). *, ** and *** signify the statistical difference between the groups at $p \leq 0.05$, $p \leq 0.01$, and $p \leq 0.001$, respectively.*

3.3.5 Zonation biased cholangiocyte profiling upon PNRHs cultured on liver ECM blend silk scaffolds under static culture conditions

3.3.5.1 Gene expression analysis

The expression levels of hepatic progenitor genes (HNF4α) and cholangiocyte genes (CK-19 and Sox9) were distinct in PNRHs cultured on LECM-SF scaffolds **(Figure 3.6 A)**. Over 10 days, HNF4α expression remarkably increased ($p \leq 0.01$) in PNRHs cultured on BA:dLS (2:0) and BA:dLS (0.5:1.5) compared to that in PNRHs cultured on BA:dLS (1.5:0.5) and BA:dLS (1:1) **(Figure 3.6 A, i)**. However, at day 30, the PNRHs cultured on BA:dLS (0.5:1.5) expressed HNF4α at levels 1.6 to 2.1 fold higher ($p \leq 0.001$) than the levels in PNRHs cultured on BA:dLS (2:0), BA:dLS (1:1), and BA:dLS (1.5:0.5). Similarly, CK-19 and Sox9 expression significantly increased in PNRHs cultured on BA:dLS (0.5:1.5) compared to that in PNRHs cultured on BA:dLS (2:0), BA:dLS (1.5:0.5), and BA:dLS (1:1) at day 30 **(Figure 3.6 A, ii-iii)**. At day 30, CK-19 expression in PNRHs cultured on BA:dLS (0.5:1.5) was 2.5 fold higher ($p \leq 0.001$) than that in other scaffold variants **(Figure 3.6 A, ii)**. Similarly, Sox9 expression in PNRHs cultured on BA:dLS (0.5:1.5) was 2.1 fold higher ($p \leq 0.01$) than PNRHs cultured on other scaffold variants **(Figure 3.6 A, iii)**.

3.3.5.2 Immunostaining for protein expression

Immunostaining displayed a differential expression of HNF4α and CK-19 upon PNRHs culture in LECM-SF scaffolds **(Figure 3.6 B, i-ii)**. Granular expression of HNF4α was observed in the cytoplasm of hepatocyte aggregates along with preferential nucleus expression. Spheroidal culture of hepatocytes has been reported to affect the nucleus localization of HNF4α due to the phosphorylation of HNF4α by SRC tyrosinase kinase [270, 274]. The percentage area of $HNF4\alpha^+$ cells in PNRHs cultured on BA:dLS (2:0), BA:dLS (1.5:0.5), BA:dLS (1:1), and BA:dLS (0.5:1.5) were 1.1 ± 0.1, 0.7 ± 0.2, 0.6 ± 0.1, and 2.1 ± 0.3, respectively **(Figure 3.6 B, iii)**. The percentage area of $CK\text{-}19^+$ cells in PNRHs cultured on BA:dLS (2:0), BA:dLS (1.5:0.5), BA:dLS (1:1), and BA:dLS (0.5:1.5) were 4.4 ± 0.4, 2.9 ± 0.7, 3.3 ± 0.6, and 9.7 ± 1.3, respectively **(Figure 3.6 B, iv)**. The scaffold with higher ECM, BA:dLS (0.5:1.5) supported increased HNF4α and CK-19 expression in cultured PNRHs, as corroborated from the percentage area of $HNF4\alpha^+$ and $CK\text{-}19^+$ cells ($p \leq 0.01$) **(Figure 3.6 B, iii-iv)**. As a further indication of cholangiocyte functions supported by BA:dLS (0.5:1.5), immunostaining for Sox9 demonstrated an increased expression in PNRHs cultured on BA:dLS (0.5:1.5) **(Figure 3.6 C)**.

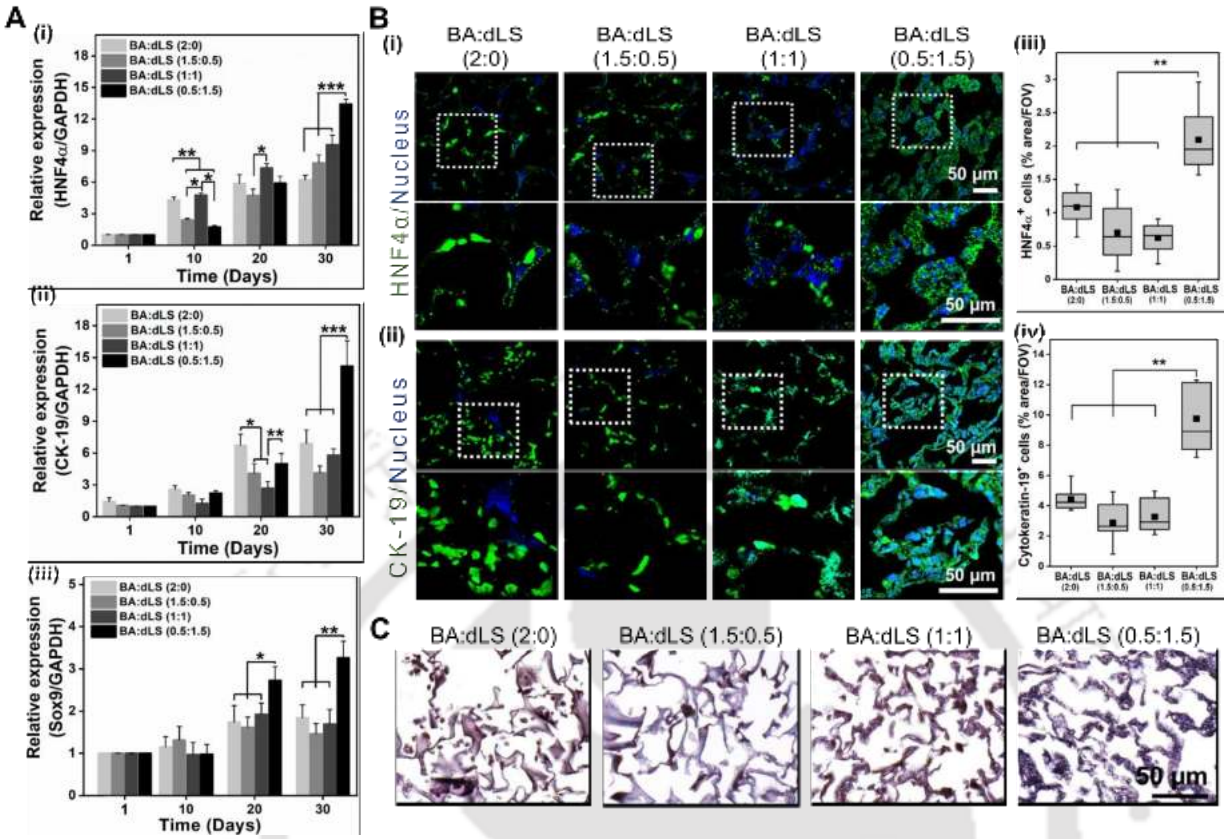

Figure 3.6. Liver-specific endodermal and cholangiocyte functions in the static culture of PNRHs seeded liver ECM blend silk scaffolds over 30 days. *(A) Relative expression of (i) HNF4α, (ii) CK-19, and (iii) Sox9. Data are represented as average ± standard error of mean (n=3). *, ** and *** signify the statistical difference between the groups at $p \leq 0.05$, $p \leq 0.01$, and $p \leq 0.001$, respectively. (B) Representative CLSM immunofluorescence images showing the expression of (i) HNF4α and (ii) CK-19; quantification of percentage area of (iii) HNF4α- and (iv) CK-19-positive cells per scaffold FOV processed from immunofluorescence images (n=9 from each group). The white box represents the area shown in the high magnification image. Scale bar: 50 µm. C. Immunostained images showing the Sox9 expression. Scale bar: 50 µm.*

3.3.6 Zonation biased synthetic and metabolic function profiling upon PNRHs cultured on liver ECM blend silk scaffolds as a single system upon perfusion bioreactor culture

Under static conditions, each scaffold variant supported a unique pattern of synthetic, metabolic, and cholangiocyte functions in cultured PNRHs, which might be associated with microenvironmental cues and physicochemical properties of scaffolds. Taken together, the PNRHs cultured on BA:dLS (0.5:1.5) closely recapitulated the zone 1 PP-specific liver functions, and PNRHs cultured on BA:dLS (1.5:0.5) mimicked the zone 3 PC-specific liver functions. With respect to this, the PNRHs seeded scaffolds were stacked as a single whole system in the perfusion

bioreactor chamber as the media infuses through BA:dLS (0.5:1.5), then BA:dLS (1:1), and diffuses out from BA:dLS (1.5:0.5), and matured over 45 days, as illustrated in schematics **(Figure 3.7 A)**. As BA:dLS (2:0) demonstrated higher compressive modulus, acellular BA:dLS (2:0) was placed at the bottom of the whole system to withhold mechanical stress during media perfusion. The H&E stained longitudinal section (LS) and cross-section (CS) of PNRHs cultured on scaffolds presented uniform hepatocyte infiltration into scaffolds after 35 days of maturation in the perfusion bioreactor **(Figure 3.7 B)**. Comparatively, PNRHs distribution increased in BA:dLS (0.5:1.5) mimicking PP region, compared to BA:dLS (1:1) and BA:dLS (1.5:0.5).

3.3.6.1 Gene expression analysis

The expression levels of synthetic genes (ALB and FIB), and phase-I and phase-II drug-metabolizing genes (GSTA1, CYP1A2, A1AT, and CYP2E1) upon perfusion bioreactor culture of PNRHs seeded on a single whole system were quantified **(Figure 3.7 C)**. After 30 days of maturation, BA:dLS (0.5:1.5) supported an increased ALB expression about 1.8 and 5 fold higher than BA:dLS (1:1) and BA:dLS (1.5:0.5), respectively **(Figure 3.7 C, i)**. At 45 days, ALB expression was 2.2 fold higher ($p \leq 0.01$) in PNRHs cultured on BA:dLS (0.5:1.5) than that in PNRHs cultured on BA:dLS (1:1) and BA:dLS (1.5:0.5), resembling PP functions. However, FIB expression remarkably increased ($p \leq 0.001$) in PNRHs cultured on BA:dLS (1:1) and BA:dLS (1.5:0.5) about 3.1 fold higher than that in PNRHs cultured on BA:dLS (0.5:1.5) over 45 days maturation **(Figure 3.7 C, ii)**. The expression levels of GSTA1 and CYP1A2 were 1.8 fold higher in PNRHs cultured on BA:dLS (1.5:0.5) and BA:dLS (1:1) than those in PNRHs cultured on BA:dLS (0.5:1.5) over 45 days **(Figure 3.7 C, iii-iv)**. Similarly, A1AT expression was 3.9 fold higher in PNRHs cultured on BA:dLS (1.5:0.5) and BA:dLS (1:1) than that in PNRHs cultured on BA:dLS (0.5:1.5) ($p \leq 0.001$) **(Figure 3.7 C, v)**. CYP2E1 expression was 1.3 times higher in PNRHs cultured on BA:dLS (1.5:0.5) and BA:dLS (1:1) than that in PNRHs cultured on BA:dLS (0.5:1.5) ($p \leq 0.01$) **(Figure 3.7 C, vi)**. Taken together, expression levels of drug-metabolizing genes were significantly higher in scaffolds resembling the PC region in the bioreactor.

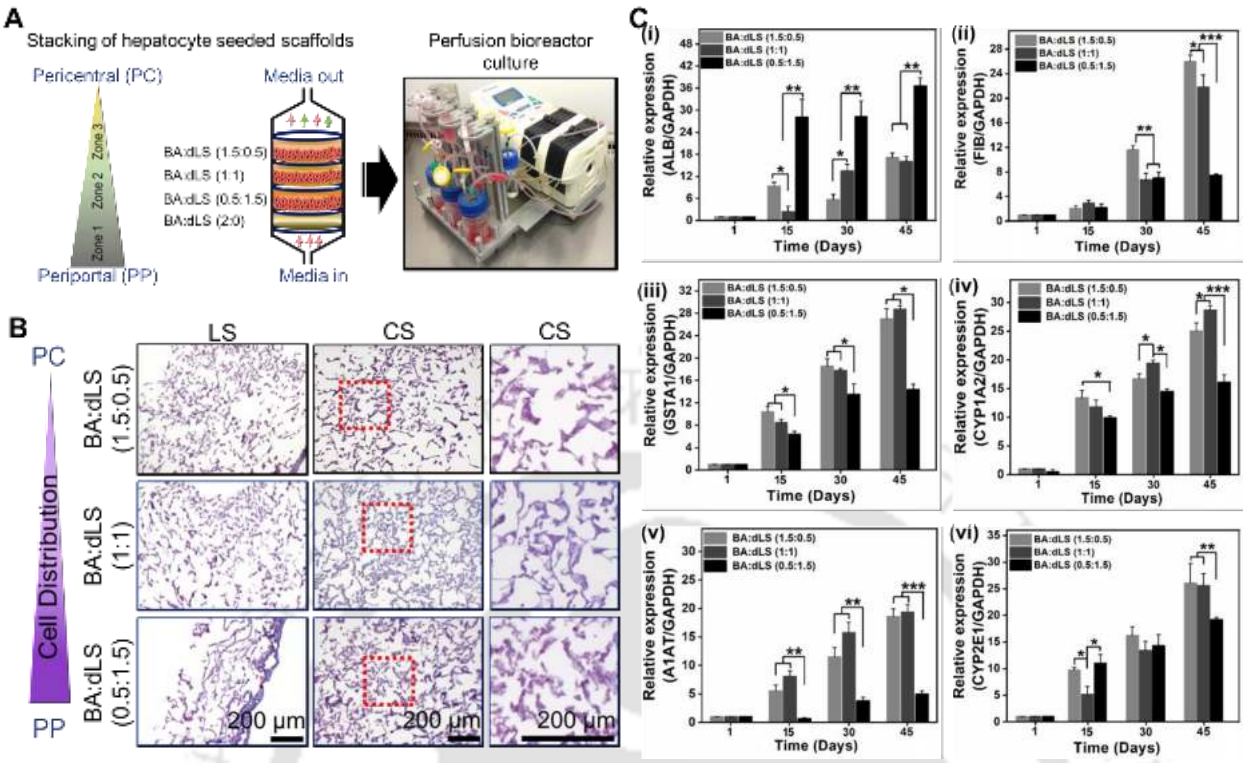

Figure 3.7. Liver-specific synthetic and detoxification functions in perfusion bioreactor culture of PNRHs seeded liver ECM blend silk scaffolds over 45 days. *(A) Schematics showing the stacking arrangement of PNRHs seeded liver ECM blend silk scaffolds and maturing in perfusion bioreactor over 45 days. (B) H&E images showing the cellular distribution. The red box in CS represents the area shown in the CS high magnification image. Scale bar: 200 µm. (C) Relative expression of synthetic gene markers (i) ALB and (ii) FIB, and detoxification gene markers (iii) GSTA1, (iv) CYP1A2, (v) A1AT, and (vi) CYP2E1. PP and PC represent periportal and pericentral regions, respectively; LS- Longitudinal section of scaffolds; CS-Cross section of scaffolds. Data are represented as average ± standard error of mean (n=3). *, ** and *** signify the statistical difference between the groups at $p \leq 0.05$, $p \leq 0.01$, and $p \leq 0.001$, respectively.*

3.3.6.2 Immunostaining for protein expression

PNRHs cultured on BA:dLS (0.5:1.5), BA:dLS (1:1), and BA:dLS (1.5:0.5) and matured as a single system in perfusion bioreactor were immunostained for albumin and fibronectin **(Figure 3.8 A, i-ii)**. Peculiarly, a gradient of albumin expression with higher expression was observed in PNRHs cultured on BA:dLS (0.5:1.5), mimicking the zone 1 PP region, and lower albumin levels in PNRHs cultured on BA:dLS (1:1) and BA:dLS (1.5:0.5) **(Figure 3.8 A, i)**. This was validated from the quantification results, where the percentage area of albumin$^+$ cells was higher ($p \leq 0.001$) in PNRHs cultured on BA:dLS (0.5:1.5) than those in PNRHs cultured on BA:dLS (1:1) and BA:dLS (1.5:0.5) **(Figure 3.8 A, iii)**. The percentage area of albumin$^+$ cells in

PNRHs cultured on BA:dLS (0.5:1.5), BA:dLS (1:1), and BA:dLS (1.5:0.5) were 8.2 ± 0.8, 1.8 ± 0.4, and 1.2 ± 0.2, respectively. However, fibronectin expression was similar among PNRHs cultured on BA:dLS (1:1) and BA:dLS (1.5:0.5) compared to that in PNRHs cultured on BA:dLS (0.5:1.5) **(Figure 3.8 A, ii)**. The percentage area of fibronectin^{+} cells in PNRHs cultured on BA:dLS (0.5:1.5), BA:dLS (1:1), and BA:dLS (1.5:0.5) were 1.9 ± 0.3, 2.9 ± 0.4, and 5.6 ± 0.7, respectively, in which PNRHs cultured on BA:dLS (1.5:0.5) presented enhanced fibronectin ($p \leq 0.05$) expression compared to that in the other two scaffolds **(Figure 3.8 A, iv)**. Similarly, arginase-1 immunostaining of the culture system revealed a gradient arginase-1 expression, with higher levels in PNRHs cultured on BA:dLS (0.5:1.5), mimicking the zone 1 PP region **(Figure 3.8 B)**.

3.3.6.3 Effect on albumin synthesis, urea secretion, and cytochrome P450 activity

The albumin and urea secreted by a single system into the conditioned media were quantified at days 1, 10, 20, 30, and 45 upon maturation in the perfusion bioreactor **(Figure 3.8 C, i-ii)**. The total albumin increased ($p \leq 0.01$) by 4.8 fold at day 30 compared to days 10 and 20 of maturation **(Figure 3.8 C, i)**. Over 45 days, the total albumin secreted into the medium was 940.7 ± 40.2 µg, which was 1.8 times higher than that at day 30. However, total urea secreted into the media gradually increased until 30 days (8498.9 ± 628.2 µg) and maintained a similar level up to 45 days (9177.5 ± 118.2 µg) **(Figure 3.8 C, ii)**. The total urea secreted in the medium at days 30 and 45 was higher ($p \leq 0.001$) than that on days 10 and 20. Furthermore, the CPR activity of PNRHs cultured in each scaffold was analyzed at predefined time points **(Figure 3.8 C, iii)**. Similar to gene expression analysis, the CPR activity of PNRHs cultured on BA:dLS (1.5:0.5) and BA:dLS (1:1) were significantly higher than the CPR activity of PNRHs cultured on BA:dLS (0.5:1.5) at days 30 and 45. Over 45 days, the CPR activity of PNRHs cultured on BA:dLS (0.5:1.5), BA:dLS (1:1), and BA:dLS (1.5:0.5) were 0.29 ± 0.02 mU/mg, 0.54 ± 0.02 mU/mg, and 0.43 ± 0.03 mU/mg, respectively. The CPR activity of PNRHs cultured on BA:dLS (1:1) was higher ($p \leq 0.01$) than that of PNRHs cultured on BA:dLS (1.5:0.5) and BA:dLS (0.5:1.5), respectively, confirming higher CPR activity towards the PC region.

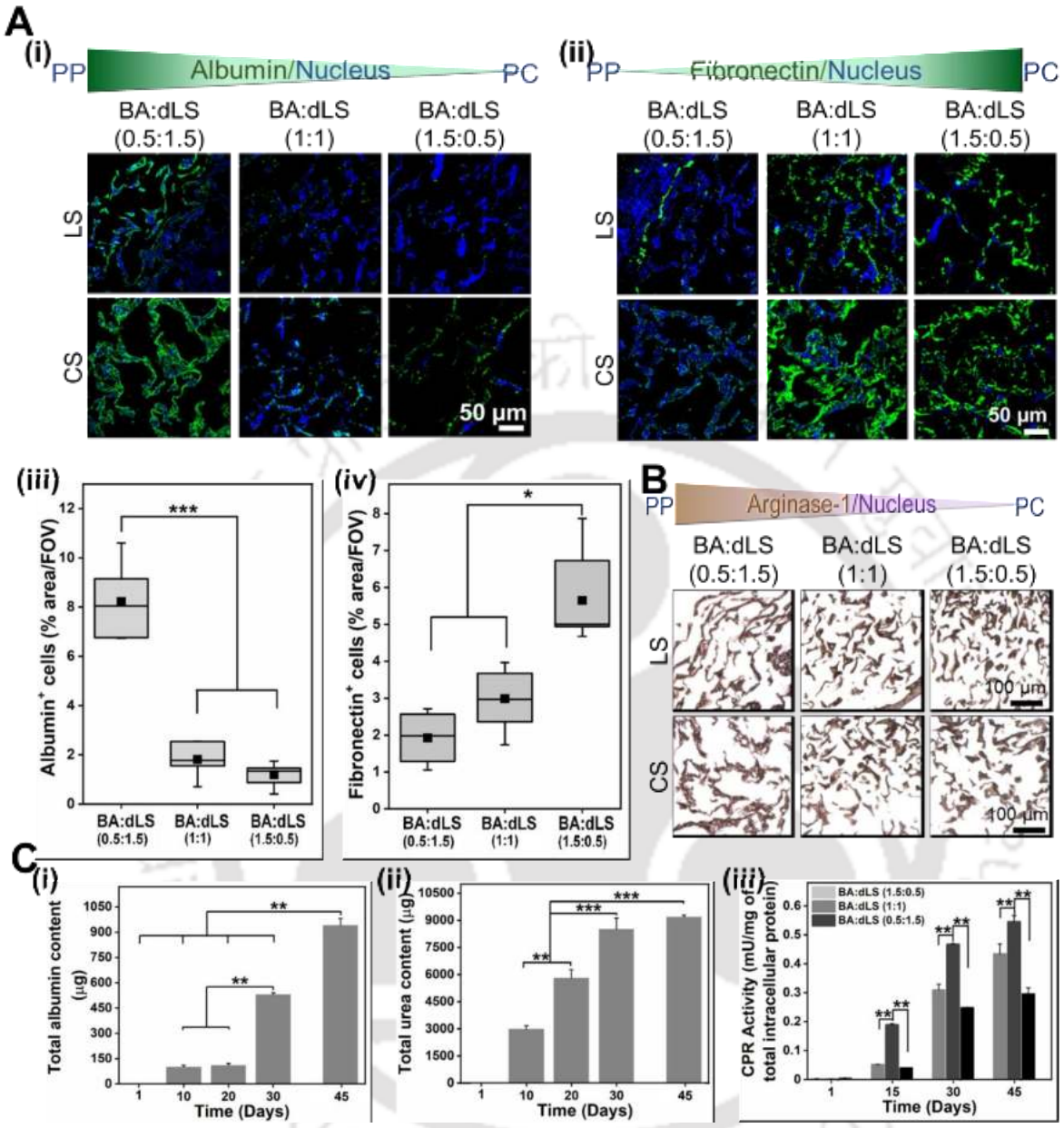

Figure 3.8. Liver-specific synthetic and detoxification functions in perfusion bioreactor culture of PNRHs seeded liver ECM blend silk scaffolds over 45 days. *(A) Representative CLSM immunofluorescence images showing the gradient expression of (i) albumin and (ii) fibronectin; quantification of percentage area of (iii) albumin- and (iv) fibronectin-positive cells per scaffold FOV processed from immunofluorescence images (n=9 from each group). Scale bar: 50 µm. (B) Immunostained images showing arginase-1expression. Scale bar: 100 µm. (C) Biochemical quantitative estimation of total (i) albumin, (ii) urea, and (iii) cytochrome P450 activity. PP and PC represent periportal and pericentral regions, respectively; LS-Longitudinal section of scaffolds; CS-Cross section of scaffolds. Data are represented as average ± standard error of mean (n=3). *, ** and *** signify the statistical difference between the groups at $p \leq 0.05$, $p \leq 0.01$, and $p \leq 0.001$, respectively.*

3.3.7 Zonation biased cholangiocyte profiling upon PNRHs cultured on liver ECM blend silk scaffolds as a single system upon perfusion bioreactor culture

3.3.7.1 Gene expression analysis

The expression levels of hepatic progenitor genes (HNF4α), and cholangiocyte genes (CK-19, Sox9) were assessed in PNRHs cultured as a single system upon maturation in perfusion bioreactor **(Figure 3.9 A)**. The HNF4α expression was similar up to 15 days in PNRHs cultured on all three scaffolds; however, HNF4α expression increased ($p \leq 0.01$) in PNRHs cultured on BA:dLS (0.5:1.5) than PNRHs cultured on BA:dLS (1.5:0.5) and BA:dLS (1:1) at days 30 and 45 **(Figure 3.9 A, i)**. HNF4α expression in PNRHs cultured on BA:dLS (0.5:1.5) significantly increased by about 4 fold at day 30 compared to that at day 15 and increased by 1.3 times at day 45 than that at day 30. Similarly, the expression of CK-19 and Sox9 increased in PNRHs cultured on BA:dLS (0.5:1.5), mimicking the zone 1 PP region, compared to expression in PNRHs cultured on BA:dLS (1.5:0.5) and BA:dLS (1:1) **(Figure 3.9 A, ii-iii)**. The CK-19 expression was enhanced ($p \leq 0.01$) in PNRHs cultured on BA:dLS (0.5:1.5) compared to that in PNRHs cultured on BA:dLS (1.5:0.5) and BA:dLS (1:1) at days 15, 30 and 45 upon bioreactor culture **(Figure 3.9 A ii)**. Subsequently, Sox9 expression was 2.5 fold higher in PNRHs cultured on BA:dLS (0.5:1.5), mimicking the PP zone 1 region, compared to that in PNRHs cultured on BA:dLS (1.5:0.5) and BA:dLS (1:1) at days 30 and 45 of maturation **(Figure 3.9 A, iii)**.

3.3.7.2 Immunostaining for protein expression

Upon maturation as a single system in the perfusion bioreactor, both LS and CS of PNRHs cultured on BA:dLS (0.5:1.5), BA:dLS (1:1), and BA:dLS (1.5:0.5) was immunostained for HNF4α and CK-19 **(Figure 3.9 B)**. A similar trend was evidenced in HNF4α and CK-19 expression, following a gradient with increased expression in PNRHs cultured on BA:dLS (0.5:1.5), resembling the zone 1 PP region **(Figure 3.9 B-C)**. A granular HNF4α expression was observed in the cytoplasm of hepatocyte aggregates along with preferential nucleus expression. Spheroidal culture of hepatocytes has been reported to affect the nucleus localization of HNF4α due to the phosphorylation of HNF4α by SRC tyrosinase kinase [270, 274]. Also, the percentage area of $HNF4\alpha^+$ cells in PNRHs cultured on BA:dLS (0.5:1.5), BA:dLS (1:1), and BA:dLS (1.5:0.5) were 6.1 ± 0.7, 1.9 ± 0.3, and 1.9 ± 0.4, respectively, with increased ($p \leq 0.01$) $HNF4\alpha^+$ cells in PNRHs cultured on BA:dLS (0.5:1.5) **(Figure 3.9 C, i)**. Intense CK-19 staining was observed along the cell membrane with minimal positive staining in the cytoplasm. Similarly, the

percentage area of CK-19$^+$ cells in PNRHs cultured on BA:dLS (0.5:1.5), BA:dLS (1:1), and BA:dLS (1.5:0.5) were 6.9 ± 1.3, 0.9 ± 0.2, and 1.1 ± 0.2 respectively, with significantly ($p \leq 0.001$) higher CK-19$^+$ cells in PNRHs cultured on BA:dLS (0.5:1.5) **(Figure 3.9 C, ii)**. Furthermore, immunostaining for Sox9 followed a gradient with remarkably increased Sox9 expression in PNRHs cultured on BA:dLS (0.5:1.5), recapitulating zone 1 PP function **(Figure 3.9 D)**.

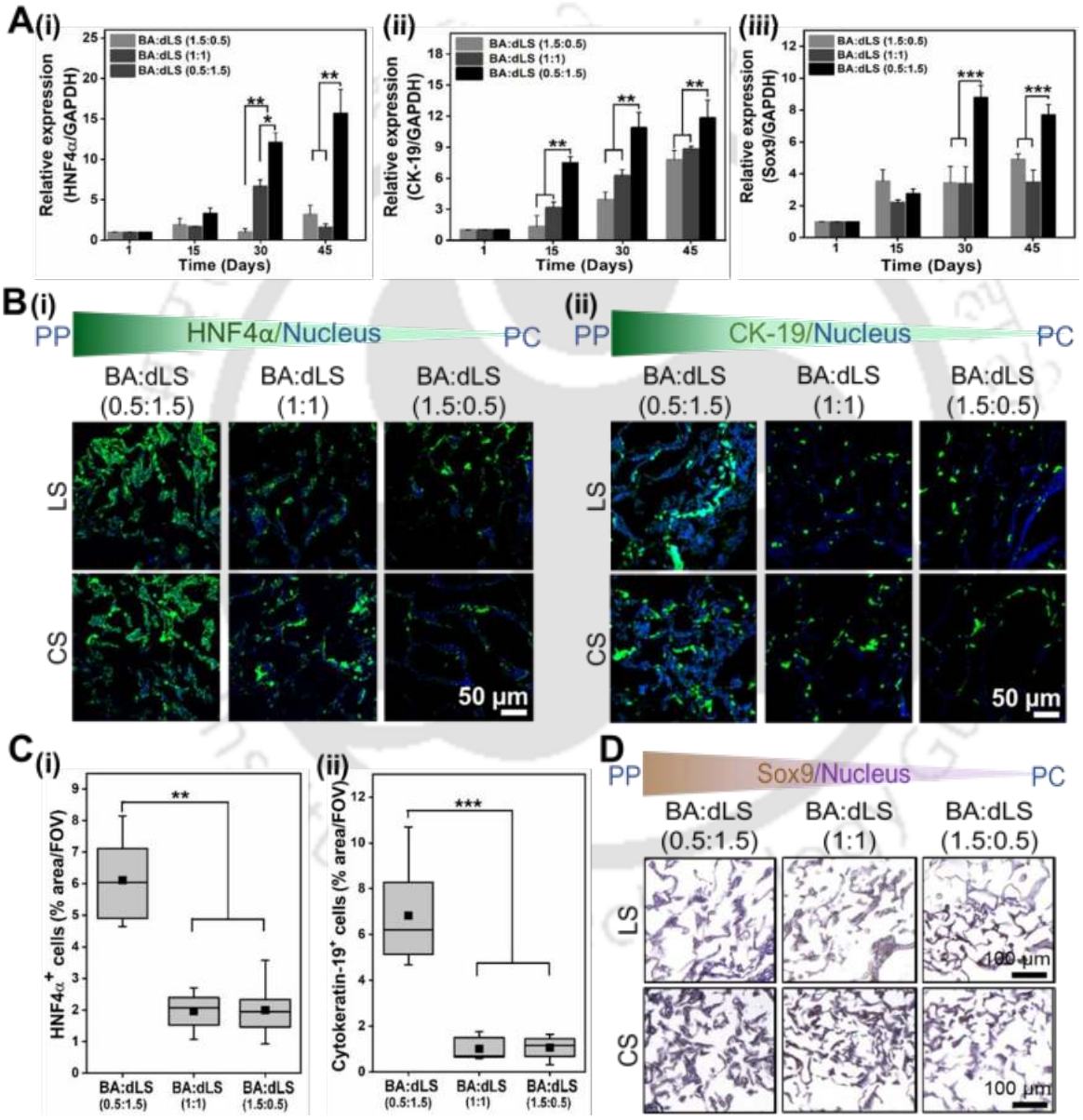

Figure 3.9. Liver-specific endodermal and cholangiocyte functions in perfusion bioreactor culture of PNRHs seeded liver ECM blend silk scaffolds over 45 days. *(A) Relative expression of (i) HNF4α, (ii) CK-19, and (iii) Sox9. Data are represented as average ± standard error of mean (n=3). *, ** and *** signify the statistical difference between the groups at $p \leq 0.05$, $p \leq 0.01$, and*

p ≤ 0.001, respectively. (B) Representative CLSM immunofluorescence images showing the gradient expression of (i) HNF4α and (ii) CK-19. Scale bar: 50 µm. (C) Quantification of percentage area of (i) HNF4α- and (ii) CK-19-positive cells per scaffold FOV processed from immunofluorescence images (n=9 from each group). (D) Representative immunostained images showing Sox9 expression. Scale bar: 100 µm. PP and PC represent periportal and pericentral regions, respectively; LS- Longitudinal section of scaffolds; CS-Cross section of scaffolds.

3.3.8 *In vitro* inflammatory response and hemocompatibility assessment towards scaffolds

The *in vitro* inflammatory response toward LECM-SF scaffolds showed a similar response in all variants **(Figure 3.10 A)**. The positive control, LPS at 500 ng/mL, induced enhanced ($p \leq 0.01$) IL-1β release of 1128.8 ± 61.7 pg/mL compared to those of LECM-SF scaffolds variants and negative control (TCP). After exposure to BA:dLS (2:0), BA:dLS (1.5:0.5), BA:dLS (1:1), and BA:dLS (0.5:1.5), RAW 264.7 macrophages secreted comparable IL-1β levels of 533.3 ± 47.0 pg/mL, 610 ± 36.0 pg/mL, 435.5 ± 38.3 pg/mL, and 402.2 ± 55.0 pg/mL, respectively, comparable to IL-1β release in the negative control, TCP (436.6 ± 61.7 pg/mL). Moreover, the IL-1β release in response to scaffolds was remarkably lower ($p \leq 0.01$) than that of LPS treatment. The thrombogenic attribute of scaffolds assessed by estimating the LDH activity of adhered platelets in BA:dLS (2:0), BA:dLS (1.5:0.5), BA:dLS (1:1), and BA:dLS (0.5:1.5), which were 0.87 ± 0.22 mU/mL, 0.20 ± 0.06 mU/mL, 0.35 ± 0.05 mU/mL, and 0.17 ± 0.05 mU/mL respectively **(Figure 3.10 B)**. The LDH activity of adhered platelets was higher ($p \leq 0.01$) in BA:dLS (2:0) compared to BA:dLS (1.5:0.5), BA:dLS (1:1), and BA:dLS (0.5:1.5).

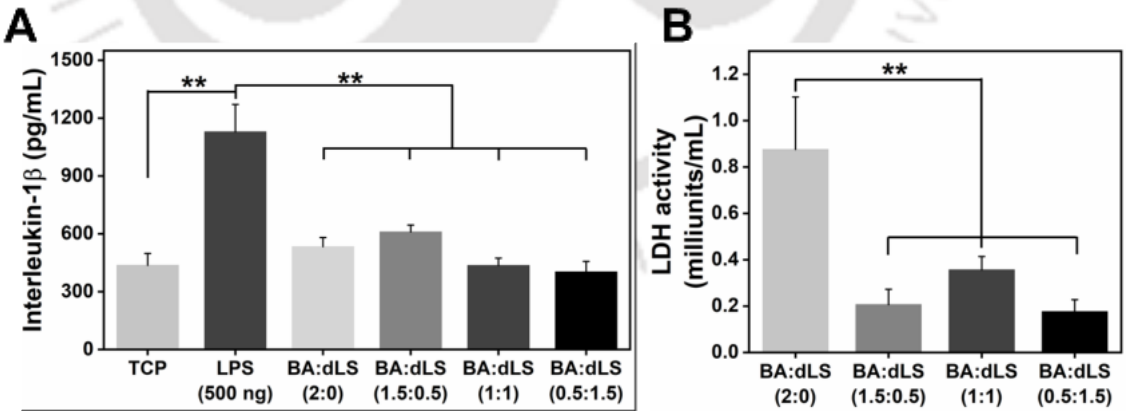

Figure 3.10. Immunocompatibility and hemocompatibility of liver ECM blend silk scaffolds. *(A) Assessment of in vitro immune response towards liver ECM blend silk scaffolds using RAW macrophages by measuring the secreted interleukin-1β. (B) In vitro hemocompatibility towards liver ECM blend silk scaffolds. Data are represented as average ± standard error of mean (n=4). ** signifies the statistical difference between the groups at p ≤ 0.01.*

3.3.9 Host foreign body response towards scaffolds in the subcutaneous rat model

The host response toward LECM-SF scaffolds, as examined from H&E images, confirmed host cell infiltration in the implanted scaffolds at 1 and 3 weeks post implantation. **(Figure 3.11 A)**. Histological examination revealed that scaffold morphology was maintained until 1 week, followed by its steady degradation and increased host cell infiltration at 3 weeks. Masson's trichrome staining of explants evaluated tissue remodeling in the implant site at 1 and 3 weeks, and collagen fibers were not distinctly visible at 1 week **(Figure 3.11 A)**. At 3 weeks post implantation, collagen deposition in fibrous form was visualized in and around the implanted scaffold. At 1 week, the number of multinucleate giant cells quantified from H&E images were lower ($p \leq 0.01$) in BA:dLS (1:1) and BA:dLS (0.5:1.5) compared to that in BA:dLS (2:0) and BA:dLS (1.5:0.5) **(Figure 3.11 B)**. A reduced ($p \leq 0.01$) multinucleate giant cells was observed at 3 weeks compared to those at 1 week in all the implants. Immunofluorescence staining of explants at 1 and 3 weeks against CD31 showed the presence of blood vessels **(Figure 3.12)**, which was further quantified to assess the angiogenesis toward LECM-SF scaffolds **(Figure 3.11 C)**. The blood vessels were statistically insignificant among all samples at 1 week, although BA:dLS (0.5:1.5) exhibited an increased ($p \leq 0.001$) number of blood vessels than BA:dLS (2:0) implant. While comparing the blood vessels in each scaffold variant at 1 week and 3 weeks, only the higher ECM variant, BA:dLS (0.5:1.5) showed a lesser ($p \leq 0.01$) number of blood vessels at 3 weeks compared to that at 1 week.

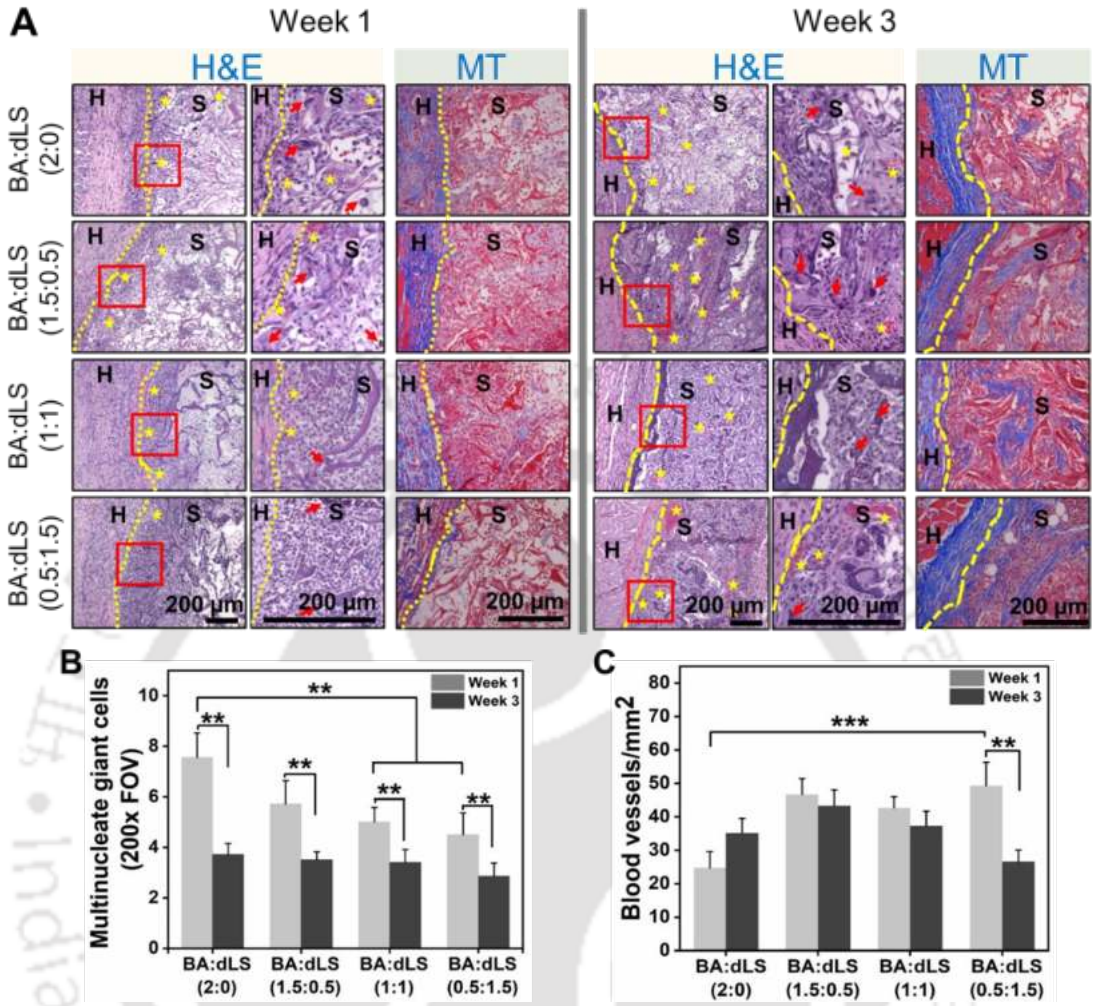

Figure 3.11. Host response toward liver ECM blend silk scaffolds assessed in the subcutaneous rat model. *(A) H&E and Masson's Trichrome (MT) images of explants from 1 and 3 weeks post implantation. The yellow dashed line demarcates the host tissue (H) and scaffold (S). The yellow star and red arrows indicate the presence of blood vessels and multinucleate giant cells, respectively. The red box represents the area magnified in the H&E images. Scale bar: 200 µm. Quantification of (B) Multinucleate giant cells; (C) Number of blood vessels processed from H&E and CD31 stained images, respectively (n=9 from each group). Data are represented as average ± standard error of mean. n=3 implants. ** and *** signify the statistical difference between the groups at $p \leq 0.01$ and $p \leq 0.001$, respectively.*

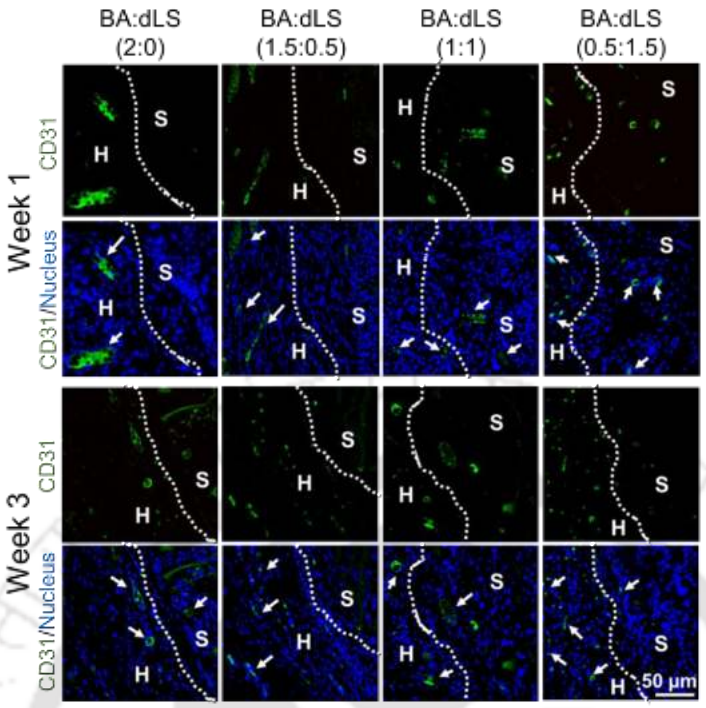

Figure 3.12. Angiogenesis towards liver ECM blend silk scaffolds. *CD31 staining images of explants from 1 and 3 weeks post implantation. The white dashed line demarcates the host tissue (H) and scaffold (S). The white arrows indicate the presence of blood vessels. Scale bar: 50 µm.*

3.3.10 Macrophage modulation towards scaffolds in subcutaneous rat model

A detailed macrophage response toward LECM-SF scaffolds was investigated by staining and quantifying the percentage area of pro-inflammatory macrophages ($CCR7^+$) and anti-inflammatory macrophages ($CD163^+$) at 1 and 3 weeks post implantation **(Figure 3.13)**. Overall, similar pan-macrophages ($CD68^+$, stained green) response toward all scaffolds were observed, and both pro-inflammatory ($CCR7^+$, stained red) and pro-remodeling ($CD163^+$, stained red) activated macrophages were evidenced **(Figure 3.13 A)**. However, individual scaffolds activated distinct macrophage phenotypes, as confirmed from percentage area quantification of $CCR7^+$ and $CD163^+$ macrophages **(Figure 3.13 B-C)**. The scaffolds with higher ECM, BA:dLS (1:1) and BA:dLS (0.5:1.5) stimulated remarkably lower ($p \leq 0.01$) percentage areas of $CCR7^+$ macrophages compared to those in BA:dLS (2:0) and BA:dLS (1.5:0.5) at 1 and 3 weeks post implantation **(Figure 3.13 B)**. The percentage area of $CCR7^+$ cells were reduced ($p \leq 0.05$) in BA:dLS (2:0) and BA:dLS (0.5:1.5) implants at 3 weeks compared to those at 1 week post implantation. Meanwhile, the $CD163^+$ pro-remodeling macrophages increased significantly in all scaffold implants over 3 weeks compared to levels at 1 week **(Figure 3.13 C)**. The percentage area of $CD163^+$ pro-

remodeling macrophages in BA:dLS (2:0), BA:dLS (1.5:0.5), BA:dLS (1:1), and BA:dLS (0.5:1.5) explants were 3.2 ± 0.6, 3.0 ± 0.7, 4.5 ± 0.9, and 6.4 ± 0.8, respectively, at 3 weeks. Relatively, BA:dLS (0.5:1.5) implant showed an increased ($p \leq 0.01$) $CD163^+$ pro-remodeling macrophage activation compared to BA:dLS (2:0) and BA:dLS (1.5:0.5) at 3 weeks. Furthermore, the M2-like: M1-like ratio of macrophages at the implant site was evaluated by measuring $CD163^+/CCR7^+$ cells **(Figure 3.13 D)**. At 1 week, scaffolds presented a similar trend of $CD163^+/CCR7^+$ macrophages; however, at 3 weeks each scaffold displayed a unique $CD163^+/CCR7^+$ ratio. The $CD163^+/CCR7^+$ macrophages in BA:dLS (2:0), BA:dLS (1.5:0.5), BA:dLS (1:1), and BA:dLS (0.5:1.5) were 0.9 ± 0.2, 0.9 ± 0.2, 2.3 ± 0.3, and 4.1 ± 0.4, respectively. At 3 weeks, increased ($p \leq 0.001$) M2-like: M1-like ratios of macrophages were noticed in BA:dLS (1:1) and BA:dLS (0.5:1.5) compared to those in BA:dLS (2:0) and BA:dLS (1.5:0.5). Also, BA:dLS (1:1) and BA:dLS (0.5:1.5) showed an increased ($p \leq 0.01$) M2-like: M1-like ratios of macrophages at 3 weeks compared to those at 1 week.

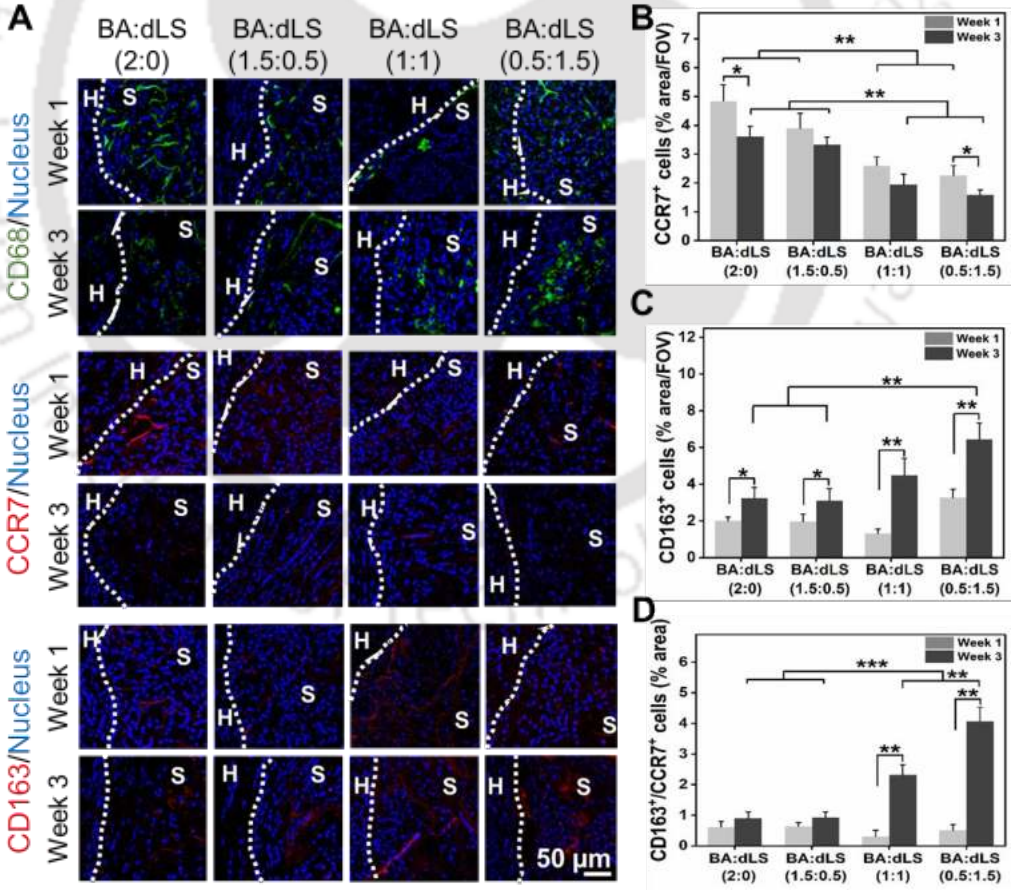

Figure 3.13. Macrophage activation toward liver ECM blend silk scaffolds assessed in the subcutaneous rat model. *(A) Representative immunofluorescence images showing the expression*

*of pan-macrophage marker CD68-stained green; M1-like pro-inflammatory macrophage marker CCR7-stained red; M2-like anti-inflammatory marker CD163-stained red. The nucleus is counterstained with DAPI and shown in blue. The white dashed line demarcates the host tissue (H) and scaffold (S). Scale bar: 50 µm. Quantification of percentage area for (B) CCR7- and (C) CD163-positive cells per scaffold FOV, and (D) M2-like: M1-like ratio of $CD163^{+}/CCR7^{+}$ cells processed from immunofluorescence images (n=9 from each group). Data are represented as average ± standard error of mean. n=3 implants. *, ** and *** signify the statistical difference between the groups at $p \leq 0.05$, $p \leq 0.01$, and $p \leq 0.001$, respectively.*

3.4 Discussion

The establishment of a physiologically relevant *in vitro* liver model resembling native zonation is in high demand for its robust application in the bioartificial liver (BAL), regenerative therapeutics, and high-throughput drug screening liver model. The present study provides the first evidence of developing an *in vitro* liver model recapitulating hepatocyte metabolic heterogeneity induced as a result of altering liver ECM proportion in scaffolds and mimicking the oxygen gradient. The collective findings suggest that each liver ECM blend silk (LECM-SF) scaffold variant supports distinct metabolic functions of cultured primary neonatal rat hepatocytes (PNRHs). In accordance with static functional properties, a single *in vitro* liver system mimicking physiological liver zonation was assembled in a perfusion bioreactor, where scaffolds were stacked following the order BA:dLS (0.5:1.5), BA:dLS (1:1), and BA:dLS (1.5:0.5). The scaffold with high liver ECM content, BA:dLS (0.5:1.5) supported zone 1 PP-specific mature hepatocytes and cholangiocyte-like functions, as evident from increased albumin secretion and $CK\text{-}19^{+}$ bile-duct formation. However, BA:dLS (1:1) and BA:dLS (1.5:0.5) scaffolds exhibited zone 3 PC-specific detoxifying functions, as observed from the expression of phase-I and phase-II metabolizing enzymes and cytochrome P450 activity. Finally, following subcutaneous implantation, scaffolds showed a shift to pro-remodeling macrophage activation at 3 weeks. Comparatively, wounds implanted with BA:dLS (1:1) and BA:dLS (0.5:1.5) scaffolds exhibited an increased M2-like: M1-like macrophage activation, evidencing its utilization as immunomodulatory tissue-engineered construct toward liver regeneration.

Liver ECM-based 3D matrices are a promising platform for regulating physiological attributes of cultured hepatocytes, which reproduce native ECM microenvironment niche through multiparametric cues, thus promoting cellular maturation and cell-ECM interaction [288]. However, individual ECM protein has proven to be inadequate in maintaining a native cell

phenotype and promoting lineage-specific differentiation of progenitor cells compared to tissue-specific ECM [114, 125, 284]. To facilitate hepatocyte functions, several groups have fabricated liver ECM-based 2D and 3D platforms. Lonekal *et al.* compared functional attributes of primary rat hepatocytes (PRHs) when cultured in (i) media supplemented with various liver ECM sources and (ii) hydrogel composed of liver ECM from various sources. Results showed that porcine and canine liver ECM maintained a mature PRHs phenotype compared to human and rat liver ECM [284]. In our earlier study, porous BA scaffolds fabricated by coalescing BM and AA silk fibroin assisted PNRHs growth as clusters that in turn maintained albumin synthesis, urea secretion, and CYP activity [271]. ECM incorporation in designing 3D matrices for tissue engineering applications provides a suitable milieu by enhancing cell-cell and cell-matrix interactions [289]. Herein, we have fabricated LECM-SF scaffolds for the first time that assimilates biocompatible and mechanical traits of silk fibroin [271, 290] and native-mimicry liver ECM [291]. Histological and biochemical investigation of isolated porcine liver ECM met the decellularization criteria, signifying effective cell removal and structural ECM preservation [287]. The liver ECM isolation protocol followed in this study is likely to preserve collagen I, collagen IV, fibronectin, and laminin in ECM and supported hepatic differentiation of bone marrow-derived mesenchymal stem cells, as reported by Jiang *et al.* [44]. A shift in the amide peaks and higher β-sheet content observed in LECM-SF scaffolds confirmed β-sheet induction and integral stability after EDC/NHS crosslinking, as evidenced from FTIR deconvolution analysis. FESEM morphological characterization showed an interconnected porous network in the range of 40-120 μm with a distinct pore morphology and porosity above 80%, supplementing hepatocyte infiltration, attachment, and migration [271, 292]. Factors such as porosity, swelling ratio, and stability are crucial for matrices to be employed in perfusion bioreactor culture and BAL, as it defines the multidirectional diffusion of nutrients. The enhanced swelling ratio observed in BA:dLS (1:1) and BA:dLS (0.5:1.5) might be due to its larger pore size and increased porosity **(Figure 3.2)**. The *in vitro* degradation rate of scaffolds was investigated using a nonspecific Protease XIV enzyme that mimics native MMPs. The higher degradation rates observed in BA:dLS (1:1) and BA:dLS (0.5:1.5) scaffolds might be attributed to their increased hydrophilicity and access to protease enzyme, as confirmed from swelling ratio results. Developing scaffolds mimicking the biomechanical properties of native ECM is reported to show prime functions in BAL and liver tissue engineering applications [285]. Clinical data showed that the stiffness of native liver tissue

increases drastically up to 4.1-21.9 kPa during fibrosis due to aberrant ECM deposition, thus distorting angiogenesis and hepatic regeneration [293]. In our study, the compressive modulus was reduced in scaffolds possessing liver ECM compared to that in blank silk scaffolds and was similar to the healthy liver (1.5-4.5 kPa) **(Figure 3.2 H-I)**.

The fabricated LECM-SF scaffolds were first applied to characterize the hepatocyte-matrix interaction for cell viability, distribution, and its effect on proliferation. All scaffold variants supported the PNRHs attachment along the pore wall and spheroidal cluster formation, albeit maintained a similar proliferation rate over 30 days in static culture conditions **(Figure 3.3)**. Hepatocyte clusters formed in BA:dLS (0.5:1.5) scaffold might be associated with a high amount of liver ECM in scaffolds. Many reports have observed that individual components of ECM like collagen, fibronectin, and proteoglycans or the whole ECM influence an aggregate or spheroidal formation of hepatocytes owing to the physical cues influencing optimal cell-cell and cell-ECM interactions [66, 294]. Hepatocyte aggregates have shown to be effective in maintaining the native liver phenotype, hepatocyte polarity, and enhanced liver-specific synthetic and detoxification functions [218, 275]. Each scaffold variant presented a unique PNRHs metabolic activity, including synthetic and detoxification functions over 30 days in static culture. The mature hepatocyte functions, albumin secretion, and urea synthesis were remarkably enhanced in the scaffold with higher ECM, BA:dLS (0.5:1.5) over 30 days. It has been reported that liver ECM hydrogel promotes matured hepatocyte functions, including albumin and urea secretion, due to the presence of GAGs and proteoglycans in ECM [114]. However, at day 30, we observed a significant reduction in the expression of drug-metabolizing enzymes and CYP protein levels in PNRHs cultured on BA:dLS (0.5:1.5), while it was prevailed in BA:dLS (1:1) and BA:dLS (1.5:0.5) **(Figure 3.4-3.5)**. The decrease in CYP activity observed in BA:dLS (0.5:1.5) might be due to its lower mechanical properties. Conventionally, neonatal and fetal liver comprise hepatoblasts in the ductal plates, which are referred as transit-amplifying cells that expand to hepatocytic and biliary progenitor cells in adult livers [295]. Gene expression and immunostaining indicated that transcription factors crucial for cholangiocyte differentiation were enhanced in PNRHs cultured on BA:dLS (0.5:1.5). HNF4α, a crucial transcription factor in liver physiology, regulates metabolism, differentiation, and proliferation of hepatocytes [198]. In naive conditions, cholangiocyte maturation from hepatoblasts or progenitor cells is based on microenvironmental cues from ECM, MSCs, and matured hepatocytes around the portal vein [282]. Indeed, the

transcription factors (HNF4α and Sox9) were expressed significantly higher in BA:dLS (0.5:1.5), which in turn supported CK-19 expression presenting cholangiocyte-like cell differentiation **(Figure 3.6)**. Therefore, it is presumed that in addition to microenvironmental cues from liver ECM, BA:dLS (0.5:1.5) scaffold might have additional unidentified physicochemical properties that promoted differentiation of hepatic progenitor cells in PNRHs to functional cholangiocyte [282].

Given the ability of ECM matrices to modulate the functional behavior of PNRHs, we sought to mimic zonation-specific functions in our liver model system by simulating oxygen gradient using a perfusion bioreactor [34]. To recapitulate the spatiotemporal arrangements of hepatocytes, liver model system comprising PNRHs cultured on LECM-SF scaffolds were sequentially stacked following BA:dLS (0.5:1.5), BA:dLS (1:1), and BA:dLS (1.5:0.5), with an acellular BA:dLS (2:0) scaffold at the bottom to withhold physiological stress during nutrient infusion. Responsiveness to ECM alteration with oxygen gradient was further stimulated by maturing the *in vitro* liver model system over 45 days in perfusion bioreactor culture leading to enhanced albumin secretion and urea synthesis **(Figure 3.7-3.8)**. The heat map comparing the relative expression of synthetic, detoxification, endodermal, and cholangiocyte specific markers in PNRHs cultured on BA:dLS (1.5:0.5), BA:dLS (1:1), and BA:dLS (0.5:1.5) under static (day 30) versus perfusion (days 30 and 45) conditions were plotted by normalizing to day 1 values as baseline **(Figure 3.14)**. On day 30, the heat map analysis revealed distinct gene expression profiles in the perfusion culture of PNRHs seeded BA:dLS (1.5:0.5), BA:dLS (1:1), and BA:dLS (0.5:1.5) versus static culture and in particular showed significantly higher expression levels of ALB, GSTA1, CYP1A2, CYP2E1, CK-19, and Sox9. Moreover, at day 45, perfusion culture supported a gradient expression of all genes in PNRHs seeded BA:dLS (1.5:0.5), BA:dLS (1:1), and BA:dLS (0.5:1.5). Altogether, BA:dLS (1.5:0.5) supported a higher expression level of detoxification (GSTA1, CYP1A2, A1AT, CYP2E1) and synthetic (FIB) genes; and BA:dLS (0.5:1.5) supported a higher expression level of endodermal, cholangiocyte (HNF4α, CK-19, and Sox9) and synthetic (ALB) genes at day 45 under perfusion conditions **(Figure 3.14)**.

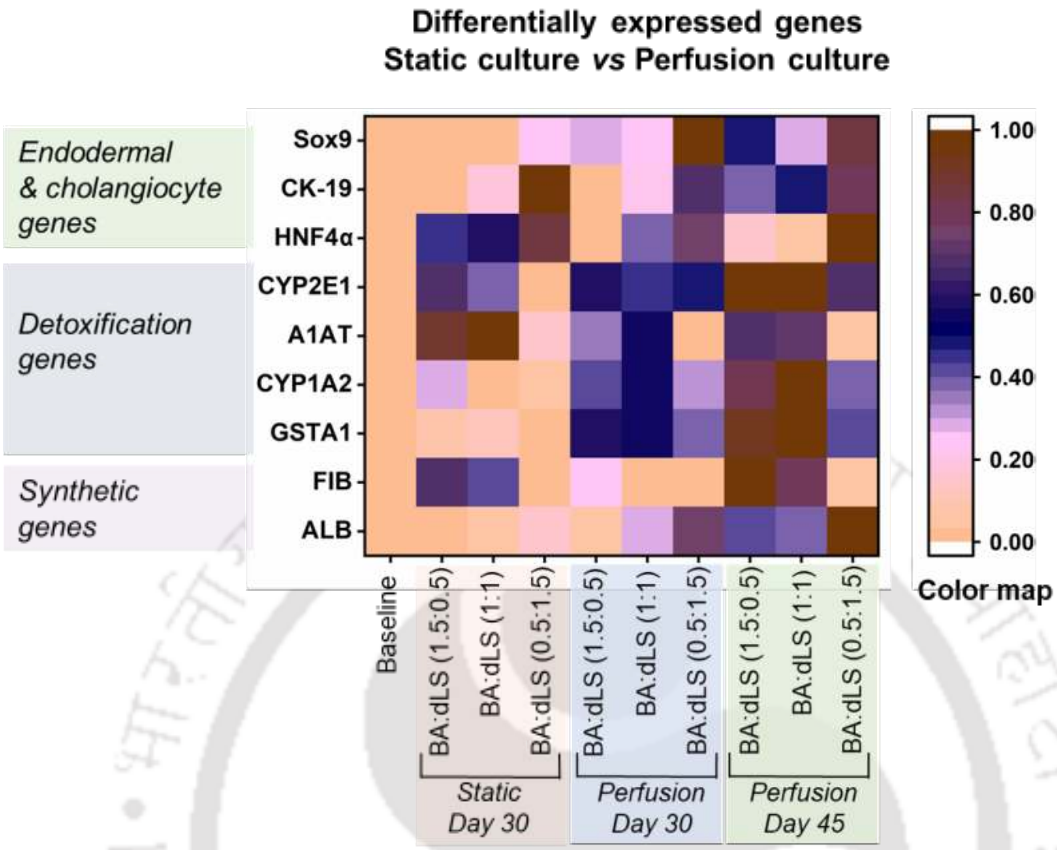

Figure 3.14. Relative expression of genes under static culture versus perfusion bioreactor culture. *Heat map showing the relative expression levels of synthetic genes (albumin-ALB, fibronectin-FIB), detoxification genes (glutathione S-transferase alpha 1-GSTA1, cytochrome P450 1A2-CYP1A2, alpha-1 antitrypsin-A1AT, cytochrome P450 2E1-CYP2E1), endodermal & cholangiocyte genes (hepatocyte nuclear factor 4α-HNF4α, cytokeratin 19-CK19, SRY-box transcription factor9-Sox9) in PNRHs cultured on LECM-SF scaffolds during static (day 30) versus perfusion bioreactor conditions (day 30 and day 45).*

Increased oxygen availability and higher ECM concentration around BA:dLS (0.5:1.5) supported zone 1 PP-specific albumin synthesis, as corroborated from earlier reports [34, 114]. Enhanced CYP activity and higher fibronectin expression witnessed in PNRHs cultured on BA:dLS (1:1) and BA:dLS (1.5:0.5) scaffolds might be attributed to reduced oxygen availability as observed in zone 3 PC regions **(Figure 3.7-3.8)** [34]. Among many factors, a gradient in oxygen concentration around the upstream PP portal vein and downstream PC central vein has been shown to play a crucial role in modulating gene expression, and hepatocyte heterogeneity resulting in liver zonation [34, 37]. For instance, the partial pressure of oxygen in the PP blood has been reported to be high, about 60-65 mmHg, which increases the capacity of oxidative energy

metabolism in the PP region. The high expression of carbomylphosphate synthetase and taurocholic acid uptake carrier in the PP zone aids in urea formation and bile formation, respectively [5]. However, partial pressure of oxygen falls to 30-35 mmHg in perivenous blood, increasing the capacity of xenobiotic metabolism and glucose uptake through the expression of cytochrome P450 and glucokinase, respectively [37]. *In vitro* liver culture systems imposing oxygen gradient have been reported, in which oxygen concentration contributed to the heterogeneous expression of CYP, nitrogen metabolism, drug detoxification mechanisms, [35, 36] as also observed in the current study. *In vitro* liver models recapitulating the zonation of detoxification functions have been investigated for evaluating the zonation dependent drug response or zonal hepatotoxicity [34, 194]. The liver model developed in the present study demonstrated differential expression of drug detoxification markers and CYP activity. Evaluating with zone 3 specific hepatotoxic drugs, including acetaminophen and tamoxifen, would further validate the potential of the current liver model for studying drug metabolism and toxicology applications [35, 194]. As an indicator of hepatocyte polarity, the liver bile canaliculi network distribution should be preserved [194]. In our study, the liver model system allowed a continuous bile duct formation around PP-like BA:dLS (0.5:1.5), which is intriguing **(Figure 3.9)**. A functional biliary ductular channel formation was observed as a result of coculturing primary hepatocytes with cholangiocytes and stromal cells in the spheroid form [296]. The polarized hepatocytes organized at the core of spheroids formed bile canaliculi with the aid of tight junctions, while cholangiocytes have resided at the periphery of hepatic microtissue [296]. The bile duct observed in the present study might be a striking correlation between the progenitor cells and native-mimicry ECM components in PNRHs and 3D matrix, respectively. However, further studies are needed to assess the potential of liver ECM in differentiating progenitor cells to cholangiocytes. Notably, the liver model system under continuous perfusion offered improvement in (i) compartmentalization of metabolic activity through an oxygen gradient, (ii) bidirectional diffusion of nutrients and metabolites, and (iii) a bile duct development.

The 3D scaffolds employed for BAL demand antithrombogenic attributes to prevent thrombosis as it is in the vicinity of a patient's plasma [297]. The procoagulant sites on the matrix determine platelet adhesion from circulating blood, leading to thrombogenicity [294]. It has been reported that the prothrombotic nature of the intact vascular network in the decellularized whole organ limits its use in clinical transplantation [298]. In this study, the LDH activity measurement

signified that blending liver ECM with silk drastically reduced the platelet adhesion, thus supporting hemocompatibility **(Figure 3.10)**. *In vitro* macrophage response toward scaffolds investigated using RAW 264.7 cells showed that the IL-1β release in response to scaffolds variants and negative control (TCP) was similar, confirming minimal acute inflammatory response toward LECM-SF scaffolds. IL-1β, a critical pro-inflammatory cytokine, is known to induce iNOS secretion resulting in the acute inflammatory response [259]. Hypothetically, biomaterials mimicking native tissue are more likely to promote site-appropriate functional remodeling by minimizing the adverse foreign body reaction and immune responses [299]. We note that the host response and macrophage activation toward scaffolds varied based on ECM proportion in the matrix, as evaluated in the subcutaneous rat model. Histomorphologic examination of explants at 1 and 3 weeks indicated multinucleate giant cell formation and new blood vessels in and around the implanted scaffolds **(Figure 3.11-3.12)**. At 3 weeks, all LECM-SF scaffold variants showed increased cellular infiltration and early tissue ingrowth, supporting tissue integration, as evidenced from neovascularization and increased collagen deposition [162, 299]. A decreased number of multinucleate giant cells and active ECM deposition over 3 weeks led us to assess the macrophage immunomodulation due to inherent scaffold properties. All scaffolds induced an initial M1-like macrophage activation at the wound site at 1 week and switched over to M2-like macrophage activation over 3 weeks. Comparatively, as the ECM content in the scaffold increases, M2-like macrophage activation was improved over 3 weeks **(Figure 3.13)**. This is further supported by increased M2-like: M1-like macrophage subpopulation and reduced multinucleate giant cells observed in BA:dLS (1:1) and BA:dLS (0.5:1.5), indicating the likelihood of constructive tissue remodeling outcome [125, 299].

The current study developed an *in vitro* liver model system using liver ECM and silk fibroin as biomaterials and simulated oxygen gradient by maturing in perfusion bioreactor to accomplish liver zonation specific metabolic heterogeneity of hepatocytes. As observed from PP specific synthetic functions and PC specific metabolizing functions, the liver model as a whole represents a potential platform for BAL devices, drug screening model, and for studying liver physiology. Also, the platform would find its application as implantable constructs aiding liver regeneration. Furthermore, coculturing with non-parenchymal cells would improve cellular crosstalk, and evaluation of the developed liver model as a BAL cellular component in performing liver functions

is required to investigate its efficacy as a treatment option. However, the results are noteworthy, and the potential clinical implications of the present study are promising, owing to achieving liver zone-specific functions.

3.5 Significant Findings

1. The fabricated liver ECM blend silk (LECM-SF) scaffolds by altering the ECM proportion supported long-term liver-specific functions and recapitulated metabolic heterogeneity of primary neonatal rat hepatocytes (PNRHs).
2. The LECM-SF scaffolds are highly porous, and possess high water uptake capacity, thus supporting optimal nutrient diffusion and hepatocyte infiltration. Although altering the ECM in scaffolds had no significant effect on PNRHs proliferation, a distinct pattern of synthetic, metabolic, and cholangiocyte functions was witnessed by individual scaffold variants upon static culture conditions.
3. Following the functional attributes of PNRHs in static culture, a perfusion bioreactor was employed to enable an oxygen diffusion gradient, where PNRHs seeded LECM-SF scaffolds are stacked in sequence, mimicking the physiological liver zonation as the media flows from the PP to the PC region.
4. Over 45 days of maturation, the whole *in vitro* liver system recapitulating native-mimicry liver zonation was developed, where the scaffold with a higher liver ECM supported PP functions (synthetic and cholangiocyte); and scaffolds with least ECM supported PC functions (detoxification and ECM production).
5. Furthermore, scaffolds with increased ECM showed minimal platelet adhesion and higher pro-remodeling macrophage response, supporting hemocompatibility and tissue remodeling.
6. Altogether, our results encourage the use of an *in vitro* liver system resembling hepatocytes metabolic heterogeneity as a valuable tool in bioartificial liver devices, transplantable constructs, a liver model for studying physiology, and a high-throughput drug screening platform.

CHAPTER 4

Mimicking native liver lobule microarchitecture in vitro with parenchymal and non-parenchymal cells using 3D bioprinting for drug toxicity and drug screening applications

This chapter investigates the bioengineering of *in vitro* liver model recapitulating the native liver microarchitecture and cellular physiology to achieve cellular crosstalks and hepatic metabolic functions for hepatotoxicity prediction. A human vascularized liver model was bioprinted with a novel liver ECM-based bioink laden with human adipose mesenchymal stem cell-derived hepatocyte-like cells, human umbilical vein endothelial cells, and human hepatic stellate cells. The developed clinically relevant vascularized liver model showed a dose-dependent toxic response and would provide a robust platform for pharmaceutical companies.

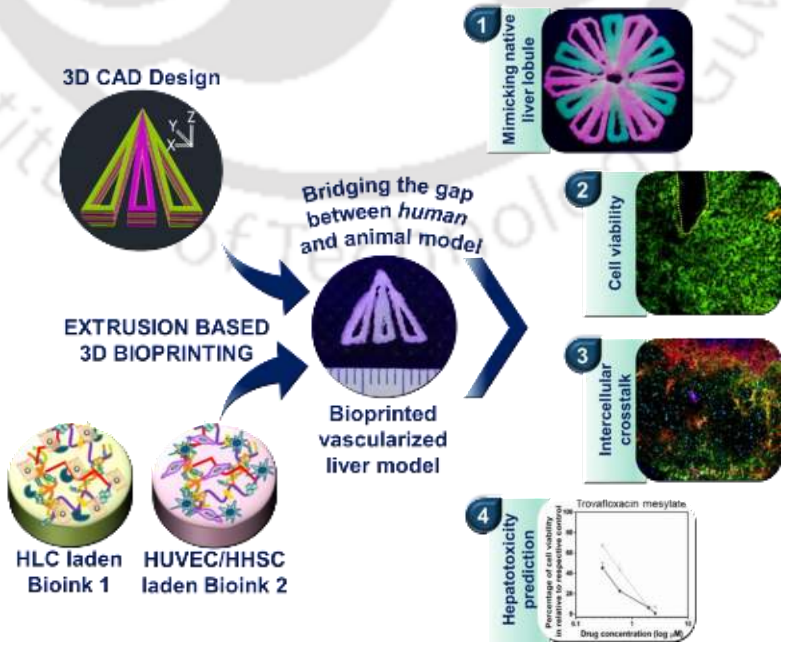

ABSTRACT

Bioengineering an *in vitro* liver model recapitulating the native liver microarchitecture consisting of parenchymal and non-parenchymal cells is crucial in achieving cellular crosstalk and hepatic metabolic functions for accurate hepatotoxicity prediction. Bioprinting holds the promise of engineering constructs with precise control over the spatial distribution of multiple cells. Two distinct tissue-specific liver extracellular matrix (ECM)-based bioinks with excellent printability and rheological attributes are formulated for supporting parenchymal and non-parenchymal cells. A physiologically relevant human vascularized liver model is bioprinted with a novel liver ECM-based bioink laden with human adipose mesenchymal stem cell-derived hepatocyte-like cells (HLCs), human umbilical vein endothelial cells (HUVECs), and human hepatic stellate cells (HHSCs) using an extrusion-based bioprinting approach and validated for hepatotoxicity assessment. The HLC/HUVEC/HHSC-laden liver model resembles native alternate cords of hepatocytes with a functional sinusoidal lumen-like network in both horizontal and vertical directions, demonstrating enhanced albumin production, urea synthesis, and cytochrome P450 (CPR) activity. Furthermore, the liver model is evaluated for drug toxicity assessment following 24 h exposure to different concentrations of (i) non-hepatotoxicants aspirin and dexamethasone, (ii) idiosyncratic hepatotoxicant trovafloxacin mesylate, and (iii) clinical hepatotoxicant acetaminophen and troglitazone. A follow-up cell viability and metabolic competence evaluation by estimating DNA concentration, lactate dehydrogenase activity, and CPR activity revealed a dose-dependent clinically relevant hepatotoxic response. These results corroborated that the developed clinically relevant vascularized liver model is affordable and would aid pharmaceutical companies in speeding up the drug development and provide a robust platform for hepatotoxicity screening.

The findings of this chapter are published in a peer reviewed journal:

Janani G., Priya S., Dey S., and Mandal B.B. "*Mimicking native liver lobule microarchitecture in vitro with parenchymal and non-parenchymal cells using 3D bioprinting for drug toxicity and drug screening applications*". **ACS Applied Materials & Interfaces**, 2022, 14 (8), 10167-10186

4.1 Introduction

Drug-induced liver injury (DILI), a leading cause for high rates of FDA-approved drug withdrawal from the market is due to inadequate drug safety, efficacy, and toxicity assessments in preclinical and animal models during drug development [300]. 18-30% of such drug withdrawals are mainly due to adverse drug reaction (ADR), resulting in hepatotoxicity and acute liver failure [301]. A recent study by Wouters *et al*. estimated that the median investment cost for research and development of a single drug accounts for approximately $985 million, including the expenditures on failed clinical trials [302]. The plausible reason for ADR in humans is the discordance in hepatotoxicity findings (~45%), which occurs due to variation in genetics, toxicological mechanisms, and drug-metabolizing pathways between conventional animal models and humans [301]. DILI is caused by (i) direct hepatotoxicity and (ii) idiosyncratic hepatotoxicity, the former is predictable, dose-related, and shows insignificant individual differences; indeed, the latter is rare, highly unpredictable, and shows significant inter-individual differences related to age, gender, and genetic polymorphisms [303-305]. Together with the limitations of cost, ethical requirements, and ADR predictions in animal models, human *in vitro* liver models recapitulating native physiology have gained importance over the past decade in drug toxicology assessment [306].

Existing liver culture systems for drug screening include native liver slices, hepatoma cell lines, human primary hepatocytes, and stem cell-derived hepatocytes [73, 272]. Spheroids of hepatoma cell lines and human induced pluripotent stem cells (hiPSCs) were explored to predict hepatotoxicity as an imaging-based toxicity model [73, 307]. However, traditional monolayer culture and spheroids were limited in maintaining native morphology, diffusion gradient, long-term viability, and liver functions [145, 297]. Therefore, three-dimensional (3D) liver systems with a vision to improve hepatic metabolic performance were fabricated and investigated for hepatotoxicity prediction [308]. The highly vascularized liver involves in selective uptake, metabolism, detoxification, biotransformation, and elimination of xenobiotics, toxins, and complex molecules [309]. Evidently, liver development and functions necessitate paracrine communication between parenchymal (hepatocytes) and non-parenchymal (endothelial, Kupffer, and stellate) cells [309]. The advancements in scaffold design, cellular sources, tissue-specific biomaterials, and 3D bioprinting have enabled significant control over cell-cell and cell-matrix interactions in bioengineered liver models, which assisted in reproducing liver functions. Several

high-throughput systems, including hepatocellular microarrays, organ-on-a-chip, bioprinted models, and patterned co-culture of liver cells, were evaluated for maintaining long-term hepatic functions [299]. However, 3D constructs with cellular components >200 µm demonstrated diffusional limitations, thus cell-laden constructs with vascularized endothelial channels were proposed to enhance nutrient diffusion, drug perfusion, and cellular functionality [300].

A substantial body of evidence revealed that 3D *in vitro* liver tissue comprising a co-culture of hepatocytes and non-parenchymal cells (NPCs) predicted hepatotoxicity more accurately than the liver model with only hepatocytes, as the inclusion of NPCs contributed significantly to the inflammatory components of DILI [193, 195, 300]. Endothelial channels in HepG2/C3A-laden gelatin methacryloyl hydrogel delayed the permeability of Acetaminophen [300]. Similarly, a microfluidic OrganoPlate LiverTox^{TM} liver-on-a-chip model system, wherein hiPSC-derived hepatocytes were cultured with endothelial and THP1-derived macrophages retained hepatic functions and predicted time-dependent hepatotoxicity [200]. Beyond the impact of multicellular components, spatial patterning and precise interactions of hepatocytes, endothelial cells, and stellate cells with extracellular matrix (ECM) have shown to be critical in achieving native-like liver physiological functions, drug permeabilization, and drug metabolism [195]. The highly vascularized liver is covered with a thin fibrillar Glisson's capsule and consists of small repeated functional hexagonal subunits called lobules [310]. Each lobule comprises a rich population of hepatocytes arranged in linear cords, that are segregated by fenestrated sinusoids lined with sinusoidal endothelial cells, Kupffer cells, and liver stellate cells [310]. A compartmentalized scaffold-free liver tissue encompassing primary hepatocytes, endothelial cells, and stellate cells maintained higher levels of albumin, cytochrome P450 activity and showed dose-dependent toxicity for Trovafloxacin [195, 310]. So far, very few 3D liver models resembling the native spatiotemporal arrangement and multicellular composition have been fabricated for predicting DILI. A bottom-up 3D bioprinting approach offered the bioprinting of a vascularized hepatic lobule structure embedded with HepG2/C3A and endothelial cells with increased albumin and urea secretion [153, 311]. Furthermore, 3D scaffold functionalized with bioactive ECM components, including fibronectin, collagen, decellularized liver ECM maintained angiogenesis, hepatocyte polarity, detoxification, and synthetic functions [281, 312].

Taken together, a bioengineered liver model mimicking spatiotemporal arrangement and cellular composition of the native liver has become decisive for researchers and pharmaceutical

companies. National Research Council report suggests that the *in vitro* liver model for accurate drug toxicity prediction should address (i) similar dose-response relationships as humans, (ii) considering the variability of responses due to heterogeneity in the human population, and (iii) assessing multiple compounds [309]. In this study, a physiologically relevant *in vitro* liver model system with a hepatic sinusoid network was bioprinted for the first time, wherein the 3D CAD design trails alternate cords of parenchymal and NPCs using an extrusion bioprinting technique, and was further evaluated for its sensitivity in drug toxicity assessment. Various bioprinting techniques, such as droplet-based bioprinting, inkjet bioprinting, vat polymerization-based bioprinting, digital light processing, and extrusion-based bioprinting facilitate precise deposition of cells encapsulated in bioinks at pre-defined positions in a sequential layer approach [313-315]. The most widely used extrusion-based bioprinting approach in tissue engineering research offers the advantages of printing biological materials (i) with a wide range of viscosities, (ii) that undergo shear thinning and temperature-sensitive crosslinking, and (iii) encapsulated with high cell densities [315, 316]. Furthermore, pneumatic-driven multi-nozzle extrusion bioprinting could extrude multi-material bioinks in the individual and subsequent layers to form continuous microfilaments, which are subsequently deposited in a layer-by-layer fashion and finally stacked to form a self-standing, stable structure with fidelity [315]. A tissue-specific liver ECM bioink was formulated with bulking agent gelatin and bioactive silk fibroin isolated from mulberry (*Bombyx mori*, BM) and non-mulberry (*Antheraea assamensis,* AA) to improve the rheological characteristics and support liver cell functionality [281, 291]. The blend of BM and AA silk fibroin has been in eminence in liver tissue engineering due to its excellent mechanical robustness, biocompatibility, minimal immune response, and intrinsic arginine-glycine-aspartate (RGD) motif [281, 290]. Furthermore, the self-gelling attribute of blend silk fibroin following the green aqueous process has led us to incorporate silk fibroin as a bioactive material with liver ECM to formulate multifunctional bioinks for fabricating complex self-standing structures [291, 317]. In parenchymal bioink 1, β-D galactose was incorporated explicitly to augment hepatocyte attachment, polarity, and liver-specific functions by activating the asialoglycoprotein receptor [114]. The parenchymal bioink 1 hydrogel layer was encapsulated with a high cell density of human adipose mesenchymal stem cell-derived hepatocyte-like cells (HLCs); and the NPC bioink 2 hydrogel layer was encapsulated with human umbilical vein endothelial cells (HUVECs) and

human hepatic stellate cells (HHSCs) as supporting cells. The HLC/HUVEC/HHSC-laden vascularized liver model demonstrated enhanced urea synthesis, albumin production, and cytochrome P450 activity over 15 days. The bioprinted liver constructs laden with (i) HLC and (ii) HLC/HUVEC/HHSC were assessed for their potential in screening hepatotoxicity toward non-hepatotoxicants (aspirin and dexamethasone), idiosyncratic hepatotoxicant (trovafloxacin mesylate), and hepatotoxicants (acetaminophen and troglitazone). The present study would pave the way for pharmaceutical companies to use the bioprinted 3D *in vitro* vascularized liver model as a humanized preclinical drug screening assessment model.

4.2 Materials and Methods

4.2.1 Preparation of the liver ECM and silk fibroin solution

The liver ECM was obtained by decellularization of the porcine liver using the chemical decellularization method followed by enzymatic solubilization **(Figure 4.1)** [281]. In brief, thin liver slices were subjected to a freeze-thaw cycle and rinsed with 0.1M phosphate-buffered saline (PBS) and Milli-Q water to instigate cell lysis. Then, the liver slices were decellularized with TritonX-100 (1% v/v) and ammonium hydroxide solution (0.1% v/v) for 4 days with frequent changes. The resulting liver ECM scaffolds were freeze-dried and digested in a pepsin buffered solution (1% w/v in 0.01 N HCl, 37°C) to acquire a final liver ECM solution of 10 mg/mL. The liver ECM solution was brought up to physiological pH (7.4), and strained through a 70 µm cell strainer to dissociate the aggregates and obtain liver ECM-derived microparticles.

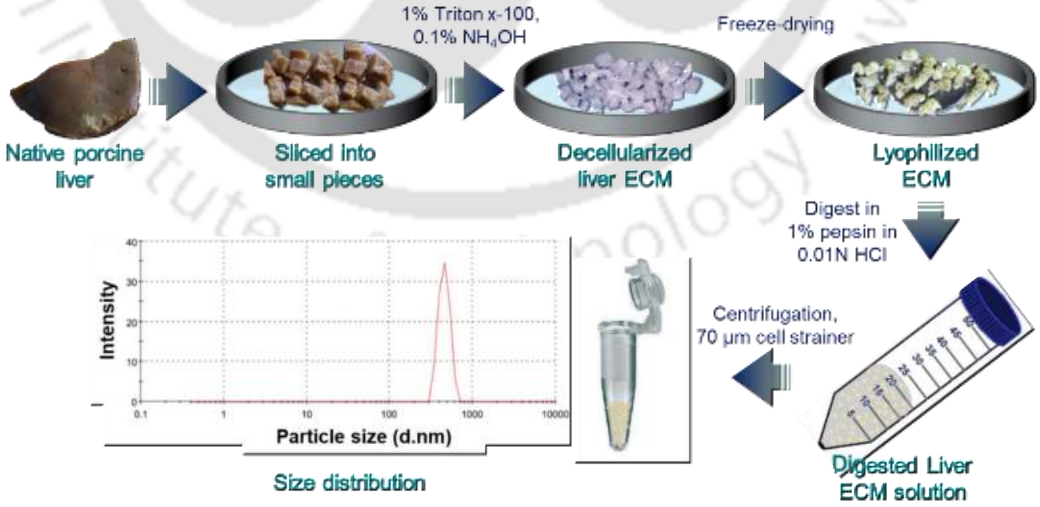

Figure 4.1. Schematic representation of decellularization process and pepsin digestion to obtain liver extracellular matrix (ECM)-derived solution. *Dynamic Light Scattering of liver ECM solution showing size distribution of liver ECM derived microparticles.*

The regenerated mulberry BM silk fibroin was acquired by dissolving BM silk fibers obtained after degumming (0.02 M sodium carbonate solution, 95°C, 30 min) in lithium bromide solution (9.3 M, 60°C, 4 h) followed by dialysis for 2 days [271, 281]. The regenerated non-mulberry AA silk fibroin solution was obtained by extruding AA silk fibroin from silk glands, dissolving in sodium dodecyl sulfate solution (1% w/v), followed by dialysis at 4°C for 4 h [281]. Then, the BA silk fibroin was prepared by combining regenerated 1% (w/v) BM and 1% (w/v) AA silk fibroin at an equal ratio of 1:1 [271].

4.2.2 Cell culture

4.2.2.1 Differentiation of human adipose-derived mesenchymal stem cells toward hepatocyte-like cells and their characterization

The human adipose-derived mesenchymal stem cells **(**ADMSCs) were cultured and maintained in a HiPer high glucose Dulbecco's Modified Eagle Medium (DMEM), 10% (v/v) FBS, 1% (v/v) L-Glutamine, and 2 ng/mL basic fibroblast growth factor (bFGF). The ADMSCs were differentiated toward hepatocyte-like cells (HLCs) using a two-stage protocol; definitive endodermal differentiation for 7 days followed by hepatocyte differentiation for 11 days [108, 318]. The ADMSCs were cultured for 7 days in endodermal differentiation media containing high glucose DMEM supplemented with 10% (v/v) FBS, 0.1% (v/v) L-glutamine, 20 ng/mL hepatocyte growth factor (HGF), 10^{-7} mM dexamethasone, 10 ng/mL oncostatin M, and 10 ng/mL bFGF. Then, the medium was changed to hepatocyte differentiation media containing high glucose DMEM supplemented with 10% (v/v) FBS, 0.1% (v/v) L-glutamine, 40 ng/mL HGF, 10 ng/mL oncostatin M and 1X ITS. The differentiation media was replenished every second day. The hepatic differentiation was characterized by gene expression analysis and immunolabeling for hepatocyte-specific markers. The total RNA was collected from ADMSCs and HLCs using the TRIzol reagent, and cDNA was prepared using a high-capacity cDNA reverse transcription kit (Thermo Fisher Scientific, Applied Biosystems, USA) [283]. The expression of mature hepatic markers including albumin, alpha-fetoprotein (AFP), hepatocyte nuclear factor 4α (HNF4α), and cytochrome P450 2E1 (CYP2E1) was analyzed using SYBR Green PCR Master mix in a quantitative 7500 Fast Real-Time Polymerase Chain Reaction (RT-PCR, Applied Biosystems, USA). The list of primers is provided in **Table 4.1**.

Table 4.1. *Forward and reverse primer sequence for real-time polymer chain reaction*

S. No.	Gene Name	Accession Number	Sequence
1.	h-GAPDH	NM_001357943.2	**F** 5'-GACCTGACCTGCCGTCTA-3'
			R 5'-GTTGCTGTAGCCAAATTCGTT-3'
2.	h-ALB	NM_000477.6	**F** 5'-GTGCTAATTTCCCTCCGTTTGTC-3'
			R 5'-GCAACCTCACTCTTGTGTGC-3'
3.	h-AFP	NM_001134.3	**F** 5'-AGCTTGGTGGTGGATGAAAC-3'
			R 5'-CCCTCTTCAGCAAAGCAGAC-3'
4.	h-HNF4α	NM_000457.6	**F** 5'-CGAAGGTCAAGCTATGAGGACA-3'
			R 5'-ATCTGCGATGCTGGCAATCT-3'
5.	h-CYP1A2	NM_000761.4	**F** 5'-GCACTATCAGGACTTTGACA-3'
			R 5'-TTGGTCACAAGGTACATGAG-3'
6.	h-CYP2E1	NM_000773.4	**F** 5'-CGTGGAAATGGAGAAGGAAA-3'
			R 5'-GGTGATGAACCGCTGAATCT-3'
7.	h-CK-19	NM_002276.5	**F** 5'-AGCATGAAAGCTGCCTTGGA-3'
			R 5'-CCTGATTCTGCCGCTCACTATC-3'
8.	h-CD31	XM_032908315.1	**F** 5'-TCCGATGATAACCACTGCAA-3'
			R 5'-TGGTGGAGTCTGGAGAGGA-3'
9.	h-vWF	NM_000552.5	**F** 5'-TCTTCCAGGACTGCAACAAG-3'
			R 5'-TCCGAGATGTCCTCCACATA-3'
10.	h-Desmin	NM_001382713.1	**F** 5'-CATCGCGGCTAAGAACATTT-3'
			R 5'-GCCTCATCAGGGAATCGTTA-3'

Human glyceraldehyde-3-phosphate dehydrogenase (GAPDH) was used as a housekeeping gene, followed by functional gene expression was calculated using the delta Ct method. Subsequently, ADMSCs, hepatic endodermal cells (after 7 days), and matured HLCs (after 18 days) were immunolabeled for stem cell Sox9 marker and hepatocyte-specific albumin, cytokeratin 18, CYP2E1, fibronectin, and HNF4α markers. The cells at each stage were fixed in 10% (v/v) neutral buffered formalin (NBF) solution, permeabilized in 0.1 M PBS solution containing 0.1% (v/v) Triton X-100, and subjected to blocking in blocking buffer solution containing 1% (w/v) bovine serum albumin (BSA), 2% (v/v) horse serum, and 0.2% (v/v) tween

20. The primary antibodies used were (i) mouse anti-Sox9 (sc20095, 1:200 dilution), (ii) mouse anti-albumin (ab10241, 1:200 dilution), (iii) rabbit anti-cytokeratin 18 (ab133263, 1:300 dilution) (iv) rabbit anti-CYP2E1 (NBP2-67021, 1:200 dilution), (v) mouse anti-fibronectin (ab6328, 1:100 dilution), and (vi) rabbit anti-HNF4α (ab201460, 1:1000 dilution) diluted in blocking buffer and incubated with cells at 4°C overnight. Then, the cells were incubated with corresponding secondary antibodies, and nuclei were counterstained with DAPI. The fluorescence images were captured using a Nikon ECLIPSE Ti2 inverted microscope (NIKON Instruments Inc.) and processed using ImageJ software (NIH, USA).

4.2.2.2 Culturing human umbilical vein endothelial cells and human hepatic stellate cells

The primary HUVECs characterized for the von Willebrand Factor (vWF), cluster of differentiation 31 (CD31), and HHSCs characterized for Desmin were procured from the ScienCell Research Laboratories, USA. HUVECs were cultured in ECGM (endothelial cell growth medium, ScienCell) supplemented with 5% (v/v) FBS, 1% (v/v) endothelial cell growth supplement, and 1% (v/v) Penicillin/streptomycin (P/S) solution. Similarly, the SCGM (stellate cell growth medium, ScienCell) supplemented with 2% (v/v) FBS, 1% (v/v) P/S solution, and 1% (v/v) stellate cell growth supplement was used to culture HHSCs. The HUVECs and HHSCs were subcultured at 80% confluency, and cells at <5 passage were used for bioprinting.

4.2.3 Bioink formulation, printability, and FTIR examination

The basic liver ECM-based ink for encapsulating HLCs, HUVECs, and HHSCs was optimized by blending different concentrations of liver ECM-derived microparticles (0.5% - 3%, w/v) and BA silk fibroin solution (0.5% - 3%, w/v) with bulking agent gelatin (1% - 9%, w/v) and evaluating their printability. Furthermore, β-D galactose, a specific ligand known for augmenting hepatocyte attachment, was incorporated as an additive in bioink 1 [114]. The HLCs were seeded on a 48-well plate and cultured in DMEM suspended with different concentrations (1, 10, 20, 30, 40, 50, 60, 80, 100, 500, and 1000 mM) of β-D galactose for 7 days. At day 3 and day 7, the cellular viability was evaluated using an MTT reagent, followed by the percentage of cell viability (%) was calculated by normalizing the DNA concentration of HLCs cultured with different β-D galactose concentrations to HLCs cultured only in media. From the percentage of cell viability graph **(Figure 4.2)**, 40 mM β-D galactose was chosen as an optimal cytocompatible concentration to incorporate into bioink 1. Moreover, an enzyme-based horseradish peroxidase (HRP)/ hydrogen

peroxide (H_2O_2) crosslinking procedure was employed to augment β-sheets in bioinks, where 15 units of HRP and 1.65 mM H_2O_2 were added per 1 mL of bioink [291]. Then, the HRP/H_2O_2 crosslinked bioink solution was loaded into a 10 mL CELLINK syringe with a 27G blunt needle and incubated at 37°C for 30-40 min to ensure complete gelation. The printability was evaluated by extruding bioink using a BIO X 3D bioprinter (CELLINK). The optimized concentration of each constituent in formulated bioink 1 and bioink 2 from printability assessment **(Figure 4.4)** are listed in **Table 4.2**. The basic liver ECM-based ink with β-D galactose was labeled as bioink 1 and used to encapsulate HLCs. Only basic liver ECM-based ink was labeled as bioink 2 and used to encapsulate both HUVECs and HHSCs. Furthermore, the structural analysis of hydrogels formed from bioink 1, bioink 2, and blend (bioink1/bioink 2 = 1:1) before and after enzymatic HRP/H_2O_2 crosslinking was analyzed using attenuated total reflection mode Fourier Transform Infrared (FTIR, PerkinElmer FTIR Spectrum Two, USA) spectroscopy. The spectra were recorded in the range of 2000 cm^{-1} - 850 cm^{-1} at 4 cm^{-1} spectral resolution.

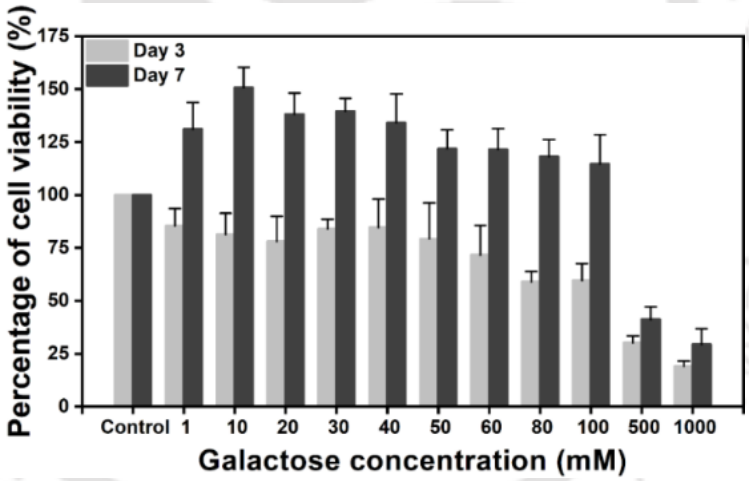

Figure 4.2. Assessment of cellular viability of HLCs on treatment with different concentrations of β-D galactose after day 3 and day 7 of culture using MTT assay. *Data are represented as Mean ± SD (n = 3).*

Table 4.2. *Concentration of each constituent in formulated bioink 1 and bioink 2*

Bioinks	Final concentration in bioink				
	BM silk fibroin (w/v)	**AA silk fibroin (w/v)**	**Liver ECM (w/v)**	**Gelatin (w/v)**	**β-D galactose (mM)**
HLC laden bioink-1	1%	1%	1%	7%	40
HUVEC/ HHSC laden bioink-2	1%	1%	1%	7%	-

4.2.4 Rheological characterization

The acellular crosslinked bioink 1 and bioink 2 were subjected for rheological characterizations by assessing the (i) optimal gelation time, (ii) amplitude sweep, (iii) frequency sweep, (iv) optimal printing temperature, and (v) thixotropic nature using MCR 302 Anton Par Rheometer (Austria) fitted with 25 mm diameter parallel plate at a set gap of 1 mm. The gelation time was assessed from dynamic oscillatory profiling at a constant shear strain (γ) of 0.01% and oscillatory strain (ω) of 10 rad/s. The temperature sweep profiling was performed for a range of 4°C – 45°C at ω = 10 rad/s to determine the optimal printing temperature. Then, the yield point and linear viscoelastic region (LVER) of bioinks were studied at constant ω = 10 rad/s from amplitude sweep analysis performed at a range of shear strain γ = 0.0001% - 5%. The LVER obtained from the amplitude sweep was noted and used for performing frequency sweep analysis at varying oscillatory strain ω = 0.01 - 100 rad/s. Furthermore, the deformation, self-standing, and complex viscosity property of the bioink were analyzed using a three interval thixotropic test (3ITT) by alternating shear strain and angular frequency at 25°C from low (γ = 0.1% and ω = 10 rad/s) to higher (γ = 10% and ω = 100 rad/s) range. The results were recorded and processed using Anton Paar RheoCompass software.

4.2.5 CAD designing and printing of 3D printed liver model

A 3D liver lobule-like structure was designed using AutoCAD software (Autodesk), dimensions were optimized using Slic3r and Repetier Host software, and a CAD file was exported to the STL format. The parameters were configured and sliced with layer thickness 0.45 mm, printing speed 4 mm/s, and fill density 20%, and the final STL file was converted into G-code and imported for printing in BIO X 3D Bioprinter. The design of the bioprinted liver model was

inspired by the native liver lobule structure, where sheets of hepatocytes are arranged in complementary patterns with NPCs and comprise HLCs in the bioink 1 layer and HUVECs and HHSCs in the bioink 2 layer. A total of six layers were printed following layer-by-layer assembly, wherein bioink 1 and bioink 2 were printed alternatively in both horizontal and vertical directions to facilitate the paracrine signaling among hepatocytes and NPCs.

4.2.6 Physicochemical characterizations and immunocompatibility analysis of the 3D printed liver model

4.2.6.1 Physicochemical characterizations

Prior to cell-laden bioprinting, the acellular printed construct was investigated for surface morphology and pore size using Zeiss field emission scanning electron microscopy (FESEM, Sigma, USA). The printed constructs were lyophilized, sputter-coated with gold, and scanned at a resolution of 4 cm^{-1} under FESEM, and the pore size was determined by processing the acquired images using ImageJ software. Simultaneously, the acellular printed constructs with only bioink 1, bioink 2, and blend ink were assessed for water uptake ability and integral stability by swelling ratio and *in vitro* degradation studies, respectively [271]. Briefly, the initial dry weight (DM_{it}) of constructs was noted, incubated in 0.1 M PBS at 37°C for 7 h, the swollen weight of constructs at predetermined time points was measured (M_{pd}), and the swelling ratio was calculated by,

$$\text{Swelling ratio (\%)} = (DM_{it} - M_{pd})/ DM_{it} \times 100$$

The *in vitro* degradation rate was assessed in a hydrolytic 0.1 M PBS environment and enzymatic 2 U/mL protease XIV (Sigma-Aldrich, USA) conditions over 18 days. After measuring the initial dry weight (DM_{it}) of constructs, samples were incubated at 37°C in 0.1 M PBS and 2 U/mL Protease XIV solution. Every 3 days, the incubated constructs were removed, rinsed in Milli-Q water to remove the residual solution, and the dry weight of constructs post lyophilization at predetermined time points (DM_{pd}) was measured. The mass remaining (%) of printed constructs was calculated using,

$$\text{Mass degraded (\%)} = [(DM_{it} - DM_{pd})/ DM_{it}] \times 100$$

$$\text{Mass remaining (\%)} = 100 - \text{Mass degraded (\%)}$$

4.2.6.2 Immunocompatibility analysis

The bioink was characterized for antithrombogenicity, *in vitro* immunogenicity, host response, and *in vivo* immunocompatibility [281, 317]. The sterile hydrogels composed of bioink 1, bioink 2, and only gelatin of 5 mm diameter × 2 mm height were incubated at 37°C for 2 h with platelet-rich plasma (PRP) collected from porcine blood. Then, the lactate dehydrogenase (LDH) activity of platelets adhered on hydrogels was quantified using the LDH assay kit to determine hemocompatibility. Subsequently, the murine RAW 264.7 macrophage cell line cultured in a 24-well plate was exposed to sterile hydrogels composed of bioink 1 and bioink 2 of 5 mm diameter × 2 mm height for 24 h at 37°C. The amount of pro-inflammatory cytokine IL-1β released in media in response to hydrogels was measured using an IL-1β ELISA kit (Sigma-Aldrich, USA). The IL-1β release in response to 500 ng/mL of lipopolysaccharide (LPS) treatment and only media was taken as a positive control and negative control, respectively. The host cell response and macrophage stimulation toward hydrogels were studied post implantation in the subcutaneous pocket of Sprague Dawley rats. Animal experiments were performed following the Institutional Animal Ethical Committee, National Institute of Pharmaceutical Education and Research-Guwahati, Assam, India. The sterilized hydrogels composed of gelatin and formulated blend bioinks were implanted in a subcutaneous pocket, and explants along with surrounding host tissue collected at week 1 and week 2 post implantation were fixed in 10% (v/v) NBF and examined for cellular infiltration using Hematoxylin and Eosin (H&E) staining. Furthermore, the angiogenesis, macrophage infiltration, pro-inflammatory macrophage stimulation, and pro-remodeling macrophage stimulation toward implants were determined by immunostaining for CD31, CD68, CCR7, and CD163, respectively. The fluorescence images were captured using a Nikon ECLIPSE Ti2 inverted microscope and processed using ImageJ software.

4.2.7 Bioprinting and evaluation of liver cell performance in the bioprinted liver model

4.2.7.1 Cell-laden bioink preparation and bioprinting

For cell-laden bioink preparation, HLCs at a density of 2×10^6 cells/mL were mixed in bioink 1; and HUVECs and HHSCs at a density of 1.4×10^6 cells/mL and 0.4×10^6 cells/mL, respectively, were mixed in bioink 2. The cell-laden bioinks were loaded in respective sterile CELLINK syringe, centrifuged at 400 rpm for 2 min to remove any bubbles, and incubated at 37°C for 40 min to ensure gelation. The instructed G-code was imported to the Bio X 3D bioprinter, and the bioink was dispensed through 27G needle following extrusion-based bioprinting at 5-8 mm/s

speed and 15-20 kPa pressure. The bioprinted liver model was cultured at 37°C in a culture medium composed of a 2:1:1 ratio of high glucose DMEM, ECGM, and SCGM, and matured over 15 days.

4.2.7.2 Evaluation of cellular viability and proliferation in bioprinted liver model

The cellular viability of bioprinted constructs laden with (i) HLC and (ii) HUVEC/HHSC was evaluated at day 5 and day 10 of the culture period with calcein-AM/ethidium homodimer-1 staining (Thermo Fisher Scientific, USA). Subsequently, the viability of HLC/HUVEC/HHSC-laden bioprinted liver constructs cultured for 1 week and 2 weeks were analyzed. Briefly, the bioprinted liver constructs were washed with 0.1 M PBS, incubated with 40 µM of calcein-AM (green fluorescence) and 20 µM of ethidium homodimer-1 (red fluorescence) for 30 - 40 min at 37°C. The live/dead images of bioprinted constructs were captured by Z-stacking 15 images at an interval of 10 µm using LSM 880 confocal laser scanning microscopy (CLSM, Zeiss). Acquired images were processed using ImageJ software to obtain a 3D surface plot to apprehend the distribution of live (green) and dead (red) cells. Simultaneously, the HLC/HUVEC/HHSC-laden bioprinted liver model at day 10 of the culture period was fixed in NBF, incubated in 15% and 30% sucrose preservation solution for 6 h and 12 h, respectively, cryosectioned laterally at 10 µm thickness, stained with H&E, and images were captured at the bright field using a Nikon ECLIPSE Ti2 microscope.

Cellular proliferation of bioprinted constructs laden with (i) HLC, (ii) HUVEC/HHSC, and (iii) HLC/HUVEC/HHSC over 15 day culture period was assessed by quantifying the total DNA concentration using the PicoGreen dsDNA assay kit (Thermo Fisher Scientific, USA), following the manufacturer's instructions. The bioprinted constructs collected at days 1, 5, 10, and 15 were homogenized at 4°C for 4 h using cell lysis buffer encompassing Tris HCl, glycerol, NaCl, and protease inhibitors and centrifuged at 3000 rpm to obtain the cell lysate in the supernatant [271]. The cell lysate was incubated with TE buffer and Quant-it PicoGreen dsDNA reagent for 5-10 min under dark conditions. The fluorescence was measured at an excitation and emission wavelength of 480 nm and 520 nm using Tecan Multiplate Reader Infinite M200 PRO (Switzerland), and the DNA concentration in the sample was calculated from the standard curve plotted using Lambda DNA.

4.2.7.3 Gene expression analysis

The expression of parenchymal hepatocyte genes (albumin; cytokeratin-19; cytochrome P450 1A2-CYP1A2; cytochrome P450 2E1-CYP2E1), non-parenchymal HUVEC genes (CD31; vWF), non-parenchymal HHSC gene (desmin) in HLC/HUVEC/HHSC-laden bioprinted liver model at days 1, 5, 10, and 15 of culture period was analyzed using a 7500 Fast RT-PCR. The total RNA was extracted using TRIzol, chloroform, isopropanol, and DNA diluent. The RNA was estimated using a NanoDrop (Thermo Fisher Scientific), and cDNA was synthesized using a high-capacity cDNA reverse transcription kit [283]. Quantitative RT-PCR was performed with sets of human-specific primers **(Table 4.1)** and human GAPDH as a housekeeping gene, using SYBR Green PCR Master mix in the RT-PCR Detection system. The relative expression of a functional gene in the HLC/HUVEC/HHSC-laden bioprinted liver model at a predefined time point was normalized against the expression of a functional gene at day 1. Results were presented following the comparative $2^{-\Delta\Delta Ct}$ method.

4.2.7.4 Immunofluorescence staining

For immunofluorescence staining, the HLC/HUVEC/HHSC-laden bioprinted liver models matured for 1 week and 2 weeks were washed in PBS, fixed overnight at 4°C in NBF solution, permeabilized in PBS containing 0.1% (v/v) Triton X-100 solution, and subjected to blocking in PBS containing 1% (w/v) BSA, 2% (v/v) horse serum, and 0.2% (v/v) tween 20 solution. The distribution of HLCs and HHSCs in a bioprinted liver model was examined by immunolabeling and co-localizing against albumin and desmin marker. The constructs were incubated with primary antibodies, mouse anti-albumin (ab10241, 1:200 dilution), and rabbit anti-desmin (ab32362, 1:200 dilution) suspended in blocking buffer at 4°C overnight. Then, the constructs were incubated with corresponding secondary antibodies at 1:200 dilution for 3 h, and nuclei were counterstained with DAPI. Then, the vascularization in HLC/HUVEC/HHSC-laden bioprinted liver model was assessed by immunolabeling against (i) albumin (HLC) and vWF (HUVEC) marker, and (ii) CYP2E1 (HLC) and CD31 (HUVEC) marker. For albumin and vWF staining, the constructs were incubated at 4°C overnight with primary antibodies, mouse anti-albumin (ab10241, 1:200 dilution), and rabbit anti-vWF (ab6994, 1:200 dilution). Subsequently, for CYP2E1 and CD31 staining, the constructs were incubated overnight with primary antibodies, rabbit anti-CYP2E1 (NBP2-67021, 1:100 dilution), and mouse anti-CD31 (ab199012, 1:200 dilution). Post-incubation, the constructs were incubated with respective secondary antibodies at 1:200 dilution for 3 h, and

nuclei were counterstained with DAPI. Furthermore, the distribution of NPCs in the HLC/HUVEC/HHSC-laden bioprinted liver model was investigated by immunolabeling and co-localizing against CD31 (HUVEC) and desmin (HHSC) marker. The constructs were incubated overnight with primary antibodies against mouse anti-CD31 (ab199012, 1:200 dilution) and rabbit anti-desmin (ab32362, 1:200 dilution), treated with corresponding secondary antibodies at 1:200 dilution, and nuclei were counterstained with DAPI. The immunofluorescence images were visualized and captured by Z-stacking 15 images at an interval of 10 µm using LSM 880 CLSM and processed using ImageJ software to apprehend the co-distribution of both cell markers following color deconvolution, thresholding, and analyzing the 3D surface plot.

4.2.7.5 Human albumin secretion and urea synthesis assay

The conditioned media from the HLC/HUVEC/HHSC-laden bioprinted liver model collected on days 1, 5, 10, and 15 of the culture period was stored at -80°C, centrifuged at 3000g for 10 min, and estimated for albumin and urea secretion in media, as previously reported [281]. The albumin content in the supernatant was determined using the human albumin ELISA kit (Abcam, UK). The sample volume of 50 µL was incubated for 1 h in albumin antibody precoated wells, followed by serially treated with an equal volume of biotinylated albumin antibody, 1X streptavidin conjugate, and chromogen substrate for 30 min, 30 min, and 20 min respectively. Absorbance was measured at 450 nm, and the unknown albumin concentration was calculated from the standard curve generated using albumin standard at a concentration of 0-200 ng/mL. Simultaneously, the urea content in the conditioned media was measured using the urea assay kit (Sigma-Aldrich, USA) [271]. The sample volume of 50 µL was incubated with 50 µL of the reaction mix entailing substrate (peroxidase), enzyme mix, developer, and converting enzyme at 37°C for 60 min under dark conditions and intermittent shaking. Absorbance was recorded at 570 nm, and the unknown urea concentration was calculated from the standard curve generated using urea standard at a concentration of 1-5 nmol.

4.2.7.6 Lactate dehydrogenase assay

The number of viable hepatocytes is directly related to the intracellular LDH activity [292]. The intracellular LDH activity of the HLC/HUVEC/HHSC-laden bioprinted liver model at predetermined time points was determined using the LDH activity assay kit (Sigma-Aldrich, USA). Briefly, the cell lysate was isolated by incubating the constructs in cell lysis buffer as

described. The cell lysate at respective dilution was incubated for 3-5 min at 37°C with an LDH assay buffer containing LDH substrate mix under dark conditions, followed by the absorbance measurement at 450 nm in kinetic mode. The NADH generated in the unknown sample was calculated from the standard graph generated using 0-12.5 nmol/well. The LDH activity in the unknown samples was calculated using,

$$\text{LDH activity (milliunit/mL)} = (A/ \Delta T \times V)$$

where, A = amount of NADH (nmol) as calculated from the standard graph (difference in absorbance between T_2 and T_1 was used to determine the amount of NADH generated)

ΔT = difference in time between T_2 and T_1 (min)

V = sample volume (mL)

4.2.7.7 Cytochrome P450 activity

The metabolic activity of the HLC/HUVEC/HHSC-laden bioprinted liver model was evaluated using a cytochrome P450 reductase (CPR) activity assay kit (Abcam, UK) according to the manufacturer's instructions [281]. Briefly, the microsomal fraction of the cell lysate was isolated from the cultured constructs as delineated and incubated at 37°C for 10 min with a reaction buffer composed of two main components: NADPH substrate and glucose-6-phosphate. However, a similar reaction was carried out for all the samples in the presence of 1 mM CPR inhibitor. Post incubation, the absorbance was measured at 460 nm in the kinetic mode for 20 min. Subsequently, the total intracellular protein in cell lysate was assessed using the Bradford reagent, followed by absorbance measurement at 595 nm. The specific CPR activity in the bioprinted liver model at a predetermined time point was calculated in two steps using,

$$\text{CPR activity (mU/mg)} = (\Delta A/ (\Delta T \times P_c))$$

where, ΔA = difference in absorbance between T_2 and T_1 that gives the amount of glucose-6-phosphate consumed (nmol)

ΔT = difference in time between T_2 and T_1 (min)

P_c = intracellular protein concentration (mg)

Specific CPR activity in each sample = (CPR activity) – (CPR activity in the presence of inhibitor)

4.2.8 Bioprinted liver lobule model for drug-induced liver injury evaluation

The bioprinted liver constructs laden with (i) HLC and (ii) HLC/HUVEC/HHSC after maturing for 10 days were exposed to drugs for 24 h to analyze their potential in drug-induced hepatotoxicity prediction. All drugs, including non-hepatotoxicants (aspirin and dexamethasone), idiosyncratic hepatotoxicant (trovafloxacin mesylate), and hepatotoxicants (acetaminophen and troglitazone) were procured from Sigma-Aldrich, USA; and Dimethyl sulfoxide (DMSO) was used as a solvent to prepare drug solution. The C_{max}, an average maximum drug concentration found in plasma, is defined as therapeutically appropriate drug exposure levels in humans [319]. The concentrations of all drugs used for toxicity assessment are provided in **Table 4.3**, considering human C_{max}, 100 × C_{max}, or above 100 × C_{max}, as applied in earlier studies [320, 321]. The bioprinted liver model was exposed to drugs for 24 h (**Table 4.3)**, followed by estimating the cell viability, LDH activity, and CPR activity of the liver model. Subsequently, the analysis of cell viability, LDH activity, and CPR activity in the liver model matured for 10 days without any drug exposure was considered as an internal control. The cell death induced by drug exposure in the bioprinted liver model was estimated from the percentage of viable cells. The bioprinted liver constructs were homogenized using cell lysis buffer, and cellular viability was assessed by quantifying the DNA concentration in cell lysate using Quant-iT^{TM} PicoGreen dsDNA assay kit. In addition, a drug concentration showing a 50% decrease in cell viability (EC_{50}) in bioprinted liver constructs was evaluated using nonlinear curve fitting following dose-response model from a plot of drug concentration (X) versus the percentage of cell viability (Y) using OriginPro8 software. Subsequently, the LDH activity and specific CPR activity of the bioprinted liver model were measured using the LDH assay kit and CPR activity assay kit as explained in the methodology sections 4.2.7.6 and 4.2.7.7, respectively.

Table 4.3. *List of drugs and their concentration used for drug toxicity assessment in bioprinted liver model.*

S. No.	Drugs	Human C_{max} (µM)	100 × C_{max} (µM)	Concentration range tested (µM)	EC_{50} in liver model[a] (µM)	EC_{50} in liver model[b] (µM)
1.	Aspirin	5.53	552.60	5.53, 552.60 and 1000	N/A	N/A
2.	Dexamethasone	0.22	22.40	0.22, 22.40 and 500	N/A	N/A
3.	Trovafloxacin mesylate	4.08	407.80	2, 4.08, 100 and 407.80	5.45	1.04
4.	Acetaminophen	139	13900	139, 5000, 10000 and 13900	7119.43	4546.77
5.	Troglitazone	6.39	638.70	6.39, 50, 100 and 638.70	100.18	66.11

EC_{50} value of drugs in bioprinted liver model laden with HLC (liver model[a]), and bioprinted liver model laden with HLC/HUVEC/HHSC (liver model[b]), as observed in the present study

4.2.9 Statistical analysis

All the experiments, including functional characterization and drug toxicity testing, were performed in triplicates (n=3 samples), unless otherwise mentioned. Data are represented as average ± SD (standard deviation). OriginPro 8 was used for data processing and determining statistical significance. The one-way ANOVA test followed by posthoc Dunn's multiple comparison test was performed to determine statistical analysis considering significance at $p \leq 0.05$, $p \leq 0.01$, and $p \leq 0.001$.

4.3 Results

4.3.1 Design and printing of the 3D printed liver model

A 3D liver lobule mimetic CAD model was designed, wherein the structure emphasizes the native hierarchical arrangement of hepatocyte plates with the complementary sinusoidal network and space disse in both horizontal and vertical directions **(Figure 4.3 A)**. The generation of 3D bioprinted vascularized liver lobule model includes a series of steps, (i) a discrete HLC-

laden bioink 1 and HUVEC/HHSC-laden bioink 2 formulation **(Figure 4.3 B, i)**, and (ii) 3D bioprinting of the liver model using the extrusion-based bioprinting technique **(Figure 4.3 B, ii)**. A total of six layers of cell-laden hydrogels were printed in a layer-by-layer fashion, wherein each layer constituted three alternative multi-material extrusion of bioink 1 and bioink 2. The alternate layers of HLC-laden bioink 1 and HUVEC/HHSC-laden bioink 2 were maintained in an individual layer and successive layers to achieve complementary cellular arrangements of parenchymal and NPCs to mimic the native liver. The multilayered assembly of bioink 1 and bioink 2 in horizontal and vertical directions in the desired 3D pattern offered by extrusion bioprinting portrayed a stable liver model. To visualize this as a whole liver lobule model, fluorescent particles were encapsulated in gelatin, green as HLC-laden ink and pink as HUVEC/HHSC-laden ink, and printed to envisage intercellular crosstalk and ECM interaction as shown in **Figure 4.3 B, ii**. In printed constructs, base length, side length, and single-layer thickness were 11 mm, 11 mm, and 0.45 mm, respectively.

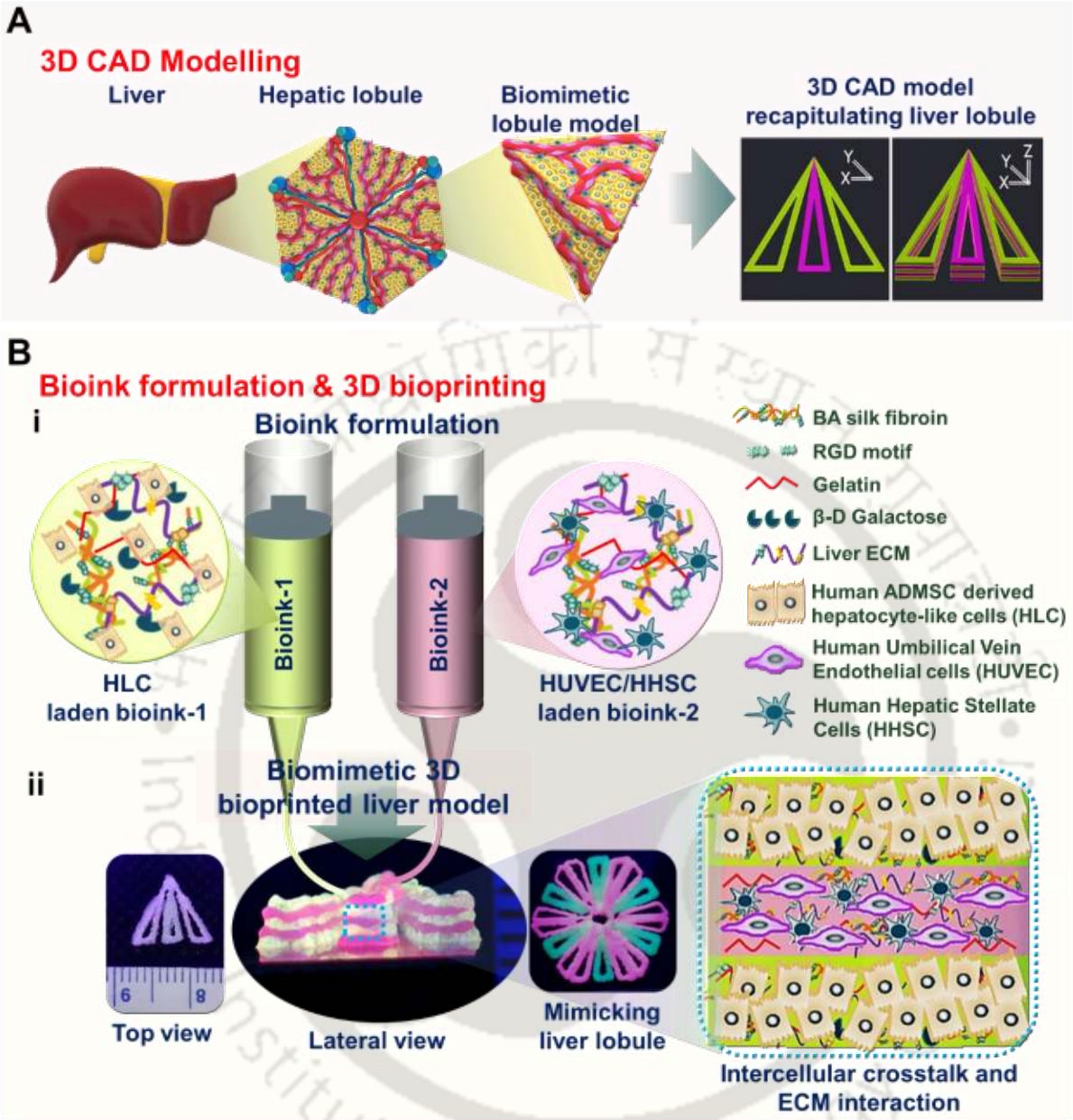

Figure 4.3. Schematic illustration of CAD designing, bioink formulation, and bioprinting of the liver lobule model. *(A) Design of the 3D bioprinted liver model similar to the native liver lobule with an alternate cellular arrangement of parenchymal and NPCs in both horizontal and vertical directions using CAD digital modeling. (B) (i) Bioink formulation encompassing HLC-laden bioink 1 and HUVEC/HHSC-laden bioink 2, and (ii) Extrusion-based bioprinting of a multilayered biomimetic liver model depicting the intercellular crosstalk and cell-matrix interaction for the high-throughput drug screening platform.*

4.3.2 Bioink formulation, printability examination, and rheological characterization

The liver ECM-derived microparticles obtained by Triton X-100/ammonium hydroxide decellularization **(Figure 4.1)** demonstrated a mean particle size of 848.8 ± 71.4 nm, as observed from dynamic light scattering analysis. A co-printable basic liver ECM ink for supporting HLCs and HUVECs/HHSCs was optimized as 1% (w/v) BM silk, 1% (w/v) AA silk, 1% (w/v) liver ECM, and 7% (w/v) gelatin from the printability examination **(Figure 4.4 A)**. Specifically, 40 mM β-D galactose, a cytocompatible concentration that maintained HLCs viability over 7 days was added as an additive in bioink 1 with basic liver ECM ink **(Figure 4.2)**. FTIR spectra for bioink 1, bioink 2, and blend before and after HRP/H_2O_2 crosslinking showed a peak shift in the amide I, amide II, and amide III bands in crosslinked hydrogels, ensuring β-sheet formation **(Figure 4.4 B)**. A peak shift in the amide I (1650-1600 cm^{-1}), amide II (1580-1510 cm^{-1}), and amide III (1250-1210 cm^{-1}) bands denoted by a, b, and c in the spectrum, respectively, confirmed conformational changes in secondary structure post-enzymatic crosslinking. The rheological properties, storage (G') and loss (G") moduli of formulated bioink 1 and bioink 2 were assessed as a function of time and temperature. The sol-gel transition occurred at 13.4 min and 11 min for bioink 1 and bioink 2, respectively, as observed from a rapid increase in G' values, and G' reached a steady value of 1560 Pa over 32 min for both bioinks **(Figure 4.4 C, i)**. While increasing the temperature, both bioinks initiated sol-gel transition at 33°C and were stable after 37°C, endorsing the HRP/H_2O_2 crosslinking, and 28°C - 34°C was chosen as the optimal printing temperature. **(Figure 4.4 C, ii)**. From the amplitude sweep analysis performed at a constant angular frequency of 10 rad/s, LVER was calculated as 0.08-0.2%, and elastic behavior (G'>G") was noticed at a low shear strain **(Figure 4.4 C, iii)**. However, with an increase in the shear strain, the elastic nature of hydrogels was lost, and the viscous nature (G">G') was gained, indicating the shear thinning effect of bioinks, owing to its viscous behavior. Frequency sweep analysis performed at a constant shear strain of 0.01% (as calculated from LVER in amplitude sweep) confirmed the integral stability of crosslinked hydrogels **(Figure 4.4 C, iv)**. From the 3ITT, G' gradually recovered for both bioinks post deformation that occurred due to the shear-thinning effect in LVER, thus corroborating that both inks would regain their elastic nature and maintain structural stability post-exposure to high shear strain **(Figure 4.4 C, v)**. Subsequently, the complex viscosity of bioinks at alternate cycles of oscillation-rotation confirmed the shear-thinning nature of bioinks **(Figure 4.4 C, vi)**.

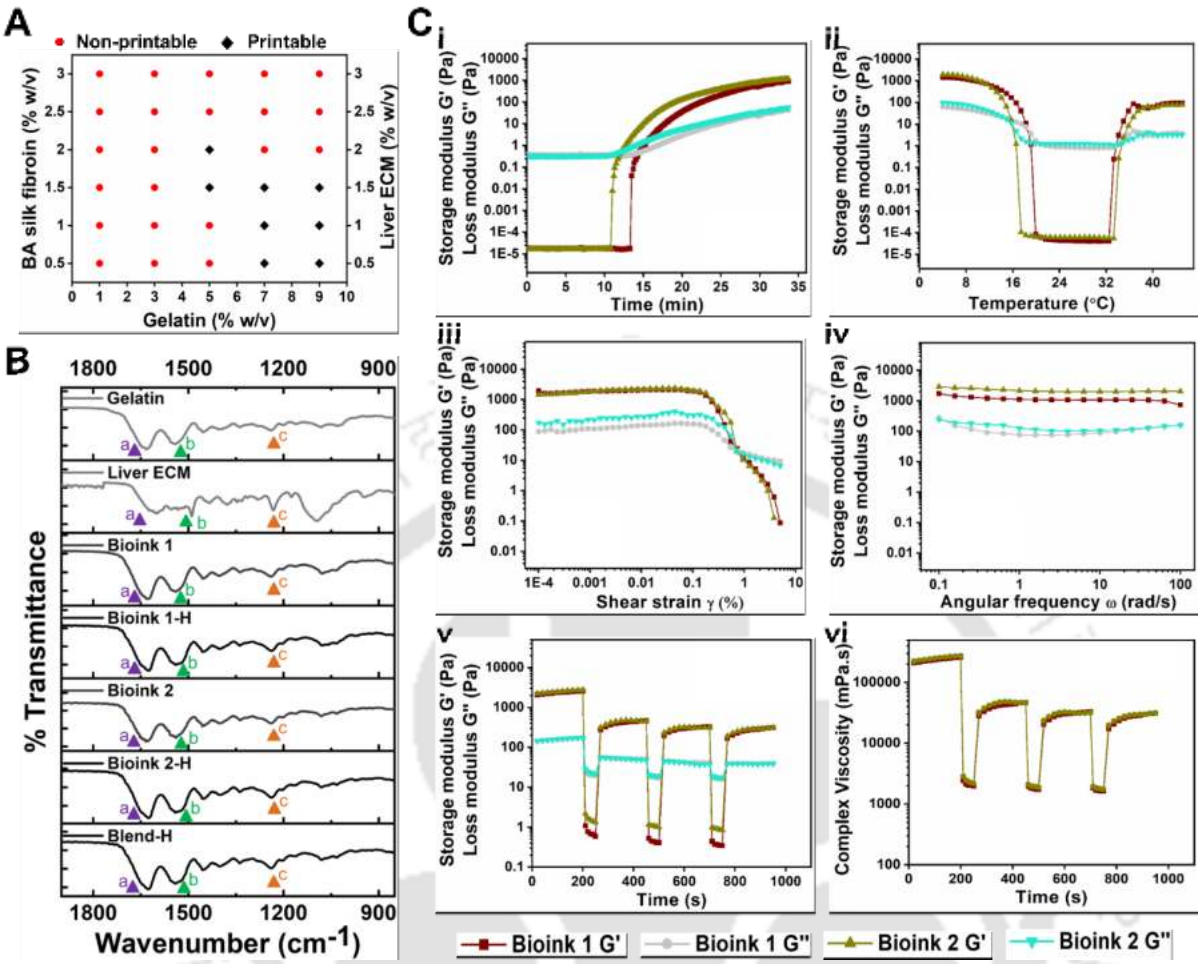

Figure 4.4. Bioink formulation for HLC (bioink 1) and HUVEC/HHSC (bioink 2) and its characterization. *(A) Printability examination. (B) FTIR spectrum of enzymatic* HRP/H_2O_2 *crosslinked (-H) and non-crosslinked bioink 1, bioink 2, and blend bioink hydrogels. a, b, and c represent amide-I, amide-II, and amide-III, respectively. (C) Rheological analysis of bioink 1 and bioink 2 (i) gelation time profile, (ii) temperature sweep profile, (iii) amplitude sweep profile, (iv) frequency sweep profile, (v) three interval thixotropic measurement, and (vi) complex viscosity.*

4.3.3 Physicochemical characterizations and immunocompatibility of the 3D printed liver model

The surface morphology, swelling ratio, *in vitro* degradation profile, hemocompatibility, and immunocompatibility of the acellular printed liver model were characterized. FESEM characterizations revealed that the printed constructs possessed interconnected struts with a pore size of 142.80 ± 28.44 µm **(Figure 4.5 A-B)**. The printed constructs with individual bioink 1 and bioink 2, and blend exhibited a distinct trend of swelling kinetics **(Figure 4.5 C-D)**. The printed constructs showed rapid water uptake and swelling within 45 min and attained an equilibrium after

1 h. At 7 h, the constructs printed with ink 2 exhibited a significantly ($p \leq 0.01$) increased swelling ratio of 872.71 ± 48.50 compared to constructs printed with blend ink (727.22 ± 26.33) and ink 1 (580.41 ± 54.97) **(Figure 4.5 C)**. Among the constructs printed with blend ink and ink 1, the constructs printed with blend ink demonstrated a higher ($p \leq 0.01$) swelling ratio. In the initial 1 h, a similar pattern of high swelling ratio ($p \leq 0.01$) was witnessed in the constructs printed with ink 2 and blend ink compared to ink 1 **(Figure 4.5 D)**. The degradation study revealed that printed constructs were stable in hydrolytic PBS conditions and significantly ($p \leq 0.001$) degraded in an enzymatic protease XIV environment **(Figure 4.5 E)**. After incubating for 18 days in PBS condition, all three variants of 3D printed constructs maintained structural integrity without any structural disruptions. However, at the end of 18 days, the printed constructs with only ink 1 displayed a minimal mass loss with a reduced ($p \leq 0.05$) percentage mass remaining of 82.20 ± 0.35% compared to printed constructs using ink 2 (93.03 ± 3.14%) and blend ink (92.89 ± 0.94%). Moreover, all variants of printed constructs subjected to an enzymatic environment showed structural disruptions by day 3, degraded rapidly by day 9, and did not indicate any significant difference in the percentage mass remaining over 18 days. An *in vitro* hemocompatibility assessment by quantification of LDH activity of adhered platelets on hydrogels revealed a minimal ($p \leq 0.01$) platelet adhesion on hydrogel fabricated using bioink 1 (2.19 ± 0.32 milliunits/mL) and bioink 2 (3.54 ± 1.35 milliunits/mL) compared to gelatin (9.39 ± 1.29 milliunits/mL) **(Figure 4.5 F, i)**. Further, the pro-inflammatory cytokine, IL-1β released from *in vitro* RAW 264.7 macrophages was much lower ($p \leq 0.05$) in response to bioink 1 and bioink 2 hydrogels with 802.22 ± 90.76 pg/mL and 729.84 ± 96.30 pg/mL, respectively than that released in the presence of LPS (1128.88 ± 142.41 pg/mL) **(Figure 4.5 F, ii)**. However, the IL-1β release in response to bioink hydrogels was comparable to the negative control, tissue culture plate (TCP). The response of macrophages toward both bioinks was statistically insignificant; thus, a blend bioink hydrogel was studied in detail for macrophage modulation and host response compared to only gelatin hydrogel after implantation in the subcutaneous pocket of Wistar rats **(Figure 4.5 G)**. Histological analysis of 1 week and 2 weeks explant revealed the infiltration of host tissue cells, including fibroblasts and macrophages in the subcutaneous pocket treated with blend bioink hydrogel compared to only gelatin hydrogel. The retrieved explants with blend bioink hydrogel samples showed higher $CD31^+$ blood vessels and $CD68^+$ macrophages at 1 week than gelatin hydrogel. However, over 2 weeks, the blood vessels and macrophage infiltration reduced in both gelatin and

blend bioink hydrogel. Furthermore, assessment of $CCR7^+$ pro-inflammatory and $CD163^+$ pro-remodeling macrophages revealed that a greater number of $CD163^+$ pro-remodeling macrophages were present in explants with blend bioink hydrogel over 2 weeks than gelatin hydrogel, supporting immunocompatibility and tissue regeneration.

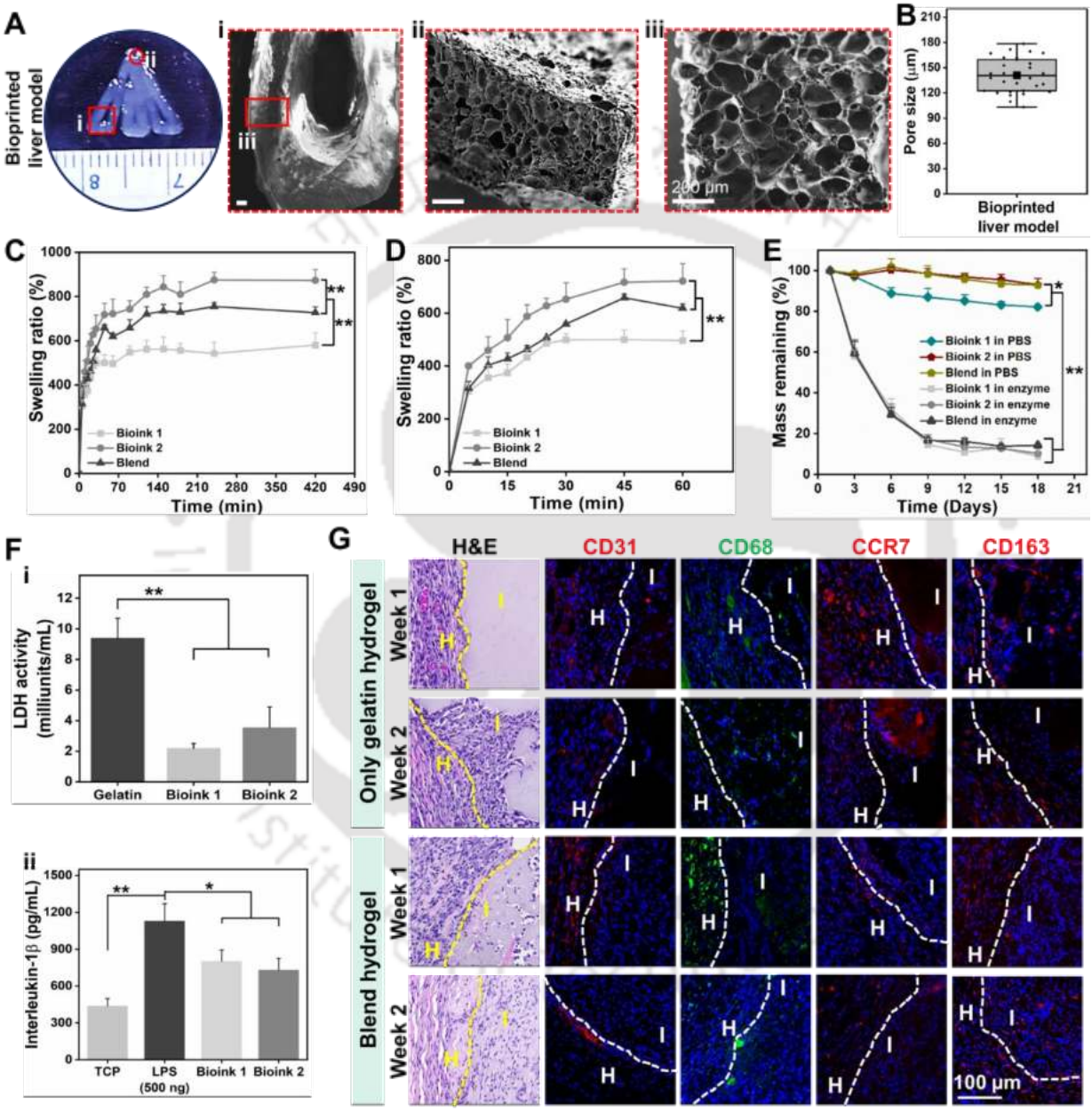

Figure 4.5. Physicochemical characterizations and immunocompatibility analysis of the 3D printed liver model. *(A) Field emission scanning electron microscopy images presenting the surface morphology and interconnected porous network of the printed liver model. Scale bar: 200 μm. (B) Pore size. (C) Swelling ratio of printed constructs up to 7 h. (D) Swelling ratio of printed constructs in the initial 1 h. (E) Degradation profile of the printed constructs in the hydrolytic*

*(PBS) and enzymatic (Protease XIV) environment. (F) Quantification of (i) LDH activity of adhered platelets, and (ii) pro-inflammatory cytokine, IL-1β, released by mouse RAW 264.7 macrophages. (G) Host acceptance and immune response toward blend hydrogel and only gelatin hydrogel after 1 week and 2 weeks of subcutaneous implantation. Host cell infiltration and blood vessel formation were observed from H&E and CD31 staining, respectively. Macrophages, pro-inflammatory macrophages, and pro-remodeling macrophages were determined by CD68, CCR7, and CD163 staining, respectively. The yellow and white dashed line delineates the host (H) and implant hydrogel (I) (n = 3). Scale bar: 100 µm. Data are represented as Mean ± SD. (n = 3, * $p \leq 0.05$, ** $p \leq 0.01$ and *** $p \leq 0.001$).*

4.3.4 Differentiation of ADMSCs toward hepatocyte-like cells

The quantitative RT-PCR data showed that matured HLCs following stage-wise differentiation **(Figure 4.6 A)** expressed mature hepatocyte-specific genes albumin, AFP, and HNF4α; indeed, ADMSC did not exhibit expression **(Figure 4.6 B)**. The CYP2E1 expression was significantly ($p \leq 0.01$) upregulated in HLCs compared to ADMSCs. After 18 days of differentiation, the ADMSCs gradually altered morphology from spindle-like mesenchymal to polygonal-like hepatocyte morphology, increasing cell-cell interaction **(Figure 4.6 C)**. The stemness characteristic Sox9 protein expression was observed in ADMSCs compared to hepatic endoderm and mature HLCs **(Figure 4.6 C)**. Hepatic endoderm cells at the end of day 7 expressed hepatic progenitor-specific markers, including albumin, CYP2E1, and fibronectin. Relatively, HLCs at the end of day 18 showed an increased expression of mature hepatocyte proteins, including albumin, cytokeratin 18, CYP2E1, fibronectin, and HNF4α.

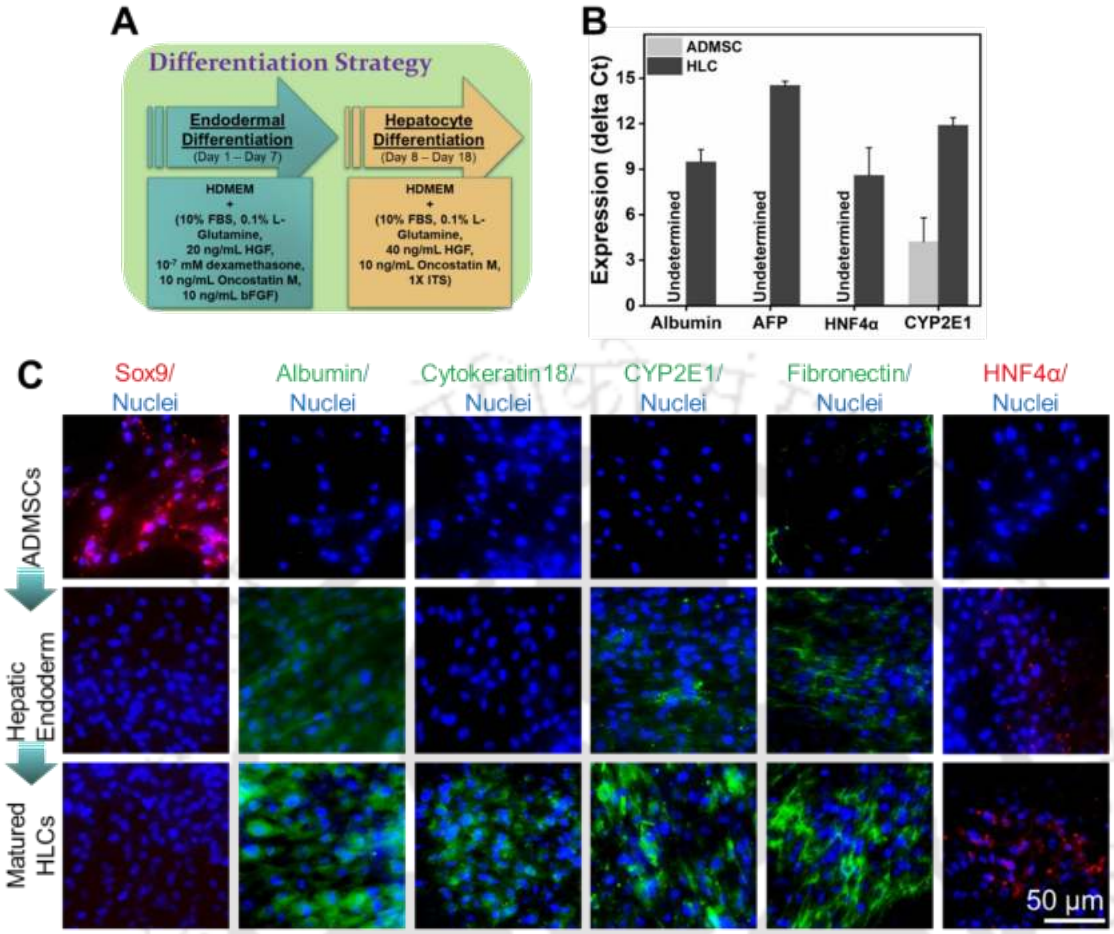

Figure 4.6. Differentiation of human adipose-derived mesenchymal stem cells (ADMSCs) toward hepatocyte-like cells (HLCs) and their characterization. *(A) Schematic representation of step-wise differentiation protocol for the generation of functional HLCs from ADMSCs. (B) Gene expression analysis for albumin, AFP, HNF4α, and CYP2E1 in ADMSCs and HLCs. (C) Immunofluorescence images of ADMSCs, hepatic endoderm, and HLCs for stem cell marker (Sox9) and functional hepatocyte markers (albumin, cytokeratin 18, CYP2E1, fibronectin, HNF4α). Scale bar: 50 µm. Data are represented as Mean ± SD. (n = 3, * $p \leq 0.05$ and ** $p \leq 0.01$).*

4.3.5 Viability, distribution, and proliferation of embedded cells in the bioprinted liver model

The HLCs were encapsulated in bioink 1, HUVECs and HHSCs were encapsulated in bioink 2, and a 3D liver lobule-like construct was bioprinted, wherein the ratio of HLC/HUVEC/HHSC was maintained as 10:7:2 **(Figure 4.7 A)**. The live/dead confocal fluorescence images of bioprinted liver construct laden with (i) HLC, (ii) HUVEC/HHSC, and (iii) HLC/HUVEC/HHSC showed that embedded cells maintained viability **(Figure 4.7 B-C)**. In HLC-laden bioprinted constructs, the HLCs showed a spheroidal organoid formation over 10 days

(Figure 4.7 B, i). On the other hand, HUVEC/HHSC-laden bioprinted constructs showed a mesenchymal morphology, and cells were attached along the pores **(Figure 4.7 B, ii)**. Similarly, the HLC/HUVEC/HHSC-laden bioprinted liver constructs revealed that encapsulated cells were viable and distributed evenly over 15 days, thus facilitating cellular infiltration in the printed constructs **(Figure 4.7 C)**. Minimal cell death was noticed at the periphery of liver constructs laden with HUVEC/HHSC and HLC/HUVEC/HHSC. Subsequently, H&E stained lateral sections of HLC/HUVEC/HHSC-laden bioprinted liver constructs showed an even distribution of embedded cells between the layers of bioprinted constructs **(Figure 4.7 D)**. Furthermore, the cell proliferation in terms of DNA concentration between three bioprinted constructs laden with (i) HLC, (ii) HUVEC/HHSC, and (iii) HLC/HUVEC/HHSC cultured over 15 days was analyzed **(Figure 4.7 E)**. The HLC-laden liver model maintained a similar DNA concentration over 15 days, indicating the absence of HLC proliferation. However, the HUVEC/HHSC-laden liver model showed enhanced proliferation on day 10 and day 15 compared to day 1 and day 5. Comparatively, the HLC/HUVEC/HHSC-laden liver model showed statistically enhanced cell proliferation than bioprinted constructs laden with HLC and HUVEC/HHSC at day 5 ($p \leq 0.01$), day 10 ($p \leq 0.01$), and day 15 ($p \leq 0.001$). Remarkably, HLC/HUVEC/HHSC-laden bioprinted constructs demonstrated increased cell proliferation over 15 days, with increased ($p \leq 0.01$) DNA concentration at day 5 (326.10 ± 35.30 ng/mL) compared to day 1 (188.42 ± 28.22 ng/mL), and increased ($p \leq 0.001$) DNA concentration at day 10 (471.81 ± 25.18 ng/mL) and day 15 (503.98 ± 32.90 ng/mL) compared to day 1 and day 5.

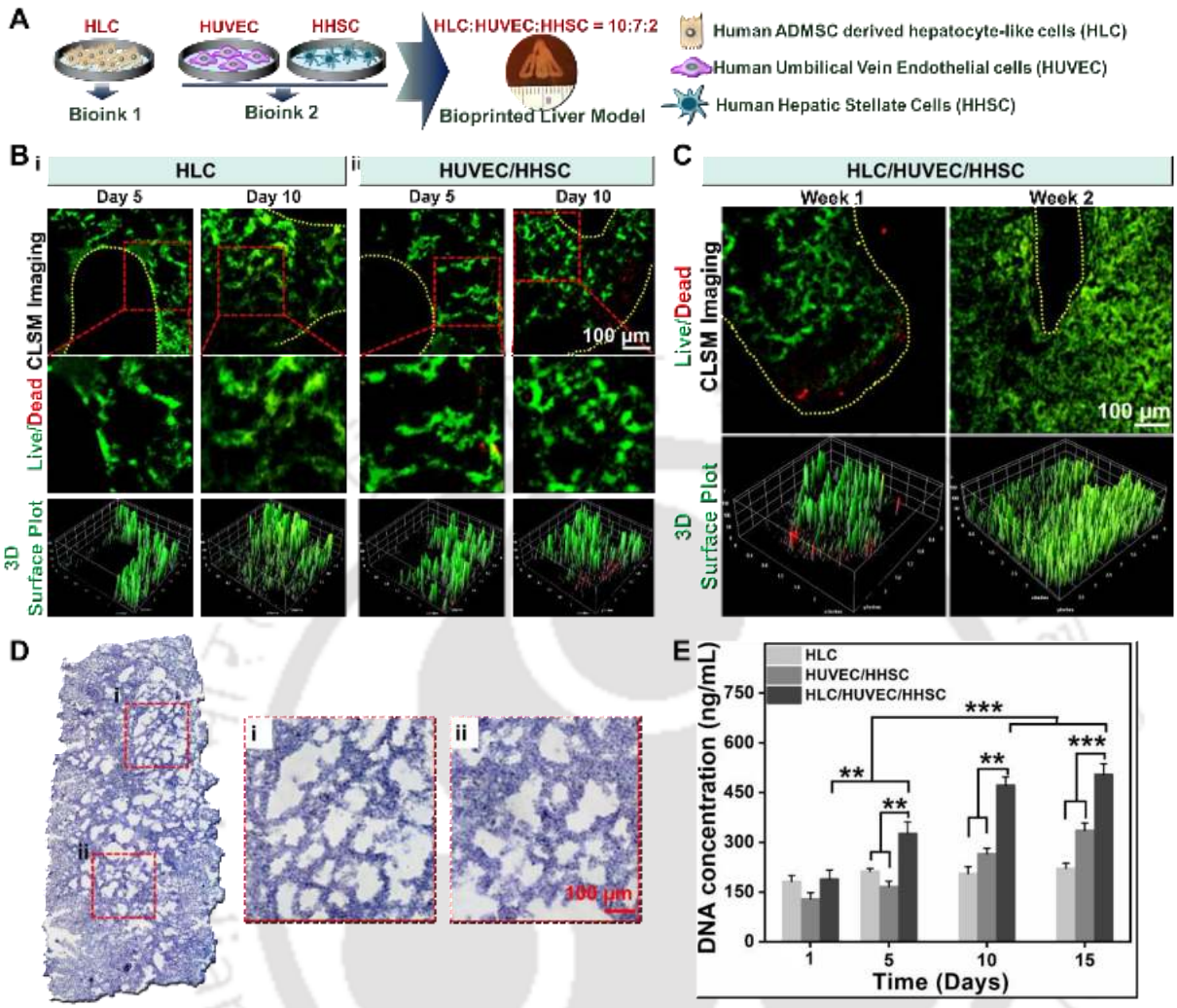

Figure 4.7. Bioprinting of liver constructs and their characterization for cellular viability, distribution, and proliferation. *(A) Schematic illustration of HLC-laden bioink 1 and HUVEC/HHSC-laden bioink 2 preparation, and their ratio for bioprinting of the liver model. (B) Confocal live/dead images and 3D surface plot analysis of the bioprinted liver model laden with (i) HLC and (ii) HUVEC/HHSC on day 5 and day 10. (C) Confocal live/dead images and 3D surface plot analysis of the HLC/HUVEC/HHSC-laden bioprinted vascularized liver model on week 1 and week 2. The live cells are stained in green, and the dead cells are stained in red. (D) H&E staining of the lateral section of the HLC/HUVEC/HHSC-laden bioprinted liver model. Scale bar: 100 µm. The yellow dashed line shows the boundary of a single layer in bioprinted constructs, and the red box shows the area shown in the higher magnification image. (E) Assessment of cellular proliferation in the bioprinted liver model laden with HLC, HUVEC/HHSC, and HLC/HUVEC/HHSC until day 15 using the PicoGreen dsDNA assay kit. Data are represented as Mean ± SD. (n = 3, ** $p \leq 0.01$ and *** $p \leq 0.001$).*

4.3.6 Functional analysis

Comparatively, the HLC/HUVEC/HHSC-laden bioprinted liver model demonstrated higher potential in maintaining cell viability and proliferation than bioprinted constructs laden with (i) HLC and (ii) HUVEC/HHSC. Furthermore, the liver-specific hepatocyte, endothelial, and stellate functions were analyzed in the HLC/HUVEC/HHSC-laden vascularized liver model.

4.3.6.1 Gene expression analysis of parenchymal and non-parenchymal markers in the bioprinted vascularized liver model

The expression level of hepatic-specific genes albumin, cytokeratin-19; phase I enzymes CYP1A2, CYP2E1; HUVEC-specific genes CD31, vWF; and HHSC-specific gene desmin in the vascularized liver model was increased over 15 days **(Figure 4.8 A-B)**. The albumin expression on day 10 significantly ($p \leq 0.01$) upregulated about 7.42 and 1.75 fold compared to day 1 and day 5, respectively, and maintained similar expression over 15 days **(Figure 4.8 A)**. However, cytokeratin-19 expression gradually upregulated over 15 days, with increased ($p \leq 0.05$) expression on day 15, about 1.42 fold greater than day 10, and a greater ($p \leq 0.001$) expression on day 10 and day 15 than day 1 and day 5. In particular, the expression levels of CYP1A2 and CYP2E1 upregulated ($p \leq 0.001$) at day 5 and maintained similar expression up to day 15 of the culture period. The endothelial cell marker, CD31 gene expression upregulated ($p \leq 0.001$) about 3.58 fold on day 10 compared to day 5 and did not exhibit any significant difference in expression levels between day 10 and day 15 **(Figure 4.8 B)**. The vWF expression gradually upregulated over 15 days, with an enhanced ($p \leq 0.05$) expression about 1.87 fold on day 15 compared to day 5. Furthermore, the desmin expression significantly ($p \leq 0.001$) upregulated over 15 days compared to day 1. Desmin expression upregulated ($p \leq 0.05$) about 2.00 and 1.45 fold on day 15 compared to day 5 and day 10, respectively.

4.3.6.2 Bioprinted vascularized liver model patterning hepatocytes and supporting cells in a physiologically relevant sinusoidal and space disse network

The HLC/HUVEC/HHSC-laden bioprinted vascularized liver model stained for multiple liver cell-specific markers to study the protein expression, and co-localization exhibited increased protein expression levels after 2 weeks compared to 1 week. From the surface plot and immunofluorescence images, higher expression of albumin (green fluorescence) positive HLCs and desmin (red fluorescence) positive HHSCs was observed over 2 weeks than 1 week **(Figure**

4.8 C). Surface plot analysis showed that the HLCs appeared as aggregates or organoids with distinct aligned HHSCs layers in the vascularized liver model after 2 weeks. Similarly, the bioprinted liver model stained for albumin (green fluorescence) and vWF (red fluorescence) demonstrated organoid growth of HLCs with a layer of a sinusoidal-like network formed by adjacent HUVECs over 2 weeks, as observed from the surface plot and immunofluorescence images **(Figure 4.8 D)**. Furthermore, the vascularized liver model stained for phase I metabolism protein CYP2E1 (green) and endothelial cell adhesion protein CD31 (red) indicated that the whole construct was well integrated, and endothelial cells formed a vascular network **(Figure 4.9 A)**. Then, the distribution of HUVECs and HHSCs was evaluated by assessing the co-localization of CD31 (green) and desmin (red) protein **(Figure 4.9 B)**. Both HUVECs and HHSCs showed an increased strong expression of CD31 and desmin protein, respectively at 2 weeks compared to 1 week, suggesting the formation of vascular network with space of disse.

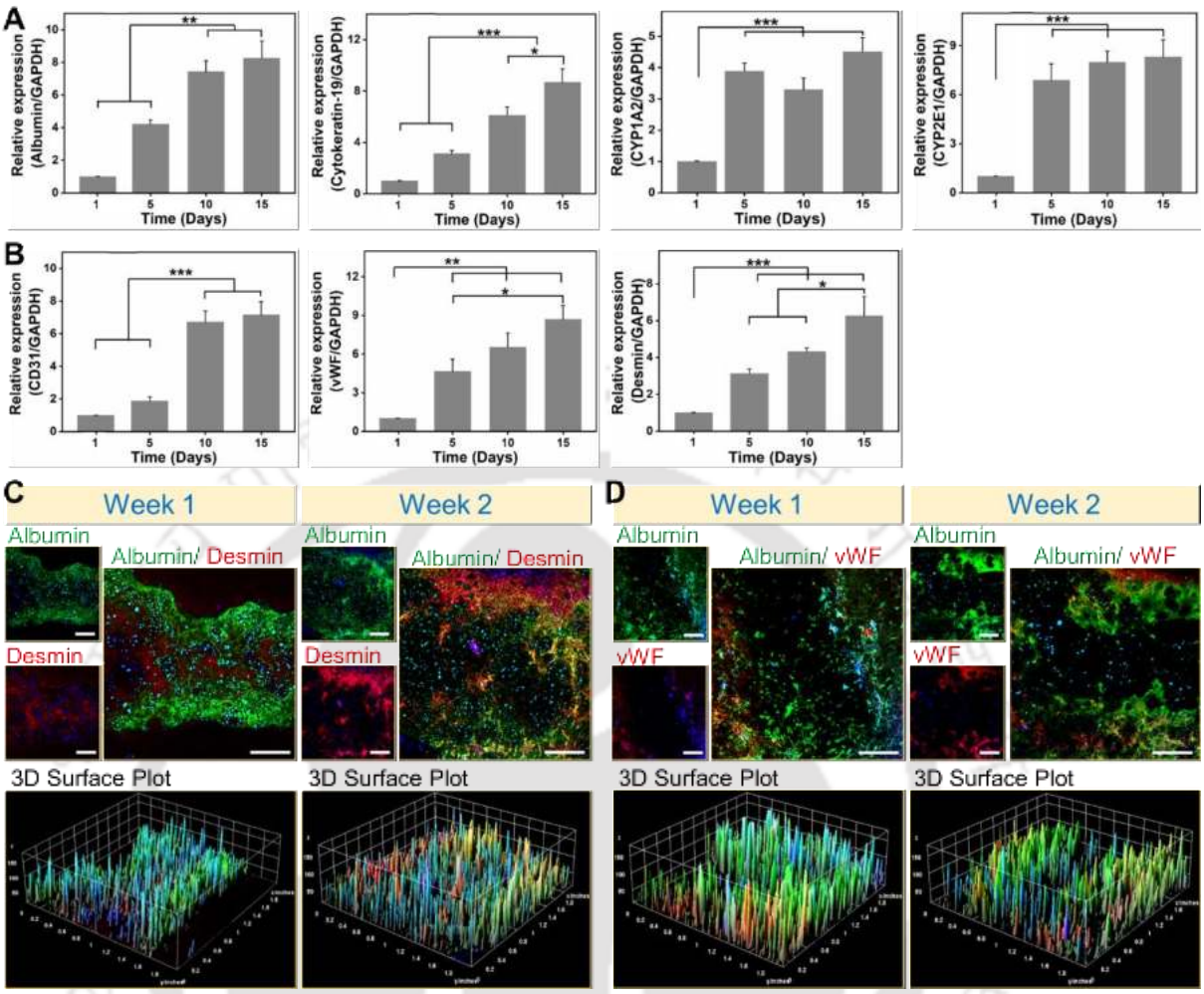

Figure 4.8. Functional assessment of the HLC/HUVEC/HHSC-laden bioprinted vascularized liver model. *Gene expression analysis of (A) hepatocyte specific markers albumin, cytokeratin – 19, CYP1A2, and CYP2E1. (B) Gene expression analysis of HUVEC specific biomarkers CD31, vWF, and HHSC specific marker desmin. (n = 3, * $p \leq 0.05$, ** $p \leq 0.01$ and *** $p \leq 0.001$). Data are represented as Mean ± SD. Confocal z-stack immunostaining images and 3D surface plot of the bioprinted vascularized liver model stained for (C) albumin (green), desmin (red), and nucleus (blue) and (D) albumin (green), vwf (red), and nucleus (blue) representing the distribution of both parenchymal (HLC) and non-parenchymal (HUVEC/HHSC) cells over 1 week and 2 weeks of the culture period. Scale bar: 200 µm.*

4.3.6.3 Hepatic functions of the bioprinted vascularized liver model

Detailed hepatocyte-specific functions, including synthetic functions, nitrogen metabolism, and detoxification ability in the HLC/HUVEC/HHSC-laden vascularized liver model were determined by albumin production, urea synthesis, CPR activity, and LDH activity **(Figure 4.9 C-H)**.

4.3.6.3.1 Albumin production and urea synthesis

The total albumin content secreted from the vascularized liver model significantly ($p \leq 0.001$) increased on day 10 (99.60 ± 10.24 ng) and day 15 (131.99 ± 17.81 ng) compared to day 1 (25.15 ± 5.52 ng) and day 5 (47.15 ± 8.62 ng) **(Figure 4.9 C)**. The albumin secretion was normalized to the total DNA content in the bioprinted liver construct, which demonstrated an increased ($p \leq 0.01$) albumin secretion of about 0.14 ± 0.03 ng/ng of DNA on day 5 and 0.22 ± 0.02 ng/ng of DNA on day 10 compared to day 1 **(Figure 4.9 D)**. A similar trend of increased ($p \leq 0.001$) albumin production normalized to total DNA was noticed on day 10 and day 15 compared to day 1 and day 5. Similarly, an increased ($p \leq 0.001$) total urea content of 375.61 ± 41.04 µg on day 15 and 298.99 ± 8.11 µg on day 10 was observed compared to 87.85 ± 7.91 µg on day 1 and 173.45 ± 8.90 µg on day 5 **(Figure 4.9 E)**. The urea content normalized to total DNA of liver constructs was statistically ($p \leq 0.001$) enhanced on day 15 (0.82 ± 0.08 ng/ng of DNA) and day 10 (0.63 ± 0.06 ng/ng of DNA) compared to day 1 (0.24 ± 0.02 ng/ng of DNA) and day 5 (0.53 ± 0.03 ng/ng of DNA) **(Figure 4.9 F)**. Both albumin production and urea synthesis by the vascularized liver model increased in a time-dependent manner up to day 10 of the culture period and maintained similar synthetic functions from day 10 to day 15.

4.3.6.3.2 Cytochrome P450 reductase and lactate dehydrogenase activity

The CPR activity and LDH activity of the vascularized liver model increased with an increase in culture time from day 1 to day 10 and maintained similar activity from day 10 to day 15 **(Figure 4.9 G-H)**. The total CPR activity on day 5, day 10, and day 15 was 0.16 ± 0.01 mU/mg of total intracellular protein, 0.21 ± 0.01 mU/mg of total intracellular protein, and 0.22 ± 0.01 mU/mg of total intracellular protein, respectively **(Figure 4.9 G)**. Statistical analysis revealed that CPR activity on day 10 increased ($p \leq 0.01$) by about 1.8 and 1.2 fold compared to day 1 and day 5, respectively, and on day 15 increased ($p \leq 0.01$) by about 2.0 and 1.4 fold compared to day 1 and day 5, respectively. The bioprinted vascularized liver constructs presented an LDH activity of 1.49 ± 0.10 milliunits/mL, 2.12 ± 0.18 milliunits/mL, and 2.74 ± 0.19 milliunits/mL on day 5, day 10, and day 15, respectively **(Figure 4.9 H)**. The LDH activity on day 15 was significantly ($p \leq 0.01$) increased about 6.34, 1.83, and 1.28 fold compared to day 1, day 5, and day 10, respectively.

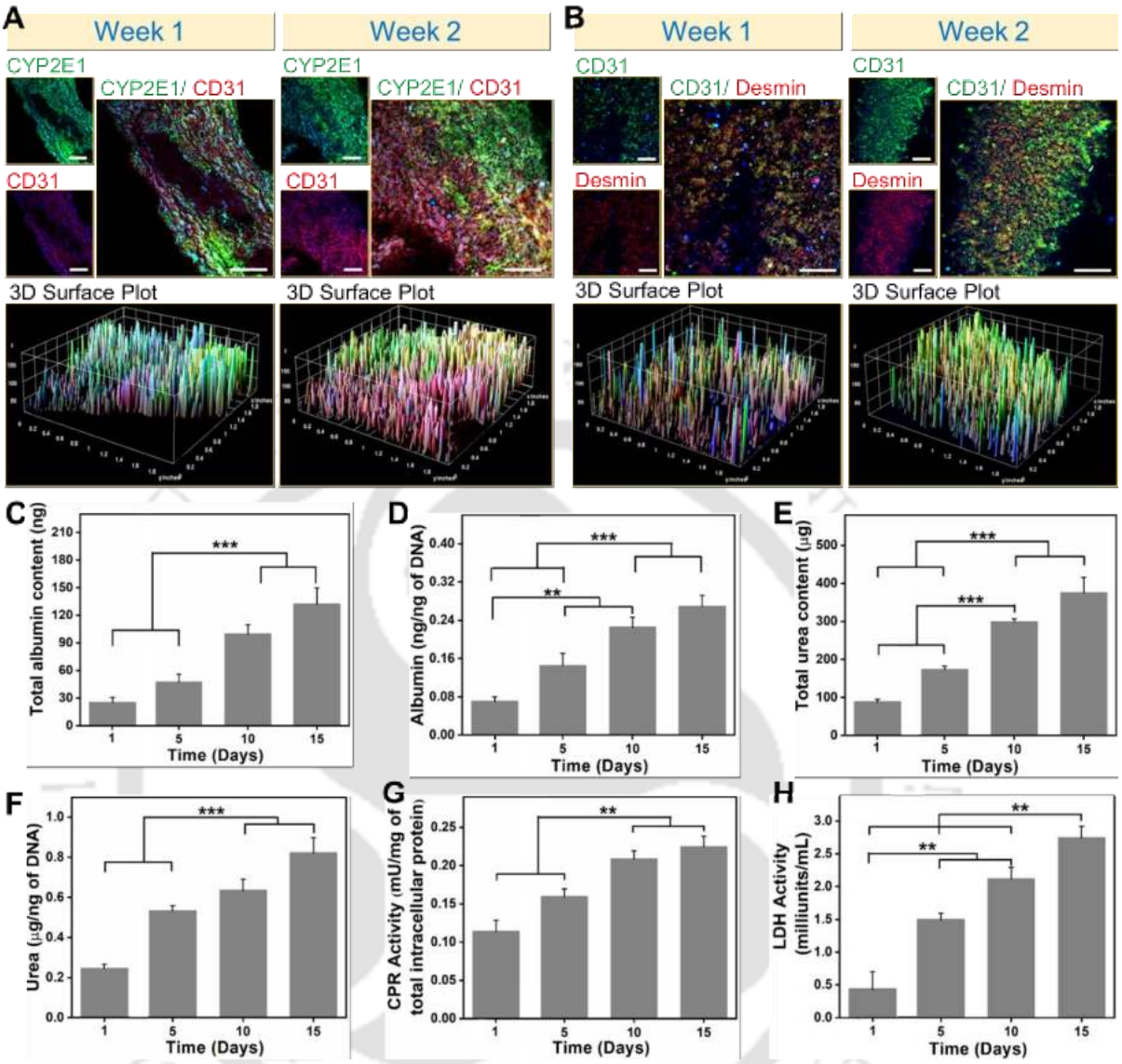

Figure 4.9. Functional assessment of the HLC/HUVEC/HHSC-laden bioprinted vascularized liver model. *Confocal z-stack immunostaining images and 3D surface plot of bioprinted vascularized liver model stained for (A) CYP2E1 (green), CD31 (red), and nucleus (blue) and (B) CD31 (green), desmin (red), and nucleus (blue) to visualize the distribution of both parenchymal (HLC) and non-parenchymal (HUVEC/HHSC) cells over 1 week and 2 weeks of the culture period. Scale bar: 200 µm. Biochemical estimation of (C) Total albumin content, (D) Albumin per ng of DNA, (E) Total urea content, (F) Urea per ng of DNA, (G) CPR activity, and (H) LDH activity. Data are represented as Mean ± SD. (n = 3, * $p \leq 0.05$, ** $p \leq 0.01$ and *** $p \leq 0.001$).*

4.3.7 Bioprinted hepatocyte liver model and Bioprinted vascularized liver model in predicting hepatotoxicity

The metabolic competence of the bioprinted liver model laden with (i) HLC and (ii) HLC/HUVEC/HHSC in predicting hepatotoxicity was evaluated using non-hepatotoxicants (aspirin and dexamethasone), idiosyncratic hepatotoxicant (trovafloxacin mesylate), and known hepatotoxicants (acetaminophen and troglitazone) treated for 24 h **(Table 4.3)**. The bioprinted liver constructs without any drug treatment were considered an internal control. The cytotoxicity was analyzed by estimating DNA concentration and LDH activity, and hepatic metabolism competence was assessed from CPR activity.

4.3.7.1 Bioprinted liver models in predicting aspirin and dexamethasone toxicity assessment

Initially, the bioprinted liver models were matured for 10 days, followed by exposed to non-hepatotoxic drugs, aspirin, and dexamethasone for 24 h, and evaluated for drug toxicity **(Figure 4.10 A)**. An increased cellular viability and metabolism function was observed in the HLC/HUVEC/HHSC-laden vascularized liver model compared to the HLC-laden liver model; however, they are insignificant with their respective internal control **(Figure 4.10)**. From the percentage of cell viability assessment, aspirin and dexamethasone at higher concentrations exhibited >80% cell viability in the liver model laden with (i) HLC and (ii) HLC/HUVEC/HHSC **(Figure 4.10 B)**. However, aspirin at 1000 µM concentration (greater than 100 × C_{max}) demonstrated minimal cytotoxicity, with reduced DNA concentration and intracellular LDH activity in both liver models compared to their respective internal control **(Figure 4.10 C, i-ii)**. The drug metabolism functions were similar in the liver constructs exposed to increased aspirin concentration and were statistically insignificant with their respective internal control **(Figure 4.10 C, iii)**. Subsequently, dexamethasone at varying concentrations showed no effect on the overall viability and metabolism of liver constructs, as evinced from similar DNA concentration, intracellular LDH activity, and CPR activity to internal control **(Figure 4.10 D)**.

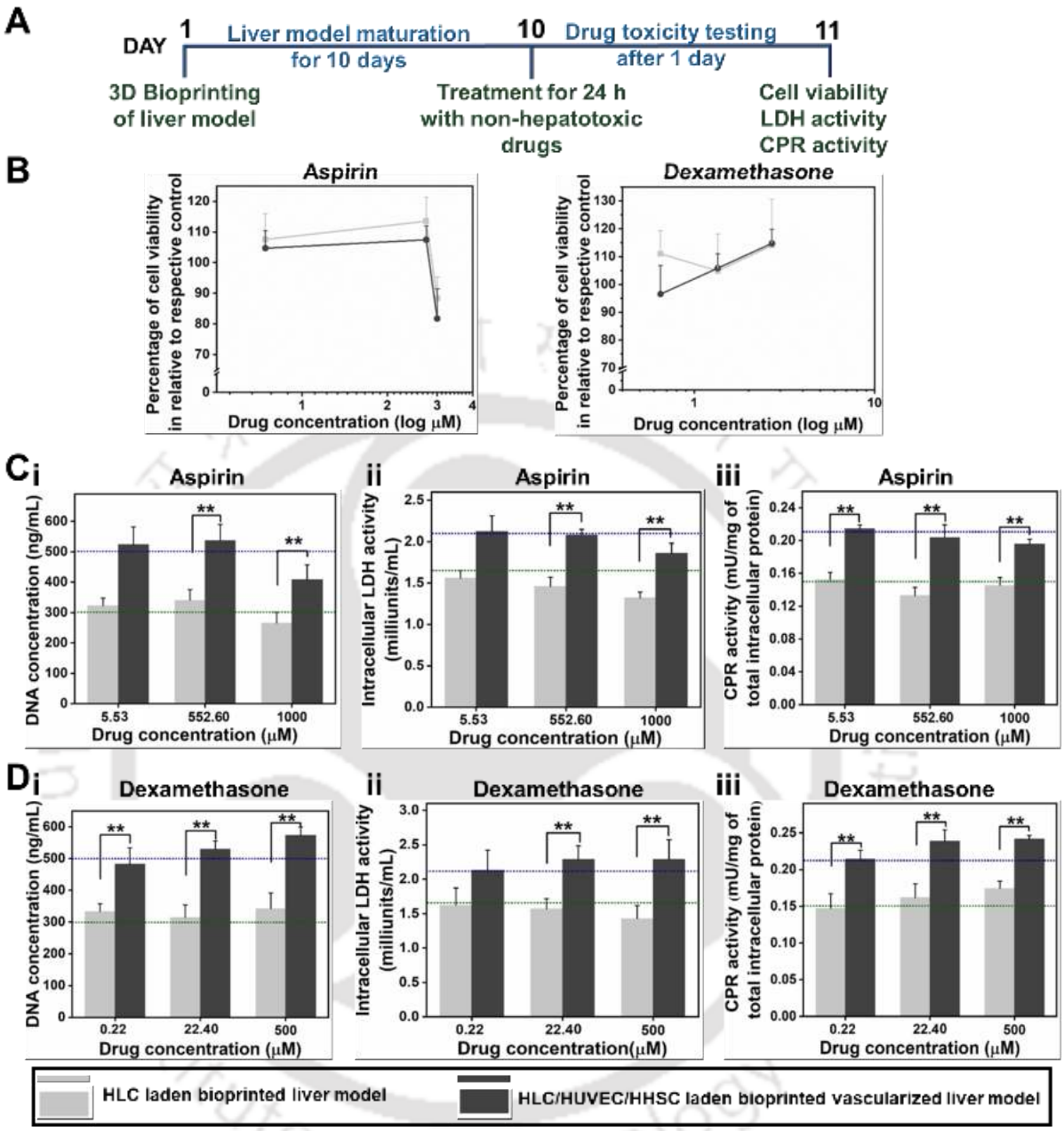

Figure 4.10. Bioprinted liver model laden with (i) HLC and (ii) HLC/HUVEC/HHSC in drug toxicity prediction using non-hepatotoxic drugs. *(A) Schematic illustration showing the exposure of matured 3D bioprinted liver model for 24 h with non-hepatotoxicity drugs followed by drug-induced hepatotoxicity assessment. (B) Percentage of cell viability after 24 h treatment with non-hepatotoxic drugs, aspirin and dexamethasone in the bioprinted liver model. Treatment of non-hepatotoxic drugs (C) Aspirin and (D) Dexamethasone followed by estimating (i) DNA content, (ii) intracellular LDH activity, and (iii) CPR activity. The green and blue dashed line represents the activity of bioprinted constructs laden with (i) HLC and (ii) HLC/HUVEC/HHSC, respectively, in an internal control. Data are represented as Mean ± SD. (n = 3, * $p \leq 0.05$, ** $p \leq 0.01$ and *** $p \leq 0.001$).*

4.3.7.2 Trovafloxacin mesylate toxicity assessment in bioprinted liver models

The hepatotoxicity induced by idiosyncratic and hepatotoxic drugs following 24 h treatment was investigated **(Figure 4.11 A)**. An idiosyncratic drug, trovafloxacin mesylate induced dose-dependent toxicity with a significant decrease in the percentage of cell viability with an increase in the drug concentration **(Figure 4.11 B)**. The HLC/HUVEC/HHSC-laden vascularized liver model showed the toxicity effect at a lower dose with an EC_{50} of 1.04 µM; indeed, HLC-laden liver constructs showed the toxicity effect at a higher dose with an EC_{50} of 5.45 µM, as extrapolated from the dose-response curve and percentage of cell viability. The effect of trovafloxacin mesylate on the DNA concentration and intracellular LDH activity was more pronounced, with significantly ($p \leq 0.001$) reduced cellular viability at 4.08 µM, 100 µM, and 407.80 µM compared to 2 µM in both liver models **(Figure 4.11 C, i-ii)**. At human C_{max} 4.08 µM of trovafloxacin mesylate, the DNA concentration was reduced to 43.13% in the HLC-laden liver model and 22.60% in the HLC/HUVEC/HHSC-laden liver model **(Figure 4.11 C, i)**. Similarly, at 4.08 µM trovafloxacin mesylate treatment, the intracellular LDH activity in the HLC-laden liver model and vascularized liver model was reduced to 0.52 ± 0.11 milliunits/mL and 0.38 ± 0.09 milliunits/mL, respectively **(Figure 4.11 C, ii)**. The vascularized liver model presented significantly increased CPR activity at different doses of trovafloxacin mesylate treatment compared to the HLC-laden liver model **(Figure 4.11 C, iii)**. The metabolism protein, total CPR activity was reduced ($p \leq 0.001$) in liver constructs exposed to trovafloxacin mesylate treatment at 4.08 µM, 100 µM, and 407.80 µM compared to 2 µM.

4.3.7.3 Acetaminophen toxicity assessment in bioprinted liver models

The liver models experienced a concentration-dependent cytotoxicity effect with acetaminophen, with an EC_{50} of 4546.77 µM in the HLC/HUVEC/HHSC-laden liver model and EC_{50} of 7119.43 µM in the HLC-laden liver model, as extrapolated from the dose-response curve and percentage of cell viability **(Figure 4.11 B)**. Both liver models showed no cytotoxic behavior at human C_{max} 139 µM of acetaminophen treatment and presented a comparable level of DNA concentration, intracellular LDH activity, and CPR activity to their respective internal control **(Figure 4.11 D)**. Liver models showed a significant ($p \leq 0.001$) reduction in their cell viability at 5000 µM, 10000 µM, and 13900 µM compared to 139 µM of acetaminophen treatment **(Figure 4.11 D, i)**. However, the vascularized liver model did not demonstrate a statistical difference in intracellular LDH activity and CPR activity at 139 µM and 5000 µM of acetaminophen treatment

(Figure 4.11 D, ii-iii). The intracellular LDH activity was remarkably ($p \leq 0.01$) reduced at 10000 µM and 139000 µM acetaminophen in both liver models compared to 139 µM and 5000 µM treatment **(Figure 4.11 D, ii)**. The HLC/HUVEC/HHSC-laden liver model presented significantly ($p \leq 0.05$) increased CPR activity at 139 µM and 5000 µM acetaminophen treatment compared to the HLC-laden liver model **(Figure 4.11 D, iii)**. However, the CPR activity of the HLC/HUVEC/HHSC-laden liver model exposed to 10000 µM and 139000 µM of acetaminophen was diminished ($p \leq 0.01$) compared to 139 µM and 5000 µM of acetaminophen.

4.3.7.4 Troglitazone toxicity assessment in bioprinted liver models

The liver models experienced a concentration-dependent cytotoxicity effect with troglitazone, with an EC_{50} of 66.11 µM in the HLC/HUVEC/HHSC-laden bioprinted liver model and an EC_{50} of 100.18 µM in the HLC-laden liver model, as extrapolated from the dose-response curve and percentage of cell viability **(Figure 4.11 B)**. Both liver models showed no cytotoxic effect at human C_{max} 6.39 µM of troglitazone and demonstrated a similar DNA concentration, intracellular LDH activity, and CPR activity as an internal control **(Figure 4.11 E)**. The HLC/HUVEC/HHSC-laden liver model experienced a more cytotoxic effect at 50 µM and 100 µM of troglitazone with cell viability of 58.08 ± 1.8% and 28.68 ± 3.0% compared to the HLC-laden liver model with cell viability of 68.96 ± 4.6% and 41.20 ± 4.0%, respectively **(Figure 4.11 E, i)**. Both liver models showed a significant ($p \leq 0.01$) reduction in cell viability at 100 µM and 638.70 µM compared to 6.39 µM and 50 µM of troglitazone **(Figure 4.11 E, i)**. Similarly, a drastically reduced ($p \leq 0.01$) intracellular LDH activity and CPR activity were noticed in both liver models exposed to 100 µM and 638.70 µM compared to 6.39 µM and 50 µM **(Figure 4.11 E, ii-iii)** of troglitazone. However, at 50 µM troglitazone, the intracellular LDH activity in the HLC- laden liver model and HLC/HUVEC/HHSC-laden liver model was reduced to 1.12 ± 0.11 milliunits/mL and 1.55 ± 0.12 milliunits/mL, respectively **(Figure 4.11 E, ii)**. The vascularized liver model presented significantly increased CPR activity at 6.39 µM ($p \leq 0.01$) and 50 µM ($p \leq 0.05$) of troglitazone treatment compared to the HLC-laden liver model **(Figure 4.11 E, iii)**.

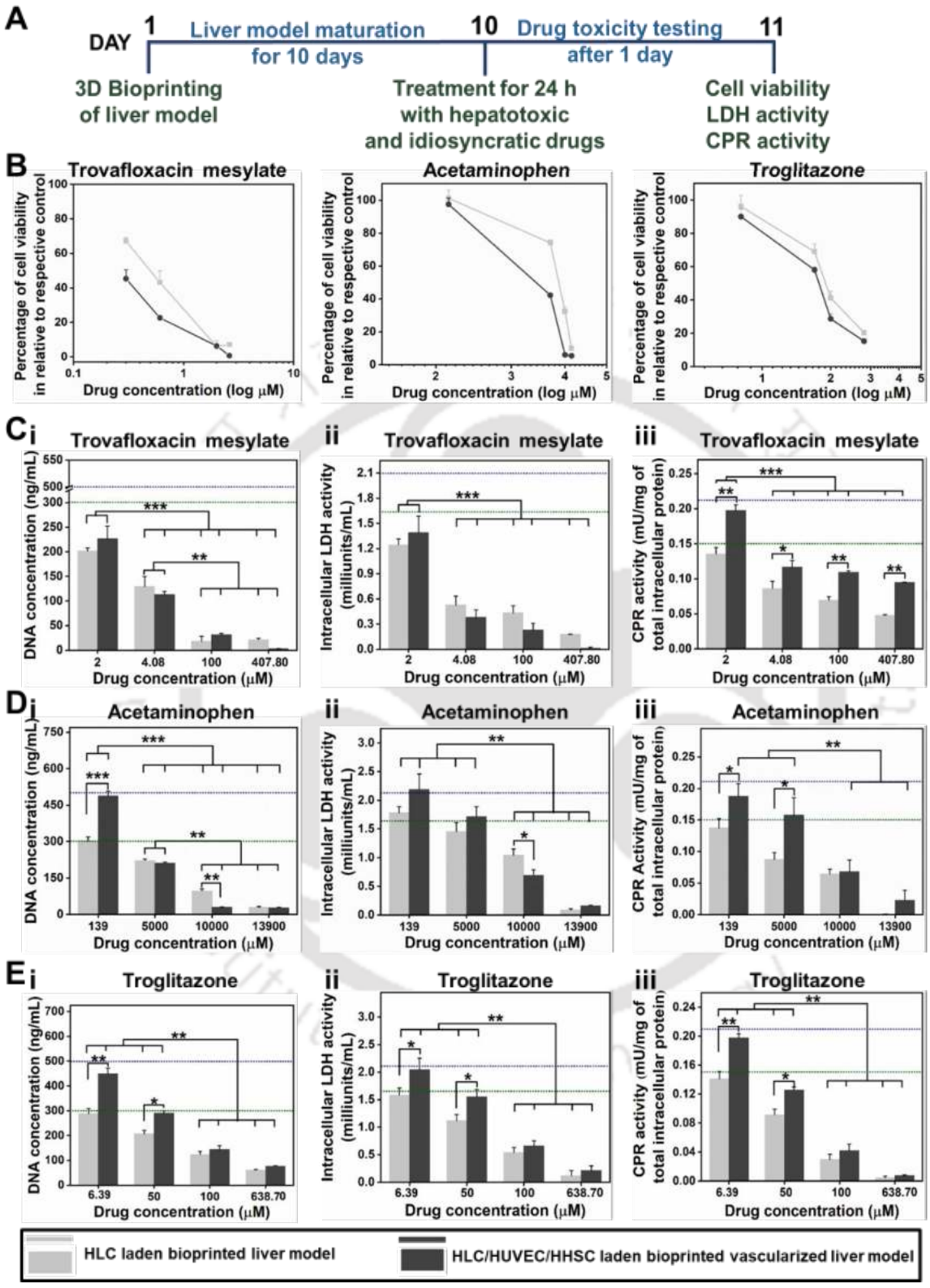

Figure 4.11. Bioprinted liver model laden with (i) HLC and (ii) HLC/HUVEC/HHSC in drug toxicity prediction using idiosyncratic and hepatotoxic drugs. *(A) Schematic illustration showing*

*the exposure of matured 3D bioprinted liver model for 24 h with idiosyncratic and hepatotoxic drugs followed by drug-induced hepatotoxicity assessment. (B) Percentage of cell viability after 24 h treatment with idiosyncratic drug trovafloxacin mesylate and hepatotoxic drugs acetaminophen and troglitazone in the bioprinted liver model. Treatment of (C) Trovafloxacin mesylate, (D) Acetaminophen, and (E) Troglitazone followed by estimating the (i) DNA content, (ii) intracellular LDH activity, and (iii) CPR activity. The green and blue dashed line represents the activity of bioprinted constructs laden with (i) HLC and (ii) HLC/HUVEC/HHSC, respectively, in an internal control. Data are represented as Mean ± SD. (n = 3, * $p \leq 0.05$, ** $p \leq 0.01$ and *** $p \leq 0.001$).*

4.4 Discussion

The shortfall of conventional animal models in human hepatotoxicity evaluation due to the discrepancies in the activity of drug metabolism markers has led to the development of preclinical *in vitro* human liver models [195, 301]. Many approaches have been accomplished in developing a 3D *in vitro* liver model for drug toxicity applications; indeed, they are limited in reconstructing the spatiotemporal architecture, cellular composition, and cell-ECM interactions as in native liver lobule. To the best of our knowledge, this is the first report that developed a physiologically relevant 3D bioprinted vascularized liver model with a layer-by-layer assembly of HLCs and HUVECs/HHSCs in horizontal and vertical directions for drug toxicity evaluation **(Figure 4.3)**. A novel 3D CAD model of the liver lobule patterning HLCs and HUVECs/HHSCs in a complementary arrangement was designed to reflect the native liver lobule with hepatocyte cords in close contact with a sinusoidal network [146]. An ideal liver ECM-based bioink that undergoes a sol-gel transition under physiological conditions and provides distinct microenvironmental cues for encapsulated cells was formulated to bioprint cell-laden constructs. The printed constructs were physicochemically characterized and bioprinted following multi-material extrusion, in which the parenchymal layer comprised HLC-laden bioink 1, and the NPC layer comprised HUVEC/HHSC-laden bioink 2. Explicitly, the HLC formed spheroidal organoids, and HUVECs and HHSCs exhibited mesenchymal morphology in the vascularized liver model. The bioprinted liver model assisted enhanced cellular viability, proliferation, and liver-specific albumin production, urea synthesis, and CPR activity over 15 days. Furthermore, the vascularized liver model exposed to idiosyncratic and hepatotoxic drugs predicted DILI accurately.

The hepatotoxicity prediction in existing liver systems was limited due to the lack of native microenvironmental cues, hepatocyte polarity, and metabolic functions [73, 195, 205]. *In vitro* liver models encompassing liver ECM preserved significant ECM components, including growth

factors, cytokines, and chemokines that in turn aided in maintaining an aggregate culture, polarity, zonation, and metabolic competence of hepatocytes [273, 281, 322]. An ideal bioink hydrogel providing heterotypic cellular interactions, cell-matrix interactions, and mimics tissue-specific physiological conditions is critical during bioprinting of cell-laden liver constructs [281, 312, 323]. Herein, we fabricated liver ECM-based bioink for cell encapsulation, with bulking agent gelatin and bioactive silk fibroin to augment the rheological behavior, post-printing features, and liver cell functionality [317]. Thus, the inclusion of silk fibroin in bioink not only acted as a reinforcing supportive material, indeed provided active biological cues for enhanced cellular attachment through integrin mediated pathway [291, 317]. Aiming to develop liver ECM-based bioink, a co-printable basic liver ECM bioink composition was optimized as 7% (w/v) gelatin, 1% (w/v) BM, 1% (w/v) AA, and 1% (w/v) liver ECM **(Figure 4.4)**. In addition, a cytocompatible β-D galactose concentration of 40 mM was included as an additive in basic liver ECM bioink for parenchymal bioink 1 to supplement HLC attachment and proliferation through activation of the asialoglycoprotein receptor [114]; however, basic liver ECM bioink was considered as NPC bioink 2. Bioinks subjected to enzymatic HRP/H_2O_2 crosslinking induced β-sheets as a result of oxidation of phenolic hydroxyl groups followed by dityrosine bond formation, which is also corroborated from FTIR data, confirming the stability and structural integrity of bioprinted constructs [317]. Previous investigations have revealed that HRP/H_2O_2 enzymatic crosslinking at mild reaction conditions is an effective cytocompatible crosslinking approach and catalyzes hydrogelation to generate cell-laden bioprinted constructs with good shape fidelity [291, 324]. The cell viability and cell proliferation results also confirmed the cytocompatibility of bioink, substantiating the nontoxic nature of the concentration of HRP and H_2O_2 employed in the current study. Rheological characterizations indicated that the gelation of bioinks was depended on time and temperature with sol-gel transition after 10-15 min at a physiological temperature of 37°C. From amplitude sweep analysis and 3ITT, a shear-thinning effect of bioink at the LVER was observed, followed by regaining their elastic behavior post-deformation, substantiating a viscous nature during extrusion and stability after extrusion. The layers of acellular printed constructs were interconnected with a pore size of 142.80 ± 28.44 μm, ensuring the transport of nutrients, oxygen, and drugs to the encapsulated cells, which is crucial in cellular viability and drug testing **(Figure 4.5)** [300, 311]. The formation of larger pores is permissive for an increased swelling ratio of the liver construct, that assisted in the nutrient uptake [281]. The printed constructs maintained integral stability in

hydrolytic conditions over 18 days, displaying improved mechanical properties, indeed rapidly degraded in an enzymatic proteolytic environment supporting an ideal implantable matrix for liver tissue engineering. The biocompatibility evaluation of *in vitro* models containing native ECM is crucial to circumvent the immunogenic responses of decellularized ECM [325]. The *in vitro* hemocompatibility assay, *in vitro* macrophage study, and *in vivo* subcutaneous implantation revealed that bioink hydrogel was hemocompatible, minimally immunogenic, and promoted angiogenesis with pro-remodeling macrophage activation, substantiating the biocompatibility of liver ECM-based bioink hydrogel **(Figure 4.5)** [290]. Moreover, the hemocompatible and immunocompatible *in vitro* liver model possess potential to test human blood specimens for predicting DILI in future endeavors [326].

In addition to bioink formulation and designing, the selection of cell sources for bioprinting is significant to attain a functional liver model. Mesenchymal stem cells, especially human ADMSCs were employed to facilitate the functional HLCs, owing to several advantages, including availability and cytokine secretion [108, 152]. Gene expression studies and immunofluorescence staining confirmed the expression of hepatocyte-specific markers in HLCs, evincing the purity of the HLCs population in bioink 1 preparation **(Figure 4.6)**. Significant studies have shown clear benefits of co-culturing hepatocytes with NPCs, that encouraged multicellular interplay, viability, and long-term maintenance of liver-specific synthetic and metabolic functions compared to only hepatocyte culture [153, 195]. Furthermore, NPCs play an intriguing role in DILI, contributing to the inflammatory mechanisms of hepatotoxicity and progression of liver fibrosis [193, 195]. For example, endothelial cells form leaky capillaries and assist in the bidirectional perfusion of nutrients, drugs, and toxic metabolites, and stellate cells transdifferentiate to myofibroblasts and secrete pro-inflammatory cytokines in a fibrogenic environment [193]. Taken together, we incorporated NPCs into our *in vitro* liver model to resemble paracrine signaling and multiple liver cell components for achieving accurate DILI prediction. HUVECs and HHSCs were selected as NPCs for formulating bioink 2; explicitly, HUVECs were chosen over sinusoidal endothelial cells considering the prospective interaction of umbilical vein with fetal liver, and HHSCs supported the hepatocytes by ECM remodeling [7, 327]. The vascularized liver model over maturation induced HLC aggregation and maintained the viability of embedded HLCs, HUVECs, and HHSCs **(Figure 4.7)**. No proliferation observed in only the HLC-laden liver model might be attributed to the differentiated HLC in the constructs. An increased cell proliferation observed in the

HLC/HUVEC/HHSC-laden bioprinted liver model compared to the liver model laden with only HLC and HUVEC/HHSC over 15 days was attributed to paracrine interactions and cell-matrix interactions offered by bioink properties and multicellular components [73, 197]. In line with the viability, the phenotypic and functional maintenance of liver cells in *in vitro* liver construct is a great challenge [33]. The controlled spatial distribution of alternating cords of HLCs and HUVECs/HHSCs in horizontal and vertical directions might facilitate the physiologically relevant cell-matrix and local paracrine interactions in the bioprinted liver model [152, 328]. The vascularized liver model preserved the expression of mature hepatic, endothelial cell, and stellate markers over 15 days **(Figure 4.8)**. The co-localization for (i) albumin and desmin and (ii) albumin and vWF in the liver model substantiated the spatial distribution of hepatocytes with stellate cells and endothelial cells, respectively. The CYP2E1 and CD31 staining over time presented a development of a sinusoidal-like network with metabolically active hepatocytes, thus instigating the vascularization in the liver model **(Figure 4.9)**. Thus, immunostaining offered advancements in understanding the cell distribution in the HLC/HUVEC/HHSC-laden liver model, signifying that a well-integrated construct with an effective cell-cell interaction assisted in the formation of hepatocytes aggregates and a sinusoidal lumen with space disse [311]. Previous studies also presented a sinusoidal lumen formation in bioprinted constructs while co-culturing hepatocytes with endothelial cells [152, 153]. Furthermore, our vascularized liver model maintained liver-specific metabolic activities, including albumin production, urea secretion, and CPR activity. The improved albumin gene expression is correlated with the albumin immunostaining and albumin production from the liver model over 15 days **(Figure 4.8-4.9)**. An increased expression of CYP1A2, CYP2E1, and quantitative functional CPR activity in the liver model is significant as it is involved in metabolizing 80% of drugs [329].

The precise control over patterning multiple liver cells in different directions using extrusion-based bioprinting in generating the liver model has led to achieving longevity of metabolic competence, which will significantly enhance the sensitivity of DILI prediction [306]. The vascularized liver model exhibited mature hepatocyte-specific synthetic and metabolic functions comprising a sinusoidal-like endothelial and space disse network on day 10. The potential of NPCs in liver models was evaluated by exposing the matured liver models laden with (i) only HLC and (ii) HLC/HUVEC/HHSC to known drugs for 24 h. Aspirin and dexamethasone did not exhibit cytotoxicity in both models, even at a higher concentration **(Figure 4.10)**. The liver

model printed with co-culture of HLC and HUVEC/HHSC showed more sensitivity toward idiosyncratic and hepatotoxic drugs than only the HLC-laden liver model **(Figure 4.11)**. Identification of hepatotoxic perpetrators during the preclinical phase of drug development is a prime way to prevent DILI. The hepatotoxicity prediction in "gold standard" 2D monolayer culture of patient-specific human hepatocytes has been diminished due to limited availability, rapid dedifferentiation of hepatocytes, and reduced liver-specific functions [193, 195, 330]. Trovafloxacin mesylate, a well-known anti-infective idiosyncratic drug, was withdrawn from the market following one year of FDA approval due to ADR [195]. Trovafloxacin mesylate showed strong hepatotoxicity in the HLC/HUVEC/HHSC-laden liver model with an EC_{50} of 1.04 µM (lesser than human C_{max}), compared to the HLC-laden liver model with an EC_{50} of 5.45 µM [195, 331]. This was similar to clinically relevant doses and in line with the 3D HepG2 spheroid model with an EC_{50} of 5.6 µM [320]. Interestingly, the vascularized liver model demonstrated increased drug sensitivity compared to the 3D liver tissue manufactured by Organovo (San Diego, USA), in which scaffold-free 3D printed liver tissue comprising primary hepatocytes, HUVECs, and HHSCs demonstrated EC_{50} of 20 µM [195]. Furthermore, the sensitivity of liver models in response to hepatotoxic drugs, acetaminophen metabolized by CYP2E1 and CYP1A2, and troglitazone metabolized by CYP3A4 were evaluated [320]. The vascularized liver model was sensitive toward acetaminophen and troglitazone with an EC_{50} of 4546.77 µM and 66.11 µM, respectively, which was lesser than 100 × human C_{max}.

The model in the present study was more sensitive in predicting hepatotoxicity than previously reported 3D liver tissues [73, 195, 319, 332]. The vascularized liver model investigated for predicting acute drug response could also be employed as a suitable *in vitro* model for anticipating chronic drug exposure owing to the maintenance of long-term functions. The chronic drug response occurs due to the accumulation of toxic byproducts and drug resistivity [301]. After long-term and repeated drug exposures, the vascularized liver would demonstrate higher sensitivity leading to substantially lower EC_{50}, due to the cumulative effect of toxic products and drug exposure [301]. The more evident toxicity effect noticed in the HLC/HUVEC/HHSC-laden liver model might be attributed to increased sensitivity in the co-culture model involving the paracrine interactions of the damaged hepatocytes with endothelial cells and stellate cells [198, 332]. Furthermore, higher sensitivity toward drug clearance in the presence of NPCs is owing to

the additional secondary response exhibited by NPCs through activation of immune cells, steatosis, and fibrosis after a primary injury caused by hepatocytes [301]. In addition, the metabolic competence measured in terms of CPR activity was higher in the vascularized liver model than that in the HLC-laden liver model. Notably, these hepatotoxicity effects were observed without including any inflammatory cytokines or Kupffer cells.

Our findings provide a physiologically relevant liver model with native-like sinusoidal lumen and space disse that maintains the long-term metabolic competence of hepatocytes and provides insights into precise human hepatotoxicity prediction. The functional advancements in the vascularized liver model deliver a relevant preclinical model for drug screening with minimal screening time and cost that can remediate DILI and found applications in personalized medicine and speed up the drug development process. Our future studies using the vascularized liver model are aimed toward deciphering the molecular events of hepatotoxicity after long-term and repeated drug exposures, which enables testing a panel of hepatotoxic drugs. In addition, the vascularized liver model offers a potential platform for understanding liver cellular physiology, glycogen storage, and lipid accumulation; and for developing *in vitro* liver disease models such as alcoholic fatty liver disease and non-alcoholic fatty liver disease for drug design and development. The immunocompatible bioink hydrogel would demonstrate superior performance as implantable constructs and bioartificial liver. Follow-up studies with the bioprinted liver model would be performed to assess repeated-dose drug toxicity and multiple drug toxicity for an extended period. Furthermore, efforts will focus on the inclusion of primary human hepatocytes, Kupffer cells, and bile duct epithelium in the developed liver model and drug toxicity assessment under continuous perfusion conditions to resemble native DILI prediction.

4.5 Significant Findings

1. The present study successfully fabricated and functionally characterized a physiologically relevant *in vitro* human vascularized liver model for hepatotoxicity testing.
2. Herein, we formulated a liver ECM-based bioink to encapsulate liver cells, designed a 3D CAD model inspired by the native liver lobule architecture, and functionally characterized the bioprinted liver model.
3. Over maturation, the HLCs formed hepatic organoids, and HUVECs and HHSCs together formed a sinusoidal-like network in the bioprinted vascularized liver model that assisted in

achieving liver-specific functions over 2 weeks, including albumin production, urea synthesis, and cytochrome P450 activity.

4. Drug toxicity assessment using idiosyncratic and hepatotoxic drugs revealed that the HLC/HUVEC/HHSC-laden bioprinted vascularized liver model possessed increased metabolic competence and predicted human hepatotoxicity compared to only the HLC-laden liver model.
5. The benefits recorded by the bioprinted vascularized liver model in drug toxicity prediction could be a result of the combination of compartmentalized design of constructs, tissue-specific bioink to augment cell-ECM interactions and co-culture with NPCs.
6. In the future, the inclusion of immune cells in the liver model and drug response study under perfusion conditions could improve toxicological studies.
7. The vascularized liver model represented a high-throughput drug screening platform and could find prospective applications in understanding cellular physiology and developing liver disease models.

CHAPTER 5

Silk fibroin bioscaffold from Bombyx mori and Antheraea assamensis elicits a distinct host response and macrophage activation paradigm in vivo and in vitro

This chapter investigates the host response, angiogenesis, and macrophage activation profiling towards *Bombyx mori* and *Antheraea assamensis* silk bioscaffolds, individually and as a blend (BA) after evaluation in a partial thickness rat abdominal wall defect model. Liver ECM and small intestinal submucosa ECM that were recognized for constructive tissue remodeling, and polypropylene mesh that was associated with pro-inflammatory macrophage phenotype activation were used as controls. Effect of degradation products of bioscaffolds on macrophage activation was evaluated using naive bone marrow-derived macrophages (BMDM) and pro-inflammatory activated BMDM. This study has the potential for understanding the macrophage phenotype stimulated by silk bioscaffolds in directing tissue regeneration.

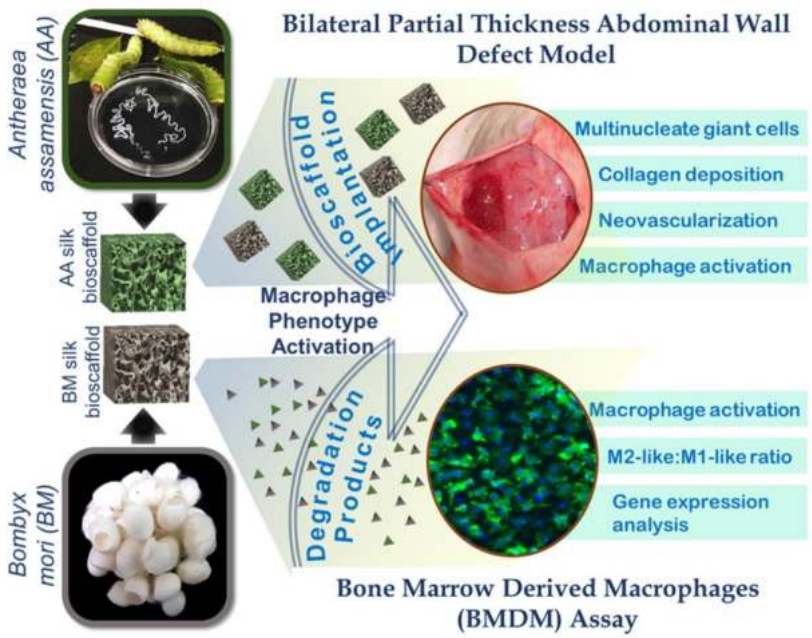

ABSTRACT

Biomaterials composed of silk fibroin from both mulberry and non-mulberry silkworm varieties have been investigated for their utility in tissue engineering and drug delivery, but these studies have largely excluded any evaluation of host immune response. The present study compares the macrophage activation response towards mulberry (*Bombyx mori*, BM) and non-mulberry (*Antheraea assamensis*, AA) silk types, individually and as a blend (BA) in a partial thickness rat abdominal wall defect model and *in vitro* primary murine bone marrow-derived macrophage (BMDM) assay. Biologic materials composed of liver extracellular matrix (LECM) and small intestinal submucosa (SIS) ECM that are recognized for constructive tissue remodeling, and polypropylene mesh that is associated with pro-inflammatory macrophage phenotype activation are used as controls in the animal model. The AA silk graft shows a host response similar to SIS with few foreign body multinucleate giant cells, vascularization, high CD206 expression, and high M2-like: M1-like macrophage phenotype ratio. Exposure to AA silk degradation products *in vitro* induces a higher arginase: iNOS ratio in both naive BMDM and pro-inflammatory activated BMDM; and higher Fizz1: iNOS ratio in pro-inflammatory activated BMDM. These data suggest that the AA silk supports a pro-remodeling macrophage response with potential therapeutic applications.

The findings of this chapter are under submission:

Janani G., Zhang L., Badylak S.F., and Mandal B.B. "*Silk fibroin bioscaffold from Bombyx mori and Antheraea assamensis elicits a distinct host response and macrophage activation paradigm in vivo and in vitro*".

5.1 Introduction

Silk polymer produced by a wide variety of insects and arachnids has been used for centuries as sutures and wound dressings in its native fiber form [106, 290]. Among all potential silk sources, silkworm silk-based biomaterials are most prevalent in the field of healthcare applications, including sutures, tissue engineering, diagnostics, optical devices, controlled drug delivery systems, and implantable devices [290]. Based on feeding habitat and environmental factors, silkworms are classified into globally distributed mulberry silkworms (*Bombycidae* family) and heterogeneously distributed non-mulberry silkworms (*Saturniidae* and *Lasiocampidae* family) [333]. Silkworm silk consists of two main components: (i) core fibroin protein and (ii) a glue-like sericin protein [290]. Sericin has been reported to elicit an allergic or inflammatory response compared to fibroin protein [334]. Silk proteins isolated from various types are characterized by amino acid composition, thus imparting distinct physicochemical properties [42, 290]. Mulberry *Bombyx mori* (BM) silk fibroin, a heterodimer of Heavy chain, Light chain, and P25 glycoprotein is isolated from cocoons. Indeed, non-mulberry *Antheraea assamensis* (AA) silk fibroin, a homodimer of Heavy chain is isolated from silk glands due to difficulty in dissolving the degummed AA silk fibers [42, 290]. The polyglycine alanine repeats present in the heavy chain of BM silk fibroin contribute to its hydrophobicity. The polyalanine repeats and a high basic/acidic amino acid ratio in AA silk fibroin contribute to its increased hydrophobicity, mechanical strength and extensibility [42]. Mechanically resilient and easily processable silk fibroin biopolymer is amenable to fabrication in a diverse range of 2D and 3D matrices with defined cytocompatibility and resorbability characteristics [106, 283, 290]. BM silk-based constructs, including Restylane silk, silk sutures, SERI surgical scaffold, and silk thread were extensively tested in clinical studies for breast and abdominal wall reconstruction applications [290, 335]. Porous BM silk constructs employed for fascial defect repair augmentation showed a suitable tensiometry strength yet induced fibrosis as part of the foreign body response [336]. During the past decade, the AA silk fibroin has been investigated for tissue engineering applications due to its desirable mechanical strength, polyalanine repeats, and presence of intrinsic RGD motifs [41, 42, 337]. The blend (BA) bioscaffold fabricated from BM and AA in an equal proportion was hypothesized to possess physicochemical properties of both silk proteins and explored for liver, bone, and vascular tissue engineering applications [271, 281, 338, 339]. In our previous study, a comprehensive physicochemical characterization of BM silk, AA silk, and BA silk scaffolds showed a similar

pore size and porosity in all types of silk scaffolds [271]. Indeed, AA silk bioscaffolds presented fibrous morphology, higher mechanical strength, and slower degradation compared with BM silk due to the presence of polyalanine repeats, α-helices, and β-sheets in non-mulberry silk-based matrices [271, 340, 341]. The biodegradation rate of silk scaffolds is regulated by their molecular weight, processing conditions, amino acid composition, crystallinity, β-sheet content, and pore size [340, 341]. A brief macrophage response study towards silk biomaterials in our previous work in *in vitro* mouse macrophage cell-line (RAW 264.7) and *in vivo* subcutaneous implantation showed minimal macrophage response towards AA silk and BA silk bioscaffolds compared to BM silk [271]. Few studies have ventured into exploring the inflammatory response towards BM silk-based matrices, including films [342], electrospun mats [343], and hydrogels [344] using RAW 264.7, human monocyte cell line (THP1), and *in vivo* subcutaneous implantation. Upon subcutaneous implantation, electrospun BM mats fabricated from a blend of fibroin and sericin elicited a discrete macrophage response and vascularization depending on the sericin concentration [343]. Subcutaneous injection of BM silk hydrogels elicited a similar innate immune response as observed with polyethylene glycol hydrogels [344]. However, the effect of mulberry (BM) silk and non-mulberry (AA) silk on *in vitro* primary monocytes or monocyte-derived macrophages and their comparison to ECM controls have not been studied [345]. Although the tissue response to BM silk biomaterials has been generally described [345, 346], the effect of these BM silk, AA silk, and BA silk biomaterials upon foreign body response, angiogenesis, and macrophage activation state in comparison with ECM controls has not been studied.

Macrophage phenotype at the implantation site has been shown to be a predictor of downstream clinical outcomes [347-349]. Implantation of any material elicits protein adsorption, platelet activation, provisional matrix formation, and immune cell activation as part of the inflammatory response [350, 351]. In the present study, the *in vivo* host response to BM silk, AA silk, and BA silk biomaterials was evaluated in the context of cell infiltration, foreign body response, macrophage phenotype activation, angiogenesis, tissue remodeling, and extracellular matrix (ECM) deposition. The response was compared to that of naturally derived ECM bioscaffolds, including liver ECM (LECM) and small intestinal submucosa ECM (SIS), and polypropylene (PP) surgical mesh. Several studies have evaluated the use of porcine SIS for dermal, cardiovascular, and musculoskeletal applications in preclinical animal studies and human clinical applications [352]. The immune response to SIS bioscaffold has been well characterized

and showed relatively rapid degradation and pro-remodeling macrophage phenotype activation [353, 354]. Liver ECM-based matrices supported the engraftment of hepatocytes and stellate cells, and induced functional phenotypic maturation under a continuous perfusion system [125]. PP surgical mesh has been shown to promote a dominant pro-inflammatory macrophage phenotype post implantation as part of the foreign body response in a partial thickness abdominal wall defect model [353]. Mulberry and non-mulberry silk scaffolds differed in mass loss, amino acid content, peptide fragments, crystallinity, α-helix, and β-sheet upon degradation in *in vitro* and *in vivo* [340]. Herein, we investigated the macrophage activation response of the degradation products of BM silk, AA silk, and BA silk bioscaffolds upon exposure to primary murine bone marrow-derived macrophages (BMDM) and pro-inflammatory activated BMDM. The response was compared to that of degradation products of naturally derived ECM bioscaffolds, LECM and SIS.

The objective of the present study was to characterize macrophage activation state elicited by silk bioscaffolds, BM silk ($M_{BM\ silk}$), AA silk ($M_{AA\ silk}$), BA silk ($M_{BA\ silk}$) in comparison with macrophage activation elicited by ECM bioscaffolds, LECM (M_{LECM}), SIS (M_{SIS}), and surgical PP mesh ($M_{PP\ mesh}$).

5.2 Materials and Methods

5.2.1 Overview and experimental design

The host response towards silk bioscaffolds compared to ECM bioscaffolds and PP mesh was evaluated in both *in vitro* and *in vivo* studies. The test articles were implanted in a bilateral partial thickness abdominal wall defect model and studied for their impact on host cell infiltration, angiogenesis, connective tissue formation, and macrophage phenotype activation. *In vitro* macrophage activation effects were studied using primary murine bone marrow-derived macrophages (BMDM).

5.2.2 Materials

Three variants of silk fibroin bioscaffolds were prepared from (i) *Bombyx mori* (BM) silk fibroin, (ii) *Antheraea assamensis* (AA) silk fibroin, and (iii) a blend of *Bombyx mori* and *Antheraea assamensis* (BA) silk fibroin according to the established protocols [271]. The isolation of BM silk fibroin solution includes degumming of BM cocoons, dissolution of degummed fibers in 9.3M lithium bromide solution, and subsequent dialysis for 48 h. The native silk protein was isolated from the silk glands of 5th instar AA silkworms, dissolved in 1% (w/v) sodium dodecyl

sulfate solution, and dialyzed for 4 h to obtain AA silk fibroin solution. The porous silk fibroin bioscaffolds were prepared by the freeze-drying method: BM, AA, and BA silk fibroin solution of 3% (w/v) were lyophilized, followed by β-sheet induction through ethanol treatment [271, 281].

Two different ECM bioscaffolds were prepared; one from the porcine liver (LECM) [355] and the second from porcine small intestinal submucosa (SIS) [354, 356]. Both ECM bioscaffolds were prepared by vacuum pressing according to previously established tissue decellularization protocols [354, 355, 357]. Briefly, porcine liver slices (~5 mm thick) were gently massaged to assist cell lysis and then incubated for 1 h at 37°C in 0.02% (v/v) trypsin/ 0.05% (w/v) ethylenediaminetetraacetic acid solution. After every enzymatic and detergent treatment, the liver slices were subjected to deionized water washes and gentle mechanical massaging. Subsequently, the liver slices were mechanically agitated in 3% (v/v) Triton X-100 solution for 1 h and 4% (w/v) sodium deoxycholic acid solution for 1 h on an orbital shaker [355]. The decellularized liver slices were disinfected with 0.1% (v/v) peracetic acid (PAA) in ethanol solution and labeled as LECM. The harvested small intestine was cut longitudinally and mechanically abraded to remove the superficial layers of tunica mucosa, tunica muscularis externa, and tunica serosa. The remnant sheets of tunica submucosa and basilar portions of tunica mucosa were disinfected with PAA to accomplish decellularization and labeled as SIS [354, 356]. Both LECM and SIS bioscaffolds met described decellularization requirements, i.e., no visible intact cell nuclei and DNA concentration of <50 ng/mg dry weight of LECM and SIS [287].

C.R. BARD surgical mesh (C.R. BARD, Warwick, RI, USA) composed of PP, was used in the current study as a positive pro-inflammatory control. The description of materials and their composition are listed in **Table 5.1**. The test articles of fixed size and dry weight (1.5 × 1.5 cm, 20 mg) were placed in a sealed sterilization pouch and subjected to terminal sterilization with ETO gas following 16 h cycle at 50°C (Series 3plus EOG sterilizer, Anderson Sterilizers, NC) to meet FDA sterility guidelines [358].

Table 5.1. *Description, composition, and category of the materials tested in the current study*

S. No.	Material Description	Composition	Category
1.	*Bombyx mori (BM silk)*	3% (w/v), Dry weight = 20 mg	Bio-resorbable scaffold
2.	*Antheraea assamensis (AA silk)*	3% (w/v), Dry weight = 20 mg	Bio-resorbable scaffold
3.	Blend silk scaffold *(BA silk)* (BM:AA → 1:1)	3% (w/v), Dry weight = 20 mg	Bio-resorbable scaffold
4.	Acellular porcine Liver ECM sheets *(LECM)*	Dry weight = 20 mg	Bio-resorbable vacuum pressed LECM sheets
5.	Acellular porcine Small Intestinal Submucosa *(SIS)*	Dry weight = 20 mg	Bio-resorbable vacuum pressed SIS sheets
6.	Polypropylene Mesh *(PP mesh)*	Dry weight = 20 mg	Non-resorbable surgical mesh

5.2.2.1 *In vivo* study

A bilateral partial thickness abdominal wall defect model was employed to assess the host response to all test articles [353]. The histomorphologic findings, connective tissue deposition, vascularization, and macrophage activation phenotypes were evaluated at day 14 and day 35 post implantation.

5.2.2.2 *In vitro* study

The primary macrophages isolated from murine bone marrow are reliable and commonly used to assess *in vitro* macrophage phenotype study [359]. The effect of degradation products of all bioscaffolds on macrophage activation was evaluated *in vitro* using naive BMDM and pro-inflammatory activated BMDM. The degradation products of silk bioscaffolds (BM silk, AA silk, and BA silk) and ECM bioscaffolds (LECM and SIS) were exposed to naive and pro-inflammatory activated BMDM by adding to the culture media. The macrophage phenotype activation and transcriptional activity of pro-inflammatory and pro-remodeling markers in response to

degradation products of bioscaffolds were evaluated by immunolabeling and gene expression assay, respectively.

5.2.3 Partial thickness abdominal wall defect model and scaffold implantation

The rat bilateral partial thickness abdominal wall defect model was employed to examine the host response toward test articles (BM silk, AA silk, BA silk, LECM, SIS, and PP mesh) in comparison to the unrepaired (i.e., injury alone) abdominal wall defect (Defect) [347, 353]. Animal procedures were conducted in accordance with the Institutional Animal Care and Use Committee (IACUC) guidelines at the University of Pittsburgh (IACUC Approval Number: 18123831). Sprague-Dawley rats weighing 300-500 g were randomly sorted into seven discrete groups in triplicates (n=3 for each time point, day 14 and day 35).

Animals were anesthetized using 2% isoflurane in oxygen, and lower abdomen was shaved and scrubbed with Betadine (povidone-iodine) solution. Sterile drapes were placed around the surgical area, and the surgical plane of anesthesia (2% isoflurane in oxygen) was maintained during surgery. A midline incision was made through the skin, and the underlying lateral muscular abdominal wall was exposed by bluntly dissecting the subcutaneous tissue. Bilateral 1.5 cm × 1.5 cm defects were created by removing the external and internal abdominal oblique muscular layers while leaving the underlying transversalis fascia and peritoneum intact [347]. The muscle layers were identified from their orientation, wherein the external oblique fibers were directed inferiorly and medially, the internal oblique fibers were directed perpendicular to the external oblique, and transversalis fascia was directed horizontally. Uniformity in defect size and shape was maintained among all the groups using a ruler method, which was ensured by implanting the test articles of fixed size 1.5 cm × 1.5 cm in the defect area (**Table 5.1**). The control group was left unrepaired. The scaffold was sutured to surrounding abdominal musculature using a non-absorbable 4-0 PROLENE® suture to secure the implant at the defect site and assist in demarcating the implant at the time of explant. A minimal amount of suture material was used to minimize the host response to the suture itself. The skin was closed using a 3-0 resorbable VICRYL® suture. Post-surgery, animals received 0.01-0.05 mg/kg of Buprenorphine Hydrochloride for analgesia and 20 mg of Baytril for three days.

5.2.4 Explant of test articles

On day 14 and day 35 post implantation, euthanization using CO_2 inhalation and cervical dislocation were performed as per the American Veterinary Medical Association (AVMA) guidelines. Under aseptic conditions, the surgical sites were exposed, the full-thickness abdominal wall comprising the test article and a small amount of surrounding native tissue was excised and fixed in 10% (v/v) Neutral Buffered Formalin (NBF) for subsequent histologic processing.

5.2.5 Histologic assessment

The NBF fixed samples were trimmed as 5 µm thickness sections and stained with hematoxylin and eosin (H&E, Thermo Fisher), and Masson's Trichrome (Sigma Aldrich) stain. Briefly, slides were cleared with xylene, rehydrated using a gradient of ethanol treatment (100%, 95%, 90%, 70%, and 50%), and stained independently for H&E and Masson's Trichrome. Subsequently, all stained tissue sections were processed for a gradient of ethanol (50%, 70%, 90%, 95%, and 100%) treatment, xylene treatment, and DPX mounting. For each test article, the host tissue-implant interface marking the suture ends and the middle sections were imaged at different magnification fields (50×, 100×, 200×, and 400×) using a Zeiss Axio Observer microscope. The cellularity and the number of foreign body multinucleate giant cells (MGC) at the implant site per 200× field of view (FOV) were determined. The cellularity was quantified using CellProfiler Image Analysis (http://www.cellprofiler.org) software, and three independent blinded observers performed the scoring of MGC.

5.2.6 Immunolabeling

Neovascularization and macrophage phenotypes at the implant site were investigated using immunolabeling. Prior to incubation with primary antibodies, tissue sections were deparaffinized using xylene treatment, rehydrated using a gradient of ethanol treatment, and dipped in running tap water for 2 min. The hydrated sections were immersed in citrate buffer (10 mM citric acid solution, pH 6.0) at 95°C - 100°C for 20 min and then washed twice with TRIS buffer/Tween 20 solution, pH 7.0 for 5 min. The tissue sections were incubated in blocking buffer comprising 2% (v/v) normal horse serum, 1% (w/v) bovine serum albumin (BSA), 0.1% (v/v) Triton X-100, 0.1% (v/v) Tween 20 for 1 h to minimize non-specific binding.

5.2.6.1 CD31 immunolabeling and quantification

After incubating the tissue sections in the blocking buffer, a primary antibody against the endothelial cell adhesion molecule CD31 (mouse anti-rat CD31, BD) at 1:150 dilution in the blocking buffer was applied and incubated at 4°C overnight. The sections were washed with PBS followed by incubation with the fluorophore-conjugated secondary antibody Alexa-594 (donkey anti-mouse, Invitrogen) at 1:200 dilution in blocking buffer for 1 h under dark conditions. The PBS washing step was repeated, and nuclei were labeled with DAPI (4'-6-diamidino-2-phenylindole). Subsequently, the slides were mounted using a fluorescent mounting medium (Dako) and stored at 4°C until imaging. The fluorescent images were captured randomly at 200× magnification field in the host tissue-implant interface using the Nuance multispectral imaging system. The extent of angiogenesis was evaluated by quantifying the blood vessel density, i.e., the number of microvessels was divided from the total area of 200× magnification image. Three independent blinded observers quantified the total number of blood vessels/mm^2.

5.2.6.2 Macrophage phenotype quantification

The macrophage activation state at day 14 and day 35 was examined by immunolabeling and quantifying for (i) macrophage (CD68) and M1-like pro-inflammatory (TNF-α) marker, and (ii) macrophage (CD68), M1-like pro-inflammatory (CD86), and M2-like pro-remodeling (CD206) marker. For CD68 and TNF-α immunostaining, primary antibodies against CD68 (mouse anti-rat CD68, AbD Serotec) and TNF-α (rabbit anti-human TNF-α, Abcam) diluted at 1:150 in blocking buffer were applied and incubated at 4°C overnight. After PBS washing, the tissue sections were incubated in fluorescence conjugated secondary antibodies, Alexa-594 (donkey anti-mouse, Invitrogen) and Alexa-488 (donkey anti-rabbit, Invitrogen), for 1 h. The nuclei were counterstained with DAPI and mounted with Dako medium. For CD68, CD86, and CD206 immunolabeling, primary antibodies against CD68 (mouse anti-rat CD68, AbD Serotec) at 1:150 dilution, CD86 (rabbit anti-human CD86, Abcam) at 1:150 dilution, and CD206 (goat anti-mouse CD206, R&D Systems) at 1:100 dilution suspended together in blocking buffer were applied and incubated overnight at 4°C. The tissue sections were washed with PBS and incubated with secondary antibodies, Alexa-594 (donkey anti-mouse, Invitrogen) at 1:200 dilution, Alexa-488 (donkey anti-goat, Invitrogen) at 1:200 dilution, and PerCp-Cy5.5 (donkey anti-rabbit, Santa Cruz) at 1:300 dilution in blocking buffer for 1 h. The nuclei were counterstained with DAPI and mounted with Dako medium.

Fluorescent images were captured randomly at the host tissue-implant interface for each tissue section at three different 200× fields using the Nuance multispectral imaging system. The number of macrophages expressing each marker per FOV was quantified using CellProfiler Image analysis software. The total number of macrophages co-expressing CD68 and TNF-α were quantified and denoted as pro-inflammatory macrophages. The percentage of pro-inflammatory macrophages was calculated by dividing the number of pro-inflammatory macrophages ($CD68^+TNF\text{-}\alpha^+$) from the total macrophages ($CD68^+$) in the same field. In the second staining, the total number of macrophages expressing CD68, co-expressing CD68 and CD86, and co-expressing CD68 and CD206 in the same field were quantified and denoted as macrophages, pro-inflammatory macrophages, and pro-remodeling macrophages, respectively. The subpopulation of macrophages expressing $CD68^+CD86^+CD206^+$ was denoted as "triple-labeled cells". The M1-like (pro-inflammatory) subpopulation and M2-like (pro-remodeling) subpopulation was calculated by subtracting the triple-labeled cells from $CD68^+CD86^+$ and $CD68^+CD206^+$, respectively. From these values, the M2-like: M1-like ratio of macrophages was calculated by dividing the number of M2-like macrophages by M1-like macrophages.

5.2.7 *In vitro* macrophage response

5.2.7.1 Derivation of silk and ECM degraded products

Degradation products of bioscaffolds were prepared by enzymatic digestion as previously described [353]. Briefly, silk and ECM bioscaffolds were lyophilized and milled using a Wiley Mill to produce particulate forms (i.e., powders) (< 60 μm). The milled powders at 100 mg dry weight were enzymatically digested in pepsin solution (10 mg of pepsin (Sigma Aldrich, Cat No. P7012) in 10 mL of 0.01N HCl) for 48 h at constant stirring to yield 10 mg/mL of individual silk and ECM digests. The pepsin solution without the particulate powders digested, as described above, was used as a pepsin control for all *in vitro* experiments.

5.2.7.2 Macrophage preparation

All procedures were approved and performed according to the IACUC guidelines at the University of Pittsburgh (IACUC Approval number: 18083483). Monocytes were isolated from the bone marrow of adult female C57BL/6 mice obtained from Jackson Laboratories (Bar Harbor, ME) and differentiated into BMDM as described [353, 359]. Briefly, tibia and femur bones were harvested after sacrificing the animal by CO_2 euthanasia and cervical dislocation. Under sterile

conditions, tibia and femur bones were transected at both the ends, and the bone marrow cavity was flushed repeatedly with complete DMEM medium (high glucose DMEM + 10% (v/v) fetal bovine serum + 100 U/mL Penicillin + 100 µg/mL Streptomycin) using a 30G needle to harvest marrow cells. The harvested monocytes were washed twice to remove the tissue debris, plated at a cell density of 10^6 cells/mL of macrophage complete medium, and cultured for 7 days at 37°C, 5% CO_2. The macrophage complete medium was composed of macrophage-colony-stimulating factor (MCSF) containing DMEM medium, supplemented with 10% (v/v) L929 cell supernatant, 10 mM non-essential amino acids, 10 mM HEPES buffer, and 50 µM beta-mercaptoethanol. The macrophage complete medium was changed every 48 h to promote naive macrophage (Mϕ) differentiation.

5.2.7.3 Cytotoxicity assay

The non-cytotoxic/cytocompatible concentration of the degradation products of bioscaffolds against BMDM was evaluated using the quantitative MTT assay (Vibrant MTT Cell Proliferation Assay Kit) and Live/Dead staining (LIVE/DEAD™ Viability/Cytotoxicity Kit). Exosome deprived media obtained by ultracentrifugation (Beckman Coulter Optima L-90K Ultracentrifuge) of complete DMEM media at 100,000 g, 4°C for 16 h was used for all *in vitro* macrophage activation studies. Briefly, naive BMDM cultured in a 96 well plate (Mϕ) were treated with degradation products of each bioscaffold and pepsin solution at 0.00195 mg/mL, 0.0039 mg/mL, 0.0078 mg/mL, 0.0156 mg/mL, 0.0325 mg/mL, 0.0625 mg/mL, 0.125 mg/mL, 0.25 mg/mL, 0.5 mg/mL and 1 mg/mL in exosome deprived DMEM medium for 24 h at 37°C, 5% CO_2. For MTT assay, the macrophages after treatment were washed with PBS and incubated with 100 µL of DMEM medium (without FBS and antibiotics) containing 1.2 mM MTT (3-(4,5-dimethylthiazol-2-yl)-2,5-diphenyl-tetrazolium bromide) for 2 h. After incubation, 75 µL of MTT media was removed and incubated in 50 µL of dimethyl sulfoxide at 37°C for 10 min, followed by absorbance measurement at 570 nm. The fold change in metabolic activity of BMDM treated with an individual concentration of bioscaffolds degradation products was calculated relative to the BMDM treated with only pepsin at the same concentration. Cell viability was assessed using the Live/Dead viability staining kit as per the manufacturer's instructions. After treatment with degradation products, the BMDM were washed with PBS and incubated with 2µM Calcein-AM and 4µM Ethidium homodimer solution for 15 min. The fluorescence images were captured at

three different 200× fields using a Zeus live-cell microscope: the live cells were stained green, and dead cells were stained red.

5.2.7.4 Effect of degradation products on naive and pro-inflammatory macrophages

A maximum non-cytotoxic dose of 0.125 mg/mL of degradation products of bioscaffolds, as selected from MTT assay and live/dead staining, was used to evaluate its effect on macrophage phenotypes in two distinct studies. In the first study, the Mϕ were exposed to 0.125 mg/mL of bioscaffolds degradation products or pepsin solution suspended in exosome depleted medium for 24 h at 37°C, 5% CO_2. The canonical cytokine controls included were (i) M1-like pro-inflammatory phenotype, induced by treating the Mϕ with 20 ng/mL of IFN-γ and 100 ng/mL of LPS; and (ii) M2-like pro-remodeling phenotype, induced by treating the Mϕ with 20 ng/mL of IL-4 for 24 h at 37°C, 5% CO_2. In the second study, the Mϕ were first induced to a pro-inflammatory phenotype by treating with 20 ng/mL of IFN-γ and 100 ng/mL of LPS for 6 h followed by treatment with 0.125 mg/mL of degradation products of bioscaffolds, pepsin, and cytokine controls for 24 h. In both the studies, the degradation products of bioscaffolds, pepsin, and macrophage activation controls were prepared in an exosome deprived medium. After 24 h treatment, cells were washed with sterile PBS and fixed in 2% paraformaldehyde for immunolabeling studies. In addition, cell lysates harvested with TRIzol reagent were stored at -80°C for gene expression studies.

5.2.7.5 Immunolabeling for macrophage phenotypes

Macrophage phenotypes after exposure to degradation products of bioscaffolds were assessed by immunolabeling for the pan-macrophage marker (F4/80), pro-inflammatory "M1-like" marker (iNOS), and two pro-remodeling "M2-like" markers (arginase and Fizz1). Briefly, macrophages were incubated for 1 h in blocking buffer comprised of 2% (v/v) normal house serum, 1% (w/v) BSA, 0.1% (v/v) Triton X-100, 0.1% (v/v) Tween 20 in PBS solution to prevent nonspecific binding. The primary antibodies used were (i) monoclonal rat anti-murine F4/80 (Novus Biologicals), (ii) polyclonal rabbit anti-murine iNOS (Novus Biologicals), (iii) polyclonal rabbit anti-liver arginase (Abcam), and (iv) polyclonal rabbit anti-murine Fizz1 (RELMα) (Peprotech) diluted at 1:100 in blocking buffer and incubated with macrophages at 4°C overnight. The primary antibody solution was aspirated, washed three times with PBS, and then incubated with fluorophore-conjugated secondary antibodies (i) Alexa Fluor 488 goat anti-rat (Invitrogen)

(for F4/80 wells) and (ii) Alexa Fluor 488 goat anti-rabbit (Invitrogen) (for iNOS, Arginase, and Fizz1 wells) diluted at 1:200 in blocking buffer for 1 h at room temperature. The secondary antibody solution was aspirated, washed with PBS, and counterstained for nuclei using DAPI solution for 5 min. Fluorescence images were captured randomly at three 200× fields in each well using a Zeus live-cell microscope. The light exposure time for F4/80 (pan-macrophages), iNOS (M1-like), arginase and Fizz1 (M2-like) in macrophages treated with silk and ECM digests was standardized based on their respective cytokine treated controls. The number of positive macrophages for each marker was quantified from the macrophages (stained in green) co-localized with DAPI (stained in blue) using CellProfiler Image Analysis Software. The percent of positive cells for each marker was calculated by dividing the number of positive macrophages by total macrophages (DAPI positive). Further, the arginase: iNOS and Fizz1: iNOS ratio was determined by dividing the arginase positive cells and Fizz1 positive cells by the respective iNOS positive cells.

5.2.7.6 Gene expression profile

The transcriptional activation of cytokines, chemoattractants, surface markers, and metabolic markers in both naive macrophages and pro-inflammatory activated macrophages exposed to 0.125 mg/mL of degradation products of bioscaffolds was evaluated through real-time quantitative polymerase chain reaction (qPCR). The TRIzol reagent of 800 µL was added to treated macrophages, and cell lysates were collected using a cell scraper. The cell lysate solution was mixed with 200 µL of chloroform, vortexed for 15 s, and centrifuged at 12,000g, 4°C for 10 min. The top aqueous layer was carefully transferred to a fresh tube, mixed with 1:10 volume of 3M sodium acetate and 1:1 volume of 2-propanol, and centrifuged at 18,000g, 4°C for 20 min to obtain RNA pellet. The RNA pellet was washed with 1 mL of 75% ethanol at 18,000g, 4°C for 15 min, and then air-dried RNA pellet was re-suspended in 20 µL of nuclease-free water. The isolated RNA of 1 µg was converted to cDNA using the High Capacity cDNA Reverse Transcription Kit (Invitrogen) as per the manufacturer's instructions. qPCR was performed using PowerUp™ SYBR® Green Master Mix to determine the transcriptional activity of macrophage markers. The results were represented as $\log_{10}(2^{-\Delta\Delta Ct})$, where the expression level of the gene of interest was normalized with expression levels of GAPDH (housekeeping gene) and relative to Mϕ (first study) and activated macrophages (second study).

5.2.8 Statistical analysis

All data are presented as mean ± standard error of mean (SEM) and are from three technical and three biological replicates (unless otherwise mentioned). Statistical analysis and mean value differences between the sample groups were performed using Origin software (Origin 2018b, OriginLabs, USA) with a non-parametric one-way analysis of variance (ANOVA) via a Kruskal-Wallis test followed by post-hoc Dunn's multiple comparison test. A p-value of $p \leq 0.05$ and $p \leq 0.01$ was considered to be statistically different between the samples.

5.3 Results

5.3.1 Partial thickness abdominal wall defect model and histomorphologic quantification

The test articles (BM silk, AA silk, BA silk, LECM, SIS, and PP mesh) did not induce edema at the implant site and were easily identifiable at the time of explant **(Figure 5.1)**. The bioscaffolds (BM silk, AA silk, BA silk, LECM, and SIS) showed good integration with host tissue and variable degrees of degradation at 35 days. PP surgical mesh showed modest integration with the host tissue through 35 days.

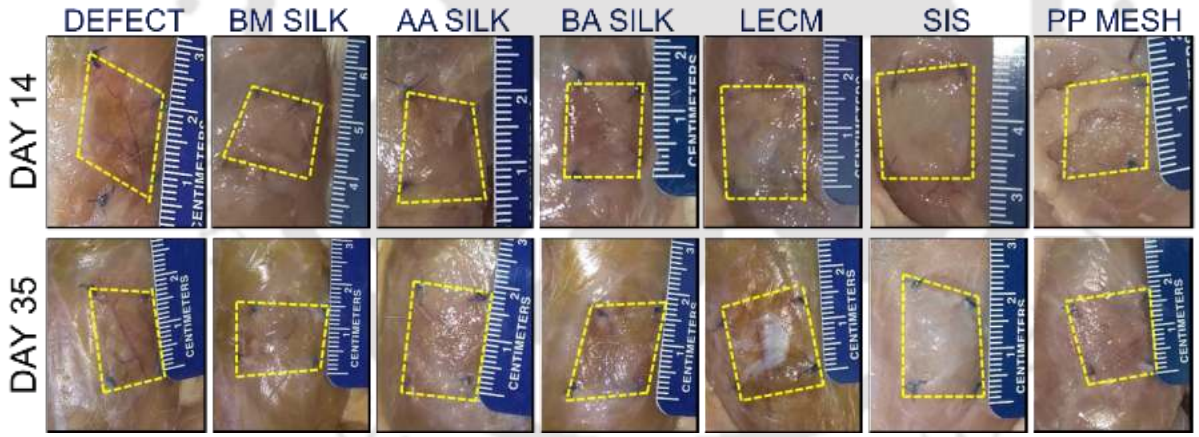

Figure 5.1. The gross view of materials implanted in the bilateral partial thickness abdominal wall defect model during the explant collection at day 14 and day 35. *N = 3 biological replicates and 3 technical replicates per group.*

The cellularity (total number of infiltrated cells), and the number of foreign MGC at the implant site per 200× FOV were evaluated from H&E stained images **(Figure 5.2)**. Among bioscaffolds, cellularity was considerably higher in BM silk, AA silk, and BA silk ($p \leq 0.01$) and SIS ($p \leq 0.05$) compared to LECM **(Figure 5.3 A)**. Over 35 days, cellularity remained high in silk bioscaffolds compared to LECM, SIS, defect alone, and PP mesh ($p \leq 0.01$). Among silk bioscaffolds, BA silk showed higher cellularity than BM silk ($p \leq 0.05$). At day 14 and day 35 post

implantation, ECM bioscaffolds showed fewer MGC than silk bioscaffolds, defect alone, and PP mesh ($p \leq 0.01$) **(Figure 5.3 B)**. At day 14, the silk bioscaffolds, BM silk (9.82 ± 2.03), AA silk (6.01 ± 1.26), BA silk (8.71 ± 2.02) showed a greater ($p \leq 0.01$) number of MGC than LECM (2.05 ± 0.73) and SIS (2.12 ± 0.92). Compared to PP mesh, MGC were substantially fewer in BA silk ($p \leq 0.05$); and AA silk, LECM, SIS ($p \leq 0.01$) bioscaffolds at 14 days.

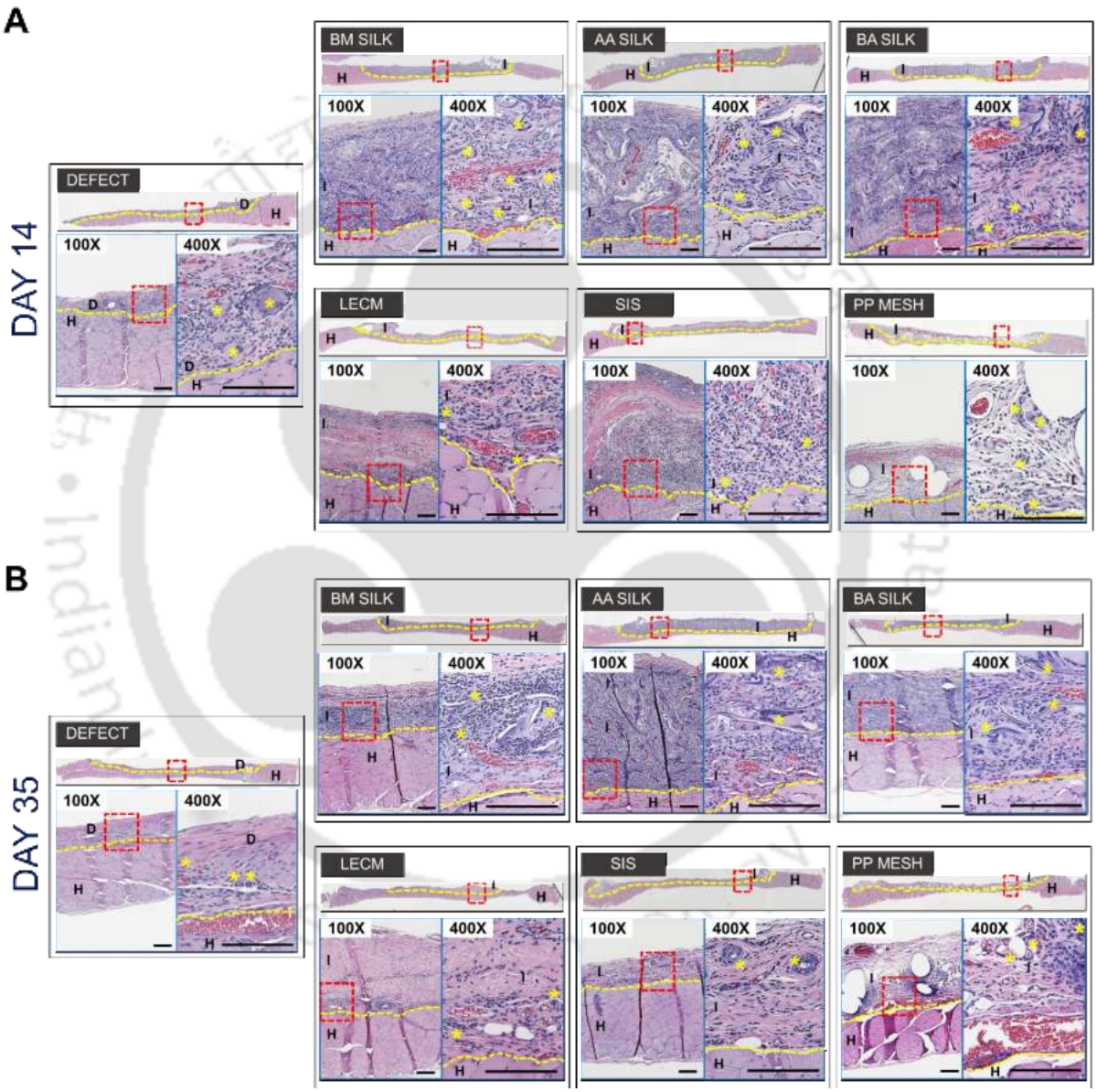

Figure 5.2. Host cellular response towards the test articles and defect alone at day 14 and day 35 post implantation. *Representative H&E stained histologic cross-sections of the defect alone site (unrepaired abdominal wall), and the defect repaired with the test articles (BM silk, AA silk, BA silk, LECM, SIS, and PP mesh) at (A) day 14 and (B) day 35 post implantation. The full-thickness defect site, including the host tissue and the implant, exhibits integration of the test*

articles with the host tissue. Low magnification (100×) image depicts the extent of vascularization, cell response, and cellularity at the host tissue-implant interface. High magnification (400×) image shows the MGC and cell thickness layer at the interface. The red box in the low magnification image represents the area displayed in the high magnification image. Dashed yellow line demarcates the host tissue (H) from defect (D) or implant (I), and yellow stars show the presence of MGC. Scale bar: 200 µm. N = 3 biological replicates and 3 technical replicates per group.

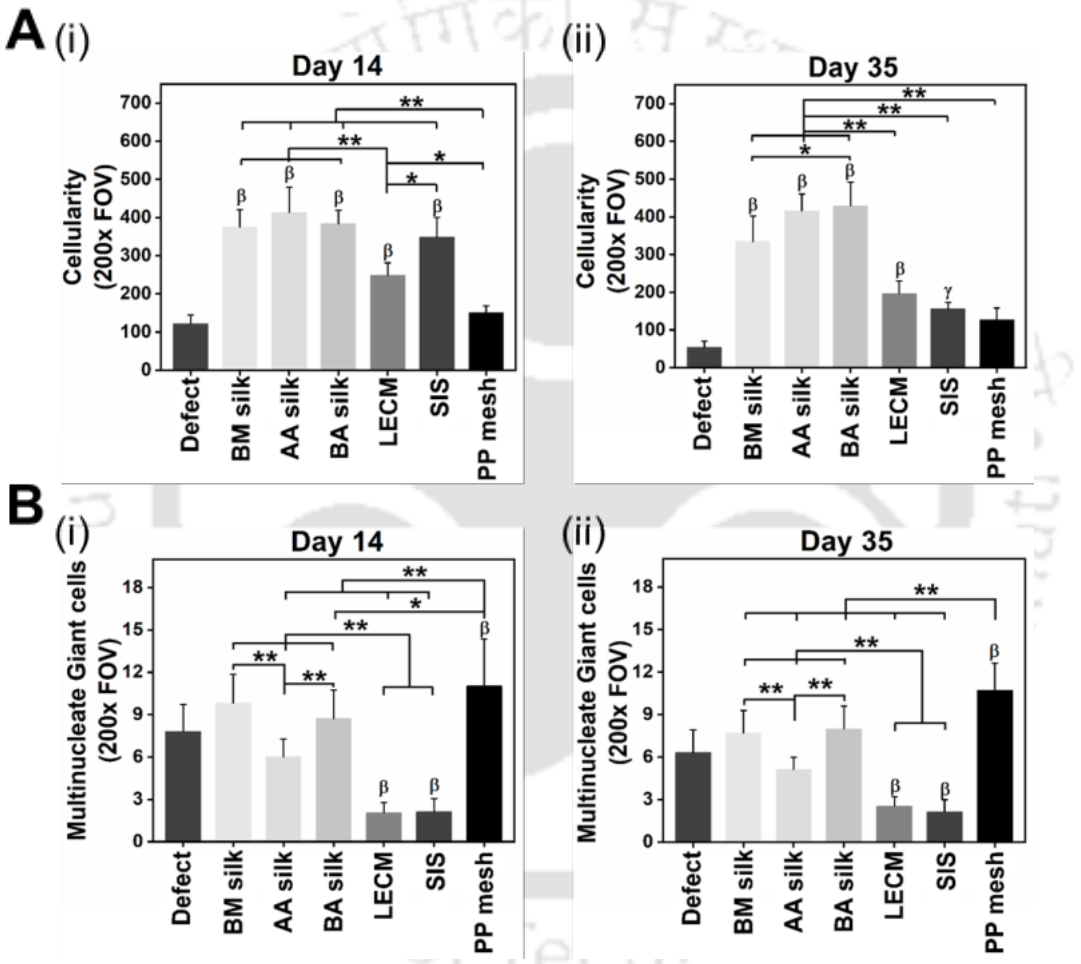

Figure 5.3. Quantification of histomorphologic profile around the host tissue-implant interface. *(A) The cellularity or the number of cells infiltrated towards the test articles per 200× FOV at (i) day 14 and (ii) day 35 post implantation. (B) The number of MGC at the implant site per 200× FOV at (i) day 14 and (ii) day 35 post implantation. Data are presented as average ± standard error of mean; N = 3 biological replicates and 3 technical replicates per group; γ and β indicate $p \leq 0.05$ and $p \leq 0.01$ statistically significant to defect alone (unrepaired abdominal wall); * and ** indicate statistical significance at $p \leq 0.05$ and $p \leq 0.01$, respectively; with Dunn-Sidak post test.*

5.3.2 Connective tissue formation and blood vessel assessment

Masson's Trichrome staining of explants provided information about the connective tissue formation, collagen deposition, and its organization at the implant site **(Figure 5.4)**. Prior to implantation, Masson's Trichrome staining of ECM bioscaffolds resembled organized laminate sheets of collagenous tissue and were stained in blue, whereas the silk bioscaffolds were stained in red. At day 14, the defects repaired with silk bioscaffolds showed early scaffold degradation and deposition of disorganized collagen fibers in and around the implant site, followed by organized collagen layers at 35 days. Correspondingly, ECM bioscaffolds partially degraded over 35 days and lost their distinct architecture by separation of multilaminate sheets and deposition of well-organized collagen fibers [360]. No similar histological evidence of organized collagen deposition was observed in the defect alone or PP mesh.

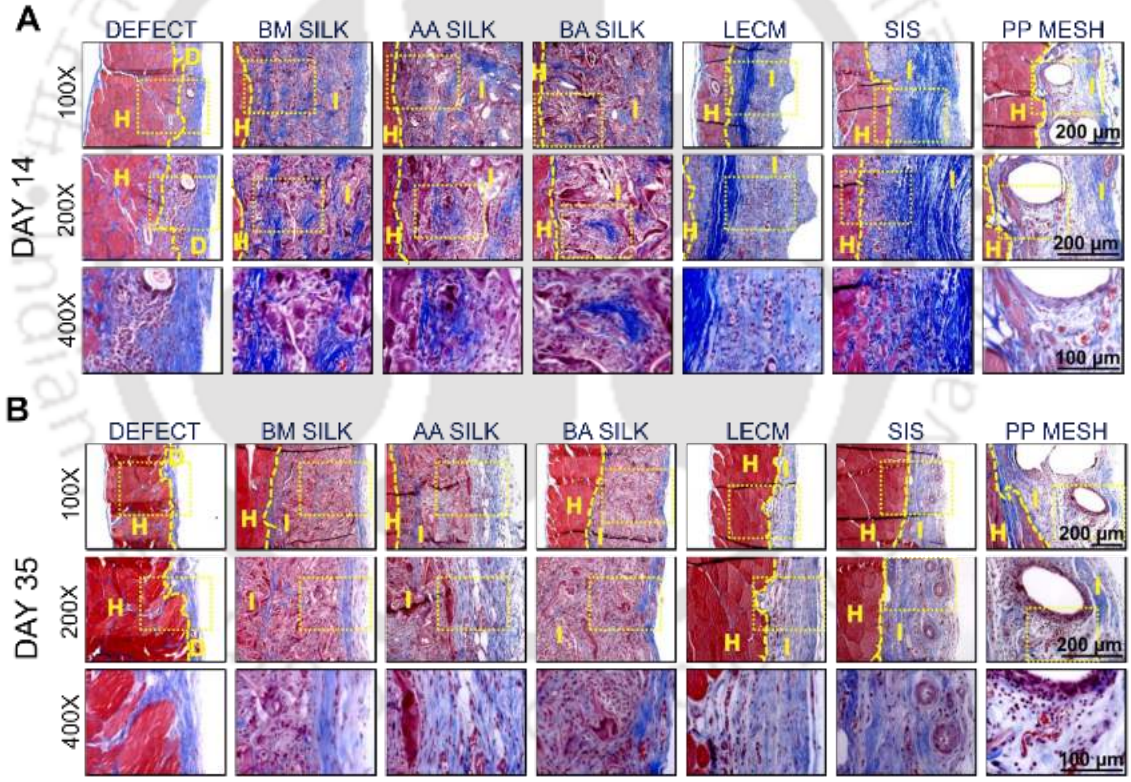

Figure 5.4. Masson's Trichrome staining of the test articles and defect alone at day 14 and day 35 post implantation. *Representative Masson's Trichrome staining images of the defect alone (unrepaired abdominal wall) and the defect repaired with the test articles at (A) day 14 and (B) day 35 post implantation. The blue, red, and dark red in the images depict the collagen fibers, cytoplasm, and nucleus, respectively. Low magnification images (100× and 200×) represent the collagen layer deposition at the host tissue-implant interface and around the implant; scale bar: 200 µm. High magnification images (400×) display the organization and intervention of the*

collagen layers at the implant site; scale bar: 100 µm. Yellow box in the low magnification image represents the area displayed in the high magnification image. Dashed yellow line demarcates the host tissue (H) from defect (D) or implant (I). N = 3 biological replicates and 3 technical replicates per group.

Vascularization was examined by CD31 immunolabeling. The number of CD31 positive blood vessels per mm^2 at day 14 and day 35 post implantation was quantified **(Figure 5.5 A)**. At day 14, the number of blood vessels per mm^2 was higher ($p \leq 0.01$) in defects repaired with AA silk, LECM, SIS, and PP mesh than defect alone site and BA silk implant **(Figure 5.5 C)**. At day 35, the number of blood vessels per mm^2 was higher ($p \leq 0.01$) in defects repaired with BM silk and PP mesh than defect alone site **(Figure 5.5 D)**. Compared to PP mesh, the number of blood vessels was fewer in LECM, SIS ($p \leq 0.05$); and BA silk ($p \leq 0.01$). Among all bioscaffolds, the total number of blood vessels per mm^2 decreased significantly from 14 days to 35 days in AA silk (137.86 ± 11.4 to 99.9 ± 11.1), LECM (137.19 ± 18.5 to 82.77 ± 14.5), and SIS (163.17 ± 25.3 to 90.81 ± 10.0).

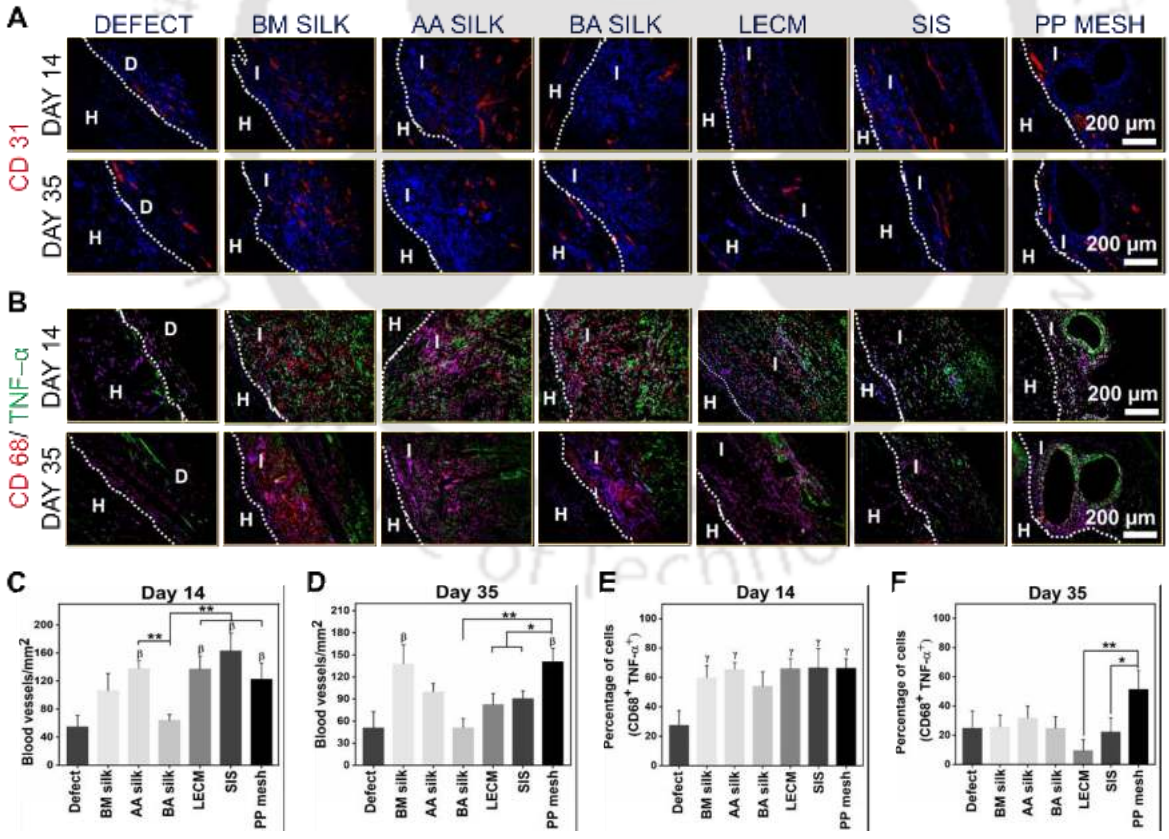

Figure 5.5. Immunostaining and quantification of blood vessels and pro-inflammatory macrophages around the test articles and defect alone at day 14 and day 35 post implantation.

*(A) CD31 immunolabeling images of the defect alone and defect repaired with test articles at day 14 and day 35. Red: CD31 (blood vessels), Blue: DAPI (Nucleus). Scale bar: 200 µm. (B) CD68 and TNF-α immunolabeling of the defect alone and defect repaired with test articles at day 14 and day 35. Red: CD68 (macrophages), Green: TNF-α (pro-inflammatory macrophages), Blue: Nucleus, Magenta: co-localization of CD68 and Nucleus. Scale bar: 200 µm. Dashed white line demarcates the host tissue (H) from the defect (D) or implant (I). Quantification of the number of blood vessels per mm^2 at (C) day 14 and (D) day 35 post implantation. Quantification of the percentage of macrophages ($CD68^+$) co-expressing pro-inflammatory TNF-α marker at (E) day 14 and (F) day 35 post implantation. Data are presented as average ± standard error of mean; N = 3 biological replicates and 3 technical replicates per group; γ and β indicate $p \leq 0.05$ and $p \leq 0.01$ statistically significant to defect alone (unrepaired abdominal wall); * and ** indicate statistical significance at $p \leq 0.05$ and $p \leq 0.01$, respectively; with Dunn-Sidak post test.*

5.3.3 Spatiotemporal analysis of macrophage phenotype

The inflammatory response towards implanted test articles and defect alone site was assessed by immunolabeling against macrophages ($CD68^+$) and pro-inflammatory macrophages ($TNF\text{-}\alpha^+$) at the same FOV **(Figure 5.5 B)**. At day 14, AA silk and BA silk implants showed a greater number of macrophages and pro-inflammatory macrophages than defect alone, BM silk, LECM, SIS, and PP mesh **(Figure 5.6 A-B)**. At day 14, the macrophages were significantly fewer in SIS implants than defect alone. The number of macrophages was greater ($p \leq 0.01$) in AA silk implant than defect alone, LECM, SIS, and PP mesh at day 35 **(Figure 5.6 C)**. However, SIS implant showed fewer ($p \leq 0.01$) macrophages than BM silk and BA silk. At 35 days, a decline in the total number of pro-inflammatory macrophages was observed in all bioscaffolds. Among the test articles, AA silk implant induced increased pro-inflammatory expression in the macrophages compared to LECM and SIS ($p \leq 0.05$) **(Figure 5.6 D)**. At day 14, BM silk, AA silk, LECM, SIS, and PP mesh implants showed a greater ($p \leq 0.05$) percentage of M1-like, pro-inflammatory macrophages ($CD68^+TNF\text{-}\alpha^+$ cells) compared to defect alone **(Figure 5.5 E)**. However, at day 35, the percentage of $CD68^+TNF\text{-}\alpha^+$ cells markedly decreased in all defects repaired with bioscaffolds compared to the percentage present at day 14 **(Figure 5.5 F)**. Compared to PP mesh, LECM and SIS implants showed a significantly reduced percentage of $CD68^+TNF\text{-}\alpha^+$ cells.

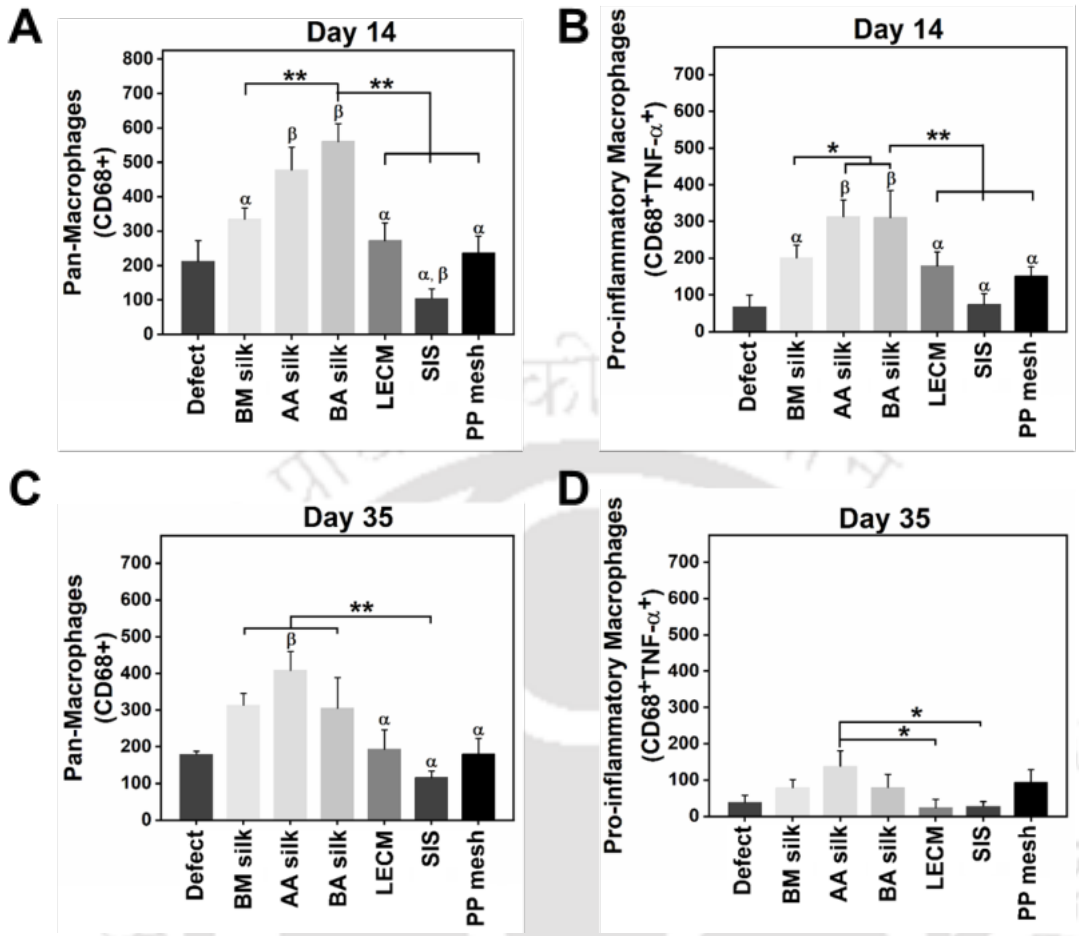

Figure 5.6. Quantification of macrophages and pro-inflammatory macrophages subpopulation around the host tissue-implant interface. *Number of (A, C) macrophages ($CD68^+$) and (B, D) pro-inflammatory macrophages ($CD68^+TNF\text{-}\alpha^+$) at (A, B) day 14 and (C, D) day 35 post implantation. Data are presented as average ± standard error of mean; N = 3 biological replicates and 3 technical replicates per group; β indicates $p \leq 0.01$ statistically significant to defect alone (unrepaired abdominal wall); α indicates statistical significance at $p \leq 0.01$ to AA silk; * and ** indicate statistical significance at $p \leq 0.05$ and $p \leq 0.01$, respectively; with Dunn-Sidak post test.*

Triple macrophage staining for CD68 (pan-macrophage marker), CD86 (M1 subtype pattern expressed in antigen-presenting cells for activating T cells), and CD206 (M2 subtype pattern that enhances healing) showed the spatiotemporal distribution of distinct M1 and M2 macrophage subpopulation at day 14 and day 35 post implantation in the same FOV **(Figure 5.7 A-B)** [361]. The macrophages ($CD68^+$) co-expressing CD86, and $CD68^+$ macrophages co-expressing CD206 offered insights regarding the number of pro-inflammatory macrophages and pro-remodeling macrophages, respectively. All the variants of bioscaffolds induced a spike of pro-inflammatory macrophage response at 14 days, followed by a transition towards pro-remodeling

macrophages at 35 days. Macrophages exhibit transient polarization states during tissue remodeling in response to microenvironmental cues from the implant [349]. The ratio of pro-remodeling to pro-inflammatory macrophages (M2-like: M1-like ratio) is a relevant metric as it is associated with the extent of wound healing and tissue remodeling. At day 14, the presence of M1-like pro-inflammatory macrophages ($CD68^+CD86^+$ cells) differed among the materials; specifically, the macrophage population showed significantly greater numbers ($p \leq 0.01$) in AA silk (283.58 ± 119.0 cells) and BA silk (274.70 ± 67.4 cells) implants than LECM (88.35 ± 20.3 cells), SIS (40 ± 14.32 cells), and PP mesh (120.93 ± 36.25 cells) implants **(Figure 5.7 C, i)**. The subpopulation of M2-like pro-remodeling macrophages ($CD68^+CD206^+$ cells) in defect alone and the defects repaired with BM silk, AA silk, BA silk, LECM, SIS, and PP mesh were 43.5 ± 23.94 cells, 115.77 ± 46.03 cells, 113.58 ± 41.02 cells, 151 ± 34.76 cells, 57.21 ± 14.0 cells, 102.7 ± 45.0 cells, and 38.62 ± 9.4 cells respectively **(Figure 5.7 D, i)**. Statistical analysis showed that pro-remodeling macrophages were greater in BM silk ($p \leq 0.05$) and BA silk ($p \leq 0.01$) implant than defect alone. Compared to PP mesh, the pro-remodeling macrophages were higher in defects repaired with silk bioscaffolds ($p \leq 0.01$); and SIS ($p \leq 0.05$). Among bioscaffolds, the pro-remodeling macrophages were greater in BM silk ($p \leq 0.05$) and BA silk ($p \leq 0.01$) than LECM. However, $CD68^+CD86^+CD206^+$ macrophages were greater in defects repaired with BA silk compared to LECM, SIS, PP mesh, and defect alone ($p \leq 0.01$) **(Figure 5.7 E, i)**. Variation existed in the subpopulation of pro-inflammatory and pro-remodeling macrophages among the implanted test articles reflected in the M2-like: M1-like ratio of macrophages **(Figure 5.7 F, i)**. An increased ($p \leq 0.01$) M2-like: M1-like ratio was observed in SIS (3.89 ± 0.96) than BM silk (0.69 ± 0.26), AA silk (0.38 ± 0.19), BA silk (0.40 ± 0.17), LECM (0.57 ± 0.18), PP mesh (0.15 ± 0.05), and defect alone (0.41 ± 0.12).

After 35 days, the subpopulation of M1-like pro-inflammatory macrophages was greater ($p \leq 0.01$) in BM silk (191.55 ± 99.3 cells), AA silk (169.43 ± 89.1 cells), and BA silk (221.27 ± 62.7 cells) than SIS (21.25 ± 13.1 cells) and defect alone (7.11 ± 2.6 cells) **(Figure 5.7 C, ii)**. Despite a similar number of pro-inflammatory macrophages around silk bioscaffolds, the defects repaired with AA silk and BA silk showed a greater number of M2-like pro-remodeling macrophages compared to defect alone, LECM, SIS, PP mesh ($p \leq 0.01$); and BM silk ($p \leq 0.05$) **(Figure 5.7 D, ii)**. The subpopulation of pro-remodeling macrophages in defect alone, BM silk, AA silk, BA silk, LECM, SIS, and PP mesh implants were 2.44 ± 0.9 cells, 67.33 ± 35.5 cells,

201.87 ± 100.2 cells, 237.81 ± 67.4 cells, 20.14 ± 6.1 cells, 30.00 ± 15.6 cells, and 23.46 ± 8.2 cells respectively. Likewise, the number of $CD68^{+}CD86^{+}CD206^{+}$ macrophages increased ($p \leq 0.01$) in AA silk and BA silk compared to LECM, SIS, PP mesh, and defect alone **(Figure 5.7 E, ii)**. The M2-like: M1-like ratio of macrophages was statistically significant between the bioscaffolds **(Figure 5.7 F, ii)**. The M2-like: M1-like ratio in AA silk and SIS implants was higher ($p \leq 0.01$) than the defect alone site. The defects repaired with AA silk, BA silk, and SIS showed a higher ($p \leq 0.01$) M2-like: M1-like ratio than PP mesh. Among bioscaffolds, AA silk and SIS showed a higher M2-like: M1-like ratio than BM silk and LECM ($p \leq 0.01$); SIS showed a higher M2-like: M1-like ratio than BA silk ($p \leq 0.05$); BA silk showed higher ($p \leq 0.05$) M2-like: M1-like ratio than BM silk.

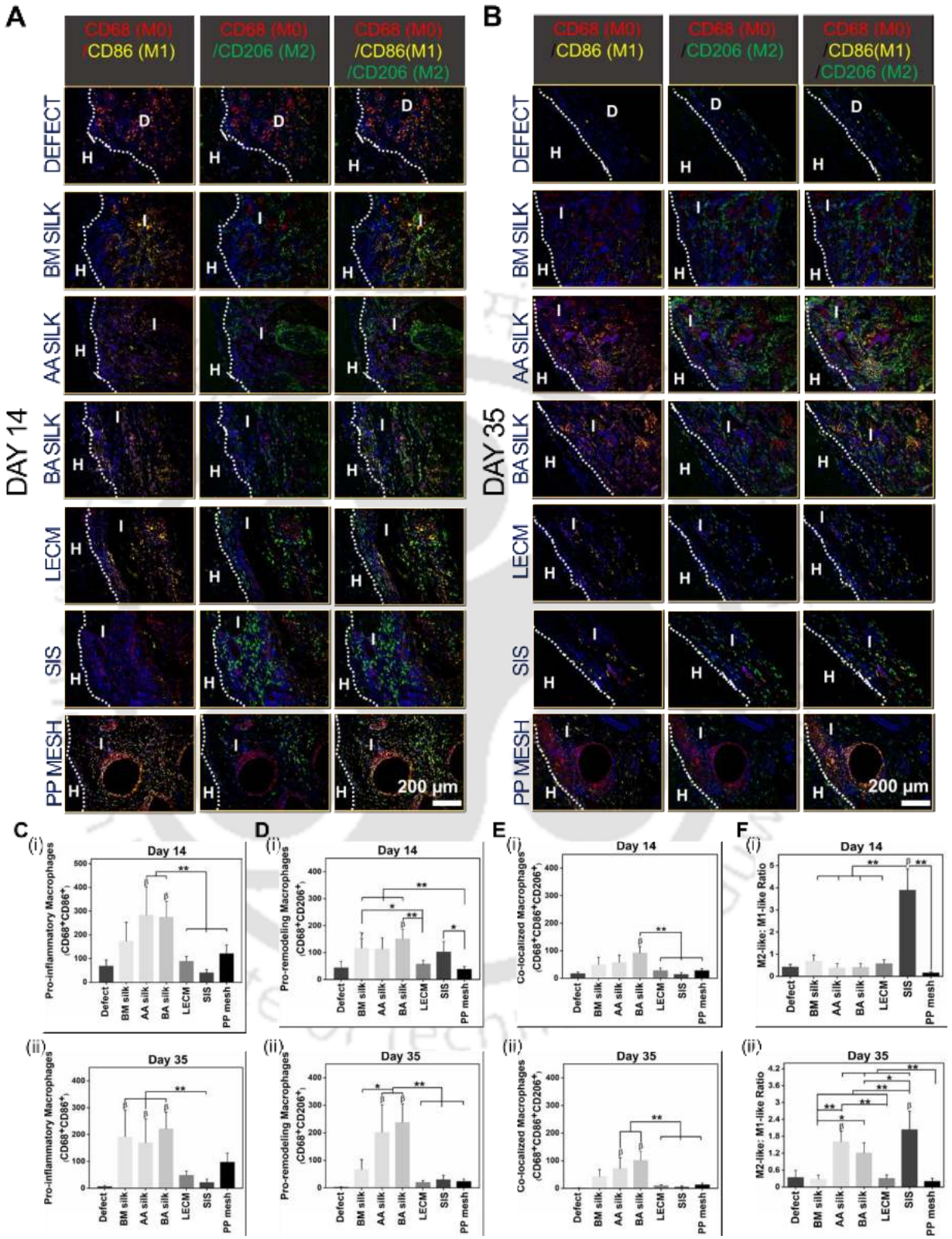

Figure 5.7. Immunolabeling and quantification of macrophage phenotypes around the test articles and defect alone at day 14 and day 35 post implantation. *Immunolabeling for the*

*macrophage (CD68), pro-inflammatory macrophage (CD86), and pro-remodeling macrophage (CD206) in the defect alone and defect repaired with implanted test articles at (A) day 14 and (B) day 35 post implantation. Red: CD68 (macrophages), Yellow: CD86 (pro-inflammatory macrophages), Green: CD206 (pro-remodeling macrophages), Blue: Nucleus, Magenta: co-localization of CD68 and Nucleus, Orange: co-localization of CD68 and CD86. Scale bar: 200 µm. Dashed white line demarcates the host tissue (H) from the defect (D) or implant (I). Quantification of (C) number of pro-inflammatory macrophages ($CD68^+CD86^+$), (D) number of pro-remodeling macrophages ($CD68^+CD206^+$), (E) number of triple labeled macrophages ($CD68^+CD86^+CD206^+$), (F) M2-like: M1-like ratio of macrophages at (i) day 14 and (ii) day 35 post implantation. Data are presented as average ± standard error of mean; N = 3 biological replicates and 3 technical replicates per group; γ and β indicate $p \leq 0.05$ and $p \leq 0.01$ statistically significant to defect alone (unrepaired abdominal wall); * and ** indicate statistical significance at $p \leq 0.05$ and $p \leq 0.01$, respectively; with Dunn-Sidak post test.*

5.3.4 Effect of degradation products of bioscaffolds upon naive macrophages

A maximum non-cytotoxic dose of 0.125 mg/mL of degradation products of bioscaffolds, as selected from MTT assay and live/dead staining **(Figure 5.8)**, was used to evaluate its effect on macrophage activation state in two distinct studies.

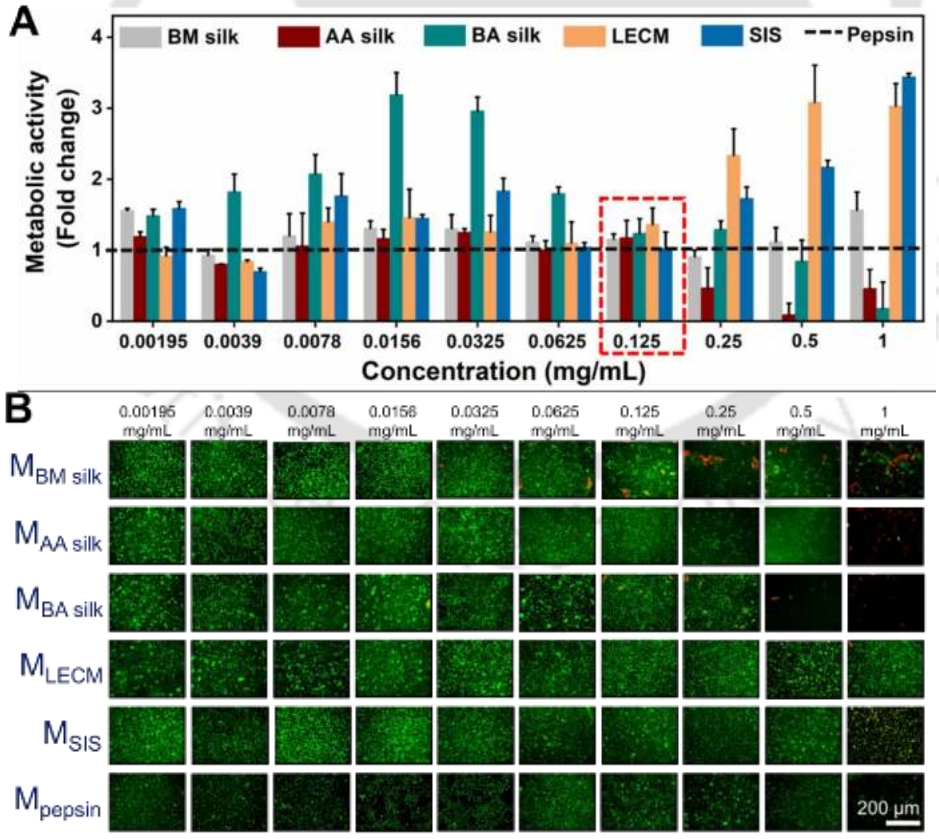

Figure 5.8. Dose-response cytotoxicity study of degradation products of all variants of silk and ECM bioscaffolds against macrophages. *(A) The metabolic activity of BMDM treated with*

different concentrations of degradation products of BM silk, AA silk, BA silk, LECM, and SIS bioscaffolds, where the values are normalized to the metabolic activity of BMDM treated with a respective dose of pepsin. The dashed black line represents the metabolic activity of macrophages towards different concentrations of pepsin. The red box signifies the non-cytotoxic concentration of degradation products of silk and ECM bioscaffolds against macrophages. (B) The live/dead staining images of the macrophages exposed to different concentrations of degradation products of BM silk, AA silk, BA silk, LECM, and SIS bioscaffolds. Live cells are stained in green, whereas the dead cells are stained in red. Scale bar: 200 µm. Data are presented as average ± standard error of mean; N = 3 biological replicates and 3 technical replicates.

The Mϕ showed a distinct macrophage phenotype activation after exposure to degradation products of bioscaffolds, as assessed by immunolabeling against pan-macrophage marker (F4/80), M1-like pro-inflammatory macrophage marker (iNOS), and M2-like pro-remodeling macrophage markers (Arginase and Fizz1) **(Figure 5.9 A)**. All treatment groups showed an equivalent number of F4/80 positive macrophages; accordingly, no statistical difference was observed **(Figure 5.9 B, i)**. The percent of iNOS positive macrophages was fewer ($p \leq 0.01$) in LECM treated Mϕ compared to AA silk, and SIS treated Mϕ **(Figure 5.9 B, ii)**. Compared to the negative control (only pepsin), BM silk, BA silk, and LECM treated Mϕ showed fewer ($p \leq 0.01$) iNOS positive cells. The percent of arginase positive macrophages in BM silk, AA silk, BA silk, LECM, and SIS treated Mϕ was 13.08 ± 5.7%, 26.64 ± 12.7%, 6.75 ± 2.3%, 10.12 ± 3.4%, and 11.34 ± 3.7%, respectively **(Figure 5.9 B, iii)**. AA silk treated Mϕ showed a greater ($p \leq 0.01$) number of arginase positive cells than BA silk, LECM, and pepsin control. The Fizz1 positive macrophages were greater ($p \leq 0.01$) in BM silk, AA silk, BA silk, and LECM treated groups than SIS treated Mϕ **(Figure 5.9 B, iv)**. As macrophages showed a unique pattern of iNOS, arginase, and Fizz1 after exposure to each biomaterial, the ratio of arginase: iNOS and Fizz1: iNOS was determined **(Figure 5.9 C)**. The arginase: iNOS ratio in BM silk, AA silk, BA silk, LECM, and SIS treated macrophages was 0.79 ± 0.2, 2.06 ± 0.7, 0.32 ± 0.1, 3.20 ± 1.2, and 0.58 ± 0.2, respectively **(Figure 5.9 C, i)**. AA silk and LECM treated Mϕ showed a significantly enhanced arginase: iNOS ratio compared to BM silk, BA silk, SIS, and pepsin control. Similarly, Fizz1: iNOS ratio evaluated in BM silk (2.45 ± 0.9), AA silk (2.81 ± 1.7), BA silk (1.00 ± 0.2), LECM (8.56 ± 1.8), and SIS (0.20 ± 0.1) treated macrophages was statistically significant **(Figure 5.9 C, ii)**. Compared to pepsin control, the Fizz1: iNOS ratio was higher in AA silk ($p \leq 0.05$), BM silk ($p \leq 0.01$), and LECM ($p \leq 0.01$) treated macrophages. The Fizz1: iNOS ratio was higher ($p \leq 0.01$) in BM silk, and AA silk treated Mϕ

than SIS. LECM treated Mϕ showed a higher ($p \leq 0.01$) Fizz1: iNOS ratio than BM silk, AA silk, BA silk, and SIS treated macrophages.

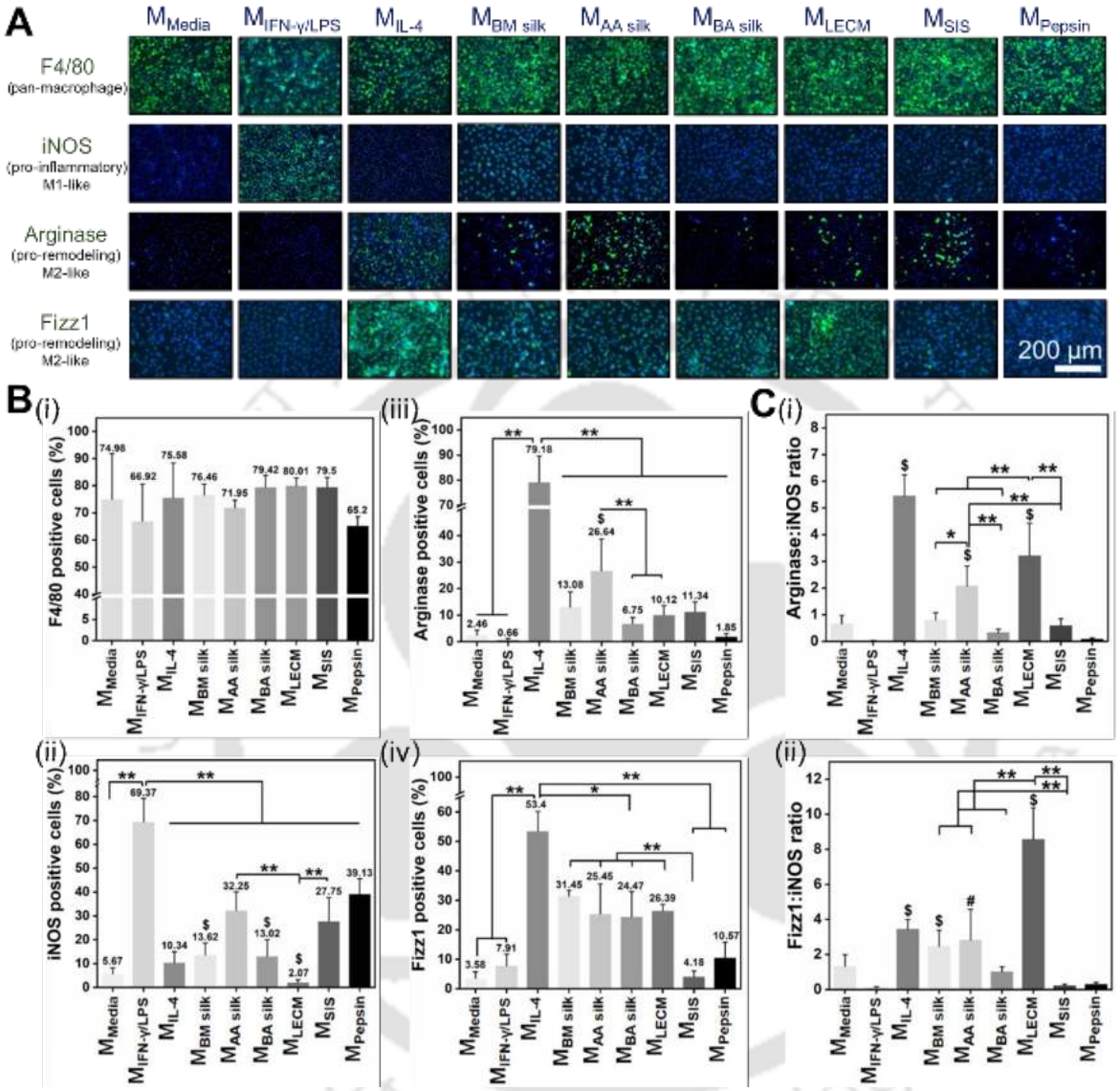

Figure 5.9. In vitro macrophage phenotype response to degradation products of silk (BM silk, AA silk, and BA silk) and ECM (LECM and SIS) bioscaffolds. *Primary murine BMDM were exposed to 0.125 mg/mL of degradation products of bioscaffolds for 24 h. A known cytokine controls, $M_{IFN-\gamma/LPS,}$ and $M_{IL-4,}$ were included for pro-inflammatory and pro-remodeling macrophage phenotypes, respectively. (A) Immunolabeling for pan-macrophage marker (F4/80), M1-like pro-inflammatory marker (iNOS), and M2-like pro-remodeling markers (Arginase and Fizz1). Scale bar: 200 µm. (B) Percentage quantification of macrophage phenotypes for (i) F4/80, (ii) iNOS, (iii) Arginase, and (iv) Fizz1. (C) The ratio of (i) arginase: iNOS and (ii) Fizz1: iNOS. Data are presented as average ± standard error of mean; N = 3 biological replicates and 3 technical replicates per group; # and $ indicate $p \leq 0.05$ and $p \leq 0.01$ statistically significant to*

*pepsin. * and ** indicate statistical significance at $p \leq 0.05$ and $p \leq 0.01$, respectively; with Dunn-Sidak post test.*

The transcriptional activity of pro-inflammatory genes (iNOS, TNF-α, IL-1β, IL-6, and MCP1) and pro-remodeling genes (Arginase, Fizz1, YM1, IL-10, and IL1-Ra) associated with macrophage polarization, cytokines, and chemoattractants in Mϕ exposed to degradation products of bioscaffolds was evaluated **(Figure 5.10)**. The Mϕ exposed to degradation products of bioscaffolds showed no difference in iNOS expression. The expression levels of TNF-α, IL-1β, IL-6, and MCP1 were distinct among bioscaffolds treated macrophages **(Table 5.2)**. The radar plots showed reduced expression levels of TNF-α, IL-1β, IL-6, and MCP1 in Mϕ exposed to AA silk, AA silk, BM silk, and AA silk, respectively **(Figure 5.10 B)**. A discrete expression of Arginase, Fizz1, IL-10, and IL1-Ra was observed among bioscaffolds treated macrophages **(Figure 5.10 C)**. The p-values representing the reduced expression of pro-inflammatory genes and increased expression of pro-remodeling genes in Mϕ exposed to degradation products of bioscaffolds are summarized in **Table 5.2**. From radar plots, the increased expression of arginase, Fizz1, and IL-1Ra was observed in Mϕ exposed to BA silk, AA silk, and BA silk, respectively **(Figure 5.10 D)**.

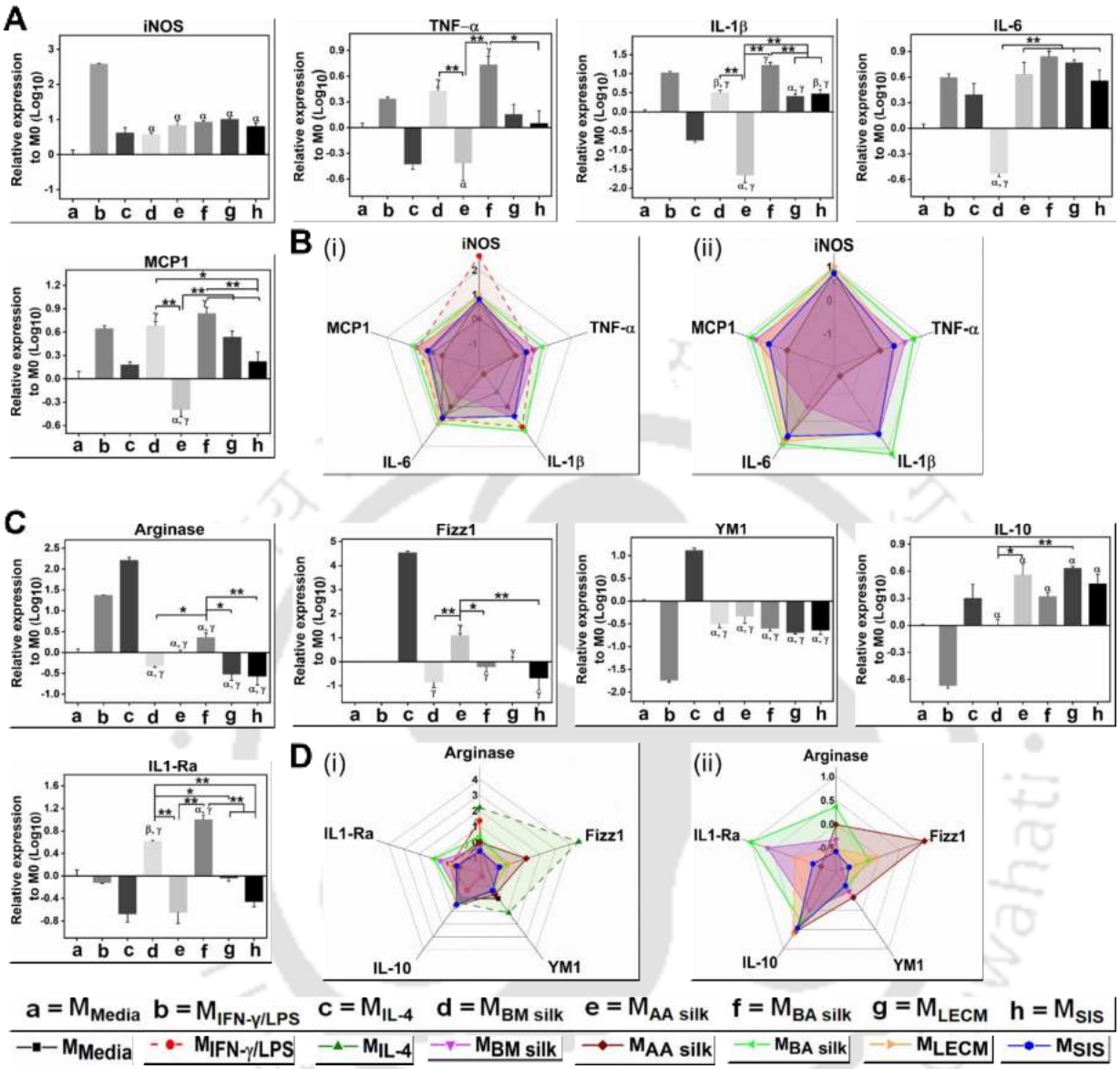

Figure 5.10. Relative transcriptional activity of pro-inflammatory genes and pro-remodeling genes in macrophages after the effect of degradation products of silk (BM silk, AA silk, and BA silk) and ECM (LECM and SIS) bioscaffolds. *Primary murine BMDM were exposed to 0.125 mg/mL of degradation products of silk and ECM bioscaffolds for 24 h. A known cytokine controls, $M_{IFN\text{-}\gamma/LPS}$ and $M_{IL\text{-}4,}$ were included for pro-inflammatory and pro-remodeling macrophage phenotypes, respectively. (A) Transcriptional level of pro-inflammatory genes (iNOS, TNF-α, IL-1β, IL-6, and MCP1). (B) Radar plots of averaged relative expression of pro-inflammatory genes in (i) media control, cytokines treated controls, silk and ECM bioscaffolds treated macrophages, and (ii) BM silk, AA silk, BA silk, LECM and SIS bioscaffolds treated macrophages. (C) Transcriptional level of pro-remodeling genes (Arginase, Fizz1, YM1, IL-10, and IL1-Ra). (D) Radar plots of averaged relative expression of pro-remodeling genes in (i) media control, cytokines treated controls, silk and ECM bioscaffolds treated macrophages, and (ii) BM silk, AA*

*silk, BA silk, LECM and SIS bioscaffolds treated macrophages. Data are presented as average ± standard error of mean; N = 3 biological replicates and 2 technical replicates per group; α and β indicate $p \leq 0.01$ and $p \leq 0.05$ statistical significance to pro-inflammatory cytokine control (20 ng/mL IFN-γ and 100 ng/mL LPS); γ and ε indicate $p \leq 0.01$ and $p \leq 0.05$ statistical significance to pro-remodeling cytokine control (20 ng/mL of IL-4); * and ** indicate statistical significance at $p \leq 0.05$ and $p \leq 0.01$, respectively; with Dunn-Sidak post test.*

Table 5.2. *p-values representing the reduced expression of pro-inflammatory genes and increased expression of pro-remodeling genes in macrophages after the effect of degradation products of bioscaffolds for figure 5.10. * and ** indicate statistical significance at $p \leq 0.05$ and $p \leq 0.01$, respectively; with Dunn-Sidak post test.*

		p-values of expression levels in				
		BM silk	**AA silk**	**BA silk**	**LECM**	**SIS**
Pro-inflammatory genes (Downregulated)	**iNOS**	ns between the groups				
	TNF-α		** vs. BM silk ** vs. BA silk			* vs. BA silk
	IL-1β		** vs. BM silk ** vs. BA silk ** vs. LECM ** vs. SIS		** vs. BA silk	** vs. BA silk
	IL-6	** vs. AA silk ** vs. BA silk ** vs. LECM ** vs. SIS				
	MCP1		** vs. BM silk ** vs. BA silk ** vs. LECM ** vs. SIS			* vs. BM silk ** vs. BA silk
Pro-remodeling genes (Upregulated)	**Arginase**			* vs. BM silk * vs. LECM ** vs. SIS		
	Fizz1		* vs. BA silk ** vs. BM silk ** vs. SIS			
	YM1	ns between the groups				
	IL-10		* vs. BM silk		** vs. BM silk	
	IL1-Ra	* vs. LECM ** vs. AA silk ** vs. SIS		** vs. AA silk ** vs. LECM ** vs. SIS		

5.3.5 Effect of degradation products of bioscaffolds upon pro-inflammatory activated macrophages

The response of pro-inflammatory activated macrophages after exposure to degradation products of bioscaffolds was assessed by immunolabeling against F4/80, iNOS, and Arginase and Fizz1 markers **(Figure 5.11 A)**. The cytokine controls and bioscaffolds treated macrophages showed a similar percent of F4/80 positive cells **(Figure 5.11 B, i)**. The percent of iNOS positive cells was significantly lower in pro-inflammatory activated macrophages exposed to AA silk, BA silk, and LECM compared to the pepsin control **(Figure 5.11 B, ii)**. The percent of arginase positive cells in pro-inflammatory activated macrophages exposed to BM silk, AA silk, BA silk, LECM, and SIS were 9.05 ± 4.1%, 12.61 ± 3.2%, 8.44 ± 4.5%, 5.7 ± 0.9%, and 38.76 ± 9.8% respectively **(Figure 5.11 B, iii)**. The pro-inflammatory activated macrophages exposed to SIS expressed greater ($p \leq 0.01$) arginase positive cells than BM silk, AA silk, BA silk, LECM, and pepsin control. However, the percent of Fizz1 positive cells in pro-inflammatory activated macrophages exposed to BM silk, AA silk, BA silk, LECM, and SIS was 43.12 ± 5.7%, 45.52 ± 11.3%, 32.02 ± 4.9%, 29.74 ± 5.8%, and 37.11 ± 14.4%, respectively **(Figure 5.11 B, iv)** and was statistically significant than pepsin control. The arginase: iNOS ratio was distinct in pro-inflammatory activated macrophages exposed to BM silk (0.14 ± 0.05), AA silk (0.61 ± 0.10), BA silk (0.17 ± 0.06), LECM (0.20 ± 0.09), and SIS (0.77 ± 0.19) **(Figure 5.11 C, i)**. The arginase: iNOS ratio was higher in SIS ($p \leq 0.01$), and AA silk ($p \leq 0.05$) treated pro-inflammatory activated macrophages compared to pepsin control, BM silk, and BA silk treated groups. The Fizz1: iNOS ratio in pro-inflammatory activated macrophages exposed to BM silk, AA silk, BA silk, LECM, and SIS was 0.73 ± 0.09, 2.31 ± 0.45, 1.03 ± 0.11, 0.84 ± 0.35, and 0.74 ± 0.27, respectively **(Figure 5.11 C, ii)**. The Fizz1: iNOS ratio was higher ($p \leq 0.01$) in pro-inflammatory activated macrophages exposed to AA silk compared to pepsin control, BM silk, BA silk, LECM, and SIS.

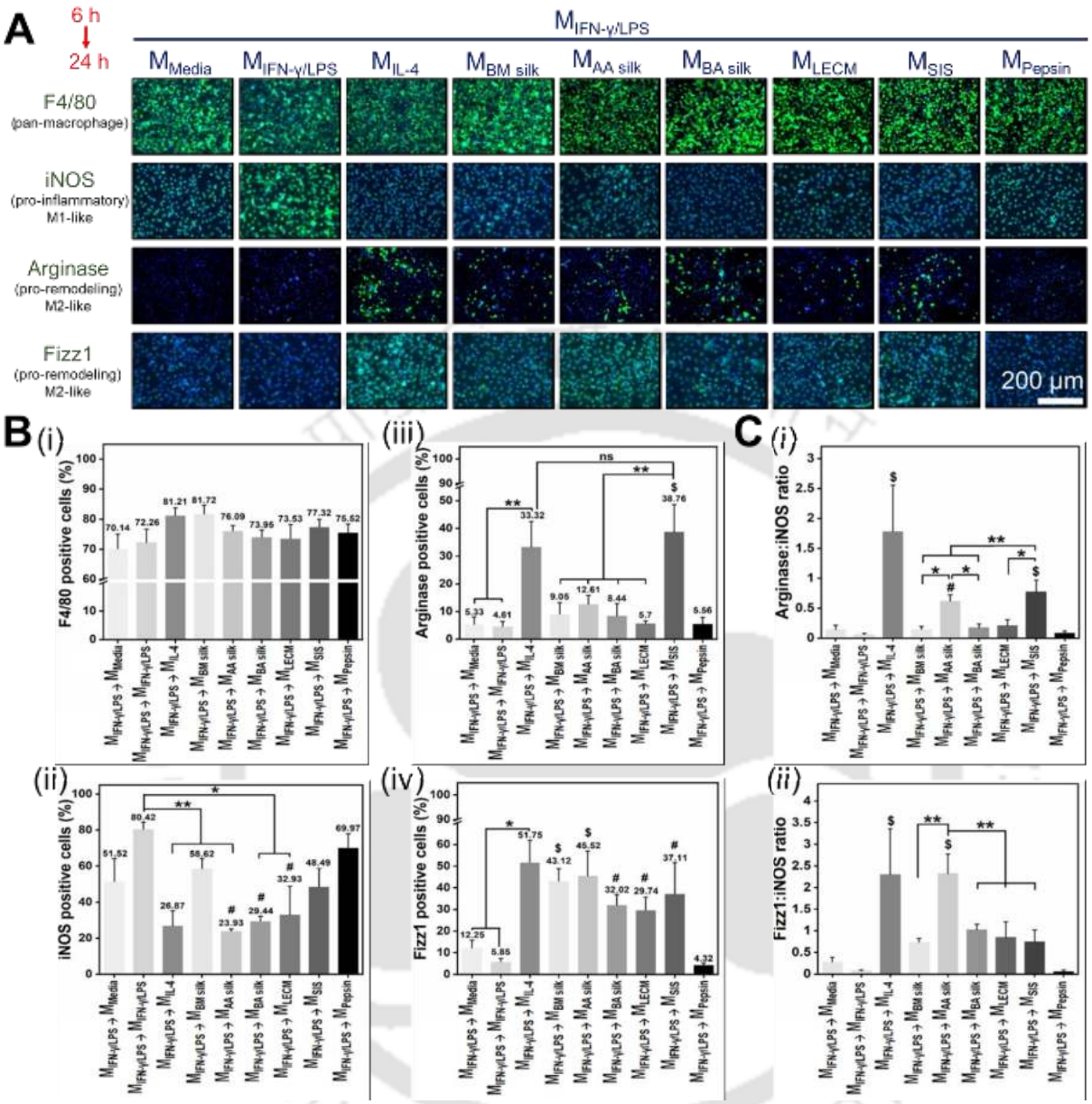

Figure 5.11. Effect of degradation products of silk (BM silk, AA silk, and BA silk) and ECM (LECM and SIS) bioscaffolds on pro-inflammatory activated macrophages. *Primary murine BMDM activated towards pro-inflammatory phenotype (IFN-γ and LPS treatment for 6 h) were exposed to 0.125 mg/mL of degradation products of silk and ECM bioscaffolds for 24 h. A known cytokine controls, $M_{IFN-\gamma/LPS}$ and M_{IL-4}, were included for pro-inflammatory and pro-remodeling macrophage phenotypes, respectively. (A) Immunolabeling for pan-macrophage marker (F4/80), M1-like pro-inflammatory marker (iNOS), and M2-like pro-remodeling markers (Arginase and Fizz1). Scale bar: 200 µm. (B) Percentage quantification of macrophage phenotype response for (i) F4/80, (ii) iNOS, (iii) Arginase, and (iv) Fizz1. (C) The ratio of (i) arginase: iNOS and (ii) Fizz1: iNOS. Data are presented as average ± standard error of mean; N = 3 biological replicates and 3 technical replicates per group; # and $ indicate $p \leq 0.05$ and $p \leq 0.01$ statistically significant*

*to pepsin, * and ** indicate statistical significance at $p \leq 0.05$ and $p \leq 0.01$, respectively, with Dunn-Sidak post test.*

The pro-inflammatory activated macrophages exposed to degradation products of bioscaffolds showed significantly unique expression of iNOS, TNF-α, IL-1β, and MCP1, and no difference was observed in IL-6 expression **(Figure 5.12 A)**. From radar plots **(Figure 5.12 B)**, reduced expression of iNOS, TNF-α, and IL-1β was observed in pro-inflammatory activated macrophages exposed to AA silk, SIS, and AA silk, respectively. The expression levels of Arginase and IL1-Ra were significantly different in pro-inflammatory activated macrophages exposed to bioscaffolds; however, no significant difference was observed in expression levels of Fizz1, YM1, and IL-10 **(Figure 5.12 C)**. The p-values representing the reduced expression of pro-inflammatory genes and increased expression of pro-remodeling genes after the effect of degradation products of bioscaffolds in pro-inflammatory activated macrophages are summarized in **Table 5.3**. Among bioscaffolds, the increased expression of arginase and IL-1Ra was observed in pro-inflammatory activated macrophages exposed to BA silk **(Figure 5.12 D)**.

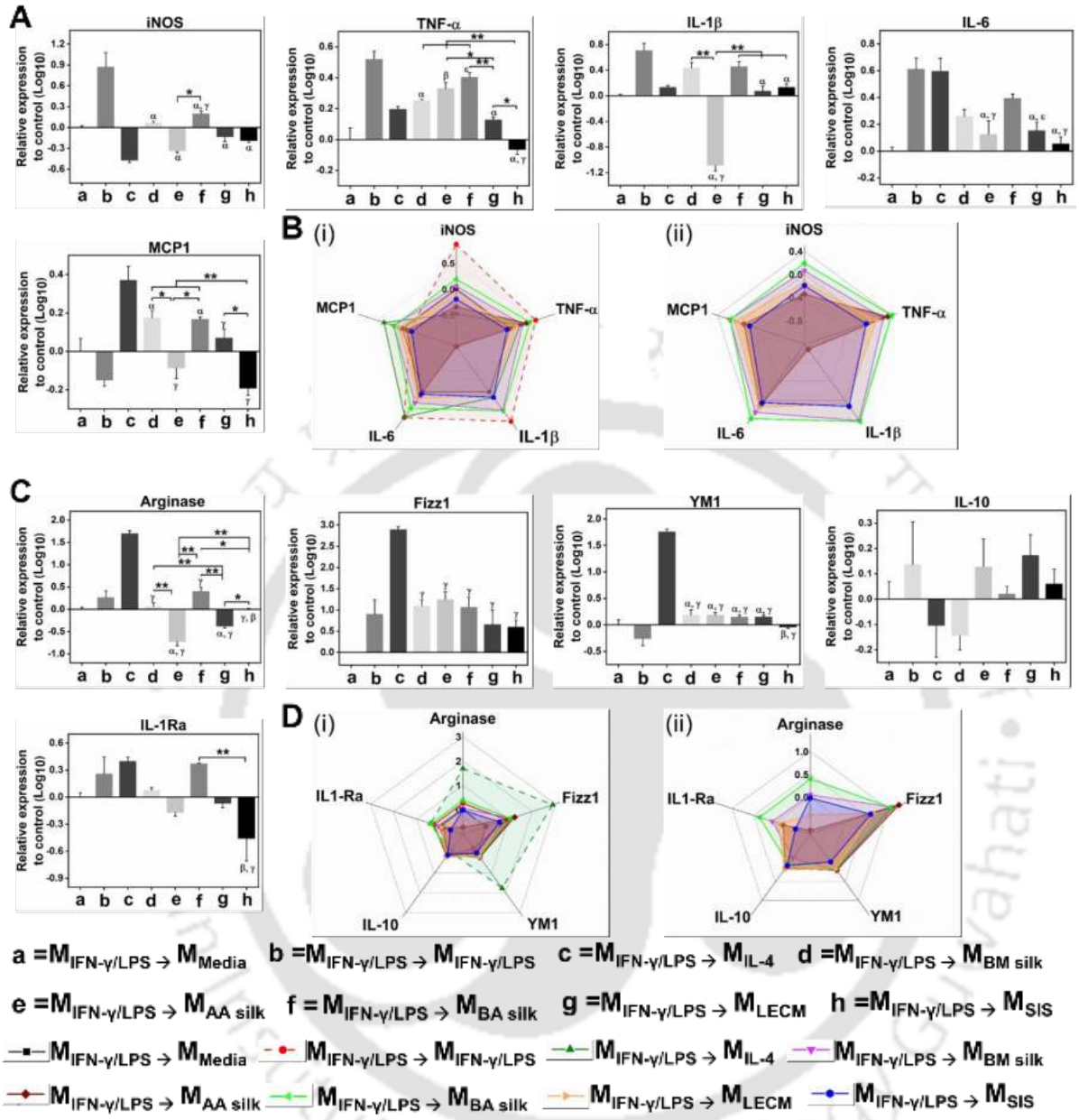

Figure 5.12. Relative transcriptional activity of pro-inflammatory genes and pro-remodeling genes after the effect of degradation products of silk (BM silk, AA silk, and BA silk) and ECM (LECM and SIS) bioscaffolds on pro-inflammatory activated macrophages. *Primary murine BMDM activated towards pro-inflammatory phenotype (IFN-γ and LPS treatment for 6 h) were exposed to 0.125 mg/mL of degradation products of silk and ECM bioscaffolds for 24 h. A known cytokine controls, $M_{IFN-\gamma/LPS}$ and $M_{IL-4,}$ were included for pro-inflammatory and pro-remodeling macrophage phenotypes, respectively. (A) Transcriptional level of pro-inflammatory genes (iNOS, TNF-α, IL-1β, IL-6, and MCP1). (B) Radar plots of averaged relative expression of pro-inflammatory genes in (i) media control, cytokines treated controls, silk and ECM treated macrophages, and (ii) BM silk, AA silk, BA silk, LECM and SIS treated macrophages. (C)*

*Transcriptional level of pro-remodeling genes (Arginase, Fizz1, YM1, IL-10, and IL1-Ra). (D) Radar plot of averaged relative expression of pro-remodeling genes in (i) media control, cytokines treated controls, silk and ECM treated macrophages, and (ii) BM silk, AA silk, BA silk, LECM and SIS treated macrophages. Data are presented as average ± standard error of mean; N = 3 biological replicates and 2 technical replicates per group; α and β indicate $p \leq 0.01$ and $p \leq 0.05$ statistically significant to pro-inflammatory cytokine control (20 ng/mL IFN-γ and 100 ng/mL LPS); γ and ε indicate $p \leq 0.01$ and $p \leq 0.05$ statistically significant to pro-remodeling cytokine control (20 ng/mL of IL-4); * and ** indicate statistical significance at $p \leq 0.05$ and $p \leq 0.01$, respectively; with Dunn-Sidak post test.*

Table 5.3. *p-values representing the reduced expression of pro-inflammatory genes and increased expression of pro-remodeling genes after the effect of degradation products on pro-inflammatory activated macrophages for figure 5.12. * and ** indicate statistical significance at $p \leq 0.05$ and $p \leq 0.01$, respectively; with Dunn-Sidak post test.*

		p-values of expression levels in				
		BM silk	**AA silk**	**BA silk**	**LECM**	**SIS**
Pro-inflammatory genes (Downregulated)	**iNOS**		* vs. BA silk			
	TNF-α				* vs. AA silk ** vs. BA silk	* vs. LECM ** vs. BM silk ** vs. AA silk ** vs. BA silk
	IL-1β		** vs. BM silk ** vs. BA silk ** vs. LECM ** vs. SIS			
	IL-6	ns between the groups				
	MCP1		* vs. BM silk * vs. BA silk			* vs. LECM ** vs. BM silk ** vs. BA silk
Pro-remodeling genes (Upregulated)	**Arginase**	** vs. AA silk ** vs. LECM		* vs. SIS ** vs. AA silk ** vs. LECM		* vs. LECM ** vs. AA silk
	Fizz1	ns between the groups				
	YM1	ns between the groups				
	IL-10	ns between the groups				
	IL1-Ra			** vs. SIS		

5.4 Discussion

The biocompatibility assessment, as defined by the Food and Drug Administration (FDA), includes safety and functionality evaluation during host tissue-biomaterial interaction [362]. The biocompatibility and constructive remodeling potential of a material can be evaluated using a partial thickness rat abdominal wall defect model [347, 363]. *In vitro* macrophage activation effects are investigated using reliable and commonly used primary murine bone marrow-derived macrophages (BMDM) [359]. The effect of degradation products of bioscaffolds, produced by exposure of all bioscaffolds to pepsin, on macrophage activation was evaluated using naive BMDM and pro-inflammatory activated BMDM. Each type of silk fibroin significantly impacted macrophage activation, which was distinct from canonical cytokine controls. The most notable findings were AA silk bioscaffold implant showed a predominant M2 pro-remodeling macrophage phenotype with fewer MGC and an increased M2-like: M1-like ratio of macrophage subpopulation following implantation in partial thickness rat abdominal wall defect model. Moreover, the BMDM response to AA silk bioscaffolds degradation products showed pronounced pro-remodeling macrophage activation, as evident from increased arginase: iNOS and Fizz1: iNOS ratio. Results of the present study suggest that AA silk bioscaffold activates pro-remodeling macrophage polarization driven constructive tissue remodeling.

All animals used in the study survived the surgery without any adverse postoperative events through the predetermined day 14 or day 35 endpoints. Post implantation, three distinct phases of a host tissue response can be described: (i) inflammatory phase, (ii) proliferative phase, and (iii) tissue remodeling phase [345, 347]. Immediately after implantation, the biomaterial associated adsorbed proteins include signals for migration of polymorphonuclear leukocytes, predominantly neutrophils and macrophages [364]. Biomaterial adsorbed proteins interact with cell adhesion receptors of migrated cells at the host tissue-implant interface to initiate cell infiltration and immune cell activation [351]. During the course of study, the bioscaffolds showed good integration with host tissue and an increased cellularity compared to defect alone site and PP surgical mesh. The host response toward the biomaterial includes neovascularization, infiltration of macrophages, and fibroblasts at the implantation site [353, 365]. The microenvironmental cues and endogenous stimuli, including the adsorbed proteins, regulate infiltrated macrophages to adhere and fuse to form MGC [365]. At 35 days, the number of MGC was substantially fewer in all the variants of bioscaffolds ($p \leq 0.01$) compared to PP mesh, which might be attributed to the non-resorbable

nature of PP mesh [363]. AA silk showed fewer ($p \leq 0.01$) MGC than BM silk and BA silk at 14 days and 35 days. A greater number of MGC present in BM silk and BA silk bioscaffolds might be attributed to phagocytosis of large-sized BM silk based degradation products [345]. The MGC is generally a characteristic of a chronic innate immune response. Masson's Trichrome staining of explants showed the early degradation of bioscaffolds and deposition of collagen fibers over 35 days.

Macrophages possessing potential plasticity play a crucial role in physiological processes in response to foreign materials, damaged tissue, and infectious agents [353]. Classically activated M1 macrophages produce a high level of inducible nitric oxide synthase (iNOS) and secrete pro-inflammatory cytokines and chemokines such as IL-1β, IL-6, and TNF-α [359]. Taken together, an increased number of pro-inflammatory macrophages and MGC in defects repaired with BM silk shows foreign body response, which was also reported in a rat model for facial augmentation [336]. Implantation of surgical PP mesh typically intensified the pro-inflammatory response, leading to a foreign body reaction with an increased number of MGC, higher percentage of TNF-α positive cells, and decreased M2-like: M1-like ratio. AA silk implant showed a higher M2-like: M1-like ratio over 35 days, similar to SIS implant supporting tissue remodeling. The presence of fibronectin, factor X, iC3b, fibrinogen, vitronectin, and RGD motifs at the implant surface acts as a fundamental adhesion receptor for immune cells [366]. It is plausible that RGD motifs of indigenous AA silk fibroin might be attributed to increased cell infiltration observed in AA silk and BA silk bioscaffolds, thus promoting cell attachment by integrin mediated pathway [271]. AA silk bioscaffold has been reported to maintain native cell phenotype and enhance functional properties of *in vitro* cultured cells, owing to intrinsic RGD motifs and bioactivity of AA silk fibroin [271, 290]. The neovascularization of implanted bioscaffolds was dependent on the continued presence of both pro-inflammatory and pro-remodeling macrophage subpopulations [367, 368]. A sequential release of VEGF, PDGF-BB, and MMP9 from the recruited M1, M2a, and M2c macrophages, respectively at the implant site, stabilized pericytes, supported sprouting, and guided new vessel formation [367]. The difference in host biological response and macrophage phenotype activation observed toward BM, and AA silk bioscaffolds might be attributed to their distinct amino acid sequences and physicochemical properties [369].

Following implantation of a resorbable biomaterial, the immune response is governed, in part, by its degradation products and surface charges in the course of graft remodeling [351]. The

monocytes and macrophages at the implantation site play a prime role in the migration and proliferation of fibroblasts and stem cells by releasing cytokines and growth factors [370]. Primary monocyte-derived macrophages have been used in an established cell culture model for *in vitro* evaluation of (i) cellular viability, (ii) macrophage activation, and (iii) maturation [353, 370]. The classical M1 macrophage phenotype induced by bacterial cell wall component (LPS) and IFN-γ secretes pro-inflammatory cytokines and nitric oxide resulting in pathogen killing [371]. The alternative M2 macrophage phenotype induced by IL-4 helps in ECM production, clearance of apoptotic cells, mitigation of the inflammatory response, and release of chemotactic factors like IL-10, supporting tissue remodeling [372]. In both studies, the canonical cytokine controls included were (i) M1-like pro-inflammatory phenotype that was induced by treating the Mϕ with 20 ng/mL of IFN-γ and 100 ng/mL of LPS; and (ii) M2-like pro-remodeling phenotype that was induced by treating the Mϕ with 20 ng/mL of IL-4. Among bioscaffolds, Mϕ exposed to degradation products of LECM bioscaffolds showed a pro-remodeling macrophage phenotype, with increased arginase: iNOS and Fizz1: iNOS ratio. Degradation products of SIS and AA silk bioscaffolds transitioned pro-inflammatory activated BMDM to a pro-remodeling phenotype, as observed from increased arginase: iNOS ratio (in SIS and AA silk treatment) and Fizz1: iNOS (in AA silk treatment).

The degradation products of all the variants of bioscaffolds downregulated the expression of iNOS, IL-1β, and MCP1 in pro-inflammatory activated BMDM compared to naive BMDM. The IL-6 was downregulated in the pro-inflammatory activated BMDM exposed to AA silk, BA silk, LECM, and SIS. The increased TNF-α expression observed in pro-inflammatory activated BMDM exposed to AA silk degradation products was consistent with a higher number of pro-inflammatory macrophages ($CD68^{+}TNF\text{-}\alpha^{+}$) in defects repaired with AA silk at 14 days. Among the pro-remodeling genes, YM1 was upregulated in the pro-inflammatory activated BMDM exposed to degradation products of all bioscaffolds compared to naive BMDM. The degradation products of silk biomaterials showed a significant difference in the macrophage activation response upon exposure to naive BMDM and pro-inflammatory activated BMDM. Previous reports have shown that primary structures and condensed structures in regenerated mulberry and non-mulberry silk fibroin influence a difference in degradation behavior [340, 373]. Comparatively, non-mulberry silk is more resistant to enzymatic degradation due to the presence of abundant polyalanine repeats, and high α-helix and β-sheets [340]. Naive BMDM and pro-

inflammatory activated BMDM exposed to degradation products of BM silk, AA silk, and BA silk bioscaffolds expressed similar Fizz1 positive cells and were statistically insignificant. Fizz1, a resistin-like molecule α (RELMα) expression, is characterized by alternatively activated murine M2a macrophages that promote wound healing during tissue repair upon stimulation via Th2-type cytokines such as IL-4 and IL-13 via the STAT6 pathway [359, 374]. Thus, Fizz1 expression data indicate that BM silk and AA silk biomaterials support similar tissue repair and healing mechanisms. AA silk degradation products treated naive BMDM, and pro-inflammatory activated BMDM showed an increased Arginase: iNOS ratio that is associated with alternatively activated macrophages induced by Il-4 cytokine. High arginase expression in murine macrophages, a characteristic of M2a macrophages, has been reported to be crucial for tissue repair, cell proliferation, and synthesis of ECM components [374, 375]. It is presumed that, at least in part, the mechanisms by which AA silk bioscaffold modulate the pro-remodeling macrophage activation response include the polyalanine repeats, cryptic peptides, RGD motifs, high crystalline primary structures and amino acid composition derived from AA silk degradation products [290, 340, 376]. The *in vitro* ability of macrophages to adopt the M2 phenotype following M1 activation is known as deactivated macrophages (M2c) [375], which possess unique gene and protein expression pattern and promotes wound healing with increased ECM deposition [367].

In summary, the present study highlights the comparison of macrophage phenotype activation and tissue response towards mulberry silk, non-mulberry silk, LECM, SIS, and surgical mesh. There are some limitations in the current study. The innate or acute immune response comprising the characterization of (i) provisional matrix on implanted materials, (ii) neutrophils recruitment, and (iii) secretion of reactive oxygen species and proteolytic enzymes towards silk biomaterials must be elucidated. Further investigations using transcriptional profiling and flow cytometric analysis to quantify the macrophage subpopulation are still needed to be studied.

5.5 Significant Findings

1. The potential implications of the present study are noteworthy. AA silk implants elicited predominantly pro-remodeling macrophage response with fewer MGC than BM silk, supporting a more constructive tissue remodeling response.
2. It was observed that the source, amino acid sequences, and physicochemical properties of silk fibroin play a significant role in determining the macrophage phenotype participating in downstream clinical outcomes.
3. Furthermore, the AA silk degradation products were able to direct pro-remodeling macrophage activation by demonstrating an increased arginase: iNOS in BMDM and Fizz1: iNOS in pro-inflammatory activated BMDM.
4. Additional characterization studies in terms of metabolic and cytokine secretion are required to have a comprehensive understanding of macrophage phenotype towards silk biomaterials.
5. On the whole, this study has the potential for understanding the macrophage phenotype stimulated by intrinsic BM silk and AA silk bioscaffolds in directing tissue regeneration through modulating macrophage polarization *in vivo* and *in vitro*.
6. Further, a complete understanding of the molecular interactions of silk bioscaffolds with the host cells that influence macrophage polarization could provide the opportunity for immune-informed silk biomaterials in tissue-specific constructive remodeling.

CHAPTER 6

Intraperitoneal administration of liver-derived extracellular matrix hydrogel promotes regeneration and alleviates liver fibrosis in acetaminophen-induced liver injury

This chapter investigates a facile therapeutic approach in treating liver fibrosis. The therapeutic role of liver extracellular matrix and *Antheraea assamensis* hydrogel in attenuating acetaminophen (APAP)-induced liver failure and subsequently promoting liver regeneration was studied using *in vitro* primary mouse hepatocytes and mouse model of APAP-induced liver injury. LECM stimulated early regeneration by inducing cyclin D1, decreasing p21, and promoting hepatocyte proliferation with increased Ki67 and PCNA expression. Our study has revealed that LECM is a potential hepatoprotective and therapeutic solution in attenuating APAP-induced liver injury and stimulating compensatory liver regeneration after APAP overdose.

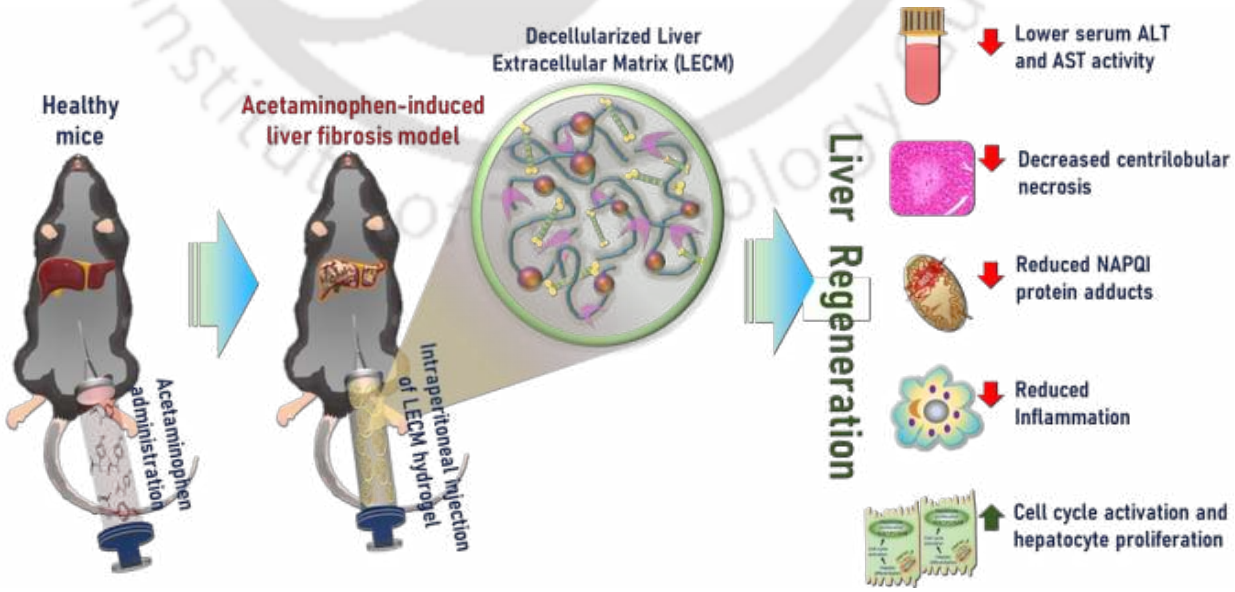

ABSTRACT

Acetaminophen (APAP) overdose causes severe hepatotoxicity and inhibits subsequent liver regeneration leading to liver failure. Liver extracellular matrix (LECM) and *Antheraea assamensis* (AA) silk fibroin have been recently explored for various clinical applications owing to its therapeutic potential. In the present study, the therapeutic role of LECM and AA in attenuating APAP-induced liver failure and subsequently promoting liver regeneration was studied using *in vitro* primary mouse hepatocytes and an APAP-induced liver fibrosis mouse model. In *in vitro* model, LECM and AA increased the metabolic activity of APAP-induced hepatocytes by activating the cell cycle and inhibiting caspase 3 activity. The mouse model of APAP-induced liver injury after severe APAP overdose (600 mg/kg) was treated intraperitoneally, 1 h post APAP with LECM and AA, and investigated after 24 h and 48 h for critical roles of APAP metabolism, formation of APAP-protein adducts, necrotic cell death, sterile inflammatory response, followed by recovery or regeneration. Histological examination suggested that both LECM and AA treatment attenuated the initiation and progression of APAP-induced liver injury by reducing necrosis, APAP-protein adducts, and inflammation. Strikingly, LECM stimulated early regeneration following APAP overdose by inducing cyclin D1, decreasing p21, and promoting hepatocyte proliferation with increased Ki67 and PCNA expression at 24 h. Indeed, hepatocyte proliferation was observed at 48 h in animals receiving AA treatment with increased Ki67 and PCNA expression. Our study has revealed that LECM as a potential hepatoprotective and therapeutic solution in attenuating APAP-induced liver injury and stimulating compensatory liver regeneration after APAP overdose in a clinically relevant model.

The findings of this chapter are under preparation for manuscript submission:

Janani G., Zhang L., Roy N., Johnson S.A., Bhushan B., Duncan A.W., Mandal B.B., and Badylak S.F. "*Intraperitoneal administration of liver-derived extracellular matrix hydrogel promotes regeneration and alleviates liver fibrosis in acetaminophen-induced liver injury*". **Manuscript under preparation**

6.1 Introduction

Acetaminophen (N-acetyl-para-aminophenol; APAP), well known as Paracetamol and Tylenol, is used as an over-the-counter medicine antipyretic and analgesic medicine worldwide at therapeutic doses [377]. However, APAP overdose leads to hepatotoxicity and drug-induced liver injury (DILI) in the Western world and developed countries, accounting for 50% of all acute liver failure (ALF) cases [378, 379]. The pathophysiology of APAP-induced liver injury and repair mechanism is complex and includes three interlinked phases (i) initiation, (ii) progression, and (iii) recovery/regeneration [377]. The initiation phase occurs within the initial 6 h administration of the toxic dose of APAP in the mouse model. Intrinsically, APAP is metabolized by cytochrome P450 2E1 (CYP2E1) to form a highly reactive toxic metabolic N-acetyl-p-benzoquinone imine (NAPQI), which is eliminated by hepatic glutathione conjugation under physiological conditions [377, 380]. APAP overdose causes glutathione depletion, and excess NAPQI accumulates in mitochondria forming cellular protein adducts, resulting in reactive oxygen species (ROS) generation, mitochondrial oxidative damage, DNA fragmentation, and ultimately centrilobular necrosis [377, 381]. The progression phase is initiated in 6 h to 24 h after initial cell death by the damaged hepatocytes [382]. The necrotic cells in the centrilobular zone release endogenous damage-associated molecular patterns (DAMPs) and proteolytic enzymes, leading to substantial recruitment of inflammatory cells and mediating localized inflammation [377, 380]. The recovery or regeneration phase after APAP-induced ALF is dose-dependent and was observed after 24 h of APAP administration to 96 h [382]. The repair mechanism is associated with the removal of necrotic debris by the invading immune cells, followed by compensatory hepatocellular proliferation that is activated by extensive paracrine and exocrine signaling via growth factors and cytokines [383]. At high doses of APAP, the recovery phase slows down, and liver regeneration is inhibited, leading to multi-organ failure and death [383]. Currently, N-acetylcysteine (NAC) therapy within 8 h of APAP overdose is the only approved and successful pharmacological intervention for APAP hepatotoxicity in clinical practice, which acts as a ROS scavenger by replenishing glutathione and blocking hepatic damage [380, 384, 385]. However, orthotopic liver transplantation is the ultimate treatment approach for patients with advanced ALF, and this procedure is limited by cost, shortage of healthy donors, and life-long use of immunosuppressive drugs [386].

The need for a potential therapeutic molecule has led researchers to investigate the therapeutic efficacy of natural herbal products, growth factors, cytokines, stem cells, and cell-derived molecules in attenuating ALF and facilitating regeneration [378, 385]. The pretreatment of natural products associated with anti-oxidative and anti-inflammatory activities has effectively prevented APAP-induced toxicity by scavenging ROS [383, 387, 388]. However, any intervention would be clinically relevant only when the treatment material has been administered post-APAP intoxication and shown therapeutic potential in attenuating the APAP-induced liver injury [385]. Mesenchymal stem cell (MSC) therapies, including intravenous administration of human umbilical cord-derived MSC and adipose-derived MSC after APAP intoxication, improved survival rates and promoted tissue repair owing to its immunomodulatory and anti-inflammatory properties [386, 389]. Despite decades of research on exploring a therapeutic solution for APAP-induced liver injury, a novel hepatoprotective bioactive compound that alleviates the APAP-induced liver injury and promotes the regeneration of damaged liver when administered after APAP intoxication is yet unknown. Researchers have highlighted that timely stimulation of liver regeneration after APAP overdose through vascular endothelial growth factor [390], and epidermal growth factor receptor [379] reduced necrosis and assisted in hepatocyte proliferation. In recent years, the prominent role of liver-specific extracellular matrix (LECM) hydrogel in liver tissue engineering is emerging, owing to the presence of growth factors, cytokines, and cell-secreted exosomes in LECM [207, 391, 392]. LECM hydrogels have maintained hepatic phenotype and promoted the differentiation and functionality of cultured primary hepatocytes *in vitro* [47, 281]. An injectable LECM hydrogel improved the viability and hepatic functions of primary transplanted hepatocytes *in vivo* over subcutaneous implantation compared to collagen hydrogels, providing a suitable matrix for liver tissue engineering [224, 391]. Similarly, silk fibroin isolated from non-mulberry silkworm *Antheraea assamensis* (AA), a proteinaceous biomaterial with intrinsic RGD motifs has been explored for functional remodeling of various tissues like cartilage, skin, blood vessels, and bone [290]. Molecular studies have revealed that AA silk fibroin possesses a higher percentage (3.9%) of alkaline amino acids, including histidine, arginine, and lysine, which were reported to have strong antioxidant activity [42, 206]. Overall, these studies highlighted stimulating liver regeneration using bioactive molecules after APAP overdose in patients as a plausible therapeutic option.

The role of LECM and AA hydrogel in attenuating APAP-induced liver injury and subsequent liver regeneration is unknown, which was investigated in the present study in *in vitro* primary mouse hepatocytes (PMH) and *in vivo* APAP-induced liver fibrosis mouse model. We administered the therapeutic agent intraperitoneally (i.p.) 1 h after APAP overdose (600 mg/kg) in injectable hydrogel format and compared the protective role of LECM and AA hydrogels with the gold standard NAC treatment. We performed *in vitro* metabolic activity and gene expression analysis to assess the hepatoprotective effects of LECM and AA hydrogel on PMH subjected to APAP-induced cell damage. Further, the hepatoprotective potential of LECM and AA hydrogel in attenuating APAP-induced liver fibrosis mouse model was explored by assessing the APAP metabolism, NAPQI accumulation, necrotic cell death, sterile inflammatory response followed by liver regeneration.

6.2 Materials and Methods

6.2.1 Experimental Design

The present study aims to determine the therapeutic effect of liver extracellular matrix (LECM) hydrogel and *Antheraea assamensis* (AA) silk hydrogel upon APAP-induced liver fibrosis model in *in vitro* primary mouse hepatocytes (PMH) and *in vivo* mice model. All animal experiments were performed in accordance with the Institutional Animal Care and Use Committee (IACUC) at the University of Pittsburgh. For *in vitro* studies, LECM hydrogel and AA hydrogel were supplemented in the media in APAP-induced PMH, followed by the metabolic activity and gene expression profile of hepatocytes were assessed to examine the protective effect of supplements. For *in vivo* studies, treatment groups including LECM hydrogel and AA hydrogel were intraperitoneally (i.p.) administered 1 h following 600 mg/kg APAP intoxication in mice. Similarly, NAC treatment i.p. 1 h following 600 mg/kg APAP intoxication, served as the positive control. The animals were sacrificed at 24 h and 48 h post-treatment, and the protective effect of treatment groups upon APAP-induced liver fibrosis injury was assessed in terms of serum ALT, serum AST, necrotic area, formation of APAP-protein adducts, CYP2E1 expression, macrophage infiltration, and cell proliferation.

6.2.2 Preparation of LECM and AA hydrogels

LECM was obtained by decellularizing healthy porcine liver using a combined enzymatic and chemical decellularization method [355]. Under constant stirring, thin liver slices were

incubated in 0.02% (v/v) trypsin/ 0.05% (w/w) ethylenediaminetetraacetic acid (EDTA) solution for 1 h, followed by incubated in 3% (v/v) Triton X-100 solution for 1 h. A deionized water wash and gentle mechanical massaging were included between the steps to facilitate cell removal. Then, the liver slices were incubated in 4% (w/v) sodium deoxycholic acid solution, washed with deionized water, disinfected with 0.1% (v/v) peracetic acid solution, lyophilized, and milled to obtain dry LECM powder. The decellularization efficiency was assessed by DNA quantification, Hematoxylin and Eosin (H&E, ThermaFisher Scientific) staining, and 4'-6'-diamidino-2-phenylindole (DAPI) staining of native liver and LECM. The posterior and middle silk glands harvested from the 5th instar fully matured healthy AA silkworms were squeezed to extrude silk proteins [281]. The silk proteins were dissolved in 1% (w/v) sodium dodecyl sulfate (SDS) solution, dialyzed against deionized water at 4°C, lyophilized, and stored as AA silk pellets. The lyophilized LECM and AA were enzymatically digested as previously described [393], with pepsin (1 mg/mL in 0.01 N HCl) by incubating 10 mg of LECM and AA powder at room temperature (RT) for 48 h under constant stirring. The LECM and AA digest of 10 mg/mL were neutralized to physiological pH of 7.4 using 10X phosphate-buffered saline (PBS) and 0.1 M NaOH at 4°C. Then, the digest was diluted with 1X PBS at 4°C to the desired concentration for *in vitro* and *in vivo* studies. The temperature was gradually increased to 37°C allowing gelation to form LECM and AA hydrogels.

6.2.3 Effect of LECM and AA hydrogels as treatments in *in vitro* APAP-induced liver fibrosis model

6.2.3.1 Isolation of primary mouse hepatocytes via enzymatic liver perfusion

The PMH were isolated from healthy adult male C57BL/6 mice (Jackson Laboratories, Bar Harbor, Maine) using a two-step collagenase/DNase perfusion method [394]. Following general anesthesia (20 mg/mL ketamine and 2 mg/mL xylazine) induction, a catheter was gently introduced into the portal vein or inferior vena cava, and the liver was circulated with 0.3 mg/mL collagenase II and 0.05 mg/mL DNase solution. The digested livers were dispersed in wash media comprising DMEM-F12 media with 5% (v/v) FBS to dissociate liver cells. The liver cell suspension was passed through a 70 µm cell strainer and centrifuged twice at 600 rpm for 3 min to separate the parenchymal hepatocytes in the pellet. The isolated PMH with >85% cell viability (by Trypan blue staining) were seeded at a density of 6×10^4 cells per well in Corning Primaria^{TM}

24 well plates. The DMEM-F12 culture media with 0.5% (v/v) FBS and 1X ITS supplement was used for all experiments.

6.2.3.2 Generation of *in vitro* APAP-induced liver fibrosis model and treatment

An *in vitro* APAP-induced liver fibrosis model was developed after 24 h of cell attachment. The APAP stock solution of 10 mM was prepared freshly in warm culture media and maintained at 37°C until APAP dissolved completely. On day 2, the PMH were treated with 5 mM and 7.5 mM APAP suspended in culture media for 24 h at 37°C, and PMH without APAP treatment were labeled as healthy **(Figure 6.2 A)**. After 24 h of APAP disease induction on day 3, the hepatocytes were treated with LECM hydrogel (50 µg, 100 µg, and 200 µg) and AA hydrogel (25 µg, and 50 µg) suspended in culture media and incubated at 37°C for 24 h. The fresh media was replenished in healthy and APAP groups. After 24 h of LECM and AA treatments on day 4, the metabolic activity and gene expression profile of hepatocytes were assessed.

6.2.3.3 Assessment of metabolic activity

The metabolic activity of healthy, APAP, APAP + LECM, and APAP + AA in *in vitro* 5 mM and 7.5 mM APAP-induced liver fibrosis model was determined using the alamar blue assay. At the end of 24 h treatment on day 4, the media was removed, and cells were treated with 250 µL of 10% (v/v) alamar blue solution suspended in culture media for 4 h at 37°C. The reduced alamar blue dye solution was transferred to a fresh 96 well-plate, and absorbance was recorded at 570 nm and 600 nm. The metabolic activity of healthy, APAP, APAP + LECM, and APAP + AA groups was calculated from the percentage reduction in alamar blue and represented as fold change relative to the metabolic activity of healthy PMH. From alamar blue assay, 100 µg LECM and 25 µg AA as supplements showed significantly improved metabolic activity in the 7.5 mM APAP-induced liver fibrosis model, and this concentration was selected further to study the variation in gene expression among the groups.

6.2.3.4 Isolation of RNA and quantitative real-time polymerase chain reaction analysis

On day 4, the mRNA expression levels in the 7.5 mM APAP-induced liver fibrosis model treated with 100 µg LECM and 25 µg AA were assessed using quantitative real-time polymerase chain reaction (qRT-PCR). Briefly, the cell lysates were collected from healthy, APAP, APAP + LECM, and APAP + AA using TRIzol reagent, per the manufacturer's instructions. The aqueous layer from cell lysates was separated using chloroform and treated with 3M sodium acetate (1:10

volume), and 2-propanol (1:1 volume) to obtain an RNA pellet. The RNA pellet was washed with 75% (v/v) ethanol and suspended in sterile 20 µL nuclease-free water. The RNA of 1 µg was reverse transcribed to cDNA using the High Capacity cDNA Reverse Transcription Kit (Invitrogen). The relative expression levels of cell cycle regulators – Cyclin D1, Cyclin E1, Cyclin A2, Cyclin B1; cell proliferation – PCNA (Proliferating Cell Nuclear Antigen); transcription factors – EGFR (Epidermal Growth Factor Receptor), HNF4α (Hepatocyte Nuclear Factor4α); hepatocyte metabolism – Arginase 1, CYP2E1; cell cycle inhibitor – p21; and apoptosis – Caspase 3 was determined using PowerUp™ SYBR® Green Master Mix. The β-Actin expression levels were used for data normalization, and results were represented as fold change ($2^{-\Delta\Delta Ct}$) relative to expression levels of healthy PMH.

6.2.4 Effect of LECM and AA hydrogels as treatments in APAP-induced liver fibrosis mouse model

6.2.4.1 Animals, APAP-induced liver fibrosis model, treatments, and tissue collection

A total of fifty-eight healthy male C57BL/6 mice 6 to 8 weeks old (Jackson Laboratories, Bar Harbor, Maine) weighing approximately 20-30 g were randomly sorted into nine discrete groups (n=5 per healthy and group at 24 h time point, n=7 per group at 48 h time point). All animals were kept in standard laboratory conditions, fed a normal diet, and acclimatized to the environment for a week before starting the experiment. The APAP-induced liver fibrosis model was generated in mice by administering 600 mg/kg APAP i.p. after 12 h overnight fasting. The APAP solution was prepared in sterile warm saline solution and used freshly. After 1 h of APAP administration, mice were administered i.p. with (i) 5 mg/mL LECM, (ii) 5 mg/mL AA, or (iii) 5 mg/mL LECM + AA for 24 h as treatment groups, and designated as APAP + LECM, APAP + AA, and APAP + (LECM + AA), respectively. Similarly, 1200 mg/kg NAC (pH 7.4), an approved antidote for APAP-induced hepatotoxicity, was administered i.p. following 1 h APAP intoxication in the positive control group to compare the effect of NAC with LECM, AA, and LECM + AA. Animals were sacrificed at 24 h after treatment, and blood and livers were analyzed for serum activity, gene expression, and histology. Serum transaminase activity and percentage necrotic area showed that animals treated with LECM + AA group didn't recover from APAP-induced liver injury, and showed similar serum activity and necrosis as APAP animals. Accordingly, for 48 h time point, mice were administered i.p. with (i) 5 mg/mL LECM, (ii) 5 mg/mL AA, or (iii) 1200 mg/mL NAC as treatment groups, and designated as APAP + LECM, APAP + AA, and APAP + NAC,

respectively. Animals were sacrificed after 48 h treatment, followed by blood and liver were collected and processed for serum analysis, gene expression, and histology.

6.2.4.2 Serum alanine aminotransferase (ALT) and aspartate aminotransferase (AST) activity

The blood samples collected from healthy and all the treatment groups following 24 h and 48 h APAP intoxication were centrifuged at 5000 rpm, 4°C for 5 min to isolate serum, and serum was stored at -20°C until analysis. The serum samples were assessed for liver enzymes, alanine aminotransferase (ALT), and aspartate aminotransferase (AST) using Infinity™ ALT reagent and Infinity™ AST reagent (Thermo Fisher Scientific), respectively, per manufacturer's instructions. Briefly, 10 µL of serum was mixed with 100 µL of respective reagent, and absorbance was recorded at 340 nm, 37°C in kinetic mode. The ALT activity (U/L) and AST activity (U/L) were calculated using,

$$\text{Activity (U/L)} = \Delta\text{Ab/min} \times \text{Factor}$$

$$\text{Factor} = (\text{TV} \times 1000)/6.3 \times \text{SV} \times \text{P}$$

where,

ΔAb/min = Difference in absorbance per minute

TV = Total reaction volume (mL)

SV = Sample volume (mL)

P = Cuvette pathlength (cm)

6.2.4.3 Necrotic area analysis

The liver samples from healthy, APAP, and all treatment groups following 24 h and 48 h APAP intoxication were fixed in 10% (v/v) Formalin, embedded in paraffin blocks, and sectioned into 5 µm thickness. The sections were stained with H&E following standard techniques, and images were captured at the bright field using Nikon ECLIPSE Ti2 inverted microscope (NIKON Instruments Inc.). The images were processed, and the necrotic area around the centrilobular region was measured using ImageJ software (NIH, USA), followed by the percentage of necrosis (%) was calculated for each animal.

6.2.4.4 Isolation of RNA and qRT-PCR analysis

The liver samples from healthy, APAP, APAP + LECM, and APAP + AA following 24 h and 48 h APAP intoxication were snap-frozen in liquid nitrogen and stored at -80°C. The total RNA from all samples was isolated and converted to cDNA as detailed in the *methodology section 6.2.3.4*. The relative expression levels of hepatocyte metabolism markers - CYP2E1, arginase-1; kupffer cell marker – CLEC7A; cell cycle regulator maker – Cyclin D1; and cell cycle inhibitor maker – p21 were determined using PowerUp™ SYBR® Green Master Mix. The β-Actin expression levels were used for data normalization, and results were represented for each animal as fold change ($2^{-\Delta\Delta Ct}$) relative to expression levels of healthy animals.

6.2.4.5 APAP Protein Adducts Measurement

The NAPQI accumulation in the centrilobular regions of healthy, APAP, APAP + LECM, and APAP + AA following 24 h and 48 h APAP intoxication was assessed by immunohistochemistry (IHC) detection of Nitrotyrosine [383]. The sections were treated with xylene, a gradient of ethanol, running water, and citric acid-based antigen retrieval buffer (pH 6.0, 95°C for 20 min). Then, the sections were washed with 1X Tris-buffered saline containing 0.05% Tween 20 (pH 7.4) and incubated for 20 min in blocking buffer containing 2.5% (v/v) normal horse serum. The samples were sequentially incubated at RT with primary antibody against 3-nitrotyrosine (mouse monoclonal, Abcam, ab53232, 1:250) for 1 h, biotinylated universal secondary antibody solution for 30 min, and VECTASTAIN Elite ABC reagent (PK-7200, VECTOR Laboratories) for 30 min. The sections were incubated with ImmPACT DAB peroxidase substrate solution at dark conditions for 20 s, counterstained with hematoxylin, and representative images were captured at the bright field using a Nikon ECLIPSE Ti2 microscope. Ten images per animal (including lobe 1, lobe 2, and lobe 3) were processed using ImageJ software for quantifying the area of NAPQI protein adducts and the percentage area of NAPQI protein adducts per field was calculated for each animal.

6.2.4.6 Immunolabeling and quantification

The healthy, APAP, APAP + LECM, and APAP + AA following 24 h and 48 h APAP intoxication were assessed for the expression of acetaminophen metabolism marker - CYP2E1, arginase-1; macrophage marker – F4/80; transcription factor – HNF4α; and cell proliferation marker – Ki67 using immunolabeling. The primary antibodies used were CYP2E1 (Rabbit

monoclonal, Novus Biologicals, NBP2-67021, 1:100), Arginase-1 (Rabbit polyclonal, Abcam, ab91279, 1:200), F4/80 (Rat monoclonal, Novus Biologicals, NB600-404, 1:250), HNF4α (Rabbit monoclonal, Abcam, ab201460, 1:500), and Ki67 (Rabbit monoclonal, Abcam, ab16667, 1:250). The secondary antibodies used were Alexa Fluor 488 (goat anti-rabbit, Thermo Fisher Scientific, A11034, 1:250) for CYP2E1 and HNF4α; Dylight 594 (goat anti-rabbit, Abcam, ab96885, 1:100) for Arginase-1 and Ki67; and Alexa Fluor 488 (goat anti-rat, Thermo Fisher Scientific, A21212, 1:200) for F4/80. The sections were co-immunostained for F4/80 and Arginase-1 to understand the macrophage infiltration and zone-specific liver metabolism. For immunofluorescence staining, the sections after the antigen retrieval step were incubated overnight with the primary antibody solution at respective dilutions at 4°C. The sections were washed three times with 1X PBS, incubated with corresponding secondary antibody at respective dilutions for 1 h, counterstained with DAPI, and mounted with Dako fluorescent mounting media. The representative fluorescence images were captured at random places using Nikon ECLIPSE Ti2 inverted fluorescence microscope. Ten images per animal (including lobe 1, lobe 2, and lobe 3) were processed using ImageJ software, and F4/80 positive cells, HNF4α positive cells, and Ki67 positive cells for each animal were quantified.

6.2.4.7 Immunohistochemistry and quantification of PCNA positive cells

The individual cell cycle phase in the proliferating cells of healthy, APAP, APAP + LECM, and APAP + AA following 24 h and 48 h APAP intoxication was assessed by IHC detection of endogenous cell replication marker, proliferating cell nuclear antigen (PCNA), as previously described [395]. Briefly, the sections were rehydrated and incubated in a citric acid buffer for antigen retrieval (95°C, 20 min) and blocking buffer (RT, 20 min). The primary antibody against PCNA (Mouse monoclonal, CS2586, 1:200, Cell Signaling Technology) was applied to the samples and incubated at RT for 1 h. Then, the sections were serially incubated in biotinylated universal secondary antibody solution (30 min), VECTASTAIN Elite ABC reagent (30 min), and DAB peroxidase substrate solution (1 min). The sections were counterstained with hematoxylin, mounted, and images were captured at the bright field using Nikon ECLIPSE Ti2 inverted microscope. The PCNA-stained sections with distinct brown nuclei were used for PCNA scoring for each animal by randomly processing ten images per animal (including lobe 1, lobe 2, and lobe 3) [396]. The number of (i) cells in G1 phase, (ii) cells in S phase, (iii) cells in G2 phase, and (iv) cells in Mitosis was defined as cells with light brown nuclear staining, deep brown nuclear staining,

diffused brown cytoplasmic staining, and brown cytoplasmic staining with deep blue nuclear staining, respectively [382].

6.2.5 Statistical analysis

All *in vitro* data presented as bar graphs are expressed as mean ± SEM (Standard Error Mean) from three biological replicates. All *in vivo* data presented as box graphs represented individual data points from each animal, and the mean of each group was indicated as a black line in the box. A One-Way ANOVA test followed by post-hoc Dunn's multiple comparison test was used to determine the statistically significant differences between groups. Results are considered statistically significant at p-value lower than 0.05, 0.01, and 0.001.

6.3. Results

6.3.1 Variation in metabolic activity of PMH following LECM and AA treatment in *in vitro* APAP-induced liver fibrosis model

The LECM appeared translucent and showed residual DNA content of 12.55 ± 2.97 ng/mg of dry weight after decellularization, which was within the reported permissible DNA content (50 ng/mg of dry weight) in decellularized tissues **(Figure 6.1 A-B)**. The H&E and DAPI stained LECM revealed the preservation of ECM architecture and clearance of cell remnants in contrast to the native liver, confirming the decellularization efficiency **(Figure 6.1 C)**.

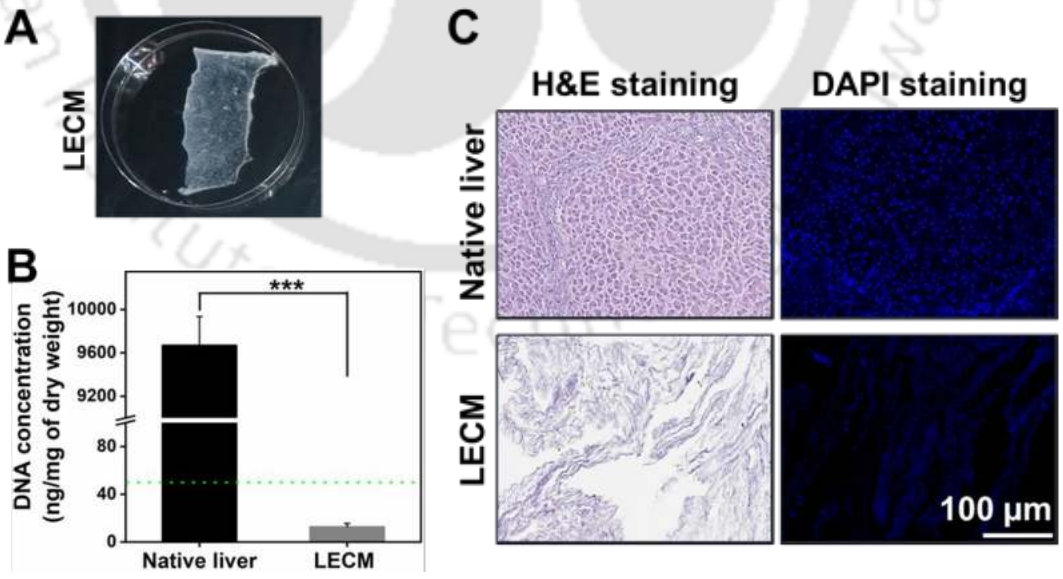

Figure 6.1. Decellularization of porcine liver and their characterization. *(A) Representative photograph of decellularized liver extracellular matrix (LECM). (B) DNA content in native liver and LECM. The green dashed line represents the permissible amount (50 ng) of DNA in the*

*decellularized tissues. Data are represented as mean ± SEM for n=3 samples per group. *** represents p ≤ 0.001. (C) H&E and DAPI staining showing the preservation of ECM architecture and the absence of cell nuclei in LECM. Scale bar: 100 µm.*

The protective effect of LECM and AA hydrogel upon *in vitro* 5 mM and 7.5 mM APAP-induced liver fibrosis model was investigated by assessing the metabolic activity of PMH on day 4 **(Figure 6.2 A)**. Exposure of 5mM APAP in PMH declined ($p \leq 0.05$) the metabolic activity of APAP-induced PMH compared to healthy **(Figure 6.2 B)**. In 5 mM APAP-induced liver fibrosis model, the APAP + (LECM 100 µg) group attenuated the APAP effect, and the metabolic activity increased ($p \leq 0.01$) compared to APAP. Then, an *in vitro* 7.5 mM APAP-induced liver disease model was generated to significantly ($p \leq 0.01$) reduce the hepatocyte metabolic activity in APAP than healthy to assess the protective effect of LECM and AA hydrogel **(Figure 6.2 C)**. In 7.5 mM APAP-induced liver fibrosis model, LECM (50 µg, 100 µg, and 200 µg), and AA (25 µg) as treatment groups attenuated the APAP effect, and the metabolic activity of PMH increased ($p \leq 0.01$) compared to APAP.

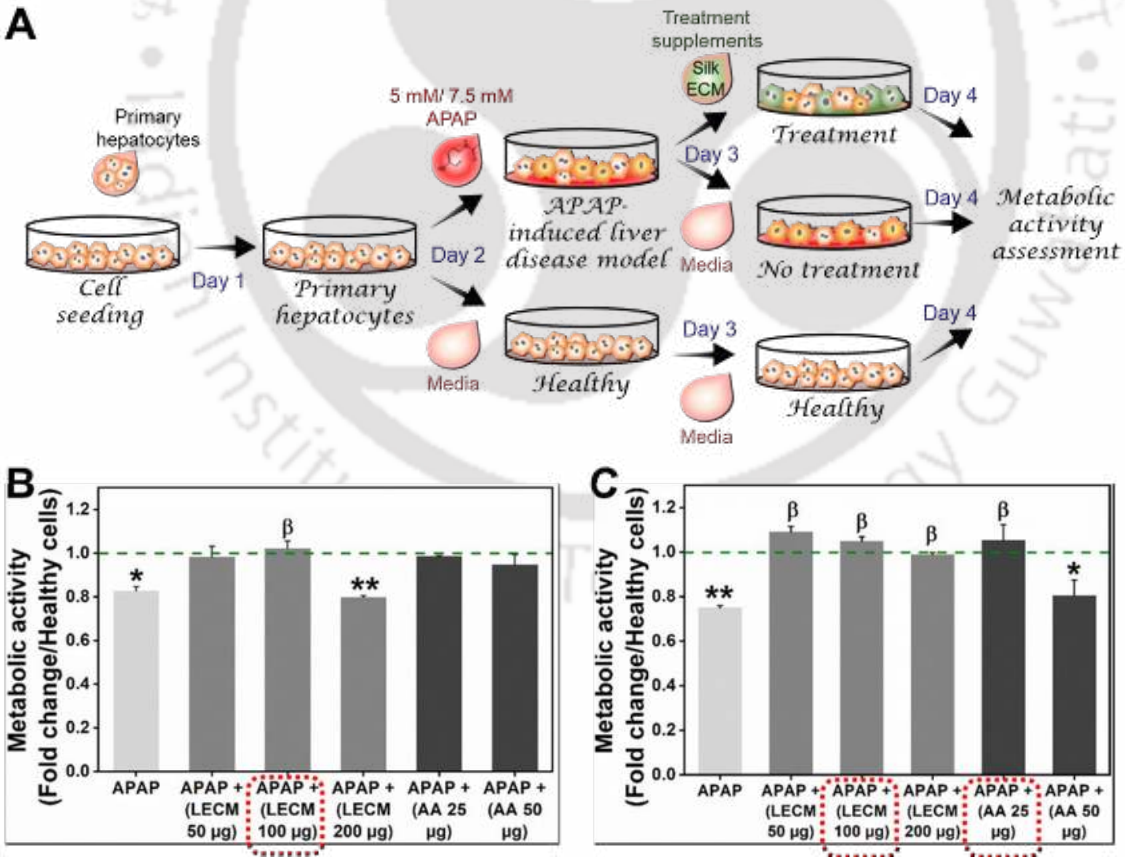

Figure 6.2. Role of LECM and AA silk as supplements in recovering damaged hepatocytes, and effects on hepatocytes metabolic activity in in vitro APAP-induced liver fibrosis model. *(A)*

*Schematics showing the generation of in vitro APAP-induced liver disease model, treatment, and metabolic analysis following treatment. (B, C) The metabolic activity of APAP (diseased hepatocytes), APAP + LECM, APAP + AA in (B) 5 mM APAP-induced liver fibrosis model and (C) 7.5 mM APAP-induced liver fibrosis model, as analyzed using alamar blue assay. Data are represented as mean ± SEM. The green dashed line represents the metabolic activity of healthy hepatocytes. * $p \leq 0.05$, ** $p \leq 0.01$ vs healthy hepatocytes; $^{\alpha}$ $p \leq 0.05$, $^{\beta}$ $p \leq 0.01$ vs APAP.*

6.3.2 Variation in cellular morphology and expression of gene markers associated with regeneration following LECM and AA treatment in *in vitro* 7.5 mM APAP-induced liver fibrosis model

The LECM (100 µg) and AA (25 µg) treatment in 7.5 mM APAP-induced liver fibrosis model modulated the PMH morphology, cell proliferation, and metabolism associated genes compared to APAP **(Figure 6.3)**. On day 3, cell death and loss of hepatocyte-like polygonal/cuboidal morphology were observed in APAP-induced PMH compared to healthy **(Figure 6.3 B)**. Post-treatment, APAP + LECM and APAP + AA retained the hepatocyte morphology with increased cell proliferation and minimal cell death compared to APAP-induced PMH. Quantitative gene expression analysis revealed a differential expression of cyclin D1, cyclin E1, cyclin A2, cyclin B1, PCNA, EGFR, HNF4α, Arginase 1, CYP2E1, p21, and Caspase 3 among the groups **(Figure 6.3 C)**. Our results showed significant downregulation of cyclin D1, cyclin A2, and cyclin B1 expression in APAP, APAP + LECM, and APAP + AA compared to healthy **(Figure 6.3 C, i)**. Relatively, the expression levels of cell cycle regulators, cyclin D1 (28.0 fold), cyclin A2 (1.8 fold), and cyclin B1 (1.4 fold) was upregulated ($p \leq 0.05$) in APAP + LECM than APAP + AA. Specifically, cyclin B1 (1.6 fold) expression was upregulated ($p \leq 0.05$) in APAP + LECM compared to APAP, and cyclin E1 (1.9 fold) expression was upregulated ($p \leq 0.05$) in APAP + AA compared to healthy. Overall, the PCNA gene, known for cell replication, was upregulated in APAP + LECM ($p \leq 0.01$) and APAP + AA ($p \leq 0.05$) with a fold increase of 1.7 and 1.5, respectively, compared to healthy. EGFR expression was downregulated ($p \leq 0.001$) in diseased and treated groups than in healthy **(Figure 6.3 C, ii)**. The expression levels of HNF4α significantly upregulated in APAP + LECM compared to APAP (1.5 fold) and healthy (2.2 fold). Arginase 1 expression was significantly upregulated in APAP and APAP + LECM compared to healthy. The Arginase 1 expression was significantly upregulated in APAP + LECM compared to APAP (1.6 fold) and APAP + AA (3.4 fold) **(Figure 6.3 C, iii)**. The expression levels of CYP2E1 were upregulated in APAP ($p \leq 0.001$), APAP + LECM ($p \leq 0.001$), and APAP + AA ($p \leq 0.01$)

compared to healthy; and p21 expression was not significant among groups **(Figure 6.3 C, iv)**. Caspase 3 expression level was significantly upregulated in APAP compared to healthy (1.9 fold), APAP + LECM (1.5 fold), and APAP + AA (1.6 fold).

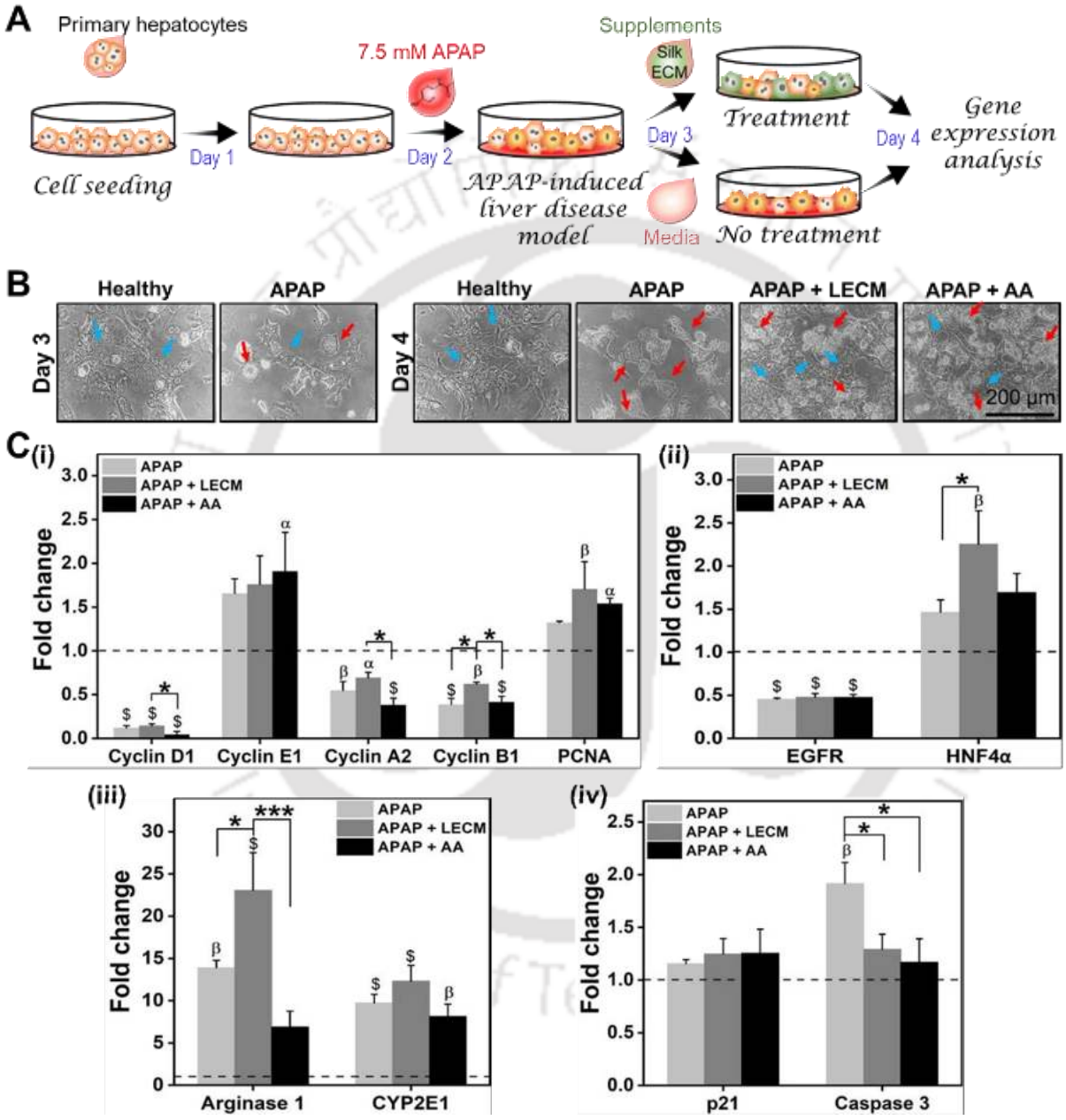

Figure 6.3. Gene expression analysis of markers associated with hepatocyte regeneration following LECM (100 µg), and AA (25 µg) treatment in in vitro 7.5 mM APAP-induced liver fibrosis model. *(A) Schematics showing the process of generating APAP-induced liver fibrosis model, treatment, and analysis. (B) Microscopic images of healthy, APAP at day 3 after seeding PMH; and healthy, APAP, APAP + LECM and APAP + AA at day 4 after seeding PMH. Scale*

*bar: 200 µm. The red and blue arrows represent the damaged and healthy hepatocytes, respectively. (C) Relative gene expression of markers associated with (i) cell division, (ii) transcription factor, (iii) metabolism, and (iv) cell cycle inhibitor and apoptosis. Data are represented as mean ± SEM. The black dashed line represents the expression of the target gene in healthy PMH. $^{\alpha}$ $p \leq 0.05$, $^{\beta}$ $p \leq 0.01$, $^{\$}$ $p \leq 0.001$ vs healthy hepatocytes; * $p \leq 0.05$, ** $p \leq 0.01$, and *** $p \leq 0.001$.*

6.3.3 ALT activity, AST activity, and liver histopathology following 24 h treatment of LECM, AA, and LECM + AA in APAP-induced liver fibrosis mice model

We investigated the protective effect of LECM, AA, and LECM + AA (administered 1 h post-APAP, i.p.) in mice following APAP overdose (600 mg/kg, i.p.) by assessing serum ALT, serum AST, histopathology, and gene expression at 24 h **(Figure 6.4 A)**. Representative images of the whole abdominal cavity and liver showed that the i.p. administered treatment samples were not precipitated or settled at 24 h **(Figure 6.4 B)**. The H&E stained liver sections showed centrilobular necrosis, a characteristic of APAP-induced liver injury **(Figure 6.4 C)**. The ALT and AST activity significantly elevated in APAP, APAP + AA, and APAP + (LECM + AA) compared to healthy **(Figure 6.4 D-E)**. Four of five animals receiving LECM and three of five animals receiving AA presented lower ALT activity than the average of ALT in the APAP group **(Figure 6.4 D)**. Compared to NAC treatment, ALT activity was significantly higher in APAP, APAP + AA, and APAP + (LECM + AA). However, ALT activity was higher in all five animals receiving a combination of LECM and AA than the average of ALT in the APAP group. Four of five animals receiving LECM and two of five animals receiving AA presented lower AST activity compared to the average of AST in the APAP group **(Figure 6.4 E)**. The ALT and AST activity in animals receiving LECM and NAC treatment were not significantly different from healthy. The histopathological approach of scoring the liver tissues for the percentage of necrosis showed diminished ($p \leq 0.001$) injury in animals receiving LECM (16.4 ± 1.9), AA (23.4 ± 3.9), and NAC (11.7 ± 3.2) treatment compared to APAP (29.2 ± 4.8) **(Figure 6.4 F)**. Comparatively, LECM alleviated ($p \leq 0.001$) APAP-induced liver injury than AA and LECM + AA; AA alleviated ($p \leq 0.001$) APAP-induced liver injury than LECM + AA. The necrotic area was higher in animals receiving LECM ($p \leq 0.05$), AA ($p \leq 0.001$), and LECM + AA ($p \leq 0.001$) treatment compared to NAC treatment.

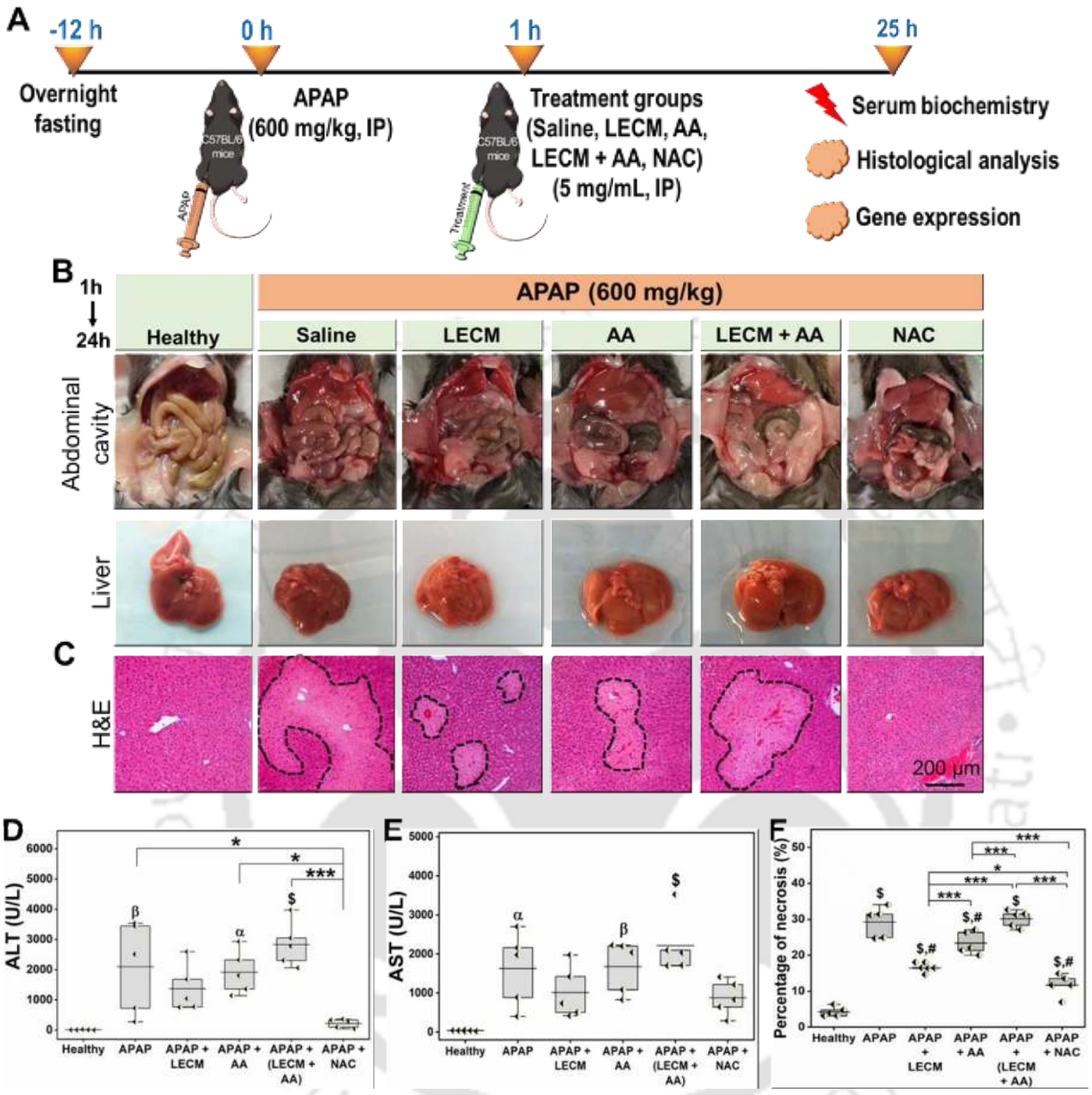

Figure 6.4. Early treatment of LECM, AA, LECM + AA, and NAC (administered 1 h post-APAP) in attenuating APAP-induced liver fibrosis injury (600 mg/kg) over 24 h. *(A) Study design depicting the timeline of 600 mg/kg APAP disease induction, treatment administration, and analysis in C57BL/6 mice. (B) Representative images of whole abdominal cavity and liver post 24 h in healthy, disease, and treatment groups. (C) H&E staining outlining the necrotic core (dashed black lines) Scale bar: 200 µm. (D) Serum ALT. (E) Serum AST. (F) Percentage of necrotic area, N = 5 mice per group. Data are represented as a box plot overlaying the individual data point from each animal, and the mean of each group is indicated as a black line in the box.* $^{\alpha}$ *p ≤ 0.05,* $^{\beta}$ *p ≤ 0.01,* $^{\$}$ *p ≤ 0.001 vs healthy animals;* $^{\#}$ *p ≤ 0.001 vs APAP; * p ≤ 0.05, ** p ≤ 0.01, and *** p ≤ 0.001.*

6.3.4 ALT activity, AST activity, and liver histopathology following 48 h treatment of LECM, and AA in APAP-induced liver fibrosis mice model

The protective effect of LECM, and AA (administered 1 h post-APAP, i.p.) in mice following APAP overdose (600 mg/kg, i.p.) was studied by assessing serum ALT, serum AST, histopathology, and gene expression at 48 h **(Figure 6.5 A)**. The gross images of the abdominal cavity and whole liver showed that the i.p. administration of treatment samples was not precipitated at 48 h **(Figure 6.5 B)**. The centrilobular necrosis scoring of H&E stained liver sections showed a higher liver injury at 48 h following APAP overdose **(Figure 6.5 C)**. The ALT activity was not significant among APAP, APAP + LECM, and APAP + AA **(Figure 6.5 C-D)**. Serum ALT activity was significantly higher in APAP, APAP + LECM, and APAP + AA compared to healthy animals **(Figure 6.5 D)**. Compared to NAC treatment, ALT activity was higher in APAP ($p \leq 0.05$), APAP + LECM ($p \leq 0.05$), and APAP + AA ($p \leq 0.001$). The AST activity was higher ($p \leq 0.05$) in animals receiving LECM and AA treatment compared to healthy **(Figure 6.5 E)**. There was no significant difference in AST activity among APAP, APAP + LECM, APAP + AA, and APAP + NAC. The percentage of necrosis scoring demonstrated that liver injury decreased ($p \leq 0.001$) in animals receiving LECM (20.9 ± 5.6), AA (26.9 ± 5.7), and NAC (8.3 ± 2.4) treatment, compared with APAP (42.4 ± 4.1) **(Figure 6.5 F)**. Comparatively, LECM alleviated ($p \leq 0.001$) APAP-induced liver injury than AA; and NAC alleviated ($p \leq 0.001$) liver injury than LECM and AA.

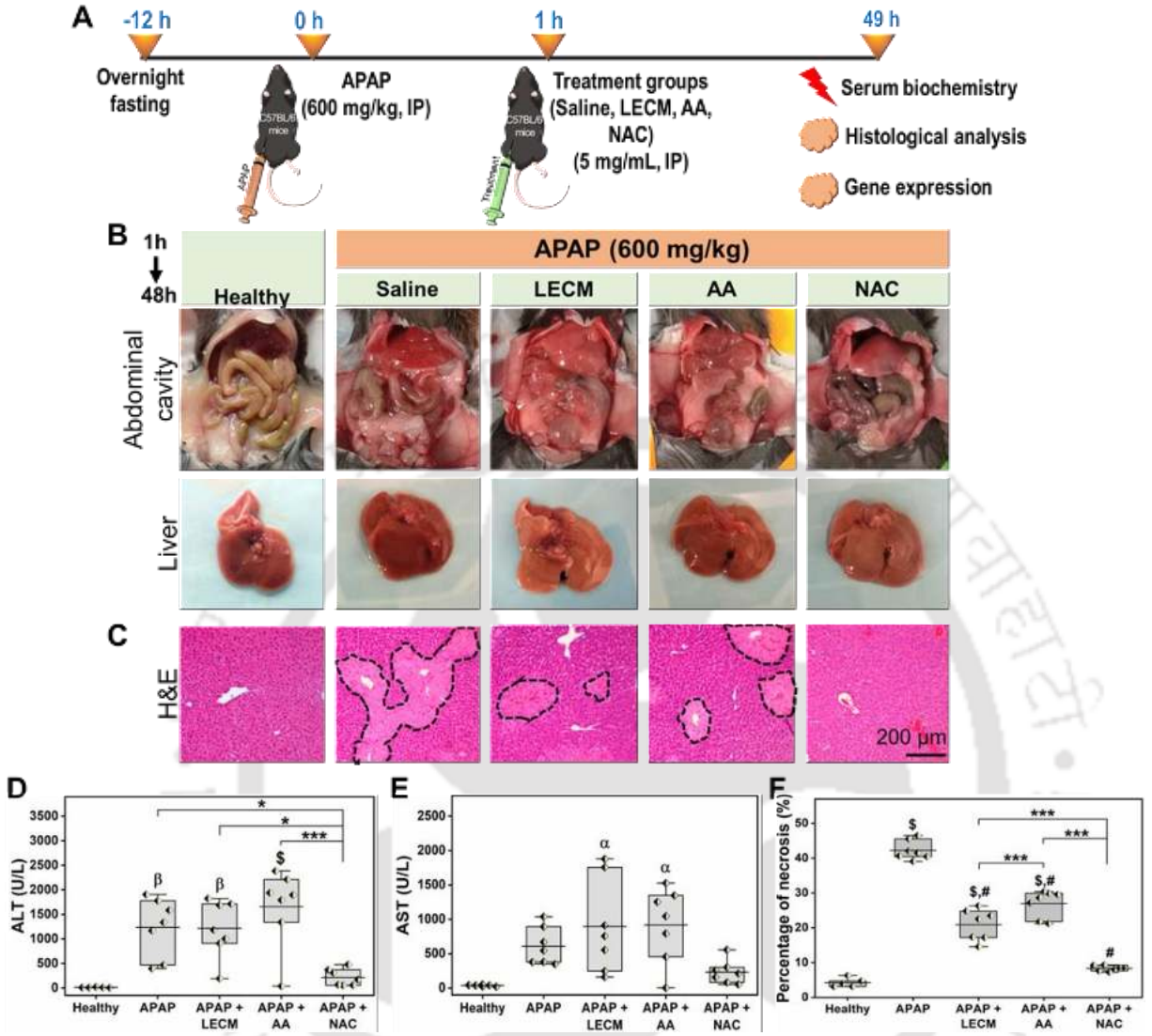

Figure 6.5. Early treatment of LECM, AA, and NAC (administered 1 h post-APAP) in attenuating APAP-induced liver fibrosis injury (600 mg/kg) over 48 h. *(A) Study design depicting the timeline of 600 mg/kg APAP disease induction, treatment administration, and analysis in C57BL/6 mice. (B) Representative images of whole abdominal cavity and liver post 48 h in healthy, disease, and treatment groups. (C) H&E staining outlining the necrotic core (dashed black lines) Scale bar: 200 µm. (D) Serum ALT. (E) Serum AST. (F) Percentage of necrotic area, N = 7 mice per group. Data are represented as a box plot overlaying the individual data point from each animal, and the mean of each group is indicated as a black line in the box.* $^{\alpha}$ *p ≤ 0.05,* $^{\beta}$ *p ≤ 0.01,* $^{\$}$ *p ≤ 0.001 vs healthy animals;* $^{\#}$ *p ≤ 0.001 vs APAP; * p ≤ 0.05, and *** p ≤ 0.001.*

6.3.5 Effect of LECM and AA treatment on initiation of APAP-induced liver fibrosis by analyzing CYP2E1 expression and NAPQI accumulation

Next, we studied the effect of LECM and AA treatment on the pathophysiology of APAP bioactivation and reactive metabolite formation in APAP-induced liver injury by analyzing CYP2E1 expression and NAPQI accumulation **(Figure 6.6 A, i)**. Healthy animals showed a marginal CYP2E1 expression around the portal triad (PT), and no expression around the central vein (CV) **(Figure 6.6 A, ii)**. CYP2E1 was strongly expressed in APAP animals over 48 h compared to 24 h **(Figure 6.6 A, iii)**. The LECM and AA treatment for 24 h and 48 h markedly reduced the CYP2E1 expression. The quantitative gene expression analysis indicated no significant difference in CYP2E1 mRNA expression among APAP and animals receiving LECM and AA treatment **(Figure 6.6 B)**. Indeed, CYP2E1 mRNA expression was upregulated ($p \leq 0.001$) in APAP + NAC compared with APAP, APAP + LECM, and APAP + AA following 24 h and 48 h. APAP animals showed an increased area of NAPQI protein adducts around CV; indeed, animals receiving LECM and AA treatment showed a reduced area of NAPQI protein adducts following 24 h and 48 h APAP overdose **(Figure 6.6 A)**. Healthy animals showed an absence of NAPQI protein adducts, and animals receiving NAC showed minimal NAPQI protein adducts at the periphery of the liver lobe. Following 24 h treatment, animals receiving LECM (19.0 ± 2.7), AA (21.2 ± 1.9), and NAC (10.6 ± 1.7) showed a lower ($p \leq 0.001$) percentage area of NAPQI protein adducts than APAP (45.5 ± 7.8) animals **(Figure 6.6 C)**. At 24 h, the percentage area of NAPQI protein adducts was not significant among APAP + NAC and APAP + LECM; however, APAP + AA showed an increased area ($p \leq 0.01$) of NAPQI protein adducts compared with APAP + NAC treatment. At 48 h, APAP + LECM (21.3 ± 5.1), APAP + AA (24.4 ± 3.6), and APAP + NAC (8.7 ± 1.9) treatment showed a lower ($p \leq 0.001$) percentage area of NAPQI protein adducts than APAP (50.7 ± 5.5) **(Figure 6.6 C)**. The APAP + LECM and APAP + AA showed a higher area ($p \leq 0.001$) of NAPQI protein adducts compared with APAP + NAC at 48 h.

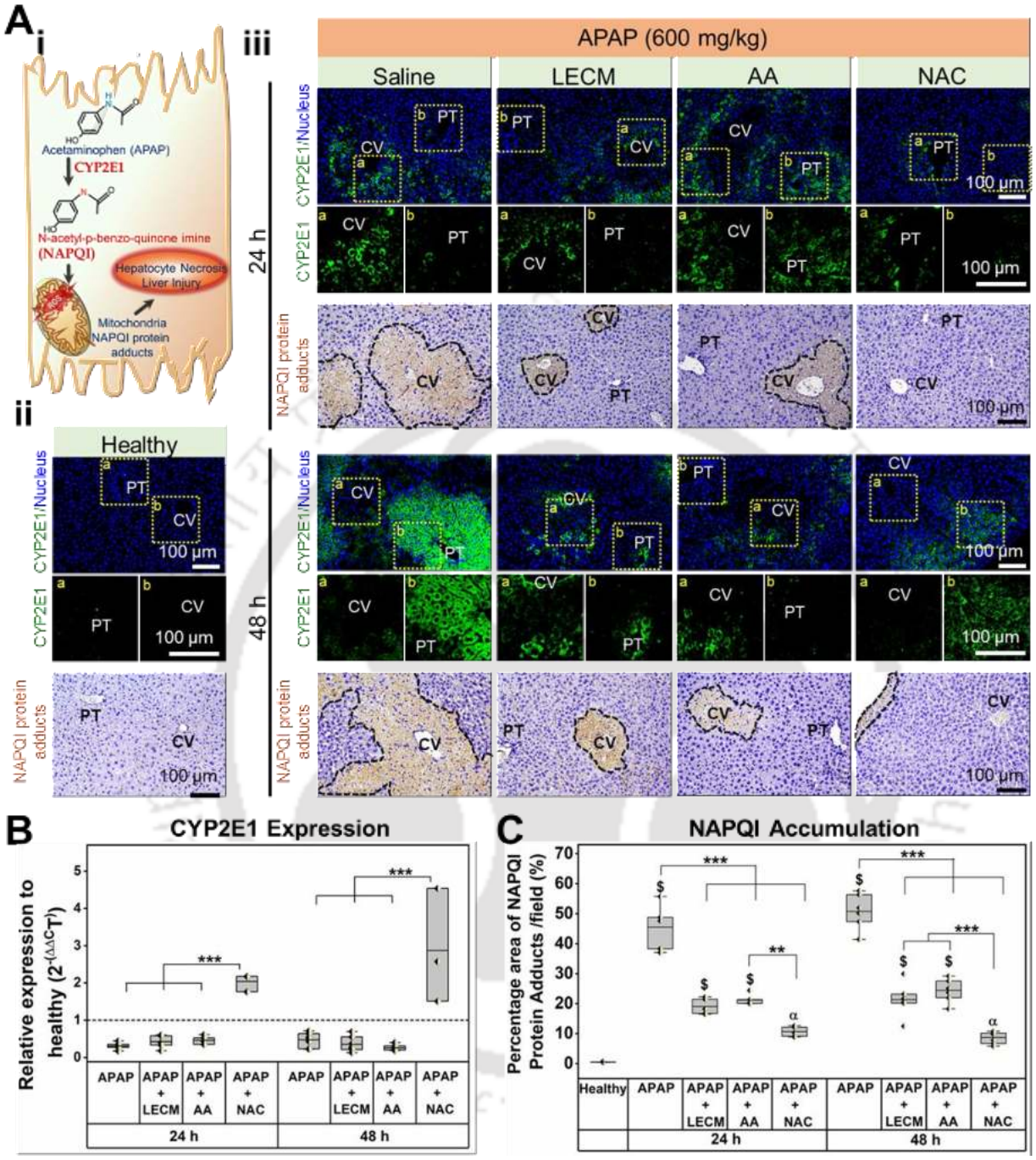

Figure 6.6. Initiation of APAP-induced liver fibrosis injury following 24 h and 48 h LECM and AA treatment. *(A) (i) Pathogenesis of APAP-induced liver injury from APAP bioactivation to reactive NAPQI metabolite formation. Immunofluorescence staining of CYP2E1 (green) and immunohistochemical staining of NAPQI protein adducts in (ii) healthy and (iii) APAP-induced liver injury animals receiving saline (negative control), LECM, AA, and NAC (positive control) treatment for 24 h and 48 h. The black dashed line outlined the area of NAPQI protein adducts. Scale bar: 100 µm, CV = Central vein, PT = portal triad. The yellow box 'a' and 'b' in the lower magnification image represents the area displayed in the higher magnification image. (B) CYP2E1*

*mRNA expression, black dashed line represents the relative expression of target gene in healthy animals. (C) Quantification of percentage area of NAPQI protein adducts. Data are represented as a box plot overlaying the individual data point from each animal, and the mean of each group is indicated as a black line in the box. $^{\alpha}$ $p \leq 0.05$, $^{\beta}$ $p \leq 0.01$, $^{\$}$ $p \leq 0.001$ vs healthy animals; * $p \leq 0.05$, ** $p \leq 0.01$ and *** $p \leq 0.001$.*

6.3.6 Effect of LECM and AA treatment on progression of APAP-induced liver fibrosis by analyzing macrophage infiltration and hepatocyte metabolism

The release of DAMPs from damaged hepatocytes activated immune cells, which is the main factor in the progression of APAP-induced liver injury **(Figure 6.7 A, i)**. The effect of LECM and AA treatment on activation of liver resident macrophages, i.e., Kupffer cell to the injury site was determined by F4/80 staining and CLEC7A mRNA expression. The immunostained liver sections showed increased infiltration of F4/80 positive immune cells in APAP animals compared with animals receiving LECM, AA, and NAC treatment over 24 h and 48 h **(Figure 6.7 A, ii-iii)**. Quantification of positive cells indicated that F4/80 positive Kupffer cells were higher ($p \leq 0.001$) in APAP animals compared with healthy; and in APAP animals at 48 h compared to 24 h **(Figure 6.7 B)**. Following 24 h treatment, F4/80 positive Kupffer cells were lower ($p \leq 0.001$) in animals receiving LECM (7.4 ± 0.3), AA (7.3 ± 0.3), and NAC (2.4 ± 0.1) compared with APAP (20.2 ± 0.6) animals. Similarly, over 48 h, F4/80 positive Kupffer cells were lower ($p \leq 0.001$) in animals receiving LECM (6.4 ± 0.1), AA (5.9 ± 0.1), and NAC (2.1 ± 0.1) compared with APAP (31.7 ± 0.5) animals. The expression levels of CLECL7A were 2.9 fold higher ($p \leq 0.001$) in APAP animals at 48 h compared to 24 h **(Figure 6.7 C)**. Furthermore, the CLECL7A mRNA expression was downregulated ($p \leq 0.001$) in animals receiving LECM, AA, and NAC treatment than APAP animals over 48 h. The immunofluorescence stained sections showed that arginase-1 expression, which is constitutively expressed by healthy periportal hepatocytes, was relatively decreased in APAP animals over 24 h and 48 h **(Figure 6.7 A)**. The Arginase-1 mRNA expression was upregulated ($p \leq 0.001$) in APAP + NAC at 48 h compared to 24 h **(Figure 6.7 D)**. Following 48 h treatment, arginase-1 mRNA expression was upregulated ($p \leq 0.001$) in APAP + NAC compared with APAP, APAP + LECM, and APAP + AA.

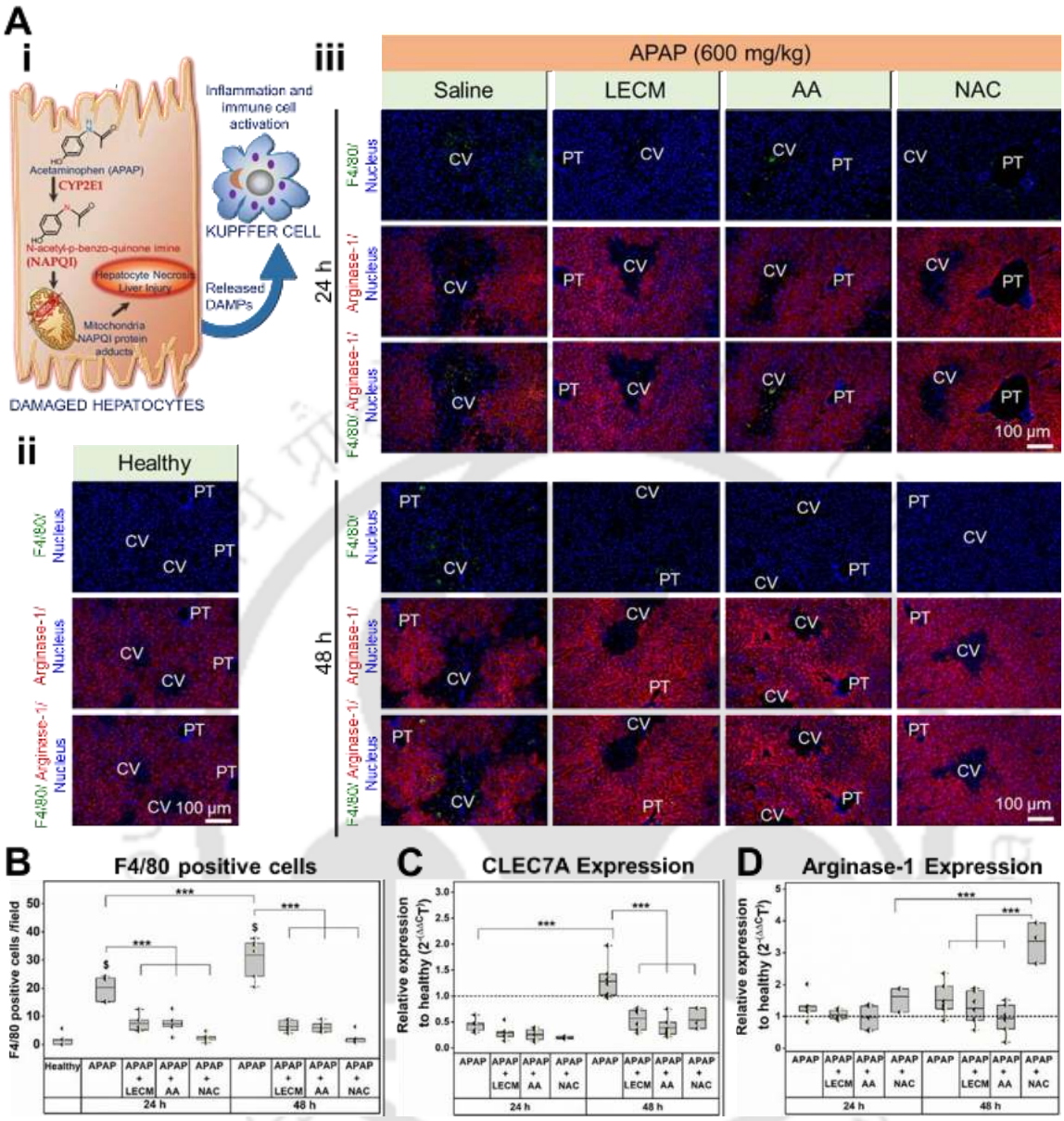

Figure 6.7. Progression of APAP-induced liver fibrosis injury following 24 h and 48 h LECM and AA treatment by macrophage activation and hepatocyte metabolism. *(A) (i) Pathogenesis of APAP-induced liver injury showing the release of DAMPs from damaged hepatocytes and initiating inflammation. Immunofluorescence staining of F4/80 (green) and Arginase-1 (red) in (ii) healthy and (iii) APAP-induced liver injury animals receiving saline (negative control), LECM, AA, and NAC (positive control) treatment over 24 h and 48 h. Scale bar: 100 µm, CV = Central vein, PT = portal triad. (B) Quantification of F4/80 positive cells. (C) CLEC7A mRNA expression, (D) Arginase-1 mRNA expression. The black dashed line in figure C and D represent the relative expression of target gene in healthy animals. Data are represented as a box plot overlaying the individual data point from each animal, and the mean of each group is indicated as a black line in the box.* $^{\$}$ *$p \leq 0.001$ vs healthy animals; *** $p \leq 0.001$.*

6.3.7 Effect of LECM and AA treatment on liver regeneration following APAP overdose by analyzing hepatic differentiation and proliferation

6.3.7.1 Cyclin D1 and p21 mRNA expression

We studied the mRNA expression levels of cell cycle regulator - Cyclin D1 and cell cycle inhibitor - p21 [28] **(Figure 6.8 A-B)**. At 24 h, Cyclin D1 mRNA level was markedly upregulated ($p \leq 0.01$) in animals receiving LECM treatment with a 3.4 and 9.1 fold increase compared with AA and NAC treatment **(Figure 6.8 A)**. AT 24 h, p21 mRNA levels was induced ($p \leq 0.001$) in APAP + NAC compared with APAP, APAP + LECM, and APAP + AA **(Figure 6.8 B)**. The p21 mRNA expression was also upregulated in animals receiving NAC treatment at 24 h than 48 h. Comparatively, APAP + LECM showed reduced ($p \leq 0.05$) p21 mRNA expression than APAP + AA at 24 h.

6.3.7.2 HNF4α and Ki67 expression following LECM and AA treatment in APAP-induced liver injury

Then, we studied the liver regeneration following LECM and AA treatment in APAP-induced liver injury using immunostaining for HNF4α and Ki67, which are associated with the maintenance of adult hepatocyte phenotype and proliferation, respectively **(Figure 6.8 C)**. The immunostained liver sections showed robust proliferation in APAP + LECM group with increased expression of HNF4α and Ki67 **(Figure 6.8 C, iii)**. At 24 h, HNF4α-positive cells were significantly higher in APAP + LECM (108.1 ± 23.3) compared to APAP (9.6 ± 5.7), APAP + AA (38.7 ± 9.9), and APAP + NAC (17.3 ± 7.4) **(Figure 6.8 D)**. Remarkably at 48 h, HNF4α-positive cells were higher ($p \leq 0.001$) in APAP + LECM (200.9 ± 54.3) and APAP + AA (133.4 ± 36.2) compared to APAP (2.6 ± 0.9), and APAP + NAC (3.5 ± 1.7). The HNF4α-positive cells increased ($p \leq 0.001$) in APAP + LECM and APAP + AA at 48 h compared to 24 h. Quantification of Ki-67 positive cells showed an increased ($p \leq 0.001$) cell proliferation in animals receiving LECM and AA treatment at 48 h compared to 24 h **(Figure 6.8 E)**. At 48 h, Ki67-positive cells were higher ($p \leq 0.001$) in APAP + LECM (114.3 ± 26.6) and APAP + AA (63.9 ± 21.8) compared to APAP (3.9 ± 2.7), and APAP + NAC (1.7 ± 1.1). At 48 h, HNF4α-positive cells and Ki-67 positive cells were higher ($p \leq 0.001$) in APAP + LECM compared to APAP + AA. Compared to healthy animals, HNF4α-positive cells and Ki67-positive cells were significantly higher in APAP + LECM at 24 h and 48 h, and APAP + AA at 48 h.

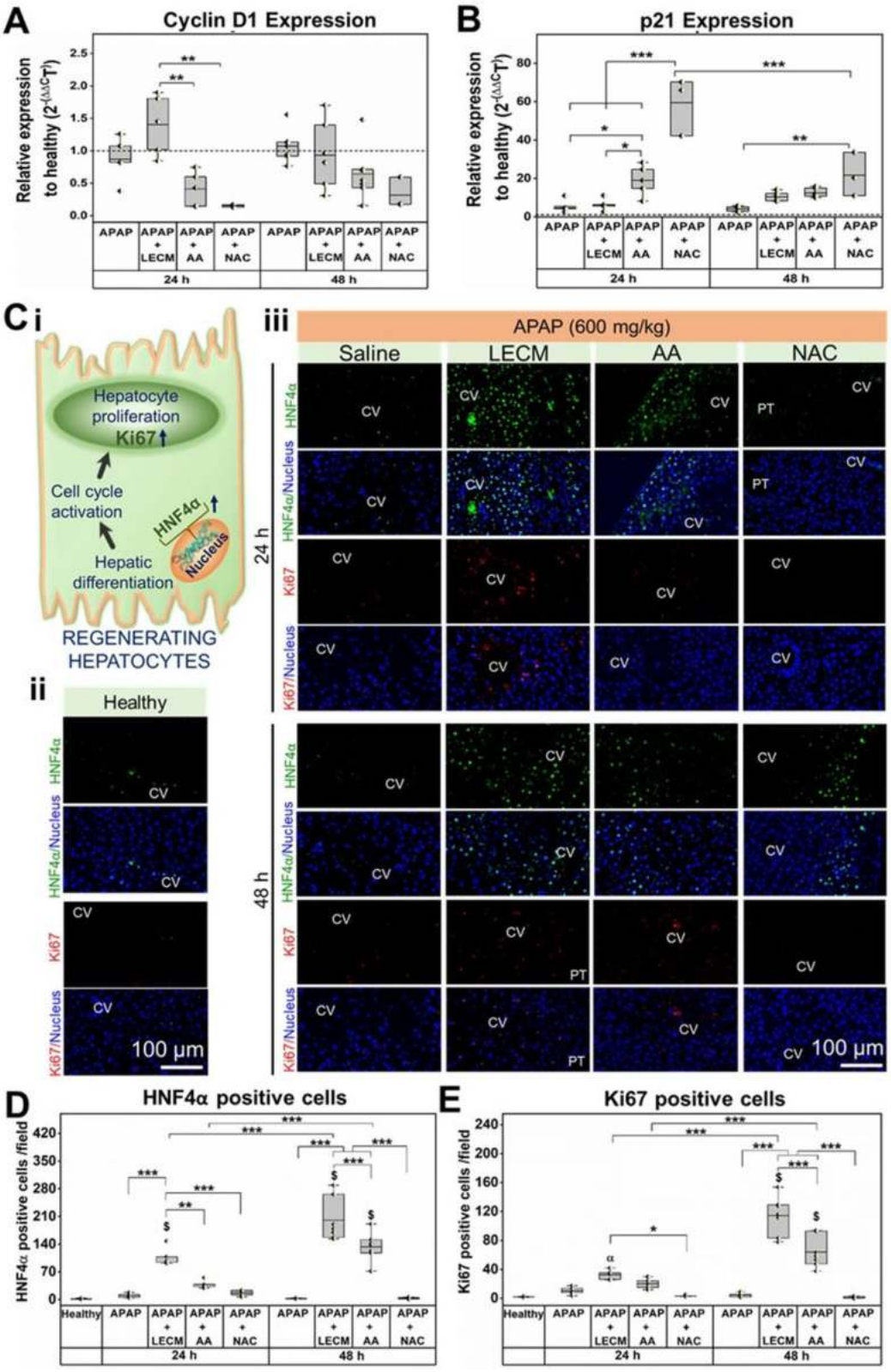

Figure 6.8. Effect of LECM and AA treatment on hepatic differentiation and proliferation in APAP-induced liver fibrosis injury over 24 h and 48 h. *(A) Cyclin D1 mRNA expression, (B) p21*

mRNA expression. The black dashed line in figure A and B represents the relative expression of target gene in healthy animals. (C) (i) Recovery of APAP-induced liver injury showing cell cycle activation and hepatic proliferation. Immunofluorescence staining of HNF4α (green) and Ki67 (red) in (ii) healthy, and (iii) APAP-induced liver injury animals receiving saline (negative control), LECM, AA, and NAC (positive control) treatment over 24 h and 48 h. Scale bar: 100 µm, CV = Central vein, PT = portal triad. (D) Quantification of HNF4α-positive cells. (E) Quantification of Ki67-positive cells. Data are represented as a box plot overlaying the individual data point from each animal, and the mean of each group is indicated as a black line in the box. $^{\alpha}$ *$p \leq 0.05$,* $^{\$}$ *$p \leq 0.001$ vs healthy animals; * $p \leq 0.05$, ** $p \leq 0.01$ and *** $p \leq 0.001$.*

6.3.8 Effect of LECM and AA treatment on liver regeneration following APAP overdose by analyzing hepatic differentiation and proliferation

Next, the liver regeneration following LECM and AA treatment in APAP-induced liver injury was studied using PCNA IHC to determine cell cycle activation and cell proliferation **(Figure 6.9 A)**. The PCNA-stained liver sections showed evidence of hepatocytes entering the cell cycle in APAP, APAP + LECM, APAP + AA, and APAP + NAC at 24 h and 48; indeed, no PCNA-positive cells were observed in healthy animals **(Figure 6.9 B-C)**.

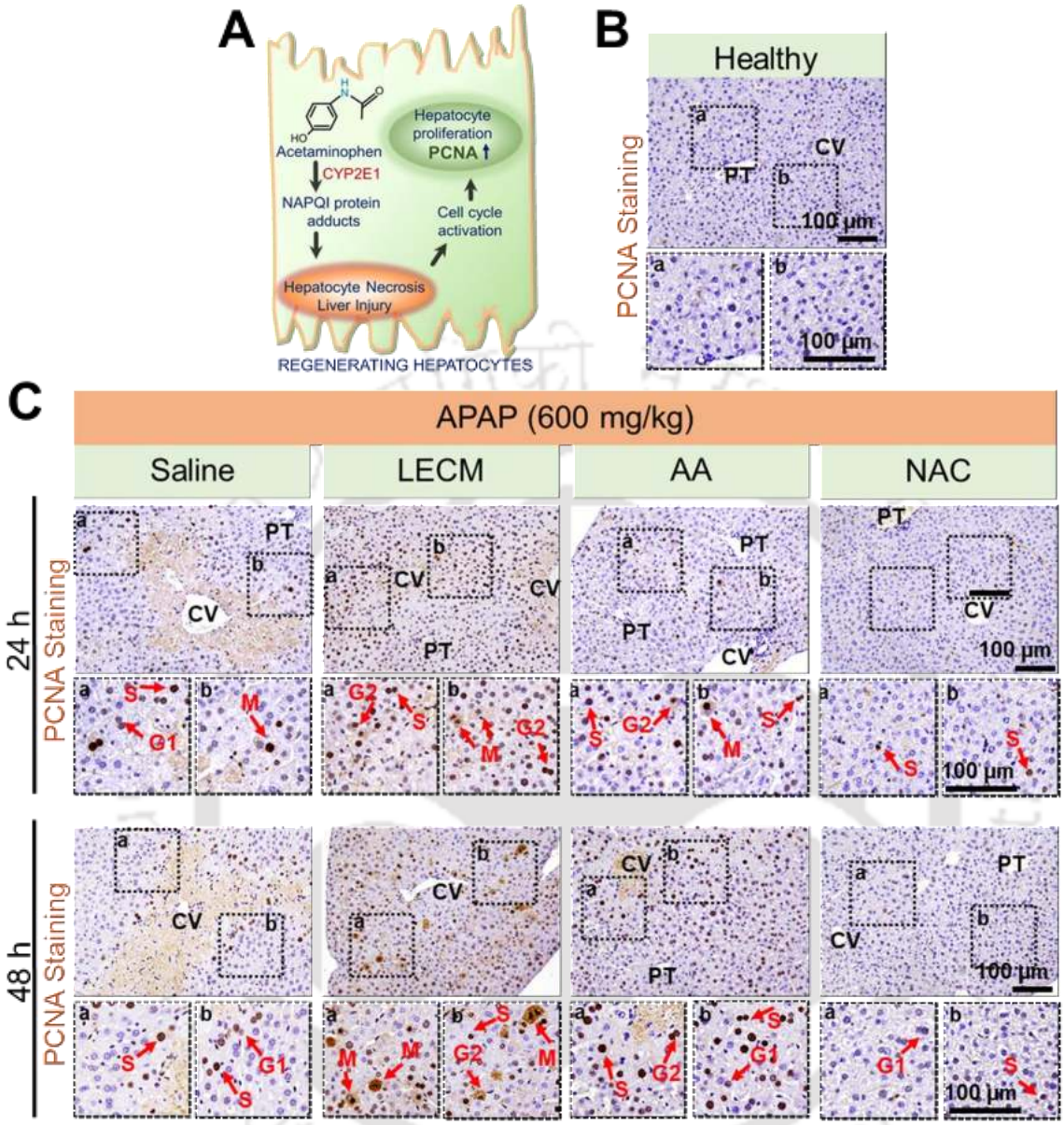

Figure 6.9. Effect of LECM and AA treatment on hepatic regeneration in APAP-induced liver fibrosis injury over 24 h and 48 h. *(A) Regeneration of APAP-induced liver fibrosis injury in mice demonstrating cell cycle progression and hepatic proliferation. Immunohistochemical staining of PCNA in (B) healthy and (C) APAP-induced liver injury animals receiving saline (negative control), LECM, AA, and NAC (positive control) treatment over 24 h and 48 h. Scale bar: 100 µm, CV = Central vein, PT = portal triad. The black box 'a' and 'b' in the lower magnification image represents the area displayed in the higher magnification image. The red arrows with inscriptions show the cells in G1, S, G2, and M phases.*

The quantification of PCNA-positive cells, cells in G1, S, G2, and M phase showed robust proliferation in APAP + LECM and APAP + AA over 48 h **(Figure 6.10 A)**. An increase in total

PCNA-positive cells was noticed after 48 h in APAP ($p \leq 0.01$), APAP + LECM ($p \leq 0.001$), APAP + AA ($p \leq 0.001$) compared to 24 h **(Figure 6.10 B)**. At 24 h, animals receiving LECM (107.5 ± 21.9) and AA (64.6 ± 13.4) treatment showed a higher ($p \leq 0.001$) number of PCNA-positive cells compared to NAC (17.4 ± 3.2). APAP + LECM showed a higher ($p \leq 0.001$) number of PCNA-positive cells compared to APAP, and APAP + NAC. At 48 h, the total PCNA-positive cells were higher ($p \leq 0.001$) in APAP + LECM (161.9 ± 12.1) and APAP + AA (125.4 ± 15.4) compared to APAP (71.0 ± 11.3) and APAP + NAC (15.5 ± 5.5). Comparatively, animals receiving LECM treatment showed a higher ($p \leq 0.001$) number of PCNA-positive cells than AA. The LECM and AA treatment induced more ($p \leq 0.001$) cells entering to G1 phase at 48 h than 24 h **(Figure 6.10 C)**. The cells entering the G1 phase in APAP, APAP + LECM, APAP + AA, and APAP + NAC at 24 h were 23.8 ± 7.3, 43.6 ± 10.2, 33.3 ± 11.9, and 11.1 ± 1.8. Cells in G1 phase were higher in APAP + LECM compared to APAP ($p \leq 0.05$), and APAP + NAC ($p \leq 0.001$); and APAP + AA compared to APAP + NAC ($p \leq 0.05$). Over 48 h, cells entering the G1 phase were in APAP, APAP + LECM, APAP + AA, and APAP + NAC were 43.5 ± 9.1, 88.6 ± 11.0, 69.3 ± 13.4, and 8.3 ± 2.5. Over 48 h, cells entering the G1 phase were significantly higher in animals receiving LECM and AA treatment compared to APAP and NAC. Comparatively, cells in the G1 phase were higher ($p \leq 0.01$) in APAP + LECM than APAP + AA. At 24 h, cells entering S phase were higher ($p \leq 0.001$) in APAP + LECM (57.3 ± 16.8) compared to APAP + AA (28.8 ± 9.0) and APAP + NAC (6.4 ± 2.8) **(Figure 6.10 D)**. Animals receiving AA treatment showed a higher ($p \leq 0.01$) number of cells in the S phase than NAC. At 48 h, APAP + LECM (62.0 ± 8.2) and APAP + AA (50.8 ± 7.8) showed a higher ($p \leq 0.001$) number of cells in the S phase compared to APAP (25.4 ± 6.1), and APAP + NAC (6.0 ± 3.3). Over 48 h, cells in the S phase were higher in APAP + AA than 24 h. A very few cells entered the G2 phase at 24 h in APAP and all treatment groups **(Figure 6.10 E)**. Over 48 h, cells in the G2 phase were higher in APAP + LECM compared to APAP ($p \leq 0.001$), APAP + AA ($p \leq 0.01$), and APAP + NAC ($p \leq 0.001$). Cells in the G2 phase increased ($p \leq 0.05$) in APAP + LECM at 48 h compared to 24 h. Over 24 h and 48 h, mitoses were more ($p \leq 0.001$) evident in APAP + LECM compared to APAP, APAP + AA, and APAP + NAC **(Figure 6.10 F)**. At 48 h, APAP + AA showed a higher ($p \leq 0.001$) number of cells in Mitosis than APAP + NAC.

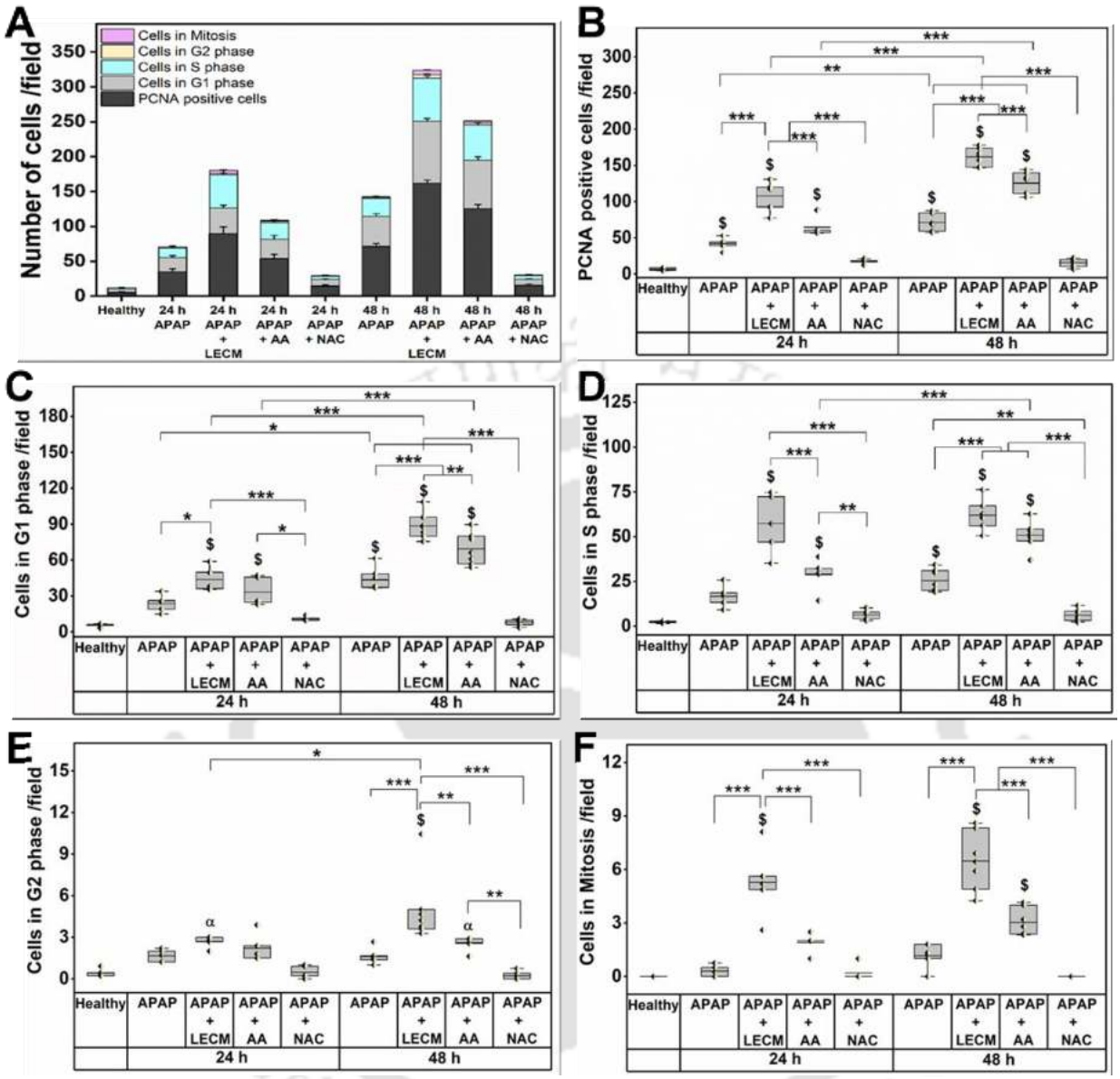

Figure 6.10. Effect of LECM and AA treatment on hepatic regeneration in APAP-induced liver fibrosis injury over 24 h and 48 h. *(A) Stacked bar graph showing the number of PCNA positive cells in different phases of cell cycle in healthy, APAP, APAP + LECM, APAP + AA over 24 h and 48 h. Quantification of (B) Total PCNA positive cells. (C) Cells in G1 phase. (D) Cells in S phase. (E) Cells in G2 phase. (F) Cells in Mitosis. Data are represented as a box plot overlaying the individual data point from each animal, and the mean of each group is indicated as a black line in the box.* $^{\alpha}$ *$p \leq 0.05$,* $^{\$}$ *$p \leq 0.001$ vs healthy animals; * $p \leq 0.05$, ** $p \leq 0.01$ and *** $p \leq 0.001$.*

6.4 Discussion

The present study highlights that liver injury following APAP overdose can be mitigated, and subsequent liver regeneration can be promoted by i.p. injection of LECM hydrogel derived from healthy porcine liver. *In vitro* observations suggested that LECM treatment can increase the metabolic activity of APAP-induced PMH, upregulate cyclin B1, HNF4α, and Arginase 1 expression, and downregulate the Caspase 3 expression. Furthermore, *in vivo* findings elaborated the role of LECM in alleviating liver injury and subsequently promoting hepatocyte proliferation following APAP overdose through activating cyclin D1, Ki67, inhibiting p21, and maintaining HNF4α. This study also demonstrates that AA treatment can alleviate APAP-induced liver injury by reducing cell death and promoting cell proliferation in *in vitro* PMH and *in vivo* mouse model. Overall, our *in vitro* and *in vivo* evidence revealed that LECM remarkably facilitates recovery or regeneration following APAP overdose, and AA inhibits the progression of APAP-induced liver injury.

Several researchers have investigated the pathophysiology of APAP-induced hepatotoxicity and liver regeneration after APAP overdose [378, 382, 383, 397]. However, liver regeneration was inhibited at high doses of APAP, i.e., higher than 550 mg/kg APAP in C57BL/6J mouse leads to significant liver injury, with cell cycle arrest, elevated serum transaminases, and decreased cyclin D1 expression [382]. Previous studies have recommended using the mouse model of APAP-induced liver injury as a popular mechanistic model for investigating new therapeutic interventions as mice closely mimic the human pathophysiology, where the treatment needs to be provided after APAP administration [385]. Injectable acellular matrix hydrogels derived from decellularized ECM and native biomaterials have been proven to be a potential therapeutic material facilitating tissue impairment, remodeling, and cell infiltration [393, 398]. The studies that LECM and AA maintained the native cellular phenotype and facilitated functional tissue remodeling corroborate the critical role of these biological materials in promoting liver regeneration following ALF [47, 224, 290]. In this context, we investigated the hepatoprotective potential of LECM and AA hydrogel in mitigating APAP-induced liver damage. An *in vitro* culture of primary mouse and human hepatocytes exposed to APAP after initial cell attachment replicates the native APAP metabolism, NAPQI generation, and cell death [24]. We observed dose-dependent toxicity in PMH following 5 mM and 7.5 mM APAP treatment, with significant cell death in 7.5 mM APAP-induced liver fibrosis model attributed to APAP metabolic activation [399]. The LECM treatment

facilitated the regeneration after APAP-induced cell damage in 7.5 mM APAP-induced liver fibrosis model by significantly increasing metabolic activity, upregulating cyclin B1, HNF4α, and arginase 1 and downregulating caspase 3 expression. However, AA treatment facilitated the recovery after APAP-induced injury by decreasing the caspase 3 expression and increasing metabolic activity. The LECM treatment after APAP-induced hepatotoxicity promoted the PMH to enter the cell cycle, particularly the G2 phase and Mitosis, corroborating the hepatoprotective effect of tissue-specific LECM. Previous studies have proposed that treatment strategies activating the cell cycle and decreasing the caspase 3 activity might be crucial in promoting liver regeneration after ALF [24, 385, 400].

Based on the *in vitro* results, we investigated the therapeutic role of LECM, AA, and NAC in 600 mg/kg APAP-induced liver injury mice model over two time points 24 h and 48 h, where the treatment groups were i.p. injected 1 h after APAP administration. Liver failure induced by 600 mg/kg APAP has been considered a lethal dose in mice due to active inhibition of critical promitogenic pathways leading to cell cycle progression and liver regeneration [382, 401]. The intraperitoneal route of treatment administration has been widely used in rodents, allows quick reabsorption into surrounding tissues, and has shown to be effective in protecting the carbon tetrachloride-induced liver failure in a rat model by reducing necrosis and inflammation [402]. The biomarkers of hepatocyte death, serum ALT and AST levels peaked at 24 h and subsided at 48 h in all the groups, demonstrating initiation of liver injury before 24 h [377]. A decline in serum transaminases observed during the later phase of APAP hepatotoxicity is attributed to the limited half-life of serum markers in the circulation [382, 403]. Along with the increase in serum transaminases, the end result of the initiation and progression phase of APAP-induced liver injury is extensive centrilobular necrosis and necrotic cell death caused by irreversible mitochondrial injury and DNA fragmentation [377]. H&E stained liver sections demonstrated centrilobular necrosis with nuclear fragmentation in all animals receiving APAP **(Figure 6.11)**. Further, necrosis score analysis showed strikingly reduced cell death in animals receiving LECM treatment at both 24 h and 48 h with 16% and 20% cell death, respectively compared to APAP animals with 29% and 42% cell death at 24 h and 48 h, respectively. However, AA treatment showed reduced cell death at 48 h with 26% cell death. These data suggested that LECM favored protection of APAP-induced liver injury and subsequent regeneration at early time point, indeed AA supported recovery after 24 h.

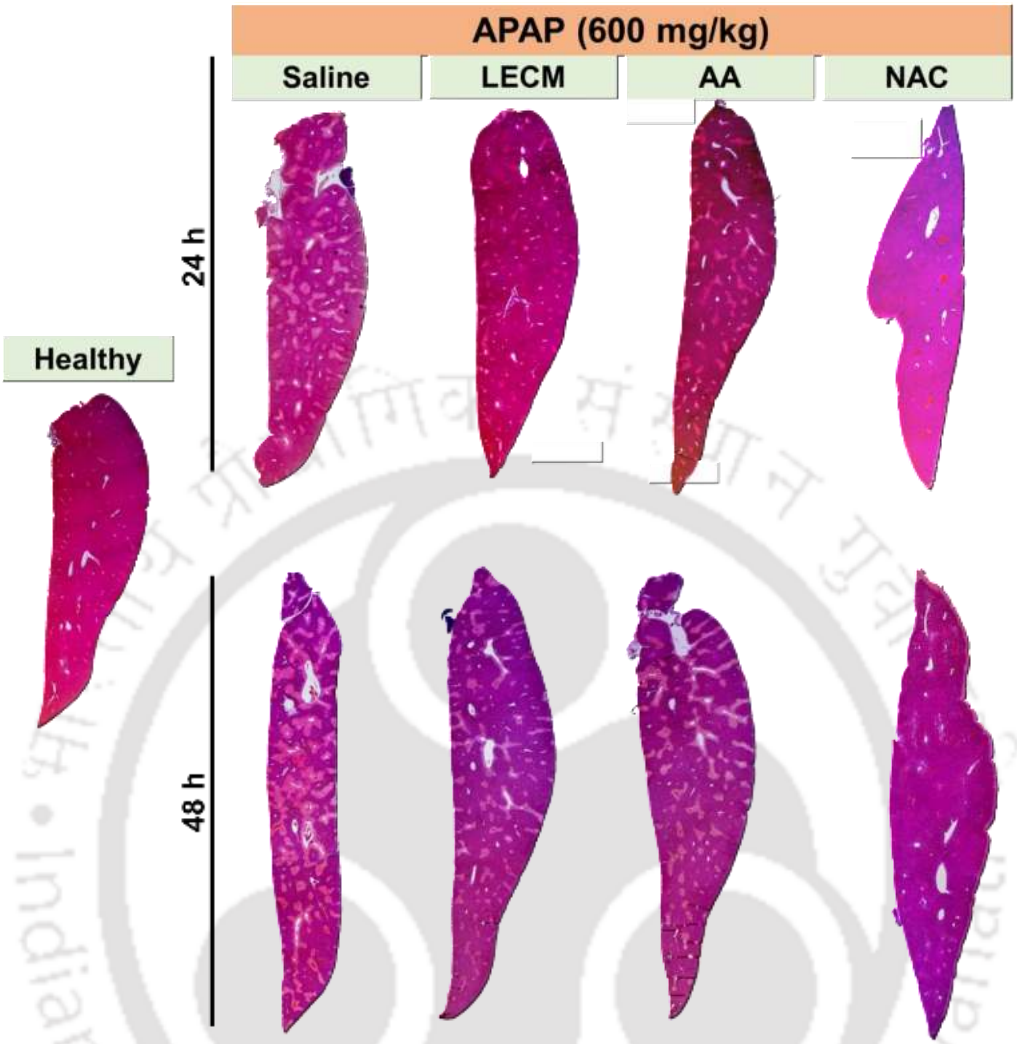

Figure 6.11. Representative photographs of liver lobe showing the necrotic area*, taken stitching the H&E stained liver sections from healthy, APAP, APAP + LECM, APAP + AA, and APAP + NAC following 24 h and 48 h.*

APAP metabolism is predominantly mediated by CYP2E1, which converts APAP to toxic NAPQI metabolite resulting in glutathione depletion, oxidative stress, and necrotic cell death [378]. Previous studies showed that inhibiting or knocking out CYP2E1 activity in mice reduces APAP-induced hepatotoxicity [389, 404]. Immunohistology results indicated a strong CYP2E1 expression in APAP at 48 h compared to 24 h, but CYP2E1 expression was reduced in animals receiving LECM, AA, and NAC treatment at both 24 h and 48 h. An increased area of NAPQI protein adducts causes elevated levels of free radicals such as ROS, leading to hepatocyte necrosis [405]. Over 48 h, LECM and AA treatment showed a reduced percentage area of NAPQI protein adducts with 21% and 24% compared to APAP animals with 50%, evidencing minimal necrosis.

Therefore, minimal CYP2E1 expression leading to the reduced area of NAPQI protein adducts in LECM and AA treatment animals over 24 h and 48 h corroborated similar hepatoprotective effects of LECM and AA hydrogel. During APAP-induced liver injury and hepatocyte death, the release of DAMPs initiates a sterile innate inflammatory response resulting in the activation of liver-specific resident Kupffer cells to produce chemokines, and facilitate infiltration of neutrophils and monocytes to the site of injury [406, 407]. Recruitment of monocytes and Kupffer cells is controversial and holds a crucial factor in both recovery and aggravation of liver injury [408]. Immunostaining and quantification for F4/80 (macrophage marker) positive cells combined with mRNA analysis for Kupffer cell marker CLEC7A showed a reduced number of macrophages in animals receiving LECM, AA, and NAC treatment over 24 h and 48 h. Moreover, an increased F4/80 positive macrophages and upregulated CLEC7A expression were observed in APAP animals at 48 h compared to 24 h. These data corroborated that a higher number of necrotic cells in APAP animals mediated an increased inflammation and progression of liver injury at 48 h, and lesser hepatocyte death in animals receiving treatment supported minimal inflammation, which was also observed from necrosis score analysis and NAPQI protein adduct quantification [409]. Arginase-1, a metalloenzyme is involved in the urea cycle and concentrated explicitly by the periportal hepatocytes [410]. The liver sections co-stained with F4/80 and Arginase-1 showed that the cell death due to APAP was more concentrated in the pericentral hepatocytes, i.e., centrilobular cell death and macrophage infiltration was in close proximity to the centrilobular region.

The effect of LECM and AA treatment on liver regeneration following APAP-induced injury was investigated by assessing the expression of cell cycle regulators, cyclin D1 and p21 that play a significant role in liver regeneration [378]. The cyclin D1 activation is associated with the cells entering the cell cycle by binding to cyclin-dependent kinase 4 and β-catenin, committing to DNA replication, and p21 activation was associated with cell cycle inhibitor [28, 382, 411]. Bhushan *et al*. 2014 has reported inhibition of liver regeneration with induction of p21 and decreased cyclin D1 in animals receiving APAP overdose (600 mg/kg) [382]. Our most remarkable finding was that LECM treatment in the APAP-induced fibrosis model induced the cyclin D1 expression and inhibited the p21expressin at the initial time point 24 h preceding the start of the regenerative phase in LECM treatment, indeed this was not observed in AA and NAC treatment. NAC treatment increased p21 expression at 24 h and 48 h demonstrating the cell cycle arrest. Previous studies have reported that inducing cyclin D1 and inhibiting p21 through various

treatment approaches such as cerium oxide nanoparticles, EGFR activation, and exosomes promote liver regeneration following APAP-induced ALF [379, 392, 412]. HNF4α, a nuclear transcription factor regulates hepatocyte differentiation in embryonic development, maintains adult hepatic phenotype, and is involved in various liver-specific metabolic functions [413]. Immunostaining for HNF4α presented a higher number of HNF4α positive cells in animals receiving LECM and AA treatment at 48 h. A recent study has highlighted that hepatocytes modulate the HNF4α activity while switching between differentiated and proliferative states, and HNF4α reexpression is critical during the termination phase of liver regeneration [414]. These studies suggested that newly proliferating hepatocytes around CV in animals receiving both LECM and AA treatment got differentiated and maintained the adult hepatocyte functions. Further, we studied liver regeneration by immunolabeling for standard cell proliferation markers, Ki-67 and PCNA in all diseased and treatment groups [415]. The endogenous cell replication marker, PCNA provides insight into cell cycle activation and proliferation by distinguishing individual cell cycle phases, including G1, S, G2, and M during cell division [382]. After LECM treatment, some of the cells underwent DNA synthesis and were in the S phase and Mitosis by 24 h, and a majority of the cells were in the S phase and Mitosis by 48 h. The cell division was activated at 24 h in LECM treatment with an increased number of proliferating cells compared to AA treatment, which was also corroborated from Ki-67 immunostained images. Similarly, intravenous administration of human umbilical cord-derived MSC into BALB/c mice after 600 mg/kg APAP intoxication improved hepatocyte proliferation and prevented liver injury [386]. An increased proliferation observed in animals receiving AA treatment might be attributed to the bioactive properties and RGD motifs in silk fibroin [290]. The liver ECM hydrogels are reported to retain structural and biological signals such as growth factors and cytokines, which might play a crucial role in activating the cell cycle and proliferation [207, 391]. Overall, these data support that LECM treatment stimulates timely liver regeneration at high doses of APAP by facilitating initial entry into the cell cycle, decreasing cell cycle arrest, and promoting hepatocyte proliferation at 24 h.

The findings of the present study possess significant clinical utilizations. Stimulating timely liver regeneration after severe APAP overdose in liver injury patients, which inhibits compensatory liver regeneration, holds therapeutic potential. Early i.p. administration (post 1 h APAP) of LECM hydrogel attenuated liver failure after APAP overdose and stimulated liver regeneration at 24 h. Besides, early i.p. administration (post 1 h APAP) of AA hydrogel prevented

progression of APAP-induced liver failure and stimulated delayed liver regeneration at 48 h. Future studies would focus on including initial time points to investigate the efficacy of LECM and AA hydrogel in preventing the initiation of liver failure. Furthermore, a detailed mechanistic understanding of the proposed LECM and AA therapeutic option in promoting liver regeneration and signaling pathways that regulate recovery needs to be evaluated.

6.5 Significant Findings

1. In summary, our results indicate for the first time, to our knowledge, that i.p. administration of LECM and AA hydrogel attenuated liver injury after severe APAP overdose via reduced NAPQI accumulation, oxidative stress, centrilobular necrosis, and inflammation.
2. Our results demonstrate that the AA silk fibroin enhanced hepatocyte proliferation at 48 h following APAP overdose. The antioxidant property of AA silk fibroin might assist in protecting the APAP-induced liver injury by scavenging the generated ROS, and peptides and RGD motifs in AA silk fibroin might be associated with increased proliferation.
3. In comparison, both *in vitro* and *in vivo* studies demonstrate that LECM treatment after APAP overdose aids in the onset of early liver regeneration by activating the cell cycle through cyclin D1 expression, decreasing cell death, and maintaining matured hepatic functions.
4. The tissue-specific LECM possesses immunomodulatory and antioxidant properties and offers dynamic reciprocity between hepatocytes and cell secretome in the ECM.
5. Our study suggested that LECM treatment as a potential alternative therapeutic strategy to stimulate early liver regeneration after liver failure.

Summary and Future Perspectives

Summary and Future Perspectives

Liver cirrhosis, a late stage of fibrosis occurs as scar tissue progresses and is associated with impaired self-regenerative ability, progressive liver inflammation, and fibrosis. The gold standard "Liver transplantation" treatment approach possesses various limitations, and alternative tissue engineering-based therapeutics were explored, followed by its promising prospects in the bioartificial liver and regenerative applications (*discussed in Chapter 1*). Developing an ideal 3D matrix for a physiologically relevant *in vitro* liver model and liver regenerative applications involves the following crucial facets (i) a biomimetic matrix, (ii) physicochemical attributes, (iii) hepatocyte aggregate culture, (iv) liver zonation, (v) recapitulating liver microarchitecture, (v) constructive tissue remodeling, (vi) minimal inflammation, and (vii) liver regeneration **(Figure 6.12)**. Herein, we have progressively fabricated an ideal 3D matrix and employed advanced fabrication techniques and perfusion culture systems to generate liver models. Amalgamating tissue-specific liver extracellular matrix (ECM) with silk fibroin from both mulberry and non-mulberry silk sources, studying macrophage phenotype activation in response to silk and liver ECM biomaterials, and investigating the regenerative potential of developed biomaterials are the novel highlights of the present thesis.

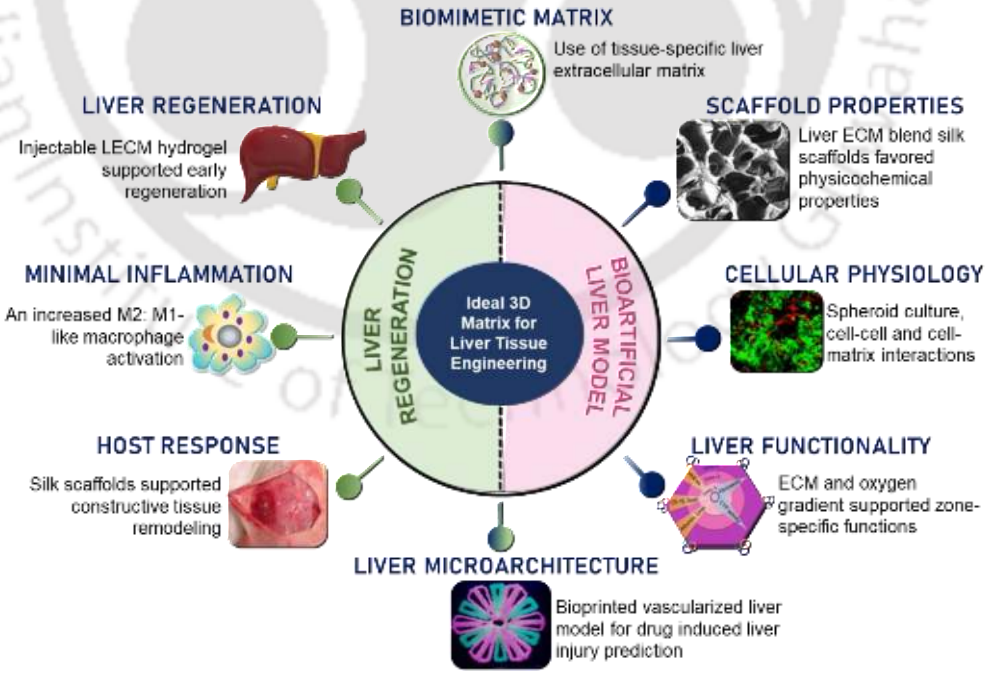

Figure 6.12. *Schematic illustration presenting the key findings of this thesis work.*

We first focused on maintaining functional hepatocyte clusters for an extended period, as hepatocyte clusters displayed higher functionality, emphasizing both cell-cell and cell-matrix interactions. Modulating the cell-matrix interactions and physicochemical properties of the 3D scaffold facilitates the formation of hepatocyte aggregates. The porous and hemocompatible blend 3D silk scaffold (BA) fabricated by amalgamating mechanically resilient RGD containing *Antheraea assamensis* (AA) silk fibroin and *Bombyx mori* (BM) silk fibroin assisted the self-aggregation of functional hepatocyte clusters (< 100 μm) and maintained albumin secretion, ureagenesis, and cytochrome P450 activity over 3 weeks, as evaluated using HepG2 and primary rat hepatocytes (*as described in Chapter 2*). Further, the BA silk scaffold was functionalized with decellularized liver extracellular matrix solution (dLS) to resemble tissue-specific biomimetic cues and dynamic interplay between cells and matrix to accomplish hepatocyte polarity, growth, liver functions, and long-term stability. The porous liver ECM blend silk (LECM-SF) scaffolds possess high water imbibing capacity supporting nutrient diffusion and compressive modulus similar to a healthy liver. *Chapter 3* provides the first evidence of developing an *in vitro* liver zonation model recapitulating hepatocyte metabolic heterogeneity induced as a result of altering liver ECM proportion in scaffolds and mimicking the oxygen gradient using a perfusion bioreactor. The primary neonatal rat hepatocytes seeded LECM-SF scaffolds were stacked in sequence and matured over 45 days in perfusion bioreactor, wherein scaffolds with higher liver ECM supported periportal specific synthetic and cholangiocyte functions; and scaffolds with least ECM supported pericentral specific detoxification and ECM production functions (*as described in Chapter 3*). While LECM-SF biomaterial provides biomimetic cues, recapitulating spatiotemporal arrangement and cellular composition of the native liver has become decisive in developing *in vitro* liver models for drug screening applications. Two distinct tissue-specific bioinks were formulated with LECM, BA silk, β-D galactose, and gelatin for supporting parenchymal and non-parenchymal cells (NPCs). *Chapter 4* highlights the bioprinting of the liver model system with a hepatic sinusoid network, wherein the 3D CAD design trails alternate cords of parenchymal (hADMSC-derived HLCs) and NPCs (HUVECs and HHSCs) using an extrusion bioprinting technique. The HLC/HUVEC/HHSC-laden vascularized liver model maintained hepatic functions over 2 weeks, showed increased metabolic competence, and predicted hepatotoxicity. The developed clinically relevant vascularized liver model would provide a robust high-throughput platform for hepatotoxicity screening (*as described in Chapter 4*). For liver regenerative

applications, investigating the host response and macrophage phenotype activation state towards the biomaterial at the implantation site is crucial, which has been shown to be a predictor of downstream clinical outcomes. Chapter 5 presents and compares the host response and macrophage activation state elicited by BM, AA, BA, and LECM biomaterial to small intestinal submucosa extracellular matrix (SIS) and polypropylene surgical mesh (PP mesh). The findings of this *Chapter 5* are AA silk implants elicited predominantly pro-remodeling macrophage response with fewer multinucleate giant cells than BM silk, supporting a more constructive tissue remodeling response. Degradation products of AA silk bioscaffold directed pro-remodeling macrophage activation through increased arginase: iNOS in bone marrow-derived macrophages (BMDM) and Fizz1: iNOS in pro-inflammatory activated BMDM. This chapter potentially provided the macrophage phenotype stimulated by intrinsic BM silk and AA silk in directing the tissue regeneration, which is crucial while performing *in vivo* study (*as described in Chapter 5*). From this work, we took forward AA silk and LECM to investigate their therapeutic prospects in attenuating liver fibrosis and promoting liver regeneration in acetaminophen (APAP)-induced liver fibrosis mouse model. *Chapter 6* presented that intraperitoneal administration of LECM and AA hydrogel attenuated APAP-induced liver injury through reduced NAPQI accumulation, oxidative stress, centrilobular necrosis, and inflammation. Comparatively, intraperitoneal administration of tissue-specific LECM hydrogel aided the early onset of liver regeneration by activating the cell cycle through cyclin D1, Ki67, and PCNA expression. This study suggested the potential alternative therapeutic strategy of LECM in stimulating liver regeneration after liver failure (*as described in Chapter 6*).

The future perspectives of this thesis are enumerated in the following sections:

1. Employing **human-induced pluripotent stem cells (hiPSCs) and primary human hepatocytes (PHHs)** hold great promise in developing patient-specific personalized *in vitro* liver models owing to their phenotypic characteristics and significant aspects of human hepatic metabolism.
2. The tissue-resident **Kupffer cells** regulate inflammation orchestrating the immune responses between parenchymal and non-parenchymal cells, making it a crucial component while developing *in vitro* liver models for drug toxicity screening and *in vitro* liver disease

models. The inclusion of Kupffer cells in *in vitro* models would confer adequate cellular crosstalk and improve the hepatotoxicity prediction.

3. Functionalization of 3D scaffolds with **bioactive molecules like tissue-specific matrix-bound nanovesicles, liver cell-secreted exosomes, and platelet-rich plasma** would further confer adequate bioactivity of scaffolds instructing biomimetic cues.
4. Bioengineered *in vitro* liver zonation model and bioprinted liver model developed in this thesis that closely resembles native liver physiology could be treated with potential chemicals, cytokines, agents, and molecules to develop prospective liver fibrosis models. Further, miniaturization of ***in vitro*** **liver disease models** following advanced strategies would allow investigation of molecular mechanisms and pathogenesis underpinning complex liver diseases, find therapeutic targets to treat liver disease, and in regenerative medicine.
5. Emerging **microfluidic technologies encompassing advanced computational models** would allow miniaturization of *in vitro* liver models and prediction of flow patterns, shear stress, and mass transfer more accurately.
6. The therapeutic potential and immunogenic attributes of tissue-specific liver ECM hydrogel are investigated in this thesis. Herein, Liver ECM hydrogel promoted hepatocyte proliferation and liver regeneration following APAP overdose in the acetaminophen-induced liver fibrosis mouse model. Analysis of the **therapeutic potential of liver ECM hydrogel in human-specific *in vitro* and *in vivo* liver disease models** would further ascertain their preclinical efficacy.
7. Validation of developed *in vitro* models as an extracorporeal bioartificial liver support system and drug toxicity screening with an array of drug compounds through various phases of human clinical trials could enable **high throughput, spin-off, and technology transfer**.

Bibliography

[1] Taub R. *Liver regeneration: from myth to mechanism*. Nature Reviews Molecular Cell Biology, 2004, 5 (10): 836-847.

[2] da Silva Morais A, Vieira S, Zhao X, Mao Z, Gao C, Oliveira JM, Reis RL. *Advanced biomaterials and processing methods for liver regeneration: state-of-the-art and future trends*. Advanced Healthcare Materials, 2020, 9 (5): 1901435.

[3] Stanger BZ. *Cellular homeostasis and repair in the mammalian liver*. Annual Review of Physiology, 2015, 77: 179-200.

[4] Del Campo JA, Gallego P, Grande L. *Role of inflammatory response in liver diseases: Therapeutic strategies*. World Journal of Hepatology, 2018, 10(1): 1-7.

[5] Jungermann K, Keitzmann T. *Zonation of parenchymal and nonparenchymal metabolism in liver*. Annual Review of Nutrition, 1996, 16(1): 179-203.

[6] Felmlee DJ, Baumert TF, Grün D. *Zooming in on liver zonation*. Hepatology, 2018, 67(2): 784-787.

[7] Si-Tayeb K, Lemaigre FP, Duncan SA. *Organogenesis and development of the liver*. Developmental Cell, 2010, 18(2): 175-189.

[8] Heydari Z, Najimi M, Mirzaei H, Shpichka A, Ruoss M, Farzaneh Z, Montazeri L, Piryaei A, Timashev P, Gramignoli R, Nussler A, Baharvand H, Vosough M. *Tissue engineering in liver regenerative medicine: Insights into novel translational technologies*. Cells, 2020, 9(2): 304.

[9] Zaret KS. *Regulatory phases of early liver development: Paradigms of organogenesis*. Nature Reviews Genetics, 2002, 3(7): 499-512.

[10] Forbes SJ, Newsome PN. *Liver regeneration-mechanisms and models to clinical application*. Nature Reviews Gastroenterology & Hepatology, 2016, 13(8): 473-485.

[11] Michalopoulos GK, Bhushan B. *Liver regeneration: Biological and pathological mechanisms and implications*. Nature Reviews Gastroenterology & Hepatology, 2021, 18(1): 40-55.

[12] Faccioli LA, Dias ML, Paranhos BA, dos Santos Goldenberg RC. *Liver cirrhosis: An overview of experimental models in rodents*. Life Sciences, 2022, 301: 120615.

[13] Marcellin P, Kutala BK. *Liver diseases: A major, neglected global public health problem requiring urgent actions and large-scale screening*. Liver International, 2018, 38: 2-6.

[14] Tanaka M, Miyajima A. *Liver regeneration and fibrosis after inflammation*. Inflammation and Regeneration, 2016, 36(1): 19.

[15] Mallat A, Lotersztajn S. *Cellular mechanisms of tissue fibrosis. 5. Novel insights into liver fibrosis*. American Journal of Physiology-Cell Physiology, 2013, 305(8): C789-C799.

[16] Bhatia SN, Underhill GH, Zaret KS, Fox IJ. *Cell and tissue engineering for liver disease*. Science Translational Medicine, 2014, 6(245): 245sr2-245sr2.

[17] Dutkowski P, Linecker M, DeOliveira ML, Müllhaupt B, Clavien P-A. *Challenges to liver transplantation and strategies to improve outcomes*. Gastroenterology, 2015, 148(2): 307-323.

[18] Palakkan AA, Hay DC, PR AK, TV K, Ross JA. *Liver tissue engineering and cell sources: Issues and challenges*. Liver International, 2013, 33(5): 666-676.

[19] Mirdamadi ES, Kalhori D, Zakeri N, Azarpira N, Solati-Hashjin M. *Liver tissue engineering as an emerging alternative for liver disease treatment*. Tissue Engineering Part B: Reviews, 2020, 26(2): 145-63.

[20] Lee SY, Kim HJ, Choi D. *Cell sources, liver support systems and liver tissue engineering: Alternatives to liver transplantation*. International Journal of Stem Cells, 2015, 8(1): 36-47.

[21] Berthiaume F, Maguire TJ, Yarmush ML. *Tissue engineering and regenerative medicine: History, progress, and challenges*. Annual Review of Chemical and Biomolecular Engineering, 2011, 2: 403-430.

[22] Matai I, Kaur G, Seyedsalehi A, McClinton A, Laurencin CT. *Progress in 3D bioprinting technology for tissue/organ regenerative engineering*. Biomaterials, 2020, 226: 119536.

[23] Zhu L, Wang Z, Xia H, Yu H. *Design and fabrication of the vertical-flow bioreactor for compaction hepatocyte culture in drug testing application*. Biosensors, 2021, 11(5): 160.

[24] Godoy P, Hewitt NJ, Albrecht U, Andersen ME, Ansari N, Bhattacharya S, et al. *Recent advances in 2D and 3D in vitro systems using primary hepatocytes, alternative hepatocyte sources and non-parenchymal liver cells and their use in investigating mechanisms of hepatotoxicity, cell signaling and ADME*. Archives of Toxicology, 2013, 87(8): 1315-1530.

[25] Peter JO, Chan K, Silber PM. *Human and animal hepatocytes in vitro with extrapolation in vivo*. Chemico-biological Interactions, 2004, 150(1): 97-114.

[26] Dunn JC, Tompkins RG, Yarmush ML. *Long-term in vitro function of adult hepatocytes in a collagen sandwich configuration*. Biotechnology Progress, 1991, 7(3): 237-245.

[27] LeCluyse EL, Audus KL, Hochman JH. *Formation of extensive canalicular networks by rat hepatocytes cultured in collagen-sandwich configuration*. American Journal of Physiology - Cell Physiology, 1994, 266(6): C1764-C1774.

[28] Fausto N. *Liver regeneration*. Journal of Hepatology, 2000, 32: 19-31.

[29] Zhang J, Zhao X, Liang L, Li J, Demirci U, Wang S. *A decade of progress in liver regenerative medicine*. Biomaterials, 2018, 157: 161-176.

[30] Kim K, Ohashi K, Utoh R, Kano K, Okano T. *Preserved liver-specific functions of hepatocytes in 3D co-culture with endothelial cell sheets*. Biomaterials, 2012, 33(5): 1406-1413.

[31] Wang Y, Yao HL, Cui CB, Wauthier E, Barbier C, Costello MJ, Moss N, Yamauchi M, Sricholpech M, Gerber D, Loboa EG, Reid LM. *Paracrine signals from mesenchymal cell populations govern the expansion and differentiation of human hepatic stem cells to adult liver fates*. Hepatology, 2010, 52 (4), 1443-1454.

[32] Sassi L, Ajayi O, Campinoti S, Natarajan D, McQuitty C, Siena RR, Mantero S, Coppi Pd, Pellegata AF, Chockshi S, Urbani L. *A perfusion bioreactor for longitudinal monitoring of bioengineered liver constructs*. Nanomaterials, 2021, 11(2): 275.

[33] Yamada M, Utoh R, Ohashi K, Tatsumi K, Yamato M, Okano T, Seki M. *Controlled formation of heterotypic hepatic micro-organoids in anisotropic hydrogel microfibers for long-term preservation of liver-specific functions*. Biomaterials, 2012, 33(33), 8304-8315.

[34] Allen JW, Khetani SR, Bhatia SN. *In vitro zonation and toxicity in a hepatocyte bioreactor*. Toxicological Sciences, 2005, 84(1), 110-119.

[35] McCarty WJ, Usta OB, Yarmush ML. *A microfabricated platform for generating physiologically-relevant hepatocyte zonation*. Scientific Reports, 2016, 6(1): 1-10.

[36] Allen JW, Bhatia SN. *Formation of steady-state oxygen gradients in vitro: Application to liver zonation*. Biotechnology and Bioengineering, 2003, 82(3): 253-262.

[37] Jungermann K, Kietzmann T. *Oxygen: modulator of metabolic zonation and disease of the liver*. Hepatology, 2000, 31(2): 255-260.

[38] Burke ZD, Reed KR, Yeh S-W, Meniel V, Sansom OJ, Clarke AR, Tosh D. *Spatiotemporal regulation of liver development by the Wnt/β-catenin pathway*. Scientific Reports, 2018, 8(1): 1-9.

[39] Aigner TB, DeSimone E, Scheibel T. *Biomedical applications of recombinant silk-based materials*. Advanced Materials, 2018, 30(19): 1704636.

[40] Abbott A, Coburn JM. *HepaRG maturation in silk fibroin scaffolds: Toward developing a 3D in vitro liver model*. ACS Biomaterials Science & Engineering, 2021.

[41] Kundu S, Kundu B, Talukdar S, Bano S, Nayak S, Kundu J, Mandal BB, Bhardwaj N, Botlagunta M, Dash BC, Acharya C. *Nonmulberry silk biopolymers*. Biopolymers, 2012, 97(6): 455-467.

[42] Gupta KA, Mita K, Arunkumar KP, Nagaraju J. *Molecular architecture of silk fibroin of Indian golden silkmoth, Antheraea assama*. Scientific Reports 2015, 5(1): 1-17.

[43] Kukla DA, Stoppel WL, Kaplan DL, Khetani SR. *Assessing the compatibility of primary human hepatocyte culture within porous silk sponges*. RSC Advances, 2020, 10(62): 37662-37674.

[44] Jiang W-C, Cheng Y-H, Yen M-H, Chang Y, Yang VW, Lee OK. *Cryo-chemical decellularization of the whole liver for mesenchymal stem cells-based functional hepatic tissue engineering*. Biomaterials, 2014, 35(11): 3607-3617.

[45] Shupe T, Williams M, Brown A, Willenberg B, Petersen BE. *Method for the decellularization of intact rat liver*. Organogenesis, 2010, 6(2): 134-136.

[46] Coronado RE, Somaraki-Cormier M, Natesan S, Christy RJ, Ong JL, Halff GA. *Decellularization and solubilization of porcine liver for use as a substrate for porcine hepatocyte culture: Method optimization and comparison*. Cell Transplantation, 2017, 26(12): 1840-1854.

[47] Loneker AE, Faulk DM, Hussey GS, D'Amore A, Badylak SF. *Solubilized liver extracellular matrix maintains primary rat hepatocyte phenotype in-vitro*. Journal of Biomedical Materials Research Part A, 2016, 104(4): 957-965.

[48] Panwar A, Das P, Tan LP. *3D hepatic organoid-based advancements in LIVER tissue engineering*. Bioengineering, 2021, 8(11): 185.

[49] Lorente S, Hautefeuille M, Sanchez-Cedillo A. *The liver, a functionalized vascular structure*. Scientific Reports, 2020, 10(1): 1-10.

[50] Hoshiba T, Otaki T, Nemoto E, Maruyama H, Tanaka M. *Blood-compatible polymer for hepatocyte culture with high hepatocyte-specific functions toward bioartificial liver development*. ACS Applied Materials & Interfaces, 2015, 7(32): 18096-18103.

[51] Reid LM, Fiorino AS, Sigal SH, Brill S, Holst PA. *Extracellular matrix gradients in the space of Disse: Relevance to liver biology*. Wiley Online Library, 1992, 15(6), 1198-1203.

[52] Miyajima A, Tanaka M, Itoh T. *Stem/progenitor cells in liver development, homeostasis, regeneration, and reprogramming*. Cell Stem Cell, 2014, 14(5): 561-574.

[53] Poisson J, Lemoinne S, Boulanger C, Durand F, Moreau R, Valla D, Rautou P-E. *Liver sinusoidal endothelial cells: Physiology and role in liver diseases*. Journal of Hepatology 2017, 66(1): 212-227.

[54] Sørensen KK, Simon-Santamaria J, McCuskey RS, Smedsrød B. *Liver sinusoidal endothelial cells*. Comprehensive Physiology, 2011, 5(4): 1751-1774.

[55] Asahina K, Tsai SY, Li P, Ishii M, Maxson Jr RE, Sucov HM, Tsukamoto H. *Mesenchymal origin of hepatic stellate cells, submesothelial cells, and perivascular mesenchymal cells during mouse liver development*. Hepatology, 2009, 49(3): 998-1011.

[56] Kolios G, Valatas V, Kouroumalis E. *Role of Kupffer cells in the pathogenesis of liver disease*. World Journal of Gastroenterology: WJG, 2006, 12(46): 7413.

[57] Dixon LJ, Barnes M, Tang H, Pritchard MT, Nagy LE. *Kupffer cells in the liver*. Comprehensive Physiology, 2013, 3(2): 785.

[58] Gebhardt R. *Metabolic zonation of the liver: Regulation and implications for liver function*. Pharmacology & Therapeutics, 1992, 53(3), 275-354.

[59] Smith DM. *The ontogenetic history of the mitochondria of the hepatic cell of the white rat*. Journal of Morphology, 1931, 52(2): 485-511.

[60] Kietzmann T. *Metabolic zonation of the liver: The oxygen gradient revisited*. Redox Biology, 2017, 11: 622-630.

[61] Cunningham RP, Porat-Shliom N. *Liver Zonation - Revisiting old questions with new technologies*. Frontiers in Physiology, 2021: 1433.

[62] Schofield CA, Walker TM, Taylor MA, Patel M, Vlachou DF, Macina JM, Vidgeon-Hart MP, Williams A, McGill PJ, Newman CF, Sakatis MZ. *Evaluation of a three-dimensional primary human hepatocyte spheroid model: Adoption and industrialization for the enhanced detection of drug-induced liver injury*. Chemical Research in Toxicology, 2021, 34(12): 2485-2499.

[63] Miyamoto D, Hara T, Hyakutake A, Nakazawa K. *Changes in HepG2 spheroid behavior induced by differences in the gap distance between spheroids in a micropatterned culture system*. Journal of Bioscience and Bioengineering, 2018, 125(6): 729-735.

[64] Mueller-Klieser W, Freyer J, Sutherland R. *Influence of glucose and oxygen supply conditions on the oxygenation of multicellular spheroids*. British Journal of Cancer, 1986, 53(3): 345-353.

[65] Landry J, Bernier D, Ouellet C, Goyette RA, Marceau N. *Spheroidal aggregate culture of rat liver cells: Histotypic reorganization, biomatrix deposition, and maintenance of functional activities*. The Journal of Cell Biology, 1985, 101(3): 914-923.

[66] Jiang H-L, Kim Y-K, Cho K-H, Jang Y-C, Choi Y-J, Chung J-H, Cho C-S. *Roles of spheroid formation of hepatocytes in liver tissue engineering*. International Journal of Stem Cells, 2010, 3(2): 69-73.

[67] Hardelauf H, Frimat J-P, Stewart JD, Schormann W, Chiang Y-Y, Lampen P, . *Microarrays for the scalable production of metabolically relevant tumour spheroids: A tool for modulating chemosensitivity traits*. Lab on a Chip, 2011, 11(3): 419-428.

[68] Huang B-W, Gao J-Q. A*pplication of 3D cultured multicellular spheroid tumor models in tumor-targeted drug delivery system research*. Journal of Controlled Release, 2018, 270: 246-259.

[69] Zhu X, Wu Q, He Y, Gao M, Li Y, Peng W, Li S, Liu Y, Zhang R, Bao J. *Fabrication of size-controllable and arrangement-orderly HepG2 spheroids for drug screening via decellularized liver matrix-derived micropattern array chips*. ACS Omega, 2022, 7(2): 2364-2376.

[70] Pingitore P, Sasidharan K, Ekstrand M, Prill S, Lindén D, Romeo S. *Human multilineage 3D spheroids as a model of liver steatosis and fibrosis*. International Journal of Molecular Sciences, 2019, 20(7): 1629.

[71] Bell CC, Hendriks DF, Moro SM, Ellis E, Walsh J, Renblom A, Puigvert F, Dankers ACA, Jacobs F, Snoeys J, Sison-Young RL, Jenkins RE, Nordling Å, Mkrtchian S, Park BK, Kitteringham NR, Goldring CEP, Lauschke VM, Ingelman-Sundberg M. *Characterization of primary human hepatocyte spheroids as a model system for drug-induced liver injury, liver function and disease*. Scientific Reports, 2016, 6(1): 1-13.

[72] Bell CC, Chouhan B, Andersson LC, Andersson H, Dear JW, Williams DP, Söderberg M. *Functionality of primary hepatic non-parenchymal cells in a 3D spheroid model and contribution to acetaminophen hepatotoxicity*. Archives of Toxicology, 2020, 94(4): 1251-1263.

[73] Lee G, Kim H, Park JY, Kim G, Han J, Chung S, Yang JH, Jeon JS, Woo D-H, Han C, Kim SK, Park H-J, Kim J-H. *Generation of uniform liver spheroids from human pluripotent stem cells for imaging-based drug toxicity analysis*. Biomaterials, 2021, 269: 120529.

[74] Ramli MNB, Lim YS, Koe CT, Demircioglu D, Tng W, Gonzales KAU, Tan CP, Szczerbinska I, Liang H, Soe EL, Lu Z, Ariyachet C, Yu KM, Koh SH, Yaw LP, Jumat NHB, Lim JSY, Wright G, Shabbir A, Dan YY, Ng H-H, Chan Y-S. *Human pluripotent stem cell-derived organoids as models of liver disease*. Gastroenterology, 2020, 159: 1471-1486. e12.

[75] Chen S, Wang J, Ren H, Liu Y, Xiang C, Li C, Lu S, Shi Y, Deng H, Shi X. *Hepatic spheroids derived from human induced pluripotent stem cells in bio-artificial liver rescue porcine acute liver failure*. Cell Research, 2020, 30(1): 95-97.

[76] Ye S, Boeter JW, Penning LC, Spee B, Schneeberger K. *Hydrogels for liver tissue engineering*. Bioengineering, 2019, 6(3): 59.

[77] Xia T, Zhao R, Liu W, Huang Q, Chen P, Waju YN, Al-Ani MK, Lv Y, Yang L. *Effect of substrate stiffness on hepatocyte migration and cellular Young's modulus*. Journal of Cellular Physiology, 2018, 233(9): 6996-7006.

[78] Xia T, Zhao R, Feng F, Yang L. *The effect of matrix stiffness on human hepatocyte migration and function - an in vitro research*. Polymers, 2020, 12(9): 1903.

[79] Higuchi A, Kurihara M, Kobayashi K, Su Cho C, Akaike T, Hara M. *Albumin and urea production by hepatocytes cultured on extracellular matrix proteins-conjugated poly (vinyl alcohol) membranes*. Journal of Biomaterials Science, Polymer Edition, 2005, 16(7): 847-860.

[80] Meng D, Lei X, Li Y, Kong Y, Huang D, Zhang G. *Three dimensional polyvinyl alcohol scaffolds modified with collagen for HepG2 cell culture*. Journal of Biomaterials Applications 2020;35:459-70.

[81] Liu T, van den Berk L, Wondergem JA, Tong C, Kwakernaak MC, Braak Bt, Heinrich D, Water Bvd, Kieltyka RE. *Squaramide-based supramolecular materials drive HepG2 spheroid differentiation*. Advanced Healthcare Materials, 2021, 10(11): 2001903.

[82] Cui J, Wang H, Shi Q, Sun T, Huang Q, Fukuda T. *Multicellular co-culture in three-dimensional gelatin methacryloyl hydrogels for liver tissue engineering*. Molecules, 2019, 24(9): 1762.

[83] Wang X, Yu X, Yan Y, Zhang R. *Liver tissue responses to gelatin and gelatin/chitosan gels*. Journal of Biomedical Materials Research Part A: An Official Journal of The Society for Biomaterials, The Japanese Society for Biomaterials, and The Australian Society for Biomaterials and the Korean Society for Biomaterials, 2008, 87(1): 62-68.

[84] Rajalekshmi R, Shaji AK, Joseph R, Bhatt A. *Scaffold for liver tissue engineering: Exploring the potential of fibrin incorporated alginate dialdehyde-gelatin hydrogel*. International Journal of Biological Macromolecules, 2021, 166: 999-1008.

[85] Sk MM, Das P, Panwar A, Tan LP. *Synthesis and characterization of site selective photo-crosslinkable glycidyl methacrylate functionalized gelatin-based 3D hydrogel scaffold for liver tissue engineering*. Materials Science and Engineering: C, 2021, 123: 111694.

[86] Vasanthan KS, Subramaniam A, Krishnan UM, Sethuraman S. *Influence of 3D porous galactose containing PVA/gelatin hydrogel scaffolds on three-dimensional spheroidal morphology of hepatocytes*. Journal of Materials Science: Materials in Medicine, 2015, 26(1): 1-20.

[87] Malinen MM, Kanninen LK, Corlu A, Isoniemi HM, Lou Y-R, Yliperttula ML, Urtti AO. *Differentiation of liver progenitor cell line to functional organotypic cultures in 3D nanofibrillar cellulose and hyaluronan-gelatin hydrogels*. Biomaterials, 2014, 35(19): 5110-5121.

[88] Serna-Márquez N, Rodríguez-Hernández A, Ayala-Reyes M, Martínez-Hernández LO, Peña-Rico MÁ, Carretero-Ortega J, Hautefeuille M, Vázquez-Victoria G. *Fibrillar collagen type I participates in the survival and aggregation of primary hepatocytes cultured on soft hydrogels*. Biomimetics, 2020, 5(2): 30.

[89] Aghdam SK, Khoshfetrat AB, Rahbarghazi R, Jafarizadeh-Malmiri H, Khaksar M. *Collagen modulates functional activity of hepatic cells inside alginate-galactosylated chitosan hydrogel microcapsules*. International Journal of Biological Macromolecules, 2020, 156: 1270-1278.

[90] Jiang J, Tan Y, Liu A, Yan R, Ma Y, Guo L, Sun J, Guo Z, Fan H. *Tissue engineered artificial liver model based on viscoelastic hyaluronan-collagen hydrogel and the effect of EGCG intervention on ALD*. Colloids and Surfaces B: Biointerfaces, 2021, 206: 111980.

[91] Seale N, Ramaswamy S, Shih Y-R, Verma I, Varghese S. *Macroporous dual compartment hydrogels for minimally invasive transplantation of primary human hepatocytes*. Transplantation, 201, 102(9): e373-e381.

[92] Song W, Lu Y-C, Frankel AS, An D, Schwartz RE, Ma M. *Engraftment of human induced pluripotent stem cell-derived hepatocytes in immunocompetent mice via 3D co-aggregation and encapsulation*. Scientific Reports, 2015, 5(1): 1-13.

[93] Zhao Y, Xu B, Liang W, Ding Y, Li J, Zhang Y, Xu F, Zhou H, Xu Y. *Multisite injection of bioengineered hepatic units from collagen hydrogel and neonatal liver cells in parenchyma improves liver cirrhosis*. Tissue Engineering Part A, 2019, 25(15-16): 1167-1174.

[94] Bate TS, Gadd VL, Forbes SJ, Callanan A. *Response differences of HepG2 and primary mouse hepatocytes to morphological changes in electrospun PCL scaffolds*. Scientific Reports, 2021, 11(1): 1-13.

[95] Lewis PL, Green RM, Shah RN. *3D-printed gelatin scaffolds of differing pore geometry modulate hepatocyte function and gene expression*. Acta Biomaterialia, 2018, 69: 63-70.

[96] Fasolino I, Guarino V, Marrese M, Cirillo V, Vallifuoco M, Tamma M, Vassallo V, Bracco A, Calise F, Ambrosia L. *HepG2 and human healthy hepatocyte in vitro culture and co-culture in PCL electrospun platforms*. Biomedical Materials, 2017, 13(1): 015017.

[97] Gao Y, Callanan A. *Influence of surface topography on PCL electrospun scaffolds for liver tissue engineering*. Journal of Materials Chemistry B, 2021, 9(38): 8081-8093.

[98] Mobarra N, Soleimani M, Ghayour-Mobarhan M, Safarpour S, Ferns GA, Pakzad R, Pasalar P. *Hybrid poly-l-lactic acid/poly (ε-caprolactone) nanofibrous scaffold can improve biochemical and molecular markers of human induced pluripotent stem cell-derived hepatocyte-like cells*. Journal of Cellular Physiology, 2019, 234(7): 11247-11255.

[99] Wang B, Jakus AE, Baptista PM, Soker S, Soto-Gutierrez A, Abecassis MM, Shah RN, Wertheim JA. *Functional maturation of induced pluripotent stem cell hepatocytes in extracellular matrix-a comparative analysis of bioartificial liver microenvironments*. Stem Cells Translational Medicine, 2016, 5(9): 1257-1267.

[100] Liu M, Yang J, Hu W, Zhang S, Wang Y. *Superior performance of co-cultured mesenchymal stem cells and hepatocytes in poly (lactic acid-glycolic acid) scaffolds for the treatment of acute liver failure*. Biomedical Materials, 2016, 11(1): 015008.

[101] Liu X, Zhou L, Heng P, Xiao J, Lv J, Zhang Q, Hickey ME, Tu Q, Wang J. *Lecithin doped electrospun poly (lactic acid)-thermoplastic polyurethane fibers for hepatocyte viability improvement*. Colloids and Surfaces B: Biointerfaces, 2019, 175: 264-271.

[102] Verma SK, Modi A, Bellare J. *Three-dimensional multiscale fiber matrices: Development and characterization for increased HepG2 functional maintenance for bio-artificial liver application*. Biomaterials science, 2018, 6(2): 280-291.

[103] Ghahremanzadeh F, Alihosseini F, Semnani D. *Investigation and comparison of new galactosylation methods on PCL/chitosan scaffolds for enhanced liver tissue engineering*. International Journal of Biological Macromolecules, 2021, 174: 278-288.

[104] Raposo CD, Costa R, Petrova KT, Brito C, Scotti MT, Cardoso MM. *Development of novel galactosylated PLGA nanoparticles for hepatocyte targeting using molecular modelling*. Polymers, 2020, 12(1): 94.

[105] Vasanthan KS, Subramanian A, Krishnan UM, Sethuraman S. *Role of biomaterials, therapeutic molecules and cells for hepatic tissue engineering*. Biotechnology Advances, 2012, 30(3): 742-752.

[106] Holland C, Numata K, Rnjak-Kovacina J, Seib FP. *The biomedical use of silk: Past, present, future*. Advanced Healthcare Materials, 2019, 8(1): 1800465.

[107] Lee-Montiel FT, George SM, Gough AH, Sharma AD, Wu J, DeBiasio R, Vernetti LA, Taylor DL. *Control of oxygen tension recapitulates zone-specific functions in human liver microphysiology systems*. Experimental Biology and Medicine, 2017, 242(16): 1617-1632.

[108] Gandomani MG, Lotfi AS, Tamandani DK, Arjmand S, Alizadeh S. *The enhancement of differentiating adipose derived mesenchymal stem cells toward hepatocyte like cells using gelatin cryogel scaffold*. Biochemical and Biophysical Research Communications, 2017, 491(4): 1000-1006.

[109] Klaas M, Möll K, Mäemets-Allas K, Loog M, Järvekülg M, Jaks V. *Long-term maintenance of functional primary human hepatocytes in 3D gelatin matrices produced by solution blow spinning*. Scientific Reports, 2021, 11(1): 1-13.

[110] Jiankang H, Dichen L, Yaxiong L, Bo Y, Hanxiang Z, Qin L, Bingheng L, Yi L. *Preparation of chitosan-gelatin hybrid scaffolds with well-organized microstructures for hepatic tissue engineering*. Acta Biomaterialia, 2009, 5(1): 453-461.

[111] Huang F, Cui L, Peng CH, Wu XB, Han BS, Dong YD. *Preparation of three-dimensional macroporous chitosan–gelatin B microspheres and HepG2-cell culture*. Journal of Tissue Engineering and Regenerative Medicine, 2016, 10(12): 1033-1040.

[112] Zhang Y, Wang QS, Yan K, Qi Y, Wang GF, Cui YL. *Preparation, characterization, and evaluation of genipin crosslinked chitosan/gelatin three-dimensional scaffolds for liver tissue engineering applications*. Journal of Biomedical Materials Research Part A, 2016, 104(8): 1863-1870.

[113] German CL, Madihally SV. *Type of endothelial cells affects HepaRG cell acetaminophen metabolism in both 2D and 3D porous scaffold cultures*. Journal of Applied Toxicology, 2019, 39(3): 461-472.

[114] Feng Z-Q, Chu X, Huang N-P, Wang T, Wang Y, Shi X, Ding Y, Gu Z-Z. *The effect of nanofibrous galactosylated chitosan scaffolds on the formation of rat primary hepatocyte aggregates and the maintenance of liver function*. Biomaterials, 2009, 30(14): 2753-2763.

[115] Fan J, Shang Y, Yuan Y, Yang J. *Preparation and characterization of chitosan/galactosylated hyaluronic acid scaffolds for primary hepatocytes culture*. Journal of Materials Science: Materials in Medicine, 2010, 21(1): 319-327.

[116] Rajendran D, Hussain A, Yip D, Parekh A, Shrirao A, Cho CH. *Long-term liver-specific functions of hepatocytes in electrospun chitosan nanofiber scaffolds coated with fibronectin*. Journal of Biomedical Materials Research Part A, 2017, 105(8): 2119-2128.

[117] Aleahmad F, Ebrahimi S, Salmannezhad M, Azarnia M, Jaberipour M, Hoseini M, Talaei-Khozani T. *Heparin/collagen 3D scaffold accelerates hepatocyte differentiation of Wharton's jelly-derived mesenchymal stem cells*. Tissue Engineering and Regenerative Medicine, 2017, 14(4): 443-452.

[118] Xu L, Wang S, Sui X, Wang Y, Su Y, Huang L, Zhang Y, Chen Z, Chen Q, Du H, Zhang Y. *Mesenchymal stem cell-seeded regenerated silk fibroin complex matrices for liver regeneration in an animal model of acute liver failure*. ACS Applied Materials & Interfaces, 2017, 9(17): 14716-14723.

[119] Elkayam T, Amitay-Shaprut S, Dvir-Ginzberg M, Harel T, Cohen S. *Enhancing the drug metabolism activities of C3A-a human hepatocyte cell line-by tissue engineering within alginate scaffolds*. Tissue engineering, 2006, 12 (5): 1357-1368.

[120] Lin N, Lin J, Bo L, Weidong P, Chen S, Xu R. *Differentiation of bone marrow-derived mesenchymal stem cells into hepatocyte-like cells in an alginate scaffold*. Cell proliferation, 2010, 43(5): 427-434.

[121] Gao C, Yang Y, Zhang Y, Qian M, Yang J. *HGF gene delivering alginate/galactosylated chitosan sponge scaffold for three-dimensional coculture of hepatocytes/3T3 cells*. DNA and Cell Biology, 2020, 39(3): 451-458.

[122] Moghe PV, Berthiaume F, Ezzell RM, Toner M, Tompkins RG, Yarmush ML. *Culture matrix configuration and composition in the maintenance of hepatocyte polarity and function*. Biomaterials, 1996, 17(3): 373-385.

[123] Zhang X, Chen X, Hong H, Hu R, Liu J, Liu C. *Decellularized extracellular matrix scaffolds: Recent trends and emerging strategies in tissue engineering*. Bioactive materials, 2022, 10: 15-31.

[124] Wang Y, Nicolas CT, Chen HS, Ross JJ, De Lorenzo SB, Nyberg SL. *Recent advances in decellularization and recellularization for tissue-engineered liver grafts*. Cells Tissues Organs, 2017, 204(3-4): 125-136.

[125] Faulk DM, Wildemann JD, Badylak SF. *Decellularization and cell seeding of whole liver biologic scaffolds composed of extracellular matrix*. Journal of Clinical and Experimental Hepatology, 2015, 5(1): 69-80.

[126] Uygun BE, Soto-Gutierrez A, Yagi H, Izamis M-L, Guzzardi MA, Shulman C, Milwid J, Kobayashi N, Tilles A, Berthiaume F, Hertle M. *Organ reengineering through development of a transplantable recellularized liver graft using decellularized liver matrix*. Nature Medicine, 2010, 16(7): 814-820.

[127] Shaheen MF, Joo DJ, Ross JJ, Anderson BD, Chen HS, Huebert RC, Li Y, Amiot B, Young A, Zlochiver V, Nelson E. S*ustained perfusion of revascularized bioengineered livers heterotopically transplanted into immunosuppressed pigs*. Nature Biomedical Engineering, 2020, 4(4): 437-445.

[128] Ravichandran A, Murekatete B, Moedder D, Meinert C, Bray LJ. *Photocrosslinkable liver extracellular matrix hydrogels for the generation of 3D liver microenvironment models*. Scientific Reports, 2021, 11(1): 1-12.

[129] Hussein KH, Park K-M, Yu L, Kwak H-H, Woo H-M. *Decellularized hepatic extracellular matrix hydrogel attenuates hepatic stellate cell activation and liver fibrosis*. Materials Science and Engineering: C, 2020, 116: 111160.

[130] Kostallari E, Valainathan S, Biquard L, Shah VH, Rautou P-E. *Role of extracellular vesicles in liver diseases and their therapeutic potential*. Advanced Drug Delivery Reviews, 2021, 175: 113816.

[131] Gao J, Wei B, de Assuncao TM, Liu Z, Hu X, Ibrahim S, Cooper SA, Cao S, Shah VH, Kostallari E. *Hepatic stellate cell autophagy inhibits extracellular vesicle release to attenuate liver fibrosis*. Journal of Hepatology, 2020, 73(5): 1144-1154.

[132] Kostallari E, Hirsova P, Prasnicka A, Verma VK, Yaqoob U, Wongjarupong N, Roberts LR, Shah VH. *Hepatic stellate cell-derived PDGFRα-enriched extracellular vesicles promote liver fibrosis in mice through SHP2*. Hepatology (Baltimore, Md), 2018, 68(1): 333.

[133] Povero D, Pinatel EM, Leszczynska A, Goyal NP, Nishio T, Kim J, Kneiber D, de Araujo Horcel L, Eguchi A, Ordonez PM, Kisseleva T. *Human induced pluripotent stem cell–derived extracellular vesicles reduce hepatic stellate cell activation and liver fibrosis*. JCI insight, 2019, 4(14).

[134] Du Y, Li D, Han C, Wu H, Xu L, Zhang M, Zhang J, Chen X. *Exosomes from human-induced pluripotent stem cell–derived mesenchymal stromal cells (hiPSC-MSCs) protect liver against hepatic ischemia/reperfusion injury via activating sphingosine kinase and sphingosine-1-phosphate signaling pathway*. Cellular Physiology and Biochemistry, 2017, 43(2): 611-625.

[135] Bruno S, Pasquino C, Sanchez MBH, Tapparo M, Figliolini F, Grange C, Chiabotto G, Cedrino M, Deregibus MC, Tetta C, Camussi G. *HLSC-derived extracellular vesicles attenuate liver fibrosis and inflammation in a murine model of non-alcoholic steatohepatitis*. Molecular Therapy, 2020, 28(2): 479-489.

[136] Tan CY, Lai RC, Wong W, Dan YY, Lim S-K, Ho HK. *Mesenchymal stem cell-derived exosomes promote hepatic regeneration in drug-induced liver injury models*. Stem Cell Research & Therapy, 2014, 5(3): 1-14.

[137] Verstegen MM, Willemse J, Van Den Hoek S, Kremers G-J, Luider TM, van Huizen NA, Willemssen FE, Metselaar HJ, IJzermans JN, van der Laan LJ, de Jonge J. *Decellularization of whole human liver grafts using controlled perfusion for transplantable organ bioscaffolds*. Stem Cells and Development, 2017, 26(18): 1304-1315.

[138] Debnath T, Mallarpu CS, Chelluri LK. *Development of bioengineered organ using biological acellular rat liver scaffold and hepatocytes*. Organogenesis, 2020, 16(2): 61-72.

[139] Jaramillo M, Yeh H, Yarmush ML, Uygun BE. *Decellularized human liver extracellular matrix (hDLM)-mediated hepatic differentiation of human induced pluripotent stem cells (hIPSCs)*. Journal of Tissue Engineering and Regenerative Medicine, 2018, 12(4): e1962-e1973.

[140] Lewis PL, Su J, Yan M, Meng F, Glaser SS, Alpini GD, Green RM, Sosa-Pineda B, Shah RN. *Complex bile duct network formation within liver decellularized extracellular matrix hydrogels*. Scientific reports, 2018, 8(1): 1-14.

[141] Zhao C, Li Y, Peng G, Lei X, Zhang G, Gao Y. *Decellularized liver matrix-modified chitosan fibrous scaffold as a substrate for C3A hepatocyte culture*. Journal of Biomaterials Science, Polymer Edition, 2020, 31(8): 1041-1056.

[142] Agarwal T, Maiti TK, Ghosh SK. *Decellularized caprine liver-derived biomimetic and pro-angiogenic scaffolds for liver tissue engineering*. Materials Science and Engineering: C, 2019, 98: 939-948.

[143] Saleh T, Ahmed E, Yu L, Song SH, Park KM, Kwak HH, Woo HM. *Conjugating homogenized liver-extracellular matrix into decellularized hepatic scaffold for liver tissue engineering*. Journal of Biomedical Materials Research Part A, 2020, 108(10): 1991-2004.

[144] Asadi M, Lotfi H, Salehi R, Mehdipour A, Zarghami N, Akbarzadeh A, Alizadeh E. *Hepatic cell-sheet fabrication of differentiated mesenchymal stem cells using decellularized extracellular matrix and thermoresponsive polymer*. Biomedicine & Pharmacotherapy, 2021, 134: 111096.

[145] Guguen-Guillouzo C, Guillouzo A. *General review on in vitro hepatocyte models and their applications*. Hepatocytes: Springer, 2010, 1-40.

[146] Agarwal T, Banerjee D, Konwarh R, Esworthy T, Kumari J, Onesto V, Das P, Lee BH, Wagener FA, Makvandi P, Mattoli V. *Recent advances in bioprinting technologies for engineering hepatic tissue*. Materials Science and Engineering: C, 2021, 112013.

[147] Dey M, Ozbolat IT. *3D bioprinting of cells, tissues and organs*. Scientific Reports, 2020, 10(1): 1-3.

[148] Murphy SV, Atala A. *3D bioprinting of tissues and organs*. Nature Biotechnology, 2014, 32(8): 773-785.

[149] Goulart E, de Caires-Junior LC, Telles-Silva KA, Araujo BHS, Rocco SA, Sforca M, de Sousa IL, Kobayashi GS, Musso CM, Assoni AF, Oliveira D. *3D bioprinting of liver spheroids*

derived from human induced pluripotent stem cells sustain liver function and viability in vitro. Biofabrication, 2019, 12(1): 015010.

[150] Bouwmeester MC, Bernal PN, Oosterhoff LA, van Wolferen ME, Lehmann V, Vermaas M, Buchholz MB, Peiffer QC, Malda J, van der Laan LJ, Kramer NI. *Bioprinting of human liver-derived epithelial organoids for toxicity studies*. Macromolecular Bioscience, 2021, 21(12): 2100327.

[151] Yang H, Sun L, Pang Y, Hu D, Xu H, Mao S, Peng W, Wang Y, Xu Y, Zheng YC, Du S. *Three-dimensional bioprinted hepatorganoids prolong survival of mice with liver failure*. Gut, 2021, 70(3): 567-574.

[152] Ma X, Qu X, Zhu W, Li Y-S, Yuan S, Zhang H, Liu J, Wang P, Lai CSE, Zanella F, Feng GS. *Deterministically patterned biomimetic human iPSC-derived hepatic model via rapid 3D bioprinting*. Proceedings of the National Academy of Sciences, 2016, 113(8): 2206-2211.

[153] Kang D, Hong G, An S, Jang I, Yun WS, Shim JH, Jin S. *Bioprinting of multiscaled hepatic lobules within a highly vascularized construct*. Small, 2020, 16(13): 1905505.

[154] Hong G, Kim J, Oh H, Yun S, Kim CM, Jeong YM, Yun WS, Shim JH, Jang I, Kim CY, Jin S. *Production of multiple cell-laden microtissue spheroids with a biomimetic hepatic-lobule-like structure*. Advanced Materials, 2021, 33(36): 2102624.

[155] Son J, Hong SJ, Lim JW, Jeong W, Jeong JH, Kang HW. *Engineering tissue-specific, multiscale microvasculature with a capillary network for prevascularized tissue*. Small Methods, 2021, 5(10): 2100632.

[156] Moradi E, Jalili-Firoozinezhad S, Solati-Hashjin M. *Microfluidic organ-on-a-chip models of human liver tissue*. Acta Biomaterialia, 2020, 116: 67-83.

[157] Ma C, Peng Y, Li H, Chen W. *Organ-on-a-chip: A new paradigm for drug development*. Trends in Pharmacological Sciences, 2021, 42(2): 119-133.

[158] Scott SM, Ali Z. *Fabrication methods for microfluidic devices: An overview*. Micromachines, 2021, 12(3): 319.

[159] Deng J, Wei W, Chen Z, Lin B, Zhao W, Luo Y, Zhang X. *Engineered liver-on-a-chip platform to mimic liver functions and its biomedical applications: A review*. Micromachines, 2019, 10(10): 676.

[160] Kang YB, Sodunke TR, Lamontagne J, Cirillo J, Rajiv C, Bouchard MJ, Noh M. *Liver sinusoid on a chip: Long-term layered co-culture of primary rat hepatocytes and endothelial cells in microfluidic platforms*. Biotechnology and Bioengineering, 2015, 112(12): 2571-2582.

[161] Mi S, Yi X, Du Z, Xu Y, Sun W. *Construction of a liver sinusoid based on the laminar flow on chip and self-assembly of endothelial cells*. Biofabrication, 2018, 10(2): 025010.

[162] Banaeiyan AA, Theobald J, Paukštyte J, Wölfl S, Adiels CB, Goksör M. *Design and fabrication of a scalable liver-lobule-on-a-chip microphysiological platform*. Biofabrication, 2017, 9(1): 015014.

[163] Ya S, Ding W, Li S, Du K, Zhang Y, Li C, Liu J, Li F, Li P, Luo T, He L. *On-chip construction of liver lobules with self-assembled perfusable hepatic sinusoid networks*. ACS Applied Materials & Interfaces, 2021, 13(28): 32640-32652.

[164] de Mello CPP, Carmona-Moran C, McAleer CW, Perez J, Coln EA, Long CJ, Oleaga C, Riu A, Note R, Teissier S, Langer J. *Microphysiological heart–liver body-on-a-chip system with a skin mimic for evaluating topical drug delivery*. Lab on a Chip, 2020, 20(4): 749-759.

[165] Du K, Li S, Li C, Li P, Miao C, Luo T, Qiu B, Ding W. *Modeling nonalcoholic fatty liver disease on a liver lobule chip with dual blood supply*. Acta Biomaterialia, 2021, 134: 228-239.

[166] Kang YBA, Eo J, Mert S, Yarmush ML, Usta OB. *Metabolic patterning on a chip: Towards in vitro liver zonation of primary rat and human hepatocytes*. Scientific Reports, 2018, 8(1): 1-13.

[167] Bizzaro D, Russo FP, Burra P. *New perspectives in liver transplantation: From regeneration to bioengineering*. Bioengineering, 2019, 6(3): 81.

[168] Sarika P, Viha CS, Raj RS, Nirmala RJ, Kumar PA. *A non-adhesive hybrid scaffold from gelatin and gum Arabic as packed bed matrix for hepatocyte perfusion culture*. Materials Science and Engineering: C, 2015, 46: 341-347.

[169] Rebelo SP, Costa R, Silva MM, Marcelino P, Brito C, Alves PM. *Three-dimensional co-culture of human hepatocytes and mesenchymal stem cells: Improved functionality in long-term bioreactor cultures*. Journal of Tissue Engineering and Regenerative Medicine, 2017, 11(7): 2034-2045.

[170] Podichetty JT, Bhaskar PR, Singarapu K, Madihally SV. *Multiple approaches to predicting oxygen and glucose consumptions by HepG2 cells on porous scaffolds in an axial-flow bioreactor*. Biotechnology and Bioengineering, 2015, 112(2): 393-404.

[171] Kurniawan DW, Booijink R, Pater L, Wols I, Vrynas A, Storm G, Prakash J, Bansal R. *Fibroblast growth factor 2 conjugated superparamagnetic iron oxide nanoparticles (FGF2-SPIONs) ameliorate hepatic stellate cells activation in vitro and acute liver injury in vivo*. Journal of Controlled Release, 2020, 328: 640-652.

[172] Nakamura S, Ijima H. *Solubilized matrix derived from decellularized liver as a growth factor-immobilizable scaffold for hepatocyte culture*. Journal of Bioscience and Bioengineering, 2013, 116(6): 746-753.

[173] Hammond JS, Gilbert TW, Howard D, Zaitoun A, Michalopoulos G, Shakesheff KM, Beckingham IJ, Badylak SF. *Scaffolds containing growth factors and extracellular matrix induce hepatocyte proliferation and cell migration in normal and regenerating rat liver*. Journal of Hepatology, 2011, 54(2): 279-287.

[174] Park M, Yoo J-H, Lee Y-S, Lee H-J. *Lonicera caerulea extract attenuates non-alcoholic fatty liver disease in free fatty acid-induced HepG2 hepatocytes and in high fat diet-fed mice*. Nutrients, 2019, 11(3): 494.

[175] Schumacher JD, Guo GL. *Regulation of hepatic stellate cells and fibrogenesis by fibroblast growth factors*. BioMed Research International 2016, 2016.

[176] Strain AJ, Neuberger JM. *A bioartificial liver--State of the art*. Science, 2002, 295: 1005-1009.

[177] Carpentier B, Gautier A, Legallais C. *Artificial and bioartificial liver devices: Present and future*. Gut, 2009, 58(12): 1690-1702.

[178] Filippi C, Keatch SA, Rangar D, Nelson LJ, Hayes PC, Plevris JN. *Improvement of C3A cell metabolism for usage in bioartificial liver support systems*. Journal of Hepatology, 2004, 41(4): 599-605.

[179] Mavri-Damelin D, Damelin LH, Eaton S, Rees M, Selden C, Hodgson HJ. *Cells for bioartificial liver devices: The human hepatoma-derived cell line C3A produces urea but does not detoxify ammonia*. Biotechnology and Bioengineering, 2008, 99(3): 644-651.

[180] van Wenum M, Adam AA, Hakvoort TB, Hendriks EJ, Shevchenko V, van Gulik TM, Chamuleau RA, Hoekstra R. *Selecting cells for bioartificial liver devices and the importance of a 3D culture environment: a functional comparison between the HepaRG and C3A cell lines*. International Journal of Biological Sciences, 2016, 12(8): 964.

[181] Kumar A, Tripathi A, Jain S. *Extracorporeal bioartificial liver for treating acute liver diseases*. The Journal of Extra-corporeal Technology, 2011, 43(4): 195.

[182] Demetriou A, Rozga J, Podesta L, Lepage E, Morsiani E, Moscioni A, Hoffman A, McGrath M, Kong L, Rosen H, Villamil F. *Early clinical experience with a hybrid bioartificial liver*. Scandinavian Journal of Gastroenterology, 1995, 30(sup208): 111-117.

[183] Rozga J, Holzman MD, Ro M-S, Griffin DW, Neuzil DF, Giorgio T, Moscioni AD, Demetriou AA. *Development of a hybrid bioartificial liver*. Annals of Surgery, 1993, 217(5): 502.

[184] Sussman NL, Gislason GT, Conlin CA, Kelly JH. *The Hepatix extracorporeal liver assist device: Initial clinical experience*. Artificial Organs, 1994, 18(5): 390-396.

[185] Patel P, Okoronkwo N, Pyrsopoulos NT. *Future approaches and therapeutic modalities for acute liver failure*. Clinics in Liver Disease, 2018, 22(2): 419-427.

[186] Sosef MN, Abrahamse LS, van de Kerkhove M-P, Hartman R, Chamuleau RA, van Gulik TM. *Assessment of the AMC-bioartificial liver in the anhepatic pig1*. Transplantation, 2002, 73(2): 204-209.

[187] Pless G. *Artificial and bioartificial liver support*. Organogenesis, 2007, 3(1): 20-24.

[188] Sauer I, Zeilinger K, Obermayer N, Pless G, Grünwald A, Pascher A, Mieder T, Roth S, Goetz M, Kardassis D, Mas A. *Primary human liver cells as source for modular extracorporeal liver support-a preliminary report*. The International Journal of Artificial Organs, 2002, 25(10): 1001-1005.

[189] Hou Y-T, Hsu C-C. *Development of a 3D porous chitosan/gelatin liver scaffold for a bioartificial liver device*. Journal of Bioscience and Bioengineering, 2020, 129(6): 741-748.

[190] Bonalumi F, Crua C, Savina IN, Davies N, Habstesion A, Santini M, Fest-Santini S, Sandeman S. *Bioengineering a cryogel-derived bioartificial liver using particle image velocimetry defined fluid dynamics*. Materials Science and Engineering: C, 2021, 123: 111983.

[191] Sakiyama R, Blau BJ, Miki T. *Clinical translation of bioartificial liver support systems with human pluripotent stem cell-derived hepatic cells*. World Journal of Gastroenterology, 2017, 23(11): 1974.

[192] Singh VK, Seed TM. *How necessary are animal models for modern drug discovery?* Expert Opinion on Drug Discovery, 2021, 16(12), 1391-1397.

[193] Fernandez-Checa JC, Bagnaninchi P, Ye H, Sancho-Bru P, Falcon-Perez JM, Royo F, Garcia-Ruiz C, Konu O, Miranda J, Lunov O, Dejneka A. *Advanced preclinical models for evaluation of drug induced liver injury-consensus statement by the european drug-induced liver injury network* [PRO-EURO-DILI-NET]. Journal of Hepatology, 2021, 75(4): 935-959..

[194] Ahn J, Ahn J-H, Yoon S, Nam YS, Son M-Y, Oh J-H. *Human three-dimensional in vitro model of hepatic zonation to predict zonal hepatotoxicity*. Journal of Biological Engineering, 2019, 13(1): 1-15.

[195] Nguyen DG, Funk J, Robbins JB, Crogan-Grundy C, Presnell SC, Singer T, Roth AB. *Bioprinted 3D primary liver tissues allow assessment of organ-level response to clinical drug induced toxicity in vitro*. PloS One, 2016, 11(7): e0158674.

[196] Schmidt K, Berg J, Roehrs V, Kurreck J, Al-Zeer MA. *3D-bioprinted HepaRG cultures as a model for testing long term aflatoxin B1 toxicity in vitro*. Toxicology Reports, 2020, 7: 1578-1587.

[197] Gori M, Giannitelli SM, Torre M, Mozetic P, Abbruzzese F, Trombetta M, Traversa E, Moroni L, Rainer A. *Biofabrication of hepatic constructs by 3D bioprinting of a cell-laden thermogel: An effective tool to assess drug-induced hepatotoxic response*. Advanced Healthcare Materials, 2020, 9(21): 2001163.

[198] Knowlton S, Tasoglu S. *A bioprinted liver-on-a-chip for drug screening applications*. Trends in Biotechnology, 2016, 34(9): 681-682.

[199] Ma C, Zhao L, Zhou E-M, Xu J, Shen S, Wang J. *On-chip construction of liver lobule-like microtissue and its application for adverse drug reaction assay*. Analytical Chemistry, 2016, 88(3): 1719-1727.

[200] Bircsak KM, DeBiasio R, Miedel M, Alsebahi A, Reddinger R, Saleh A, Shun T, Vernetti LA, Gough A. *A 3D microfluidic liver model for high throughput compound toxicity screening in the OrganoPlate®*. Toxicology, 2021, 450: 152667.

[201] Trask Jr OJ, Moore A, LeCluyse EL. *A micropatterned hepatocyte coculture model for assessment of liver toxicity using high-content imaging analysis*. Assay and Drug Development Technologies, 2014, 12(1): 16-27.

[202] Messner S, Agarkova I, Moritz W, Kelm J. *Multi-cell type human liver microtissues for hepatotoxicity testing*. Archives of Toxicology, 2013, 87(1): 209-213.

[203] Chao P, Maguire T, Novik E, Cheng K-C, Yarmush M. *Evaluation of a microfluidic based cell culture platform with primary human hepatocytes for the prediction of hepatic clearance in human*. Biochemical Pharmacology, 2009, 78(6): 625-632.

[204] Ewart L, Apostolou A, Briggs SA, Carman CV, Chaff JT, Heng AR, Jadalannagari S, Janardhanan J, Jang KJ, Joshipura SR, Kadam M. *Qualifying a human Liver-Chip for predictive toxicology: Performance assessment and economic implications*. BioRxiv, 2021.

[205] Tsamandouras N, Kostrzewski T, Stokes CL, Griffith LG, Hughes DJ, Cirit M. *Quantitative assessment of population variability in hepatic drug metabolism using a perfused three-dimensional human liver microphysiological system*. Journal of Pharmacology and Experimental Therapeutics, 2017, 360(1): 95-105.

[206] Mandal BB, Kundu S. *A novel method for dissolution and stabilization of non-mulberry silk gland protein fibroin using anionic surfactant sodium dodecyl sulfate*. Biotechnology and Bioengineering, 2008, 99(6): 1482-1489.

[207] Park K-M, Hussein KH, Hong S-H, Ahn C, Yang S-R, Park S-M, Kweon O-K, Kim B-M, Woo H-M. *Decellularized liver extracellular matrix as promising tools for transplantable bioengineered liver promotes hepatic lineage commitments of induced pluripotent stem cells*. Tissue Engineering Part A, 2016, 22(5-6): 449-460.

[208] Janmey PA, Miller RT. *Mechanisms of mechanical signaling in development and disease*. Journal of Cell Science, 2011, 124(1): 9-18.

[209] Adwan H, Fuller B, Seldon C, Davidson B, Seifalian A. *Modifying three-dimensional scaffolds from novel nanocomposite materials using dissolvable porogen particles for use in liver tissue engineering*. Journal of Biomaterials Applications, 2013, 28(2): 250-261.

[210] Lim Y-S, Kim WR. *The global impact of hepatic fibrosis and end-stage liver disease*. Clinics in Liver Disease, 2008, 12(4): 733-746.

[211] Murray CJ, Lopez AD. *Alternative projections of mortality and disability by cause 1990–2020: Global burden of disease study*. The Lancet, 1997, 349(9064): 1498-1504.

[212] Kumaran V. *Liver Transplantation in India*. Textbook of Surgical Gastroenterology, Volumes 1 & 2, 2016: 1172.

[213] Rehm J, Samokhvalov AV, Shield KD. *Global burden of alcoholic liver diseases*. Journal of Hepatology, 2013, 59(1): 160-168.

[214] Stange J. *Extracorporeal liver support*. Organogenesis, 2011, 7(1): 64-73.

[215] Coward SM, Legallais C, David B, Thomas M, Foo Y, Mavri-Damelin D, Hodgson HJ, Selden C. *Alginate-encapsulated HepG2 cells in a fluidized bed bioreactor maintain function in human liver failure plasma*. Artificial Organs, 2009, 33(12): 1117-1126.

[216] Glicklis R, Shapiro L, Agbaria R, Merchuk JC, Cohen S. *Hepatocyte behavior within three-dimensional porous alginate scaffolds*. Biotechnology and Bioengineering, 2000, 67(3): 344-353.

[217] Chua K-N, Lim W-S, Zhang P, Lu H, Wen J, Ramakrishna S, Leong KW, Mao H-Q. *Stable immobilization of rat hepatocyte spheroids on galactosylated nanofiber scaffold*. Biomaterials, 2005, 26(15): 2537-2547.

[218] Feng Z-Q, Chu X-H, Huang N-P, Leach MK, Wang G, Wang Y-C, Ding Y-T, Gu Z-Z. *Rat hepatocyte aggregate formation on discrete aligned nanofibers of type-I collagen-coated poly (L-lactic acid)*. Biomaterials, 2010, 31(13): 3604-3612.

[219] Yang Y, Li J, Pan X, Zhou P, Yu X, Cao H, Wang Y, Li L. *Co-culture with mesenchymal stem cells enhances metabolic functions of liver cells in bioartificial liver system*. Biotechnology and Bioengineering, 2013, 110(3): 958-968.

[220] Jain E, Damania A, Shakya AK, Kumar A, Sarin SK, Kumar A. *Fabrication of macroporous cryogels as potential hepatocyte carriers for bioartificial liver support*. Colloids and Surfaces B: Biointerfaces, 2015, 136: 761-771.

[221] Lee HW, Kook Y-M, Lee HJ, Park H, Koh W-G. *A three-dimensional co-culture of HepG2 spheroids and fibroblasts using double-layered fibrous scaffolds incorporated with hydrogel micropatterns*. RSC Advances, 2014, 4(105): 61005-61011.

[222] Bokhari M, Carnachan RJ, Cameron NR, Przyborski SA. *Culture of HepG2 liver cells on three dimensional polystyrene scaffolds enhances cell structure and function during toxicological challenge*. Journal of Anatomy, 2007, 211(4): 567-576.

[223] Yang Z, Xu LS, Yin F, Shi YQ, Han Y, Zhang L, Jin HF, Nie YZ, Wang JB, Hao X, Fan DM, Zhou XM. *In vitro and in vivo characterization of silk fibroin/gelatin composite scaffolds for liver tissue engineering*. Journal of Digestive Diseases, 2012, 13(3): 168-178.

[224] Lee JS, Shin J, Park H-M, Kim Y-G, Kim B-G, Oh J-W, Cho S-W. *Liver extracellular matrix providing dual functions of two-dimensional substrate coating and three-dimensional injectable hydrogel platform for liver tissue engineering*. Biomacromolecules, 2013, 15(1): 206-218.

[225] Fan J, Yang J. *Preparation and characterization of a chitosan/galactosylated hyaluronic acid/heparin scaffold for hepatic tissue engineering*. Journal of Biomaterials Science, Polymer Edition, 2017, 28(6): 569-581.

[226] Nishida Y, Taniguchi A. *A three-dimensional collagen-sponge-based culture system coated with simplified recombinant fibronectin improves the function of a hepatocyte cell line*. In Vitro Cellular & Developmental Biology-Animal, 2016, 52(3): 271-277.

[227] Angioni MM, Bellofatto K, Merlin S, Menegon S, Perra A, Petrelli A, Sulas P, Giordano S, Columbano A, Follenzi A. *A long term, non-tumorigenic rat hepatocyte cell line and its malignant counterpart, as tools to study hepatocarcinogenesis*. Oncotarget, 2017, 8(9): 15716-15731

[228] Berthiaume F, Moghe PV, Toner M, Yarmush ML. *Effect of extracellular matrix topology on cell structure, function, and physiological responsiveness: Hepatocytes cultured in a sandwich configuration*. The FASEB Journal, 1996, 10(13): 1471-1484.

[229] Bhardwaj N, Singh YP, Devi D, Kandimalla R, Kotoky J, Mandal BB. *Potential of silk fibroin/chondrocyte constructs of muga silkworm Antheraea assamensis for cartilage tissue engineering*. Journal of Materials Chemistry B, 2016, 4(21): 3670-3684.

[230] Shefa AA, Amirian J, Kang HJ, Bae SH, Jung H-I, Choi H-j, Lee SY, Lee B-T. *In vitro and in vivo evaluation of effectiveness of a novel TEMPO-oxidized cellulose nanofiber-silk fibroin scaffold in wound healing*. Carbohydrate Polymers, 2017, 177: 284-296.

[231] Chouhan D, Chakraborty B, Nandi SK, Mandal BB. *Role of non-mulberry silk fibroin in deposition and regulation of extracellular matrix towards accelerated wound healing*. Acta Biomaterialia, 2017, 48: 157-174.

[232] Yang M, Shuai Y, Sunderland KS, Mao C. *Ice-templated protein nanoridges induce bone tissue formation*. Advanced Functional Materials, 2017, 27(44): 1703726.

[233] Hu K, Lv Q, Cui F, Feng Q, Kong X, Wang H, Huang L, Li T. *Biocompatible fibroin blended films with recombinant human-like collagen for hepatic tissue engineering*. Journal of Bioactive and Compatible Polymers, 2006, 21(1): 23-37.

[234] She Z, Jin C, Huang Z, Zhang B, Feng Q, Xu Y. *Silk fibroin/chitosan scaffold: Preparation, characterization, and culture with HepG2 cell*. Journal of Materials Science: Materials in Medicine, 2008, 19(12): 3545-3553.

[235] Kasoju N, Bora U. *Silk fibroin based biomimetic artificial extracellular matrix for hepatic tissue engineering applications*. Biomedical Materials, 2012, 7(4): 045004.

[236] Gupta P, Kumar M, Bhardwaj N, Kumar JP, Krishnamurthy C, Nandi SK, Mandal BB. *Mimicking form and function of native small diameter vascular conduits using mulberry and non-mulberry patterned silk films*. ACS Applied Materials & Interfaces, 2016, 8(25): 15874-15888.

[237] Kundu B, Kundu S. *Bio-inspired fabrication of fibroin cryogels from the muga silkworm Antheraea assamensis for liver tissue engineering*. Biomedical Materials, 2013, 8(5): 055003.

[238] Rockwood DN, Preda RC, Yücel T, Wang X, Lovett ML, Kaplan DL. *Materials fabrication from Bombyx mori silk fibroin*. Nature Protocols, 2011, 6(10): 1612-1631.

[239] Bhardwaj N, Sow WT, Devi D, Ng KW, Mandal BB, Cho N-J. *Silk fibroin-keratin based 3D scaffolds as a dermal substitute for skin tissue engineering*. Integrative Biology, 2015, 7(1): 53-63.

[240] Hussein KH, Park KM, Ghim JH, Yang SR, Woo HM. *Three dimensional culture of HepG2 liver cells on a rat decellularized liver matrix for pharmacological studies*. Journal of Biomedical Materials Research Part B: Applied Biomaterials, 2016, 104(2): 263-273.

[241] Satelli A, Hu J, Xia X, Li S. *Potential function of exogenous vimentin on the activation of wnt signaling pathway in cancer cells*. Journal of Cancer, 2016, 7(13): 1824.

[242] Nakajima H, Itakura M, Kubo T, Kaneshige A, Harada N, Izawa T, Azuma Y-T, Kuwamura M, Yamaji R, Takeuchi T. *Glyceraldehyde-3-phosphate dehydrogenase (GAPDH) aggregation causes mitochondrial dysfunction during oxidative stress-induced cell death*. Journal of Biological Chemistry, 2017, 292(11): 4727-4742.

[243] Bierwolf J, Lutgehetmann M, Feng K, Erbes J, Deichmann S, Toronyi E, Stieglitz C, Nashan B, Ma PX, Pollok JM. *Primary rat hepatocyte culture on 3D nanofibrous polymer scaffolds for toxicology and pharmaceutical research*. Biotechnology and Bioengineering, 2011, 108(1): 141-50.

[244] Meier V, Tron K, Batusic D, Elmaouhoub A, Ramadori G. *Expression of AFP and Rev-Erb A/Rev-Erb B and N-CoR in fetal rat liver, liver injury and liver regeneration*. Comparative Hepatology, 2006, 5(1): 1-12.

[245] Choi DK, Mukherjee R, Yun JW. *Gender-dependent gene expressions in brown adipose tissue of lean and obese rats fed a high fat diet*. Biotechnology and Bioprocess Engineering, 2012, 17(5): 1080-1092.

[246] Kumar V, Mundra V, Mahato RI. *Nanomedicines of Hedgehog inhibitor and PPAR-γ agonist for treating liver fibrosis*. Pharmaceutical Research, 2014, 31(5): 1158-1169.

[247] Li J, Wan Y, Na S, Liu X, Dong G, Yang Z, Yang J, Yue J. *Sex-dependent regulation of hepatic CYP3A by growth hormone: Roles of HNF6, C/EBPα, and RXRα*. Biochemical Pharmacology, 2015, 93(1): 92-103.

[248] Yang Z, Tu Q, Maitz MF, Zhou S, Wang J, Huang N. *Direct thrombin inhibitor-bivalirudin functionalized plasma polymerized allylamine coating for improved biocompatibility of vascular devices*. Biomaterials, 2012, 33(32): 7959-7971.

[249] Krimm S, Bandekar J. *Vibrational spectroscopy and conformation of peptides, polypeptides, and proteins*. Advances in Protein Chemistry, 1986, 38: 181-364.

[250] Nevskaya N, Chirgadze YN. *Infrared spectra and resonance interactions of amide-I and II vibrations of α-helix*. Biopolymers, 1976, 15(4): 637-648.

[251] Liu Z, Takeuchi M, Nakajima M, Hu C, Hasegawa Y, Huang Q, Fukuda T. *Three-dimensional hepatic lobule-like tissue constructs using cell-microcapsule technology*. Acta Biomaterialia, 2017, 50: 178-187.

[252] Chen Z, Lian F, Wang X, Chen Y, Tang N. *Arginine–glycine–aspartic acid–polyethylene glycol–polyamidoamine dendrimer conjugate improves liver-cell aggregation and function in 3-D spheroid culture*. International Journal of Nanomedicine, 2016, 11: 4247.

[253] Okudaira T, Amimoto N, Mizumoto H, Kajiwara T. *Formation of three-dimensional hepatic tissue by the bottom-up method using spheroids*. Journal of Bioscience and Bioengineering, 2016, 122(2): 213-218.

[254] Clark A, Wheeler S, Young C, Stockdale L, Neiman JS, Zhao W, Stolz DB, Venkataramanan R, Lauffenburger D, Griffith L, Wells A. *A liver microphysiological system of tumor cell dormancy and inflammatory responsiveness is affected by scaffold properties*. Lab on a Chip, 2017, 17(1): 156-168.

[255] Yucel T, Lovett ML, Kaplan DL. *Silk-based biomaterials for sustained drug delivery*. Journal of Controlled Release, 2014, 190: 381-397.

[256] Malay AD, Sato R, Yazawa K, Watanabe H, Ifuku N, Masunaga H, Hikima T, Guan J, Mandal BB, Damrongasakkul S, Numata K. *Relationships between physical properties and sequence in silkworm silks*. Scientific Reports, 2016, 6(1): 1-11.

[257] Reardon PJT, Konwarh R, Knowles JC, Mandal BB. *Mimicking hierarchical complexity of the osteochondral interface using electrospun silk-bioactive glass composites*. ACS Applied Materials & Interfaces, 2017, 9(9): 8000-8013.

[258] Sen K, Babu K. *Studies on Indian silk. I. Macrocharacterization and analysis of amino acid composition*. Journal of Applied Polymer Science, 2004, 92(2): 1080-1097.

[259] Chitrangi S, Nair P, Khanna A. *Three-dimensional polymer scaffolds for enhanced differentiation of human mesenchymal stem cells to hepatocyte-like cells: a comparative study*. Journal of Tissue Engineering and Regenerative Medicine, 2017, 11(8), 2359-2372.

[260] Lutolf M, Hubbell J. *Synthetic biomaterials as instructive extracellular microenvironments for morphogenesis in tissue engineering*. Nature Biotechnology, 2005, 23(1): 47-55.

[261] Mandal BB, Grinberg A, Gil ES, Panilaitis B, Kaplan DL. *High-strength silk protein scaffolds for bone repair*. Proceedings of the National Academy of Sciences, 2012, 109(20): 7699-7704.

[262] Loh QL, Choong C. *Three-dimensional scaffolds for tissue engineering applications: Role of porosity and pore size*. Tissue Engineering Part B: Reviews, 2013, 19(6): 485-502.

[263] Wang X, Yan Y, Lin F, Xiong Z, Wu R, Zhang R, Lu Q. *Preparation and characterization of a collagen/chitosan/heparin matrix for an implantable bioartificial liver*. Journal of Biomaterials Science, Polymer Edition, 2005, 16(9): 1063-1080.

[264] Powers MJ, Rodriguez RE, Griffith LG. *Cell-substratum adhesion strength as a determinant of hepatocyte aggregate morphology*. Biotechnology and Bioengineering, 1997, 53(4): 415-426.

[265] Shin H-S, Kook Y-M, Hong HJ, Kim Y-M, Koh W-G, Lim J-Y. *Functional spheroid organization of human salivary gland cells cultured on hydrogel-micropatterned nanofibrous microwells*. Acta Biomaterialia, 2016, 45: 121-132.

[266] Qiu P, Qu X, Brackett DJ, Lerner MR, Li D, Mao C. *Silica-based branched hollow microfibers as a biomimetic extracellular matrix for promoting tumor cell growth in vitro and in vivo*. Advanced Materials, 2013, 25(17): 2492-2496.

[267] Yamada M, Hori A, Sugaya S, Yajima Y, Utoh R, Yamato M, Seki M. *Cell-sized condensed collagen microparticles for preparing microengineered composite spheroids of primary hepatocytes*. Lab on a Chip, 2015, 15(19): 3941-3951.

[268] Du Y, Chia S-m, Han R, Chang S, Tang H, Yu H. *3D hepatocyte monolayer on hybrid RGD/galactose substratum*. Biomaterials, 2006, 27(33): 5669-5680.

[269] Gundersen GG, Worman HJ. *Nuclear positioning*. Cell, 2013, 152(6): 1376-1389.

[270] Dubois V, Staels B, Lefebvre P, Verzi MP, Eeckhoute J. *Control of cell identity by the nuclear receptor HNF4 in organ pathophysiology*. Cells, 2020, 9(10): 2185.

[271] Janani G, Nandi SK, Mandal BB. *Functional hepatocyte clusters on bioactive blend silk matrices towards generating bioartificial liver constructs*. Acta Biomaterialia, 2018, 67: 167-182.

[272] Price R, Ball S, Renwick A, Barton P, Beamand J, Lake B. *Use of precision-cut rat liver slices for studies of xenobiotic metabolism and toxicity: Comparison of the Krumdieck and Brendel tissue slicers*. Xenobiotica, 1998, 28(4): 361-371.

[273] Li Y, Wu Q, Wang Y, Li L, Chen F, Shi Y, Bao J, Bu H. *Construction of bioengineered hepatic tissue derived from human umbilical cord mesenchymal stem cells via aggregation culture in porcine decellularized liver scaffolds*. Xenotransplantation, 2017, 24(1): e12285.

[274] Fekry B, Ribas-Latre A, Baumgartner C, Deans JR, Kwok C, Patel P, Fu L, Berdeaux R, Sun K, Kolonin MG, Wang SH, Yoo S-H, Sladek FM, Eckel-Mahan K. *Incompatibility of the circadian protein BMAL1 and HNF4α in hepatocellular carcinoma*. Nature Communications, 2018, 9(1): 1-17.

[275] Tao F, Sayo K, Sugimoto K, Aoki S, Kojima N. *Development of a tunable method to generate various three-dimensional microstructures by replenishing macromolecules such as extracellular matrix components and polysaccharides*. Scientific Reports, 2020, 10(1): 1-12.

[276] Gantenbein-Ritter B, Potier E, Zeiter S, van der Werf M, Sprecher CM, Ito K. *Accuracy of three techniques to determine cell viability in 3D tissues or scaffolds*. Tissue Engineering Part C: Methods, 2008, 14(4): 353-358.

[277] Garidel P, Schott H. *Fourier-transform midinfrared spectroscopy for analysis and screening of liquid protein formulation*s. *Part 2: Detailed analysis and applications*. BioProcess Int, 2006, 4(6): 48-55.

[278] Saylor J, Ma Z, Goodridge HS, Huang F, Cress AE, Pandol SJ, Shiao SL, Vidal AC, Wu L, Nickols NG, Gertych A, Knudsen BS. *Spatial mapping of myeloid cells and macrophages by multiplexed tissue staining*. Frontiers in Immunology, 2018, 9: 2925.

[279] Wang Y, Kim MH, Shirahama H, Lee JH, Ng SS, Glenn JS, Cho N-J. *ECM proteins in a microporous scaffold influence hepatocyte morphology, function, and gene expression*. Scientific Reports, 2016, 6(1): 1-13.

[280] Smyrek I, Stelzer E. *Quantitative three-dimensional evaluation of immunofluorescence staining for large whole mount spheroids with light sheet microscopy*. Biomedical Optics Express, 2017, 8(2): 484-499.

[281] Janani G, Mandal BB. *Mimicking physiologically relevant hepatocyte zonation using immunomodulatory silk liver extracellular matrix scaffolds toward a bioartificial liver platform*. ACS Applied Materials & Interfaces, 2021, 13(21): 24401-24421.

[282] Dianat N, Dubois-Pot-Schneider H, Steichen C, Desterke C, Leclerc P, Raveux A, Combettes L, Weber A, Corlu A, Dubart-Kupperschmitt A. *Generation of functional cholangiocyte-like cells from human pluripotent stem cells and HepaRG cells*. Hepatology, 2014, 60(2): 700-714.

[283] Janani G, Kumar S, Mandal BB. *Fiber-reinforced silk* composite *for enhanced urokinase production using high-density perfusion culture and bioactive molecule supplementation*. ACS Biomaterials Science & Engineering, 2019, 5(11): 6137-6151.

[284] Gupta P, Moses JC, Mandal BB. *Surface patterning and innate physicochemical attributes of silk films concomitantly govern vascular cell dynamics*. ACS Biomaterials Science & Engineering, 2018, 5(2): 933-949.

[285] Boulet-Audet M, Vollrath F, Holland C. *Identification and classification of silks using infrared spectroscopy*. Journal of Experimental Biology, 2015, 218(19): 3138-3149.

[286] Shen L, Hillebrand A, Wang DQ-H, Liu M. *Isolation and primary culture of rat hepatic cells*. Journal of Visualized Experiments: JoVE 2012, 64: e3917.

[287] Crapo PM, Gilbert TW, Badylak SF. *An overview of tissue and whole organ decellularization processes*. Biomaterials, 2011, 32(12): 3233-3243.

[288] Ekins S, Murray GI, Burke MD, Williams JA, Marchant NC, Hawksworth GM. *Quantitative differences in phase I and II metabolism between rat precision-cut liver slices and isolated hepatocytes*. Drug metabolism and disposition, 1995, 23(11): 1274-1279.

[289] Hay ED. *Cell biology of extracellular matrix*. Springer Science & Business Media, 1991.

[290] Janani G, Kumar M, Chouhan D, Moses JC, Gangrade A, Bhattacharjee S, Mandal BB. *Insight into silk-based biomaterials: From physicochemical attributes to recent biomedical applications*. ACS Applied Bio Materials, 2019, 2(12): 5460-5491.

[291] Moses JC, Saha T, Mandal BB. *Chondroprotective and osteogenic effects of silk-based bioinks in developing 3D bioprinted osteochondral interface*. Bioprinting, 2020, 17: e00067.

[292] Chao ES, Dunbar D, Kaminsky LS. *Intracellular lactate dehydrogenase concentration as an index of cytotoxicity in rat hepatocyte primary culture*. Cell Biology and Toxicology, 1988, 4(1): 1-11.

[293] Gantenbein B, Croft AS, Larraillet MAD. *Mammalian Cell Viability Methods in 3D Scaffolds for Tissue Engineering*. Fluorescence Methods for Investigation of Living Cells and Microorganisms, 2020: 1-25.

[294] Koide N, Shinji T, Tanabe T, Asano K, Kawaguchi M, Sakaguchi K, Koide Y, Mori M, Tsuji T. *Continued high albumin production by multicellular spheroids of adult rat hepatocytes formed in the presence of liver-derived proteoglycans*. Biochemical and Biophysical Research Communications, 1989, 161(1): 385-391.

[295] Du Y, Li N, Yang H, Luo C, Gong Y, Tong C, Gao Y, Lu S, Long M. *Mimicking liver sinusoidal structures and functions using a 3D-configured microfluidic chip*. Lab on a Chip, 2017, 17(5): 782-794.

[296] Garnier D, Li R, Delbos F, Fourrier A, Collet C, Guguen-Guillouzo C, Chesné C, Nguyen TH. *Expansion of human primary hepatocytes in vitro through their amplification as liver progenitors in a 3D organoid system*. Scientific Reports, 2018, 8(1): 1-10.

[297] Lübberstedt M, Müller-Vieira U, Mayer M, Biemel KM, Knöspel F, Knobeloch D, Nüssler AK, Gerlach JC, Zeilinger K. *HepaRG human hepatic cell line utility as a surrogate for primary*

human hepatocytes in drug metabolism assessment in vitro. Journal of Pharmacological and Toxicological Methods, 2011, 63(1): 59-68.

[298] Mehrotra S, Moses JC, Bandyopadhyay A, Mandal BB. *3D printing/bioprinting based tailoring of in vitro tissue models: Recent advances and challenges*. ACS Applied Bio Materials, 2019, 2(4): 1385-1405.

[299] Ware BR, Khetani SR. *Engineered liver platforms for different phases of drug development*. Trends in Biotechnology, 2017, 35(2): 172-183.

[300] Massa S, Sakr MA, Seo J, Bandaru P, Arneri A, Bersini S, Zare-Eelanjegh E, Jalilian E, Cha B-H, Antona S, Enrico A, Gao Y, Hassan S, Acevedo JP, Dokmeci MR, Zhang YS, Khademhosseini A, Shin SR. *Bioprinted 3D vascularized tissue model for drug toxicity analysis*. Biomicrofluidics, 2017, 11(4): 044109.

[301] Miranda JP, Serras AS, Rodrigues JS, Cipriano M, Rodrigues AV, Oliveira NG. *A critical perspective on 3D liver models for drug metabolism and toxicology studies*. Frontiers in Cell and Developmental Biology, 2021, 9: 626805.

[302] Wouters OJ, McKee M, Luyten J. *Estimated research and development investment needed to bring a new medicine to market, 2009-2018*. Jama, 2020, 323(9): 844-853.

[303] Tolosa L, Jiménez N, Pérez G, Castell JV, Gómez-Lechón MJ, Donato MT. *Customised in vitro model to detect human metabolism-dependent idiosyncratic drug-induced liver injury*. Archives of Toxicology, 2018, 92(1): 383-399.

[304] Jin M, Yi X, Liao W, Chen Q, Yang W, Li Y, Li S, Gao Y, Peng Q, Zhou S. *Advancements in stem cell-derived hepatocyte-like cell models for hepatotoxicity testing*. Stem Cell Research & Therapy, 2021, 12(1): 1-13.

[305] Gomez-Lechon MJ, Castell JV, Donato MT. *Hepatocytes-the choice to investigate drug metabolism and toxicity in man: in vitro variability as a reflection of in vivo*. Chemico-biological Interactions, 2007, 168(1): 30-50.

[306] Underhill GH, Khetani SR. *Bioengineered liver models for drug testing and cell differentiation studies*. Cellular and Molecular Gastroenterology and Hepatology, 2018, 5(3): 426-439.

[307] Fey SJ, Wrzesinski K. *Determination of drug toxicity using 3D spheroids constructed from an immortal human hepatocyte cell line*. Toxicological Sciences, 2012, 127(2): 403-411.

[308] Ronaldson-Bouchard K, Vunjak-Novakovic G. *Organs-on-a-chip: A fast track for engineered human tissues in drug development*. Cell Stem Cell, 2018, 22(3): 310-324.

[309] Soldatow VY, LeCluyse EL, Griffith LG, Rusyn I. *In vitro models for liver toxicity testing*. Toxicology Research, 2013, 2(1): 23-39.

[310] Ng WL, Chua CK, Shen Y-F. *Print me an organ! Why we are not there yet*. Progress in Polymer Science, 2019, 97: 101145.

[311] Cuvellier M, Ezan F, Oliveira H, Rose S, Fricain J-C, Langouët S, Legagneux V, Baffet G. *3D culture of HepaRG cells in GelMa and its application to bioprinting of a multicellular hepatic model*. Biomaterials, 2021, 269: 120611.

[312] Lee H, Han W, Kim H, Ha D-H, Jang J, Kim BS, Cho D-W. *Development of liver decellularized extracellular matrix bioink for three-dimensional cell printing-based liver tissue engineering*. Biomacromolecules, 2017, 18(4): 1229-1237.

[313] Ng WL, Lee JM, Zhou M, Chen Y-W, Lee K-XA, Yeong WY, Shen Y-F. *Vat polymerization-based bioprinting-process, materials, applications and regulatory challenges*. Biofabrication, 2020, 12(2): 022001.

[314] Ng WL, Huang X, Shkolnikov V, Goh GL, Suntornnond R, Yeong WY. *Controlling droplet impact velocity and droplet volume: Key factors to achieving high cell viability in sub-nanoliter droplet-based bioprinting*. International Journal of Bioprinting, 2022, 8(1).

[315] Ramesh S, Harrysson OL, Rao PK, Tamayol A, Cormier DR, Zhang Y, Rivero IV. *Extrusion bioprinting: Recent progress, challenges, and future opportunities*. Bioprinting, 2021, 21: e00116.

[316] Gu Z, Fu J, Lin H, He Y. *Development of 3D bioprinting: From printing methods to biomedical applications*. Asian Journal of Pharmaceutical Sciences, 2020, 15(5): 529-557.

[317] Mehrotra S, de Melo BA, Hirano M, Keung W, Li RA, Mandal BB, Shin SR. *Nonmulberry silk based ink for fabricating mechanically robust cardiac patches and endothelialized myocardium-on-a-chip application*. Advanced Functional Materials, 2020, 30(12): 1907436.

[318] Lee J-S, Yoon H, Yoon D, Kim GH, Yang HT, Chun W. *Development of hepatic blocks using human adipose tissue-derived stem cells through three-dimensional cell printing techniques*. Journal of Materials Chemistry B, 2017, 5(5): 1098-1107.

[319] Cosgrove BD, King BM, Hasan MA, Alexopoulos LG, Farazi PA, Hendriks BS, Griffith LG, Sorger PK, Tidor B, Xu JJ, Lauffenburgher DA. *Synergistic drug–cytokine induction of hepatocellular death as an in vitro approach for the study of inflammation-associated idiosyncratic drug hepatotoxicity*. Toxicology and Applied Pharmacology, 2009, 237(3): 317-330.

[320] Ramaiahgari SC, Den Braver MW, Herpers B, Terpstra V, Commandeur JN, van de Water B, Price LS. *A 3D in vitro model of differentiated HepG2 cell spheroids with improved liver-like*

properties for repeated dose high-throughput toxicity studies. Archives of Toxicology, 2014, 88(5): 1083-1095.

[321] Khetani SR, Kanchagar C, Ukairo O, Krzyzewski S, Moore A, Shi J, Aoyama S, Aleo M, Will Y. *Use of micropatterned cocultures to detect compounds that cause drug-induced liver injury in humans*. Toxicological Sciences, 2013, 132(1): 107-117.

[322] Zahmatkesh E, Ghanian MH, Zarkesh I, Farzaneh Z, Halvaei M, Heydari Z, Moeinvaziri F, Othman A, RuoB M, Piryaei A, Gramignoli R, Yakhkeshi S, Nussler A, Najimi M, Baharvand H, Vosough M. *Tissue-specific microparticles improve organoid microenvironment for efficient maturation of pluripotent stem-cell-derived hepatocytes*. Cells, 2021, 10(6): 1274.

[323] Sasaki K, Akagi T, Asaoka T, Eguchi H, Fukuda Y, Iwagami Y, Yamada D, Noda T, Wada H, Gotoh K, Kawamoto K, Doki Y, Mori M, Akashi M. *Construction of three-dimensional vascularized functional human liver tissue using a layer-by-layer cell coating technique*. Biomaterials, 2017, 133: 263-274.

[324] Sakai S, Mochizuki K, Qu Y, Mail M, Nakahata M, Taya M. *Peroxidase-catalyzed microextrusion bioprinting of cell-laden hydrogel constructs in vaporized ppm-level hydrogen peroxide*. Biofabrication, 2018, 10(4): 045007.

[325] Croce S, Peloso A, Zoro T, Avanzini MA, Cobianchi L. *A hepatic scaffold from decellularized liver tissue: Food for thought*. Biomolecules, 2019, 9(12): 813.

[326] Lee J-H, Ho K-L, Fan S-K. *Liver microsystems in vitro for drug response*. Journal of Biomedical Science, 2019, 26(1): 1-10.

[327] Giraudi PJ, Becerra VJB, Marin V, Chavez-Tapia NC, Tiribelli C, Rosso N. *The importance of the interaction between hepatocyte and hepatic stellate cells in fibrogenesis induced by fatty accumulation*. Experimental and Molecular Pathology, 2015, 98(1): 85-92.

[328] Kang HK, Sarsenova M, Kim D-H, Kim MS, Lee JY, Sung E-A, Kook MG, Kim NG, Choi SW, Ogay V, Kang K-S. *Establishing a 3D in vitro hepatic model mimicking physiologically relevant to in vivo state*. Cells, 2021, 10(5): 1268.

[329] Wienkers LC, Heath TG. *Predicting in vivo drug interactions from in vitro drug discovery data*. Nature Reviews Drug discovery, 2005, 4(10): 825-833.

[330] Cox CR, Lynch S, Goldring C, Sharma P. *Current perspective: 3D spheroid models utilizing human-based cells for investigating metabolism-dependent drug-induced liver injury*. Frontiers in Medical Technology, 2020, 2: 14.

[331] Lazarczyk DA, Goldstein NS, Gordon SC. *Trovafloxacin hepatotoxicity*. Digestive Diseases and Sciences, 2001, 46(4): 925-926.

[332] Zhou Y, Shen JX, Lauschke VM. *Comprehensive evaluation of organotypic and microphysiological liver models for prediction of drug-induced liver injury*. Frontiers in Pharmacology, 2019, 10: 1093.

[333] Kundu B, Kurland NE, Bano S, Patra C, Engel FB, Yadavalli VK, Kundu SC. *Silk proteins for biomedical applications: Bioengineering perspectives*. Progress in Polymer Science, 2014, 39(2): 251-267.

[334] Aramwit P, Kanokpanont S, De-Eknamkul W, Srichana T. *Monitoring of inflammatory mediators induced by silk sericin*. Journal of Bioscience and Bioengineering, 2009, 107(5): 556-561.

[335] Jewell M, Daunch W, Bengtson B, Mortarino E. *The development of SERI® Surgical Scaffold, an engineered biological scaffold*. Annals of the New York Academy of Sciences, 2015, 1358(1): 44-55.

[336] Spelzini F, Konstantinovic ML, Guelinckx I, Verbist G, Verbeken E, De Ridder D, Deprest J. *Tensile strength and host response towards silk and type I polypropylene implants used for augmentation of fascial repair in a rat model*. Gynecologic and Obstetric Investigation, 2007, 63(3): 155-162.

[337] Konwarh R, Bhunia BK, Mandal BB. *Opportunities and challenges in exploring Indian nonmulberry silk for biomedical applications*. Proceedings of the Indian National Science Academy, 2017, 83: 85-101.

[338] Moses JC, Dey S, Bandyopadhyay A, Agarwala M, Mandal BB. *Silk based bioengineered diaphyseal cortical bone unit enclosing an implantable bone marrow towards atrophic non-union grafting*. Advanced Healthcare Materials, 2022, 11(6) :2102031.

[339] Gupta P, Chaudhuri GR, Janani G, Agarwala M, Ghosh D, Nandi SK, Mandal BB. *Functionalized silk vascular grafts with decellularized human Wharton's Jelly improves remodeling via immunomodulation in rabbit jugular vein*. Advanced Healthcare Materials, 2021, 10(19): 2100750.

[340] You R, Xu Y, Liu Y, Li X, Li M. *Comparison of the in vitro and in vivo degradations of silk fibroin scaffolds from mulberry and nonmulberry silkworms*. Biomedical Materials, 2014, 10(1): 015003.

[341] Umuhoza D, Yang F, Long D, Hao Z, Dai J, Zhao A. *Strategies for tuning the biodegradation of silk fibroin-based materials for tissue engineering applications*. ACS Biomaterials Science & Engineering, 2020, 6(3): 1290-1310.

[342] Meinel L, Hofmann S, Karageorgiou V, Kirker-Head C, McCool J, Gronowicz G, Zichner L, Langer R, Vunjak-Novakovic G, Kaplan DL. *The inflammatory responses to silk films in vitro and in vivo*. Biomaterials, 2005, 26(2): 147-155.

[343] Wang Y, Yao D, Li L, Qian Z, He W, Ding R, Liu H, Fan Y. *Effect of electrospun silk fibroin-silk sericin films on macrophage polarization and vascularization*. ACS Biomaterials Science & Engineering, 2020, 6(6): 3502-3512.

[344] Gorenkova N, Maitz MF, Böhme G, Alhadrami HA, Jiffri EH, Totten JD, Werner C, Carswell HVO, Seib FP. *The innate immune response of self-assembling silk fibroin hydrogels*. Biomaterials Science, 2021, 9(21): 7194-7204.

[345] Thurber AE, Omenetto FG, Kaplan DL. *In vivo bioresponses to silk proteins*. Biomaterials, 2015, 71: 145-157.

[346] Reeves AR, Spiller KL, Freytes DO, Vunjak-Novakovic G, Kaplan DL. *Controlled release of cytokines using silk-biomaterials for macrophage polarization*. Biomaterials, 2015, 73: 272-283.

[347] Sicari B, Turner N, Badylak SF. *An in vivo model system for evaluation of the host response to biomaterials*. Wound Regeneration and Repair: Springer, 2013, 3-25.

[348] Brown BN, Londono R, Tottey S, Zhang L, Kukla KA, Wolf MT, Daly KA, Reing JE, Badylak SF. *Macrophage phenotype as a predictor of constructive remodeling following the implantation of biologically derived surgical mesh materials*. Acta Biomaterialia, 2012, 8(3): 978-987.

[349] Witherel CE, Abebayehu D, Barker TH, Spiller KL. *Macrophage and fibroblast interactions in biomaterial-mediated fibrosis*. Advanced Healthcare Materials, 2019, 8(4): 1801451.

[350] Wilson CJ, Clegg RE, Leavesley DI, Pearcy MJ. *Mediation of biomaterial-cell interactions by adsorbed proteins: A review*. Tissue engineering, 2005, 11(1-2): 1-18.

[351] Franz S, Rammelt S, Scharnweber D, Simon JC. *Immune responses to implants–a review of the implications for the design of immunomodulatory biomaterials*. Biomaterials, 2011, 32(28): 6692-6709.

[352] Musahl V, Abramowitch SD, Gilbert TW, Tsuda E, Wang JHC, Badylak SF, L-Y Woo S. T*he use of porcine small intestinal submucosa to enhance the healing of the medial collateral*

ligament-a functional tissue engineering study in rabbits. Journal of Orthopaedic Research, 2004, 22(1): 214-220.

[353] Molina CP, Giglio R, Gandhi RM, Sicari BM, Londono R, Hussey GS, Bartolacci JG, Quijano Luque LM, Cramer MC, Dziki JL, Crapo PM, Badylak SF. *Comparison of the host macrophage response to synthetic and biologic surgical meshes used for ventral hernia repair*. Journal of Immunology and Regenerative Medicine, 2019, 3: 13-25.

[354] Gilbert TW, Stewart-Akers AM, Simmons-Byrd A, Badylak SF. *Degradation and remodeling of small intestinal submucosa in canine Achilles tendon repair*. JBJS, 2007, 89(3): 621-630.

[355] Sellaro TL, Ravindra AK, Stolz DB, Badylak SF. *Maintenance of hepatic sinusoidal endothelial cell phenotype in vitro using organ-specific extracellular matrix scaffolds*. Tissue Engineering, 2007, 13(9): 2301-2310.

[356] Hussey GS, Dziki JL, Lee YC, Bartolacci JG, Behun M, Turnquist HR, Badylak SF. *Matrix bound nanovesicle-associated IL-33 activates a pro-remodeling macrophage phenotype via a non-canonical, ST2-independent pathway*. Journal of Immunology and Regenerative Medicine, 2019, 3: 26-35.

[357] Cramer MC, Badylak SF. *Extracellular matrix-based biomaterials and their influence upon cell behavior*. Annals of Biomedical Engineering, 2020, 48(7): 2132-2153.

[358] Dearth CL, Keane TJ, Carruthers CA, Reing JE, Huleihel L, Ranallo CA, Kollar EW, Badylak SF. *The effect of terminal sterilization on the material properties and in vivo remodeling of a porcine dermal biologic scaffold*. Acta Biomaterialia, 2016, 33: 78-87.

[359] Huleihel L, Dziki JL, Bartolacci JG, Rausch T, Scarritt ME, Cramer MC, Vorobyov T, LoPresti ST, Swineheart IT, White LJ, Brown BN, Badylak SF. *Macrophage phenotype in response to ECM bioscaffolds*. Seminars in Immunology: Elsevier, 2017, 29: 2-13.

[360] Song Z, Peng Z, Liu Z, Yang J, Tang R, Gu Y. *Reconstruction of abdominal wall musculofascial defects with small intestinal submucosa scaffolds seeded with tenocytes in rats*. Tissue engineering Part A, 2013, 19(13-14): 1543-1553.

[361] Fearing BV, Van Dyke ME. *In vitro response of macrophage polarization to a keratin biomaterial*. Acta Biomaterialia, 2014, 10(7): 3136-3144.

[362] Williams DF. *On the mechanisms of biocompatibility*. Biomaterials, 2008, 29(20): 2941-2953.

[363] Faulk DM, Londono R, Wolf MT, Ranallo CA, Carruthers CA, Wildemann JD, Dearth CL, Badylak SF. *ECM hydrogel coating mitigates the chronic inflammatory response to polypropylene mesh*. Biomaterials, 2014, 35(30): 8585-8595.

[364] Kobayashi SD, Voyich JM, Burlak C, DeLeo FR. *Neutrophils in the innate immune response*. Archivum Immunologiae Et Therapiae Experimentalis-English Edition- 2005, 53(6): 505.

[365] Sheikh Z, Brooks PJ, Barzilay O, Fine N, Glogauer M. *Macrophages, foreign body giant cells and their response to implantable biomaterials*. Materials, 2015, 8(9): 5671-5701.

[366] Lowell CA, Berton G. *Integrin signal transduction in myeloid leukocytes*. Journal of Leukocyte Biology, 1999, 65(3): 313-320.

[367] Spiller KL, Anfang RR, Spiller KJ, Ng J, Nakazawa KR, Daulton JW, Vunjak-Novakovic G. *The role of macrophage phenotype in vascularization of tissue engineering scaffolds*. Biomaterials, 2014, 35(15): 4477-4488.

[368] Agrawal H, Tholpady SS, Capito AE, Drake DB, Katz AJ. *Macrophage phenotypes correspond with remodeling outcomes of various acellular dermal matrices*. 2012.

[369] Julier Z, Park AJ, Briquez PS, Martino MM. *Promoting tissue regeneration by modulating the immune system*. Acta Biomaterialia, 2017, 53: 13-28.

[370] Lock A, Cornish J, Musson DS. *The role of in vitro immune response assessment for biomaterials*. Journal of Functional Biomaterials, 2019, 10(3): 31.

[371] Martinez FO, Gordon S. *The M1 and M2 paradigm of macrophage activation: time for reassessment*. F1000prime Reports, 2014, 6.

[372] Murray PJ, Allen JE, Biswas SK, Fisher EA, Gilroy DW, Goerdt S, Gordon S, Hamilton JA, Ivashkiv LB, Lawrence T, Locati M, Mantovani A, Martinez FO, Mege J-L, Mosser DM, Natoli G, Saeij JP, Schultze JL, Shirey KA, Sica A, Suttles J, Udalova I, van Ginderachter JA, Vogel SN, Wynn TA. *Macrophage activation and polarization: Nomenclature and experimental guidelines*. Immunity, 2014, 41(1): 14-20.

[373] Guo C, Li C, Kaplan DL. *Enzymatic degradation of Bombyx mori silk materials: A review*. Biomacromolecules, 2020, 21(5): 1678-1686.

[374] Novak ML, Koh TJ. *Macrophage phenotypes during tissue repair*. Journal of Leukocyte Biology, 2013, 93(6): 875-881.

[375] Rőszer T. *Understanding the mysterious M2 macrophage through activation markers and effector mechanisms*. Mediators of Inflammation 2015, 2015.

[376] Lopresti ST, Brown BN. *Host response to naturally derived biomaterials*. Host response to biomaterials: Elsevier, 2015, 53-79.

[377] Bhushan B, Apte U. *Acetaminophen Test Battery (ATB): A comprehensive method to study acetaminophen-induced acute liver injury*. Gene Expression, 2020, 20(2): 125.

[378] Bhushan B, Apte U. *Liver regeneration after acetaminophen hepatotoxicity: Mechanisms and therapeutic opportunities*. The American Journal of Pathology, 2019, 189(4): 719-729.

[379] Bhushan B, Chavan H, Borude P, Xie Y, Du K, McGill MR, Lebofsky M, Jaeschke H, Krishnamurthy P, Apte U. *Dual role of epidermal growth factor receptor in liver injury and regeneration after acetaminophen overdose in mice*. Toxicological Sciences, 2017, 155(2): 363-378.

[380] Barman P, Mukherjee R, Prusty B, Suklabaidya S, Senapati S, Ravindran B. *Chitohexaose protects against acetaminophen-induced hepatotoxicity in mice*. Cell Death & Disease, 2016, 7(5): e2224-e2224.

[381] Gong L, Zhou H, Wang C, He L, Guo C, Peng C, Li Y. *Hepatoprotective effect of forsythiaside a against acetaminophen-induced liver injury in zebrafish: Coupling network pharmacology with biochemical pharmacology*. Journal of Ethnopharmacology, 2021, 271: 113890.

[382] Bhushan B, Walesky C, Manley M, Gallagher T, Borude P, Edwards G, Monga SPS, Apte U. *Pro-regenerative signaling after acetaminophen-induced acute liver injury in mice identified using a novel incremental dose model*. The American Journal of Pathology, 2014, 184(11): 3013-3025.

[383] Papackova Z, Heczkova M, Dankova H, Sticova E, Lodererova A, Bartonova L, Poruba M, Cahova M. *Silymarin prevents acetaminophen-induced hepatotoxicity in mice*. PloS One, 2018, 13(1): e0191353.

[384] De Andrade KQ, Moura FA, Dos Santos JM, De Araújo ORP, de Farias Santos JC, Goulart MOF. *Oxidative stress and inflammation in hepatic diseases: therapeutic possibilities of N-acetylcysteine*. International Journal of Molecular Sciences, 2015, 16(12): 30269-30308.

[385] Jaeschke H, Adelusi OB, Akakpo JY, Nguyen NT, Sanchez-Guerrero G, Umbaugh DS, Ding W-X, Ramachandran A. *Recommendations for the use of the acetaminophen hepatotoxicity model for mechanistic studies and how to avoid common pitfalls*. Acta Pharmaceutica Sinica B, 2021, 11(12): 3740-3755.

[386] Liu Z, Meng F, Li C, Zhou X, Zeng X, He Y, Mrsny RJ, Liu M, Hu X, Hu J-F, Li T. *Human umbilical cord mesenchymal stromal cells rescue mice from acetaminophen-induced acute liver failure*. Cytotherapy, 2014, 16(9): 1207-1219.

[387] Yang S, Kuang G, Jiang R, Wu S, Zeng T, Wang Y, Xu F, Xiong L, Gong X, Wan J. *Geniposide protected hepatocytes from acetaminophen hepatotoxicity by down-regulating CYP 2E1 expression and inhibiting TLR 4/NF-κB signaling pathway*. International Immunopharmacology, 2019, 74: 105625.

[388] Chang L, Xu D, Zhu J, Ge G, Kong X, Zhou Y. *Herbal therapy for the treatment of acetaminophen-associated liver injury: Recent advances and future perspectives*. Frontiers in Pharmacology, 2020, 11: 313.

[389] Huang Y-J, Chen P, Lee C-Y, Yang S-Y, Lin M-T, Lee H-S, Wu Y-M. *Protection against acetaminophen-induced acute liver failure by omentum adipose tissue derived stem cells through the mediation of Nrf2 and cytochrome P450 expression*. Journal of Biomedical Science, 2016, 23(1): 1-12.

[390] Donahower BC, McCullough SS, Hennings L, Simpson PM, Stowe CD, Saad AG, Kurten RC, Hinson JA, James LP. *Human recombinant vascular endothelial growth factor reduces necrosis and enhances hepatocyte regeneration in a mouse model of acetaminophen toxicity*. Journal of Pharmacology and Experimental Therapeutics, 2010, 334(1): 33-43.

[391] Saldin LT, Cramer MC, Velankar SS, White LJ, Badylak SF. *Extracellular matrix hydrogels from decellularized tissues: Structure and function*. Acta Biomaterialia, 2017, 49: 1-15.

[392] Tassinari R, Cavallini C, Olivi E, Taglioli V, Chiara Z, Ferroni O, Ventura C. *Protective effects of lyophilized exosomes derived from porcine liver against acetaminophen damage on HepG2 cells*. BMC Complementary Medicine and Therapies, 2021.

[393] Naranjo JD, Saldin LT, Sobieski E, Quijano LM, Hill RC, Chan PG, Torres C, Dziki JL, Cramer MC, Lee YC, Das R, Bajwa AK, Nossair R, Klimak M, Marchal L, Patel S, Velankar SS, Hansen KC, McGrath K, Badylak SF. *Esophageal extracellular matrix hydrogel mitigates metaplastic change in a dog model of Barrett's esophagus*. Science advances, 2020, 6(27): eaba4526.

[394] Wilkinson PD, Delgado ER, Alencastro F, Leek MP, Roy N, Weirich MP, Stahl EC, Otero PA, Chen MI, Brown WK, Duncan AW. *The polyploid state restricts hepatocyte proliferation and liver regeneration in mice*. Hepatology, 2019, 69(3): 1242-1258.

[395] Elsayed Elgarawany G, Abdou AG, Maher Taie D, Motawea SM. *Hepatoprotective effect of artichoke leaf extracts in comparison with silymarin on acetaminophen-induced hepatotoxicity in mice*. Journal of Immunoassay and Immunochemistry, 2020, 41(1): 84-96.

[396] Lu EM-C, Ratnayake J, Rich AM. *Assessment of proliferating cell nuclear antigen (PCNA) expression at the invading front of oral squamous cell carcinoma*. BMC Oral Health, 2019, 19(1): 1-7.

[397] de Moraes ACN, de Andrade CBV, Ramos IPR, Dias ML, Batista CMP, Pimentel CF, de Carvalho JJ, Goldenberg RCDS. *Resveratrol promotes liver regeneration in drug-induced liver disease in mice*. Food Research International, 2021, 142: 110185.

[398] Ghuman H, Mauney C, Donnelly J, Massensini AR, Badylak SF, Modo M. *Biodegradation of ECM hydrogel promotes endogenous brain tissue restoration in a rat model of stroke*. Acta Biomaterialia, 2018, 80: 66-84.

[399] Xie Y, McGill MR, Dorko K, Kumer SC, Schmitt TM, Forster J, Jaeschke H. *Mechanisms of acetaminophen-induced cell death in primary human hepatocytes*. Toxicology and Applied Pharmacology, 2014, 279(3): 266-274.

[400] Kučera O, Endlicher R, Rychtrmoc D, Lotková H, Sobotka O, Červinková Z. *Acetaminophen toxicity in rat and mouse hepatocytes in vitro*. Drug and Chemical Toxicology, 2017, 40(4): 448-456.

[401] Chen Q, Yan D, Zhang Q, Zhang G, Xia M, Li J, Zhan W, Shen E, Li Z, Lin L, Chen YH, Wan X. *Treatment of acetaminophen-induced liver failure by blocking the death checkpoint protein TRAIL*. Biochimica et Biophysica Acta (BBA)-Molecular Basis of Disease, 2020, 1866(1): 165583.

[402] Foroutan T, Ahmadi F, Moayer F, Khalvati S. *Effects of intraperitoneal injection of magnetic graphene oxide on the improvement of acute liver injury induced by CCl 4*. Biomaterials Research, 2020, 24(1): 1-9.

[403] Ramachandran A, Jaeschke H. *Acetaminophen toxicity: Novel insights into mechanisms and future perspectives*. Gene Expression, 2018, 18(1): 19.

[404] Abdelmegeed MA, Moon K-H, Chen C, Gonzalez FJ, Song B-J. *Role of cytochrome P450 2E1 in protein nitration and ubiquitin-mediated degradation during acetaminophen toxicity*. Biochemical Pharmacology, 2010, 79(1): 57-66.

[405] Jaeschke H, McGill MR, Ramachandran A. *Oxidant stress, mitochondria, and cell death mechanisms in drug-induced liver injury: lessons learned from acetaminophen hepatotoxicity*. Drug Metabolism Reviews, 2012, 44(1): 88-106.

[406] Nguyen NT, Umbaugh DS, Sanchez-Guerrero G, Ramachandran A, Jaeschke H. *Kupffer cells regulate liver recovery through induction of chemokine receptor CXCR2 on hepatocytes after acetaminophen overdose in mice*. Archives of Toxicology, 2022, 96(1): 305-320.

[407] Antoniades CG, Quaglia A, Taams LS, Mitry RR, Hussain M, Abeles R, Possamai LA, Bruce M, McPhail M, Starling C, Wagner B, Barnardo A, Pomplun S, Auzinger G, Bernal W, Heaton N, Vergani D, Thursz MR, Wendon J. *Source and characterization of hepatic macrophages in acetaminophen-induced acute liver failure in humans*. Hepatology, 2012, 56(2): 735-746.

[408] Sun YY, Li XF, Meng XM, Huang C, Zhang L, Li J. *Macrophage phenotype in liver injury and repair*. Scandinavian Journal of Immunology, 2017, 85(3): 166-174.

[409] Zigmond E, Samia-Grinberg S, Pasmanik-Chor M, Brazowski E, Shibolet O, Halpern Z, Varol C. *Infiltrating monocyte-derived macrophages and resident kupffer cells display different ontogeny and functions in acute liver injury*. The Journal of Immunology, 2014, 193(1): 344-53.

[410] Yan BC, Gong C, Song J, Krausz T, Tretiakova M, Hyjek E, Al-Ahmadie H, Alves V, Xiao S-Y, Anders RA, Hart JA. *Arginase-1: A new immunohistochemical marker of hepatocytes and hepatocellular neoplasms*. The American Journal of Surgical Pathology, 2010, 34(8): 1147.

[411] Satyanarayana A, Kaldis P. *Mammalian cell-cycle regulation: Several Cdks, numerous cyclins and diverse compensatory mechanisms*. Oncogene, 2009, 28(33): 2925-2939.

[412] Córdoba-Jover B, Arce-Cerezo A, Ribera J, Pauta M, Oró D, Casals G, Fernández-Varo G, Casals E, Puntes V, Jiménez W, Morales-Ruiz M. *Cerium oxide nanoparticles improve liver regeneration after acetaminophen-induced liver injury and partial hepatectomy in rats*. Journal of Nanobiotechnology, 2019, 17(1): 1-12.

[413] Parviz F, Matullo C, Garrison WD, Savatski L, Adamson JW, Ning G, Kaestner KH, Rossi JM, Zaret KS, Duncan SA. *Hepatocyte nuclear factor 4α controls the development of a hepatic epithelium and liver morphogenesis*. Nature Genetics, 2003, 34(3): 292-296.

[414] Huck I, Gunewardena S, Espanol-Suner R, Willenbring H, Apte U. *Hepatocyte nuclear factor 4 alpha (HNF4α) activation is essential for termination of liver regeneration*. Hepatology, 2019, 70(2): 666-681.

[415] He L, Pu W, Liu X, Zhang Z, Han M, Li Y, Huang X, Han X, Li Y, Liu K, Shi M, Lai L, Sun R, Wang Q-D, Ji Y, Tchorz JS, Zhou B. *Proliferation tracing reveals regional hepatocyte generation in liver homeostasis and repair*. Science, 2021, 371(6532): eabc4346.

Appendix

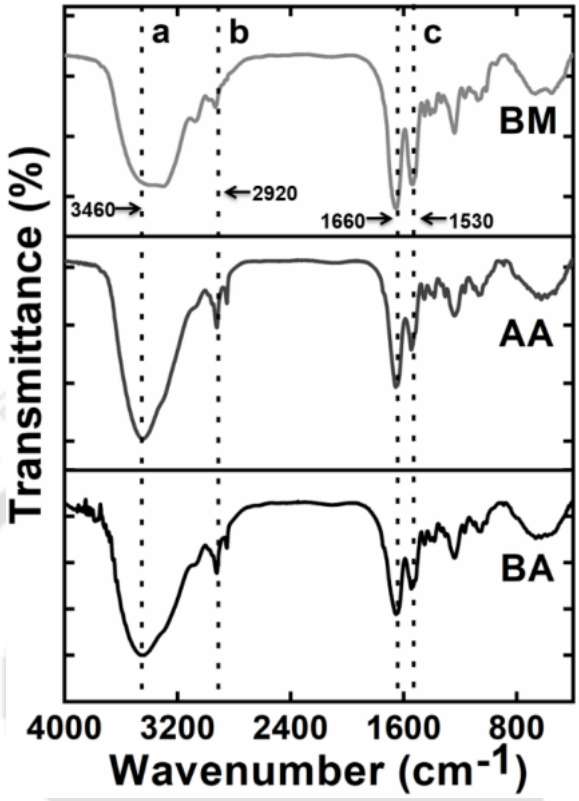

Figure A2.1. *FTIR spectrum of BM, AA and BA silk scaffolds over the range of 4000 – 500 cm^{-1}.*

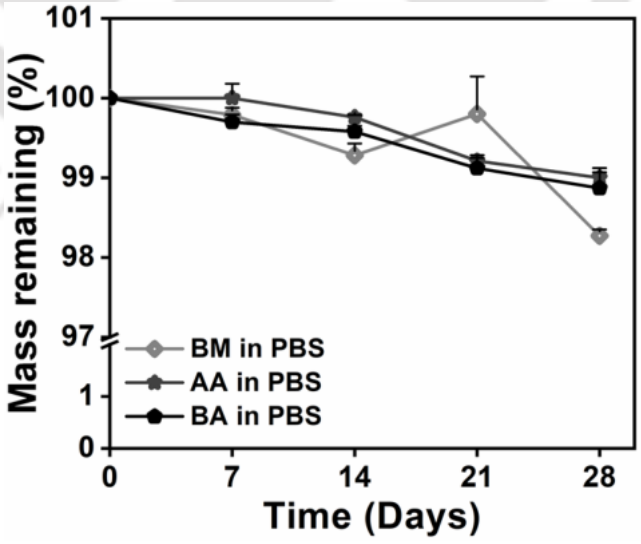

Figure A2.2. *Degradation profile of BM, AA and BA silk scaffolds over 28 days in the presence of PBS.*

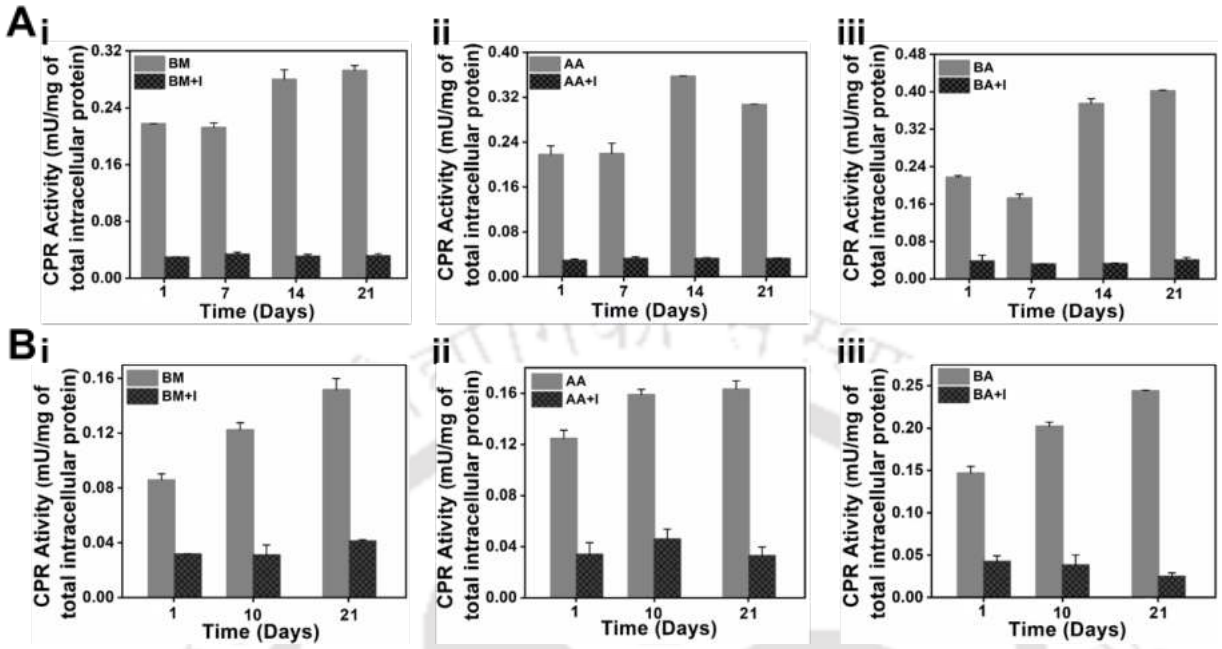

Figure A2.3. *Cytochrome P450 activity by (A) HepG2 cells and (B) primary neonatal rat hepatocytes cultured on (i) BM, (ii) AA and (iii) BA scaffolds with and without inhibitor over 21 days. Data are represented as mean ± S.D. (n=4).* $^{\#}$ *and* ** *signify the statistical difference between the groups at* $p \leq 0.05$ *and* $p \leq 0.01$*, respectively.*

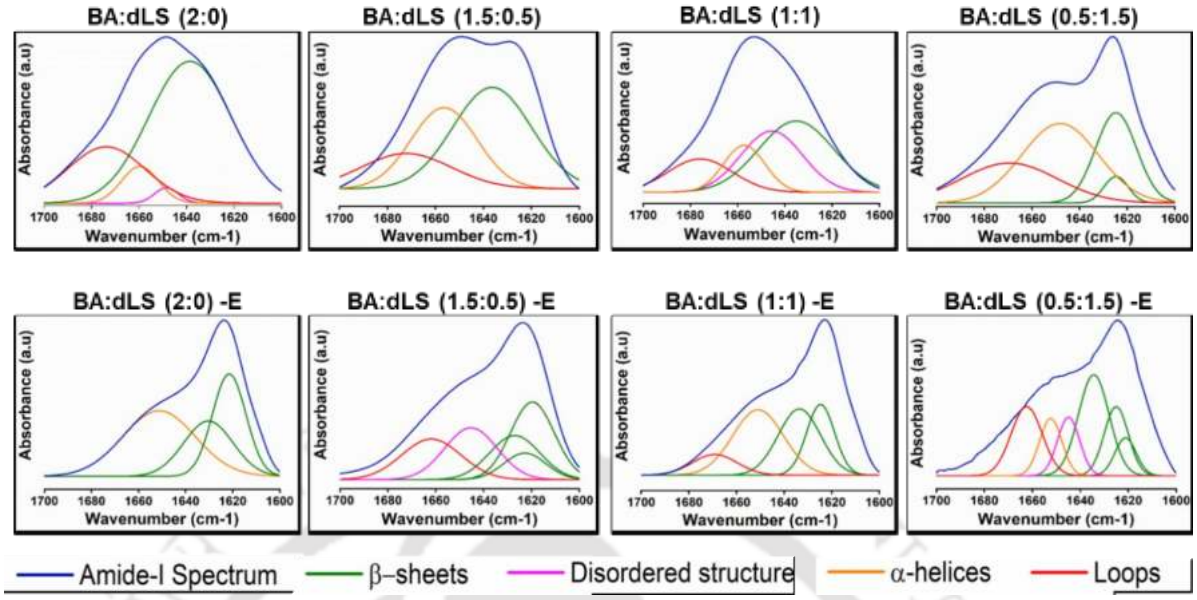

Figure A3.1. *Deconvolution of amide-I peak of untreated LECM-SF scaffolds (BA:dLS (2:0), BA:dLS (1.5:0.5), BA:dLS (1:1), BA:dLS (0.5:1.5)) and EDC/NHS crosslinked scaffolds (BA:dLS (2:0) -E, BA:dLS (1.5:0.5) -E, BA:dLS (1:1) -E, BA:dLS (0.5:1.5) –E) indicating conformational changes in secondary structure.*

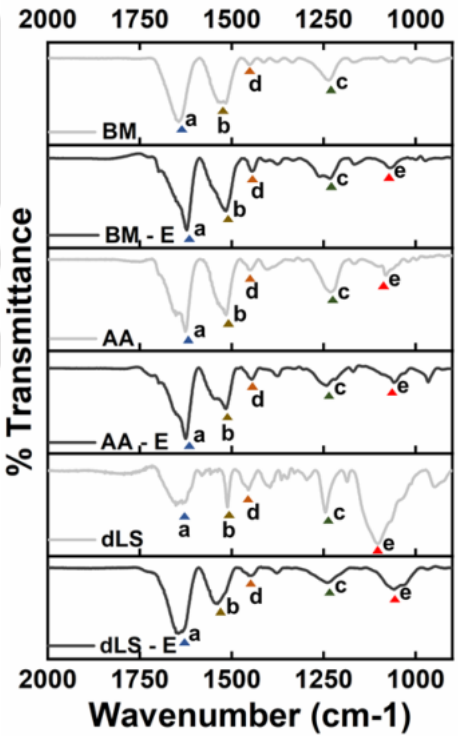

Figure A3.2. *FTIR spectrum of BM silk, AA silk and isolated dLS before (BM, AA, dLS) and after (BM -E, AA -E, dLS –E) EDC-NHS crosslinking.*

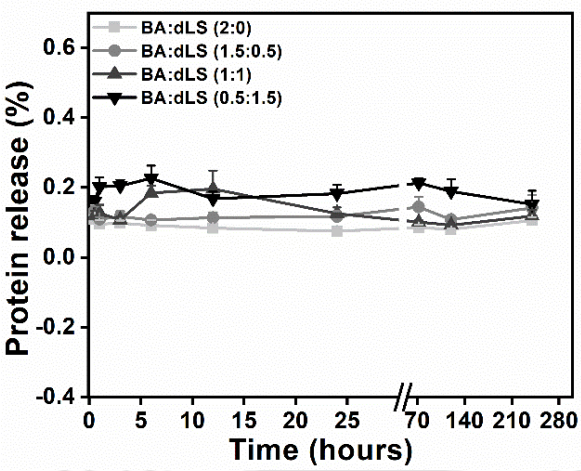

Figure A3.3. *Protein release from LECM-SF scaffolds over 10 days. Data are represented as average ± standard error mean (n=6).*

List of Publications

I. Publications from Ph.D. Thesis

(A) Journal Publications

1. **Janani G.**, Priya S., Dey S., and Mandal B.B. *Mimicking native liver lobule architecture in vitro with parenchymal and non-parenchymal cells using 3D bioprinting for drug toxicity and drug screening applications*. **ACS Applied Materials & Interfaces**, 2022, 14 (8), 10167-10186.

2. **Janani G.**, and Mandal B.B. *Mimicking physiologically relevant hepatocyte zonation using immunomodulatory silk liver extracellular matrix scaffolds towards bioartificial liver platform.* **ACS Applied Materials & Interfaces,** 2021, 13 (21), 24401-24421.

3. **Janani G.**, Kumar M., Chouhan D., Moses J.C., Gangrade A., Bhattacharjee S. and Mandal B.B. *Insight into silk-based biomaterials: From physicochemical attributes to recent biomedical applications.* **ACS Applied Bio Materials,** 2019, 2 (12), 5460-5491.

4. **Janani G.**, Nandi S.K., and Mandal B.B. *Functional hepatocyte clusters on bioactive blend silk matrices towards generating bioartificial liver constructs.* **Acta Biomaterialia**, 2018, *67*, 67-182.

5. **Janani G.,** Zhang L., Badylak S.F., and Mandal B.B. *Silk fibroin bioscaffold from Bombyx mori and Antheraea assamensis elicits a distinct host response and macrophage activation paradigm in vivo and in vitro.* (Manuscript under submission)

6. **Janani G.,** Zhang L., Roy N., Johnson S.A., Bhushan B., Duncan A.W., Mandal B.B., and Badylak S.F. *Intraperitoneal administration of liver-derived extracellular matrix hydrogel promotes regeneration and alleviates liver fibrosis in acetaminophen-induced liver injury model.* (Manuscript under preparation)

7. **Janani G.,** and Mandal B.B. *Bioengineered 3D liver constructs for bioartificial liver, drug screening models, and liver regeneration.* (Manuscript under preparation)

(B) Patents Filed

1. Mandal B.B., **Janani G**. *"3D bioprinted vascularized liver lobule model as drug screening platform".* Indian Patent Application Number: 202131050671, Filing Date: 03rd November 2021.

2. Mandal B.B., **Janani G**. *"Silk-liver ECM composite for bioartificial liver".* Indian Patent Application Number: 202031056432, Filing Date: 24th December 2020.

3. Mandal B.B., Singh Y.P., Bandyopadhyay A., Mehrotra S., Moses J.C., Bhunia B.K., **Janani G**, Chouhan D. *"Development of silk based bioinks for 3D bioprinting and uses thereof".* Indian Patent Application Number: 201831038727, Filing Date: 12th October 2018.

(C) Conferences, Seminars, Workshop Participation/ Presentations

1. **Janani G.,** and Mandal B.B. *Maturation of liver ECM blend silk scaffolds recapitulated hepatocyte metabolic heterogeneity and native liver zonation*. **The Japan – India YNU Symposium 2021** on Sustainable Transformation (SX), Dec 27, 2021. (Oral Presentation)

2. **Janani G.,** Zhang L., Badylak S.F., and Mandal B.B. *Host response and macrophage activation profile towards mulberry and non-mulberry silk*. **TERMIS 2021 6th World Congress,** Nov 15 – 19, 2021. (Oral Presentation)

3. **Janani G.,** and Mandal B.B. *A perfusion bioreactor culture of silk liver ECM blend scaffolds facilitating functional polarity and maturation in primary hepatocytes*. **TERMIS 2021 6th World Congress,** Nov 15 – 19, 2021. (Oral Presentation)

4. Online workshop on **"3D Printing: Techniques and their Application in Biomedical Devices"** organized by North East Centre for Biological Sciences and Health Engineering, IIT Guwahati, India, July 15, 2021

5. **Janani G.,** Priya S., Dey S., and Mandal B.B. *Bioprinting of multicellular liver lobule mimetic hepatic model for predicting drug-induced liver injury*. **International Conference on Advanced Material for Better Tomorrow,** July 13 – 17, 2021. (Oral Presentation, **BEST ORAL PRESENTATION AWARD**)

6. **Janani G.,** and Mandal B.B. *Bioengineered liver model exhibiting metabolic heterogeneity recapitulating native-lime zonation*. **International Conference on Biomedical Materials Innovation-2020 (ICBMI-2020),** Dec 6 - 9, 2020. (Oral Presentation)

7. Online workshop on **"Flow Cytometry Techniques and Applications"** organized by North East Centre for Biological Sciences and Health Engineering, IIT Guwahati, India, Dec 21 - 22, 2020

8. **Janani G.**, Priya S. and Mandal, B. B. *Modeling liver microarchitecture in vitro using 3D bioprinting for personalized drug toxicity and screening applications.* **International Conference on Advances in Polymeric Materials & Human Healthcare,** Oct 16 - 18 2019, Goa, India. (Poster Presentation)

9. **Janani G.,** Priya S., and Mandal B.B. *Bioprinted 3D liver model for drug toxicity studies*. **Regenerative Engineering Symposium: Converging Engineering, Life Sciences & Translational Medicine,** Oct 27 - 28 2018, Pittsburgh, PA. (Oral Presentation)

10. **Janani G.**, Nandi S.K., and Mandal B.B. *Bioactive silk based in vitro liver construct assisting hepatocyte clusters towards functional liver recapitulation.* **Research Conclave 2018**, IIT Guwahati, India, Mar 8 – 11, 2018. (Poster presentation, **BEST POSTER AWARD**)

11. **"Advanced Origin and ImageJ"** organized by Research Conclave, IIT Guwahati, India, March 9 – 10, 2018.

12. **Janani G.,** and Mandal B.B. *A 3D silk scaffold based culture system for enhanced functionality of hepatocytes*. **Research Conclave 2017**, IIT Guwahati, India, Mar 16 – 19, 2017. (Poster presentation)

13. **"Extended Rheology Characterization"** organized jointly by Central Instruments Facility, IIT Guwahati and Anton Paar India at IIT Guwahati, India, Sep 18, 2017.

14. **"ACS on Campus"** at IIT Guwahati, India, Jan 16, 2017.

15. **Janani G.,** and Mandal B.B. *Silk scaffolds for high efficiency bioartificial liver*. **SCICON 16, International Conference on Advanced Materials**, AMRITA Vishwa Vidyapeetham University, Coimbatore, India, Dec 19 – 21, 2016. (Oral Presentation)

16. **Janani G.,** and Mandal B.B. *Exploring silk fibroin scaffolds in liver tissue engineering*. **Research Conclave 2016**, IIT Guwahati, India, Mar 17 – 20, 2016. (Poster presentation)

II. Publications from other collaborative research projects

(A) Journal Publications

1. Biswas S., Bhunia B.K., **Janani G.,** and Mandal B.B. *Silk fibroin based formulations as potential hemostatic agents*. **ACS Biomaterials Science & Engineering,** 2022, 8 (6), 2654-2663.

2. Mahendiran B., Muthusamy S., **Janani G.,** Mandal B.B., Rajendran S., and Krishnakumar G.S. *Surface modification of decellularized natural cellulose scaffolds with organosilanes for bone tissue regeneration*. **ACS Biomaterials Science & Engineering,** 2022, 8 (5), 2000-2015.

3. Mehrotra S., Singh R., Bandyopadhyay A., **Janani G.,** Dey S., and Mandal B.B. *Engineering microsphere-loaded non-mulberry silk-based 3D bioprinted vascularized cardiac patches with oxygen-releasing and immunomodulatory potential*. **ACS Applied Materials & Interfaces,** 2021, 13 (43), 50744-50759.

4. Gupta P., Chaudhuri G.R., **Janani G.,** Agarwala M., Ghosh D., Nandi S.K., and Mandal B.B. *Functionalized silk vascular grafts with decellularized human Wharton's jelly improves remodeling via immunomodulation in rabbit jugular vein*. **Advanced Healthcare Materials,** 2021, 10 (19), 2100750.

5. Mahata S., **Janani G.,** Mandal B.B., and Manivannan V. *A coumarin based visual and fluorometric probe for selective detection of Al (III), Cr (III) and Fe (III) ions through "turn-on" response and its biological application.* **Journal of Photochemistry & Photobiology, A: Chemistry,** 2021, 417, 113340.

6. Arora D., Bhunia K.B., **Janani G.,** and Mandal, B.B. *Bioactive three-dimensional silk composite in vitro tumoroid model for high throughput screening of anticancer drugs.* **Journal of Colloid and Interface Science,** 2021, 589, 438-452.

7. **Janani G.,** Kumar, S., and Mandal, B.B. *Fiber-reinforced silk composite for enhanced urokinase production using high-density perfusion culture and bioactive molecule supplementation.* **ACS Biomaterials Science & Engineering,** 2019, *5*(11), 6137-6151.

8. Chouhan, D., **Janani G.,** Chakraborty, B., Nandi, S.K., and Mandal, B.B. *Functionalized PVA–silk blended nanofibrous mats promote diabetic wound healing via regulation of extracellular matrix and tissue remodelling.* **Journal of Tissue Engineering and Regenerative Medicine,** 2018, 12(3), e1559-e1570.

(B) Patents Filed

1. Mandal B.B., and **Janani G.** *"Urokinase production through fiber reinforced silk scaffold using high density perfusion culture"*. Indian Patent Application Number: 201831024035, Filing Date: 27th June 2018.

(C) Book Chapter

1. Kumar M., **Janani G.,** Fontaine M.J., Kaplan D.L., and Mandal B.B. *Silk-based encapsulation materials to enhance pancreatic cell functions*. Transplantation, Bioengineering, and Regeneration of the Endocrine Pancreas. Academic Press 2020, 329-337.

(D) Conferences, Seminars, Workshop Participation/ Presentations

1. Gupta P., Chaudhuri G.R., **Janani G.,** Agarwala M., Ghosh D., Nandi S.K., Mandal B.B. *Decellularized human Wharton's jelly facilitates remodeling of cell-free silk vascular grafts in rabbit jugular vein via immunomodulation*. **Cardiovascular Metabolic Week (CVMW2020)**, March 12-13, 2021. (Oral Presentation)

2. Gupta P., Chaudhuri G.R., **Janani G.,** Agarwala M., Ghosh D., Nandi S.K., and Mandal B.B. *Human Wharton's Jelly-Silk Composite Grafts for Small-Diameter Vascular Tissue Engineering Applications*. **International Conference on Biomedical Materials Innovation-2020 (ICBMI-2020),** Dec 6-9, 2020. (Oral Presentation)

3. Gupta T., Arora D., **Janani G.,** and Mandal B.B. *Minimally invasive silk hydrogel for anticancer drug delivery and tissue regeneration*. **Research Conclave 2018,** IIT Guwahati, India, Mar 8 – 11, 2018. (Poster presentation)

4. Gupta T., Arora D., **Janani G.,** and Mandal B.B. *Minimally invasive silk hydrogel for anti-cancer drug delivery and tissue regeneration in a breast cancer model.* **International Symposium on Functional Materials (ISFM),** IIT Kanpur, April 13 – 15, 2018. (Oral Presentation)

5. Arora D., Bhunia B.K., **Janani G.,** and Mandal B.B. *Bioactive silk assistive 3D tumoroids for pre-clinical anticancer drug evaluation.* **Indo-Japan Bilateral Symposium on Future Perspective of Bioresource Utilization in North-Eastern Region (IJBS 17),** IIT Guwahati, India, Feb 1 – 4, 2018. (Oral Presentation, Best Oral Presentation Award)

6. Kumar S., **Janani G.,** Mandal B.B. *Enhanced urokinase production from HT-1080 cells on silk based scaffolds.* **Research Conclave 2017**, IIT Guwahati, India, Mar 16 – 19, 2017. (Poster presentation)

7. Chouhan D., **Janani G.,** Chakraborty B., Nandi S.K. and Mandal B.B. *Silk fibroin based functionalized nanofibrous mats for treating diabetic foot ulcers.* **Research Conclave 2017,** IIT Guwahati, India, Mar 16 – 19, 2017. (Poster presentation)

Awards & Achievements

1. **Fulbright Nehru Doctoral Research Fellowship (Aug 2018 - May 2019),** visited McGowan Institute for Regenerative Medicine, University of Pittsburgh for 9 months, award financed by United States India Education Foundation (USIEF) and Institute of International Education (IIE) New York.